

STUDY OF DETONATION GUN COATED ALLOYS FOR RESISTANCE TO EROSION AND CORROSION

A THESIS

*Submitted in partial fulfilment of the
requirements for the award of the degree*

of

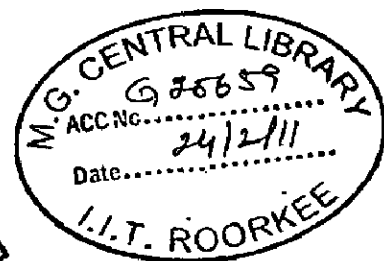
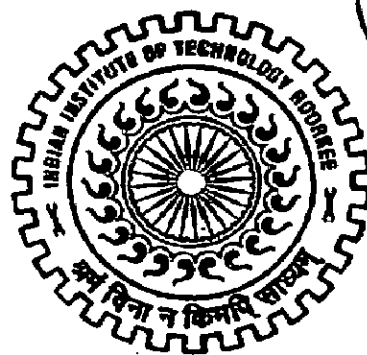
DOCTOR OF PHILOSOPHY

in

METALLURGICAL AND MATERIALS ENGINEERING

by

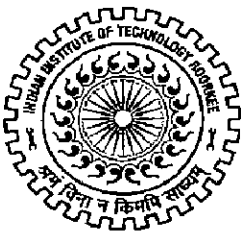
PAWAN KUMAR SAPRA



**DEPARTMENT OF METALLURGICAL AND MATERIALS ENGINEERING
INDIAN INSTITUTE OF TECHNOLOGY ROORKEE
ROORKEE - 247 667 (INDIA)**

OCTOBER, 2009

**©INDIAN INSTITUTE OF TECHNOLOGY ROORKEE, ROORKEE, 2009
ALL RIGHTS RESERVED**



INDIAN INSTITUTE OF TECHNOLOGY ROORKEE ROORKEE

CANDIDATE'S DECLARATION

I hereby certify that the work which is being presented in the thesis, entitled “**STUDY OF DETONATION GUN COATED ALLOYS FOR RESISTANCE TO EROSION AND CORROSION**” in partial fulfilment of the requirements for the award of the Degree of *Doctor of Philosophy* and submitted in the Department of Metallurgical and Materials Engineering of the Indian Institute of Technology Roorkee is an authentic record of my own work carried out during a period from January, 2005 to October, 2009 under the supervision of Dr. Satya Prakash, Professor and Dr. Surendra Singh, Assoc. Prof., Department of Metallurgical and Materials Engineering, Indian Institute of Technology Roorkee, Roorkee.

The matter presented in the thesis has not been submitted by me for the award of any other degree of this or any other Institute.

(PAWAN KUMAR SAPRA)

This is to certify that the above statement made by the candidate is correct to the best of our knowledge.

Date: 06-10-09

(Surendra Singh)
Supervisor

(Satya Prakash)
Supervisor

The Ph.D. Viva-Voice examination of **Mr. Pawan Kumar Sapra**, Research Scholar, has been held on _____.

Signature of Supervisors

Signature of External Examiner

Erosion-corrosion of materials at elevated temperatures is a major problem in various industrial processes which range from advanced coal-conversion processes, to the turbine blades of jet engines. Erosion-corrosion is a generalised wear phenomenon where the combined effect of each degradation mechanism generates more extensive mass loss than the sum of each mechanism acting independently. The operating conditions in power station boilers are conducive to fireside corrosion and erosion both in furnace wall and in the superheater and reheater areas. The erosion corrosion phenomenon results in tube wall thinning and premature failure. Erosion corrosion has become a topic of continuous investigations and great concern as it consumes the material at an unpredictably rapid rate. In steam thermal power plants where coal is used as primary fuel, the corrosion occurs in special fashions due to combustion products which change their state of matter and becomes salt as a result of high temperature. Combustion of coal generates very corrosive media particularly near the superheater tubes, forming highly corrosive ash deposits that contain alkali metals of sodium, potassium and sulphur. Ashes formed due to combustion of low grade fuels have a high concentration of compounds formed by vanadium, sodium and sulphur mainly as $\text{Na}_2\text{SO}_4\text{-V}_2\text{O}_5$ complex and sodium vanadates mixture. These compounds have very low melting points as low as 550°C . These metals easily liquefy at the operating temperatures of boilers and cause accelerated corrosion. The erosion is even more localised in its effects, and results from impact of particulates, such as coal ash, dolomite and unburnt carbon particles on surface of heated boiler tubes. So high temperature oxidation and erosion are recognized as being one of the main cause of downtimes in these installations. The materials used in these installations are fabricated from low alloy carbon steels with chromium and molybdenum as the primary alloy additions termed as boiler steels. Unfortunately T11 and T22 steels, which are commonly used in the manufacturing of conventional boilers experience accelerated erosion corrosion in high temperature boiler conditions. Although Chromium is expected to impart corrosion resistance to high temperature alloys but is not sufficient enough to form protective external scale.

Currently, the superalloys are used to increase the service life of the boilers especially in the super-heater zones of the new generation ultra-supercritical boilers. These materials being developed with high strength at elevated temperatures are highly alloyed and thus very expensive and also prone to degradation to certain environments for example Nickel based superalloys readily react with the sulphur in coal leading to high corrosion rate. The presence

of combustion gases constitutes an extreme environment and the hot corrosion is inevitable when the superalloys are used at high-temperatures for longer periods of time. A number of countermeasures are presently in use or under investigation to combat the hot corrosion such as, the use of inhibitors, control of the process parameters, development of suitable industrial alloys, and deposition of protective coatings. So in search of cost effective solutions for erosion corrosion problems, various coating techniques like thermal spraying have become attractive. The boiler steels T11 and T22 were obtained from S.G.G.S. Thermal power Plant Ropar and superalloys, namely Superni 600, Superni 718 as Ni-based, and Fe-based Superfer 800, were provided by Mishra Dhatu Nigam Limited, Hyderabad (India), for devising some means to protect them against high temperature erosive corrosive environment applications. Detonation gun spraying belongs to thermal spraying family and is used for many applications. This process has shown the development of coatings with better properties like low porosity, high strength etc. The high energy created by detonation involved in the process makes the powder closely conjoint on the surface, thereby resulting in a dense coating.

This thesis investigates the erosion and corrosion performance of Al_2O_3 -3 wt % TiO_2 thermal spray coatings deposited by detonation gun technique. As-sprayed coatings were characterized by using the combined techniques of optical microscopy, microhardness testing, X-ray diffractometry (XRD) and scanning electron microscopy/energy-dispersive analysis (SEM/EDX). The corrosion performance was evaluated in oxidising and molten salt environment and also in actual working conditions of boiler. The erosion performance was evaluated at room temperature conditions as well as under high temperature conditions, high erodent velocity, and actual boiler conditions. The corrosion behavior and morphological development were investigated by weight change kinetics, metallographs, depths of attack, metal thickness losses, and XRD analyses.

Previous research has highlighted several theoretical mechanisms under this generalized process, ranging from the erosion induced breakdown of oxide scales in corrosive environments, through to the development of oxide layers in highly erosive environments. Prior to this current work erosion corrosion experimental mechanisms has focused on bulk alloy materials with well characterised oxidation responses, under conditions of low temperature, low erodent impact velocity conditions which are readily generated within laboratory scale rigs. Few works have addressed erosion-corrosion under simulated boiler conditions of high temperature, high erodent impact velocity. The trials have been run under such testing conditions that have involved only one temperature i.e. only substrate temperature and importance of surrounding temperature has been overlooked.

Most of the published work on thermally sprayed Al_2O_3 -3 wt % TiO_2 coatings has been confined to wear and room temperature erosion. Little has been presented on the mechanism of erosion-corrosion of Al_2O_3 -3 wt % TiO_2 coatings. Most works have been conducted under milder conditions than used in the current work. In addressing the short comings in the current state of knowledge, the aim of this work was to characterise the mechanism of erosion and corrosion of D-gun sprayed Al_2O_3 -3 wt % TiO_2 thermal spray coatings under actual boiler conditions, erosion conditions and oxidising and molten salt corrosion conditions.

Al_2O_3 -3 wt % TiO_2 coatings were deposited by D-gun spraying equipment available with SVX Powder M Surface Engineering Private Limited, Greater Noida (India) under optimised conditions. The coatings, characterised in terms of microhardness, porosity content were in good agreement with the coating quality presented in the literature. The coating was deposited on two types of boiler steels designated as ASTM-SA-213-T11 and ASTM-SA-213-T22 and three superalloys namely Superni 600, Superni 718 and superfer 800. Under the given spray parameters coatings with thickness in the range of 200-220 μm and porosity less than 1% were formed. The EDX analysis has confirmed that coatings obtained in the present investigation meet the required compositions.

Solid particle erosion studies have been carried out as per G76 ASTM standard at 30° and 90° impact angle with Alumina as erodent. Erosion testing was carried out using a solid particle erosion test rig TR-471-M10 Air Jet Erosion Tester (Ducom Instruments Private Limited, Bangalore, India) capable of conducting tests at room temperature as well as high temperature. In general, Erosion resistance is measured using weight loss technique by measuring the weights before and after the test. But at high temperature, weight change measurements leads to flawed results due to oxidation of samples. In order to overcome the limitations of the weight change technique, a different technique was used for the present investigation and erosion resistance was measured in terms of volume loss after the erosion testing. The total volume loss rate, due to erosion for the test materials are compared. The effect of temperature on the coating erosion was investigated. The high temperature erosion behavior of this coating was compared with that uncoated alloy i.e. T-11, T-22 steels and Superni 600, Superni 718 and Superfer 800 superalloys.

On these coated substrates, thermal cyclic oxidation studies were performed in static air as well as in molten salt (Na_2SO_4 -60% V_2O_5) environment at 900°C for 50 cycles. The weight gain for all the coated alloys are significantly lower than the uncoated alloys subjected to oxidation and molten salt hot corrosion. The coatings showed good adherence to their respective substrates during exposure to oxidation as well as the molten salt environment. The very low porosity and the flat splat structure of the D-gun sprayed coatings have also

contributed to hot corrosion resistance as this is the desired structure, when the coatings have to perform in corrosive environment at higher temperature. In the flat splat structure the distance from the coating surface to coating/substrate interface along splat boundaries, through which the corrosive species mostly permeate, is very long.

In order to establish an understanding of the behaviour of the coatings and bare alloys in the actual working conditions, where these coatings are intended to be used, the specimens were exposed for 1500 hours to platen super-heater zone of the coal fired boiler of Shri Guru Gobind Singh Super Thermal Plant, Ropar, Punjab (India) for this study. This zone was selected for the present study as many breakdowns occurred in this power plant due to the erosion corrosion degradation of the platen superheater tubes of the coal fired boilers. The specimens were exposed to the combustion environment for 15 cycles of 100 hours heating followed by 1 hour cooling at ambient conditions. The temperature of the hanging zone was measured at regular intervals during the study and the temperature was about 700 ± 10 °C with full load of 210 MW. The erosion corrosion behavior of coated alloys is promising in comparison to substrate boiler steels. At the end of each cycle, the specimens were visually examined with respect to colour, luster, spallation tendency and adherence of the scale. Thereafter, the specimens were subjected to weight measurements. XRD and SEM/EDX techniques were used for detecting the phases present and for elemental analysis of the surface scale after exposure to boiler environments. The coatings have successfully imparted the erosion corrosion resistance to the substrate alloys in the boiler environment.

Based on these results the coatings were considered good for industrial applications. The responses of the samples in this work to oxidation, hot corrosion and erosion were considered indicative of the response of industrially applied coatings of this composition in service. This analysis makes it clear that with an appropriate choice of processing conditions a sound and adherent ceramic coating is achievable by detonation gun process using Al_2O_3 -3 wt % TiO_2 powder. Based on the findings of the present study, Al_2O_3 -3 wt % TiO_2 coatings under investigations are suggested to be tried for applications to super-heater and re-heater tubes of the boilers for protecting them against high temperature erosive corrosive environment applications.

ACKNOWLEDGEMENTS

Every success which is a result of hard efforts never tastes that good if each and every person who participated in it is not acknowledged. First and foremost, I would like to express my gratitude and acknowledgement to Dr. Satya Prakash and Dr. Surendra Singh, Department of Metallurgical and Materials Engineering, Indian Institute of Technology, Roorkee my thesis supervisors for giving me the wonderful opportunity of doing research under them. Their enthusiasm on the problem and encouragement throughout the course of this work is very much appreciable. They have always been available for discussion and guided me to accomplish the objective of this study; they have been an inspiring and driving force during the course of this work. Without their timely help, intellectual input, constructive criticism and painstaking efforts, it would not have been possible for me to complete this thesis in the present form.

I am deeply indebted to Dr. H. S. Shan, Former Professor and Head, Mechanical and Industrial Engineering Department (MIED), IIT Roorkee and Dr R. K. Sapru, former Professor and Chairman, Department of Public Administration, Panjab University, Chandigarh for inspiring me to start my research work. I would also like to thank my committee members: Professor P. S. Misra, Professor A. K. Jain, and Professor G. C. Kaushal for their time and energy in reviewing this thesis. I wish to record deep sense of gratitude to Dr. S. K. Nath, Professor and Head and Dr. V. K. Tewari, Former-Head, MMED, IIT, Roorkee, for their co-operation and support in carrying out the experimental and analysis work in the department. I would also like to thank Professor P. K Ghosh, for his valuable suggestions. I am also thankful to Dr. Harpreet Singh, Dr. Buta Singh and Dr. Tejinder Singh Sidhu for their time to time advice and guidance.

I also wish to thank the whole staff of the Department of Metallurgical and Materials Engineering, Indian Institute of Technology, Roorkee, in particular Mr. Rajinder S. Sharma, Mr. N. K. Seth, , Mr. T. K. Sharma, Mr. M. Aslam., Mr Shakti Gupta, Mr S.M. Giri, Mr. Vidya Prakash, Mr Pritam. Many thanks go to Mr. S. K. Saini, Mrs. Rekha Sharma, and Mr S. D. Sharma of Institute Instrumentation Centre, IIT, Roorkee for helping me in doing XRD, SEM and EDX work. I am also thankful to Mr. Jasbir Singh, Mr. Anish and all Technical Staff of Mechanical and Industrial Engineering Department for helping me at various stages.

Thanks are also due to Mr. Narendra Kumar without whom this thesis manuscript would not have been in the same format, infact he has helped a lot. Special thanks are due to

Mr. Vikas and Sanjay Managing Director, SVX Powder M Surface Engineering Private Limited, Greater Noida, (India) for providing facilities to deposit the coatings with Detonation Gun process. I would like to express my sincere gratitude for the library staff of IIT Roorkee, IIT Delhi and IIT Kharagpur for their kind co-operation to carry out the literature survey.

The discussions and interactions with the colleagues have been very fruitful. Many thank goes to Ph.D. fellows and friends, Mr. M. Annanth Kumar, Mr. Vikas Chawla, Mr Ram Shankar, Dr Rahul Sharma, Mr. Gurpreet Singh, Mr. Kuldeep Rana, Mrs. Priti Singh, Dr. Anupam Singhal, Dr. Balwinder Singh, Dr. R.S. Walia, Dr. S. B. Mishra, Dr Arivazhagan N., Dr. Ravindra Kumar, Mr. Manoj Mittal, Mr Gurbhinder Singh, Mr Devakumaran, Dr Hazoor Singh and Dr. M.R. Ramesh. Special thanks go to Mr. Amit Monga, Mr. Mohit Singla, Mr Saurabh, Mr Satbir Singh Sehgal, Mr Adesh Sharma and Mrs Manpreet Kaur for their everlasting support. I am also thankful to Mr. and Mrs. Akashdeep Khanna for their support.

This gives me a great opportunity to express my gratitude and reverence to my parents Sh. R. L. Sapra and Smt. Santosh Sapra and parents-in-law Sh. Romesh Chander and Smt. Suman Kanta for being a constant source of strength and support. I would like to humbly dedicate this thesis to my parents who are the spirit and source of inspiration. I would like to express my reverence and great admiration for sister-in-law, and brothers-in law, who have always been the inspiring and encouraging force for me. I am highly grateful to my Brother and Sister-in-law, Sister and Brother-in-law, for their continual co-operation during the course of this work. Special thanks to my cousins Manmohan, Yudhishtar, Ashwani, Kusum, Jyoti, Geetu, Ginni, Sugeeta, Ujjawal, Gaurav, Vinod, Savita, Vanita, Meena, Rakesh, Umesh, Monika, Mukesh, Sunny, Munny, Abhey and Ankur. Their love and support made this accomplishment possible.

My wife Rosy and loving son Pragun who missed many moments of love and care, deserves special thanks and appreciation who gave their best. At times, I believe my family is more excited than myself at the completion of this Ph.D. program. This is not to say that I am not ecstatic about this accomplishment, just an indication of the love and support that I have received from my family. My dear Grand mother has been a source of real inspiration. Rosy, my lovely wife, what can I say! You have provided me much more than just an inspiration; you have provided me the ability to live with the dynamic world and face challenges. There are no words to describe the magnitude of my gratitude. Thank you!

At this Moment, I must record my deepest regards and reverence to Almighty God and my Parents for their constant support and encouragement.


(Pawan Kumar Sapra)

PREFACE

The entire work carried out for this investigation has been presented into nine chapters.

Chapter-1 contains the introduction about the Thermal Spraying and about the erosion corrosion degradation problem faced by the various industries and their impact especially in coal fired boilers.

Chapter-2 presents the critical review of the literature regarding various aspects and mechanisms of erosion and hot corrosion. Critical review of the existing studies and detailed behaviour of coatings to counteract the erosion corrosion degradation have been made. The various preventive measures have been summarised and the detonation gun spraying is discussed in detail. After reviewing the available literature the problem has been formulated.

Chapter-3 deals with the experimental part and presents the experimental techniques and details of the experimental equipments and procedure employed for depositing the coatings, their characterization. Erosion and Hot corrosion studies and Testing procedures adopted.

Chapter-4 presents the characterisation studies which include the critical evaluation of the substrate alloys and the study regarding the characterisation of the as sprayed coatings.

Chapter-5 includes the results of erosion studies performed on uncoated as well as coated alloys at room temperature and elevated temperature and critical discussion of the study regarding the erosion behavior of substrate alloys and coatings.

Chapter-6 contains the data regarding the cyclic oxidation and molten salt studies performed on uncoated and coated alloys at 900°C along with discussion of results.

Chapter-7 deals with findings regarding the erosion corrosion behavior of uncoated and coated alloys in actual industrial environment and the results and discussion.

Chapter-8 includes the comprehensive discussions of the results with respect to the existing literature.

Chapter-9 summarises the major conclusions from the results found within the present research, and presents recommendations for future research.

CONTENTS

	Page No.
CANDIDATE'S DECLARATION	i
ABSTRACT	ii
ACKNOWLEDGEMENTS	vi
PREFACE	viii
LIST OF FIGURES	xv
LIST OF TABLES	xxxvi
LIST OF RESEARCH PUBLICATIONS	xxxvii
ABREVIATIONS	xxxix
CHAPTER 1 INTRODUCTION	1
CHAPTER 2 LITERATURE REVIEW	7
2.1 THERMAL SPRAYING – AN INTRODUCTION	7
2.2 THERMAL SPRAYING PROCESSES	8
2.2.1 <i>Electric Arc Processes</i>	8
2.2.2 <i>Plasma Spray Processes</i>	11
2.2.3 <i>Combustion Spray Processes</i>	12
2.2.3.1 <i>Low Velocity Combustion spray process</i>	12
2.2.3.2 <i>High Velocity Combustion spray process</i>	14
2.2.3.3 <i>Cold Spraying</i>	14
2.2.3.4 <i>Detonation Gun (D-gun) Spraying</i>	14
2.2.3.4.1. <i>Process parameters</i>	15
2.2.3.4.2. <i>Advantages of Detonation gun coating Technology</i>	17
2.3. ALUMINA TITANIA COATINGS	18
2.3.1 <i>Introduction</i>	18
2.3.2 <i>Thermal spraying of alumina titania</i>	19
2.4 EROSION	22
2.4.1 <i>Introduction</i>	22
2.4.2 <i>Erosion Fundamentals</i>	24

2.4.2.1 Ductile Erosion Mechanism	25
2.4.2.2 Brittle Erosion Mechanism	27
2.4.3 Erosion of Thermal Spray Coatings	28
2.4.3.1 Introduction	28
2.4.3.2 Erosion Mechanism of Thermal Spray Coating	32
2.4.3.2.1 <i>Erosion mechanisms at high temperature</i>	34
2.4.3.2.2 Factors affecting erosion	37
2.4.3.2.3 Erosion rate	39
2.4.4 Erosion in energy generation and coal gasification systems	39
2.5 HIGH TEMPERATURE CORROSION	42
2.5.1 Introduction	42
2.5.2 Role of feed composition	43
2.5.3 Corrosion Sensitive Areas	44
2.5.4 Corrosion Mechanisms	50
2.5.4.1 Oxidation	50
2.5.4.1.1 Principles of oxidation reaction	51
2.5.4.1.2 Active oxidation in Thermal power plant boiler	55
2.5.4.2 Corrosion in deposits by sulfation and molten salts	56
2.5.4.2.1 Corrosion by sulfation of chloride salts	57
2.5.4.2.2 Corrosion by chlorides at metal/oxide interface	58
2.5.4.2.3 Reaction involving molten salts mixtures	58
2.5.4.2.4 Corrosion by molten sulfates	58
2.5.4.3 Erosion Corrosion in energy generation systems	63
2.5.4.3.1 Characterisation of Gasification Environments	65
2.6 ROLE OF COATINGS IN AGGRESSIVE ENVIRONMENTS	66
2.7 PROBLEM FORMULATION	69
CHAPTER 3 EXPERIMENTAL EQUIPMENT AND ANALYTICAL METHODS	73
3.1 SELECTION OF SUBSTRATE MATERIALS	73
3.2 DEVELOPMENT OF COATINGS	73

3.2.1	Preparation of Substrate Materials	73
3.2.2	Formulation of Coatings	74
3.3	HIGH TEMPERATURE OXIDATION AND HOT CORROSION STUDIES	78
3.3.1	Experimental Setup	78
3.3.2	Oxidation Studies in Air	79
3.3.3	Hot Corrosion Studies in Molten Salt (Na_2SO_4 -60% V_2O_5)	79
3.3.3.1	Molten Salt Coating	79
3.3.3.2	Hot Corrosion Studies	80
3.4	CHARACTERISATION OF COATINGS	80
3.4.1	Measurement of Coating Thickness	80
3.4.2	Measurement of Porosity	80
3.4.3	Metallographic Studies	80
3.4.4	Measurement of Microhardness	81
3.4.5	Scanning Electron Microscopy (SEM) and Energy Dispersive X-Ray (EDX) Analysis	81
3.4.5.1	Beam-Specimen Interaction	81
3.4.5.2	Secondary Electron (SE) Imaging	82
3.4.5.3	Energy Dispersive X-ray Spectrometry (EDS)	82
3.4.5.4	X-ray Mapping	82
3.4.5.5	Back Scattered Electron (BSE) Imaging	83
3.4.5.6	Equipment Details	83
3.4.6	X-ray Diffraction (XRD)	83
3.4.6.1	Fundamentals	83
3.4.6.2	Equipment Details	85
3.5	ROOM TEMPERATURE AND ELEVATED TEMPERATURE EROSION TESTS	86
3.5.1	Experimental Setup	86
3.5.2	Erosion Studies in an Air Jet Erosion Test Rig	86
3.5.3	Analysis of eroded surfaces	89
3.5.3.1	Visual Observation	89
3.5.3.2	Erosion rate in terms of Volume loss	90
3.5.3.3	SEM/EDX Analysis	93

3.6.	EROSION-CORROSION STUDIES IN ACTUAL INDUSTRIAL ENVIRONMENT	93
3.6.1	Specimen Preparation for Testing	93
3.6.2	Analysis of erosion-corrosion products in boiler environments	95
3.6.2.1	Visual Observation	95
3.6.2.2	Weight Change Studies	95
3.6.2.3	X-Ray Diffraction (XRD) Analysis	95
3.6.2.4	SEM/EDX Analysis	95
CHAPTER 4	CHARACTERISATION OF SUBSTRATE ALLOYS AND D-GUN SPRAYED Al_2O_3-3 Wt%TiO_2 COATINGS	97
4.1	INTRODUCTION	97
4.2	SUBSTRATE ALLOYS	97
4.3	COATING DEPOSITION AND CHARACTERISATION	97
4.3.1	Morphology of coating powders and Phase Analysis	97
4.3.2	Coating Description and Visual Examination of Al_2O_3 -3wt% TiO_2 Coating	98
4.3.3	Measurements of Coating Thickness	98
4.3.4	Microhardness	98
4.3.5	Coating Porosity	104
4.3.6	Microstructure	104
4.3.7	Phase Analysis – XRD of the Coatings	104
4.3.8	SEM/ EDX (Energy dispersive X-ray) analysis	105
4.4	DISCUSSION	118
CHAPTER 5	EROSION STUDIES IN AIR JET EROSION TEST RIG	127
5.1	RESULTS	127
5.1.1	Uncoated alloys	127
5.1.1.1	Visual Examination	127
5.1.1.2	Erosion Rate	128
5.1.1.3	SEM/EDX Analysis	133
5.1.2	Al_2O_3 -3wt% TiO_2 coated alloys	148
5.1.2.1	Visual Examination	148

5.1.2.2 Erosion Rate	148
5.1.2.3 SEM/EDX Analysis	157
5.1.3 Discussion	166
5.1.3.1 Uncoated alloys	166
5.1.3.2 Al ₂ O ₃ -3wt% TiO ₂ coated alloys	176
CHAPTER 6 HIGH TEMPERATURE OXIDATION AND HOT CORROSION STUDIES	190
6.1 RESULTS AND DISCUSSION	190
6.1.1 Oxidation studies of uncoated and coated alloys in air	190
6.1.1.1 Uncoated alloys	190
6.1.1.1.1 Visual Examination	190
6.1.1.1.2 Weight Change Data	191
6.1.1.1.3 X-ray Diffraction Analysis	193
6.1.1.1.4 SEM/EDX Analysis	194
6.1.1.2 Coated alloys	214
6.1.1.2.1 Visual examination	214
6.1.1.2.2 Weight Change Data	214
6.1.1.2.3 X-ray Diffraction Analysis	215
6.1.1.2.4 SEM/EDX Analysis	215
6.1.2 Hot corrosion studies of uncoated and coated alloys in molten salt environment	236
6.1.2.1 Uncoated alloys	236
6.1.2.1.1 <i>Visual Examination</i>	236
6.1.2.1.2 <i>Weight Change Data</i>	239
6.1.2.1.3 <i>X-ray Diffraction Analysis</i>	239
6.1.2.1.4 <i>SEM/EDX Analysis</i>	240
6.1.2.2 Coated alloys	260
6.1.2.2.1 <i>Visual examination</i>	260
6.1.2.2.2 <i>Weight Change Data</i>	260
6.1.2.2.3 <i>X-ray Diffraction Analysis</i>	261
6.1.2.2.4 <i>SEM/EDX Analysis</i>	268

6.2	SUMMARY OF RESULTS	282
6.3	DISCUSSION	286
	6.3.1 Uncoated alloys	286
	6.3.2 Coated alloys	296
CHAPTER 7	EROSION CORROSION STUDIES IN ACTUAL INDUSTRIAL ENVIRONMENT	300
7.1	RESULTS	300
	7.1.1 Uncoated alloys	300
	7.1.1.1 Visual Examination	300
	7.1.1.2 Weight Change and Thickness loss data	301
	7.1.1.3 X-ray Diffraction Analysis	301
	7.1.1.4 SEM/EDX Analysis	307
	7.1.2 Al ₂ O ₃ - 3 wt% TiO ₂ coated alloys	321
	7.1.2.1 Visual Examination	321
	7.1.2.2 Weight Change and Thickness loss data	321
	7.1.2.3 X-ray Diffraction Analysis	321
	7.1.2.4 SEM/EDX Analysis	322
7.2	SUMMARY OF RESULTS	348
7.3	DISCUSSION	350
	7.3.1 Uncoated alloys	350
	7.3.2 Coated alloys	357
CHAPTER 8	COMPREHENSIVE DISCUSSION	359
CHAPTER 9	CONCLUSIONS	368
	SUGGESTIONS FOR FUTURE WORK	373
	REFERENCES	374

LIST OF FIGURES

Fig. No.	Title	Page No.
Fig. 2.1	Schematic development of the thermal spray process and mechanism of coating build-up.	9
Fig. 2.2	Summary of significant thermal spray techniques.	10
Fig. 2.3	Typical two wire arc spray system.	13
Fig. 2.4	Schematic Diagram of the Plasma spray process.	13
Fig. 2.5	Schematic Diagram of the HVOF process.	16
Fig. 2.6	Schematic of Cold Spraying Process.	16
Fig. 2.7	Schematic illustration of the Detonation Gun thermal spray system.	16
Fig. 2.8	Optical micrograph of an alumina coating used for corona rolls production, obtained by plasma-spraying.	21
Fig. 2.9	X-ray diffraction diagrams of a coarse TiO_2 powder plasma sprayed coating.	21
Fig. 2.10	A schematic view of solid particle erosion of material.	24
Fig. 2.11	Erosive mass losses as a function of impact angle for aluminium and Al_2O_3 substrates.	24
Fig. 2.12	Characteristic mechanisms of ductile erosion based on the variation in erosion conditions.	29
Fig. 2.13	Cross-sectional schematic of impact by a blunt indenter on to a brittle substrate, resulting in the formation of a conical Hertzian crack.	29
Fig. 2.14	Schematic sequence of crack formation and development as a function of indentation loading and unloading on a brittle substrate.	30
Fig. 2.15	Topographical image of an as sprayed plasma alumina coating.	45
Fig., 2.16	Schematic diagram showing the types of degradation that can occur under conditions of combined oxidation-erosion.	45
Fig. 2.17	Classification of erosion-corrosion.	46
Fig. 2.18	Schematic of the different erosion-oxidation regimes.	47

Fig. 2.19	Summary of erosion regimes observed at high temperatures.	48
Fig. 2.20	Schematic of a typical boiler and the corresponding corrosion sensitive areas.	49
Fig. 2.21	The Ellingham diagram for metallurgically important oxides.	54
Fig. 2.22	Binary phase diagram of KCl-FeCl ₂ .	59
Fig. 2.23	Temperature dependence of corrosion on superheater tubes in coal fired boilers. The dotted line is a theoretical prediction.	62
Fig. 2.24	Schematic diagram for the sulfidation mechanism and transport of oxidizing species.	62
Fig. 2.25	Schematic diagram of a typical coal fired boiler.	67
Fig. 2.26	Annual cost of corrosion in the electrical utilities industry.	68
Fig. 3.1	Detonation gun in operation at SVX Technologies, Noida	76
Fig. 3.2	Schematic Diagram of Detonation gun coating system.	77
Fig. 3.3	Schematic illustrations of the relative depths from which secondary electrons, back scattered electrons and characteristic x-rays may escape the surface to be detected.	84
Fig. 3.4	Schematic illustration of BSE grey scale variation as a function of atomic mass distribution within the sample.	84
Fig. 3.5	High Temperature Air Jet Erosion Test Rig used for erosion testing.	87
Fig. 3.6	A schematic view of High Temperature Air Jet Erosion Test Rig	88
Fig. 3.7	Scanning electron micrograph of the Alumina Eroder particles.	91
Fig. 3.8	Schematic depth-measuring method (a) Designation of sampling area. (b) Erosion depth. (c) Net missing volume of eroded area. (d) Natural volume of uneroded, bare surface. (e) Erosion wear volume loss.	92
Fig. 4.1	Optical micrographs of the substrate alloys (a) Boiler Steel T11 (b) Boiler Steel T22 (c) Superni 600 (d) Superni 718 (e) Superfer 800	99
Fig. 4.2	Scanning electron micrographs showing morphology of Al ₂ O ₃ -3wt% TiO ₂ powder.	100
Fig. 4.3	X-ray Diffraction Profile of coating powder Al ₂ O ₃ -3wt% TiO ₂ .	100

Fig. 4.4	Macrographs of specimens coated with Al ₂ O ₃ -3wt % TiO ₂ powder (a) T11, (b) T22, (c) Superni 600 (d) Superni 718 and (e) Superfer 800.	101
Fig.4.5	Scanning electron micrograph showing cross-sectional morphology of Al ₂ O ₃ -3wt%TiO ₂ D-gun sprayed coatings on substrate alloys (a) Al ₂ O ₃ -3wt%TiO ₂ coating on T11 (b) Al ₂ O ₃ -3wt%TiO ₂ coating on T22 (c) Al ₂ O ₃ -3wt%TiO ₂ coating on Superni 600 (d) Al ₂ O ₃ -3wt%TiO ₂ coating on Superni 718 and (e) Al ₂ O ₃ -3wt%TiO ₂ coating on Superfer 800	102
Fig. 4.6	Microhardness profiles of Al ₂ O ₃ -3 wt% TiO ₂ coating on different alloys along the cross-section.	103
Fig. 4.7	Average microhardness values for T11, T22, Superni 600, Superni 718 and Superfer 800 alloys.	103
Fig. 4.8	Typical Scanning electron micrographs of the surfaces of the as-sprayed Al ₂ O ₃ -3wt.% TiO ₂ coatings.	106
Fig. 4.9	Optical micrographs of a as-sprayed Al ₂ O ₃ -3 wt.% TiO ₂ coatings	106
Fig. 4.10	Cross-sectional morphology of the as-sprayed Al ₂ O ₃ -3 wt.% TiO ₂ coatings.	107
Fig. 4.11	X-ray diffraction pattern for the D-gun sprayed Al ₂ O ₃ -3 wt% TiO ₂ coated Boiler Steel T11.	108
Fig. 4.12	X-ray diffraction pattern for the D-gun sprayed Al ₂ O ₃ -3 wt% TiO ₂ coated Boiler steel T22.	108
Fig. 4.13	X-ray diffraction pattern for the D-gun sprayed Al ₂ O ₃ -3 wt% TiO ₂ coated superalloy Superni 600.	109
Fig. 4.14	X-ray diffraction pattern for the D-gun sprayed Al ₂ O ₃ -3 wt% TiO ₂ coated superalloy Superni 718.	109
Fig. 4.15	X-ray diffraction pattern for the D-gun sprayed Al ₂ O ₃ -3 wt% TiO ₂ coated superalloy Superfer 800.	110
Fig. 4.16	SEM/EDX analysis of coatings showing elemental composition (wt.%) at various points (a) Coated T11, 1000 X, (b) Coated T22, 1000 X.	111
Fig. 4.17	SEM/EDX analysis of coatings showing elemental composition (wt.%) at various points (a) Coated Superni 600, 1000 X, (b) Coated Superni 718, 1000 X and (c) Coated Superfer 800, 1000 X.	112

Fig. 4.18	Cross sectional morphology and elemental composition variation across the cross-section of Al ₂ O ₃ -3 wt%TiO ₂ coated T11 boiler steels.	113
Fig. 4.19	Cross sectional morphology and elemental composition variation across the cross-section of Al ₂ O ₃ -3 wt%TiO ₂ coated T22 boiler steels.	114
Fig. 4.20	Cross sectional morphology and elemental composition variation across the cross-section of Al ₂ O ₃ -3 wt%TiO ₂ coated superalloy Superni 600	115
Fig. 4.21	Cross sectional morphology and elemental composition variation across the cross-section of Al ₂ O ₃ -3 wt%TiO ₂ coated superalloy superfer 718.	116
Fig.4.22	Cross sectional morphology and elemental composition variation across the cross-section of Al ₂ O ₃ -3 wt%TiO ₂ coated superalloy superfer 800.	117
Fig.4.23	BSEI and elemental X-ray mappings of the cross-section of D-gun sprayed Al ₂ O ₃ -3 Wt% TiO ₂ coating on the boiler steel T11, 500X.	120
Fig.4.24	BSEI and elemental X-ray mappings of the cross-section of D-gun sprayed Al ₂ O ₃ -3 Wt% TiO ₂ coating on the boiler steel T22, 500X.	121
Fig.4.25	BSEI and elemental X-ray mappings of the cross-section of D-gun sprayed Al ₂ O ₃ -3 Wt% TiO ₂ coating on the superalloy Superni 600, 500X.	122
Fig.4.26	BSEI and elemental X-ray mappings of the cross-section of D-gun sprayed Al ₂ O ₃ -3 Wt% TiO ₂ coating on the superalloy Superni718, 500X.	123
Fig.4.27	BSEI and elemental X-ray mappings of the cross-section of D-gun sprayed Al ₂ O ₃ -3 Wt% TiO ₂ coating on the superalloy Superfer 800, 500X.	124
Fig. 5.1	Macrographs of Uncoated alloys eroded at condition 1 and impact angles of 90° and 30° (a) Boiler Steel T11 (b) Boiler Steel T22 (c) Superni 600 (d) Superni 718 (e) Superfer 800	129

Fig. 5.2	Macrographs of Uncoated alloys eroded at condition 2 and impact angles of 90° and 30° (a) Boiler Steel T11 (b) Boiler Steel T22 (c) Superni 600 (d) Superni 718 (e) Superfer 800	130
Fig. 5.3	Macrographs of Uncoated alloys eroded at condition 3 and impact angles of 90° and 30° (a) Boiler Steel T11 (b) Boiler Steel T22 (c) Superni 600 (d) Superni 718 (e) Superfer 800	131
Fig. 5.4	3D Optical Profile of the Specimen eroded at condition 1 showing depth profiles at interface and at eroded zone (a) Eroded at 30° impact Angle (b) Eroded at 90° impact Angle	134
Fig. 5.5	3D Optical Profile of the Specimen eroded at condition 2 showing depth profiles at interface and at eroded zone. (a) Eroded at 30° impact Angle (b) Eroded at 90° impact Angle	134
Fig. 5.6	3D Optical Profile of the Specimen eroded at condition 3 showing depth profiles at interface and at eroded zone. (a) Eroded at 30° impact Angle (b) Eroded at 90° impact Angle	135
Fig. 5.7	Bar diagram showing the Volume erosion rates of substrate alloys under oblique and normal impact at condition 1.	135
Fig. 5.8	Bar diagram showing the Volume erosion rates of substrate alloys under oblique and normal impact at condition 2.	136
Fig. 5.9	Bar diagram showing the Volume erosion rates of substrate alloys under oblique and normal impact at condition 3.	136
Fig. 5.10	Bar diagram showing the variation in Volume erosion rates of substrate alloys at 30° impact angle with change in test temperature.	137
Fig. 5.11	Bar diagram showing the variation in Volume erosion rates of substrate alloys at 90° impact angle with change in test temperature.	137
Fig. 5.12	Scanning Electron Macrographs and EDX analysis of uncoated alloys eroded at condition 1 and impact angle of 30° (a) Boiler Steel T11 (b) Boiler Steel T22 (c) Superni 600 (d) Superni 718 (e) Superfer 800	138

Fig. 5.13	Scanning Electron Macrographs and EDX analysis of uncoated alloys eroded at condition 1 and impact angle of 90° (a) Boiler Steel T11 (b) Boiler Steel T22 (c) Superni 600 (d) Superni 718 (e) Superfer 800	139
Fig. 5.14	Scanning Electron Macrographs and EDX analysis of uncoated alloys eroded at condition 2 and impact angle of 30° (a) Boiler Steel T11 (b) Boiler Steel T22 (c) Superni 600 (d) Superni 718 (e) Superfer 800	142
Fig. 5.15	Scanning Electron Macrographs and EDX analysis of Uncoated alloys eroded at condition 2 and impact angle of 90° (a) Boiler Steel T11 (b) Boiler Steel T22 (c) Superni 600 (d) Superni 718 (e) Superfer 800	143
Fig. 5.16	Scanning Electron Macrographs and EDX analysis of uncoated alloys eroded at condition 3 and impact angle of 30° (a) Boiler Steel T11 (b) Boiler Steel T22 (c) Superni 600 (d) Superni 718 (e) Superfer 800	146
Fig. 5.17	Scanning Electron Macrographs and EDX analysis of uncoated alloys eroded at condition 3 and impact angle of 90° (a) Boiler Steel T11 (b) Boiler Steel T22 (c) Superni 600 (d) Superni 718 (e) Superfer 800	147
Fig. 5.18	Macrographs of Al ₂ O ₃ -3 wt% TiO ₂ coated alloys eroded at condition 1 and at impact angles of 90° and 30° (a) Boiler Steel T11 (b) Boiler Steel T22 (c) Superni 600 (d) Superni 718 (e) Superfer 800	150
Fig. 5.19	Macrographs of Al ₂ O ₃ -3 wt% TiO ₂ coated alloys eroded at condition 2 and at impact angles of 90° and 30° (b) Boiler Steel T11 (b) Boiler Steel T22 (c) Superni 600 (d) Superni 718 (e) Superfer 800	151
Fig. 5.20	Macrographs of Al ₂ O ₃ -3 wt% TiO ₂ coated alloys eroded at condition 3 and at impact angles of 90° and 30° (c) Boiler Steel T11 (b) Boiler Steel T22 (c) Superni 600 (d) Superni 718 (e) Superfer 800	152

Fig. 5.21	3D Optical Profile of Al ₂ O ₃ -3 wt% TiO ₂ coated specimen eroded at condition 1 showing depth profiles at interface and at eroded zone (b) Eroded at 30° impact angle (b) Eroded at 90° impact angle	153
Fig. 5.22	3D Optical Profile of Al ₂ O ₃ -3 wt% TiO ₂ coated specimen eroded at condition 2 showing depth profiles at interface and at eroded zone (b) Eroded at 30° impact Angle (b) Eroded at 90° impact angle	153
Fig. 5.23	3D Optical Profile of Al ₂ O ₃ -3 wt% TiO ₂ coated specimen eroded at condition 3 showing depth profiles at interface and at eroded zone. (c) Eroded at 30° impact Angle (b) Eroded at 90° impact angle	154
Fig. 5.24	Bar diagram showing the volume erosion rates of coated alloys under oblique and normal impact at condition 1.	154
Fig. 5.25	Bar diagram showing the Volume erosion rates of coated alloys under oblique and normal impact at condition 2.	155
Fig. 5.26	Bar diagram showing the Volume erosion rates of coated alloys under oblique and normal impact at condition 3	155
Fig. 5.27	Bar diagram showing the variation in Volume erosion rates of coated alloys at 30° impact angle with change in test temperature	156
Fig. 5.28	Bar diagram showing the variation in Volume erosion rates of coated alloys at 90° impact angle with change in test temperature	156
Fig. 5.29	Scanning Electron Macrographs and EDX analysis of Al ₂ O ₃ -3 wt% TiO ₂ coated alloys eroded at condition 1 and impact angle of 30° (a) Boiler Steel T11 (b) Boiler Steel T22 (c) Superni 600 (d) Superni 718 (e) Superfer 800	159
Fig. 5.30	Scanning Electron Macrographs and EDX analysis of Al ₂ O ₃ -3 wt% TiO ₂ coated alloys eroded at condition 1 and impact angle of 90° (a) Boiler Steel T11 (b) Boiler Steel T22 (c) Superni 600 (d) Superni 718 (e) Superfer 800	160
Fig. 5.31	Scanning Electron Macrographs and EDX analysis of Al ₂ O ₃ -3 wt% TiO ₂ coated alloys eroded at condition 2 and impact angle of 30° (a) Boiler Steel T11 (b) Boiler Steel T22 (c) Superni 600 (d) Superni 718 (e) Superfer 800	161

Fig. 5.32	Scanning Electron Macrographs and EDX analysis of Al ₂ O ₃ -3 wt% TiO ₂ coated alloys eroded at condition 2 and impact angle of 90° (a) Boiler Steel T11 (b) Boiler Steel T22 (c) Superni 600 (d) Superni 718 (e) Superfer 800	162
Fig. 5.33	Scanning Electron Macrographs and EDX analysis of Al ₂ O ₃ -3 wt% TiO ₂ coated alloys eroded at condition 3 and impact angle of 30° (a) Boiler Steel T11 (b) Boiler Steel T22 (c) Superni 600 (d) Superni 718 (e) Superfer 800	163
Fig. 5.34	Scanning Electron Macrographs and EDX analysis of Al ₂ O ₃ -3 wt% TiO ₂ coated alloys eroded at condition 3 and impact angle of 90° Boiler Steel T11 (b) Boiler Steel T22 (c) Superni 600 (d) Superni 718 (e) Superfer 800	164
Fig. 5.35	Schematic diagram showing the erosion scar produced in general on the eroded surface at an impact angle of 90° and 30°; Mark "A" represents a localized region of material removal and Mark "B" represents the peripheral region of the elastically loaded material	169
Fig. 5.36	Schematic diagram showing the Metallic Erosion	169
Fig. 5.37	Schematic diagram showing probable erosion mechanism at low temperature.	174
Fig. 5.38	Lip fracture mode in metallic erosion	174
Fig. 5.39	Schematic oxide removal from the exposed surface at high temperature	174
Fig. 5.40	Schematic diagram showing probable mechanism of oxidation affected Erosion showing deformed zone formed due to erodent impact.	175
Fig. 5.41	Schematic Representative erosion scar on coating showing different modes of erosion in coating	178
Fig. 5.42	Schematic representation of coating fracture dependent on impact angle (a) Low Angle (b) High Angle	178
Fig. 5.43	Crack formed in bulk of a coating due to particle impingement	179
Fig. 5.44	Schematic of splat edge chipping mechanism due to particle impingement.	180

Fig. 5.45	Schematic diagram showing probable erosion mechanism of detonation gun sprayed Al ₂ O ₃ -3 Wt% TiO ₂ coatings at low impact angles due to particle impingement.	185
Fig. 5.46	Schematic illustrating the mechanism of gross splat chip formation during erosive impact as a result of low inter-splat adhesion.	186
Fig. 5.47	Schematic illustrating the mechanism of flake formation during particle impact	187
Fig. 5.48	Schematic representation of gross chip formation in the region between neighbouring indents, resulting from the large depth of erodent penetration	188
Fig. 6.1	Macrographs of substrate alloys after cyclic oxidation in air at 900°C for 50 cycles. (a) T11 (b) T22 (c) Superni 600 (d) Superni718 (e) Superfer 800	192
Fig. 6.2	Surface scale morphology and EDX analysis for boiler steels oxidised in air at 900°C for 50 cycles (a) T11, 1000 X and (b) T22, 1000 X.	197
Fig. 6.3	Surface scale morphology and EDX analysis for superalloys oxidised in air at 900°C for 50 cycles (a) superni 600, 1000 X (b) superni 718, 1000 X. and (c) superfer 800, 1000 X	198
Fig. 6.4	Weight gain plot for uncoated steels exposed to air at 900 ⁰ C for 50 cycles.	199
Fig. 6.5	Weight gain square (mg ² /cm ⁴) plot for uncoated steels exposed to air at 900 ⁰ C for 50 cycles.	199
Fig. 6.6	Weight gain plot for uncoated superalloys exposed to air at 900 ⁰ C for 50 cycles.	200
Fig.6.7	Weight gain square (mg ² /cm ⁴) plot for uncoated superalloys exposed to air at 900 ⁰ C for 50 cycles.	200
Fig. 6.8	X-ray diffraction profiles for T11 and T22 boiler steels subjected to cyclic oxidation in air at 900°C for 50 cycles. (a) T11 (b) T22	201
Fig.6.9	X-ray diffraction profiles for superalloys Superni 600 and Superni 718 subjected to cyclic oxidation in air at 900°C for 50 cycles. (a) Superni 600 (b) Superni 718	202

Fig. 6.10	X-ray diffraction profiles for superalloy superfer 800 subjected to cyclic oxidation in air at 900°C for 50 cycles.	203
Fig.6.11	Cross sectional morphology and elemental composition variation across the cross-section of boiler steel T11 exposed air at 900°C for 50 cycles, 1000 X	204
Fig.6.12	Cross sectional morphology and elemental composition variation across the cross-section of boiler steel T22 exposed air at 900°C for 50 cycles, 1000 X.	205
Fig 6.13	Cross sectional morphology and elemental composition variation across the cross-section of superalloy Superni 600 exposed air at 900°C for 50 cycles, 1000 X.	206
Fig 6.14	Cross sectional morphology and elemental composition variation across the cross-section of superalloy Superni 718 exposed air at 900°C for 50 cycles, 1000 X.	207
Fig.6.15	Cross sectional morphology and elemental composition variation across the cross-section of superalloy superfer 800 exposed air at 900°C for 50 cycles, 1000 X.	208
Fig. 6.16	BSEI and X-ray mapping of the cross-section of boiler steel T11 subjected to cyclic oxidation in air at 900°C for 50 cycles.	209
Fig. 6.17	BSEI and X-ray mapping of the cross-section of boiler steel T22 subjected to cyclic oxidation in air at 900°C for 50 cycles.	210
Fig.6.18	BSEI and X-ray mapping of the cross-section of superalloy Superni 600 subjected to cyclic oxidation in air at 900°C for 50 cycles.	211
Fig.6.19	BSEI and X-ray mapping of the cross-section of superalloy Superni 718 subjected to cyclic oxidation in air at 900°C for 50 cycles.	212
Fig. 6.20	BSEI and X-ray mapping of the cross-section of superalloy superfer 800 subjected to cyclic oxidation in air at 900°C for 50 cycles.	213
Fig.6.21	Macrographs of Al ₂ O ₃ -3wt%TiO ₂ coated substrate alloys after cyclic oxidation in air at 900°C for 50 cycles. (a) T11 (b) T22 (c) Superni 600 (d) Superni718 (e) Superfer 800	216
Fig. 6.22	Weight gain plot for Al ₂ O ₃ - 3 wt% TiO ₂ coated boiler steels T11 and T22 exposed to air at 900°C for 50cycles.	217

Fig.6.23	Weight gain square (mg^2/cm^4) plot for Al_2O_3 - 3 wt% TiO_2 coated boiler steels T11 and T22 exposed to air at 900°C for 50 cycles.	217
Fig. 6.24	Weight gain plot for Al_2O_3 - 3 wt% TiO_2 coated superalloys Superni 600, Superni 718, superfer 800 exposed to air at 900°C for 50cycles.	218
Fig.6.25	Weight gain square (mg^2/cm^4) plot for Al_2O_3 - 3 wt% TiO_2 coated superalloys Superni 600, Superni 718, superfer 800 exposed to air at 900°C for 50 cycles.	218
Fig. 6.26	X-ray diffraction profiles for Al_2O_3 -3 wt% TiO_2 coated boiler steels subjected to cyclic oxidation in air at 900°C for 50 cycles. (a) T11 (b) T22	219
Fig. 6.27	X-ray diffraction profiles for Al_2O_3 -3 wt% TiO_2 coated superalloys subjected to cyclic oxidation in air at 900°C for 50 cycles. (a) Superni 600 (b) Superni 718	220
Fig. 6.28	X-ray diffraction profiles for Al_2O_3 -3 wt% TiO_2 coated superalloy superfer 800 subjected to cyclic oxidation in air at 900°C for 50 cycles.	221
Fig. 6.29	Surface scale morphology and EDX analysis for Al_2O_3 -3wt% TiO_2 coated steels oxidized in air at 900°C for 50 cycles (a) T11, 1000 X (b) T22, 1000 X.	222
Fig. 6.30	Surface scale morphology and EDX analysis for Al_2O_3 -3wt% TiO_2 coated superalloys oxidized in air at 900°C for 50 cycles (a) Superni 600, 1000 X (b) Superni 718, 1000 X. (c) Superfer 800, 1000X.	223
Fig. 6.31	Cross sectional morphology and elemental composition variation across the cross-section of Al_2O_3 -3wt% TiO_2 Coated boiler steel T11 exposed to air at 900°C for 50 cycles, 1000 X	226
Fig 6.32	Cross sectional morphology and elemental composition variation across the cross-section of Al_2O_3 -3wt% TiO_2 Coated boiler steel T22 exposed to air at 900°C for 50 cycles, 1000 X.	227
Fig. 6.33	Cross sectional morphology and elemental composition variation across the cross-section of Al_2O_3 -3wt% TiO_2 Coated superalloy Superni 600 exposed to air at 900°C for 50 cycles, 1000 X.	228

Fig. 6.34	Cross sectional morphology and elemental composition variation across the cross-section of Al ₂ O ₃ -3wt%TiO ₂ Coated superalloy Superni 718 exposed to air at 900°C for 50 cycles, 1000 X.	229
Fig. 6.35	Cross sectional morphology and elemental composition variation across the cross-section of Al ₂ O ₃ -3wt%TiO ₂ Coated superalloy superfer 800 exposed to air at 900°C for 50 cycles, 1000 X	230
Fig.6.36	BSEI and X-ray mapping of the cross-section of Al ₂ O ₃ -3 wt%TiO ₂ coated boiler steel T11 subjected to cyclic oxidation in air at 900°C for 50 cycles.	231
Fig. 6.37	BSEI and X-ray mapping of the cross-section of Al ₂ O ₃ -3 wt%TiO ₂ coated boiler steel T22 subjected to cyclic oxidation in air at 900°C for 50 cycles.	232
Fig.6.38	BSEI and X-ray mapping of the cross-section of Al ₂ O ₃ -3 wt%TiO ₂ coated superalloy Superni 600 subjected to cyclic oxidation in air at 900°C for 50 cycles.	233
Fig. 6.39	BSEI and X-ray mapping of the cross-section of Al ₂ O ₃ -3 wt%TiO ₂ coated superalloy Superni 718 subjected to cyclic oxidation in air at 900°C for 50 cycles.	234
Fig. 6.40	BSEI and X-ray mapping of the cross-section of Al ₂ O ₃ -3 wt%TiO ₂ coated superalloy superfer 800 subjected to cyclic oxidation in air at 900°C for 50 cycles.	235
Fig.6.41	Macrographs of substrate alloys after cyclic hot corrosion in Na ₂ SO ₄ -60%V ₂ O ₅ at 900°C for 50 cycles (a) T11 (b) T22 (c) Superni 600 (d) Superni718 (e) Superfer 800	238
Fig. 6.42	Weight gain plot for uncoated boiler steels T11 and T22 subjected to cyclic hot corrosion in Na ₂ SO ₄ -60%V ₂ O ₅ at 900°C for 50 cycles.	241
Fig.6.43	Weight gain square (mg ² /cm ⁴) plot for uncoated boiler steels T11 and T22 subjected to cyclic hot corrosion in Na ₂ SO ₄ -60%V ₂ O ₅ at 900°C for 50 cycles	241
Fig. 6.44	Weight gain plot for uncoated superalloys Superni 600, Superni 718, superfer 800 subjected to cyclic hot corrosion in Na ₂ SO ₄ -60%V ₂ O ₅ at 900°C for 50 cycles.	242

Fig.6.45	Weight gain square (mg^2/cm^4) plot for uncoated Superni 600, Superni 718, Superfer 800 subjected to cyclic hot corrosion in Na_2SO_4 -60% V_2O_5 at 900°C for 50 cycles.	242
Fig.6.46	X-ray diffraction profiles for boiler steels subjected to cyclic hot corrosion in Na_2SO_4 -60% V_2O_5 at 900°C for 50 cycles. (a) T11 (b) T22	243
Fig. 6.47	X-ray diffraction profiles for superalloys Superni 600 and Superni 718 subjected to cyclic hot corrosion in Na_2SO_4 -60% V_2O_5 at 900°C for 50 cycles. (a) Superni 600 (b) Superni 718	244
Fig. 6.48	X-ray diffraction profile for superalloy superfer 800 subjected to cyclic hot corrosion in Na_2SO_4 -60% V_2O_5 at 900°C for 50 cycles.	245
Fig. 6.49	Surface scale morphology and EDX analysis for boiler steels subjected to cyclic hot corrosion in Na_2SO_4 -60% V_2O_5 at 900°C for 50 cycles (a) T11, 1000 X and (b) T22, 1000 X.	246
Fig. 6.50	Surface scale morphology and EDX analysis for superalloys subjected to cyclic hot corrosion in Na_2SO_4 -60% V_2O_5 at 900°C for 50 cycles (a) Superni 600, 1000 X and (b) Superni 718, 1000 X., (c) superfer 800, 1000 X.	247
Fig. 6.51	Cross sectional morphology and elemental composition variation across the cross-section of boiler steel T11 exposed to Na_2SO_4 -60% V_2O_5 at 900°C for 50 cycles, 200 X	250
Fig. 6.52	Cross sectional morphology and elemental composition variation across the cross-section of boiler steel T22 exposed to Na_2SO_4 -60% V_2O_5 at 900°C for 50 cycles, 200 X	251
Fig.6.53	Cross sectional morphology and elemental composition variation across the cross-section of superalloy Superni 600 exposed to Na_2SO_4 -60% V_2O_5 at 900°C for 50 cycles, 1000 X.	252
Fig.6.54	Cross sectional morphology and elemental composition variation across the cross-section of superalloy Superni 718 exposed to Na_2SO_4 -60% V_2O_5 at 900°C for 50 cycles, 1000 X.	253
Fig.6.55	Cross sectional morphology and elemental composition variation across the cross-section of superalloy superfer 800 exposed to Na_2SO_4 -60% V_2O_5 at 900°C for 50 cycles, 1000 X.	254

Fig. 6.56	BSEI and X-ray mapping of the cross-section of boiler steel T11 subjected to cyclic hot corrosion in Na ₂ SO ₄ -60%V ₂ O ₅ at 900°C for 50 cycles, 200 X	255
Fig.6.57	BSEI and X-ray mapping of the cross-section of boiler steel T22 subjected to cyclic hot corrosion in Na ₂ SO ₄ -60%V ₂ O ₅ at 900°C for 50 cycles, 200 X	256
Fig. 6.58	BSEI and X-ray mapping of the cross-section of superalloy Superni 600 subjected to cyclic hot corrosion in Na ₂ SO ₄ -60%V ₂ O ₅ at 900°C for 50 cycles, 200X.	257
Fig.6.59	BSEI and X-ray mapping of the cross-section of superalloy Superni 718 subjected to cyclic hot corrosion in Na ₂ SO ₄ -60%V ₂ O ₅ at 900°C for 50 cycles, 1000X.	258
Fig. 6.60	BSEI and X-ray mapping of the cross-section of superalloy Superfer 800 subjected to cyclic hot corrosion in Na ₂ SO ₄ -60%V ₂ O ₅ at 900°C for 50 cycles, 1000X.	259
Fig.6.61	Macrographs of Al ₂ O ₃ -3wt%TiO ₂ coated substrate alloys after cyclic hot corrosion in Na ₂ SO ₄ -60%V ₂ O ₅ at 900°C for 50 cycles (a) T11 (b) T22 (c) Superni 600 (d) Superni718 (e) Superfer 800	262
Fig. 6.62	Weight gain plot for Al ₂ O ₃ - 3 wt% TiO ₂ coated boiler steels T11 and T22 subjected to cyclic hot corrosion in Na ₂ SO ₄ -60%V ₂ O ₅ at 900°C for 50 cycles	263
Fig.6.63	Weight gain square (mg ² /cm ⁴) plot for Al ₂ O ₃ - 3 wt% TiO ₂ coated boiler steels T11 and T22 subjected to cyclic hot corrosion in Na ₂ SO ₄ -60%V ₂ O ₅ at 900°C for 50 cycles	263
Fig. 6.64	Weight gain plot for Al ₂ O ₃ - 3 wt% TiO ₂ coated superalloys Superni 600, Superni 718, superfer 800 subjected to cyclic hot corrosion in Na ₂ SO ₄ -60%V ₂ O ₅ at 900°C for 50 cycles	264
Fig.6.65	Weight gain square (mg ² /cm ⁴) plot for Al ₂ O ₃ - 3 wt% TiO ₂ coated superalloys Superni 600, Superni 718, superfer 800 subjected to cyclic hot corrosion in Na ₂ SO ₄ -60%V ₂ O ₅ at 900°C for 50 cycles	264

Fig. 6.66	X-ray diffraction profiles for Al_2O_3 -3 wt% TiO_2 coated boiler steels subjected to cyclic hot corrosion in Na_2SO_4 -60% V_2O_5 at 900°C for 50 cycles. (a) T11 (b) T22	265
Fig. 6.67	X-ray diffraction profiles for Al_2O_3 -3 wt% TiO_2 coated superalloys subjected to cyclic hot corrosion in Na_2SO_4 -60% V_2O_5 at 900°C for 50 cycles. (a) Superni 600 (b) Superni 718	266
Fig. 6.68	X-ray diffraction profiles for Al_2O_3 -3 wt% TiO_2 coated superalloy superfer 800 subjected to cyclic hot corrosion in Na_2SO_4 -60% V_2O_5 at 900°C for 50 cycles.	267
Fig. 6.69	Surface scale morphology and EDX analysis for Al_2O_3 -3wt% TiO_2 coated steels corroded in Na_2SO_4 -60% V_2O_5 at 900°C for 50 cycles (a) T11, 1000 X (b) T22, 1000 X.	270
Fig. 6.70	Surface scale morphology and EDX analysis for Al_2O_3 -3wt% TiO_2 coated superalloys corroded in Na_2SO_4 -60% V_2O_5 at 900°C for 50 cycles (a) Superni 600, 1000 X (b) Superni 718, 1000 X. (c) Superfer 800, 1000X	271
Fig.6.71	Cross sectional morphology and elemental composition variation across the cross-section of Al_2O_3 -3wt% TiO_2 Coated boiler steel T11 exposed to Na_2SO_4 -60% V_2O_5 at 900°C for 50 cycles, 1000 X	272
Fig.6.72	Cross sectional morphology and elemental composition variation across the cross-section of Al_2O_3 -3wt% TiO_2 Coated boiler steel T22 exposed to Na_2SO_4 -60% V_2O_5 at 900°C for 50 cycles, 1000 X	273
Fig.6.73	Cross sectional morphology and elemental composition variation across the cross-section of Al_2O_3 -3wt% TiO_2 Coated superalloy Superni 718 exposed to Na_2SO_4 -60% V_2O_5 at 900°C for 50 cycles, 1000 X	274
Fig.6.74	Cross sectional morphology and elemental composition variation across the cross-section of Al_2O_3 -3wt% TiO_2 Coated superalloy Superni 600 exposed to Na_2SO_4 -60% V_2O_5 at 900°C for 50 cycles, 1000 X.	275

Fig.6.75	Cross sectional morphology and elemental composition variation across the cross-section of Al ₂ O ₃ -3wt%TiO ₂ Coated superalloy superfer 800 exposed to Na ₂ SO ₄ -60%V ₂ O ₅ at 900°C for 50 cycles, 1000 X.	276
Fig. 6.76	BSEI and X-ray mapping of the cross-section of Al ₂ O ₃ -3 wt%TiO ₂ coated boiler steel T11 subjected to cyclic hot corrosion in Na ₂ SO ₄ -60%V ₂ O ₅ at 900°C for 50 cycles, 1000 X	277
Fig. 6.77	BSEI and X-ray mapping of the cross-section of Al ₂ O ₃ -3 wt%TiO ₂ coated boiler steel T22 subjected to cyclic hot corrosion in Na ₂ SO ₄ -60%V ₂ O ₅ at 900°C for 50 cycles, 1000 X	278
Fig. 6.78	BSEI and X-ray mapping of the cross-section of Al ₂ O ₃ -3 wt%TiO ₂ coated superalloy Superni 600 subjected to cyclic hot corrosion in Na ₂ SO ₄ -60%V ₂ O ₅ at 900°C for 50 cycles, 1000 X	279
Fig. 6.79	BSEI and X-ray mapping of the cross-section of Al ₂ O ₃ -3 wt%TiO ₂ coated superalloy Superni 718 subjected to cyclic hot corrosion in Na ₂ SO ₄ -60%V ₂ O ₅ at 900°C for 50 cycles, 1000 X	280
Fig.6.80	BSEI and X-ray mapping of the cross-section of Al ₂ O ₃ -3 wt%TiO ₂ coated superalloy superfer 800 subjected to cyclic hot corrosion in Na ₂ SO ₄ -60%V ₂ O ₅ at 900°C for 50 cycles, 1000 X	281
Fig. 6.81	Schematic diagram showing probable mode of oxidation attack on T22 boiler steel exposed to air at 900°C for 50 cycles.	290
Fig. 6.82	Schematic diagram showing probable mode of oxidation attack on Ni based superalloys exposed to air at 900°C for 50 cycles.	291
Fig. 6.83	Schematic diagram showing probable mode of oxidation attack on Fe- based superalloy Superfer 800 exposed to air at 900°C for 50 cycles.	292
Fig. 6.84	Schematic diagram showing probable mode of hot corrosion attack on Boiler steel T11 exposed to Na ₂ SO ₄ -60%V ₂ O ₅ environment at 900°C for 50 cycles.	293
Fig. 6.85	Schematic diagram showing probable mode of hot corrosion attack on Ni based superalloy exposed to Na ₂ SO ₄ -60%V ₂ O ₅ environment at 900°C for 50 cycles.	298

Fig. 6.86	Schematic diagram showing probable mode of hot corrosion attack on Superfer 800 superalloy exposed to Na_2SO_4 -60% V_2O_5 environment at 900°C for 50 cycles.	299
Fig. 7.1	Macrographs of uncoated substrate alloys before and after 1500 hours exposure to boiler environment: (a) T11 (b) T22 (c) Superni 600 (d) Superni718 (e) Superfer 800 (f) T11 after 1500 Hrs Exposure (g) T22 after 1500 Hrs Exposure (h) Superni 600 after 1500 Hrs Exposure (i) Superni 718 after 1500 Hrs Exposure (j) Superfer 800 after 1500 Hrs Exposure	302
Fig. 7.2	Weight change plot for uncoated alloys exposed to superheater of the coal fired boiler for 1500 hours at 700°C.	303
Fig. 7.3	Bar chart indicating the thickness lost in mm by the uncoated alloys after 1500 hours exposure to the coal fired boiler at 700°C.	303
Fig. 7.4	X-ray diffraction profiles for boiler steels exposed to superheater of the coal fired boiler for 1500 hours at 700°C. (a) T11 (b) T22	304
Fig. 7.5	X-ray diffraction profiles for superalloys exposed to superheater of the coal fired boiler for 1500 hours at 700°C (a) Superni 600 (b) Superni 718	305
Fig. 7.6	X-ray diffraction profiles for superalloy Superfer 800 exposed to superheater of the coal fired boiler for 1500 hours at 700°C.	306
Fig.7.7	Surface scale morphology and EDX analysis for boiler steel T11 exposed to superheater of the coal fired boiler for 1500 hours at 700°C.	311
Fig. 7.8	Surface scale morphology and EDX analysis for boiler steel T22 exposed to superheater of the coal fired boiler for 1500 hours at 700°C.	312
Fig. 7.9	Surface scale morphology and EDX analysis for superalloy Superni 600 exposed to superheater of the coal fired boiler for 1500 hours at 700°C.	313
Fig.7.10	Surface scale morphology and EDX analysis for superalloy Superni 718 exposed to superheater of the coal fired boiler for 1500 hours at 700°C.	314

Fig.7.11	Surface scale morphology and EDX analysis for superalloy Superfer 800 exposed to superheater of the coal fired boiler for 1500 hours at 700°C.	315
Fig. 7.12	Oxide scale morphology and elemental composition variation across the cross-section of T11 boiler steel exposed to superheater of the coal fired boiler for 1500 hours at 700°C.	316
Fig. 7.13	Oxide scale morphology and elemental composition variation across the cross-section of T22 boiler steel exposed to superheater of the coal fired boiler for 1500 hours at 700°C.	317
Fig. 7.14	Oxide scale morphology and elemental composition variation across the cross-section of Superni 600 superalloy exposed to superheater of the coal fired boiler for 1500 hours at 700°C.	318
Fig. 7.15	Oxide scale morphology and elemental composition variation across the cross-section of Superni 718 superalloy exposed to superheater of the coal fired boiler for 1500 hours at 700°C.	319
Fig. 7.16	Oxide scale morphology and elemental composition variation across the cross-section of Superfer 800 superalloy exposed to superheater of the coal fired boiler for 1500 hours at 700°C.	320
Fig. 7.17	Back scattered electron image and the corresponding x -ray mappings of cross section of uncoated T11 steel after 1500 hours exposure in boiler.	323
Fig. 7.18	Back scattered electron image and the corresponding x -ray mappings of cross section of uncoated T22 steel after 1500 hours exposure in boiler.	324
Fig. 7.19	Back scattered electron image and the corresponding x -ray mappings of cross section of uncoated superalloy Superni 600 after 1500 hours exposure in boiler.	325
Fig. 7.20	Back scattered electron image and the corresponding x -ray mappings of cross section of uncoated superalloy Superni 718 after 1500 hours exposure in boiler.	326
Fig. 7.21	Back scattered electron image and the corresponding x -ray mappings of cross section of uncoated superalloy superfer 800 after 1500 hours exposure in boiler.	327

Fig.7.22	Macrographs of $\text{Al}_2\text{O}_3\text{-3wt\%TiO}_2$ coated substrate alloys before and after 1500 hours exposure to boiler environment: (a) T11 (b) T22 (c) Superni 600 (d) Superni718 (e) Superfer 800 (f) T11 after 1500 Hrs Exposure (g) T22 after 1500 Hrs Exposure (h) Superni 600 after 1500 Hrs Exposure (i) Superni 718 after 1500 Hrs Exposure (j) Superfer 800 after 1500 Hrs Exposure	328
Fig.7.23	Weight change plot for $\text{Al}_2\text{O}_3\text{-3wt\%TiO}_2$ coated alloys exposed to platen superheater of the coal fired boiler for 1500 hours at 700°C .	329
Fig.7.24	Bar chart indicating the thickness lost in mm by the $\text{Al}_2\text{O}_3\text{-3 wt\% TiO}_2$ coated alloys after 1500 hours exposure to the coal fired boiler at 700°C .	329
Fig. 7.25	X-ray diffraction profiles for $\text{Al}_2\text{O}_3\text{-3 wt\% TiO}_2$ coated boiler steels exposed to superheater of the coal fired boiler for 1500 hours at 700°C . (a) T11 (b) T22	330
Fig. 7.26	X-ray diffraction profiles for $\text{Al}_2\text{O}_3\text{-3 wt\% TiO}_2$ coated superalloys exposed to superheater of the coal fired boiler for 1500 hours at 700°C (a) Superni 600 (b) Superni 718	331
Fig. 7.27	X-ray diffraction profiles for $\text{Al}_2\text{O}_3\text{-3 wt\% TiO}_2$ coated superalloy Superfer 800 exposed to superheater of the coal fired boiler for 1500 hours at 700°C	332
Fig.7.28	Surface scale morphology and EDX analysis for $\text{Al}_2\text{O}_3\text{-3\%TiO}_2$ coated boiler steel T11 exposed to superheater of the coal fired boiler for 1500 hours at 700°C .	333
Fig.7.29	Surface scale morphology and EDX analysis for $\text{Al}_2\text{O}_3\text{-3\%TiO}_2$ coated boiler steel T22 exposed to superheater of the coal fired boiler for 1500 hours at 700°C .	334
Fig.7.30	Surface scale morphology and EDX analysis for $\text{Al}_2\text{O}_3\text{-3\%TiO}_2$ coated superalloy Superni 600 exposed to superheater of the coal fired boiler for 1500 hours at 700°C .	335

Fig.7.31	Surface scale morphology and EDX analysis for Al_2O_3 -3% TiO_2 coated superalloy Superni 718 exposed to superheater of the coal fired boiler for 1500 hours at 700°C.	336
Fig.7.32	Surface scale morphology and EDX analysis for Al_2O_3 -3% TiO_2 coated superalloy Superfer 800 exposed to superheater of the coal fired boiler for 1500 hours at 700°C.	337
Fig. 7.33	Cross sectional morphology and elemental composition variation across the cross-section of Al_2O_3 -3 wt% TiO_2 coated T11 boiler steels exposed to superheater of the coal fired boiler for 1500 hours at 700°C.	338
Fig. 7.34	Cross sectional morphology and elemental composition variation across the cross-section of Al_2O_3 -3 wt% TiO_2 coated T22 boiler steel exposed to superheater of the coal fired boiler for 1500 hours at 700°C.	339
Fig. 7.35	Cross sectional morphology and elemental composition variation across the cross-section of Al_2O_3 -3wt% TiO_2 coated Superni 600 superalloy exposed to superheater of the coal fired boiler for 1500 hours at 700°C.	340
Fig. 7.36	Cross sectional morphology and elemental composition variation across the cross-section of Al_2O_3 -3wt% TiO_2 coated Superni 718 superalloy exposed to superheater of the coal fired boiler for 1500 hours at 700°C.	341
Fig. 7.37	Cross sectional morphology and elemental composition variation across the cross-section of Al_2O_3 -3wt% TiO_2 coated Superfer 800 superalloy exposed to platen superheater of the coal fired boiler for 1500 hours at 700°C.	342
Fig. 7.38	Back scattered electron image and the corresponding x-ray mappings of cross section of Al_2O_3 - 3 wt% TiO_2 coated T11 steel after 1500 hours exposure in boiler.	343
Fig. 7.39	Back scattered electron image and the corresponding x -ray mappings of cross section of Al_2O_3 - 3 wt% TiO_2 coated T22 steel after 1500 hours exposure in boiler.	344

Fig. 7.40	Back scattered electron image and the corresponding x -ray mappings of cross section of Al ₂ O ₃ - 3 wt% TiO ₂ coated superalloy Superni 600 steel after 1500 hours exposure in boiler.	345
Fig. 7.41	Back scattered electron image and the corresponding x -ray mappings of cross section of Al ₂ O ₃ - 3wt% TiO ₂ coated superalloy Superni 718 after 1500 hours exposure in boiler.	346
Fig. 7.42	Back scattered electron image and the corresponding x -ray mappings of cross section of Al ₂ O ₃ - 3 wt% TiO ₂ coated superalloy superfer 800 after 1500 hours exposure in boiler.	347
Fig. 7.43	Schematic diagram showing scale growth and probable erosion corrosion mechanism for the uncoated boiler steel exposed to actual boiler environment at 700°C for 1500 hours.	352
Fig. 7.44	Schematic diagram showing probable erosion corrosion mechanism for the uncoated superalloy Superni 600 exposed to actual boiler environment at 700°C for 1500 hours.	355
Fig. 7.45	Schematic diagram showing probable erosion corrosion mechanism for the uncoated superalloy Superfer 800 exposed to actual boiler environment at 700°C for 1500 hours.	356
Fig. 8.1:	Variation in Volumetric Erosion rate with change in temperature at 30° and 90° impact angles for (a) uncoated alloys and (b) Al ₂ O ₃ -3 wt% TiO ₂ coated alloys.	361
Fig. 8.2:	Bar charts showing cumulative weight gain (mg/cm ²) for the uncoated and coated alloys subjected to cyclic oxidation in air at 900°C for 50 cycles. (a) Uncoated Boiler steels (b) Coated Boiler steels (c) Uncoated Superalloys (d) Coated superalloys	364
Fig.8.3:	Bar charts showing cumulative weight gain (mg/cm ²) for the uncoated and coated alloys subjected to cyclic hot corrosion in Na ₂ SO ₄ -60%V ₂ O ₅ environment at 900°C for 50 cycles. (a) Uncoated Boiler steels (b) Coated Boiler steels (c) Uncoated Superalloys (d) Coated superalloys	365
Fig. 8.4:	Bar chart indicating the thickness lost in mm for the uncoated and Al ₂ O ₃ -3wt%TiO ₂ coated alloys after 1500 hours exposure to the coal fired boiler at 700°C.	366

LIST OF TABLES

Table No.	Title	Page No.
Table 2.1	Comparisons of different methods of thermal spray.	18
Table 2.2	Properties of Metal Oxides.	56
Table 2.3	Characterisation of coal gasification atmosphere at 1255 K.	65
Table 3.1	Chemical composition of the alloys used.	75
Table 3.2	Summary of Detonation Gun spray Equipment.	78
Table 3.3	Characteristics of Alumina-Titania Powder.	78
Table 3.4	Summary of Detonation Gun spray parameters.	78
Table 3.5	Erosion Test condition.	89
Table 3.6	Coal Analysis data.	94
Table 3.7	Chemical analysis of ash and flue gases inside the boiler.	94
Table 4.1	Coating Thickness and Porosity on coating surfaces for different specimens.	104
Table 6.1	Summary of the results for uncoated and coated alloys after high temperature cyclic oxidation in air at 900°C for 50 cycles.	282
Table 6.2	Summary of the results for uncoated and coated alloys after hot corrosion in an aggressive environment of molten salt (Na_2SO_4 -60% V_2O_5) at 900°C under cyclic conditions for 50 cycles.	284
Table 7.1	Summary of the results for uncoated and coated alloys after 1500 hours of exposure to superheater zone of the coal fired boiler at around 700°C.	348

LIST OF RESEARCH PUBLICATIONS

1. Sapra, P.K., Singh, S. and Prakash, S. (2009) "Detonation spray gun coatings against high temperature erosion in actual Boiler Environment", Int. J. of Materials and Product Technology (IJMPT) Vol. X, No. Y, pp.000-000.
2. Sapra, P.K., Singh, S., Prakash, S. and Arivazhagan, N. (2009) "Performance of Al_2O_3 -3% TiO_2 detonation gun coated ferritic steels in coal fired boiler", Int. J. Surface Science and Engineering, Vol. 3, No. 1/2, pp.145-156.
3. Sapra, P.K., Singh, S. and Prakash, S. (2008) "Evaluation of detonation gun sprayed alumina-titania coatings", Int. J. Surface Science and Engineering, Vol. 2, No. 5, pp.400-408.
4. Sapra Pawan Kumar, Singh Surendra, Prakash Satya, "Erosion-Corrosion Behaviour of Ni-based Superalloy Superni-600 in the Real Service Environment of the Boiler", International Journal of Microstructure and Materials Properties (IJMMP) (Under Review).
5. Sapra Pawan Kumar, Singh Surendra, Prakash Satya, "Elevated temperature erosion corrosion behavior of Superni-718 Superalloy in the Real Service Environment of a Boiler", Indian Journal of Engineering & Materials Sciences (Under Review).
6. Sapra Pawan Kumar, Singh Surendra, Prakash Satya, "High temperature solid particle erosion behaviour of Al_2O_3 -3 wt% TiO_2 coating produced by Detonation spray method on Fe-based superalloy." Wear (Communicated).
7. Sapra Pawan Kumar, Singh Surendra, Prakash Satya, Arivazhagan N "Performance of Fe-based Superalloy Supefer-800 in the Real Service Environment of the Boiler", International Symposium, 'Fundamental Corrosion Research in Progress' NACE Northern Area Eastern Conference "Minimizing Infrastructure Corrosion" October 26-28, 2008 Toronto, Ontario, Canada.
8. Sapra Pawan Kumar, Singh Surendra, Prakash Satya, Arivazhagan N, "High temperature erosion behavior of detonation gun-sprayed alumina-titania coatings under simulated coal-fired boiler atmospheres", (Paper No. iCAT 295) iCAT 2008: 2nd International conference on advanced Tribology 3rd - 5th December 2008, Singapore.

9. Sapra Pawan Kumar, Singh Surendra, Prakash Satya, "Elevated Temperature Erosion Response of Detonation Gun Sprayed coatings", (Abstract accepted) 4th World Tribology Congress (WTC IV), to be held from 6th - 11th September, 2009 in Kyoto, Japan.
10. Sapra Pawan Kumar, Singh Surendra, Prakash Satya, "Hot corrosion behavior of Alumina Titania coatings in molten sodium sulphate-vanadium pentoxide environment" Materials Science & Technology 2009, (Abstract Accepted) Symposium: Surface Protection for Enhanced Materials Performance, to be held from 10/25/2009 - 10/29/2009 at Pittsburgh, PA, USA.

ABBREVIATIONS

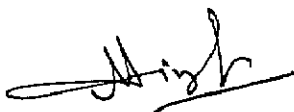
APS	Atmospheric Plasma Spray
BSEI	Back Scattered Electron Image
D-gun	Detonation Gun
EDX	Energy Dispersive X-ray Analysis
FBC	Fluidized Bed Combustor
hrs	Hours
Hv	Vickers Hardness
HVOF	High Velocity Oxy-Fuel
K_p	Parabolic Rate Constant
LPPS	Low Pressure Plasma Spray
m.p.	Melting Point
mpy	Mils per year
sec	Second
SEM	Scanning Electron Microscopy
T11	SA-213-T11 Boiler Steel
T22	SA-213-T22 Boiler Steel
VPS	Vacuum Plasma Spray
Wt%	Weight Percentage
Wt. Gain	Weight Gain
XRD	X-ray Diffraction

**Department of Metallurgical and Materials Engineering
Indian Institute of Technology Roorkee**

CERTIFICATE

Subject: Revision of PhD Thesis of Mr. Pawan Kumar Sapra

It is certified that all the revisions suggested by the examiners have been incorporated in the revised thesis, entitled “**STUDY OF DETONATION GUN COATED ALLOYS FOR RESISTANCE TO EROSION AND CORROSION**” by Mr. Pawan Kumar Sapra in partial fulfilment of the requirements for the award of the Degree of *Doctor of Philosophy*. The point wise replies of all the questions and comments made by the examiner have also been prepared separately as per the samples provided. The supervisors are fully satisfied with the revisions and the replies. The revised thesis is now resubmitted in the Department of Metallurgical and Materials Engineering of the Indian Institute of Technology Roorkee, Roorkee.



(Surendra Singh)

Supervisor

Associate Professor



(Satya Prakash)

Supervisor

Professor

Department of Metallurgical and Materials Engineering,

Indian Institute of Technology Roorkee,

Roorkee.

Date: 06-10-09

TITLE OF THE THESIS:

STUDY OF DETONATION GUN COATED ALLOYS FOR RESISTANCE TO EROSION AND CORROSION

The author sincerely thanks the examiners for the useful suggestions and the constructive comments. The Thesis has been thoroughly checked and corrections have been applied. Efforts have been made to bring the revised thesis as per the comments suggested by the examiner.

ANSWERS TO QUERIES OF REVIEWER 1

POINT BY POINT RESPONSE TO THE EXAMINERS COMMENTS	
Query 1	The rationale of the choice of the molten salt environment (Na_2SO_4 -60% V_2O_5) needs an explanation. Vanadium compounds are impurities in oil, not in coal.
Ans	Yes, Vanadium compounds are mostly present in the oils but they are also reported to be present in coal and coal burning environments (Ref. 1-7 attached). Vanadium is present typically at a concentration between 14 and 56 ppm (mg/kg) (Ref. 5). This molten salt environment has been chosen to make the testing conditions most severe.
Query 2	The choice of Ceramic coating (Al_2O_3 -3% TiO_2) also needs to be justified since its application on boiler tubes may hamper heat transfer.
Ans	Al_2O_3 - TiO_2 coatings are conventionally used for wear prevention applications and the present study was undertaken to study the high temperature erosion corrosion performance of these coatings. Yes there will be some loss of heat transfer but the tube life will be tremendously increased as this coating is withstanding the erosion and hot corrosion at laboratory level as well as in actual working conditions.
Query 3	Rapp, 1986 mentioned on p.71 should be Rapp 1981. The reference Barbooti et al 1988 mentioned on this page does not appear in the list of references
Ans	Rapp 1986 has been corrected to Rapp 1981 on page 71 and Barbooti et al 1988 reference has been included which was earlier left as a mistake.
Query 4	Page 93, The samples were hanged should read as "The Samples were hung"
Ans	Page 93, The samples were hanged has been changed to "The Samples were hung"
Query 5	Page 97 and 98 are missing
Ans	The pages 97 and 98 have been incorporated and have been checked in all the copies of the thesis which could have been left by mistake while binding the Thesis.
Query 6	The Microstructure of T11 and T22 steel shown on p. 99 show ferrite and pearlite, the structure expected in these materials and not bainite as mentioned on p 118. To avoid any confusion, higher magnification may be used.
Ans	Bainite was written by mistake and it has been corrected to pearlite at p 118. As per suggestion Higher Magnification Microstructure has also been incorporated at p 99.

Query 7	In oxidation studies the terms mass change and mass gain are preferred to weight change and weight gain
Ans	Yes, it should have been better to use mass change instead of weight gain. Here in our studies we have not taken absolute values instead difference is taken. Also few reviewers of manuscripts had suggested to use weight change in earlier publications.
Query 8	EDX gives elemental analysis, but throughout the thesis %oxides are shown alongside the SEM figures (for example, Fig. 7.8), the oxides are listed under the caption 'Elements'. These are serious mistakes.
Ans	It is agreed that EDX gives only elemental analysis. Writing Elements over the oxide was a mistake which has been corrected. The conversion to oxide is done by software and it only gives the idea regarding the approximate contents of the oxides. The figures with the elemental composition have been incorporated.
Query 9	In the discussion on the mechanism of hot corrosion , the formation of alkali pyrosulphate and trisulphates, their fluxing role and their reaction with the substrate producing FeS, Fe ₂ O ₃ and alkali sulphates should be incorporated (ASM Metals Handbook, 9 th Ed. Vol 13, p 985). Apart from catalyzing the oxidation reaction, the molten salt plays a role in the dissolution or slag type of attack of the substrate.
Ans	As per suggestions, in discussion part on Mechanism of Hot corrosion the formation of alkali pyrosulphate and trisulphates, their fluxing role and their reaction with the substrate producing FeS, Fe ₂ O ₃ and alalkali sulphates has been incorporated at p289.
Query 10	The oxidation/hot corrosion of coated samples shows step-wise progress (Figs 6.22, 6.24, 6.62, 6.64). This invariably depicts oxidation under the condition of periodic cracking of scale. Quite expectedly, the parabolic relationship has not been exhibited. An explanation for this behavior may be found on pp. 304-306 of Ref 30.
Ans	The Figures 6.22, 6.24, 6.62 and 6.64 do not represent exact parabolic relationship as pointed out, however, experimentally no evidence of cracking of the scale was found. The increments in weight gain shown in figures are of minor magnitude. Total weight gain was very less. When data of coated alloy is superimposed on the data of uncoated alloy, the discrepancy is clearly resolved as shown in the following graph (Fig.1).

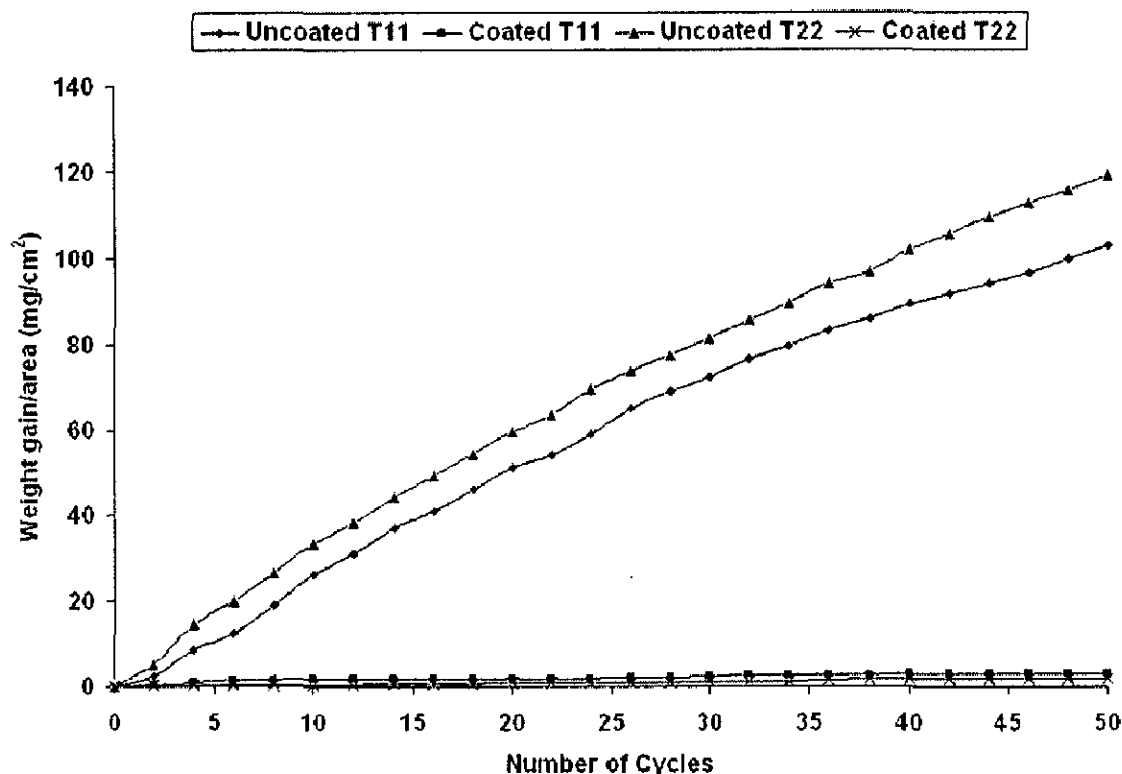


Fig.1. Weight gain plot for uncoated and Al_2O_3 - 3 wt% TiO_2 coated boiler steels T11 and T22 exposed to air at 900°C for 50cycles.

References:

1. A. G. Sykes, *Advances in Inorganic Chemistry*, 1990, Academic Press, INC, California, v. 35, p 98
2. B.V. Venkataraman and S. Sudha, 2005, "Vanadium Toxicity" *Asian J. Exp. Sci.*, Vol. 19, No. 2, 127-134
3. Chemical Profile: Vanadium: How is vanadium released by electric power plants? <http://mydocs.epri.com/docs/public/000000000001014635.pdf>
4. Helmut Sigel, Astrid Sigel, 1995, "Vanadium and its role in life", Marcel Dekker, Inc, New York, vol 31, p 634
5. M. Costigan, R. Cary, S. Dobson, "Vanadium pentoxide and other inorganic vanadium compounds" *Concise International Chemical Assessment Document 29*, p. 9. www.inchem.org/documents/cicads/cicads/cicad29.htm
6. Sang-Rin Lee, Chang-Yu Wu, 2002, Study of vanadium emission control in combustion systems by thermodynamic equilibrium analyses, *Advances in Environmental Research* Vol.7, pp.1-10
7. V. M. Goldschmidt, "Rare Elements in Coal Ashes", *Industrial and Engineering Chemistry*, Vol. 27, No. 9, pp. 1100-1102.

ANSWERS TO QUERIES OF REVIEWER 2

POINT BY POINT RESPONSE TO THE EXAMINERS COMMENTS	
MINOR COMMENTS	
Query 1	There are few typographical errors (e.g. in equation 13)
Ans	The Correction has been incorporated at page 60.
Query 2	Very occasionally a further result would have been useful, e.g. in Fig. 6.60 (p259) (& see p296), no sulphur analysis picture is given for hot corrosion in sulphate vandate salt mixture
Ans	In the mentioned figures Sulphur was not detected by the mapping so was not incorporated.
Query 3	A non academic comment; This Thesis binding created a considerable curvature when opened, making the paper hard to read. They could not be made flat
Ans	Curvature in the thesis binding may be due to considerably large number of pages (more than 400).

INTRODUCTION

Thermal spraying is a process in which materials are heated to a molten or nearly molten condition and are sprayed onto a surface to form a coating. Materials can be heated by combustion of fuel gases (similar to welding) or by using electricity. Thermal spray coatings have been widely applied to diminish the effects of erosion-oxidation in industrial environments. In this deposition technique, droplets of molten or semi-molten material are generated and projected at a surface to form a coating. All most all materials ranging from polymers through to metals, cermets and ceramics are routinely sprayed by this technique. Thermal spraying processes have been widely used for many years throughout all the major engineering industry sectors for component protection and reclamation. Recent equipment and process developments have improved the quality and expanded the potential application range for thermally sprayed coatings.

Erosion-Corrosion is a phenomenon where the combined effect of each degradation mechanism generates more extensive mass loss than the sum of each mechanism acting individually. Degradation in this manner occurs in applications associated with fluidised bed combustion and those utilizing turbines for power generation and propulsion in thermal power station

The existing coal power plants are typically 35 percent efficient, and operate at steam temperatures below 600°C. The materials used in these existing plants do not have the high-temperature strength and corrosion properties required for high temperature operation. By developing improved materials systems that can withstand higher temperatures, pulverized coal power plant efficiencies of up to 47 percent are possible. These efficiency gains, alone, would cut the release of carbon dioxide and other emissions by nearly 30 percent (Hack and Stanko, 2007). The efficiency of power plants is a strong function of the steam temperature and pressure. Research to increase both is being pursued worldwide and ultra supercritical boilers are being developed which can operate at higher temperatures. The main enabling technology in achieving the above goals has been the development of stronger high-temperature materials and the use of protective coatings (Viswanathan et al., 2006). Iron, nickel- and cobalt- base superalloys are the commercial alloys commonly used for the manufacture of components used in aggressive environments of gas turbines, steam boilers

etc. Superalloys have been developed which have strength as well as can withstand the higher temperatures and pressures present in the superheaters of advanced/supercritical boilers but they have proved to be especially susceptible to corrosion by certain coals, fuels etc most notably high-sulfur bituminous coals. The cause of this type of corrosion is generally accepted to be the presence of liquid alkali iron trisulfates on the surface of the superheater and reheater tubes beneath an overlying ash deposit. (Blough et al., 1999). During the operation of a steam boiler in thermal power plants, the evaporated salt in air will deposit directly on materials at elevated temperature, or will mix with other ash constituents and deposit onto the surface of different components, resulting in severe corrosion attack by oxidation, sulfidation and hot corrosion. It has been reported that the corrosion loss of different alloys (Fe-Ni-Cr) in the presence of salts like NaCl, Na₂SO₄ at high temperatures is 30 to 120 times higher than that without presence of salts. Coal ash corrosion is a widespread problem for superheater and reheater tubes, especially where high-sulfur, high-alkali, and high-chlorine coals are used, and is a critical problem that needs to be resolved. Approaches to solving this problem have included changing the fuel or providing protective baffling with sheaths of corrosion resistant material around selected tubes. To avoid surface attack on superalloys due to the presence of reactive alloying elements including oxidation, hot corrosion, and thermal fatigue in the most demanding applications, such as turbine blade and vanes, superalloys are often coated to improve environmental resistance. This will require protective coatings or claddings applied by various means, such as weld overlaying, laser cladding, and various forms of thermal spraying. In response to present corrosion problems, various promising coating compositions and application techniques are under development (Hack and Stanko, 2007).

Power plants are one of the major industries suffering from severe erosion and corrosion resulting in substantial losses. Major cause of premature Boiler tube failures is both hot corrosion and Erosion caused by the impact, cutting action and abrasive wear of fly ash entrained flue gases undercutting the area they strike. Maintenance cost for replacing broken tubes in some installations is very high and can be estimated at upto 54% of total production cost (Hidalgo et al 2001). In coal fired power generation, low grade fuels with sulphur, vanadium and sodium are often used. During the combustion of these low grade fuels, alkali metal sulphates and V₂O₅ vapours combine with other ash constituents and deposit onto comparatively cooler components which results in severe corrosion attack by oxidation, sulphidation, chloridation and hot corrosion. Also in boilers when sodium chloride from air/water mixes with Na₂SO₄ from the fuel and deposits on hot section components, leading to

accelerated attack of the alloy substrate. This accelerated attack often increases the corrosion loss of heat resisting alloys by over a hundred times. The performance of steels and different alloys in oxidising environment is well established but its behaviour in corrosive environments at high temperature particularly those containing sulphides, chlorides has not been studied extensively.

Corrosion of metals have received maximum attention of researchers and engineers in the field of environmental degradation of metals (Chatterjee et al, 2001). Boilers are used to burn pulverized coal, biomass and/or waste. Inside the boiler, there is a tubing system, including water and steam. The tubing is heated by the flame of the burning material. The tubes carry the steam under high pressure and are subjected from the outside to erosive and hot-corrosive wear resulting from ash and all products of burning (Kay, 1987).

A global issue exists in material selection for boiler tubes and different components in boilers and turbines. So the materials selection at elevated temperature and the corrosion and erosion behaviour of material employed in boilers and turbines is becoming an increasingly important issue for modern thermal power plants.

Corrosion may be defined as the deterioration of the materials by their reaction with surrounding and the rate increases with increase in temperature known as hot corrosion. Hot corrosion is an accelerated oxidation of material at elevated temperatures, induced by a thin film of fused salt deposits. In hot corrosion, metals and alloys are subjected to degradation at much higher rates than in gaseous oxidation, with porous non-protective oxide scale formed at the surface and sulphides permeating into the substrate. Hot corrosion is a serious problem in power generation equipments and in other energy conversion and chemical process systems.

It is believed that condensed alkali metal salts notably Na_2SO_4 , are a prerequisite to hot corrosion (Otero et al, 1992). The source of these salts may be:

- a) The direct ingestion of sea salt in a marine environment.
- b) Formation of Na_2SO_4 during the combustion of fuels containing both sodium and sulphur.
- c) The formation of (Na_2SO_4), during combustion from sodium contaminated airborne dust and sulphur in the fuel.

In energy generation processes the mechanism of hot corrosion is dependent on the formation of a liquid phase that is predominantly Na_2SO_4 or K_2SO_4 . The sulphur released from the coal, forms SO_2 with a minor amount of SO_3 and reacts with the volatilised alkalis to form Na_2SO_4 vapour, which then condenses together with fly ash on the superheater and

reheater tubes in the boiler. Such a liquid phase dissolves the chromium oxide in the protective coating, which allows the base metal to react with sulphate ions to form sulphide ions and non protective oxides (Natesan, 1976 and Rapp et al, 1981). Sulphur from fuel reacts with NaCl from ingested air during combustion in the combustor to form sodium sulphate which gets deposited on hot sections of turbine components resulting in accelerated oxidation attack. Sulphur in the fuel is generally limited to 0.3 wt% for commercial jet engines and to 1.0 wt% for marine gas turbines. NaCl comes from seawater.

High Corrosion resistance is required for high temperature materials, in addition to excellent mechanical properties; high temperature strength, good creep resistance and microstructure stability. However all these requirements can not be fulfilled by alloy development alone. So an alternate approach of surface coatings or surface treatments is commonly used. The ability of coatings to resist surface degradation over extended periods is an important contributor in safeguarding the capital investment in the structure of a vessel. Protective coatings are the first line of defense against the erosive corrosive environment. Coatings mainly serve to minimize the rate of degradation.

Erosion is a generalised wear mechanism whereby mass loss occurs through impact of discrete particles entrained in a fluid stream. According to ASTM standard G76-95, Erosion is the progressive loss of original material from a solid surface due to mechanical interaction between that surface and a fluid, a multi-component fluid, or impinging liquid or solid particles.

In coal-fired boilers, fluidized beds, and gas turbines; solid particles are produced during the combustion of heavy oils, synthetic fuels, and pulverized coal and causes erosion of materials (Zhang et al, 2000). Particle erosion has become an increasingly important material property, particularly in the field of alternative energy technology (Soderberg et al, 1981). One of the most serious problems associated with fluidized bed combustors (FBC) technology is the material loss of the combustor wall and the in-bed tubes.

Boilers and other steam power plant equipments suffer severe erosion and corrosion problems resulting in substantial losses (Prakash et al, 2001). Erosion problems contribute significantly towards partial unavailability of power in India Krishnamoorthy et al (1993). The data covering one-year duration for the boiler tube failure in the coal fired power plant in north western region of India indicates that out of the 89 number of failures, 62 failures were attributed to the erosion-corrosion by fly ash. Moreover fly ash content of the Indian coal is very high and causes severe erosion-corrosion of the materials in the power plants. In view of the high losses due to erosion-corrosion it becomes imperative to develop better

defence against such degradation by exploring newer erosion-corrosion resistant materials for the industrial applications.

The presence of fly ash and combustion gases constitutes an extreme environment, and erosion, erosion-corrosion and hot corrosion is inevitable when alloys are used at high temperatures for long periods of time (Goebel et al, 1973, Tabakoff, 1995 and Kamaraj, 2003). To improve the oxidation and corrosion resistance of alloys and to increase the service life of components at high temperatures, two approaches have been employed, adding fair amounts of Al, Cr, and Ti, and small amounts of Y, Zr and Hf to the alloy, which help to improve oxidation and corrosion resistance. Another method is coating the alloy with a protective layer using various surface treatment techniques (Wang et al, 1989). Wear and corrosion resistance of components can be greatly increased by protective coatings and this is a growing industry of considerable economic importance (Hocking, 1993).

Different surface modifications techniques like electroplating, cladding, hot dipping, and thermal spraying are used. Among these techniques the thermal spraying has grown into a well accepted industrial technology. Thermal spraying is the common name for vast gallery of techniques for coating deposition. Thermal spraying processes can be distinguished depending on the type of heat source, the gases or fuels used, and the form of precursor material fed into the source. Developments in thermal spraying as well as advances in powder and wire production have resulted in coatings with excellent properties under service conditions. So of all the available coating techniques thermal spraying is most significant because wide variety of materials can be used to produce coatings. In depositing high quality coatings advancement in technologies for deposition are needed and are being developed. The principle of formation of coatings is similar in thermal spraying techniques. The material to be deposited is melted by heat source and propelled towards the surface being coated, where they impact, flatten and solidify. To form a dense coating covering which is closely bonded to a substrate, high velocity of powders which are to be deposited is needed. Detonation Gun process is used for the deposition purpose in the present investigation. This process is used to accommodate the density and the accuracy requirement and cost. Detonation sprayed coatings get a denser microstructure and their surface hardness and adhesion strength are usually higher. On the basis of feasibility and other requirements of thermal spray coatings for protection against hot corrosion and erosion. Porosity is an important property, which influences considerably the characteristics of deposits. An important advantage of D-gun sprayed coatings is their low porosity. Porosity in the coatings is of great relevance especially in erosion. The porosities of D-gun coatings are very small:

the reported value lies between 0.5 % to 2 % (Tucker, 1982, Stachowiak and Batchelor, 2001). Detonation gun technique was proposed for the study. In past detonation technique has not been used as widely as HVOF and plasma spray.

Previous studies have pointed out the use of alumina and titania based coatings for the purpose of erosion and wear resistance and the studies have revealed that these have excellent wear and erosion resistance. There has been little literature available on oxidation or high temperature behaviour of salt mixture accelerated corrosion related to alumina and titania based coatings on boiler steels and superalloys. Previous studies have been performed at low temperatures and in environment free from salts and halogen and sulphur containing environments.

The objective of this research is to investigate experimentally the erosion corrosion behaviour of Detonation gun sprayed coatings on boiler steels and superalloys in air, molten salt (Na_2SO_4 -60% V_2O_5) and in actual working conditions of coal fired boilers of a thermal power plant. The erosion performance has been evaluated at room temperature as well as at elevated temperature. Behaviour of these coatings under different degrading environments once evaluated are compared to arrive at the best coating for given environment and temperature.

LITERATURE REVIEW

This chapter contains a critical review of the existing literature on thermal spraying along with the thermal spray techniques most commonly utilized in the deposition of coatings, erosion and erosion-corrosion behaviour of metals, alloys and protective coatings; including a comprehensive review of the behaviour of some metals, alloys and protective coatings are also included in this chapter.

2.1 THERMAL SPRAYING – AN INTRODUCTION

Surface coatings and treatments have been used to reduce material loss of components in various applications (Rogers, 1995). Thermal spraying is in general similar to welding where added material is fused to the base through a metallurgical bond, although in thermal spray coatings, the deposits adhere to the substrate mostly by mechanical interlocking.

Thermal Spray is a generic term for group of coating processes used to apply metallic or nonmetallic coatings. In Thermal spraying technique, droplets of molten or partially molten material are generated and projected at a surface to form a coating. The droplets undergo little interaction with the substrate, merely adhering to the roughened surface through physical means to form a coating. A variety of techniques falls in this category, varying in the manner in which they heat the material, the operating temperature and the velocity to which the droplets are accelerated. Through the range of operating conditions generated, any material that does not undergo sublimation or degradation upon heating can be applied as a coating. Extremely wide variety of materials ranging from polymers through to metals, cermets and ceramics are routinely sprayed (Tucker, 1994).

In this process, the coating material in the form of rod, wire or powder is fed into a high temperature heat source, where it is heated close to, or in excess of, its melting temperature. A high velocity accelerating gas or combustion gas stream accelerates the droplets of material to the substrate, where they impact and spread across the surface to form a “splat”, Fig. 2.1. The splat material deforms to match the surface topography, forming mechanical interlocking bonds as it undergoes rapid solidification (10^6 K/s).

The coating is built up by multiple particle impacts to form the fundamental heterogeneous microstructure characteristic of this technique. Due to heat and impact, the

particles flatten in the form of thin platelets and bind together with the substrate. These layers of flattened particles act as a protective coating. (Smith and Knight, 1995).

Droplets reach a variety of states prior to deposition due to the complex interaction of the heat source, velocity profiles, and particle thermal and mechanical properties. Oxidation can occur in-flight around the particle periphery, such features forming “stringers” of oxide around the deformed splats in the coating. Similarly, melting of the particles may contribute to phase dissolution in multiphase materials. Rapid solidification generates non equilibrium metastable phases and amorphous structures in the splats. Conversely particles that are not sufficiently molten do not deform significantly upon impact, potentially generating voids and porosity within the coating. The extent to which the material phases in the powder are retained in the coating, and the coating density, are critically dependent upon the deposition technique and spray parameters. The highest quality coatings are generated by high velocity particles (minimisation of exposure time to oxidation and high degree of deformation upon impact to minimise porosity), heated to a low temperature sufficient for deformation and spreading upon impact (Knight and Smith, 1998).

2.2 THERMAL SPRAYING PROCESSES

There are several thermal spraying processes. Most important and general components in these processes are as follows:

- Gun (melting of particle and accelerating towards substrate)
- Control unit (combustible gas control console or electric power control)
- Coating material (wire or powder) feeding mechanism

The various thermal spray processes are broadly classified into three categories based on their method of heating - combustion, plasma, and electric arc. Each of these categories encompasses a range of different methods, Fig. 2.2

2.2.1 Electric Arc Processes

In arc spray process, two wires are simultaneously brought into contact with each other at the nozzle. The electrical load wire causes the tips of the wires to melt when they touch. An atomizing gas such as air or nitrogen is used to strip the molten material off the wires and to transport it onto the work piece. Arc spraying is reasonably inexpensive and readily usable in the field. Low particle velocities enable maximum coating thickness for a given material (Thorpe, 1993).

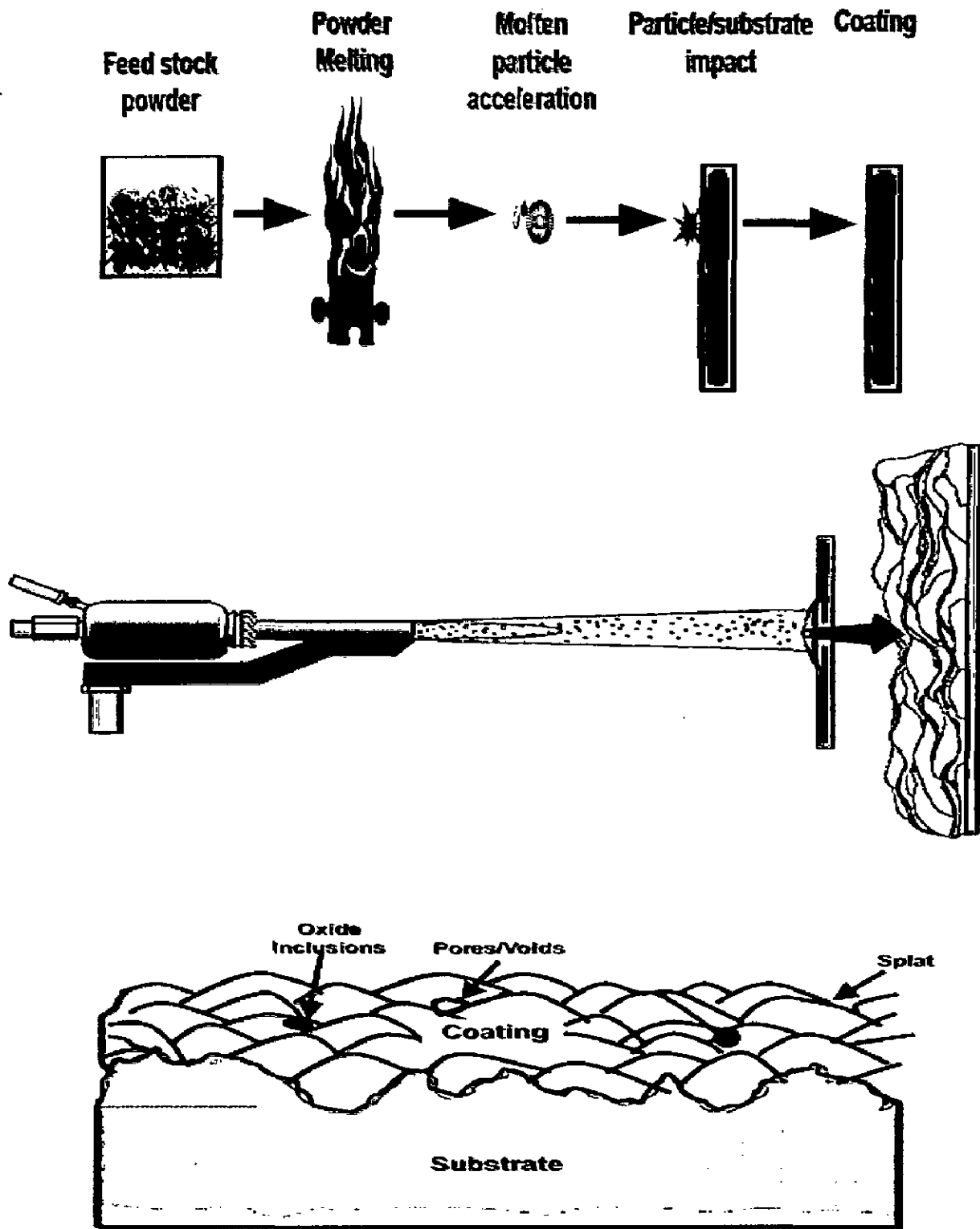


Fig. 2.1: Schematic development of the thermal spray process and mechanism of coating build-up (Engineering Manual 1110-2-3401, 1999).

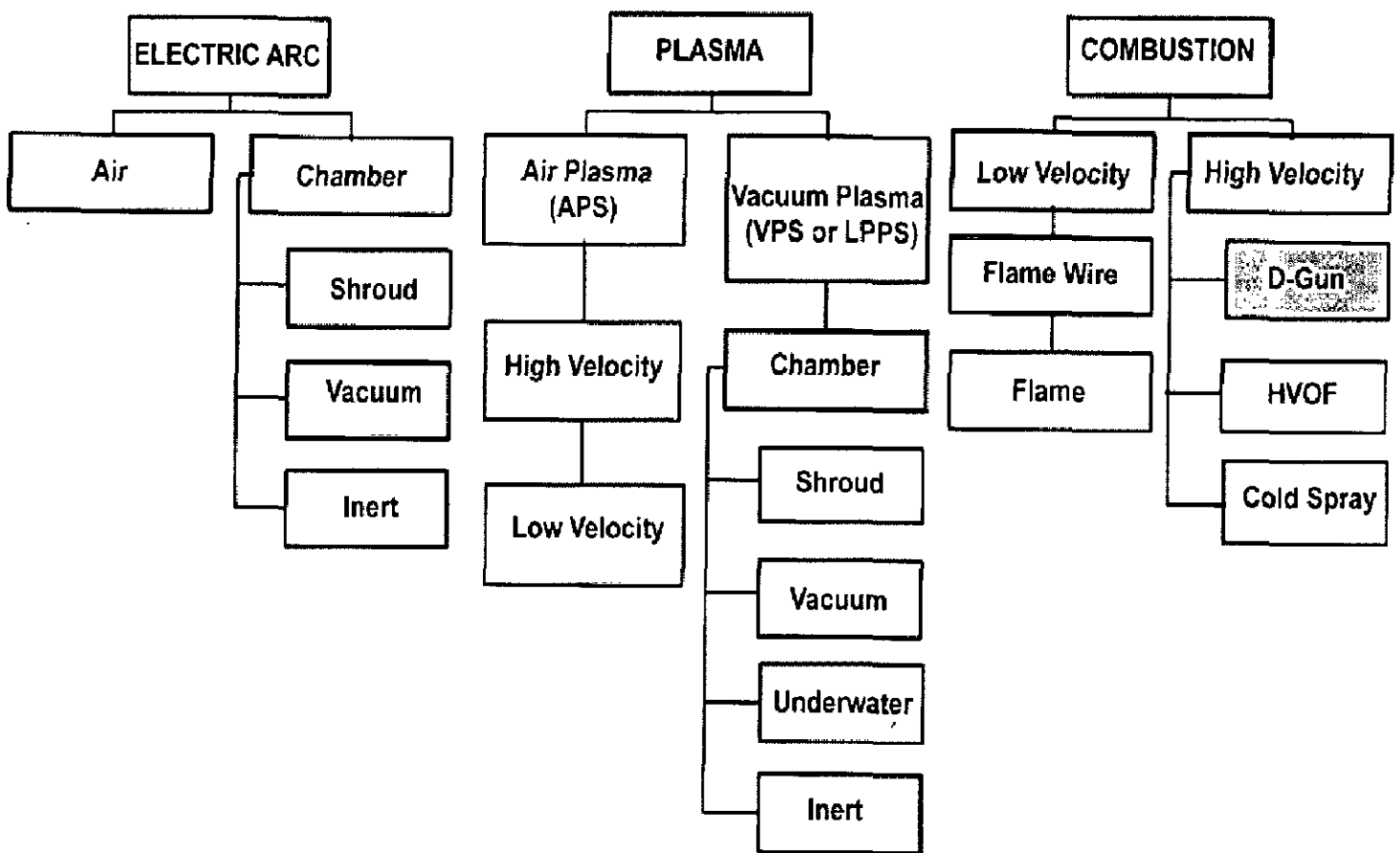


Fig. 2.2: Summary of significant thermal spray techniques (Smith, 1995).

Energy costs are lower and production rates are higher than they are with competing methods such as wire flame spray. Arc spraying may be used to apply electrically conductive materials including metals, alloys, and metal-metal oxide mixtures. Fig.2.3 shows a typical arc spray system comprised of a DC power supply, insulated power cables, a wire feed system, a compressed-air supply, controls, and an arc spray gun. Coating quality and properties can be controlled by varying the atomization pressure, air nozzle shape, power, wire feed rate, traverse speed, and standoff distance.

In Electric Arc spraying thermal spraying process, a DC electric arc is struck between two continuous consumable wire electrodes which form the spray material. Compressed gas (usually air) atomises the molten spray material into fine droplets and propels them towards the substrate. The process is simple to operate and can be used either manually or in an automated manner (Budinski, 1988; Davis, 2004).

2.2.2 Plasma Spray Processes

The process of spraying with the use of plasma has been patented by Gage et al. (1962), as well as by Giannini and Ducati (1960). The plasma spraying process uses a DC electric arc to generate a stream of high temperature ionised plasma gas, which acts as the spraying heat source. The arc is struck between two non-consumable electrodes, a tungsten cathode and a copper anode within the torch as shown in Fig. 2.4. The torch is fed with a continuous flow of inert gas, which is ionised by the DC arc, and is compressed and accelerated by the torch nozzle so that it issues from the torch as a high velocity (in excess of 2000 m/sec), high temperature (12000-16000 K) plasma jet (Thorpe, 1993). The coating material, in powder form, is carried in an inert gas stream into the plasma jet where it is heated and propelled towards the substrate. Because of the high temperature and high thermal energy of the plasma jet, materials with high melting points can be sprayed. The Plasma Spray Process is basically the spraying of molten or heat softened material onto a surface to provide a coating. Material in the form of powder is injected into a very high temperature plasma flame, where it is rapidly heated and accelerated to a high velocity. The hot material impacts on the substrate surface and rapidly cools forming a coating. Plasma spraying is used to apply surfacing materials that melt at very high temperatures.

The plasma spray process is most commonly used in normal atmospheric conditions referred as APS. Some plasma spraying is conducted in protective environments using chambers normally back filled with a protective gas at low pressure; this is referred as LPPS. Plasma spraying has the advantage that it can spray very high melting point

materials such as refractory metals like tungsten and ceramics like zirconia unlike combustion processes. Plasma sprayed coatings are generally much denser, stronger and cleaner than the other thermal spray processes with the exception of HVOF and detonation processes. Disadvantages of the plasma spray process are relative high cost and complexity of process (Heiman, 1996; Pawlowski, 1995; Davis, 2004).

2.2.3 Combustion Spray Processes

Combustion spraying uses the heat of combustion of a fuel gas (usually acetylene or propane) and oxygen mixture to melt the coating material, which can be fed into the spraying gun in two forms, either powder or solid wire/rod.

The process relies on the chemical reaction between oxygen and a fuel of combustion to produce a heat source. This heat source creates a gas stream with a temperature in excess of 3,000°C with correctly balanced conditions between oxygen and acetylene. The feed stock material to be sprayed is fed into the flame in the form of a wire or powder and compressed air is then used to atomise the molten metal and accelerate the particles onto the substrate. Combustion flame spraying uses either powder, wire or rod as the feedstock material and has found widespread usage around the world for its relative simplicity and cost effectiveness (Pawlowski, 1995; Davis, 2004).

2.2.3.1 Low Velocity Combustion spray process

The oldest form of thermal spray, flame spraying, may be used to apply a wide variety of feedstock materials including metal wires, ceramic rods, and metallic and nonmetallic powders. In flame spraying, the feedstock material is fed continuously to the tip of the spray gun where it is melted in a fuel gas flame and propelled to the substrate in a stream of atomizing gas. Common fuel gases are acetylene, propane, and methyl acetylene-propadiene. Air is typically used as the atomization gas. Oxyacetylene flames are used extensively for wire flame spraying because of the degree of control and the high temperatures offered by these gases. By gauging its appearance, the flame can be easily adjusted to be an oxidizing, neutral, or reducing flame. The lower temperature propane flame can be used for lower melting metals such as aluminum and zinc as well as polymer feedstocks. The basic components of a flame spray system include the flame spray gun, feedstock material feeding mechanism, oxygen and fuel gases with flowmeters and pressure regulator air compressor and regulator. The two consumable types give rise to the two processes powder flame spraying and wire flame spraying.

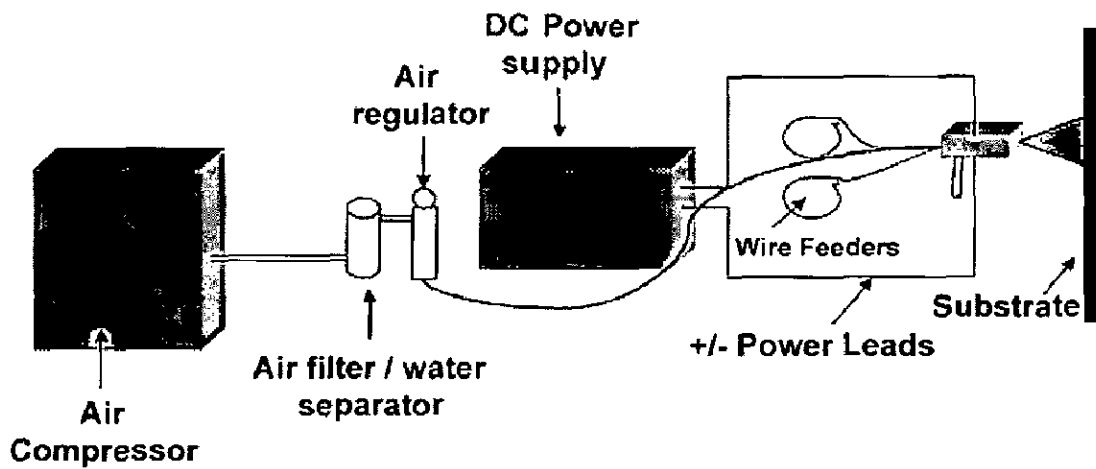


Fig. 2.3: Typical two wire arc spray system

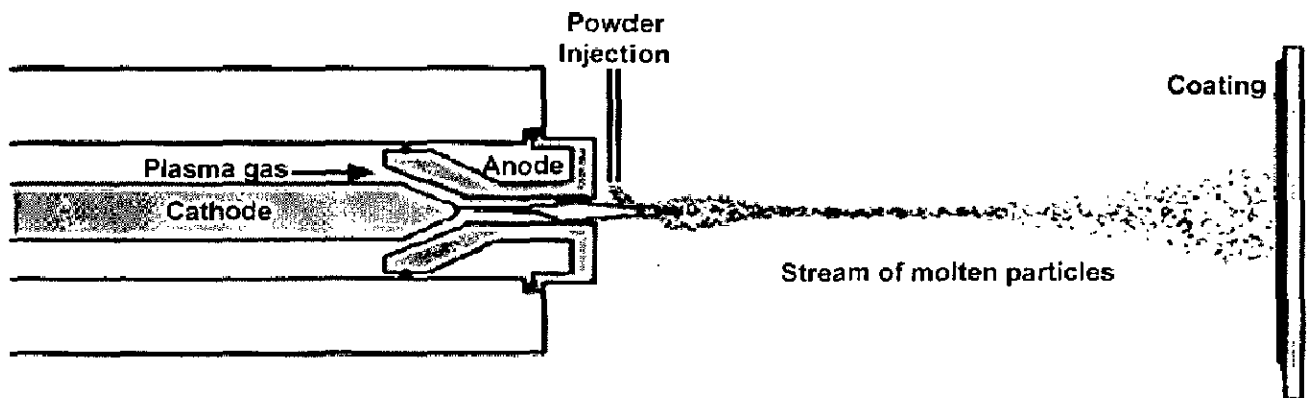


Fig. 2.4: Schematic Diagram of the Plasma spray Process

2.2.3.2 High Velocity Combustion spray process

One of the newest methods of thermal spray, High Velocity Oxy-Fuel (HVOF) Process utilizes oxygen and a fuel gas at high pressure. It was developed in late seventies and early eighties. Typical fuel gases are propane, propylene, and hydrogen. The burning gas mixture is accelerated to supersonic speeds, and a powdered feedstock is injected into the flame. The burning is continuous in this process. The schematic Diagram of the HVOF Process is shown in Fig. 2.5. The process minimizes thermal input and maximizes particle kinetic energy to produce coatings that are very dense, with low porosity and high bond strength. HVOF systems are field portable but are primarily used in fabrication shops. HVOF has been used extensively to apply wear resistant coatings for applications such as jet engine components (Bunshah, 1994; Pawlowski, 1995; Davis, 2004).

2.2.3.3 Cold Spraying

The Cold Spray or cold gas-dynamic spraying process is the next progressive step in the development of high kinetic energy coating processes. The cold-gas spraying method was developed in Novosibirsk, Russia at the end of the 1980s by Alkhimov et al. (1990). Similar in principle to the other thermal spray methods, it follows the trend of increasing particle spray velocity and reducing particle temperature as with the HVOF/HVAF processes, but to a more extreme level that it could be asked whether the process fits under the description of thermal spray. A typical cold-spraying system is shown schematically in Fig. 2.6. The Cold Spray process basically uses the energy stored in high pressure compressed gas to propel fine powder particles at very high velocities (500 - 1500 m/s). Compressed gas (usually helium) is fed via a heating unit to the gun where the gas exits through a specially designed nozzle (laval type mostly) at very high velocity. Compressed gas is also fed via a high pressure powder feeder to introduce powder material into the high velocity gas jet. The powder particles are accelerated and moderately heated to a certain velocity and temperature where on impact with a substrate they deform and bond to form a coating (Stoltenhoff, 2002).

2.2.3.4 Detonation Gun (D-Gun) Spraying

Detonation gun (D-gun) coating is a relatively new technology ejecting the melting or semi-melting state powder heated by the combustion of acetylene and oxygen to the surface of working piece at a high speed $500-1200 \text{ ms}^{-1}$. The high active energy makes the powder closely conjoint the surface and forms a layer with high strength, high hardness and good wear resistance. This technology has been widely used in many fields such as aviation, space flight, petroleum, metallurgy and machinery industry (Murakami et al., 1989).

The D-gun process was developed by Union Carbide (Poorman et al., 1955) in the early 1950s and D-gun™ sprayed coatings are available through the coating service of this organization. The detonation-gun process was also developed in the 1960s at the Paton Institute in Kiev (Ukraine) (Borisov et al., 1990; Kadyrov, 1988).

The D-Gun shown schematically in Fig. 2.7 consists of a water cooled barrel approximately one meter long, with an internal diameter of 25 mm (Pawlowski, 1995). Mixture of combustion gases, oxygen and acetylene are injected into the barrel, along with a “charge” of powder entrained in a carrier gas. A spark plug is used to ignite the mixture of gases, generating a detonation wave that reaches a maximum temperature of 4500 K and speeds in excess of 2900 m/s. The entrained powder is heated and accelerated to speeds of 750-800 m/s in the D-Gun and 900 m/s in the Super D-Gun processes respectively. The barrel is purged with nitrogen prior to the next firing, which occurs 1-15 times per second (Pawlowski, 1995; Sturgeon 1993). Each shot of powder generates a circular disc of material on the substrate, made up of multiple overlapping splats. Successive firings overlap the discs of deposited material to build up the coating. By confining the powder and combustion gases within the nozzle, air entrapment is minimised, resulting in low oxide content coatings. The high powder velocities generate significant particle deformation on impact, minimising porosity and resulting in high bond strengths. The detonation process consists of four steps: In first step, oxygen and fuel are injected into the combustion chamber; then injection of powder and nitrogen to prevent ‘backfiring’; then ignition of mixture and acceleration of powder; and finally purging of barrel by nitrogen.

2.2.3.4.1. Process parameters

In D-gun spraying, mixture of a fuel gas, usually H₂ or hydrocarbons, such as acetylene (C₂H₂), propane (C₃H₈) and butane (C₄H₁₀), with oxygen (O₂) is used as working gas. The composition giving the maximum temperature of 4500K corresponds to oxygen with 45 vol.% of acetylene (Tucker, 1982). The wave generated by detonation may attain a velocity of 2930 m/s (Smith, 1974) while the velocity of the particles reportedly reached 750 m/s in the D-gun™ and 1000 m/s in the ‘Super D-gun™’ (Irving et al., 1993). Kadyrov and Kadyrov, (1995) report velocities varying between 1000 and 3000 m/s. The barrel used in D-gun is circular with the length is in the range 450-1350mm and the diameter 21-25mm. The Firing rate is in the range 1-15 Hz. The Powder Particle sizes are usually in the range 5-60 µm. The Powder feed rate is in the range 16-40 g/min (Borisov et al., 1990). The Spray distance is reported to be about 100mm (Schwarz, 1980). The spray atmosphere is air in this process.

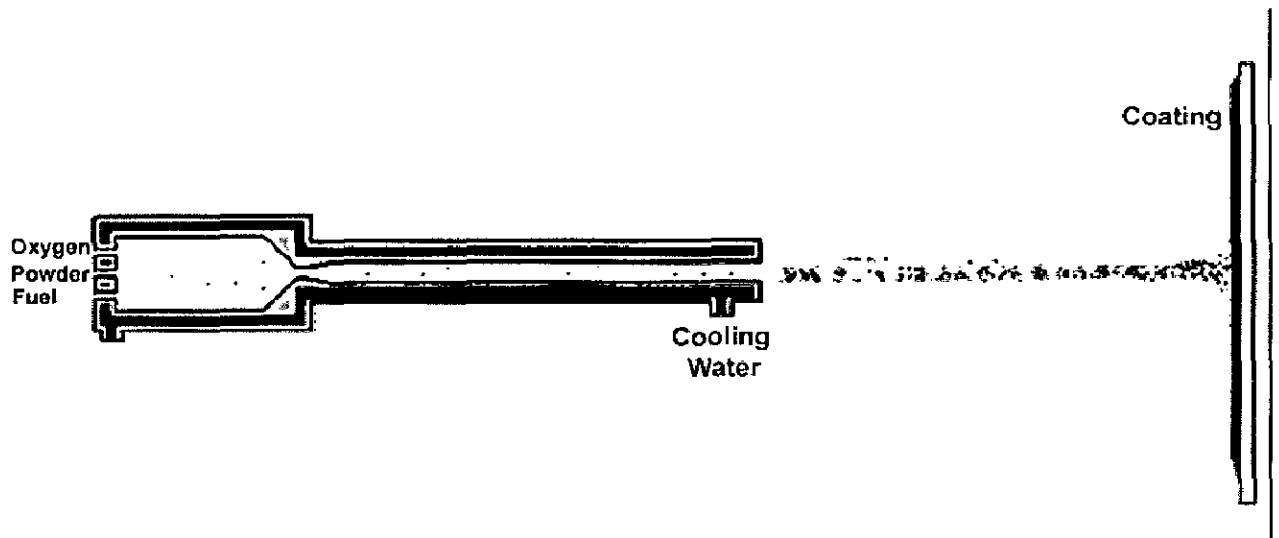


Fig. 2.5: Schematic Diagram of the HVOF Process

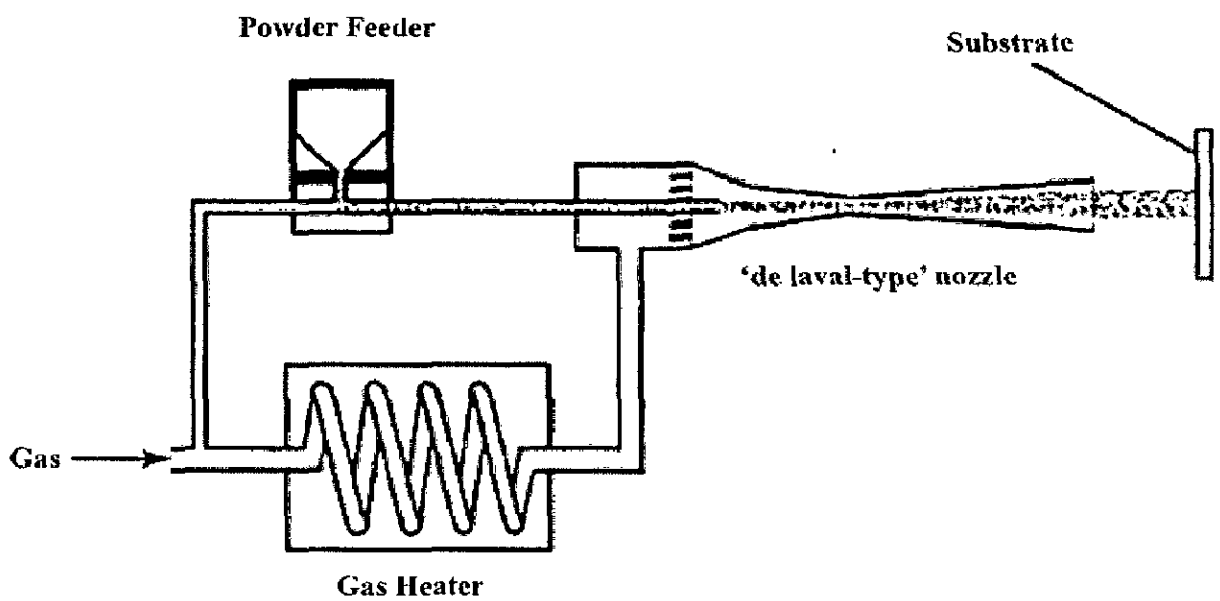


Fig. 2.6: Schematic of Cold Spraying Process (Stoltenhoff et al., 2002).

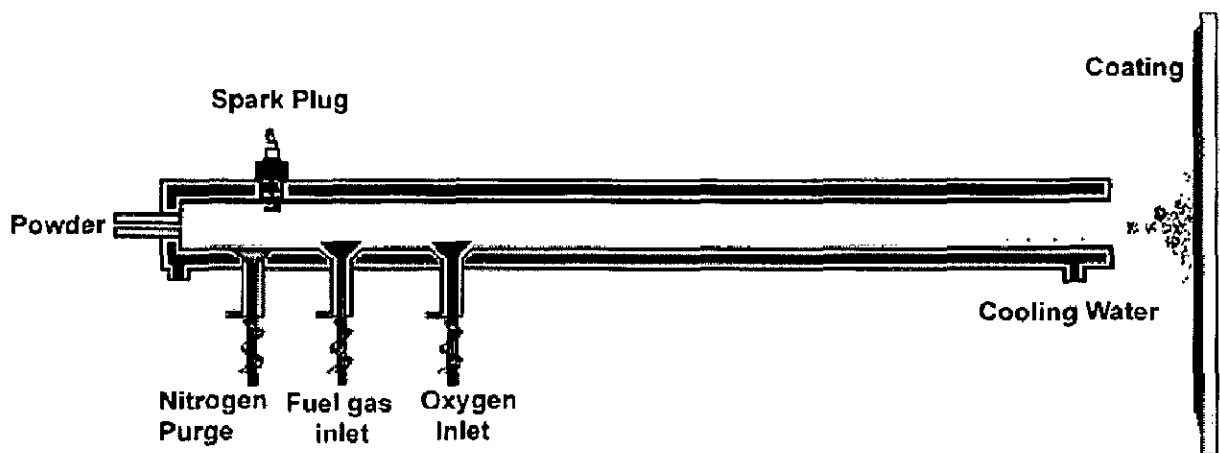


Fig. 2.7: Schematic illustration of the Detonation Gun thermal spray system.

2.2.3.4.2. Advantages of Detonation gun Coating Technology

The detonation gun (D-gun) spraying process is characterized by spray particles, which impact the surface of a substrate or a coating formed previously at the highest velocity realizable for the thermal spraying processes available at present. Therefore, the detonation gun sprayed coatings result in superior mechanical properties. Detonation gun is capable of producing the highest pressure, velocity, and density, which is not achievable by all other spraying techniques. As a result, the detonation coatings are characterized by extremely high density, microhardness, and low porosity, and are suitable for applications requiring very high standards, such as aircraft engine components and boiler components. This allows a many-fold increase in the operational lifetime of the part (Li and Ohmori, 1996; Gledhill et al., 1999; Makela et al., 1995; Saravanan et al., 2000; Ahmed and Hadfield, 1997).

A great variety of materials can be sprayed by using the detonation technology and a broad selection of base substrates can be coated. In addition to premium coating quality, the use of the detonation coating process, provides many benefits. Due to the intermittent nature of the process, the amount of heat transferred to the substrate stays very low. The substrate temperature, during spraying, does not exceed 150°C and can be maintained at room temperature, if necessary. This makes possible the spraying of precision components such as crankshafts, or turbine blades, without the danger of causing thermal deformations, or chemical changes. It is also possible to spray low melting point materials, such as plastics. The manufacturing experience has demonstrated that the use of the detonation coating process, in production, is very cost-effective; and, it results in substantial operational and maintenance cost reductions, as compared to the typical HVOF and plasma spray systems. This is due to the following factors:

- **Less Gas Used:** A high-pressure fuel and oxygen supply is not needed. The gases are fed into the combustion chamber at low pressure, slightly exceeding atmospheric pressure. The total amount of gases consumed, per unit mass of powder sprayed, is about 10 times less than the typical HVOF system.
- **Less Water Consumed:** Due to the low amount of heat transferred to the gun barrel, a special cooling system is not needed. Water consumption is very low.
- **Less Electrical Energy Consumption:** Very effective electric power consumption. Also a water chiller is not needed, which requires a lot of electricity.
- **Less Downtime:** The process is very simple to operate and very reliable. There are literally no components that can wear out.
- **Less Scrap:** There are no nozzles that can melt, or disintegrate, and spit copper on the expensive part being sprayed.

The gun barrel can be mounted at any angle, or can be fixed in the arm of a robot-manipulator. Multiple gun barrels can be installed to satisfy process requirements for high volume. Also the gun design allows to use the same unit as a grit blaster, without modifications of the barrel, or the gas supply system. This eliminates the need for a separate grit blasting booth, and it allows for a combination of surface grit blasting and further spraying, in one continuous operation (Davis, 2004; Pawlowski, 1995; Niemi et al. 1994). A brief review of few important thermal spray processes is given in Table 2.1 which compares important process characteristics associated with these techniques. The properties depicted in the table may vary depending on process settings, spray duration, spray distance, and the substrate material.

Table 2.1: Comparisons of different methods of thermal spray (Davis, 2004; Pawlowski, 1995; Kadyrov, 1995)

Type of System	Flame or Plasma Exit Temperature (°C)	Heat Transfer to Substrate (°C)	Particle Impact Velocity (m/s)	Oxide Content (%)	Porosity (%)	Adhesion (Bond Strength)
Detonation Gun	3000	20-150	800-1200	Small	0.1 - 3	Extremely high
HVOF	2500-3100	500-700	500-800	Moderate	1 - 10	Very High
Plasma Spraying	5500-8300	700-1000	200-600	Moderate to coarse	1 - 10	Very High
Wire Arc	4000-6000	500-800	240	Moderate to High	10-20	High
Flame Spraying	2500-3000	500-700	30-180	High	10-30	Low

2.3. ALUMINA TITANIA COATINGS

2.3.1 Introduction

Variety of materials viz. carbides, oxides, metallic, etc., belonging to the wear/corrosion resistant category is available commercially. The coatings can be classified into the following categories:

- (i) Metallic: NiCrAlY, Triballoy etc.
- (ii) Carbides: WC, TiC, SiC, ZrC, Cr₂C₃ etc.
- (iii) Oxides: Al₂O₃, Cr₂O₃, TiO₂, ZrO₂ etc.

The Choice of coating material depends upon the specific application.

Al₂O₃-TiO₂ Ceramics System

Ceramic coatings produced by thermal spraying are widely used in a range of industrial applications to provide wear and erosion resistance, corrosion protection and thermal insulation onto metallic substrates. Especially, alumina coatings are commonly used to resist wear by solid particle erosion (Ramm et al., 1994) and friction (Hartfield-Wunsch and Tung, 1994; Niemi et al., 1994; Kingswel et al., 1991; Kamachi et al., 1991; Naerheim et al., 1995). Ceramic coatings, prepared by the projection of a stream of molten particles at high velocity against the material to be coated, are widely used to provide wear, thermal or corrosion protection. Alumina-titania ceramic is one of the materials largely used for its wear, corrosion, and erosion resistance applications.

Al₂O₃-TiO₂ is most commonly applied ceramic coatings in thermal spray coatings. Thermally sprayed coatings, like Al₂O₃ and Cr₂O₃, have several wear protection applications in paper, printing, petrochemical, mining, food and packaging, power generation fields, thanks to their high hardness and chemical stability (Winkler et al., 2003; Xiaoou and Yufen, 2005; Tani and Nakahira, 2004; Samad et al., 2004; Heimann, 1996; Budinsky, 1995). The use of the composite in preference to pure aluminum oxide has certain advantages. Titanium oxide has a lower melting point and effectively binds alumina grains leading to higher density and wear resistance coating. (Mishra et al 2008)

2.3.2 Thermal spraying of alumina titania

Ceramic surface coatings have been used in various fields as protective coatings such as thermal barrier coatings (Haynes et al., 1996; Bartuli et al., 1995; He et al., 2000; Leushake et al., 1997; Leyens et al., 1999; Musil et al., 1997), wear protective coatings (Pantelis et al., 2000; Sundararajan et al., 1998; Zywitzki and Hoetzsch, 1995) and corrosion protective coatings. (Thornton and Chin, 1977; Arsenault et al., 1989; Emmerich et al., 1997; Pajonk and Steffans 1997; Haanapell et al., 1991; Stroosnijder et al., 1994) Ceramic coatings are increasingly being used to protect metals in corrosive environment due to their stable properties and to the possibility of tightly adhering them to the metals. (Wiklund et al., 1996)

Alumina-titania ceramic is one of the materials largely used in the APS process. It is known for its wear, corrosion, and erosion resistance applications. Al₂O₃ Alumina is highly refractory and a very stable ceramic (melting point, $T_m = 2327\text{K}$; standard enthalpy of formation, $(\Delta_f H^\circ = -1675.7 \text{ kJ/mol})$). Consequently, the oxide does not modify its composition upon spraying. At solidification, some authors have reported the formation of an amorphous phase in the lamellae, close to the interface of the substrate (Wilms and Herman,

1976). The modification of alumina with regard to the initial material occurs at solidification of the splat. The process results in formation of the $\gamma\text{Al}_2\text{O}_3$ phase instead of the stable $\alpha\text{-Al}_2\text{O}_3$ phase. McPherson (1973) explained this formation by a lower energy for nucleation from the liquid for the γ -phase than for the α -phase. The α -alumina present in the as-sprayed coatings results from inclusion of the unmelted grains (Fig. 2.8) It is possible to obtain the α -phase for the melt by alloying alumina with other oxides, such as chromia. Such alloying modifies the height of the nucleation energy barrier.

TiO_2 , being a relatively less-refractory oxide with a melting point of 2143K and a standard enthalpy of formation $\Delta_f H^\circ = -944.0$ kJ/mol, is used frequently as a coating in chemical catalysis and a dielectric in capacitors, and is being studied for such new applications as electron emitters (Tomaszek et al., 2007) or in photocatalysis (Toma et al., 2005). The oxide is often alloyed with others (Al_2O_3 , Cr_2O_3) in such compositions as, e.g. $\text{Al}_2\text{O}_3 + 13$ wt% TiO_2 , which has a liquidus at a lower temperature than the melting points of more refractory component. Commercial TiO_2 powders are often prepared by fusing and crushing and contain mainly rutile and sub-oxides, being the Magneli phases of a general formula, $\text{Ti}_x\text{O}_{2x-1}$ ($5 < x < 9$) (Berger, 2004). On plasma-spraying of coarse particles (mean size, $d_{cr} = 23\mu\text{m}$ in Fig. 2.9; rutile crystal size, $d_{cr} = 48\text{-}56$ nm) coatings are produced, having a composition similar to the initial particles, namely rutile (crystal size, $d_{cr} = 29\text{-}43$ nm, being clearly smaller than that of the powder) and sub-oxides.

Thermally Sprayed alumina-based coatings are widely used in various applications. Atmospheric plasma spraying (APS) is an economical way to deposit these coatings and is satisfactory in many cases. The properties of alumina-based coatings can be influenced by alloying. For example; an addition of TiO_2 to Al_2O_3 increases toughness and decreases porosity of coatings deposited by plasma spraying (Safai S., 1979). In the case of plasma sprayed alumina-titania coatings, the abrasion wear resistance tested using the SiC-paper grinding method has been found to increase with small additions of TiO_2 (3 wt%), whereas addition of 40 wt% TiO_2 decreased wear resistance (Filmer et al., 1990).

It is well known that engineering ceramics exhibit properties such as excellent chemical stability, corrosion resistance, and wear resistance (Safai S., 1979; Filmer et al., 1990). Ceramic coatings sprayed onto the surface of a metal can change the corrosion behavior of the substrate and can provide outstanding protection, especially under conditions in which corrosion and wear coexist at an elevated temperature (Beltzung et al., 1989; Vuoristo et al., 1991). Thermally Sprayed Al_2O_3 and $\text{Al}_2\text{O}_3\text{-TiO}_2$ coatings are being extensively developed with many outstanding properties, such as high hardness, excellent abrasive and sliding wear resistance, erosion resistance, inoxidisability, and heat insulating property. (Wang et al., 2000; Jordan et al., 2001; Goberman et al., 2002)

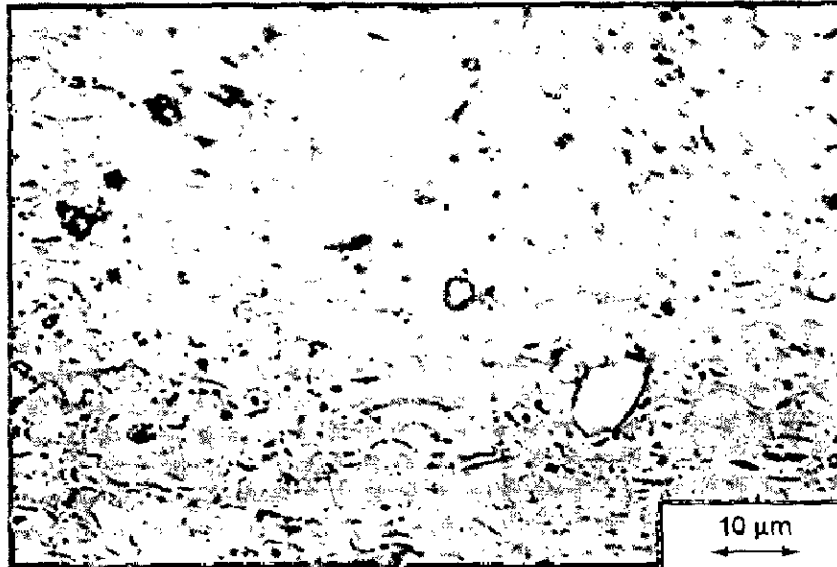


Fig. 2.8: Optical micrograph of an alumina coating used for corona rolls production, obtained by plasma-spraying (McPherson, 1973).

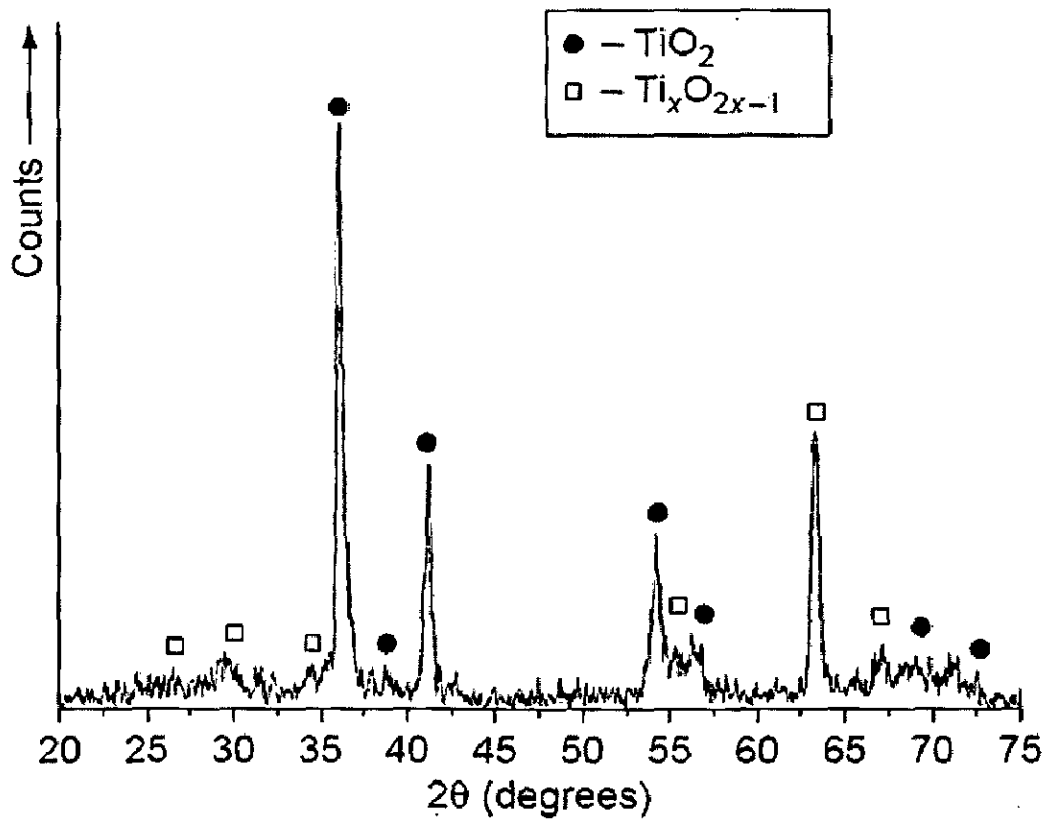


Fig. 2.9: X-ray diffraction diagrams of a coarse TiO_2 powder plasma sprayed coating (Tomaszek et al., 2006).

Alumina-titania coatings have also been used for varied applications in the automotive, transportation, textile, aerospace, and aircraft industries because of their refractory nature. The coatings produced are wear resistant, heat resistant, resistant to most acids and alkalis, and have high dielectric strength. In addition, bond strength is high, inter particle strength is high, and finish is very smooth. The coatings exhibit little evidence of through porosity. The alumina-titania coating used for the heater tube must survive thermal cycling from thermal-hydraulic testing, which promotes spalling and destruction of the insulator.

2.4 EROSION

2.4.1 Introduction

In general Erosion may be defined as metal removal caused by particle. Erosion wear mechanism involves the removal of materials from a given surface due to impact of solid particles. So Erosion is a generalised wear mechanism whereby mass loss occurs through impact of discrete particles entrained in a fluid stream. This mechanism applies to a range of situations; the use of the term in this work is in regard to mass loss by small, hard particles entrained in an air stream. The extent of erosion in this manner has been defined as:

$$\text{Erosion Rate} = \frac{\text{Mass flow rate of impinging particles}}{\text{Mass of material removed from substrate}}$$

The material loss caused by the impingement of tiny, solid particles, which have a high velocity and impact on the material surface at defined angles, is called erosive wear (Guo et al., 1995). Erosive wear is caused in the solid bodies by the action of sliding or impact of solid, liquid or gases or a combination of these (Ramesh et al., 1991). ASTM standard G76-07 (2007), defines erosion as the progressive loss of original material from a solid surface due to mechanical interaction between that surface and a fluid, a multi-component fluid, or impinging liquid or solid particles. Erosion is a serious problem in many engineering systems, including steam and jet turbines, pipelines and valves used in slurry transportation of matter, and fluidized bed combustion system (Kosel, 1992). According to Kosel (1992), solid particle erosion is a phenomenon in which a series of particles strikes and rebounds from the sliding of abrasive particles across a surface under the action of an externally applied force. He further reported that solid particle erosion is expected whenever hard particles are entrained in a gas or liquid medium impinging on a solid at any significant

velocity (greater than 1m/s). In both the cases, particles are accelerated or decelerated, and their directions of motion can be changed by the fluid, this is more significant in liquid media, and slurry erosion. A schematic view of erosion wear is shown in Fig. 2.10.

An extensive amount of research has been published in regard to the mechanisms and relative rates of erosion of materials in order to develop measures to mitigate the effect of damage. Most erosion work has focused on bulk materials, with testing primarily conducted at ambient temperature under relatively low particle impact velocities. As a result, the erosion mechanisms and effect of the variation in process variables and material properties on the erosion response have been well characterised under such conditions. The erosion response of materials under the industrially significant conditions of high temperature and/or high impact velocity is less understood.

Through this work Alumina-Titania based materials have been highlighted as possessing high erosion resistance. The positive attributes of thermal spraying have been widely exploited to apply such materials, primarily $\text{Al}_2\text{O}_3\text{-3TiO}_2$, as coatings. Similarly, while thermal spray coatings are widely utilised to mitigate the effects of erosion, few single impact studies have characterised the mechanism of degradation under high velocity impact conditions and high temperature conditions. More specifically the response of thermal spray coatings to erosion has primarily been considered from an empirical, comparative viewpoint; contrasting the erosion response with well characterised bulk materials only. Little has been presented in regard to the effect as a function of deposition technique on the coating response. Furthermore, most coating erosion resistance trials have constrained to room temperature exposures with only few publications considering the effects of high temperature exposure of the coating and its implications on the erosion mechanism and magnitude of erosion response.

Material loss of the combustor wall and the in bed tubes is one of the most serious problems associated with fluidized bed combustors (FBC) technology. The term 'wastage' is commonly used for this phenomenon, which is generally accepted to be a result of erosion or abrasive wear that may be accelerated by oxidation or high-temperature corrosion (Stringer et al., 1989). Huge levels of surface degradation of metal containment walls and heat exchanger tubing by a combined erosion-corrosion (E-C) mechanism have been experienced in some boilers, particularly fluidized bed combustors by Levy (1993). According to Kosel (1992), erosion-corrosion refers to the simultaneous, synergistic interaction between the solid particle erosion and corrosion. Erosion-corrosion is of great technical importance in several types of applications, including coal gasification or liquidification, steam turbines, jet turbines, and in

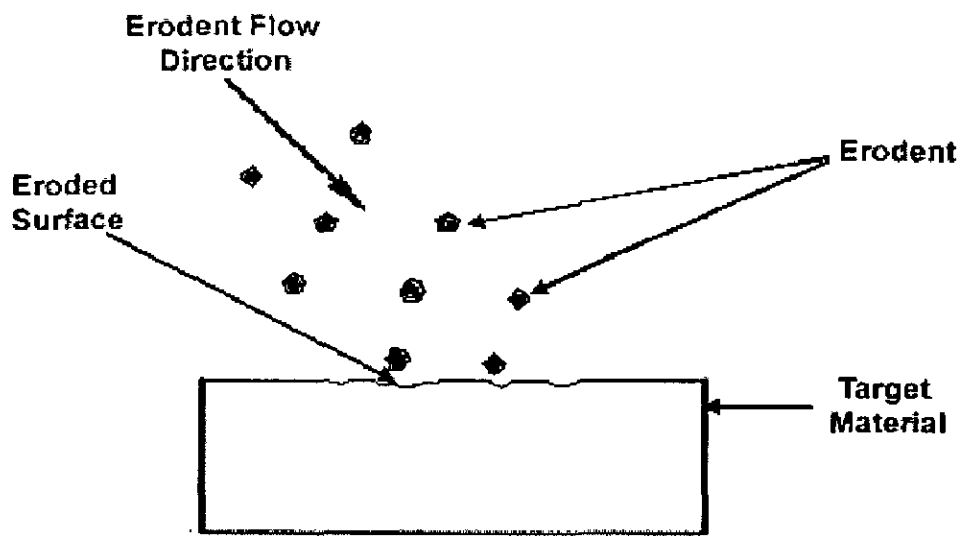


Fig. 2.10: A schematic view of solid particle erosion of material (Buckley, 1981).

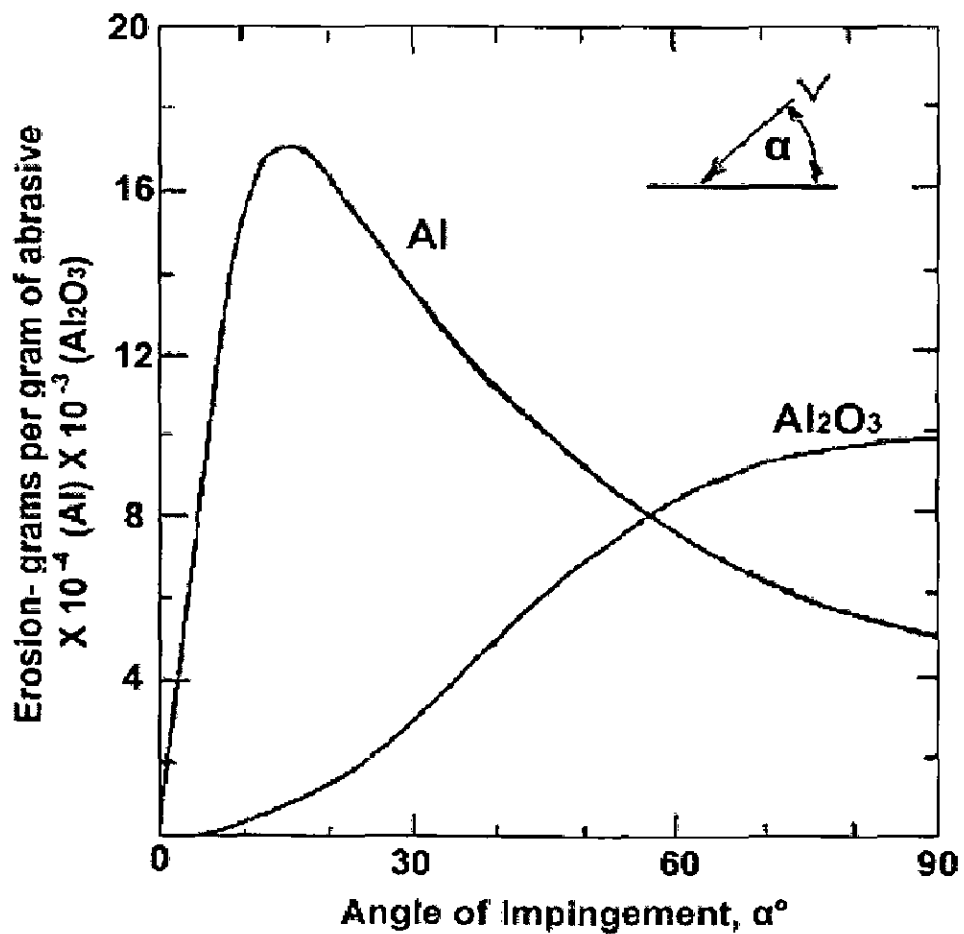


Fig. 2.11: Erosive mass losses as a function of impact angle for aluminium and Al_2O_3 substrates (Finnie, 1995)

the in-bed evaporator tubes, waterwalls, and convection pass surfaces of fluidized bed combustion systems. Material damage due to combined effect of erosion and corrosion is a problem in many industrial applications like hydraulic turbines, slurry pumps, valves, pipelines conveying solid particles (Das et al., 2006).

2.4.2 Erosion Fundamentals

In erosion, the detailed process that cause material removal is still poorly understood (Gee et al., 2003) and continuous efforts are being made in this regard. Finnie's (1960) analysis of the cutting action of a single particle launched against a ductile target and was the first model of solid particle erosion capable of predicting material removal rate. The mechanisms by which erosion mass loss occurs are broadly defined into two categories-ductile and brittle mechanisms. Such classifications were initially based on the response of classical "ductile" and "brittle" materials, which, by virtue of their erosion mechanisms, showed mass loss as a function of impact angle responses similar to those in Fig. 2.11. Subsequent work has shown that the material response as a function of impact angle depends on an extensive number of variables, well beyond those related to the material properties. For different materials under varying test conditions, different response may be generated. Variation in test conditions may generate responses characteristic of each mechanism for a single material. Such classifications are still widely used, however, in describing the material response and serve to differentiate between the two primary mechanisms of erosive mass loss.

2.4.2.1 Ductile Erosion Mechanism

As previously discussed, Finnie's analysis (1958) of the cutting action of a single particle launched against a ductile target was the first model of solid particle erosion capable of predicting material removal rate. In his scheme, the particles were assumed to be non-deforming and impacting a target, which was assumed to reach a constant flow pressure (i.e. the target is assumed perfectly plastic) immediately upon impact. By assuming that no rotation of the particles occurs during the impact process, he could solve for the trajectory of the particle in closed form as it cuts the surface, and thus predict material removal rates. This theory formed the foundation for later rigid-plastic models, which removed the restriction of particle rotation during impact. Finnie (1960) developed an analytical model to predict erosion rates that were based on the assumption that the mechanism of erosion was that of micromachining. According to him the impacting particle penetrates the target by a small amount, translates along the surface removing material ahead of it in a machining mode and

finally leaves the surface. A refined model has been developed for this mechanism by Finnie and McFadden (1978) utilizing the equation of motion of the particle tip to define an amount of target material that would be removed. The classical “ductile” erosion response, exhibits the greatest magnitudes of mass loss at low impact angles ranging from 15-30°. At higher angles the erosion rate drops away, though the rate does not tend to 0 at 90°. The severity of low angle impact damage has been related to the efficiency of the generalised “machining” mechanism postulated to account for erosive mass loss in ductile materials over these angles. This generalised mechanism has been subdivided into 3 modes of response, Fig. 2.12.

The angle impact of erosive particles i.e. the glancing angle impact of rounded erodent results in furrow indentations, with material physically displaced outwards and to the sides and terminal end of the crater. While mass loss typically does not occur by direct impact in this manner, the plastically deformed “lips” or “platelets” of highly strained material are prone to fracture or fatigue during subsequent impacts (Hutchings, 1992A; Levy, 1995). While Angular particles impart more of a “cutting” action during impact, the resulting damage dependent on one of two possible mechanisms. Type I cutting (Hutchings, 1992A), involves impact by an angular particle in a similar manner to the “ploughing” mechanism of rounded particles. The erodent particles penetrates the surface and carves out an angular furrow of material, plastically deforming material to the side of the crater and typically generating a chip or lip of material at the terminal end of the crater. As with the “ploughing” mechanism no direct material loss occurs in this process, with degradation occurring through fracture of the displaced material upon subsequent impact. Type II cutting (Hutchings, 1992 A) occurs in a similar manner to the Type I mechanism, however, rotation of the erodent particle during impact results in a machining-type action that directly “cuts” chips of material from the surface.

At higher impact angles i.e. greater than 30°, the “machining” mechanisms of mass loss become increasingly inefficient, and the mechanism of erosive mass loss is less clear. Several mechanisms have been proposed, including work hardening of the surface leading to a brittle response, delamination wear, temperature effects and extrusion (Finnie, 1995). The most widely referenced process, however, is the “platelet” mechanism (Finnie, 1995; Hutchings, 1992 B; Levy, 1995). At high impact angles the erodent particle indents the surface resulting in displacement or extrusion of material upwards and outwards (Levy 1995), generating mounds and circumferential lips of highly strained material similar to that generated by ploughing. Repeated impacts on the displaced material leads to fracture or

fatigue based loss of material. The volume of material displaced in this way is a lot lower than that generated at low angles i.e. less than 30°. In addition, many more particles are required to generate loss of the smaller deformed platelets, this lack of efficiency in material removal accounts for the lower rates of mass loss at high impact angles.

2.4.2.2 Brittle Erosion Mechanism

For brittle materials, the first known study for solid particle erosion damage has been investigated by Sheldon and Finnie (1966) who studied the erosive regime, usually referred to as hertzian fracture, where the contact between the particle and the body is exclusively elastic. In their analysis they considered dynamic forces between the surface and the particle and this resulted in a prediction of the volume removed for a material with specific properties. They also concluded that the fracture at the surface is a function of the volume of material constrained in the primary erosion zone in relation to the surface and volume flows. Unlike the classical ductile erosion response, the classical “brittle” erosion response shows the greatest rate of mass loss at high impact angles, with the rate continually decreasing to negligible degrees of mass loss at low impact angles. This response reflects the mechanism of fracture induced mass loss, whereby the extent of substrate damage is dictated by the magnitude of the vertical component of the impact load applied by the erodent particle. For a given particle impact velocity, the component of the load applied perpendicularly to the surface continually decreases with decreasing impact angle, resulting in reduced erosion damage. The erodent particle impact generates brittle fracture within the near surface zone of material, with cracks radiating outwards and downwards from the point of impact. Mass loss occurs by chipping, whereby segments of material formed by the intersection of crack networks are ejected from the surface. Initially an initiation period of negligible mass loss is typically observed, whereby particle impacts generate the extensive crack network required for steady state erosive mass loss to proceed. Generation of crack occurs by two mechanisms; broadly differentiated by whether indentation occurs by a blunt or sharp indenter. The blunt indenter under light loads generates a ring crack, termed as Hertzian crack, around the impact site that propagates down into the substrate at an angle to form a cone, Fig. 2.13 (Hutchings, 1992 A; Ruff and Wiederhorn, 1979; Hutchings, 1992 B). No plastic deformation occurs in this process as it is an elastic process (Ruff and Wiederhorn, 1979), with the extent of crack propagation dependent upon pre-existing substrate flaws, the particle diameter and substrate fracture resistance. Under more aggressive conditions, particularly with sharp indenters i.e.

erosive particles with sharp edges, cracking becomes more extensive. Evans and Wilshaw (1976, 1977) have characterised the mechanism as shown in Fig. 2.14. Indentation generates a zone of plastically deformed material around the indenter, the surrounding material being elastically loaded (Levy, 1995). According to this mechanism under the effect of loading, radial cracks propagate out from the indent perpendicular to the surface, while “medium vent” cracks propagate down into the material below the indenter. Upon unloading, lateral cracks form below the plastically deformed zone and propagate outwards and upwards towards the surface (Hutchings, 1992 A; Evans and Wilshaw, 1976). As a result, large chips of material may be formed in this process by the intersection of the various crack networks propagating from the indent (Finnie, 1995; Hutchings, 1992 A; Levy, 1995; Ruff and Wiederhorn, 1979; Levy, 1983, as well as by fracture of indented material generated by the combined action of the “wedging action” of the erodent with the cracks formed during impact (Ruff and Wiederhorn, 1979).

At low impact angles the mechanism of erosive wear of materials exhibiting brittle erosion is less clear. Finnie, (1995), has suggested that the vertical component of the erodent impact geometry determines the extent of brittle erosion. But the results cited in the review of Ruff and Wiederhorn, (1979) at low angles the response of alumina tended towards that seen in ductile metals. In their work Ruff and Wiederhorn (1979) demonstrated that no cracking occurred, while the furrows generated by glancing impact showed significant plastic deformation indicative of a “shear deformation mechanism”.

2.4.3 Erosion of Thermal Spray Coatings

2.4.3.1 Introduction

In thermal spray coatings, the complex build up of “splats” of material results in heterogeneous properties which are unlike those of bulk specimens. Given the mechanisms of erosion as a function of the bulk substrate properties as discussed previously, variation in the compositional and structural microstructure of thermal spray coatings is critical in determining their erosion response (Kingswell et al., 1991). The bonding in thermal sprayed coatings is mechanical interlocking of splats; the largely mechanical interlocking of deposits generates an inherent inter-splat weakness and the potential for void formation during deposition, potentially forming a crack network within the as-sprayed material. Also in thermal spraying, the molten or partially molten nature of the particles in-flight can lead to oxidation of the particles and dissolution of phases in composite powders, accentuating the heterogeneous variation in

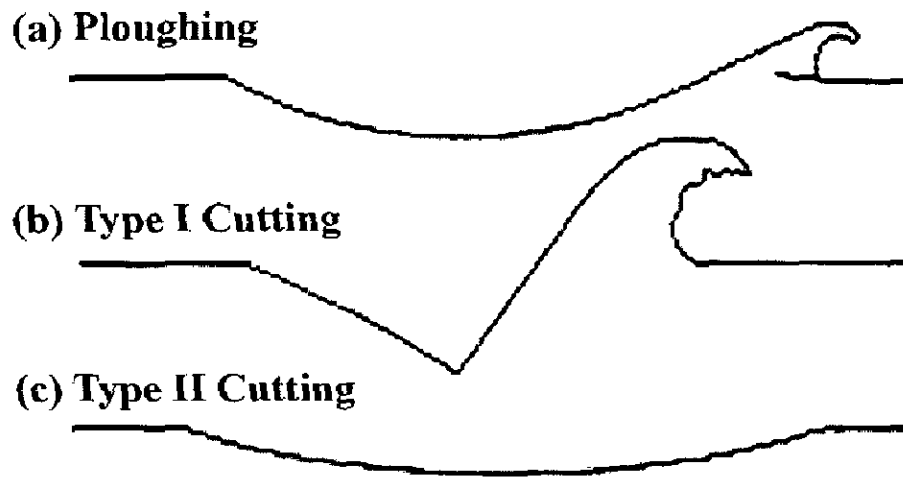


Fig. 2.12: Characteristic mechanisms of ductile erosion based on the variation in erosion conditions (Hutchings, 1992A).

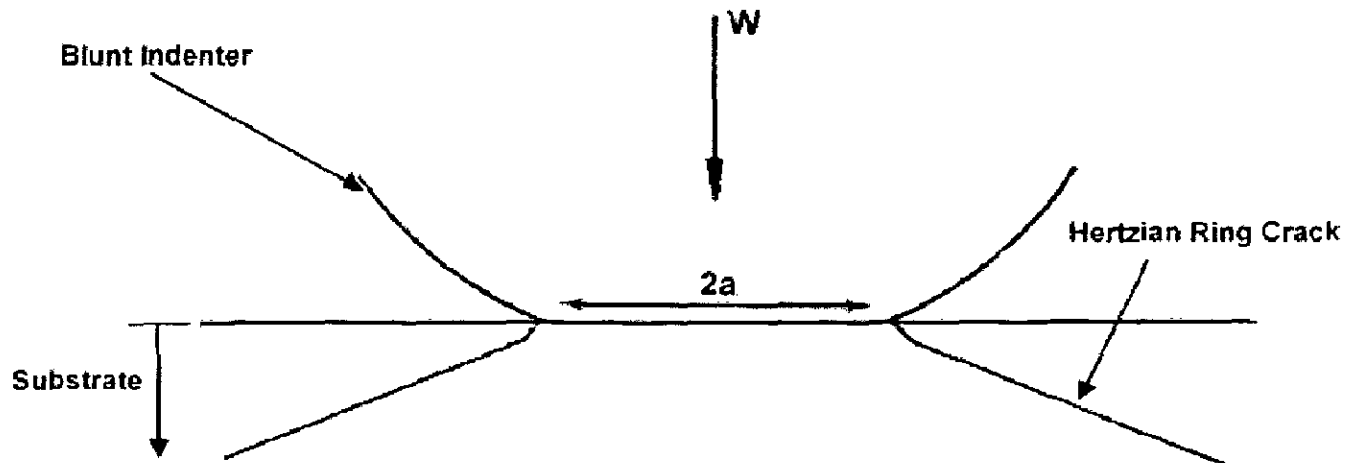


Fig. 2.13: Cross-sectional schematic of impact by a blunt indenter on to a brittle substrate, resulting in the formation of a conical Hertzian crack (Hutchings, 1992A).

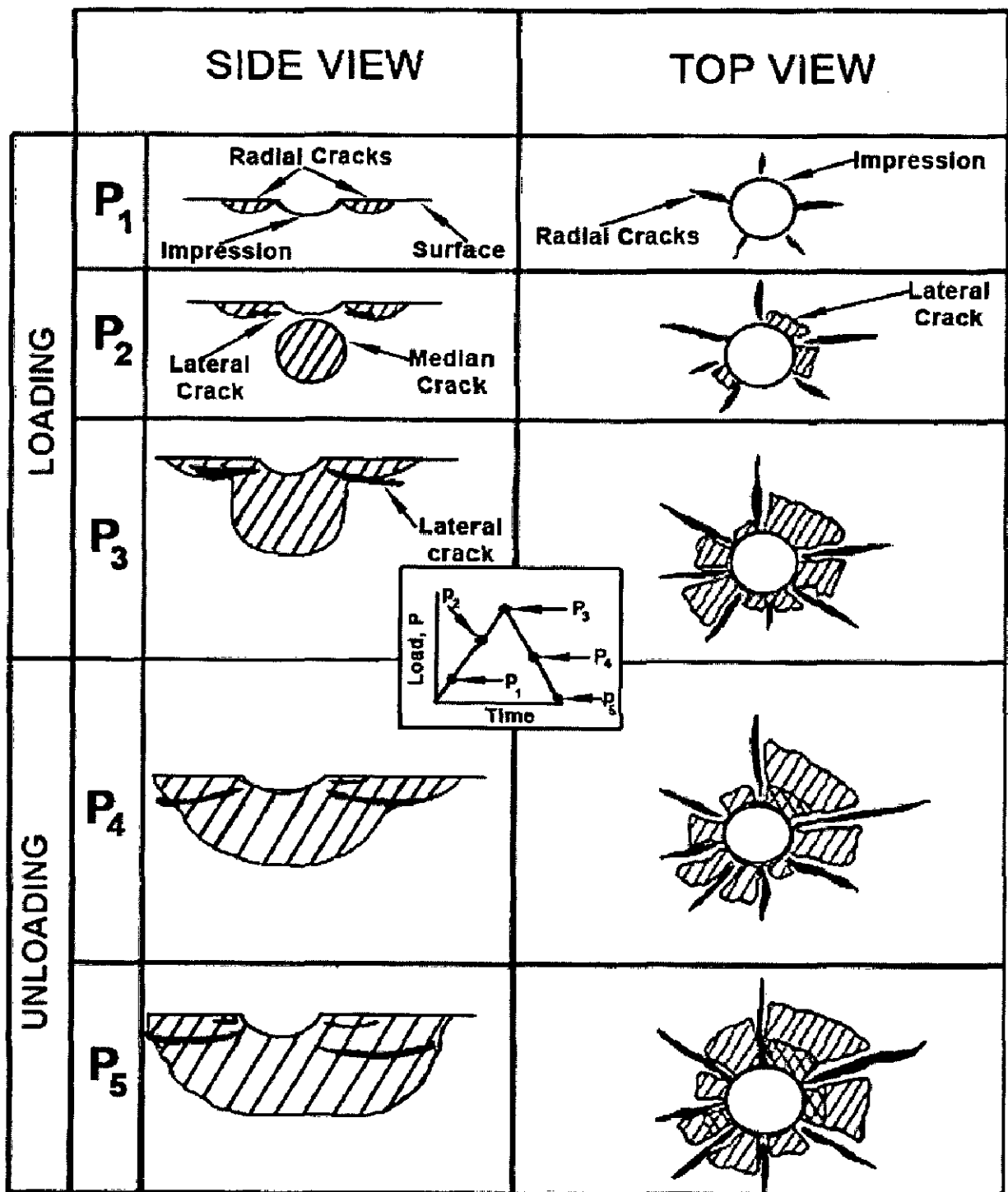


Fig. 2.14: Schematic sequence of crack formation and development as a function of indentation loading and unloading on a brittle substrate (Evans and Wilshaw, 1976).

mechanical properties and potentially reducing the inter-splat bond strength. In addition, the rapid cooling of such deposited material may result in amorphous phase formation, further complicating the brittle or ductile response of the material, or in the worst case, resulting in cracking induced by variations in the thermal expansion of the deposited material upon cooling. The significance of these microstructural characteristics on the coating erosion performance is influenced by the deposition technique, powder composition and method of manufacture, and the selection of thermal spray parameters.

The angle at which the stream of solid particles impinges the coating surface influences the rate at which the material is removed and this dependency is also influenced by the nature of the coating material (Satapathy, 2005). Many researchers have evaluated the erosion behaviors of several types of coatings. Levy, (1988) reported that in general, metals, alloys and coatings on metallic substrate erode by one of the two basic mechanisms, i.e. either by plastic deformation to failure of material or cracking and chipping of a brittle material. Further coatings that have some degree of ductility erode by a plastic deformation mechanism; while in case of brittle coatings these erode by cracking and chipping mechanism. The erosion mechanisms by which ductile and brittle coatings are removed are basically different. Levy, (1988) suggested that ductile materials including materials with relatively little measurable ductility (1% - 2% elongation) fail as a result of impacting particles causing localized plastic flow that exceeds the critical strain to failure in local areas. Structural alloys, MCrAlY coatings and other primarily metallic coatings will erode by this mechanism. When erodent particles in a gas or liquid carrier fluid strike the surface of a ductile material they initially extrude thin microplatelets of the base materials from craters, which are formed at the sites of the impacts. The platelets are then further flattened, i.e. pancake forged, by subsequent particles striking the initially deformed material. After a small number of particles have impacted the same localized area, whose size is from a few micrometers to as many as 100 μm in major diameter, part or even all of the initially extruded platelets will have been strained to their critical strain and fracture of portions of the platelets will occur.

Levy (1988) further reported that the coatings that form a layer of oxidized scale in service erode-corrode by the erosion of the scale and its replacement by oxidation of the base metal via cation diffusion. He concluded that the erosion rates of thermally sprayed coatings vary directly with their grain size and level of porosity. The presence of cracks in diffusion-type coatings results in higher erosion rates. Whereas plasma-sprayed ceramic coatings for use as thermal barriers are somewhat porous and brittle materials, that are eroded by cracking

and chipping mechanism. Moreover when the grain size of the coating is very small and there is a minimum of pores, the material loss rate is very low. Thus the greater the porosity of the coating, the easier it is for the erodent particles to knock off pieces of exposed ceramic pore walls, and the greater is the removal rate. It has also been suggested that the compositions and hardness of the coatings do not correlate with the loss rates, but their morphologies do.

Variations in erosion response may potentially occur in seemingly identical coatings sprayed with the same powder and the same deposition technique. While hardness values may be expected to take into account the significance of such features (Hawthorne et al., 1999), and therefore reflect the relative coating erosion performance, numerous studies have reported that hardness is a poor indicator of erosive wear performance for thermal spray coatings (Lathabai et al., 1998; Legoux et al., 1999; Shui et al., 1990; Sue et al., 1987; Arsenault et al., 2001; Nerz et al., 1991) and thus have agreed with Levy, (1988).

2.4.3.2 Erosion Mechanism of Thermal Spray Coating

Three principle mechanisms of erosion of thermal spray coatings based on plasma sprayed tungsten coatings have been proposed by (Kingswell et al., 1991).

- Microchipping and ploughing
- Splat fracture
- Debonding at splat boundaries

In general, low intersplat adhesive strength leads to removal of entire splats or groups of splats, primarily associated with fracture and crack propagation along splat boundaries (Kingswell et al., 1991; Hawthorne et al., 1999; Lathabai et al., 1998).

Increased inter-splat adhesion dependent on process parameters and many other factors reduces the magnitude of the erosive debris, with fracture becoming more localised within splats and associated with brittle fracture or fatigue around specific impact sites (Kingswell et al., 1991; Hawthorne et al., 1999; Lathabai et al., 1998). Mass loss then occurs in the following manner. Cracking or plastic deformation initiates near the splat boundary, generating small chips of material. Continued erosion leads to crack propagation into the splat and chipping or plastic deformation of the exposed splat edge which generates continued mass loss (Wang, 1996A; Wang and Geng, 1990; Wang, 1996 B; Wang and Lee, 1995; Wang and Verstak, 1999; Wang and Shui, 2002; Wang and Luer, 1994; Wang and Lee, 1997). Alternatively repeated impact may lead to subsurface inter-splat crack propagation via a fatigue mechanism (Wood et al., 1997). Thus mass loss in this case is generated by the

linkup of vertical erosion induced cracking, with fatigue induced splat boundary cracks. In both mechanisms, localised erosive wear in the body of splats away from the splat boundary occurs in the same manner as on bulk materials.

These fundamental mechanisms form the basis of explanations from the majority of research presented in thermal spray coating erosion across a range of deposition techniques, coating compositions and erosion testing parameters. The greatest contributor to erosive mass loss is splat boundary effects as is suggested by various researchers in the literature (Wayne et al., 1990; Kingswell et al., 1991; Latha bai et al., 1998; Legoux et al., 1999; Arsenault et al., 2001; Wood et al., 1997; Hawthorne et al., 1997; Westergard et al., 2000 ; Verdon et al., 1997; Eaton et al., 1989 ; Nicholas et al., 1999 ; Xia et al., 1999). While being an inherent weakness in as-sprayed coatings, it is evident that many mechanisms contribute to preferential fracture in the inter-splat region. The amount of inter-splat area per volume is largely a function of splat size; the significance of this is dependent upon spray parameters and test conditions. Wang, 1995A; Wang, 1995B; Levy, 1988; Levy and Wang 1988 have consistently correlated improved erosion resistance with the absence of cracks and small splat size in comparing the results of HVOF cermet coatings with arc and flame sprayed Fe based and oxide coatings.

Westergard et al., (2000) noted surprisingly little variation in the erosion of plasma sprayed alumina having similar range of precursor powder sizes. In this case the individual splats were noted to be broken up into "sub-splats", Fig. 2.15, by cracks generated by the rapid cooling rates upon impact. The density of these cracks was found to roughly increase with increasing powder size, resulting in comparable "sub-splat" size and possibly explaining the similarity in erosion performance. Irons et al., (1994) observed improved erosion performance in HVOF sprayed Cr_3C_2 -NiCr powders with an increase in initial powder size. The finer powders with significant proportions less than 16 μm , were linked to increased porosity and oxide content in the coating, degrading their performance. While a range of spray conditions were tried in this work, they concluded that these did not correlate with the optimum settings for fine powders. Hawthorne et al., 1999 and Hawthorne, 1997 also agreed to this conclusion. They suggested that the coatings thermally sprayed from the finest powder size contained many spherical particles indicating inadequate heating or low velocity at impact. Both features are functions of the spray parameters used. The results suggest that the powder size itself is not a significant variable, but the most important is whether the spray conditions used are optimised for the particular powder or not so as to generate coating microstructures of high erosion resistance.

From work of (Kingswell et al., 1991; Dallaire et al., 2001), Oxide stringers incorporated around the periphery of the splats have been highlighted as zones of preferential crack propagation and erosion. Also Aresenault et al., (2001) noted that such phases contributed to poor splat cohesion, enabling excessive splat debonding in WC-Co coatings. Work by Rabiei et al., (1999) on HVOF Fe-based alloys using wedge impression tests highlighted the preferential propagation of cracks through the very thin inter-splat oxide layers, as did Schwetzke and Kreye, (1996) in the cavitation testing of a range of HVOF coatings. Legoux et al., (1999) noted accelerated erosive attack in regions of high localised oxide content.

Porosity is also an important feature associated with splat boundaries. Voids produced by porosity resulted in reducing inter-splat cohesion Wayne et al., (1992) and also have been noted to act as crack initiation sites Schwetzke and Kreye, (1996). When exposed to the surface, enhanced erosive loss occurs through deformation around the unsupported lip of the pore (Levy A, 1983; Rogers, et al., 1991). Thus the coating response to the microstructural features is dictated by the erosion test conditions as demonstrated by various researchers in their work (Lathabia, 1998; Wood, 1997; Verdon, 1997; Eaton, 1989). Under mild test conditions (low velocity, soft erodents), erosion occurs in a similar manner to bulk samples of the same material, mass loss occurring by microchipping and platelet formation but on increasing the severity of the test conditions i.e. (higher velocity, increased hardness of erodent (e.g. SiO₂ to SiC) and increased erodent particle size) generates greater erosion rates and a transition in the mechanism of mass loss. The impact events become larger, generating more extensive cracking/fracture and leading to significant mass loss through inter-splat fracture and delamination mechanisms. The severity of erosion, however, must be considered in regard to the erosion mechanism. This has been illustrated in the work of Kingswell et al., 1991 where 160 µm particles generated significantly greater rates of erosion than larger 1500 µm particles at velocities >75 m/s. For particles of the same angularity, the authors noted that the increased contact area of larger particles enables the impact load to be dissipated over a larger area, reducing the depth of penetration and minimising erosion damage. Thus there are conflicting arguments by different researchers as far as particle size is concerned.

2.4.3.2.1 Erosion mechanisms at high temperature

The most important and the least studied is the Erosion mechanism at high temperature. Many studies concerning the interaction between erosion and a surface oxide film have been conducted [Barkalow and Pettit, 1979; Kang et al., 1985; Stephenson et al.,

1985 1986), Stephenson and Nicholls (1990), Wright et al (1991) and Stack et al (1991)]. Mechanisms of material removal have been proposed which include oxide fracture and chipping, oxide spallation at the metal-oxide interface and plastic deformation of metal substrate resulting in both oxide and metal loss.

These interactions between surface oxide and erosion have been summarised by Barkalow and Pettit (1979) using schematic diagrams typical of Fig. 2.16 which shows that for low energy particles, scale fracture does not occur and therefore metal recession rates will be determined by the oxidation process only. As the impact energy is increased and damage to the oxide scale occurs, an interaction between erosion and oxidation will result in accelerated metal loss. At still higher impact energies, deformation of the substrate produces metallic erosion. It is suggested that for materials to operate successfully at high temperatures a key requirement is the formation and maintenance of a protective oxide scale.

In another study by Kang et al., (1987) it has been suggested that the exact behaviour and the resulting morphology of the metal surface depend on the severity of erosion and the oxidation rate (Fig. 2.17). Pure erosion of the oxide dominates at high temperatures where the oxidation rate is high, while pure erosion of metal occurs at low temperature. In the erosion-enhanced oxidation regime a steady-state oxide thickness develops, with the rate of oxide formation equal to the rate of scale removal by erosion. When the erosion rate is high as compared with the scaling rate, the oxidation-affected erosion regime is entered and under these conditions a continuous oxide scale is unable to form and the metal surface comprises a composite layer of oxide, embedded erodent fragments and extruded metal. Rishel et al., (1990) modified the above model by subdividing the 'erosion-enhanced oxidation regime' into three categories: Type I, Type II and Type III, as illustrated in Fig. 2.18. The intermediate category, Type I, is the regime in which the thickness loss due to erosion is balanced by the thickness gain due to oxidation. This sub-division was proposed based on the basis of microscopy of the eroded surfaces in the various corrosion environments.

Hancock and Nicholls (1988) assumed in the first instance that oxide scales respond in a brittle manner and therefore their fracture behaviour must be quantified whereas erosion of the metallic substrate is controlled by localised plastic deformation and therefore high temperature strength must be considered. They proposed that the fracture stress of oxides can be determined using acoustic emission or resonant frequency techniques and have demonstrated the importance of both temperature and scale thickness. They estimated the localised deformation behaviour of the metallic substrate from hot hardness testing. They

concluded that structural, high temperature alloys such as the nickel base superalloys maintain their strength up to temperatures of 700°C however, at higher temperatures result in a sharp reduction in strength (Stephenson and Nicholls, 1990).

Stephenson (1989) and Stephenson and Nicholls (1993) have proposed four regimes of erosion (Fig. 2.19). According to them when the impact conditions are such that no damage results, Fig. 2.19 (a), metal loss will be predicted from the standard oxidation kinetics. Further if the erosion damage is highly localised at the surface such that only loss of oxide occurs, for example by localised fracture and chipping, Fig. 2.19 (b), but the scale remains protective, then metal loss can be expected to increase due to enhanced oxidation. In this oxide dominated regime the boundary conditions for the on-set of damage require that the fracture stress of the oxide is exceeded and that the oxide behaves as though it were of infinite thickness. They estimated this latter requirement from the modelling work of Halling and Arnell (1984) and depends on the ratio of the particle-target contact radius " a " and oxide thickness " x ." The analysis showed that the substrate has no influence on the scale surface properties when $x/a > 0.23$.

Further they proposed that the oxide modified regime Fig. 2.19 (c) occurs when the fracture strength of the oxide is exceeded and x/a is below 0.23, i.e. for relatively thin oxide scales. They reported that damage morphologies vary from through thickness scale fracture to oxide spallation, although damage to the substrate is not observed. They suggested that in this regime metal loss rates are likely to be high since the surface oxide is non-protective and linear kinetics prevails.

According to them as the relative thickness of oxide is reduced, the maximum normal force at the oxide-metal interface will increase and if the particle velocity is sufficiently high, plastic deformation of the substrate will occur. They have proposed that in this substrate dominated regime [Fig. 2.19 (d)] material removal is primarily from the substrate with a contribution from the surface oxide. Metal loss rate is determined by the erosion resistance of the metal substrate and oxidation makes only a minor contribution to the degradation process. They suggested that an interesting condition can exist where the oxide film does not fracture and its effect is to reduce the force applied to the substrate. Thus, when this applies the erosion rate will be reduced. They concluded that from knowledge of the particle, oxide and substrate properties and the impact dynamics, the boundary conditions between each regime can be quantified by considering the contact conditions at the oxide surface and how these change with oxide thickness. They also reported that the conditions for scale fracture can be determined by calculating the maximum radial tensile stress at the oxide scale surface for a

given impact event and comparing this with the fracture stress values. They estimated the contact radius assuming Hertzian behaviour with the 'effective' elastic properties of the surface which are determined using the Halling and Arnell (1984) analysis, which could be used to evaluate both the oxide dominated and oxide modified regimes. There are two important factors which differentiate the high temperature erosion of metals from their low temperature behaviour (Stephenson and Nicholls, 1995):

- (i) The surface properties of the metal may change significantly with time due to the growth of a surface oxide. The rate of growth of the oxide is a function of the temperature.
- (ii) The mechanical properties of oxide and metal may change with temperature and time.

2.4.3.2.2 Factors affecting erosion

The erosion process is caused by many factors, (Vicenzi, J. et al., 2006) among them:

- (i) flow and environmental conditions: the impingement angle, particle velocity, temperature, impingement particles per unit time and presence of corrosive agents;
- (ii) impingement particles properties: size, shape, density, hardness and friability;
- (iii) surface properties: topology, roughness, stress level and hardness

Erosion rates are affected by various factors (Kosel, 1992; Levy, 1995; Sundararajan, 1984 and Tilly 1973). Some of these important factors are impact velocity, impact angle, particle concentration, particle shape, particle size, particle density, particle friability, temperature, particle hardness, material hardness, toughness, microstructure and chemical composition etc. The erosion behaviour of HVOF sprayed NiAl intermetallic compound (IMC) coatings over a range of angles and particle velocities in air at room temperature was investigated by Hearley et al., (1999). They proposed that the maximum erosion was achieved at the highest velocity for all angles. Mishra et al., (2006) studied the effect of impact angle on erosion rate of coated and uncoated superalloys. NiCrAlY, Ni-20Cr and Ni₃Al metallic coatings were deposited on a Ni-based superalloy. For all tested samples, the erosion rates at a 30° impact angle were somewhat higher than at a 90° impact angle.

Erosion performance of coatings and the response of variations in the main erosion test variables (particle size, hardness, velocity and impact angle) has been investigated by various researchers broadly match those observed in bulk materials. Under the majority of trial conditions greater erosion rates were observed at 90° than at lower angles (Hawthorne et al., 1999; Wang and Verstak, 1999; Wood et al., 1997; Wang, 1995A; Walsh and Tabakoff,

1990; Walsh, 1992; Arsenault 1997; Wang, 1999; Sidhu et al., 2007; Mishra et al., 2006, 2008). As such these coatings were classed as exhibiting “brittle” type behaviour. Variation in this response occurred as a function of other test variables, primarily erodent velocity. At very low velocities the kinetic energy of each particle is insufficient to generate the minimum threshold load for indentation fracture (Wang and Lee, 1995). Erosive wear occurs by localised plastic deformation and the observed maximum in erosion rate shifts to lower impact angles. At higher impact velocities the erosion rate as a function of impact angle has been observed to flatten out, becoming almost independent of this variable. Under such high impact conditions the erodent particles are able to generate high stress in the coating, resulting in brittle erosion characteristics, even at low impact angles. As with bulk samples, higher particle velocities generate greater rates of erosion in cermet based coatings (Wang and Lee, 1995; Wang and Verstak, 1999; Wood et al., 1997, Walsh, 1990).

Erodent particle characteristics have received significant attention in regard to cermet coatings based on attempts at simulating fluidised bed and turbine erosion. In general, erodents with higher hardness ratios to the substrate generate greater erosion wastage (Levy, 1995). SiC is noted as the most aggressive of the commonly used erodents, followed by Al₂O₃ and SiO₂. Where mixtures of phases occur in the erodent stream, such as fluidised beds, it is the concentration of the hard phases, typically Al₂O₃ and SiO₂ that dictates the erosion rate (Wang, 1995A; Wang, 1999; Wang et al., 1991). Such behaviour is complicated by the shape of the particles, irregular particles being more aggressive than rounded erodents, as they are able to concentrate the impact energy on sharp protrusions (Levy, 1995; Wang, 1995A; Liebhard et al., 1991). Under fixed erosion conditions, the size of the erodent has been found to significantly influence the observed erosion response of cermet coatings (Walsh, 1992; Walsh et al., 1994). For particle sizes below 100 µm the erosion rate is noted to increase with increasing particle size. Above this, the so called “size effect” occurs, whereby the erosion rate plateaus out or begins to decrease with increasing erodent size (Misra and Finnie, 1981).

In ductile erosion the greatest mass loss occurs at impact angles of 15-30°. Mass loss occurs by repeated impact on platelets of material displaced by erodent impact to the point where they fracture from the surface, or as chips of material formed by direct impact. At high impact angles, these mass loss mechanisms become less efficient leading to lower rates of material wastage.

Brittle erosive mass loss occurs most significantly at high impact angles. Erodent particles impact the surface with sufficient energy to generate fracture and cracking within

the material. Mass loss occurs by chipping, whereby segments of material formed by the intersection of crack networks are ejected from the surface (Wang, 1995A; Walsh, 1992; Bahadur, 1990).

2.4.3.2.3 Erosion rate

Erosion testing consists of impinging a coated sample with a known abrasive particle utilizing compressed air as a propellant. The amount of erosion is measured either by the loss of weight or the loss of coating thickness. As per ASTM standard erosion value is the volume loss of specimen material divided by the total mass of abrasive particles that impacted the specimen (mm^3g^{-1}) [ASTM Standard G76-07]. Normalized Erosion Rate is calculated by dividing the erosion value of the specimen by erosion value of reference material (Hansen, 1979). According to Tabakoff (1995) the erosion rate is defined as the ratio between the change in the sample mass and the mass of the impacting particles. Hansen (1979) compared the erosion rates of alloys, ceramics, and cermets. He proposed that the order of material rankings would change with any change of variables such as velocity, particle type or size, and angle of impingement. He performed the erosion tests using $27\ \mu\text{m}\ \text{Al}_2\text{O}_3$ particles at normal incidence and 170 m/s at 20°C and 700°C in nitrogen. Hansen also conducted the tests with a gas-jet erosion apparatus in which particles are fed from a hopper into a nozzle, where they mix with and are accelerated by a flowing gas stream (ASTM G76). He normalized the erosion rates by defining the relative erosion factor as specimen volume loss divided by that of a standard material. As explained above, erosion resistance is normally measured using weight loss technique by measuring the weights before and after the test but at high temperatures, this leads to erroneous results due to oxidation of samples. So in order to overcome the above limitation of weight loss measurement technique erosion resistance can also be measured in terms of thickness loss (Venugopal and Agrawal, 2008). Also volume loss measurement technique has been used by Miyoshi et al, 2003 for erosion rate determination. The method has been used to evaluate surface characteristics, such as erosion volume loss and depth, surface topography, and surface roughness. The volume loss occurred after erosion testing was measured by using non contact optical profilometry.

2.4.4 Erosion in energy generation and coal gasification systems

In industrial applications and power generation such as coal burning boilers, fluidized beds and gas turbines, solid particles are produced during combustion which leads to solid particle erosion. Continued operation under particulate flow conditions adversely affects the performance of energy generation and coal gasification systems (Tabakoff, 1995). The burning of coal in thermoelectric power plants generates a huge amount of fly ash which causes intense and localized erosive wear of power plant equipment. Many power plant

engineers, as well as researchers of industrial wear problems are of the opinion that ash impacting erosion wear is the principal cause of boiler tube failure in economiser, primary superheater and reheater groups of boiler tubes (Suckling and Allen, 1995). According to them wear of boiler tubes in pulverized fuel power stations by erosion is a serious problem that often leads to unscheduled and costly outages.

Simms et al., (1995) reported that the development of coal-fired combined cycle power generation systems is receiving considerable worldwide interest. These systems, utilising both steam and gas turbines, have many advantages over conventional coal-fired power generation systems, which include increased efficiency of the electricity production and lower environmental emissions (specifically CO₂, SO_x and NO_x). According to them the influence of materials on the development of these systems can be considerable as it is necessary that components have adequate lifetimes in their operational environments. They further added that successful development and commercialisation of these new systems require that all the component parts are manufactured from appropriate materials and that these materials give predictable in-service performance.

In coal-fired power stations, about 20% of the ash produced in the boilers is deposited on the boiler walls and superheater tubes (Mbabazi et al., 2004). This deposited ash is subsequently discharged as slag and clinker during the soot blowing process. Whereas the rest of the ash is entrained in the stream of flue gas leaving the boiler. They reported that the ash-laden flue gas passes through the narrow passages between the corrugated steel plates that constitute the air heater elements. Then the ash particles collide with the surfaces of the steel air heater elements and material is eroded from the surfaces. Further in advanced stages of erosion, the plates become perforated. The air heater elements fail once they cannot maintain their structural integrity. According to them such erosion, together with the processes of blocking, fouling and corrosion, shortens the service life of the air heater elements. Once this happens, the power station unit has to be shut down in order to replace the damaged air heater elements. The resulting penalty is not only the cost of replacing the elements but also the cost of stoppage of power production. They proposed that it is desirable to predict the rate of erosion of the air heater elements in order to plan systematically for the maintenance or replacement of the air heater elements to avoid forced outages.

They further opined that in large coal-fired power stations, pulverised coal is burnt in the burners of the boilers. To improve upon the overall thermal efficiency of the boiler plant, heat exchangers are used to extract residual heat energy from the flue gas before it is released to the atmosphere and to transfer it to the combustion air supplied to the boiler burners.

According to them part of the air supplied, the 'primary air', is fed to the coal mills and is used to dry the pulverised coal and to transport the coal to the burners in the furnace. Whereas the greater part of the air supplied, the 'secondary air', is used in burning the coal. Further the heat exchangers used for preheating the combustion air are of the rotary regenerative type, commonly referred to as "air heaters". While these air heaters are prone to erosion, corrosion, blocking and fouling, particularly if the coal is of relatively poor quality, as is often the case in large South African power stations (ash content typically above 25%).

Krishnamoorthy et al., (1993) reported that the coal used in Indian power stations has large amounts of ash (about 50%) which contains abrasive mineral species such as hard quartz (up to 15%) which increase the erosion propensity of coal. They also reported that a performance review of thermal power stations indicated that erosion problems contribute significantly towards partial unavailability of power in India. They added that in coal-fired boilers, the pulverized fuel is transported to the boiler using a network of PF pipes. Components such as PF bends and elbows, multiple-port outlets, the orifice and the burner assembly are prone to high erosion wear, especially in certain locations oriented favourably for impacting wear particles.

Heat exchanger tubes immersed within a bubbling fluidized bed combustor often experience unacceptably high levels of thinning on their outer diameter and this loss in wall thickness is typically concentrated on the lower half of tubes and is frequently termed metal wastage (Stringer and Wright, 1987; MacAdam and Stringer 1995). They reported that this is consistent with aggregate impacts or any process associated with an upward particle flow. According to them, the wastage is primarily due to mechanical wear by bed particles in contact with the tubes, though an oxidation or corrosion component cannot be ruled out. They proposed that there are several macroscopic bed conditions that lead to particles with sufficient energy to cause wear. They opined that some of these are related to characteristics of the bed design or individual component failures, and others are related to intrinsic or unintentionally induced long-range flow patterns within the bed. Further they suggested that there is a general consensus however, that some of the worst wear is associated with energetic events intrinsic to bubbling bed combustors and that these events are associated in some way with bubbles themselves. They further reported that bubbles rising through tube banks are known to throw highly energetic dense aggregates of defluidized particles against tube bottoms. Also, voids, which can form beneath tubes as the entire bed undulates, will collapse against the underside of tubes with a similar effect. They concluded that the bottom of a tube is intermittently hammered by particle aggregates that strike and slide across the surface before dropping away. The study of the mechanisms of erosive wear is therefore extremely

important in order to develop suitable solutions to minimize or even eliminate maintenance procedures of such equipments.

2.5 HIGH TEMPERATURE CORROSION

2.5.1 Introduction

High-temperature corrosion is a form of corrosion that does not require the presence of a liquid electrolyte. Sometimes, this type of damage is called dry corrosion or scaling. The term oxidation is ambivalent because it can either refer to the formation of oxides or to the mechanism of oxidation of a metal (i.e., its change to a higher valence than the metallic state). Strictly speaking, high-temperature oxidation is only one type of high-temperature corrosion, but it is the most important high-temperature corrosion reaction. In most industrial environments, oxidation often participates in the high-temperature corrosion reactions, regardless of the predominant mode of corrosion (Lai, 1990). Alloys often rely upon the oxidation reaction to develop a protective scale to resist corrosion attack such as sulfidation, carburization, and other forms of high temperature attack. In general, the names of the corrosion mechanisms are determined by the most abundant dominant corrosion products. For example, oxidation implies oxides, sulfidation implies sulfides, sulfidation/oxidation implies sulfides plus oxides, and carburization implies carbides (John, 1999).

The hot corrosion degradation process of superalloys, consists of two stages i.e. initiation stage and propagation stage (Pettit and Giggins, 1987). No alloy is immune to hot corrosion attack indefinitely although there are some alloy compositions that require a long initiation time at which the hot corrosion process moves from the initiation stage to the propagation stage (Sidhu et al., 2005). However, a serious drawback of metallic material is the *deterioration in properties due to its interaction with the surrounding environments*. This results in premature failure of metallic components leading to plant shutdown and loss of economy, environmental pollution and risk to human lives. The annual direct loss of natural resources, i.e. metals, due to environmental degradation is also substantial (Chatterjee et al., 2001).

At high temperatures, metals can react “directly” with the gaseous atmosphere. Electrochemical reaction sequences remain, however, the underlying mechanism of high-temperature corrosion. High-temperature corrosion is a widespread problem in various industries such as (Roberge, 2000):

- ❖ Power generation Facilities
- ❖ Waste Incineration
- ❖ Refining and petrochemical
- ❖ Pulp and paper

- ❖ Automotive
- ❖ Aerospace and gas turbine
- ❖ Heat treating
- ❖ Mineral and metallurgical processing
- ❖ Chemical processing

A major problem of concern in the operation of thermal power plants is the issue of high temperature corrosion in boilers. High temperature boiler corrosion is a frequent cause of shutdown in thermal plants; along with problems such boiler slagging and/or fouling, and excessive refractory and metal wear. It is estimated that high temperature corrosion related shutdowns account for 70% loss of energy due to plant shutdowns. It is also estimated that corrosion-related maintenance cost accounts to a third of the annual maintenance budget and can be as high as 10% of the annual turnover (Adams et al., 2004)

2.5.2 Role of feed composition

The rate of corrosion in boilers is dependent on feed composition. It is generally assumed that this high rate of corrosion is inherent to the heterogeneous nature of the fuel and its variable chlorine content. The heterogeneous nature of the fuel makes it difficult to maintain uniform combustion conditions that are desired in steam boilers. The poor characteristics of the feed also result in product of incomplete combustion, i.e. high CO levels, occasional heat flux on the wall caused by flame impingement, and formation of aggressive deposits.

The composition of the fuel along with operating parameters influences the gas composition and deposit characteristics in the boiler tubes. Other factors such as high surface temperatures of the water wall and gas also influence high temperature corrosion in boilers. High temperatures of metal surfaces, either due to high radiation fluxes to the wall or inadequate transfer of heat to the water/steam result in the melting of deposits and acceleration of the rate of corrosion. The temperature gradient between gas temperature and the metal surface determines the condensation of vapor species, rate of deposition and the composition of the deposit. The presence of lead and zinc in the deposit lower its melting temperature. It is generally accepted that the high level of chlorides contributes to the problem of high-temperature corrosion in boilers, either in the form of HCl, Cl₂ or combined with sodium, potassium, zinc, lead, tin, and other elements.

2.5.3 Corrosion Sensitive Areas

Due to the composition of the fuel, the flue gas environment in thermal power plants is very aggressive because of gas components such as Cl_2 , HCl , S , alkali metals, These gases when cooled down form deposits on tube walls by condensation or sublimation; soft and sticky particles can also attach to the heat transfer surfaces. These deposits contain salt of chlorides and sulfates, oxides, silicates and unburned particles. Most sensitive areas attacked by corrosion are the heat transfer surfaces like water walls, screen tubes between the passes and the superheater tube bundles. Screen tubes are installed in some boilers in front of the superheater tubes bundles to reduce the temperature and velocities of the flue gas entering into the superheater tubes. Most modern thermal power plant boilers are operated at 40 bars steam pressures and steam temperature of 400°C , while some other designs, for reasons of thermal efficiency make use of even higher steam pressures and temperature. Fig. 2.20 shows a schematic of a typical waste-to-energy boiler and the corresponding corrosion sensitive areas in the facility (Rademakers et al., 2002).

Oxidation is the most important high temperature reaction. Oxidation of metals or alloys takes place when they are heated in a highly oxidizing atmosphere such as air or oxygen. An oxidation reaction is represented by the interaction of metals with oxygen to form oxide. There are a variety of factors on which the oxidation behaviors of a metal depends and the reaction mechanism involved may often be quite complex. An oxidation reaction begins with adsorption of oxygen molecules from the atmosphere, nucleation of oxides, formation of a thin oxidation layer, followed by its growth to a thicker scale (Albina et al., 2004).

The rate of corrosion in coal fired plant boilers is reported to be much higher. It is generally assumed that this high rate of corrosion is inherent to the heterogeneous nature of the fuel and its variable chlorine content. The heterogeneous nature of the fuel makes it difficult for operators to maintain uniform combustion conditions that are desired in steam boilers. The poor characteristics of the feed also result in product of incomplete combustion, i.e. high CO levels, occasional heat flux on the wall caused by flame impingement, and formation of aggressive deposits. Fuels contains alkali metals such as sodium and potassium, heavy metals such as lead, tin and zinc and various chlorine containing compounds, all of which can form potential corrosive agents. The composition of the fuel coupled with operating parameters influence the gas composition and deposit characteristics in the boiler

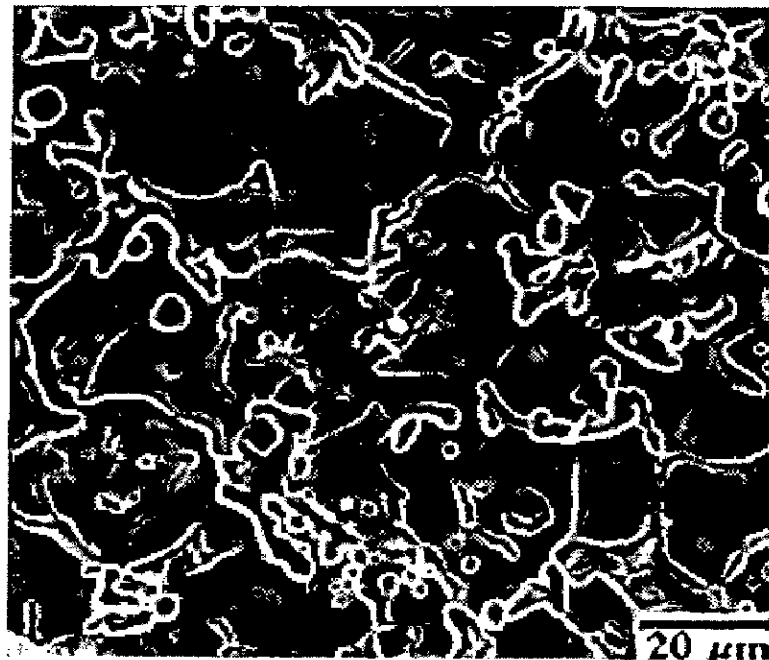


Fig. 2.15: Topographical image of an as sprayed plasma alumina coating. Note the formation of internal cracks within the splats which were noted to impact on the erosion performance (Westergard et al, 2000).

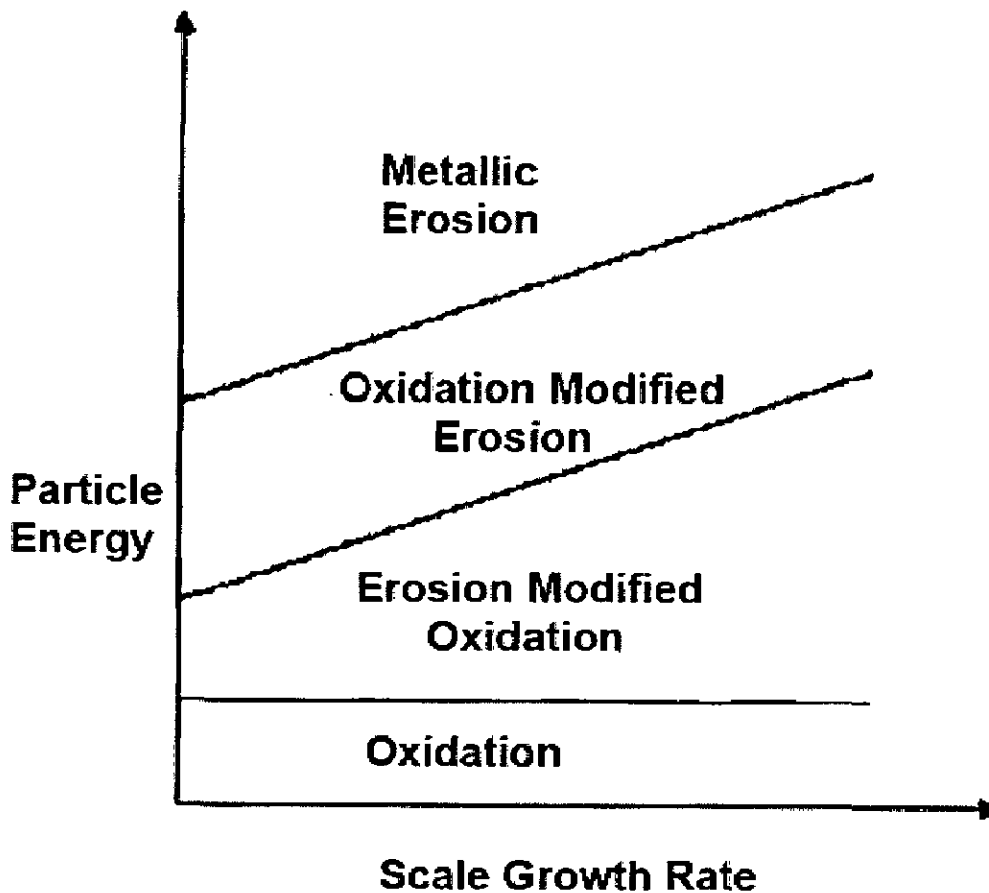


Fig. 2.16: Schematic diagram showing the types of degradation that can occur under conditions of combined oxidation-erosion (Barkalow and Pettit, 1979).

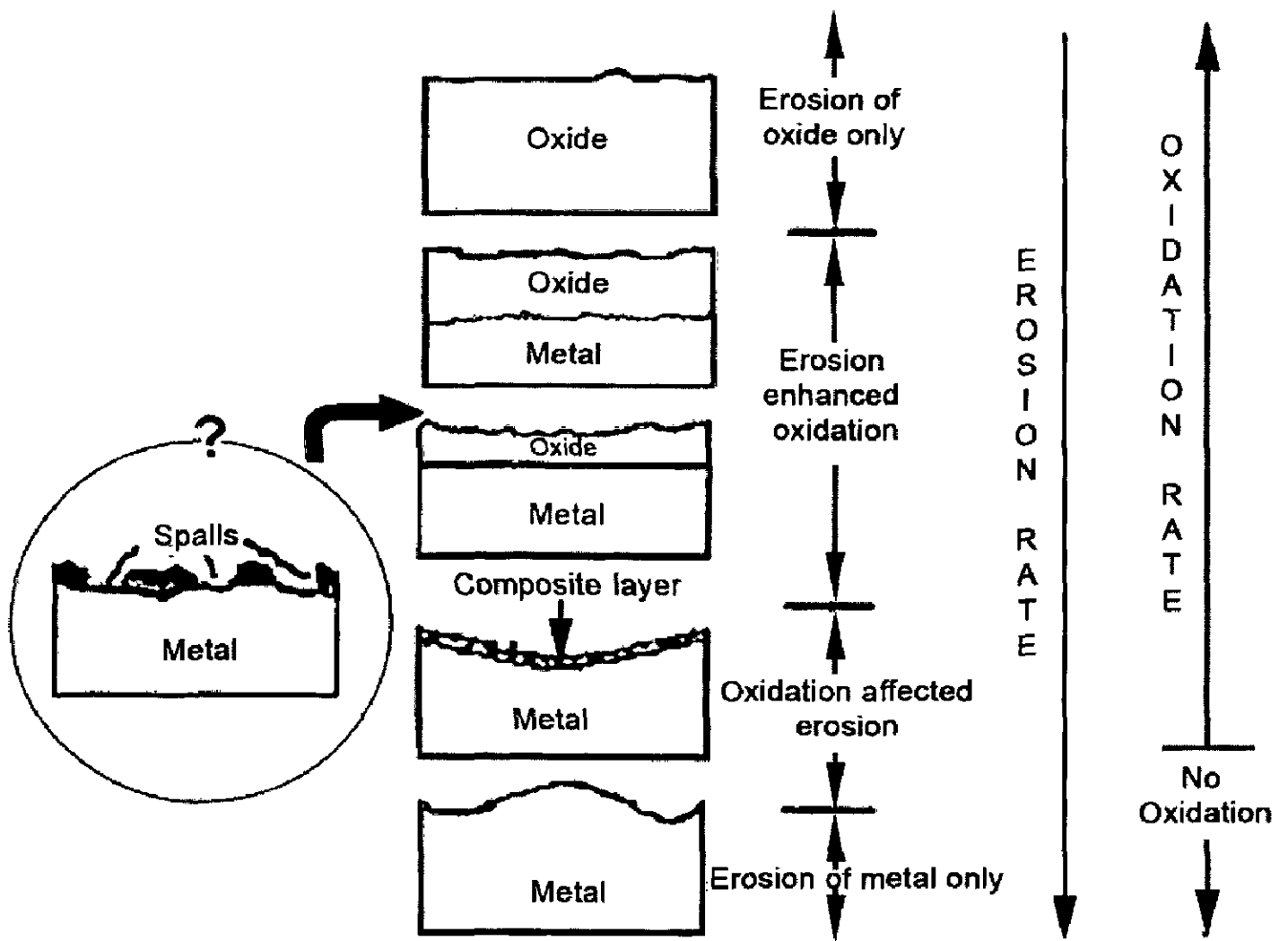


Fig. 2.17: Classification of erosion-corrosion (Kang et al., 1987).

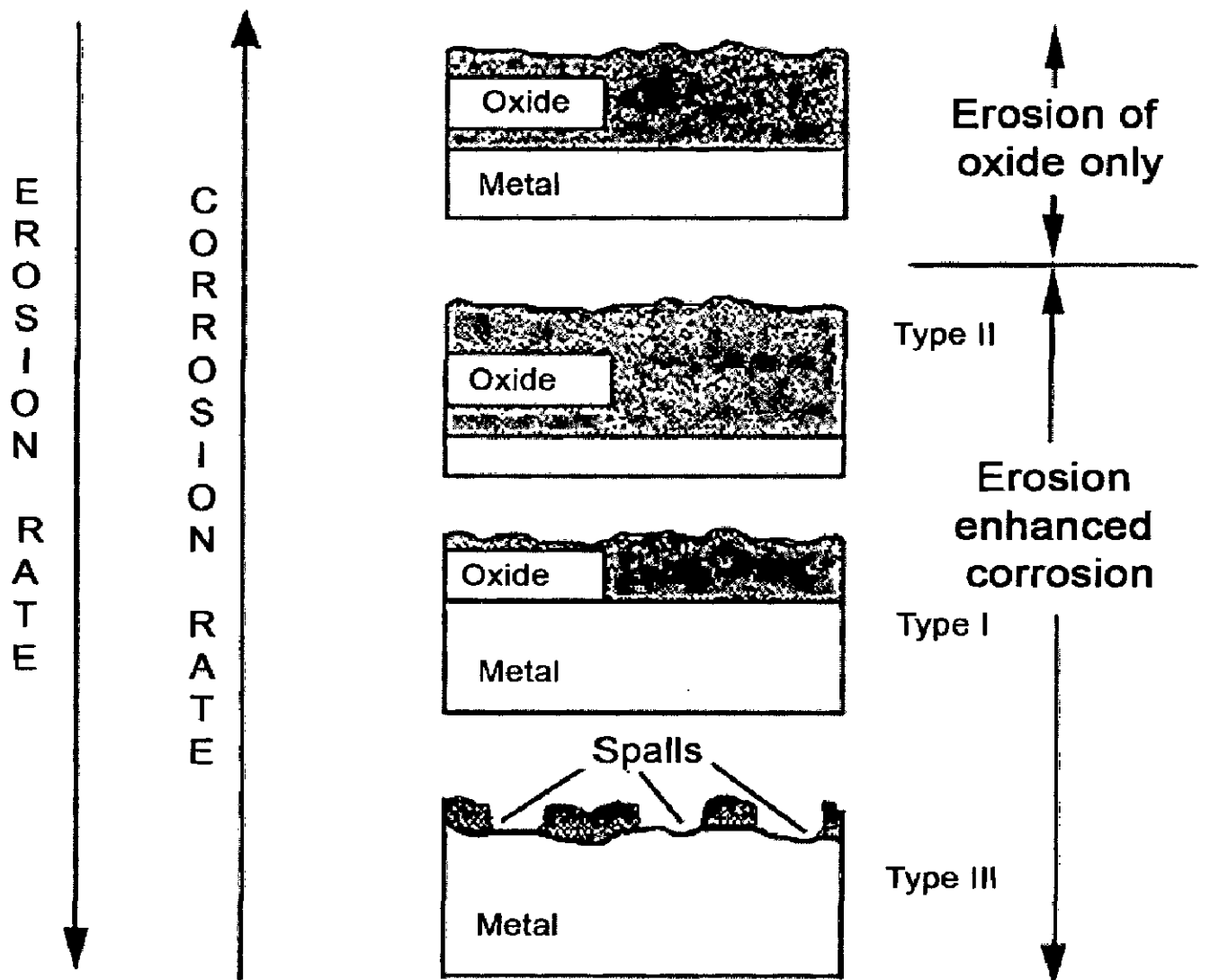


Fig. 2.18: Schematic of the different erosion-oxidation regimes (Rishel et al., 1990).

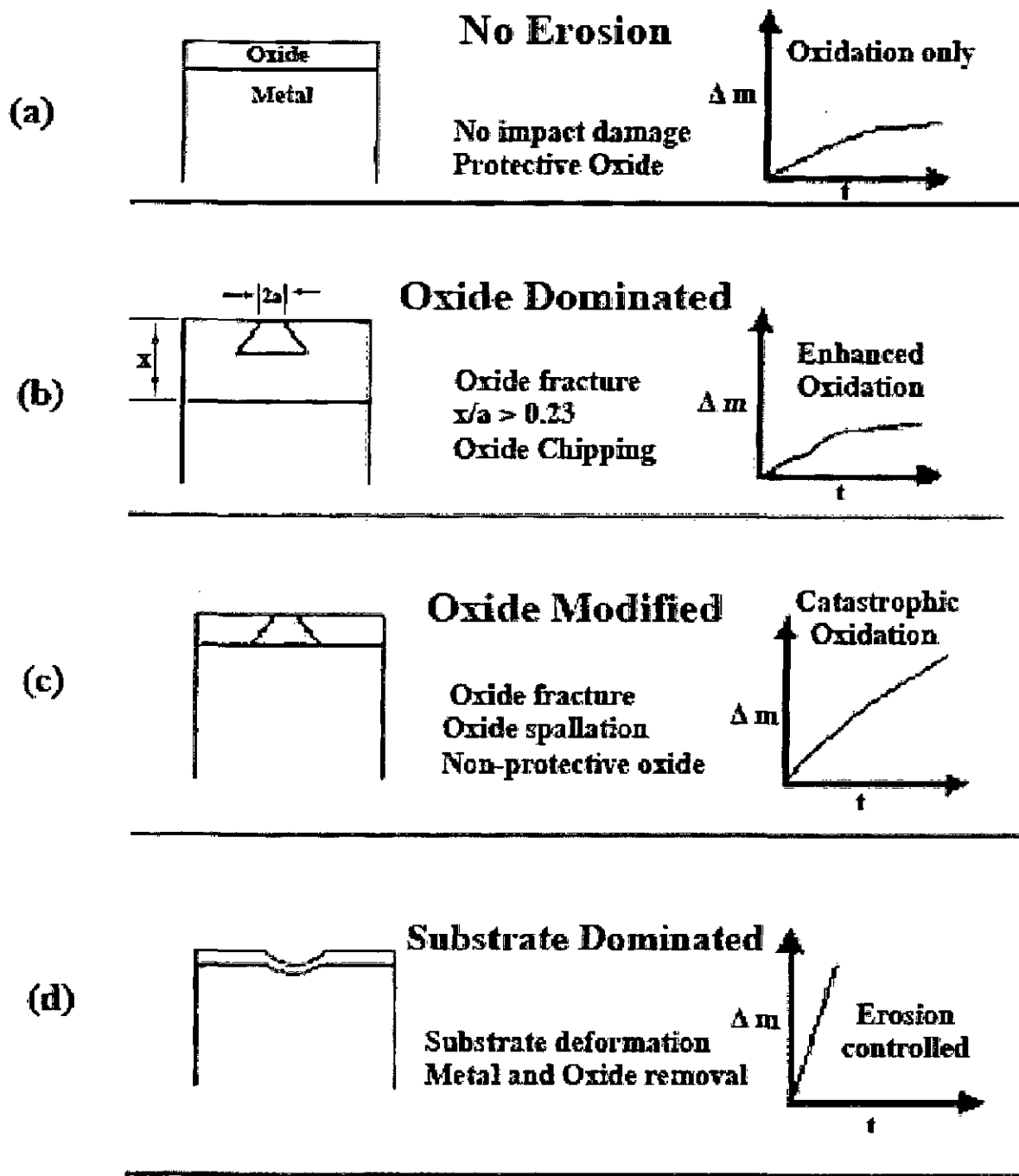


Fig. 2.19: Summary of erosion regimes observed at high temperatures (Stephenson, 1989; Stephenson and Nicholls, 1993).

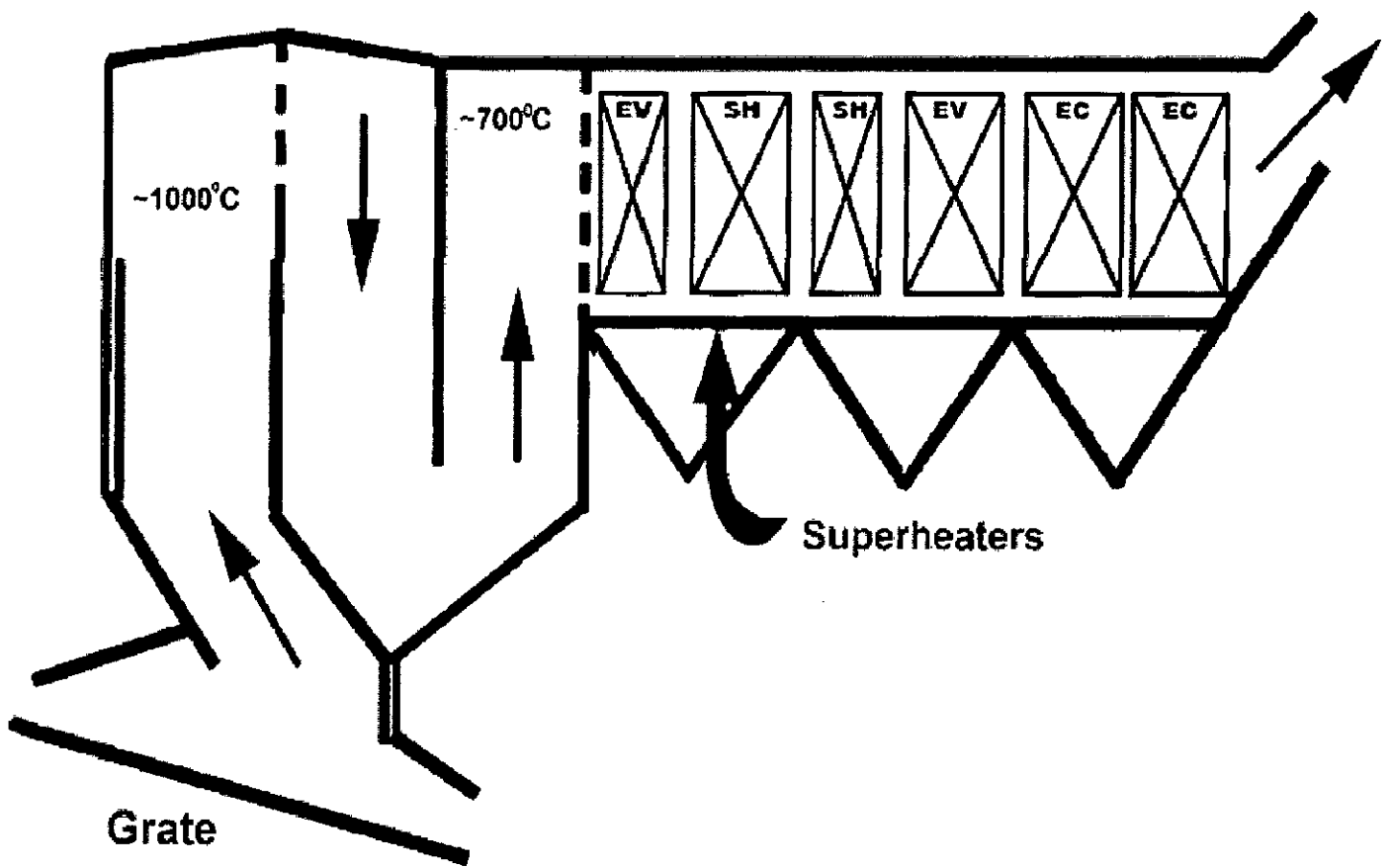


Fig. 2.20: Schematic of a typical boiler and the corresponding corrosion sensitive areas (Rademakers et al., 2002).

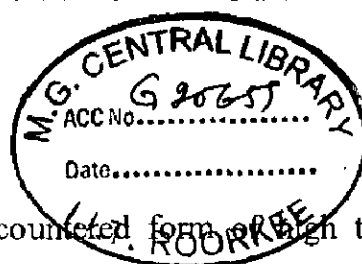
tubes. Other factors such as high surface temperatures of the waterwall and gas also influence high temperature corrosion in boilers. High temperatures of metal surfaces, either due to high radiation fluxes to the wall or inadequate transfer of heat to the water/steam result in the melting of deposits and acceleration of the rate of corrosion. The temperature gradient between gas temperature and the metal surface determines the condensation of vapor species, rate of deposition and the composition of the deposit. The presence of lead and zinc in the deposit lower its melting temperature. It is generally accepted that the high level of chlorides in waste contributes to the problem of high-temperature corrosion in boilers, either in the form of HCl, Cl₂ or combined with sodium, potassium, zinc, lead, tin, and other elements.

2.5.4 Corrosion Mechanisms

High temperature corrosion is a form of corrosion that does not require the presence of a liquid electrolyte. Alloys often rely upon oxidation reaction to develop a protective oxide to resist corrosion attacks such as sulfidation, carburization, and other forms of high temperature attacks. In general, the names of the corrosion mechanism are determined by the most abundant dominant corrosion products, i.e. oxidation for oxides, sulfidation implies sulfides, sulfidation/oxidation implies sulfides plus oxides, and carburization implies carbides. Oxidizing or reducing environments refer to the amount of oxygen present: oxidizing environment refers to oxygen rich environment, while reducing environment refers to very low oxygen concentration in the flue gas. The properties of high-temperature oxide films such as their thermodynamic stability, ionic defect structure and detailed morphology, play a crucial role in determining the oxidation resistance of a metal or alloy in a specific environment (Roberge, 2000).

2.5.4.1 Oxidation

Oxidation is the most commonly encountered form of high temperature corrosion. Oxidation is not always detrimental, e.g. as stated above most heat resistant alloys form an oxide film coating that provides corrosion resistance. The operating temperature plays a critical role in determining the oxidation rate for a given material; as temperature increases the rate of oxidation increases. Chromium oxide or chromia (Cr₂O₃) is one of the most common of those protective oxide films, thus increased chromium content in alloys is one of the most common ways of improving corrosion resistance. Other than chromium, alloying metals used to enhance oxidation resistance include aluminum, silicon, nickel and some of the rare earth metals. Alloys that rely on protective Al₂O₃ (alumina) scale formation are to be preferred over those forming



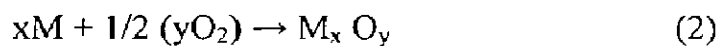
chromia for oxidation resistance above 1200°C (Lai, 1991). Austenitic steels are steels that have enough chromium and nickel to maintain austenite (ferric carbide/carbon in iron) at atmospheric temperature. Increasing the nickel content of the austenitic steels up to 30% can have strong beneficial synergistic effect with chromium. There are metallurgical considerations that impose limits on the amount of alloying additions that can be made in the design of engineering alloys, such as mechanical properties and the processing and manufacturing characteristics. Severe embrittlement tends to form in highly alloyed materials during high temperature exposure. It is therefore imperative to consider other properties besides the corrosion resistance when considering specific alloys for high-temperature applications, i.e. strength requirements. Few commercial alloys contain more than 30% chromium; silicon is usually limited to 2% and aluminum to less than 4% in wrought alloys. Yttrium, cerium and other rare elements are usually added only as a fraction of one percent (Tillack, 1992). A common approach to evade the problem of bulk alloying is the use of surface alloying. In this approach, a highly alloyed and oxidation resistant surface layer is deposited on a substrate layer that has the conventional composition and metallurgical properties.

2.5.4.1.1 Principles of oxidation reaction

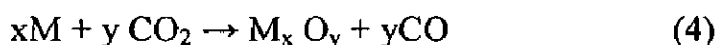
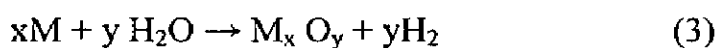
The principle of high-temperature oxidation of pure metals is described as follows (Jones, 1996). A metal, M, reacts with oxygen or other gases at high temperature by initial absorption of oxygen, and chemical reaction to form the surface oxide, by oxide nucleation and lateral growth into a continuous film that may protect the underlying metal. The film may also be thickening into a non-protective scale with various defects including cavities, microcracks and porosities (Jones, 1996). Oxidation in air by oxygen proceeds according to the reaction such as:



or generally:



A metal, M, can also be oxidized similarly by either water vapor or carbon dioxide according to the reactions,



The M_xO_y formed on the metal surface becomes a barrier between the substrate metal and oxidizing environment. Chemical thermodynamics predicts whether any reaction is

possible under given conditions, however the rate of oxidation cannot be predicted from thermodynamics. Each reactions (2), (3), and (4), for any metal is characterized thermodynamically by a standard free-energy change (ΔG°) which must be negative in order for the reaction to proceed spontaneously from left to right as written.

Since $\Delta G^\circ = \Delta H^\circ - T\Delta S^\circ$, a plot of ΔG° versus T approximates a straight line, which changes in slope where new phases form, i.e. at melting point or boiling point. These plots of standard free energy of reaction (ΔG°) as a function of temperature are known as the Ellingham diagram. Such a diagram can help visualize the relative stability of metals and their oxidized products. Fig. 2.21 shows an Ellingham diagram for many simple oxides (Gaskell, 1973). The values of ΔG° on in Ellingham diagram are expressed as kilojoules per mole of O_2 to normalize the scale and allow comparison of the stability of these oxides directly. The lower on the diagram a metal is found, the more negative the standard free energy of formation, and the more stable its oxide will be. For a given reaction (1), and assuming that the activities of M and MO_2 are taken as unity since activities of pure solids in the stable form are defined as unity at all temperatures and pressures, equation (5) may be used to express the oxygen partial pressure at which the metal and the oxide coexist (i.e. the dissociation pressure of the oxide).

The non-standard state oxygen dissociation pressures leading to oxide formation or reduction on pure metals can be found in the scales shown on the sides of the Ellingham diagram, i.e. for copper at 900°C , the oxygen dissociation pressure is about 10^{-8} atmosphere. Any oxygen pressure above this value will oxidize pure copper; any value below it will reduce copper oxide to pure copper at 900°C . Oxygen dissociation pressure ($P_{O_2/MO}$) can be obtained directly from the Ellingham diagram by drawing a straight line from the origin marked O through the free-energy line of the temperature of interest and reading the oxygen pressure from its intersection with the scale at the right side labeled (p_{O_2}). The oxidation rate of an alloy will be minimized if the oxide film has a combination of favorable properties that include: a) The film should have good adherence, to prevent flaking and spalling, b) the melting point of the oxide should be high, c) the oxide should have low vapor pressure to resist evaporation, d) the oxide film and the metal should have close to the same thermal expansion coefficients, e) the film should have high temperature plasticity to accommodate temperature differences in specific volumes of oxide and parent metal and differences in thermal expansion, and f) the film should have low electrical conductivity and low diffusion coefficients for metal ion and oxygen. Oxide scales are much stronger in compression than in

tension. If the oxide has a greater specific volume than the parent metal, as the oxide grows at the oxide metal interface, will be in compression and will be more likely protective.

Pilling and Bedworth (Roberge, 2000) proposed that the ratio of the oxide metal volume is a predictor of oxide protectiveness. The Pilling-Bedworth ratio expressed as follows:

$$\begin{aligned} PB \text{ ratio} &= \text{volume oxide produced / volume metal consumed} \\ &= \frac{Wd}{nDw} \end{aligned} \quad (6)$$

Where W = molecular weight of the oxide

D = density of the oxide

n = number of metal atoms in the oxide molecule

d = density of the metal

w = atomic weight of the metal

Often determination of the conditions under which a given corrosion product is likely to form is required (e.g., in selective oxidation of alloys). The plots of the standard free energy of reaction (ΔG°) as a function of temperature, commonly called Ellingham diagrams, can help to visualize the relative stability of metals and their oxidized products.

In general, the PB ratio should be slightly better than 1 to be protective, to foster moderate compressive stresses in the oxide and adherence to substrate metal. Very high PB ratios may result in excessive compressive stresses which buckle the film and destroy adherence. Table 2.2 lists the PB ratio of few metal/oxide systems. In practice, it has been found that PB ratios are generally poor indicators of the actual protective properties of the scale. Some reasons for this deviation from the PB rule include (Jones, 1996):

- ❖ Some oxides actually grow at the oxide-air interface, as opposed to the metal oxide interface.
- ❖ Specimen and component geometries can affect the stress distribution in the oxide films
- ❖ Continuous oxide films are observed even if $PB < 1$.
- ❖ Cracks and fissures in oxide layer can be self-healing as oxidation progresses.
- ❖ Oxide porosity is not actually predicted by the PB parameter.
- ❖ Oxides may be highly volatile at high temperatures, leading to non-protective properties, even if predicted otherwise by the PB parameter.

Six types of oxidation phenomena have been identified: (Roberge, 2000)

1. At low temperature, diffusion of oxygen and metal species through a compact oxide film

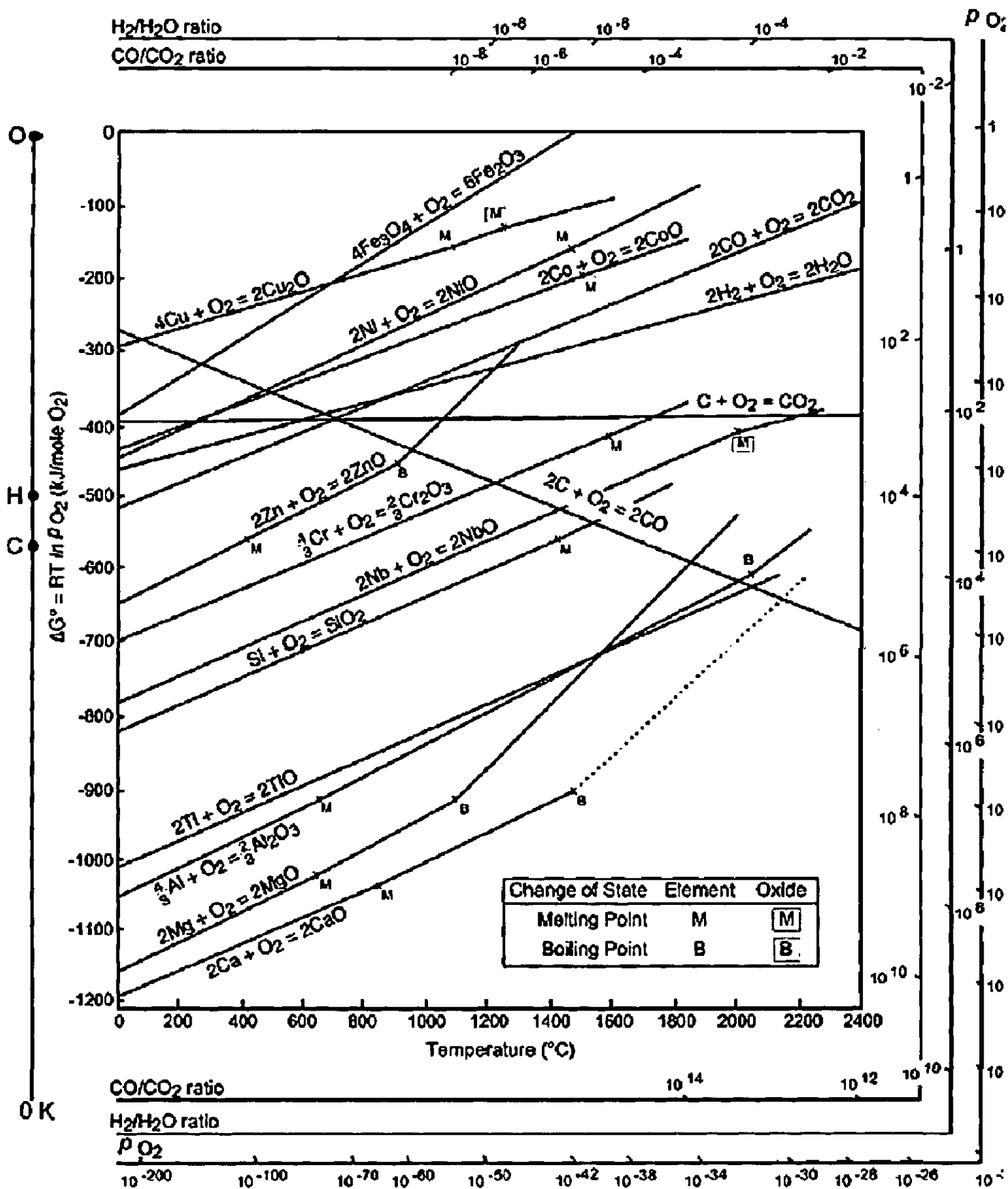


Fig. 2.21: The Ellingham diagram for metallurgically important oxides (Gaskell, 1973).

2. At moderate and high temperatures, a combination of oxide film formation and oxide volatility
3. At moderate and high temperatures, the formation of volatile metal and oxide species at the metal-oxide interface and transport through the oxide lattice and mechanically formed cracks in the oxide layer
4. At moderate and high temperatures, the direct formation of volatile oxide gases
5. At high temperature, the gaseous diffusion of oxygen through a barrier layer of volatilized oxides
6. At high temperature, spalling of metal and oxide particles.

2.5.4.1.2 Active oxidation in Thermal power plant boilers

The composition of the fuel has enormous effect on the corrosion of boilers tubes. (Prakash et al., 2001) When combusted, fuels form highly corrosive gases such as CO, Cl₂, HCl, S, alkali metals, and heavy metals such as Zn and Sn. These form deposits on the tubes and interact with the metal oxide coating. In the literature (Zahs et al., 2000; Nielsen et al., 2000; Spiegel and Grabke, 1991), it is known that the presence of chlorine in most cases prevents the formation of the protective oxide layer and causes accelerated attack in oxidizing environment. Chlorine can either be in the form of HCl, Cl₂, or combined with Na, K, Zn, Pb, Sn and other elements. Several studies in chlorine containing oxidizing atmospheres, on a number of different metals and alloys, have shown that even small changes in temperature or of the oxygen/chlorine ratio influence the corrosion behavior. The mechanism of active oxidation is described, and is generally accepted for metal temperatures above 450°C. For clarification purposes, the term deposits as used here means chlorides and sulfates due to deposition of condensed chlorides, fly ash, and others, while the term scale is used to describe the protective oxides.

The mechanism of active oxidation comprises several steps: a) the formation of chlorine at the scale surface, b) penetration of chlorine into the scale to the oxide/metal interface, c) formation of chlorides on the metal surface components, d) diffusion of chlorides outwards and, e) reaction of chloride with available oxygen in the atmosphere to give metal oxide and chlorine (Grabke et al., 1995).

Table 2.2: Properties of Metal Oxides (Jones 1996)

Metal	Oxide	PB Ratio	Protectivenessa
Aluminum	Al ₂ O ₃	1.28	P
Calcium	CaO	0.64	NP
Cadmium	CdO	1.42	NP
Cobalt	Co ₂ O ₃	2.40	P
Copper	Cu ₂ O	1.67	P
Chromium	Cr ₂ O ₃	2.02	P
Iron	FeO	1.78	P
Magnesium	MgO	0.81	P
Manganese	MnO ₂	2.37	P
Molybdenum	MoO ₃	3.27	NP
Nickel	NiO	1.70	P
Lead	PbO	1.28	NP
Silicon	SiO ₂	2.15	P
Tantalum	Ta ₂ O ₅	2.47	NP
Titanium	Ti ₂ O ₃	1.76	NP
Uranium	UO ₂	1.97	NP
Zinc	ZnO	1.58	NP
Zirconium	ZrO ₂	1.57	P

P: Protective; NP: Not Protective

2.5.4.2 Corrosion in deposits by sulfation and molten salts

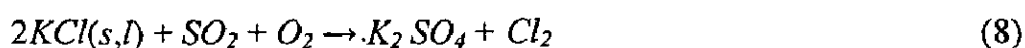
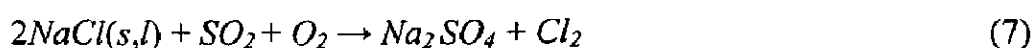
Tiwari and Prakash (1996 and 1997) have reported the hot corrosion studies on some industrial superalloys in the temperature range of 700-900°C in the environments comprising of pure Na₂SO₄, Na₂SO₄-15%V₂O₅ and Na₂SO₄-60%V₂O₅. Corrosion rates were observed to be very high in Na₂SO₄-60%V₂O₅ environment due to its low melting point. It was revealed that the severe degradation in this environment was due to the cracking of protective scale under the influence of the fluxing action of the molten salt (Tiwari 1997). Nanni et al (1987) have studied the kinetics of corrosion and the morphology of the scales formed on pure iron,

manganese and chromium with Na₂SO₄ deposits. They have reported that at all the temperatures salt coated iron has been observed to exhibit accelerated attack whereas the corrosion rate of chromium was not appreciably affected by the deposited salt. They have further suggested that the enhanced corrosion phenomenon is due to low melting liquid sulphate formation. Singh (2005) investigated the cyclic corrosion behavior of nickel based superalloy in Na₂SO₄-60%V₂O₅ environment at 900°C. Intense spalling of the scale was observed in super alloy superni 601 and weight gain including the spalled scale was enormous during the molten salt corrosion study. This NaVO₃ formed due to reaction of Na₂SO₄ and V₂O₅ acts as a catalyst (Kolta et al, 1992) and also serves as oxygen carrier to the base alloy, therefore will lead to rapid oxidation of the basic elements of the superalloys to form protective oxide scales. Simultaneously, the protective scale is destroyed or eliminated by molten salts and consequently the metal surface is exposed to direct action of aggressive environment as has been indicated in the current investigation.

2.5.4.2.1 Corrosion by sulfation of chloride salts

The effects of chloride salts on corrosion have been observed and there is an overwhelming consensus in the literature (Rademakers et al., 2002; Nielsen et al., 2000; Spiegel and Grabke, 1991; Grabke et al., 1995) that chlorides are a major factor of corrosion either in gas phase active oxidation or at low temperature oxidation. Sidhu and Prakash (2006A) studied the performance of plasma sprayed coatings in Na₂SO₄-60%V₂O₅ environment at 900°C. They reported comparatively lesser corrosion resistance offered by Ni₃Al coatings due to the internal sulphidation. Penetrated sulphur reacts with the reactive elements of the base metal to form sulphides within the metal, which eventually convert into oxides due to advancing scale metal interface.

The deposition of sulfates and chlorides occurs by condensation and/or from attachment of particles (fly ash), which may contain sulfates and alkali chlorides. Analysis of deposits has shown that the outer layers of the protective oxide scales contain sulfates such as CaSO₄, Na₂SO₄, K₂SO₄, PbSO₄, and ZnSO₄ while the inner scales contain metal chlorides like CaCl₂, KCl, PbCl₂ and ZnCl₂. The formation of sulfates in the deposit is believed to be due to the sulfation of the alkali chlorides in the deposit and is believed to occur at the outer surface of the deposit (Grabke et al., 1995). Deposited metal chlorides react with gaseous SO₂ and or SO₃ forming condensed alkali sulfates, as shown by equations (7) and (8).

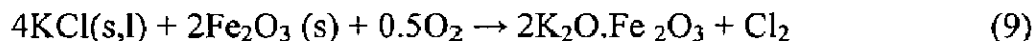


These reactions release gaseous chlorine that diffuses towards the metal/oxide interface creating a net reaction that leads to a continuous transport of metal from the

metal/oxide interface towards a higher oxygen partial pressure. Therefore, after sulfation, the reaction mechanism is similar to that of active oxidation.

2.5.4.2.2 Corrosion by chlorides at metal/oxide interface

In this case, gaseous chlorine is liberated by the reaction of condensed alkali chlorides in particular, KCl, with the metal scale (9) (Li et al., 2003):



These reactions result in high partial pressures of Cl_2 and the corrosion mechanism can proceed similar to that of active oxidation. Thermodynamics do not favor the reaction of condensed sodium chloride with oxides of iron (reaction 10) since the Gibbs free energy of formation is positive.



2.5.4.2.3 Reaction involving molten salts mixtures

Formation of salt mixtures is generally believed to be the main reason for low temperature metal corrosion, in the temperature range of 250°C to 400 °C. Salt mixtures either chloride-chloride or chlorine-sulfate, can have relatively low melting temperatures (eutectic solutions), for example, KCl has a melting point of 774°C but can form lowtemperature eutectics in solution with several other substances. Fig. 2.22 shows the binary phase diagram of KCl and FeCl_2 showing a eutectic temperature of 350°C. Once the melting point temperature is reached, the presence of a liquid phase on the surface of the metal increases the corrosion rate due to the following reasons (Nielsen et al., 2000): a) chemical reaction is faster in the liquid phase than a solid-solid reaction and b) a liquid phase provides an electrolyte, i.e. a pathway for ionic charge transfer, for the electrochemical attack.

2.5.4.2.4 Corrosion by molten sulfates

There are two types of sulfate reactions generally accepted: 1) the formation of pyrosulfates and 2) the formation of alkali metal trisulfate, from the reaction of iron oxides in contact with alkali sulfates in an oxidizing atmosphere and in the presence of sulfur dioxide. Alkali iron trisulfate is known to have serious corrosive effects but only in the liquid state. The melting points of sodium iron trisulfate and potassium iron trisulfate are at 624°C and 618°C respectively, above which catastrophic corrosion may occur. A mixture of these two compounds however, has a melting point as low as 550°C.

a) Formation of pyrosulfates (Rademakers et al., 2002; Karlsson et al., 1990; Harb and Smith, 1990): The general reaction for the formation of a liquid phase containing pyrosulfates can start with the reaction of alkali chloride deposits on metaloxide interface according to reaction (11) (Karlsson et al., 1990):

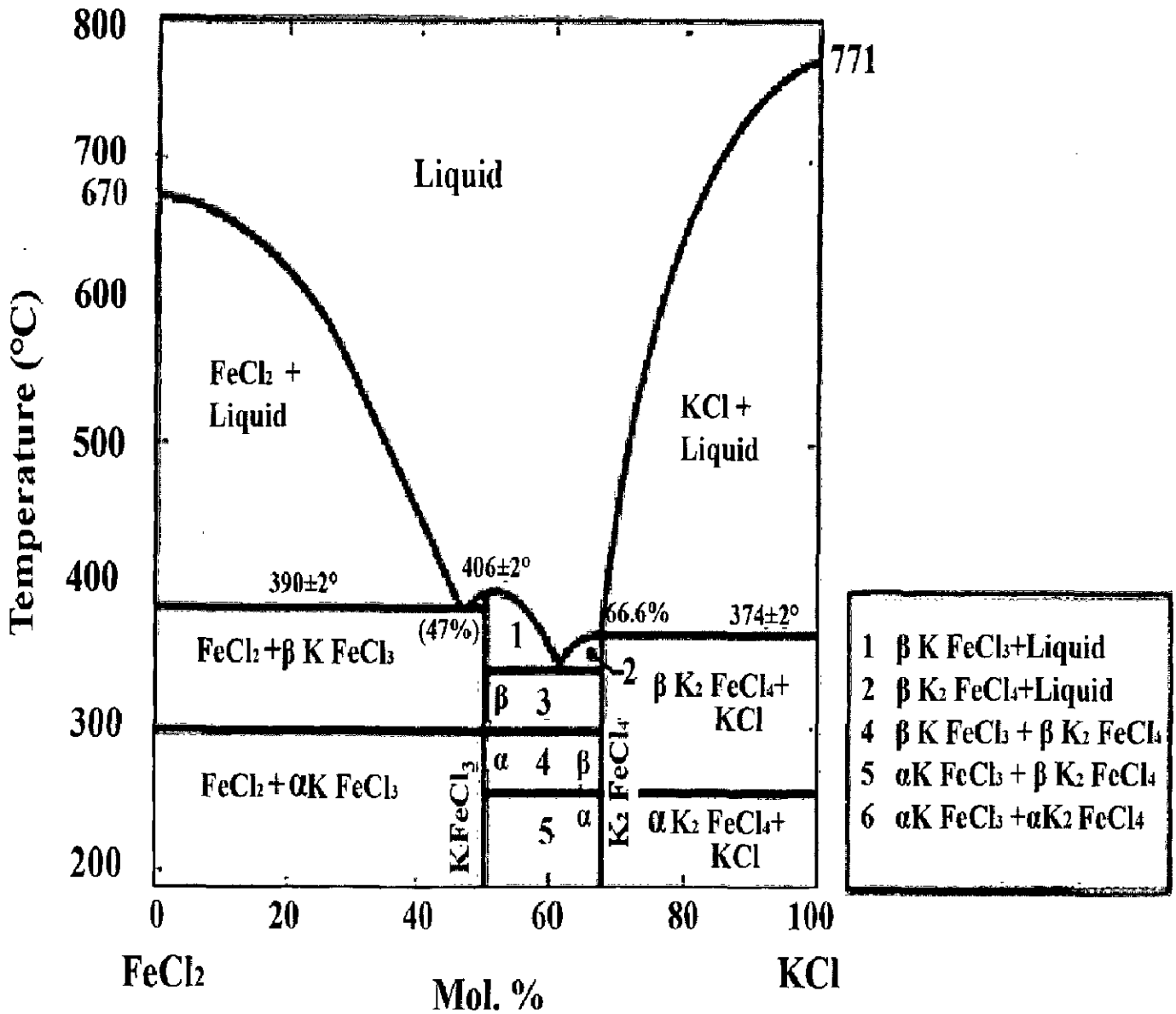
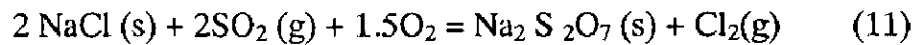


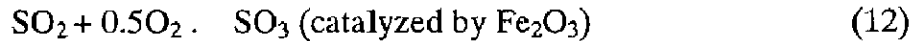
Fig. 2.22: Binary phase diagram of KCl-FeCl₂ (Neilson et al. 2000)



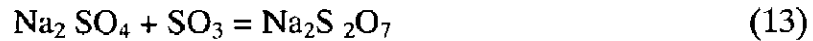
$$(\Delta G^\circ (T) = -137 + 0.308T(\text{K}) \text{ kJmol}^{-1} \text{ pyrosulfate})$$

The Gibbs free energy of the reaction is negative below 723K (450°C), and thus the reaction will only proceed below this temperature. The following mechanism has been proposed for reaction (11):

- Formation of SO₃: Given sufficient amount of SO₂ in the flue gas, SO₃ can be formed, as the oxides (iron oxide) can catalyze the oxidation of SO₂.

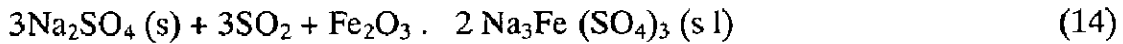


- Formation of pyrosulfates: If the deposit contains iron oxides that catalyze the oxidation of SO₂ to SO₃ then pyrosulfates can form (Rademakers et al., 2002; Harb and Smith, 1990):



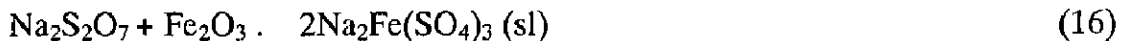
b) Formation of alkali-metal-trisulfates:

The most common form of accelerated corrosion of the superheater tubes on conventional coal-fired boilers is caused by the presence of liquid phase alkali-metal trisulfates. The deposit alkali sulfates react with SO₂ and iron oxide to form liquid alkali-iron sulfates according to reactions (14)-(15).

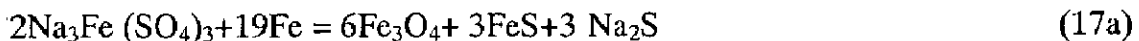


The following mechanisms describe the formation of alkali-metal trisulfates (reactions 14-15) and the subsequent corrosion of the metal:

- Formation of alkali metal trisulfate: With pyrosulfates formed (reaction 13), and at about 500°C and above, the trisulfate can attack the protective metal oxide according to reaction (16):



- Sulfidation of the metal: At 550°C and higher metal temperatures, the alkali-metal trisulfate can attack the metal according to reaction (17). The SO₃ liberated is available again to react with Na₂SO₄ resulting in cyclic corrosion reaction.



also:



This type of corrosion is generally described by what is called the basic fluxing model involving corrosive attack by forming a basic solute of the protective scale. The rate of

corrosion is observed to be a function of the metal temperature as illustrated in Fig. 2.23 (Cutler and Raask, 1981). The Fig. shows the corrosion rate of the superheater tubes of coal-fired plants at metal temperature above 550°C. The profile of the curve has something to do with the behavior of the ash deposit (which contains sulfates and chlorides (Grabke et al., 1995). At the metal temperatures at the lower end of the range for the superheater tubes, the ash deposit forms a porous layer and the normal oxidation of the metal proceeds, controlled by the growth of the protective oxide layer on the metal surface. As the metal temperatures increase (650°C), the alkali metal sulfate combustion residues form a molten layer next to the protective oxide on the surface of the metal and the corrosion rates increase rapidly over the temperature range in which the melting occurs. The reduction of corrosion rate after the peak (right side of the bell-shape curve) may be explained by the decreasing stability of the iron or chromium sulfates at higher temperatures.

The molten sulfate influences the corrosion mechanism in two ways: 1) it modifies the oxidizing potential at the outer surface of the oxide layer that is formed on the metal, and 2) it allows the dissolution of this protective oxide by the metal sulfate. The oxidation of the metal requires the transport of the oxidizing species through the molten sulfate layer. SO_3 is much more soluble than oxygen in the molten sulfate because of the chemical interaction involving the formation of the pyrosulfate ion, thus SO_3 acts as the oxidizing species under these conditions. Oxidation of the metal decreases the oxygen potential at the interface between the protective oxide and the molten sulfate layer; the chemical equilibrium between the oxy-sulfur species that are established at this interface then cause an increase in the sulfur potential to a value that is much greater than in the bulk of the flue gas. This increase in the sulfur potential then allows sulfidation of the metal to take place and leads to the formation of a scale that is less protective than that from simple oxidation. Fig. 2.24 shows a schematic diagram for the sulfur mechanism based on the increase in sulfur potential caused by transport of oxidizing species through the molten layer of the alkali metal sulfate. Molten sulfate corrosion by itself should not be a problem in waste-to-energy boilers. One of the reasons is that metal temperatures in waste-to-energy boilers, in particular the superheater tubes do not exceed 530°C. Also, the amount of sulfur in the feed is not as high as in conventional coal-fired power plants. However, the presence of chlorides can affect molten sulfate corrosion in a number of ways: Chlorides may cause the breakdown of the normally protective layer, by the same mechanism as the molten chloride salts fluxing the oxide scale. When there is a protective scale, normally SO_2/SO_3 cannot diffuse through the scale. In case the oxide break or ruptures, SO_2/SO_3 can penetrate the oxide layer, and result in increased

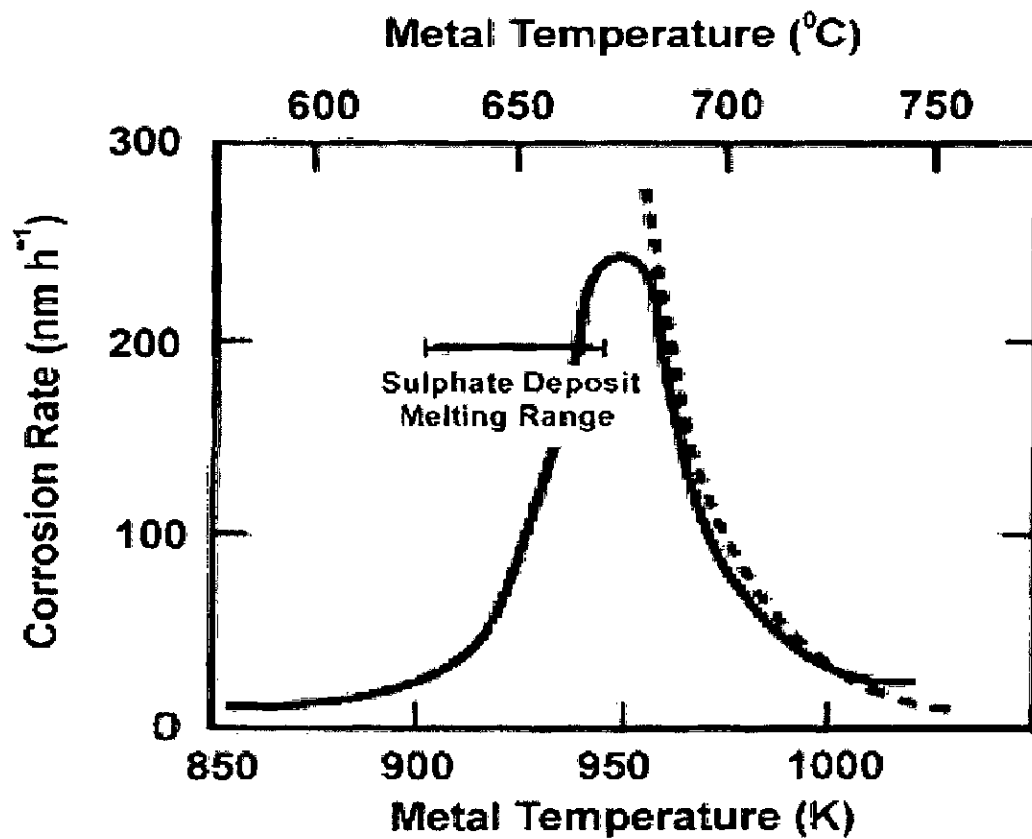


Fig. 2.23: Temperature dependence of corrosion on superheater tubes in coal fired boilers. The dotted line is a theoretical prediction (Cutler and Raask, 1981).

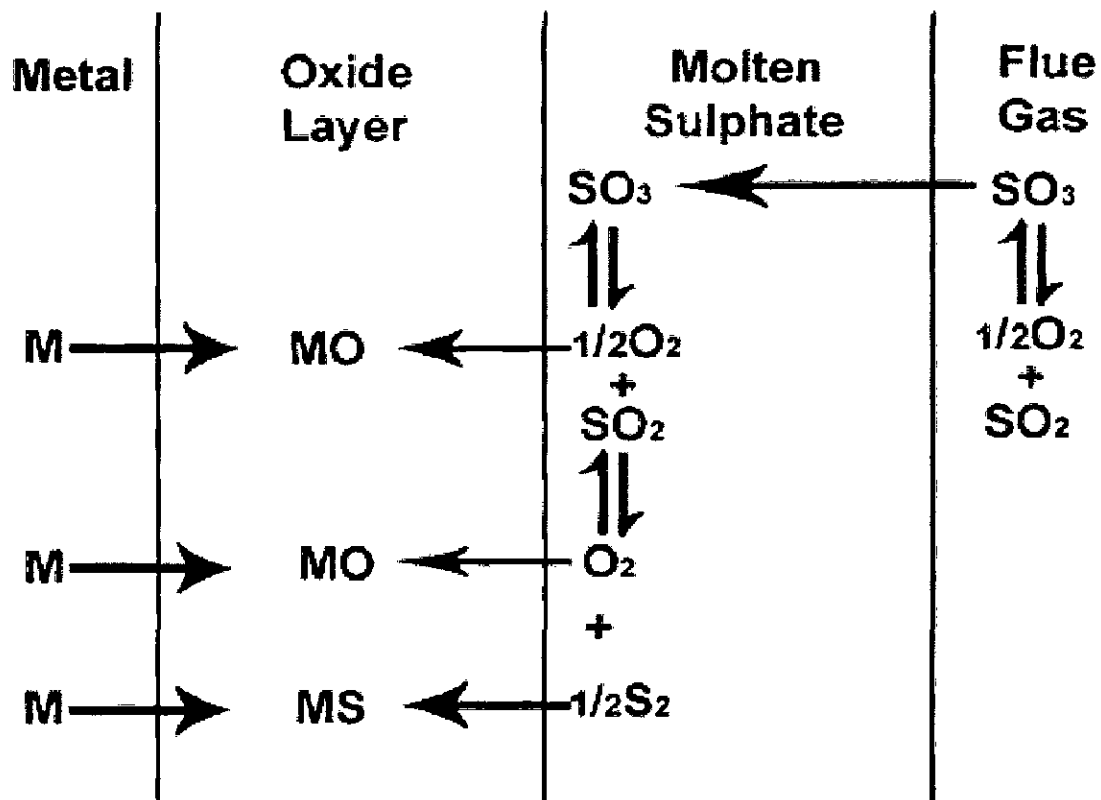


Fig. 2.24: Schematic diagram for the sulfidation mechanism and transport of oxidizing species.

sulfate corrosion of the superheater tube. Also, the presence of chlorides in the alkali sulfate decreases the melting temperature of the salt mixture, thus increasing the temperature range of corrosion up to a point where the superheaters of the waste-to-energy facilities are vulnerable (extending the lower end of the bell-shape curve of Fig. 2.23).

2.5.4.3 Erosion Corrosion in energy generation systems

Boilers are used to burn pulverized coal, biomass and/or waste. Inside the boiler, there is a tubing system, including water and steam. The tubing is heated by the flame of the burning material. The tubes, carry the steam under high pressure ($p \geq 17$ MPa) and are subjected from the outside to erosive and hot-corrosive wear resulting from ash and all products of burning (Kay, 1987). Fig. 2.25 illustrates a schematic of typical coal fired boiler. The boiler tubes could be coated with stainless-steel type 310 by air-plasma spraying (Bennett and Quigley, 1990) or high-velocity combustion spraying (Kay, 1987). Spraying can be carried out in a workshop or in situ. More, recently Langer et al., (2005a) proposed the application of self fluxing alloys to be deposited via any thermal spray method and then post-sprayed treated. Finally, Kobayashi and Yamaguchi (2004) have carefully optimized the composition and morphologies of powders to be applied via high-velocity combustion spraying on boiler tubes. The best properties were revealed by a commercial cermet, Cr_3C_2 +25 wt% NiCr, taken for comparison and two, developed by these authors, spray-dried and sintered powders where the particles included an Ni_3Al matrix and borides such as ZrB_2 , WB, CrB and MoB as reinforcements.

In many industrial applications, the surfaces undergoing high temperature corrosion are not clean; rather, surface deposits of ash and/or salt form on the components. Chemical reactions between these deposits and the protective surface oxide can lead to destruction of the oxide and rapid corrosive attack. In gas turbines, oxidized sulfur contaminants in fuel and sodium chloride from ingested air (marine atmospheres) tend to react to form sulfates that are subsequently deposited on surfaces. The presence of sodium sulfate, potassium sulfate, and calcium sulfate together with magnesium chloride has been reported in such deposits for compressor-stage components (Bornstein, 1996). Sodium sulfate is usually regarded as the dominant component of the salt deposits. The detailed mechanisms of hot corrosion have been described by Rapp and Zhang, (1994). Hot corrosion is generally considered to occur in the temperature range of 800 to 950°C, although attack at lower temperatures has also been reported. Testing has indicated that in commercial nickel- and cobalt-based alloys, chromium

additions play an important role in limiting this type of damage. Alloys with less than 15% of chromium as alloying addition are considered highly vulnerable to attack. Refinery heaters and boilers that are fired with low-grade fuels may be vulnerable to corrosion damage, especially if vanadium, sulfur, and sodium contaminants are present at high levels. Vanadium pentoxide and sodium sulfate deposits assume an important role in this type of corrosion damage. The melting point of one of these mixed compound deposits ($\text{Na}_2\text{SO}_4\text{-V}_2\text{O}_5$) can be as low as 630°C , at which point catastrophic corrosion can set in. In these severe operating conditions the use of special high-chromium alloys is required. A 50Ni-50Cr alloy has been recommended over the use of 25Cr-12Ni and 25Cr-20Ni alloys for hangers, tube sheets, and other supports. Ash and salt deposit corrosion is also a problem area in fireside corrosion of waste incinerators, in calcining operations, and in flue gas streams. (Roberge, 2000)

The corrosion portion of the annual operational and maintenance cost was estimated at \$698 million for fossil fuel, \$2,013 million for nuclear facilities, and \$75 million for hydraulic power, for a total of \$2,786 million. Thus, the total direct cost of corrosion in the electric utility industry in 1998 is estimated at \$6.889 billion per year. In comparison, an Electric Power Research Institute (EPRI) study estimated the cost of corrosion to the user/consumer to be \$17.27 billion per year. The cost to consumers includes taxes, sales, administration, and profits. This analysis indicates that the indirect costs (to the user, \$17.27 billion minus \$6.889 billion = \$10.381 billion) are 1.5 times the direct cost (to the owner/operator, \$6.9 billion). (Koch et al., 2001)

Because of the complex and often corrosive environments in which power plants operate, corrosion has been a serious problem, with a significant impact on the operation of the plants. In the 1970s and the 1980s, major efforts were spent on understanding and controlling corrosion in both nuclear and fossil fuel steam plants, and significant progress was made. However, with the aging of several plants, old problems persist and new ones appear. For example, corrosion continues to be a problem with electrical generators and with turbines. Specifically, stress corrosion cracking in steam generators in PWR plants and boiler tube failures in fossil fuel plants continue to be problems. There are further indications that aging of buried structures, such as service water piping, has started to result in leaks that cannot be tolerated. Environmental requirements and deregulation of the power industry often result in less attention being paid to corrosion and deterioration of materials of construction. If not addressed in a timely manner, these materials will corrode to the point that major repair and rehabilitation are required. The cost of corrosion will then, in the near future, increase

significantly. Fig.2.26 shows that the annual cost of corrosion in the electrical utilities sector to be \$6.9 billion, which is 14 percent of the total cost of the Utilities categories.

Table 2.3: Characterisation of coal gasification atmosphere at 1255 K (982°C), (Kane, 1980).

	Inlet	1 atm	Outlet	68 atm
	Mole Fraction	Mole Fraction	Mole Fraction	Partial Pressure, atm
H ₂	0.24	0.367	0.340	23.1
CO ₂	0.12	0.124	0.189	12.85
H ₂ S	0.01	8.8 x 10 ⁻³	9.16 x 10 ⁻³	0.623
H ₂ O	0.39	0.301	0.324	22.03
CH ₄	0.05	5.05 x 10 ⁻⁶	1.61 x 10 ⁻²	1.09
CO	0.18	0.202	0.121	8.25
NH ₃	0.01	-	-	-
SO ₂	-	2.9 x 10 ⁻⁷	6.5 x 10 ⁻⁹	4.4 x 10 ⁻⁷
COS	-	1.7 x 10 ⁻⁴	1.8 x 10 ⁻⁴	1.2 x 10 ⁻²
H	-	3.3 x 10 ⁷	3.8 x 10 ⁻⁸	2.6 x 10 ⁻⁶
CS ₂	-	2.7 x 10 ⁻⁸	2.8 x 10 ⁻⁸	1.9 x 10 ⁻⁶
S ₂	-	2.51 x 10 ⁻⁶	4.69 x 10 ⁻⁸	3.18 x 10 ⁻⁶
O ₂	-	1.01 x 10 ⁻¹⁵	2.0 x 10 ⁻¹⁷	1.37 x 10 ⁻¹⁵
log PS ₂	-	-5.599		- 5.496
log PO ₂	-	-14.994		- 14.863
log PC	-	-24.032		- 22.296

Log PC for soot formation = - 21.585 at 1255 K.

2.5.4.3.1 Characterisation of Gasification Environments

The characterisation of complex industrial atmospheres, both with respect to composition and oxidation, carburisation and sulphidation potentials is important in the

design and operation of laboratory tests for materials evaluation (Kane, 1980). The gas environments that result from the reaction of coal with steam and oxygen or air are mixtures that include CO, CO₂, CH₄, H₂, H₂S, H₂O, NH₃ and N₂. In coal gasification atmospheres that involve species such as oxygen, sulphur and carbon, it has been well established that the reliable performance of various components is strongly dependent on the sulphur contents of the gas phase, duration and temperature of exposure (Natesan, 1985). Table 2.3 enlists the characterisations similar to those prevailing in coal gasification systems.

2.6 ROLE OF COATINGS IN AGGRESSIVE ENVIRONMENTS

Electric power generation today and in the future is using and will use steam turbines, gas turbines and turbo generators, steel tubing and heat exchangers and boilers. Components consist of many parts that are welded, brazed or assembled. Each part has a specific function within the power plant. The original equipment manufacturers and the power plant customers like utilities or other power producers consider as the most important parameters of a power plant:

- ❖ Investment cost
- ❖ Operation cost
- ❖ Long-term reliability
- ❖ Availability and scheduled, short maintenance

These parameters translate into requirements for components like material cost, optimized fuel cost, high operation temperatures and long operation times without in-operation control possibilities (Schneider et al., 2006). There are two methods to reduce corrosion in boiler tubes: One is to influence the operating conditions of the heat exchanger tubes and the other is to use better corrosion resistant material. Some of the suggested ways to influence the combustion conditions are: a) improvement of the combustion process to get less corrosive environment, b) improved process control, i.e. particular control of the flue gas and temperature, and c) modification of the design, in particular flow dynamics and mixing, and the overall design of the system. With respect to application of corrosion resistant materials, there are a number of options: a) application of composite tubing consisting of two layers, with the inner layer from a boiler steel and the outer layer made from a highly corrosion-resistant material, b) application of surface welding (cladding), c) application of resistant coatings from resistant materials, e.g. high velocity oxygen flame (HVOF) to produce high quality coatings and d) application of refractory lining or ceramic tiles in particular on the wall of the first pass (Albina, 2005). Today, all power plant hardware is coated wherever no affordable and reliable structural material can be found that resists the operation environment. In general, the reaction

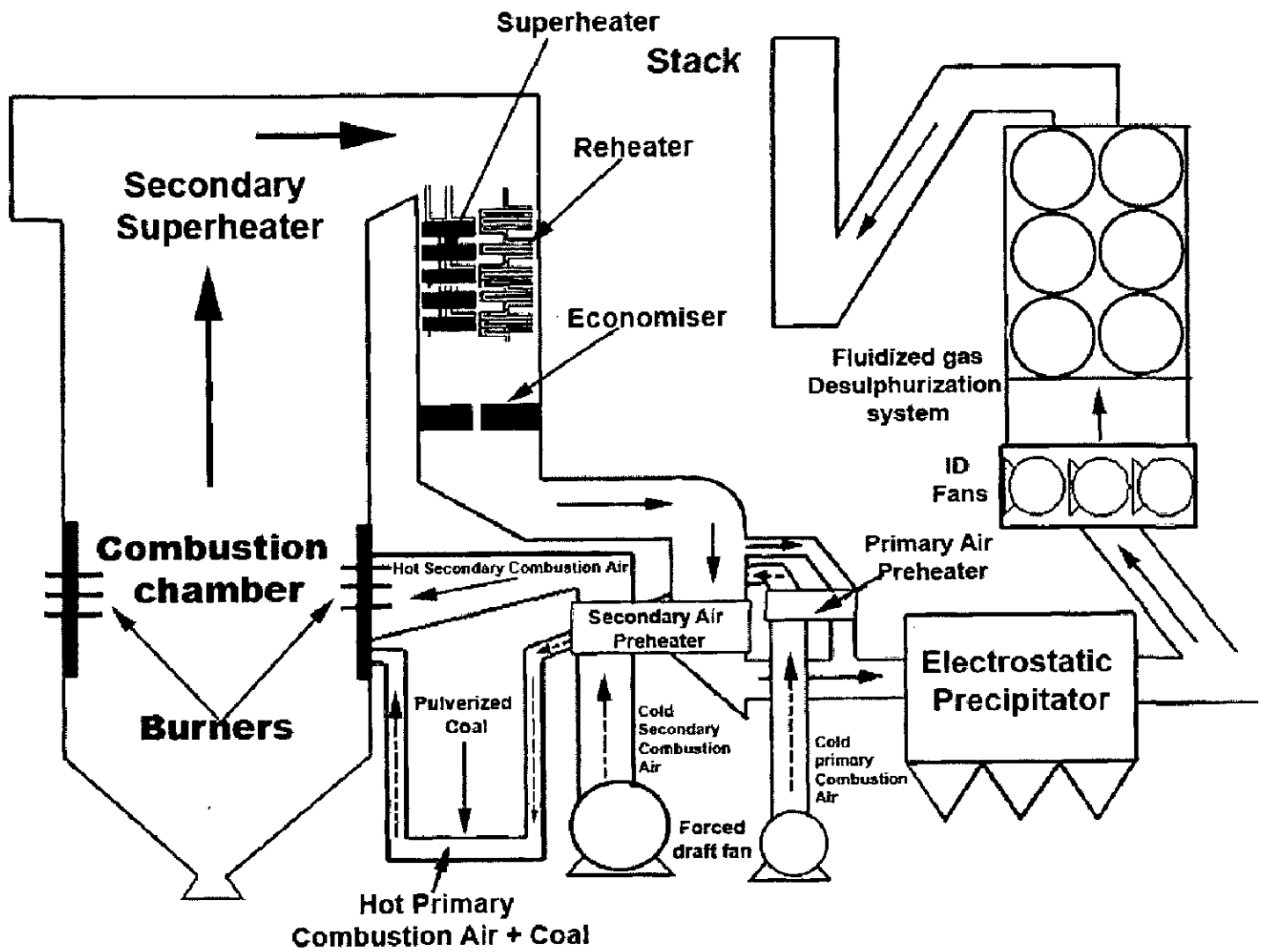


Fig. 2.25: Schematic diagram of a typical coal fired boiler (Das et al., 2006).

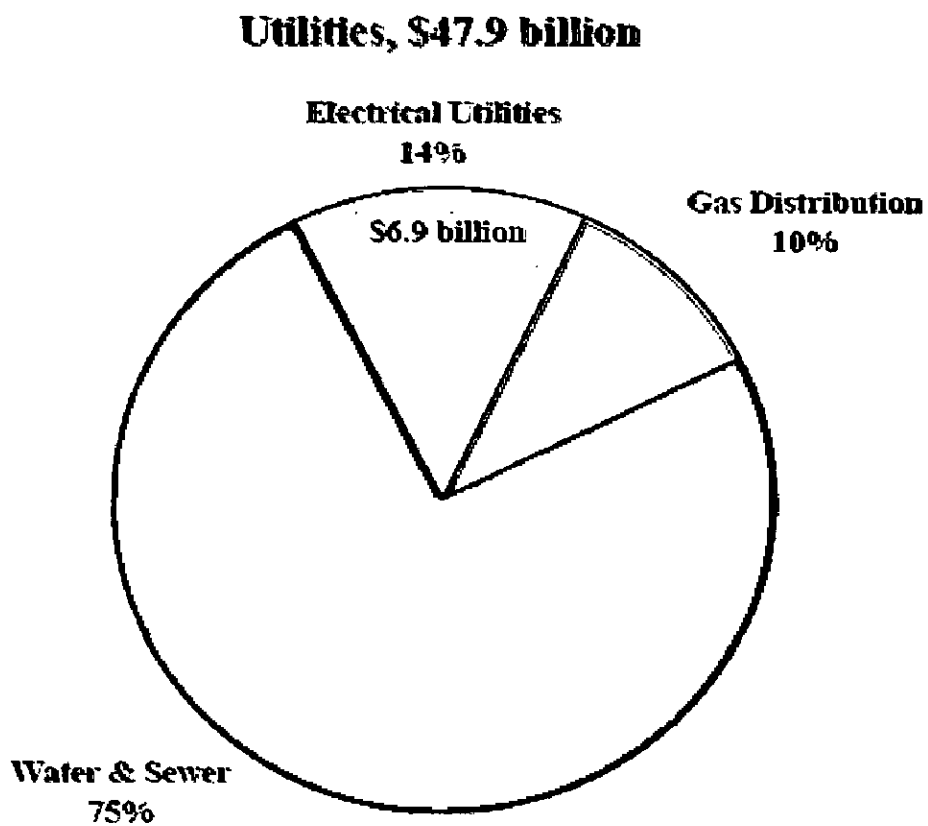


Fig. 2.26: Annual cost of corrosion in the electrical utilities industry (Koch et al., 2001).

behaviour of protective coatings in environments of their use and their interactions with the substrate during high-temperature performance is not well understood (Chatterjee et al, 2001). In context with the Indian boilers, the hot corrosion problem are relatively more severe as the Indian coal contains high ash content and therefore, the coatings can bring still more revenues. Role of thermal sprayed coatings for improving resistance to hot corrosion and erosion has been investigated by various researchers (Sidhu 2003; Singh 2005; Sidhu 2006; Mishra 2006; Singh 2006; Ramesh 2008).

Also the performance of various thermal sprayed coatings in actual industrial environment of coal fired boiler for 1000 hours has been evaluated by various researchers (Singh, 2005; Sidhu and Prakash 2005, 2006A, 2006 B and 2006C and Sidhu et al 2006) and reported better erosion corrosion resistance of coatings with respect to boiler tube steels, nickel and iron based superalloys.

2.7 PROBLEM FORMULATION

After detailed literature review, the scope of the problem and the objectives of the present study have been formulated. The present investigation is focused on the erosion corrosion evaluation of the D-gun sprayed coatings for application in power generation equipments.

As explained, components in energy generation systems required to operate at high temperature may suffer a variety of degradation processes as a consequence of complex multi component gas environment. This includes oxidation, molten salt induced attack and erosion. The development of wear and high temperature oxidation resistant system in industrial boilers is a very important topic from both engineering and an economic prospective.

There are many environments in, for instance, power generation processes where components experience mechanical wear superimposed on conditions of aqueous or high temperature corrosion. High-temperature erosion-corrosion and oxidation of the heat transfer pipes and other structural materials in the coal fired boilers are recognized as being the main cause of downtime at power generating plants, accounting for 50% to 75% of the total arrest time (Cutler, 1978).

Fire side corrosion and erosion of structural materials at elevated temperature in complex multi component gas environment that includes particulates are potential problems in many fossil fuel energy systems especially those using coal as a feed stock (Natesan, 1993). The combustion products of pulverized coal for the purpose of generating heat in a thermal power station are coarse ash, fly ash as well as the accompanying flue gases. The

coarse ash or bottom boiler ash consists of 10 to 20 % of the total ash load and fly ash consists of 80-90% of the total ash load. As suggested by the term “boiler bottom ash” the coarse ash drops out of the bottom of the boiler under the influence of gravity after combustion, while fly ash entrained in the flue gas is ducted out. The nature of fly ash is such that at high temperature it will form deposits on the boiler tubes in its path. The build up of ash deposits in its convective pass may also be detrimental from a corrosion aspect. However when passing through the latter stages of the boiler where the temperature are substantially lower, the fly-ash displays rebound as opposed to captive behavior. This causes localized erosive wear that can lead to unscheduled and costly tube failures (Suckling and Alen, 1995). Also combustion of coal generates very severe environment particularly near the superheater tubes of the boilers (Weulersse-Mouturat et al., 2004). In the combustion systems, much of the sodium and potassium is volatilized from the mineral matters in the flame to form Na_2O and K_2O vapours. The sulphur released from the coal, forms SO_2 with a minor amount of SO_3 and reacts with the volatilized alkalis to form Na_2SO_4 vapours, which then condense together with fly ash on the pendant superheater and reheater tubes in the boiler. These are the major areas where critical high-temperature fireside erosion corrosion problems are encountered. So erosion corrosion problems of the superheaters and reheaters of the boilers require some preventive measures.

Corrosion resistant materials for combustion environments are highly alloyed and thus expensive. Also, the mechanical properties of corrosion resistant alloys may not meet the requirements of structural components. The problems associated with workability, mechanical properties, and high material price can be solved by means of coatings (Morgen-Warren, 1992). Due to the continuously rising cost of the bulk materials as well as increased material requirements, the coating techniques have been given more importance in the recent times. Therefore, the use of protective coatings has been identified as a potential area for the present research.

Already research in the area of application of plasma and HVOF spray coatings on boiler tube materials and superalloys to increase resistance to erosion and hot corrosion and other degradation has been recently completed in the department. The coatings used were Ni-20Cr, Stellite-6, Ni_3Al and Ni-20Cr-10Al-1Y with bond coat Ni-20Cr-10Al-1Y. Also Cr_3C_2 -NiCr, NiCrBSi and Stellite-6 in the powder form and Ni-20%Cr in the wire form have been investigated in recent work. Also performance of NiCrAl, NiAlCrFeMo, NiCrFeSiB, WC-Co/NiCrFeSiB coatings has been investigated for protection to erosion and corrosion and the coatings have been found to be effective.

As per literature, D-gun spraying provides lower porosity levels and better adherence to substrate so D-gun spraying method has been used to form the coatings. Work has been done on alumina-titania coatings but is limited to wear applications.

The present research work has been undertaken, with an objective to explore the coating potential of Alumina Titania for high temperature applications. Attempts have been made in this work to deposit Al_2O_3 -3 wt. % TiO_2 Coatings by D-gun process on metal substrates and to establish their suitability for some typical erosion corrosion applications.

The research programme was designed to compare the erosion corrosion performance of the D-gun coated alloys with uncoated ones, for implementation in the boiler super-heaters and re-heaters, and for other future hot section components for use in similar erosive - corrosive environments.

Understanding the erosion corrosion behavior of coated alloys in various laboratory simulated environments and also contrasted by means of field testing inside real power plant boilers has become an object of scientific investigation. Thermo cyclic oxidation studies were performed in air as well as in molten salt environment (Na_2SO_4 - 60% V_2O_5) at 900 °C for 50 cycles. In both the laboratory as well in industrial environments, the experiments were conducted under cyclic conditions as the cyclic study provides the severest conditions for testing and represents the actual industrial environment where breakdown and shutdown occur frequently.

Also, the laboratory tests were performed at 900°C which is quite high the main reason being taking into consideration the overheating effects in case of boilers which has been identified the major cause of failure (Metals Handbook, 1975). Sodium and Vanadium appears to be the primary constituents of deposit formation on surfaces of heat exchangers in thermal power plants and hence (Na_2SO_4 - 60% V_2O_5) has been used as corrosive media for molten salt studies The hot corrosion environment Na_2SO_4 -60% V_2O_5 has been selected for the laboratory tests as the molten sulphate-vanadate deposits resulting from the condensation of combustion products of low grade fuels are extremely corrosive to the high-temperature materials (Rapp, 1986). Furthermore, sodium vanadyl vanadate ($\text{Na}_2\text{O} \cdot \text{V}_2\text{O}_4 \cdot 5\text{V}_2\text{O}_5$), which melts at a relatively low temperature 550°C, is found to be the most common salt deposit on the boiler superheaters (Barbooti et al., 1988). This salt mixture is very aggressive and the extremely aggressive and corrosive nature of this composition is attributed to its low melting point i.e. 500°C.

The erosion studies were carried out using a high temperature air-jet erosion test rig at a velocity of 35 ms^{-1} and impingement angles of 30° and 90°. The tests were carried out at

ambient temperature and high temperatures. High temperature erosion testing was carried out at 400°C, 900°C and 600°C, 900°C under particle velocity of 35m/s.

The two temperatures were taken for each test, sample temperature 400°C and surrounding temperature 900°C and sample temperature 600°C and surrounding temperature 900°C simulated to service conditions of boiler tubes in which sample temperature and flow gas temperature correspond to the inner and outer temperature of water wall pipes. The alumina particles of average size 50 µm were used as erodent.

Actual boiler environment studies were conducted at Guru Gobind Singh Super Thermal Plant, Ropar, Punjab (India). Coated as well as uncoated alloys were exposed to superheater zone of the coal fired boiler in the region where flue gas temperature was around 700°C. The experiments were conducted for total exposure of 1500 hrs (15 cycles, each cycle consisting of 100 hrs exposure followed by cooling at ambient conditions). The extent of erosion corrosion has been monitored by measuring thickness loss.

EXPERIMENTAL EQUIPMENT AND ANALYTICAL METHODS

The experimental techniques that have been employed are outlined in this chapter. Particular emphasis is applied to discussing the attributes of each technique that impact on the interpretation of results generated for Al_2O_3 -3% TiO_2 Coatings. This chapter presents the experimental techniques and procedures employed. Specifications of the equipments and other instruments used for the present investigation are also incorporated.

3.1 SELECTION OF SUBSTRATE MATERIALS

Selection of the substrate material for the present study has been made after consultation with SGS Thermal power Plant Ropar and Mishra Dhatu Nigham Ltd, Hyderabad (India), The alloys used for present study are Ferritic steels which are commonly used as boiler tube materials in Indian Thermal power stations namely T11 and T 22 {1Cr-0.5Mo steel "ASTM-SA213-T-11 (T11)" and 2.25Cr-1Mo steel "ASTM-SA213-T-22(T22)."} and three Super alloys (Ni- and Fe- based superalloys) having Midhani Grades, Superni 600, Superni 718, Superfer 800. The selected superalloys are widely used for steam boilers, heat exchangers and piping in the chemical industry, gas turbines, jet engines, furnace equipment, reformers and baffle plates/tubes in fertilizer plants. Boiler steels were procured in the tube form from the mentioned thermal power plant and the superalloys were procured in form of rolled sheets. Chemical composition of these alloys is given in Table 3.1.

3.2 DEVELOPMENT OF COATINGS

3.2.1 Preparation of Substrate Materials

Specimens with dimensions of approximately 21mm × 16mm × 5mm were cut from the alloy sheets and the boiler tubes for the present investigations. Grinding was carried out to remove any chips/ burrs on the specimen. Then specimens were polished with SiC papers down to 180 grit.

3.2.2 Formulation of Coatings

The coatings were deposited on the substrates using D-gun spray apparatus. Before starting the coating process, the test specimens were cleaned, degreased and shot blasted. The specimens were grit blasted by alumina (Grit 60) for better adhesion before application of the coatings by detonation spray gun process. The specimens were cleaned with acetone prior to coating. The coating work was carried out by a commercial firm namely SVX Powder M Surface Engineering Private Limited, Greater Noida (India). Detonation gun was arranged in special sound-insulated chambers (cubicles) with concrete walls as shown in Fig. 3.1. The main components of D-gun spraying system involves gas supply, powder feeding system, powder heating system, mixing chamber, barrel, coating chamber as shown in Fig. 3.2.

The main characteristics of D-gun spraying equipment are given in Table 3.2. All the process parameters were tested and optimized by the company and prior experience of the concerned technology provider helped in setting up the process parameters. The parameters were kept constant throughout the coating process and the spraying distance was maintained 185 mm. Commercially available thermal spray powder (Metco 105 SF) was used for coating deposition procured from Sulzer-Metco. The specimens were fixed in the specimen holder of detonation spray coating system and then sprayed with Al_2O_3 -3 wt% TiO_2 powder. The powder characteristics are given in Table 3.3. D-gun coating was carried out using a combustible mixture of O_2 and C_2H_2 with a frequency of 3 Hz and a spraying distance of 185 mm. The Al_2O_3 -3 wt% TiO_2 powder was placed in the powder feeding system having integrated powder heating system in order to remove any moisture from the powder. Then appropriate supply of oxygen and acetylene was given in the mixing chamber and mixture was ignited with the help of a spark plug. The ignition caused the combustion of gas mixtures and melting of the powder particles drawn into the combustion chamber. The detonation products were allowed to accelerate down the barrel resulting in high velocity. The powder particles exit with a velocity of about 700 m/s and impinged on the surface of the substrate to form a dense coating. The process was repeated several times to obtain the desired thickness of coating. The basic features of formation of detonation coatings are generally attributed to a high velocity of collision of particles against the substrate.

The gun barrel length was 1.2 m and diameter was 22 mm. Multipass coating of Al_2O_3 -3 wt% TiO_2 was formulated on all six sides of the specimens by alternatively exposing the surfaces to the barrel. In order to obtain specific coating thickness and uniformity, few optimisation trials were performed before final coating. The powders had the same composition and size range.

Table 3.1: Chemical composition of the alloys used

Alloys	Chemical Composition (wt %)														
	Fe	Ni	Cr	Ti	Al	Mo	Mn	Si	Cu	Nb+Ta	B	P	Co	S	C
T-11	Bal.		0.988			0.522	0.424	0.473				0.022		0.007	0.142
T-22	Bal.		2.502			1.081	0.472	0.426				0.022		0.008	0.141
Superni 600	9.804	73.532	15.436				0.855	0.334	0.011					0.002	0.026
Superni 718	19.932	52.944	17.244	0.991	0.545	3.133	0.021	0.032	0.012	5.10	0.005	0.005	0.01	0.005	0.021
Superfer 800	44.476	31.709	21.504	0.443	0.212		0.914	0.602	0.054					0.004	0.082



Fig. 3.1: Detonation gun in operation at SVX Technologies, Noida

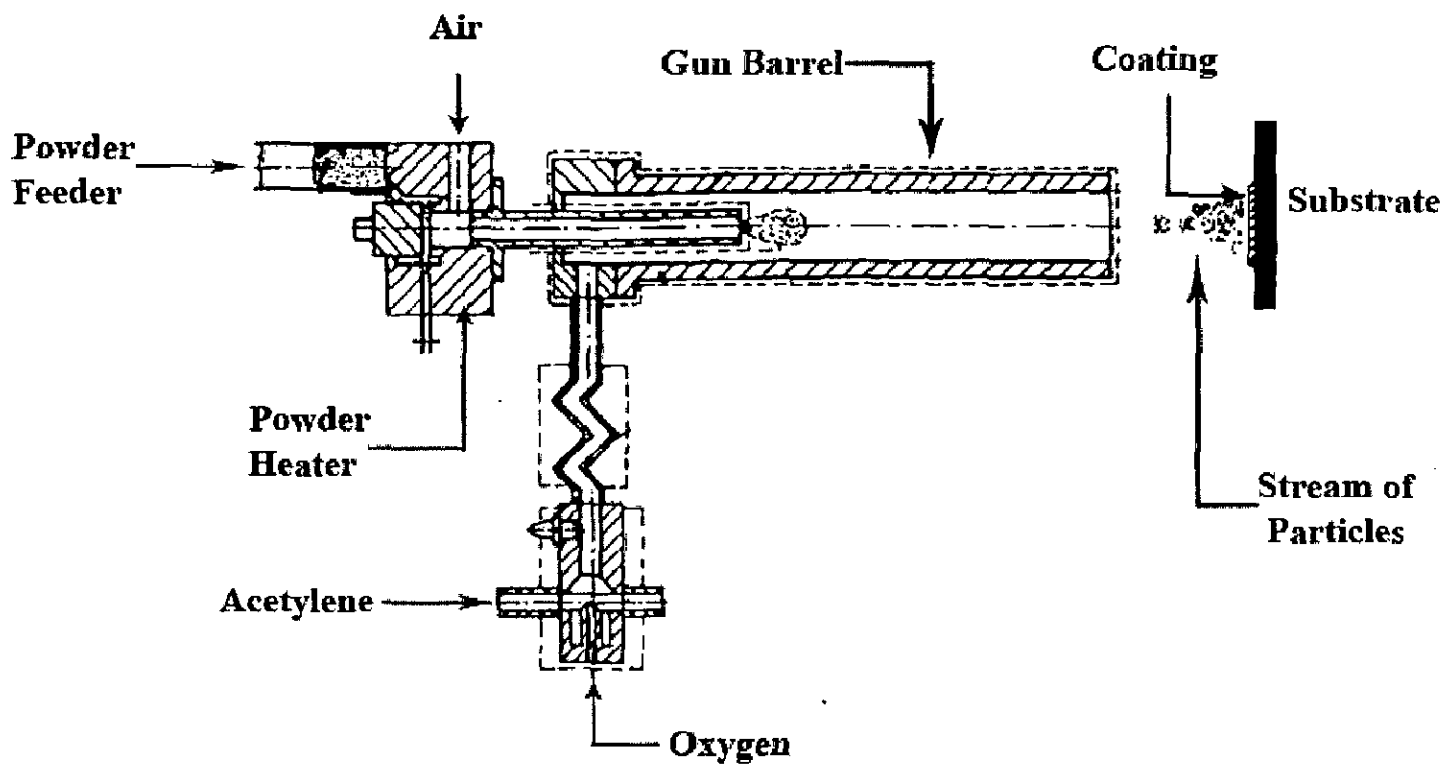


Fig. 3.2: Schematic Diagram of Detonation gun coating system (Saravanan et al., 2000)

Coating thickness obtained was from 200 to 220 μm . The process parameters for the D-gun spray process employed for applying the coatings are summarised in Table 3.4. All samples were coated with same powder and with the same parameters.

Table 3.2: Summary of Detonation Gun spray Equipment.

Barrel Length (mm)	1200
Firing Frequency (Hz)	2-4
Typical Coating Thickness per cycle (μm)	5-20
Typical Coating Thickness Achievable (μm)	Upto 500
Power Consumption	4 KW

Table 3.3: Characteristics of Alumina-Titania Powder.

Powder Description	Manufacturer	Composition (Wt %)	Particle Size	Particle Shape
Metco 101 SF	Sulzer Metco	97Al ₂ O ₃ 3TiO ₂	-22 +5 μm	Irregular Angular / Blocky, Fused and Crushed

Table 3.4: Summary of Detonation Gun spray parameters.

Spray Distance from Nozzle (mm)	185
Frequency of shots (Shot/s)	3
Carrier gas flow rate (Standard Litre/Hr)	720
Acetylene Flow Rate (Standard Litre/Hr)	2240
Oxygen Flow Rate (Standard Litre/Hr)	2720

3.3 HIGH TEMPERATURE OXIDATION AND HOTCORROSION STUDIES

3.3.1 Experimental Setup

The studies were conducted at 900°C in a laboratory silicon carbide tube furnace, Digitech, India make. The furnace was calibrated to an accuracy of $\pm 5^{\circ}\text{C}$ using Platinum/Platinum-13% Rhodium thermocouple. The uncoated as well as the coated specimens were polished down to 1 μm with alumina wheel cloth polishing to obtain similar condition of reaction before being subjected to corrosion run. Physical dimensions of the specimens were then recorded carefully with vernier caliper to evaluate their surface areas.

Subsequently the specimens were cleaned properly with acetone and dried in hot air to remove any moisture.

The prepared specimen was kept in an alumina boat and the weight of boat and specimen was measured. The alumina boats used for the studies were pre heated at a constant temperature of 1500°C for 10 hours and it was assumed that their weight would remain constant during the course of high temperature cyclic oxidation/corrosion study. Then the boat containing the specimen was kept into hot zone of the furnace set at a temperature of 900°C. The specimen along with boat was kept in the furnace for one hour in still air after which the boat with specimen was taken out and cooled at the ambient temperature for 20 minutes. Then the weight of the boat along with specimen was measured and this constituted one cycle of the oxidation study. Any spalled scale in the boat was also taken into consideration for the weight change measurements. Electronic Balance Model CB-120 (Contech, Mumbai, India) with a sensitivity of 10^{-3} g was used to conduct the weight change studies. After the end of each cycle the samples were visually examined for any change on surface and weight of samples were measured subsequently. After each cycle, the samples were critically examined for any change in color, lusture and spalling tendency of scale. All oxidation and hot corrosion studies were cyclic in this work and were carried out for 50 cycles. The reproducibility in the experiments was established by repeating hot corrosion experiments for five cases, where two specimens of the same description were subjected to similar hot corrosion test.

3.3.2 Oxidation Studies in Air

The oxidation tests at 900°C were performed on all the five base alloys as well as D-gun spray coated alloys in laboratory furnace up to 50 cycles as discussed in section 3.3.1.

3.3.3 Hot Corrosion Studies in Molten Salt (Na_2SO_4 -60% V_2O_5)

3.3.3.1 Molten Salt Coating

The D-gun spray coated as well as uncoated specimens was prepared for studies as discussed in section 3.4.1. The specimens were then heated in an oven upto 250°C and a salt mixture of Na_2SO_4 -60% V_2O_5 dissolved in distilled water was coated on the warm polished specimens with the help of a camel hair brush. The salt Na_2SO_4 was obtained from S.D. Finechem Limited Mumbai and V_2O_5 was obtained from Loba Chemie Pvt. Ltd, Mumbai. Amount of the salt coating was kept in the range of 3.0 -5.0 mg/cm². The salt coated specimens as well as the alumina boats were then dried in the oven for 3-4 hours at 100°C and weighed before being exposed to hot corrosion tests.

3.3.3.2 Hot Corrosion Studies

The uncoated as well as D-gun spray coated specimens after application of salt coating were subjected to hot corrosion in the laboratory furnace at 900°C for 50 cycles as discussed in section 3.3.1.

3.4 CHARACTERISATION OF COATINGS

3.4.1 Measurement of Coating Thickness

Thickness of the coatings was continuously monitored during the process of D-gun spraying with Minitest-2000 made in Germany. Efforts were made to obtain coatings of uniform thickness. In order to verify the thickness of coatings some of as sprayed specimens were cut along the cross-section and mounted as explained in the Section 3.3.3. BSE images were taken with the help of Field emission scanning electron microscope (FESEM). The average thickness of the coating was then measured from these BSE images and the same has been reported in Chapter 4 of the present study.

3.4.2 Measurement of Porosity

The coating porosity was measured on polished coating cross sections using image analysis. Porosity measurements for the D-gun sprayed coatings have been made from the cross-sectional micrographs of the specimens.

The Images were captured using Zeiss Axiovert 200 MAT Inverted optical microscope and Image processing was performed using the software package imaging software Zeiss AxioVision Release 4.1 (Germany). Porosity features were determined manually using a threshold function related to the image grey scale. This threshold image was converted to a black and white image, with the calculated percentage of black particles indicative of the coating porosity. Ten images were processed per sample and their averages are reported in Chapter 4.

3.4.3 Metallographic Studies

For metallographic studies across the cross-section, the D-gun spray coated specimens were cut along their cross-section with diamond cutter (Buehler's Precision Diamond Saw, Model ISOMET 1000, USA make). Thereafter, the cut sections were hot mounted in Buehler's transoptic powder so as to show their cross-sectional details. This was followed by polishing of the mounted specimens by a belt sanding machine. The specimens were then polished manually down to 1000 grit using SiC emery papers. Final polishing was carried out using cloth polishing wheel machine with 1 μm lavigated alumina powder suspension. Specimens were then washed and dried before being examined under Zeiss Axiovert 200 MAT Inverted Optical Microscope

interfaced with imaging software Zeiss AxioVision Release 4.1, Germany. The same microscope was used to obtain surface microstructures of the coatings. Cross-sectional as well as surface microstructures of the specimens used in the current study are presented in Chapter 4.

3.4.4 Measurement of Microhardness

The hardness of the coatings was tested on the polished cross section using a Vickers Hardness tester Leitz's Hardness Tester Mini Load-2 (Made in Germany). In this test a diamond indenter in the form of a square pyramid is forced into the surface [1]. Measurement is made of the two diagonal lengths of the square and correlated via conversion tables to a Vickers hardness number. Trials were conducted using a 100g load for 10 seconds, unless otherwise stated.

Microhardness of the coatings was measured by 100-gram load was provided to the needle for penetration and a hardness value was based on the relation

$$Hv = 1854.4 \times \frac{P}{d^2}$$

(Where P is the load in gram, and d is the mean of the indentation diagonal length in mm).

Because of the inhomogeneous nature of thermal spray coatings, operator judgement was required to pass or fail each indent as being representative, especially in terms of cracking. Ten representative indents were averaged for each sample. These micro hardness values are plotted as a function of distance from the coating/substrate interface in Chapter 4.

3.4.5 Scanning Electron Microscopy (SEM) and Energy Dispersive X-Ray (EDX) Analysis

3.4.5.1 Beam-Specimen Interactions (Goldstein et al).

SEM analysis is an analytical technique that exploits the electrons and x-rays generated by the interaction between an electron beam and specimen, to generate information on surface topography and specimen composition.

Interaction between the beam electrons and the specimen atoms can occur by either an elastic or inelastic process. In the elastic process a beam electron interacts with an atom and is deflected without losing a significant amount of its initial kinetic energy. The angle over which deflection occurs is large, ranging from average values of 2-5° up to 180°. Through this process, incident beam electrons can interact with the specimen and escape back out of the surface, being detected as "back scattered" electrons. During inelastic scattering an incident beam electron interacts with a substrate atom, giving up some of its initial kinetic energy. The beam electron is deflected, typically over angles <0.1° and continues into the sample. Of the

various mechanisms of beam electron-substrate atom interactions generated through inelastic scattering, those most relevant to this work involve transfer of energy to the outer band of electrons, and ejection of an inner shell electron from the atom by the beam electron. Following this interaction, the atom is in an “excited” state, relaxation of the atom resulting in the formation of “secondary” electrons and “characteristic x-rays” respectively.

The dispersive nature of the electrons of the primary beam within the specimen, combined with the multiple interactions that each electron has, means that the signals generated from the point of the incident beam are generated over a larger “interaction volume”. The energy of the electrons or x-rays formed determines the depth from which they can escape the surface and be detected, leading to significant variation in the volume of material analysed in each technique, Fig. 3.3.

3.4.5.2 Secondary Electron (SE) Imaging

During inelastic scattering the incident beam electron transfers sufficient energy to a valance band or conduction band electron in the substrate atom that it can escape the atom and travel out of the surface. These “secondary” electrons are of low energy and hence only those in the very near surface region receive enough energy to escape the surface to be detected, Fig. 3.3. Tilted surfaces generate more secondary electrons than flat regions, generating topographical contrast and the ability of surface features to be imaged.

3.4.5.3 Energy Dispersive X-ray Spectrometry (EDS)

Energy dispersive x-ray spectrometry involves analysis of the intensity of emitted x-rays as a function of their energy. The characteristic elemental x-ray energies are plotted as peaks in a spectrum. The intensity of the peaks can be correlated with the concentration of each element through the use of mathematical models. Analysis can be conducted on a specific point of material (spot scan), or over multiple points in a raster pattern to generate an “x-ray map” of the distribution of elements on a surface.

3.4.5.4 X-ray Mapping

X-ray mapping is another tool in Energy dispersive X-ray analysis of materials, X-Ray Mapping (XRM) has become a very powerful technique in understanding the distribution of elements in materials. X-ray maps from the EDS are used to examine the two-dimensional distribution of elements on a specimen surface. X-Ray maps are simply 2-dimensional images that show variations in chemical composition on the polished surface of a sample. Each map represents a single element: color variations on the map represent differences in concentration

of that element from place to place. X-Ray Map is obtained by exposing the sample under an electron beam. The counter collects X-Rays, and stores the counts at regular intervals and X-ray maps are usually collected using raw counts from the elemental peaks of interest

3.4.5.5 Back Scattered Electron (BSE) Imaging

The elements with higher atomic mass appear brighter in BSE images. In case of multi phase alloys and compounds the intensity of BSE generation is dependent upon the average atomic mass based on the mass fractions of the elements in the analysis volume. On flat surfaces, compositional distribution is reflected in varying shades of grey.

As the deflection angle of back-scattered electrons with substrate atoms is quite low, multiple interactions with the substrate atoms are required before the electron can escape the surface. The larger volume over which the back scattered electrons travel means the resolution of this technique is lower than in SE imaging. As a result of this greater analysis volume, compositional information from material below the surface appears in the BSE image. If the incident beam of electrons interacts with a secondary phase of high atomic mass beneath the surface, a higher number of electrons will be elastically scattered from this material than the surrounding matrix. As a result the back scattered electron intensity above this region will be greater than in the matrix phase alone. Essentially the BSE signal represents an average atomic mass contrast over the entire analysis zone, Fig. 3.4

3.4.5.6 Equipment Details

Surface morphology of the as-sprayed coatings was studied with the help of Scanning Electron Microscope (LEO 435VP) with an aim to understand the structure of the coatings and identify oxide inclusions, unmelted particles, pores etc. SEM/EDX Analysis was conducted with Field emission scanning electron microscope (FESEM, FEI, Quanta 200F company) with EDAX Genesis software attachment; Made in Czech Republic. SEM Imaging was conducted at an accelerating voltage of 20kV.

3.4.6 X-ray Diffraction (XRD)

3.4.6.1 Fundamentals

The X-ray Diffraction method exploits the similarity in magnitude between the wavelength of X-rays and the inter-atomic spacing of the planes of atoms in crystals, which enables X-rays to be diffracted (Cullity, 1978). The X-rays of a fixed wavelength are projected onto a sample. They penetrate the surface and are scattered by the regular array of planes of

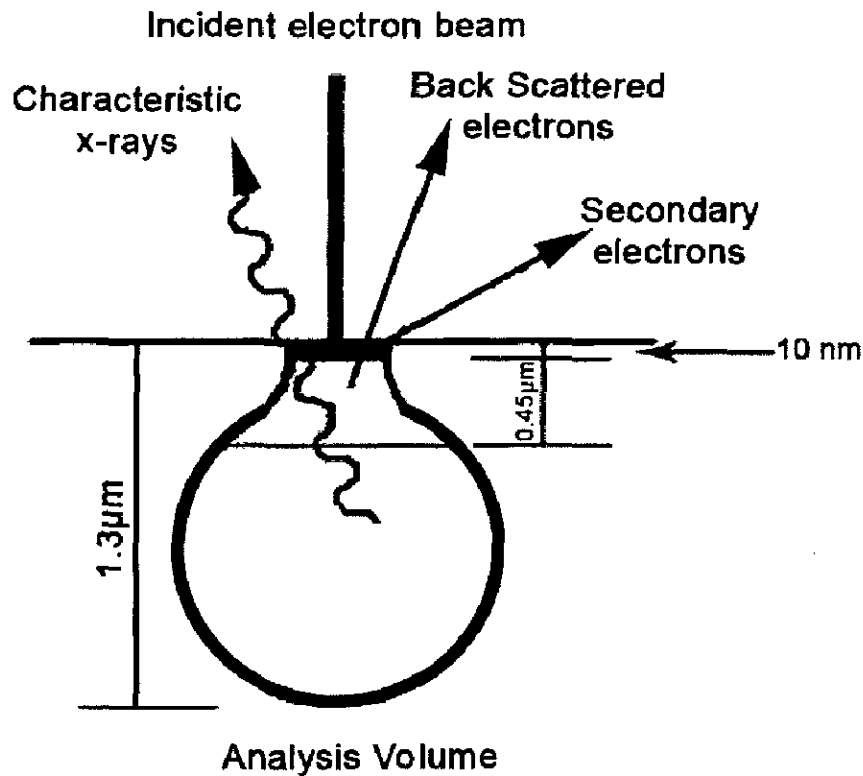


Fig. 3.3: Schematic illustrations of the relative depths from which secondary electrons, back scattered electrons and characteristic x-rays may escape the surface to be detected (Goldstein et al., 1992)

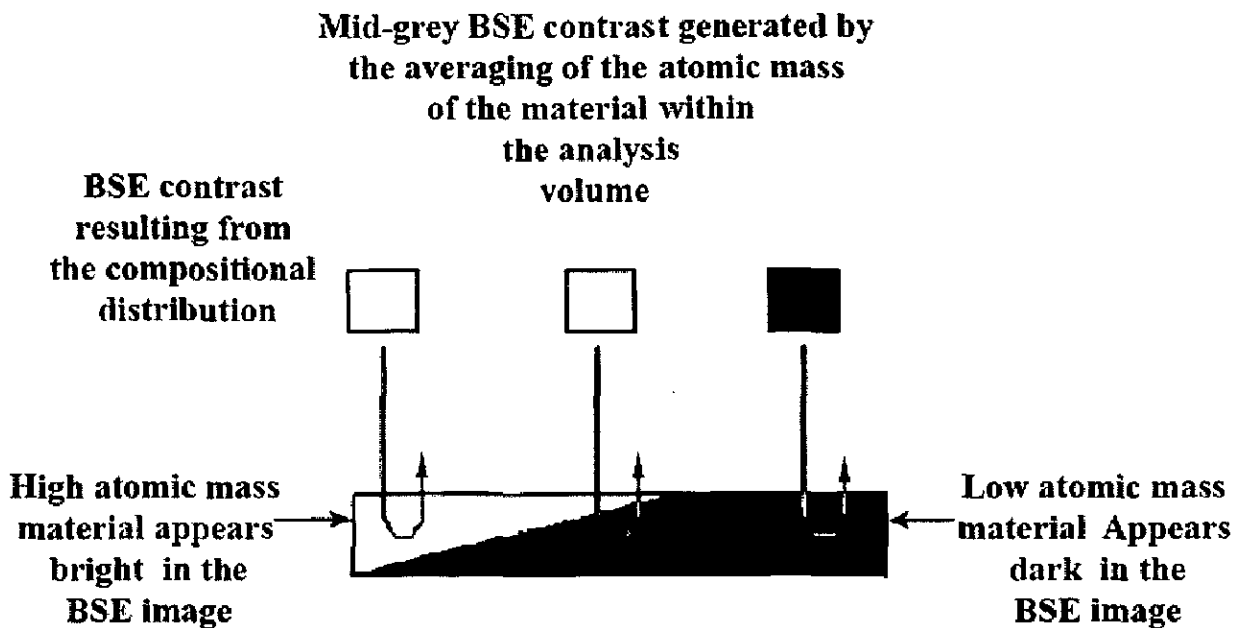


Fig. 3.4: Schematic illustration of BSE grey scale variation as a function of atomic mass distribution within the sample.

atoms, only those travelling out of the specimen in the same direction as the incident beam being detected. Within a crystal, diffraction occurs if the different distances traveled in the direction of the detector by the scattered x-rays are equal to a whole number of wavelengths. If so, the wavelengths reinforce each other through constructive interference, generating a very large intensity signal. If the variation in distance traveled does not fit this criterion, diffraction does not occur and the detector registers only a low "back ground" signal of X-rays randomly scattered in this direction. For each compound, the peaks in intensity based on the inter-atomic spacing are characteristic for a specific set of planes of atoms. As a compound has several families of crystallographic planes that may diffract X-rays, several peaks occur at different incident angles.

An X-ray spectrum is generated by scanning a range of incident angles and measuring the X-ray intensity. The peak positions within this spectrum are related to the inter-atomic spacing, d , the wavelength of the X-rays, λ , and the angle of the incident beam to the surface. The relationship between these variables is described by Bragg's Law as:

$$\lambda = 2d \sin\theta$$

Results are typically presented as spectra of intensity versus 2θ . Identification of the compounds within a spectrum is achieved by comparing the relative intensities of the various peaks and their peak positions with standard spectra within the JCPDS (Joint Committee on Powder Diffraction Standards) database. Where mixtures of phases are present, the amount of each component is proportional to the intensity and the area underneath the peaks for that compound.

3.4.6.2. Equipment Details

XRD analysis was conducted by Bruker AXS D-8 Advance Diffractometer (Germany) with $\text{CuK}\alpha$ radiation and nickel filter at 20 mA under a voltage of 35 kV. The specimens were scanned with a scanning speed of 1 Kcps in 2θ range of 20 to 120° and the intensities were recorded at a chart speed of 1 cm/min with 1°/min as Goniometer speed. Assuming height of the most prominent peak as 100%, the relative intensities were calculated for all the peaks. The diffractometer being interfaced with Bruker DIFFRAC^{plus} X-Ray diffraction software which provides 'd' values directly on the diffraction pattern. These 'd' values were then used for identification of various phases with the help of inorganic ASTM X-Ray diffraction data cards.

3.6. ROOM TEMPERATURE AND ELEVATED TEMPERATURE EROSION TESTS

3.5.1 Experimental Setup

Erosion testing was carried out using a solid particle erosion test rig TR-471-M10 Air Jet Erosion Tester (Ducom Instruments Private Limited, Bangalore, India) capable of conducting tests at room temperature as well as high temperature shown in Fig.3.5. The rig consisted of an air compressor, erodent feeding system, mixing chamber, furnace unit, specimen holder, nozzle, erodent collection chamber, pneumatic control box and electrical control box shown schematically in Fig. 3.6. The test method utilizes a repeated impact erosion approach involving a small nozzle delivering a stream of gas containing abrasive particles which impacts the surface of a test specimen.

Dry compressed air was mixed with the erodent particles, which were fed at a constant rate from hopper through erodent feeding system in the mixing chamber and then accelerated by passing the mixture through a converging nozzle made of inconel material of 4 mm diameter. These accelerated particles impacted the specimen kept in the furnace unit consisting of specimen heater and air heater. The specimen could be held at various angles with respect to the impacting particles using an adjustable sample holder. The discharge rate of the particles could be controlled by varying the frequency of motor speed in the erodent feeding system. The erodent feeding system consists of a hopper which allows erodent to fall under gravity through throat on a wheel which is rotated by a motor through timer belt. Motor speed determines the extent of discharge. Higher the speed of motor greater is the discharge and vice versa. The impact velocities of the particles could be varied by varying the pressure of the compressed air.

3.5.2 Erosion Studies in an Air Jet Erosion Test Rig

The studies were performed for uncoated as well as coated specimens for the purpose of comparison as discussed in section 3.4.1. The erosion test conditions utilized in the present study are listed in Table 3.4. A standard test procedure was employed for each erosion test. The uncoated as well as the coated specimens were polished down to 1 μ m alumina wheel cloth polishing to obtain similar condition on all the samples before being subjected to erosion run. The samples were cleaned in acetone, dried, weighed to an accuracy of 1×10^{-5} g using an electronic balance, eroded in the test rig for 3 hours and then weighed again to determine weight loss. In the present study standard alumina 50 micron (supplied with Erosion Test Rig

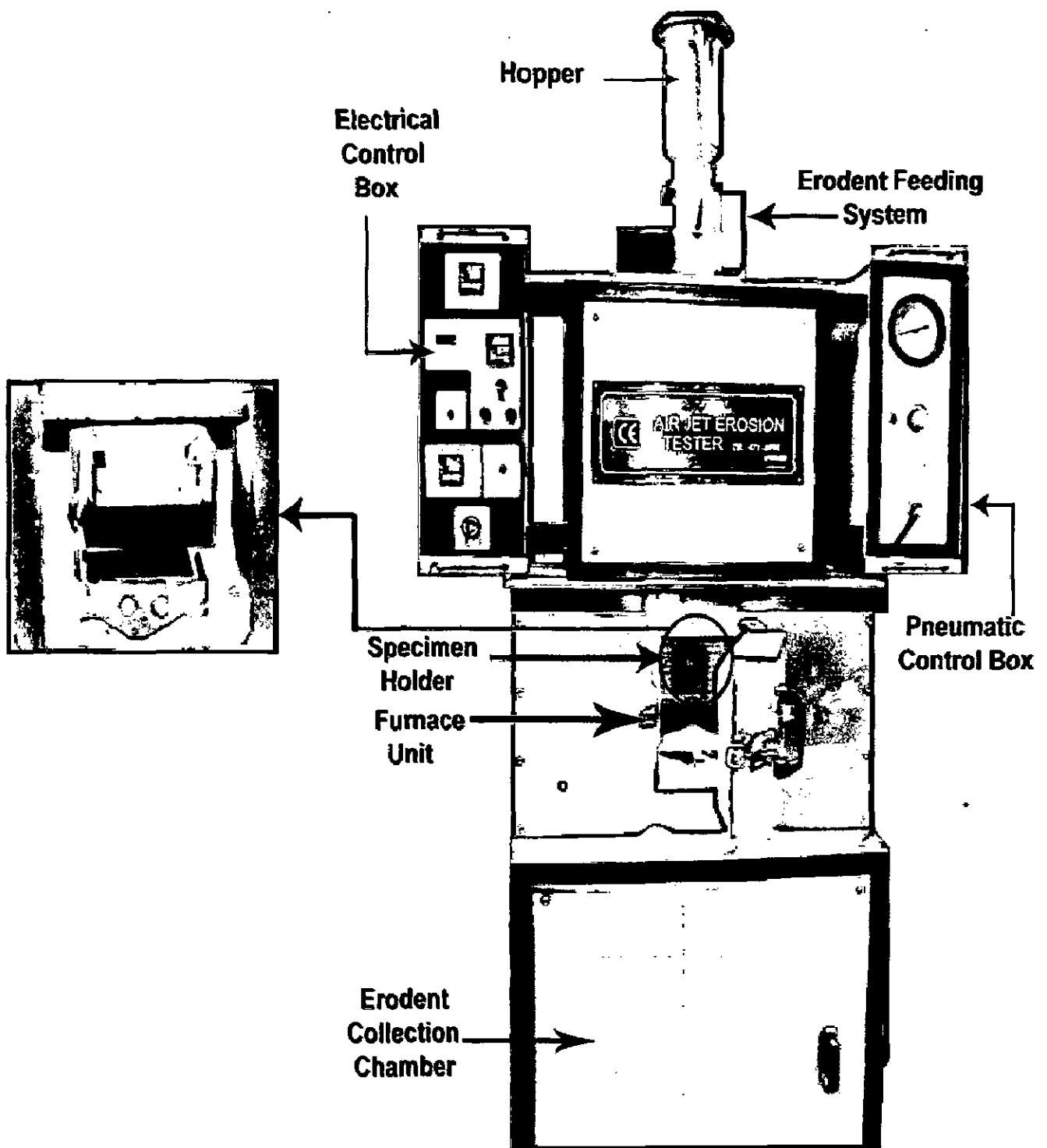


Fig. 3.5: High Temperature Air Jet Erosion Test Rig used for erosion testing.

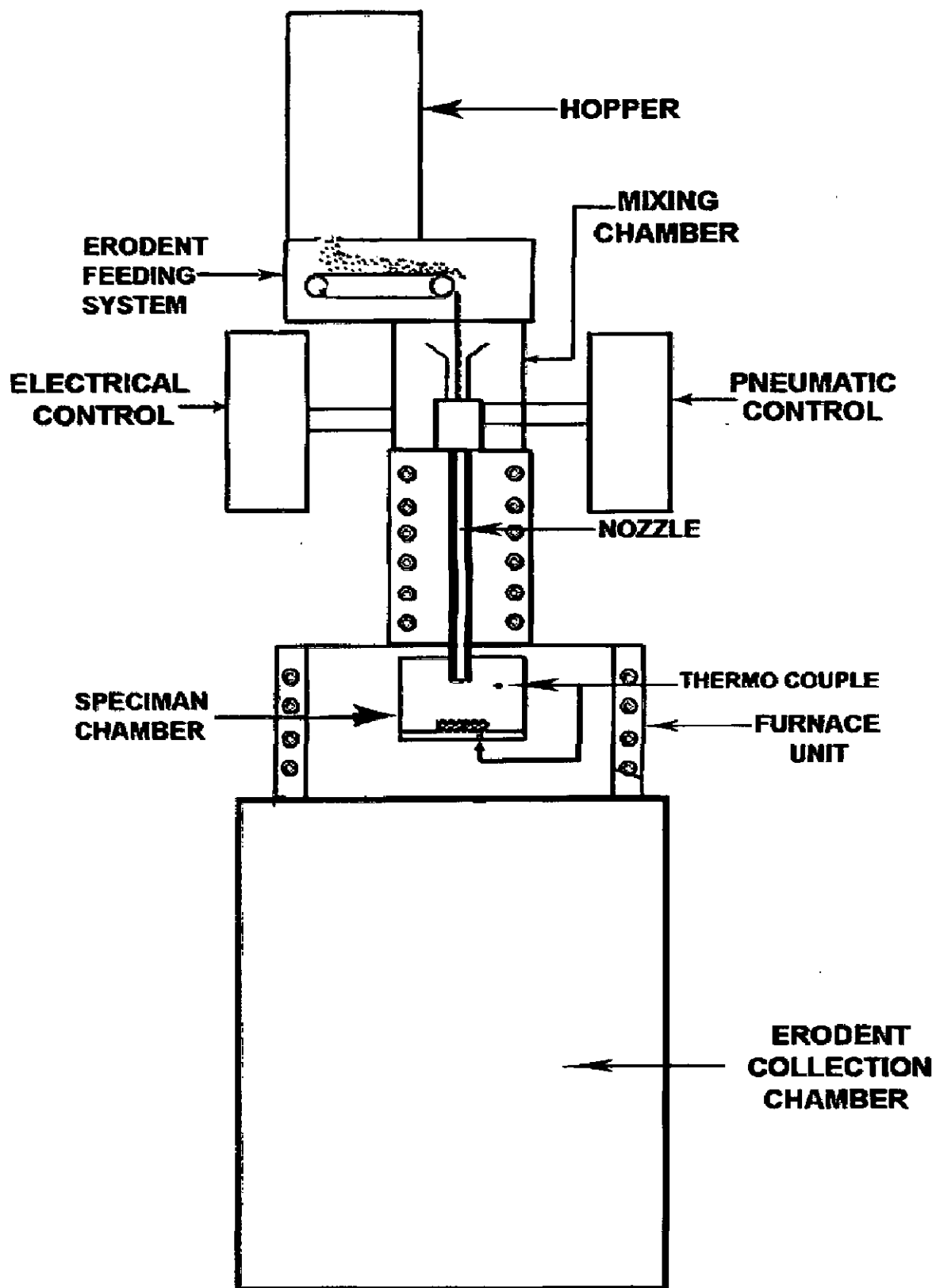


Fig. 3.6: A schematic view of High Temperature Air Jet Erosion Test Rig

by Ducom Instruments Private Limited, Bangalore, India) was used as erodent (Fig. 3.7). In general, Erosion resistance is measured using weight loss technique by measuring the weights before and after the test. But at high temperature, weight change measurements leads to flawed results due to oxidation of samples. In order to overcome the limitations of the weight change technique, a different technique was used for the present investigation. Erosion resistance was measured in terms of thickness loss after the erosion testing.

Table 3.5: Erosion Test conditions

Erodent material	Alumina (Irregular shape)
Erodent Specifications	50 micron Al ₂ O ₃
Particle velocity (m/s)	35m/s
Erodent feed rate (g/min)	2 gm/min
Impact angle (°)	30, 90
Test temperature	<ul style="list-style-type: none"> ❖ Ambient (Condition 1) ❖ Sample Temperature 400°C & Air Temperature 900°C (Condition 2) ❖ Sample Temperature 600°C & Air Temperature 900°C (Condition 3)
Nozzle diameter (mm)	4
Test time (Hrs)	3 Hours

3.5.3 Analysis of eroded surfaces

All the specimens subjected to erosion wear were analysed for the characterisation of erosion products. The analysis was performed for the surface of the eroded specimens from room temperature studies. The specimens were analysed using surface SEM, EDX and measurement of surface profiles using optical profilometer.

3.5.3.1 Visual Observation

For the specimens eroded in laboratory test rig, visual examination was made after the completion of erosion cycles and the macrographs of the eroded specimens were taken.

3.5.3.2 Erosion rate in terms of Volume loss

The volume loss occurred after erosion testing was measured by using non contact optical profilometry. The method was used to evaluate surface characteristics, such as erosion volume loss and depth, surface topography. Veeco Optical Profilometer (NT 1100, USA make) was used. Also 3-Dimensional surface topography illustrating the surface profiles of the eroded alloys and coatings were taken. This method characterizes and quantifies critical dimensions (such as area and volume of the damaged erosion wear scars), and topographical features. It has three-dimensional profiling capability with excellent precision and accuracy. The shape of a surface can be displayed by a computer-generated map developed from digital data derived from a three-dimensional interferogram of the surface.

The erosion depth was measured at six random locations to obtain the average erosion depth of an eroded scar as shown in Fig. 3.8(a) on an eroded specimen. At each location (including eroded and uneroded area) surface profiles were taken. The intact/unaffected surface (uneroded area) was used as a reference plane for the erosion depth measurement. At each erosion scar, six contour maps were obtained. The maximum erosion depth was obtained by measuring a step height between a nominal surface and a zero level of the bottom wear surface of the erosion scar in a cross-sectional profile of each contour map. Then, the mean value of the six maximum erosion depths was determined and defined as the mean erosion depth Fig. 3.8(b).

The erosion scar area was measured using Image analysis software (Image J 1.41). After performing erosion testing, the net missing volume of the eroded area (scar) was measured at six locations randomly. Afterwards, the total net missing volume of the whole eroded area was calculated. The net missing volume is equal to the negative volume minus the positive volume in the eroded area (Fig. 3.8(c)), where the negative volume is the volume above the bottom wear surface of an erosion scar and below the zero level, whereas the positive volume is the volume below the bottom wear surface of the erosion scar and above the zero level. In general, the negative volume is almost equal to the positive volume so that the net missing volume of the eroded area is negligible.

The natural volume of uneroded surface was obtained before erosion (Fig. 3.8 (d)). The natural volume of uneroded, bare area was randomly measured at six locations. Then, the total natural volume of the area, which is equal to the eroded wear scar area, was calculated.

Thus, the erosion wear volume loss can be calculated as follows which is illustrated in Fig. 3.8 (e):

Erosion volume wear loss = mean erosion depth × eroded area + net missing volume of eroded surface - natural volume of uneroded, bare surface



Fig. 3.7: Scanning electron micrograph of the Alumina Erodent particles.

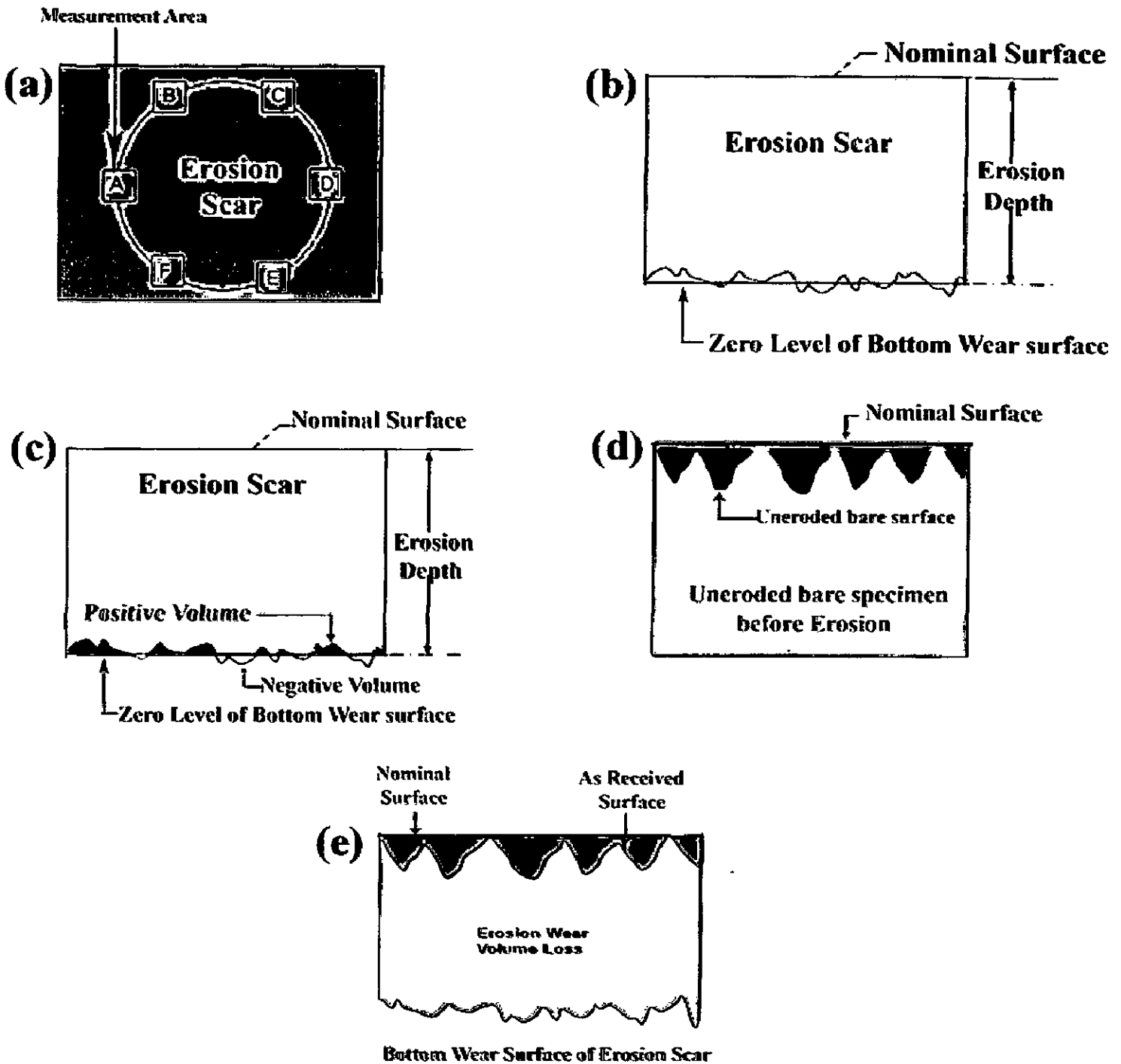


Fig. 3.8: Schematic depth-measuring method (a) Designation of sampling area. (b) Erosion depth. (c) Net missing volume of eroded area. (d) Natural volume of uneroded, bare surface. (e) Erosion wear volume loss.

The histograms illustrating the erosion rates in terms of volume loss (mm^3/g) have been plotted to compare erosion rates of different uncoated alloys and coated alloys and have been discussed in chapter 5.

3.5.3.3 SEM/EDX Analysis

Surface SEM analyses of eroded samples were conducted using Field emission scanning electron microscope (FEI Company, Quanta 200F) with EDX attachment. EDX analysis at few points of interest was taken.

3.6. EROSION-CORROSION STUDIES IN ACTUAL INDUSTRIAL ENVIRONMENT

3.6.1 Specimen Preparation for Testing

D-gun coated and uncoated specimens of size 21X16X5 mm of each alloy were exposed to superheater zone of the coal fired boiler of Guru Gobind Singh Super Thermal Plant, Ropar, Punjab (India) for this study. For hanging these samples 1 mm holes were drilled. The uncoated as well as the coated specimens were polished down to $1\mu\text{m}$ to obtain similar condition on all the samples before being subjected to boiler environment. Also physical dimensions of the specimens were measured carefully with digital Vernier Caliper to evaluate their surface areas. To evaluate the thickness loss of the samples during the exposure period, the average thickness (average of 20 measurements in each samples) was measured using micrometer screw gauge. The samples were hung in the boiler with the help of stainless steel wire and a rigid support of stainless steel rod through the soot blower dummy points at 42 m height from the base of boiler. The specimens were exposed to the combustion environment for 15 cycles. Each cycle consisted of 100 hours heating followed by 30 minutes cooling at ambient conditions. The temperature of the hanging zone was measured at regular intervals during the study and the temperature was about $700 \pm 10^\circ\text{C}$ with full load of 210 MW and volumetric flow of flue gases was $250 \text{ m}^3/\text{sec}$. After the end of each cycle the samples were visually examined for any change on surface and weight of samples were measured subsequently. The coal analysis data is reported in Table 3.6 whereas the chemical analysis of the flue gas and ash present inside the boiler is given in Table 3.7.

The samples were characterized by different methods like SEM (Scanning Electron Microscopy), EDX (Energy Dispersive X-ray Analysis).

Table 3.6: Coal Analysis data

Constituent	Wt. % age
Total moisture (inherent + surface)	10.43
Inherent moisture	7.55
Ash	34.74
Ash on fire basis (actual)	33.64
Volatile metal	21.59
Unburnt carbon in fly ash	1.35
Unburnt carbon in bottom ash	5.75

Table 3.7: Chemical analysis of ash and flue gases inside the boiler

Ash		Flue Gases	
Constituent	Wt. %age	(Volumetric flow, 250 m ³ /sec)	
Silica	53.9	Constituent	Value relative to flue gases
Al ₂ O ₃ -Fe ₂ O ₃ /Al ₂ O ₃	31.9	SO _x	236 mg/m ³
Fe ₂ O ₃	5.23	NO _x	1004 . g/m ³
Calcium oxide	1.41	CO ₂	14-16%
Magnesium oxide	1.28	O ₂	3-5 %
SO ₃	0.35	40% excess air was supplied to the Boiler for the combustion of coal.	
Na ₂ O	0.33		
K ₂ O	1.29		
Ignition loss	4.31		

3.6.2 Analysis of erosion-corrosion products in boiler environments

The samples exposed to boiler environment were analysed. The surface and cross-section of the eroded-corroded specimens from boiler environment were analysed by XRD, SEM and EDX analysis.

3.6.2.1 Visual Observation

For samples exposed to boiler environment, visual examination was made after each cycle and changes in colour, luster, growth of cracks and spalling tendency in the scales were recorded. After the completion of 15 cycles the exposed specimens were finally carefully visually examined and their macrographs were taken.

3.6.2.2 Weight Change Studies

The weight change values were calculated at the end of each cycle with the aim to approximate the kinetics of erosion-corrosion for the specimens kept in boiler environment. The weight change data were plotted with respect to number of cycles for each specimen and the plots have been given in the subsequent chapters. Because of the specimens exposed to the industrial environment, the actual working conditions of the coal fired boiler in a thermal power plant, the spalled scale could not be collected and incorporated in the weight change.

3.6.2.3 X-Ray Diffraction (XRD) Analysis

X-ray diffraction analysis was conducted for identification of different phases formed in the eroded-corroded specimen surfaces after 1500 hours exposure in the boiler, of all those specimens and results of all the analysed samples have been presented in Chapter 7.

3.6.2.4 SEM/EDX Analysis

(a) Surface Morphology

After 1500 hours exposure in the boiler of thermal power plant, SEM/EDX analysis of the eroded-corroded specimen surfaces was conducted. The specimens were scanned under the microscope and the critical areas of interests were photographed with an aim to identify the micro cracks and morphology of the surface scale.

(b) Cross-Sectional Morphology

SEM/EDX analysis for specimens was carried out along their cross-sections. Cross-sectional BSE images were taken and some points of interest identified on these images including scale/coating and substrate. EDX analysis was then conducted to ascertain elemental composition (weight %) for these points. Although these compositions correspond to selected

points along the cross-sections, still the data could be useful to approximate the distribution of various elements across the thickness of the scales.

(c) X-ray Mapping

The exposed specimens were cut along the cross-section, mounted and polished. For carrying out the EDX analysis, some critical areas of interest across the cross section of each specimen were selected and then BSEI and elemental X-ray mappings were obtained at that particular area. To evaluate different elements in the region of interest x-ray mapping of the samples was done on field emission scanning electron microscope (FEI Company, Quanta 200F) with EDX attachment. For obtaining elemental maps, image of the area to be analysed was recorded on which elemental x ray mapping was taken.

CHARACTERISATION OF SUBSTRATE ALLOYS AND D-GUN SPRAYED Al_2O_3 -3 Wt% TiO_2 COATINGS

4.1 INTRODUCTION

The chapter deals with critical evaluation of the substrate alloys and the Al_2O_3 -3 wt % TiO_2 coatings applied on them. The metallographic examination of substrate steels as well as the coatings has been discussed. Techniques like optical microscopy, X-ray diffractometry (XRD), scanning electron microscopy/energy-dispersive analysis (SEM/EDX), and micro hardness tester were used for metallographic examinations and to evaluate the physical properties like porosity and microhardness of the as-sprayed coatings. The physical properties like porosity and microhardness of as sprayed coatings have been reported and discussed with respect to the existing literature. The results of XRD and SEM/EDX analysis have been incorporated.

4.2 SUBSTRATE ALLOYS

Optical microstructures of the substrate alloys are shown in Fig. 4.1, which are explained with reference to atlas of microstructures for industrial alloys (Metals Handbook, 1972 and ASM Handbook, 1995). The microstructure of T11 and T22 steels consists of ferrite white in colour and pearlite dark in colour as shown in Fig. 4.1 (a) and (b). The microstructures of Superni 600, Superni 718 and Superfer 800, Fig. 4.1 (c), (d) and (e) respectively can be characterised by a nickel-rich γ -solid solution matrix. The microstructure of Superni 600 shows Ni-Cr-Fe solid solution containing fine as well as coarse carbides in the grains and along the grain boundaries, refer Fig. 4.1 (c). Twin boundaries are also visible in the structure of Superni 600. Whereas the microstructure of the Superfer 800 (Fig. 4.1 (e)) consists of a solid solution matrix in which some of the grains are delineated by particles of precipitated carbides at the grain boundaries and by twinning lines (Metals Handbook, 1972).

4.3 COATING DEPOSITION AND CHARACTERISATION

4.3.1 Morphology of coating powders and Phase Analysis

The morphology of powder has been evaluated using SEM. The scanning electron micrographs indicating morphology is shown in Fig. 4.2. Powder particles have irregular and

angular shape. XRD analysis of the starting powders was conducted using Bruker AXS D-8 Advance Diffractometer (Germany) with $\text{CuK}\alpha$ radiation and nickel filter at 20 mA under a voltage of 35 kV and corresponding X-ray diffraction profiles of the coating powders are shown in Fig. 4.3. The main phase detected is Al_2O_3 and the minor phase is TiO_2 . The rhombohedral α - Al_2O_3 phase along with anatase TiO_2 phase appeared in the powder.

4.3.2 Coating Description and Visual Examination of Al_2O_3 -3 wt% TiO_2 Coating

In this work five substrates were coated with Al_2O_3 -3 wt% TiO_2 powders. Coatings were sprayed using the D-gun. All samples were coated with same powder and with the same parameters. In order to obtain specific coating thickness and uniformity, few optimisation trials were performed before final coating. The powders had the same composition and size range. The Coatings were examined visually after deposition by D-gun. Macrographs for the as coated samples are shown in Fig. 4.4. Coatings have greyish appearance with rough surfaces. Coatings are uniform and found to be free from surface cracks.

4.3.3 Measurements of Coating Thickness

Scanning Electron micrographs were taken along cross-sections of the D-gun sprayed coated specimens and are shown in Fig. 4.5. Thickness of the coatings has been measured from micrographs and was found to be in the range of 200-230 μm .

4.3.4 Microhardness

Microhardness is the basic mechanical property of coatings, which are used to characterize the performance of coatings. Microhardness of the coatings on different substrate alloys has been measured along the cross-section. Profiles for microhardness versus distance from the coating-substrate interface are depicted in Fig. 4.6. The average microhardness values for T11, T22, Superni 600, Superni 718 and Superfer 800 superalloys are observed to be 194, 270, 290, 462 and 340 Hv respectively as shown in Fig. 4.7. Microhardness of the Al_2O_3 -3wt% TiO_2 coating has been found to be in a range of 862 to 1056 Hv. As velocity of powder particle was higher in D-gun spray process, the coating exhibited higher hardness.

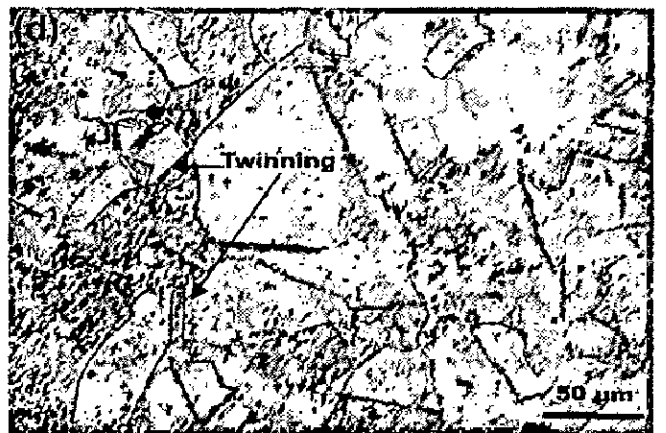
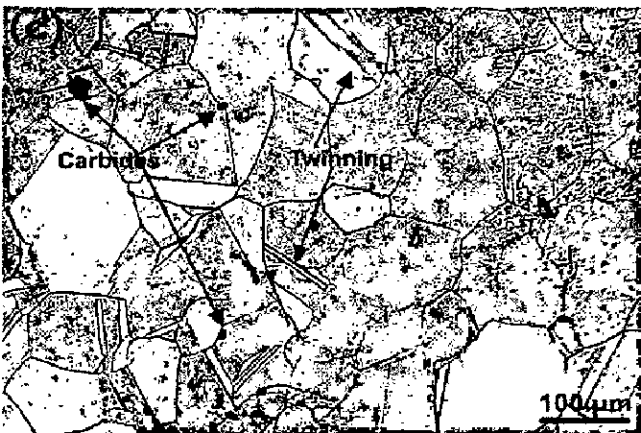
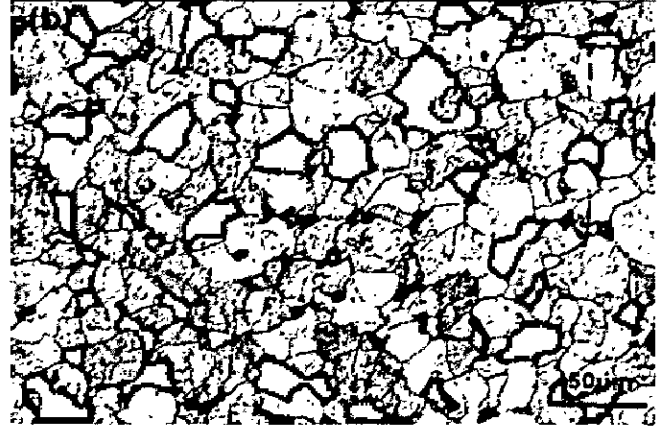
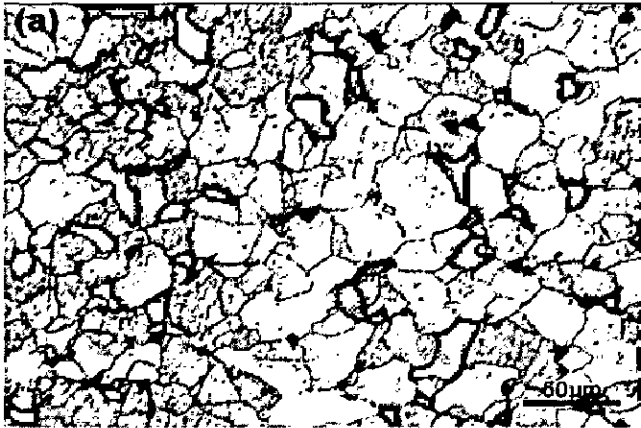


Fig. 4.1: Optical micrographs of the substrate alloys
 (a) Boiler Steel T11 (b) Boiler Steel T22 (c) Superni 600
 (d) Superni 718 (e) Superfer 800



Fig. 4.2: Scanning electron micrographs showing morphology of Al_2O_3 -3wt% TiO_2 powder.

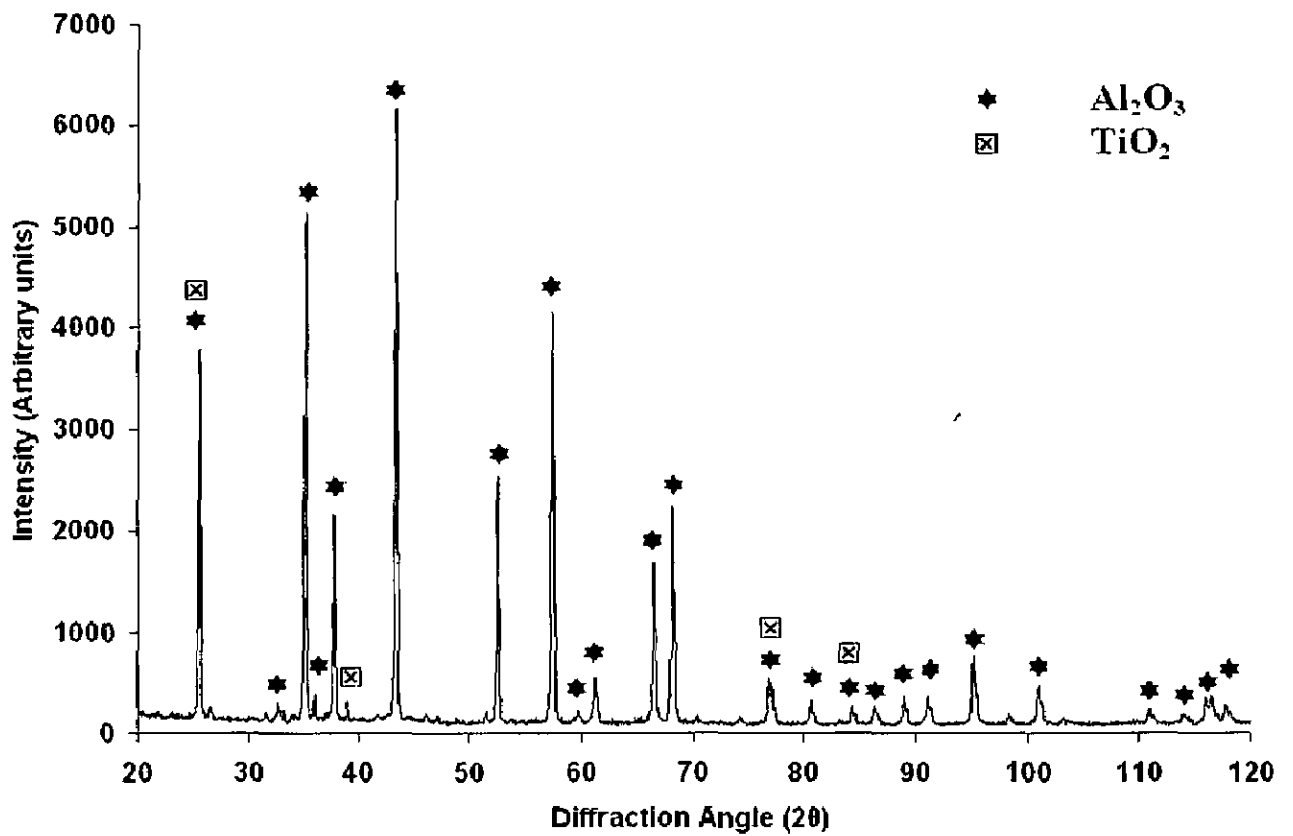


Fig. 4.3: X-ray Diffraction Profile of coating powder Al_2O_3 -3wt% TiO_2 .

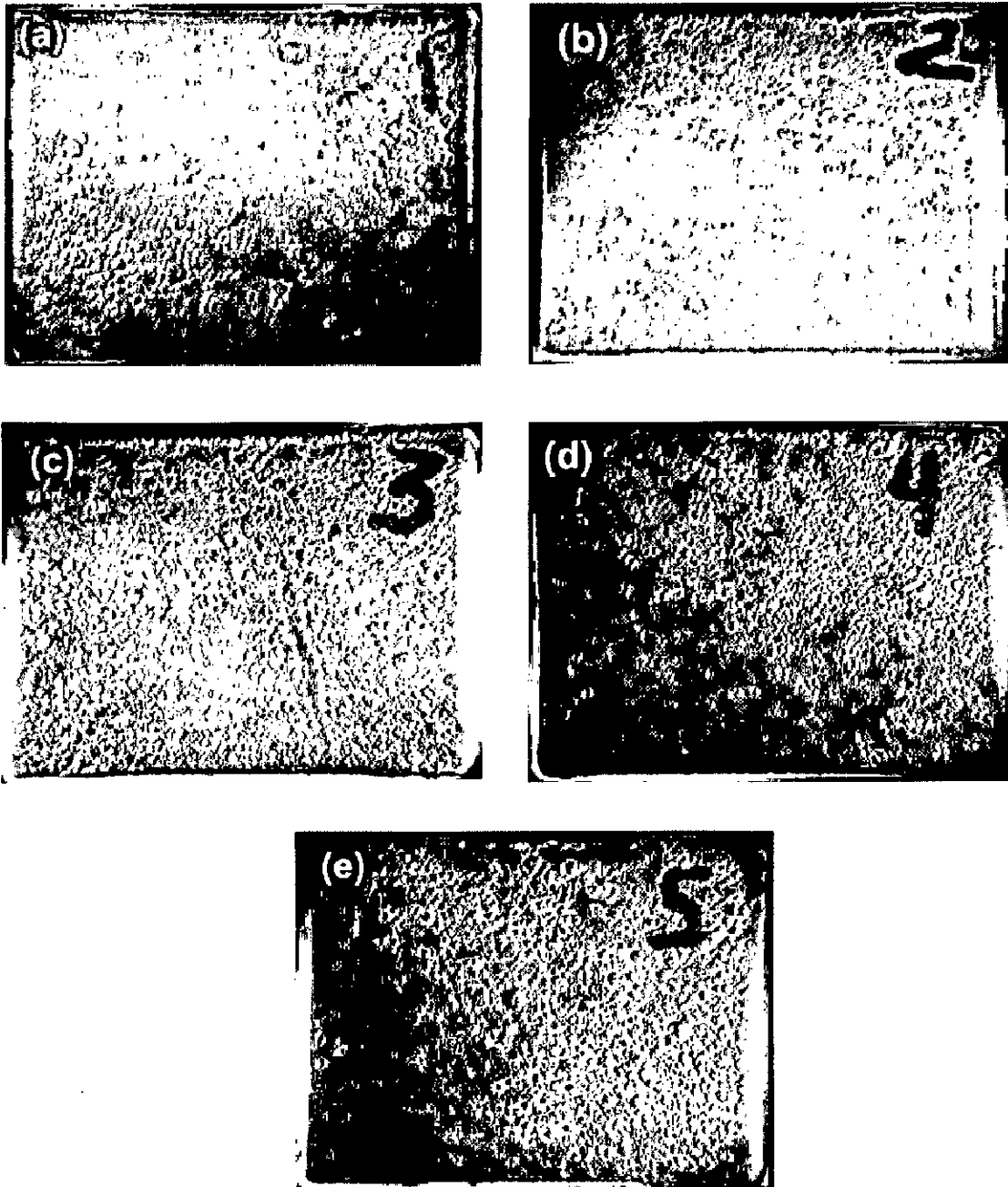


Fig. 4.4: Macrographs of specimens coated with Al_2O_3 -3 wt % TiO_2 powder (a) T11, (b) T22, (c) Superni 600 (d) Superni 718 and (e) Superfer 800.

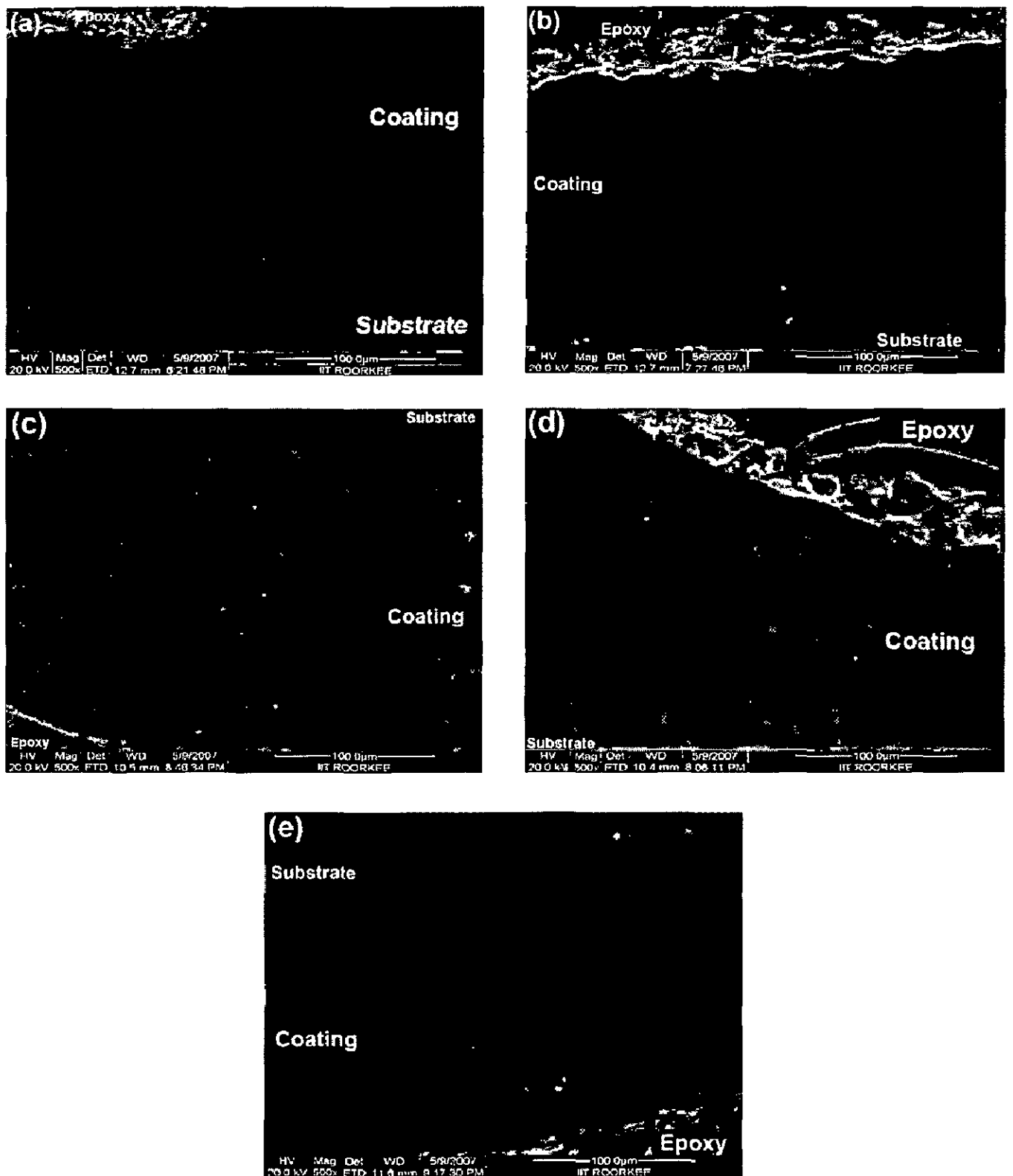


Fig.4.5: Scanning electron micrograph showing cross-sectional morphology of Al_2O_3 -3wt% TiO_2 D-gun sprayed coatings on substrate alloys (a) Al_2O_3 -3wt% TiO_2 coating on T11 (b) Al_2O_3 -3wt% TiO_2 coating on T22 (c) Al_2O_3 -3wt% TiO_2 coating on Superni 600 (d) Al_2O_3 -3wt% TiO_2 coating on Superni 718 and (e) Al_2O_3 -3wt% TiO_2 coating on Superfer 800

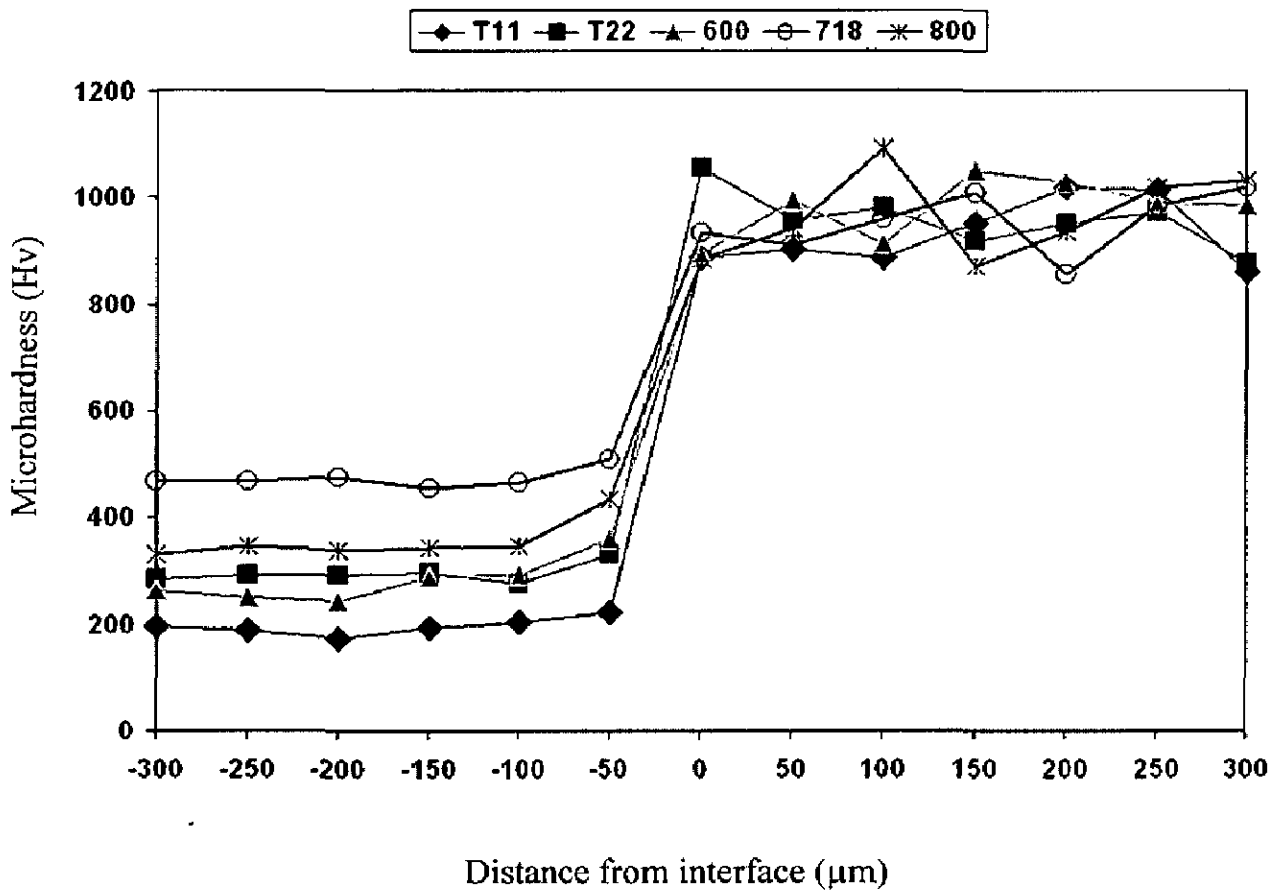


Fig. 4.6: Microhardness profiles of Al_2O_3 -3 wt% TiO_2 coating on different alloys along the cross-section.

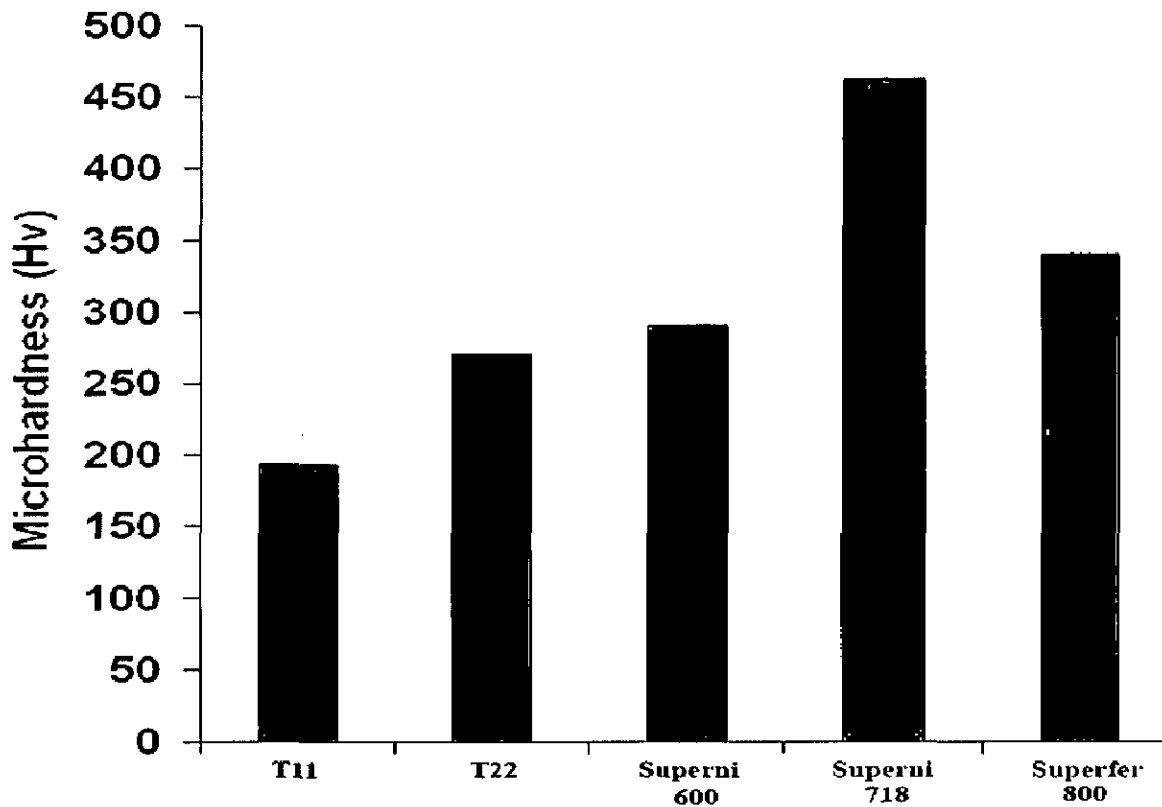


Fig. 4.7: Average microhardness values for T11, T22, Superni 600, Superni 718 and Superfer 800 alloys

4.3.5 Coating Porosity

Porosity of the coatings has a significant role to play on the erosion and corrosion resistance of thermal sprayed coatings. Dense coatings usually provide better erosion and corrosion resistance than the porous coatings. Porosity measurements were made for the D-gun sprayed Al_2O_3 -3wt% TiO_2 coatings, which are found to be in a range of 0.7-0.9 % (Table 4.1)

Table 4.1: Coating Thickness and Porosity on coating surfaces for different specimens

S. No.	Substrate	Coating Material	Coating Thickness (μm)	Porosity
1.	T11	Al_2O_3 -3 Wt% TiO_2	212	0.9%
2.	T22	Al_2O_3 -3 Wt% TiO_2	220	0.8 %
3.	Superni 600	Al_2O_3 -3 Wt% TiO_2	230	0.7 %
4.	Superni 718	Al_2O_3 -3 Wt% TiO_2	218	0.8 %
5.	Superfer 800	Al_2O_3 -3 Wt% TiO_2	215	0.7%

4.3.6 Microstructure

All the coatings produced in the present investigation were excellent in quality. It is observed that the top surface of the coating is free of cracks and porosity. All the photomicrographs exhibited very dense coatings with homogeneously dispersed porosity. Fig. 4.8 depicts the typical surface topographies of the D-gun sprayed coatings. The Al_2O_3 -3 wt.% TiO_2 coating exhibited definite splat morphologies with densely packing splats. No cracking was observed in the coating. Also there is no presence of large amount of unmelted particles. Figs 4.9 and 4.10 show the typical microstructures from the matrix for the coatings; Coatings indicated homogeneously dispersed micro porosity.

4.3.7 Phase Analysis – XRD of the Coatings

The phase composition of the as-sprayed samples was determined by X-ray diffraction (XRD). The XRD spectra of all the coatings based on the Al_2O_3 -3 wt% TiO_2 powder generally mirror the spectra presented in the literature. The spectrum is dominated by matrix phase i.e. Al_2O_3 . Small peaks of TiO_2 are also observed. No other oxide phases were

detected in analysis. The XRD results are shown in Figs 4.11 to 4.15. In the XRD spectrum of all the coated substrates, TiO₂ phase has been confined to two peaks only. XRD phase analysis revealed that coating consisted not only of α -Al₂O₃ but also γ -Al₂O₃. The results of the XRD analysis of the initial spray powder and as-sprayed coating were in good agreement with the literature, as typical peaks consisted mostly of α -alumina phase (corundum) with few peaks of titania were detected. Partial transformation of α -alumina to γ -alumina in the deposited coating is due to the spray conditions. The formation of meta-stable alumina as γ (cubic), is due to the heat conditions during the cooling process (Levin et al., 1997; McPherson 1980). It is suggested that the preferential formation of γ -Al₂O₃ is attributed to the high cooling rate (about 10⁶ K/s) of the molten particles during spraying and easy nucleation of γ -Al₂O₃ from the melt superior to α -Al₂O₃ thanks to lower interfacial energy between crystal and liquid (McPherson 1989).

4.3.8 SEM/ EDX (Energy dispersive X-ray) analysis

(a) Surface Analysis

In the case of Al₂O₃-3 wt%TiO₂ coating, one can see spheroidal grained structure. Grains have fused together due to high impact of the detonation process. Some minor cavities that are visible might have been originated at inter particle boundary regions. Particles have fused together to form larger chunks with minor cavities at the inter-boundary regions. There is presence of some unmelted particles. Most of the particles have fused to form elongated shaped structures. Flattened areas are clearly visible. SEM/EDX analysis of the coatings was done at some selected areas of interest, as shown in micrographs (Fig. 4.16 and Fig.4.17). The areas have a composition close to the powder composition.

(b) Cross-section Analysis

The BSE image and the EDX analysis across the cross section on Al₂O₃ -3 wt% TiO₂ coated alloys are shown in Fig. 4.18-4.22. In all the coated alloys the coating was quite intact and there were no cracks developed in the coating. Throughout the coating thickness, the composition is entirely of Alumina and Titania. From the cross-sectional microstructures, it can be seen that coatings consist of the lamella built up from the molten droplets impinging on the substrate. The composition contrast from backscattered electron micrographs illustrated that the Al₂O₃-3wt.% TiO₂ coating possessed distinct layered structure, i.e. aluminum-rich regions (grey) separated from titania rich regions (white). Coatings obtained with the powder exhibited a homogeneous layered structure. The white

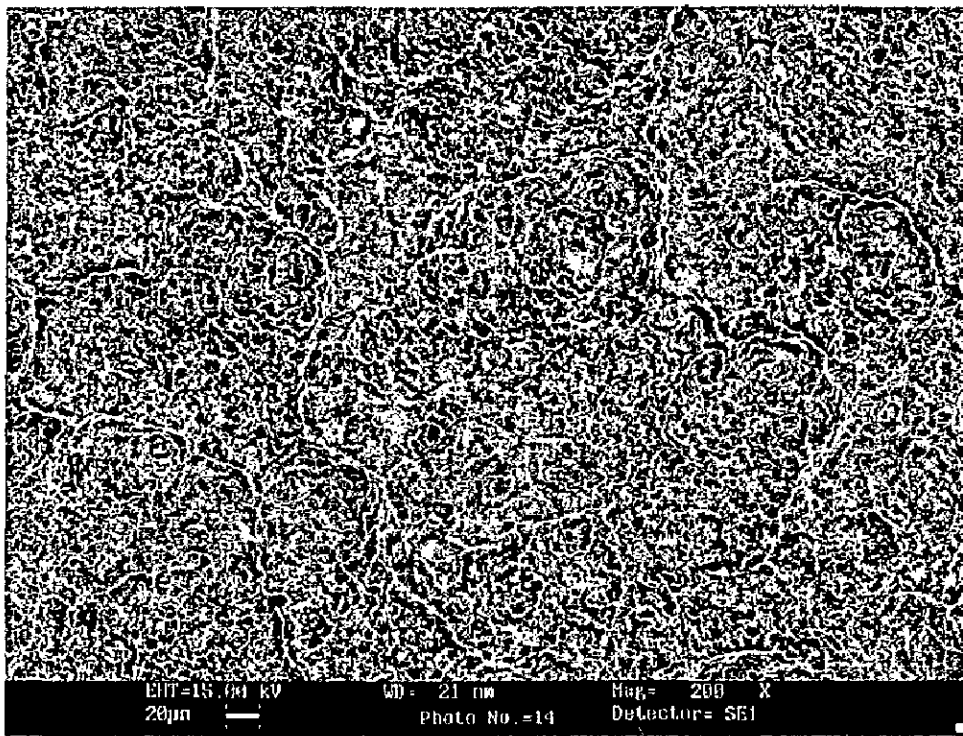


Fig. 4.8: Typical Scanning electron micrographs of the surfaces of the as-sprayed Al_2O_3 -3wt.% TiO_2 coatings

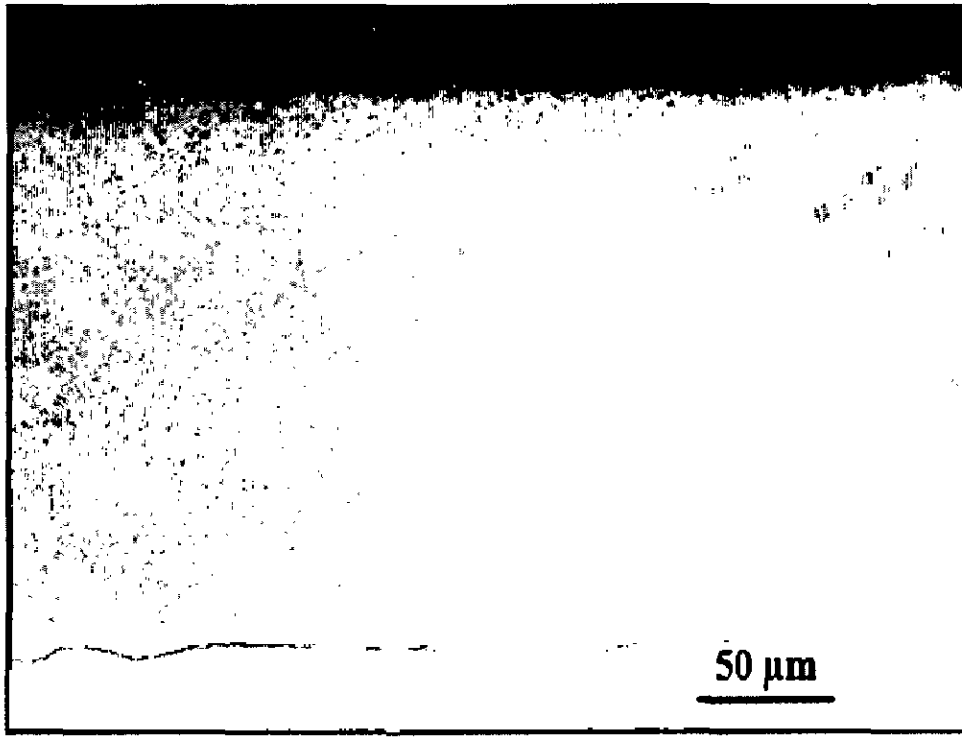


Fig. 4.9: Optical micrographs of a as-sprayed Al_2O_3 -3 wt.% TiO_2 coatings

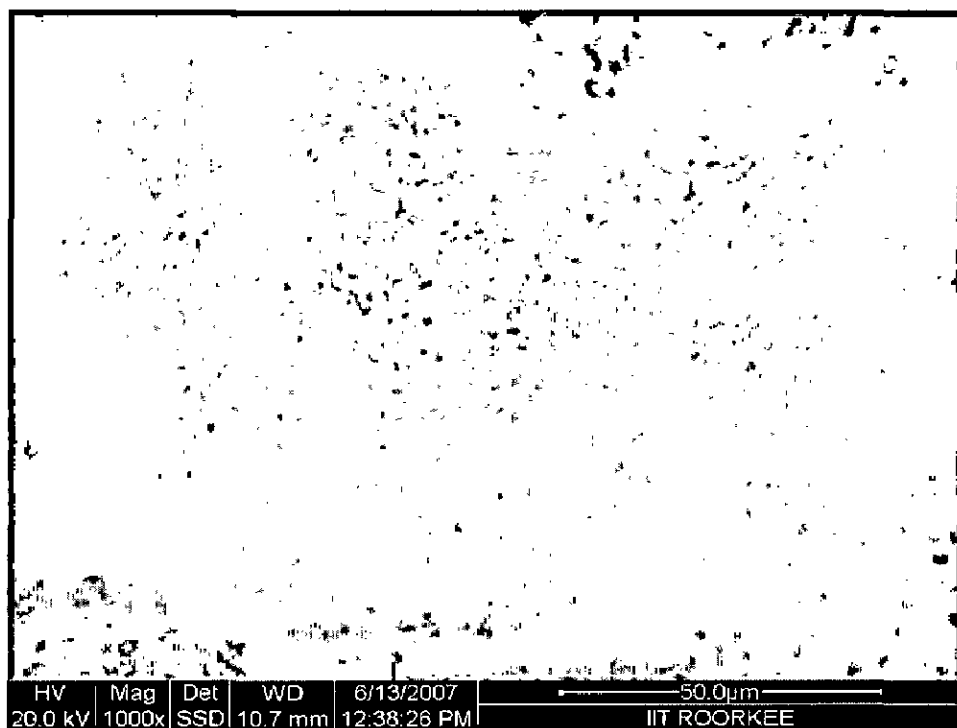


Fig. 4.10: Cross-sectional morphology of the as-sprayed Al_2O_3 -3 wt.% TiO_2 coatings:

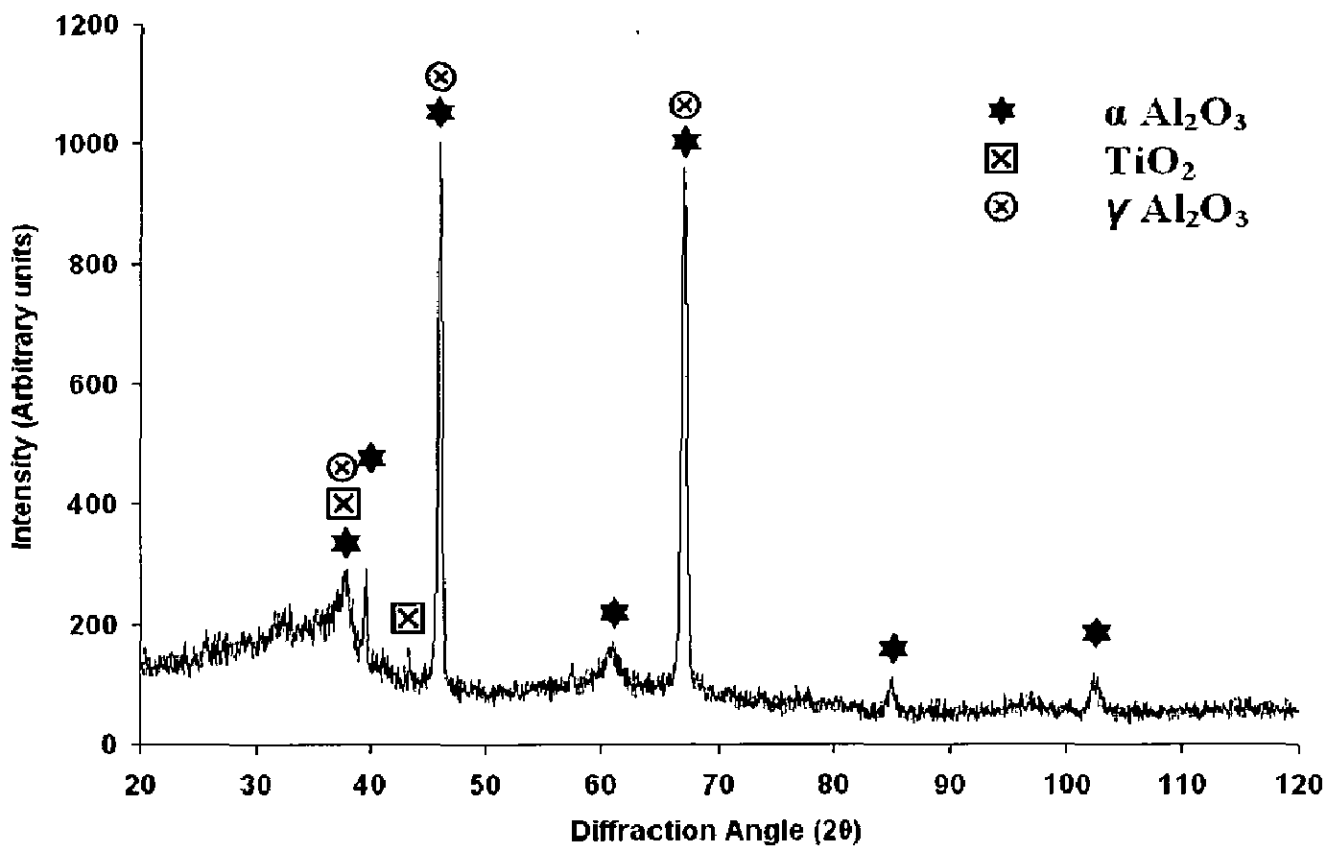


Fig. 4.11 X-ray diffraction pattern for the D-gun sprayed Al_2O_3 -3 wt% TiO_2 coated Boiler Steel T11.

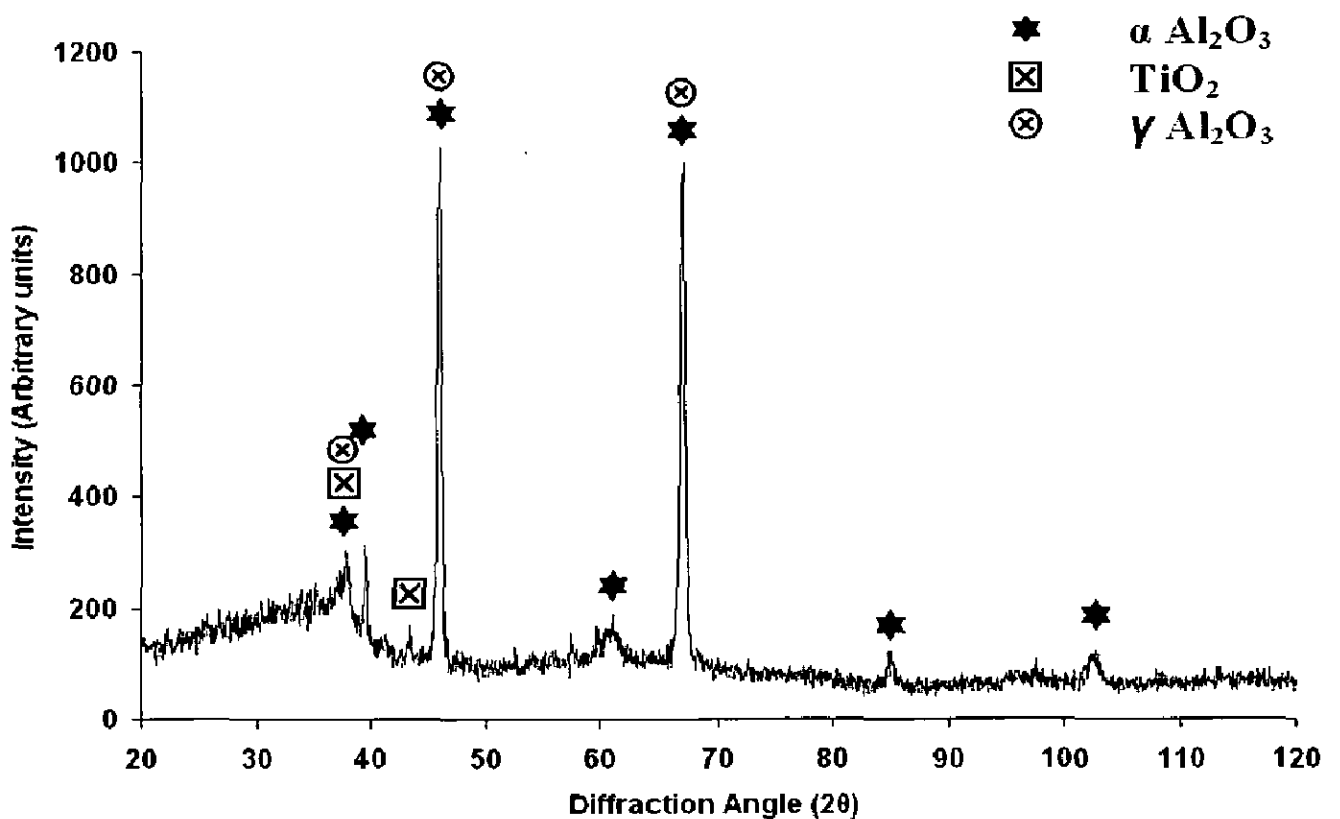


Fig. 4.12 X-ray diffraction pattern for the D-gun sprayed Al_2O_3 -3 wt% TiO_2 coated Boiler steel T22.

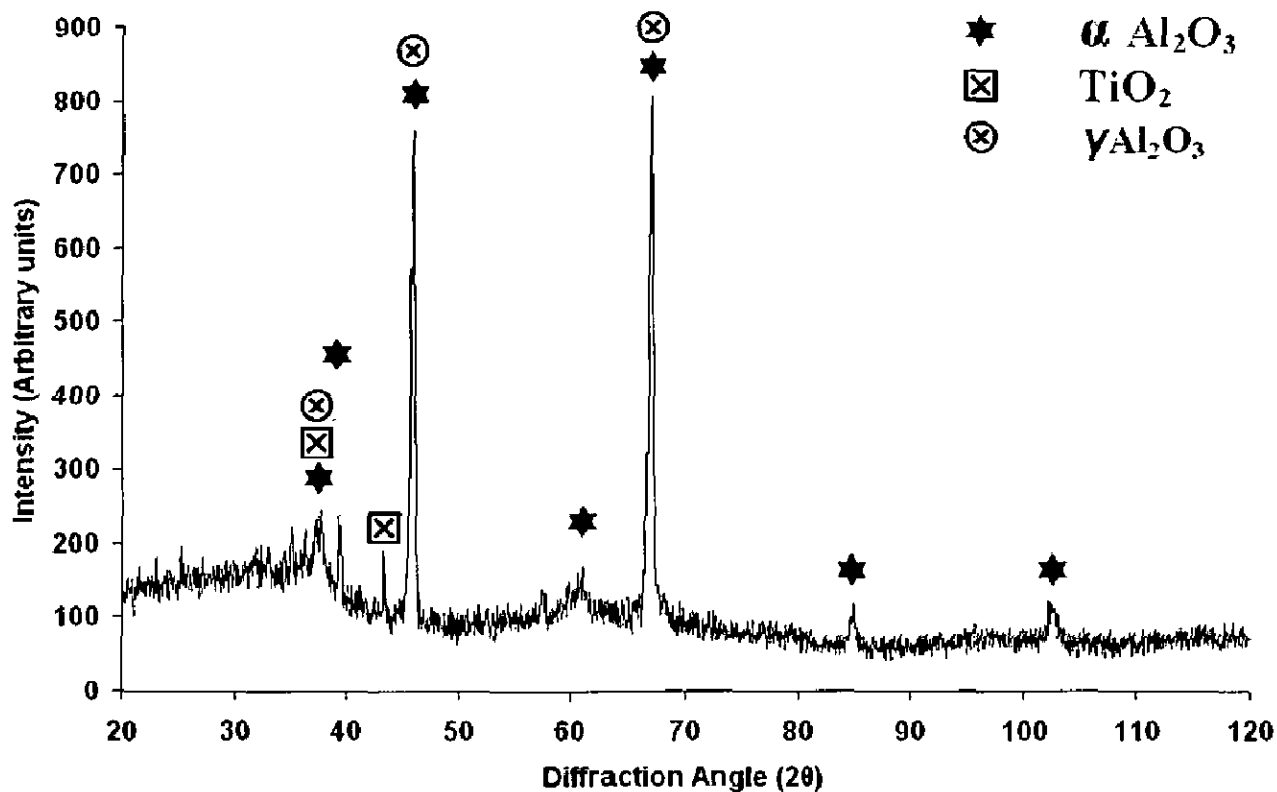


Fig. 4.13 X-ray diffraction pattern for the D-gun sprayed Al₂O₃-3 wt% TiO₂ coated superalloy Superni 600.

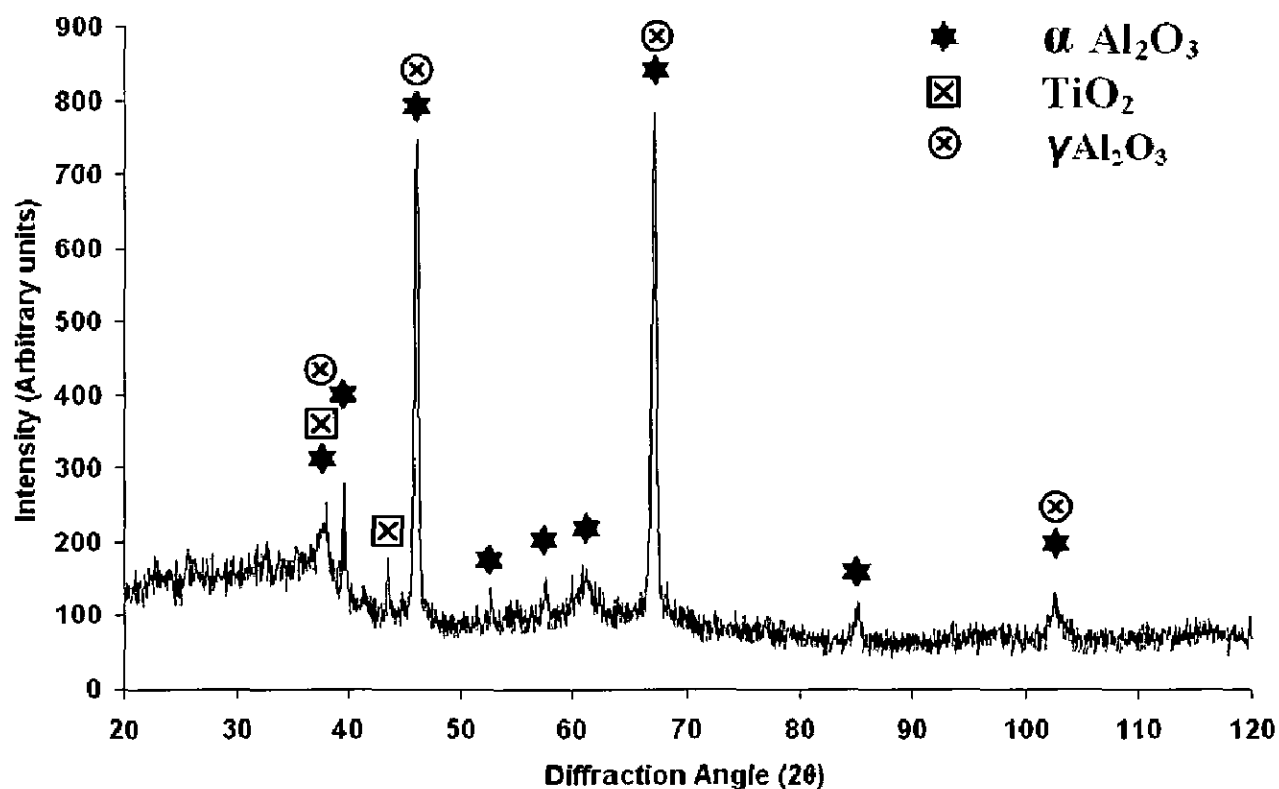


Fig. 4.14 X-ray diffraction pattern for the D-gun sprayed Al₂O₃-3 wt% TiO₂ coated superalloy Superni 718.

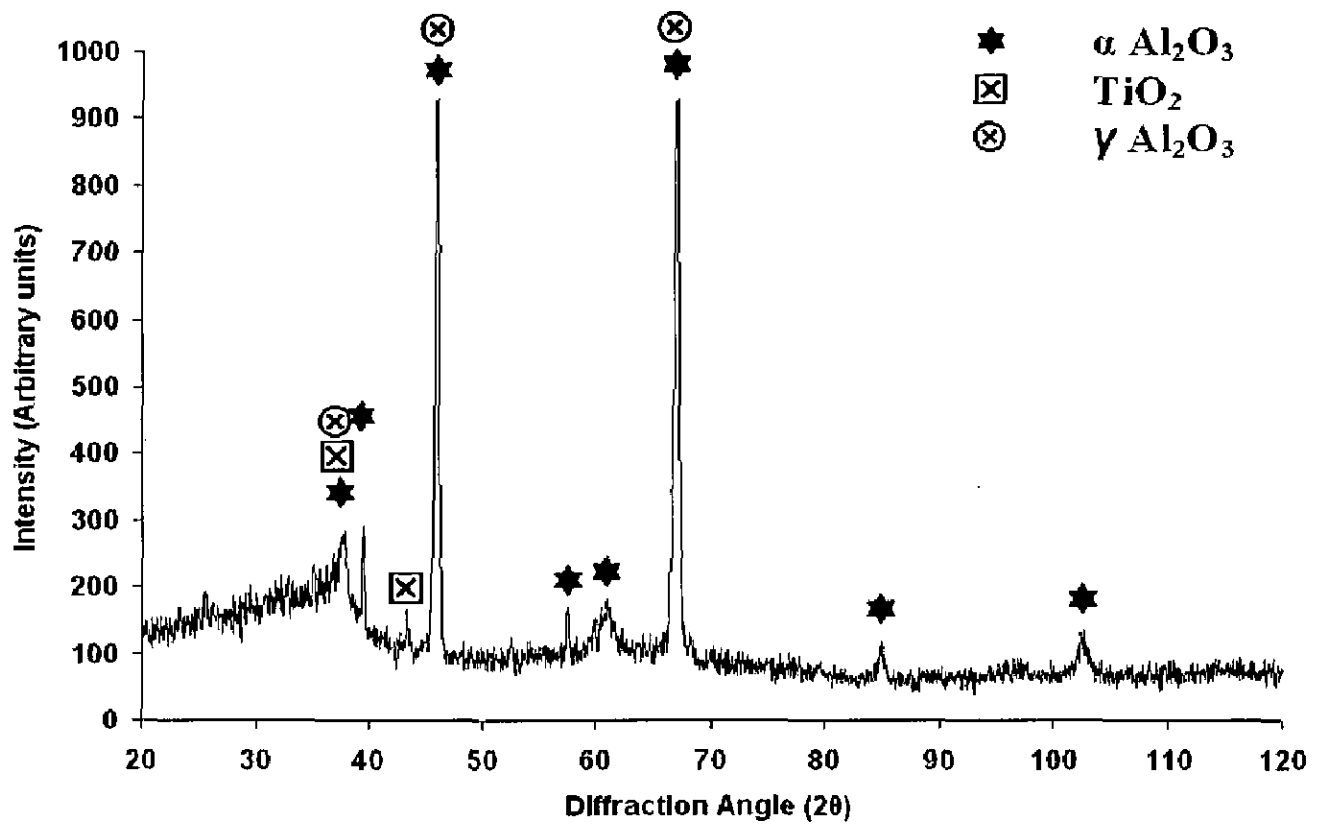


Fig. 4.15 X-ray diffraction pattern for the D-gun sprayed Al_2O_3 -3 wt% TiO_2 coated superalloy Superfer 800.

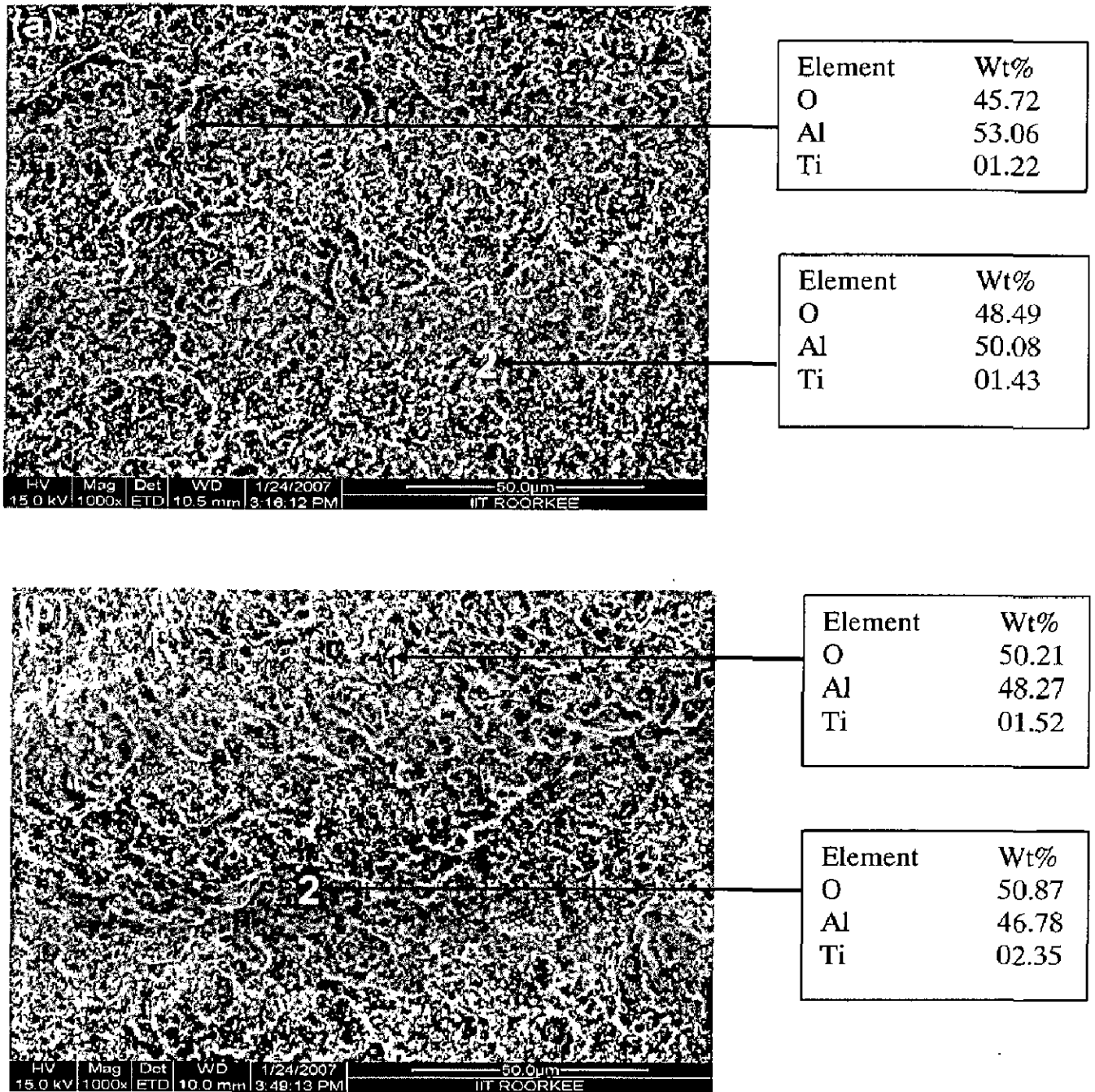


Fig. 4.16: SEM/EDX analysis of coatings showing elemental composition (wt.%) at various points (a) Coated T11, 1000 X, (b) Coated T22, 1000 X

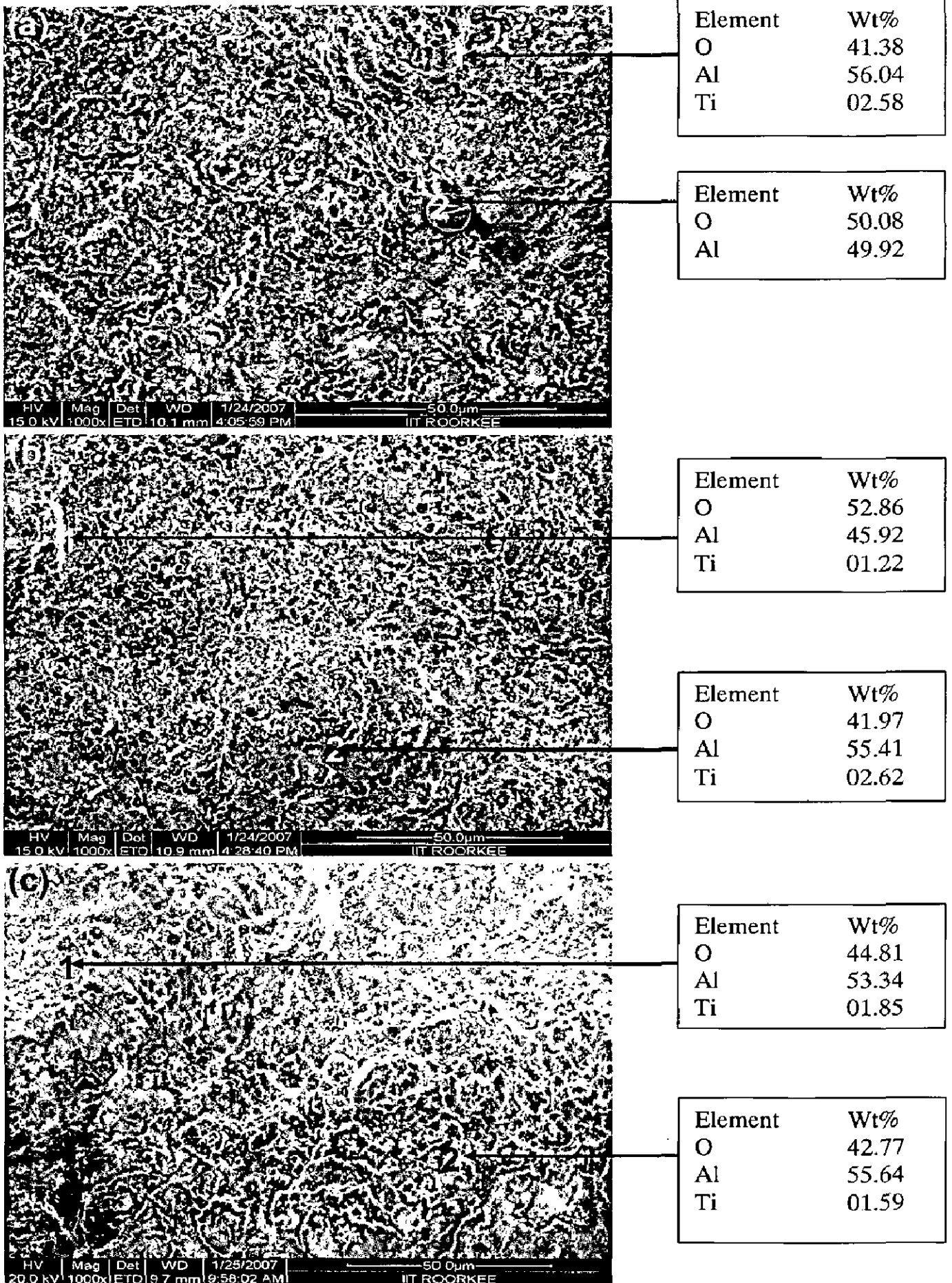


Fig. 4.17: SEM/EDX analysis of coatings showing elemental composition (wt.%) at various points (a) Coated Superni 600, 1000 X, (b) Coated Superni 718, 1000 X and (c) Coated Superfer 800, 1000 X.

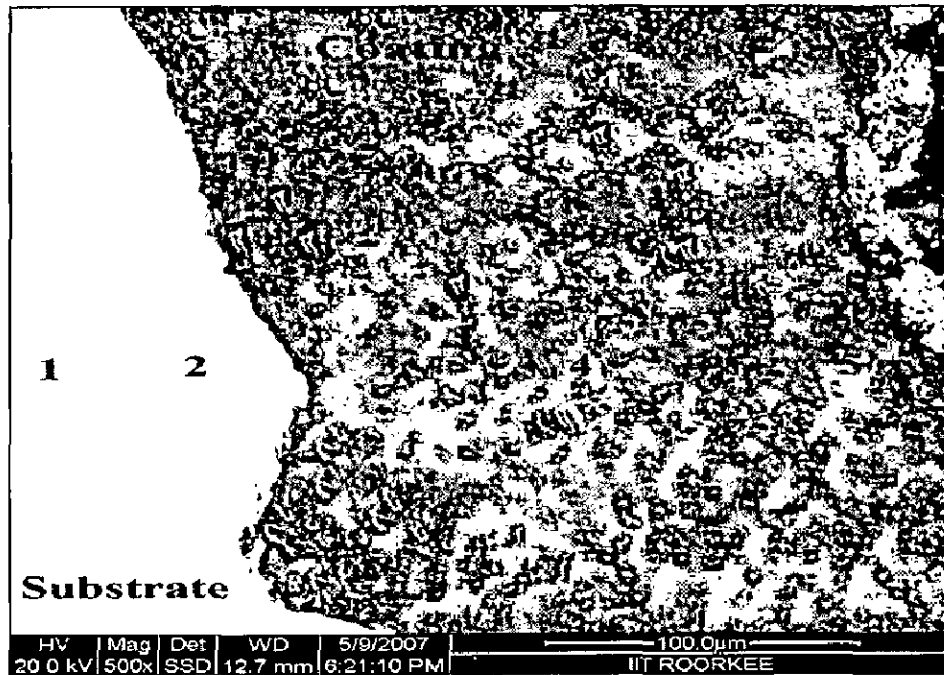
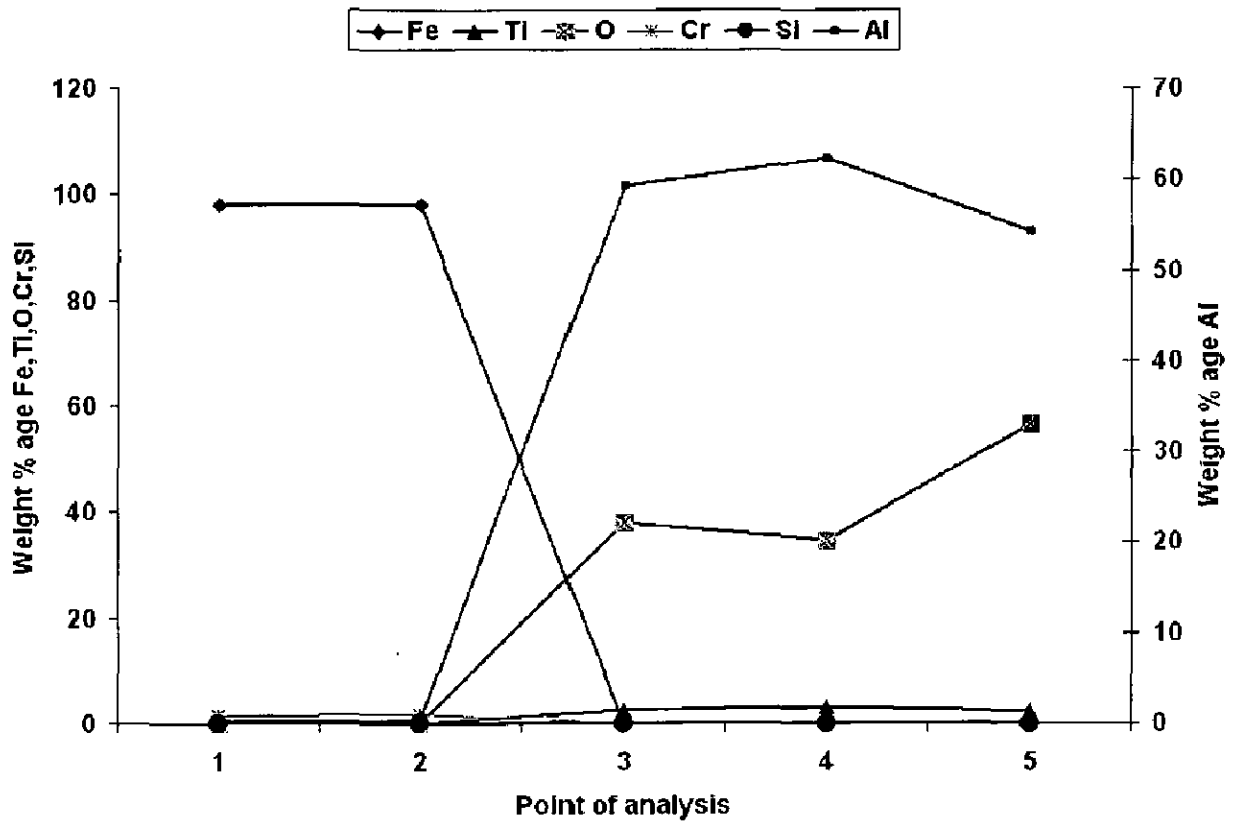


Fig. 4.18: Cross sectional morphology and elemental composition variation across the cross-section of Al_2O_3 -3 wt% TiO_2 coated T11 boiler steels

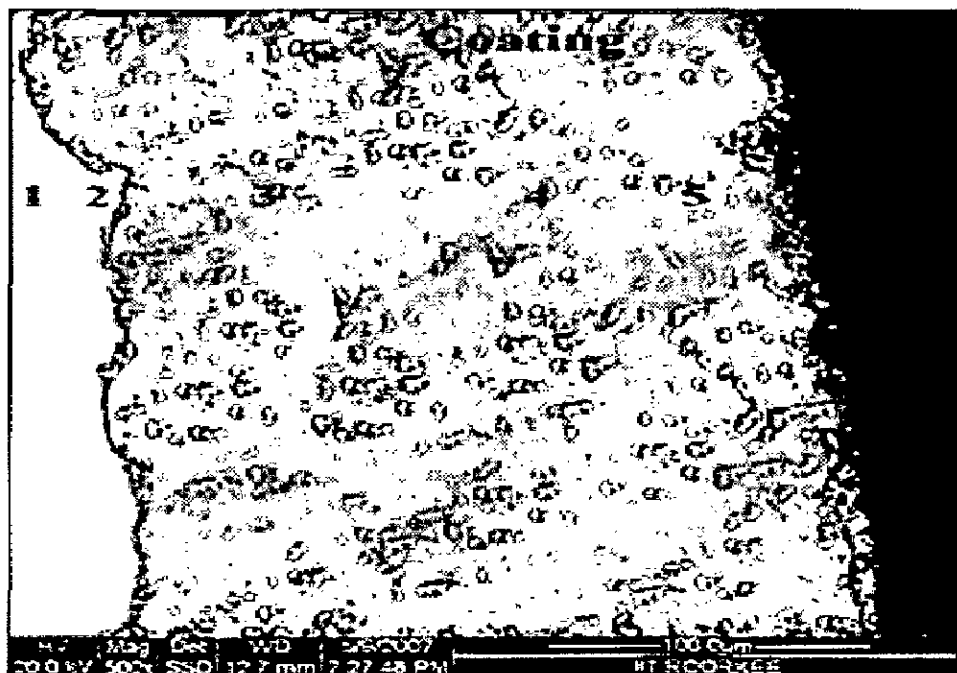
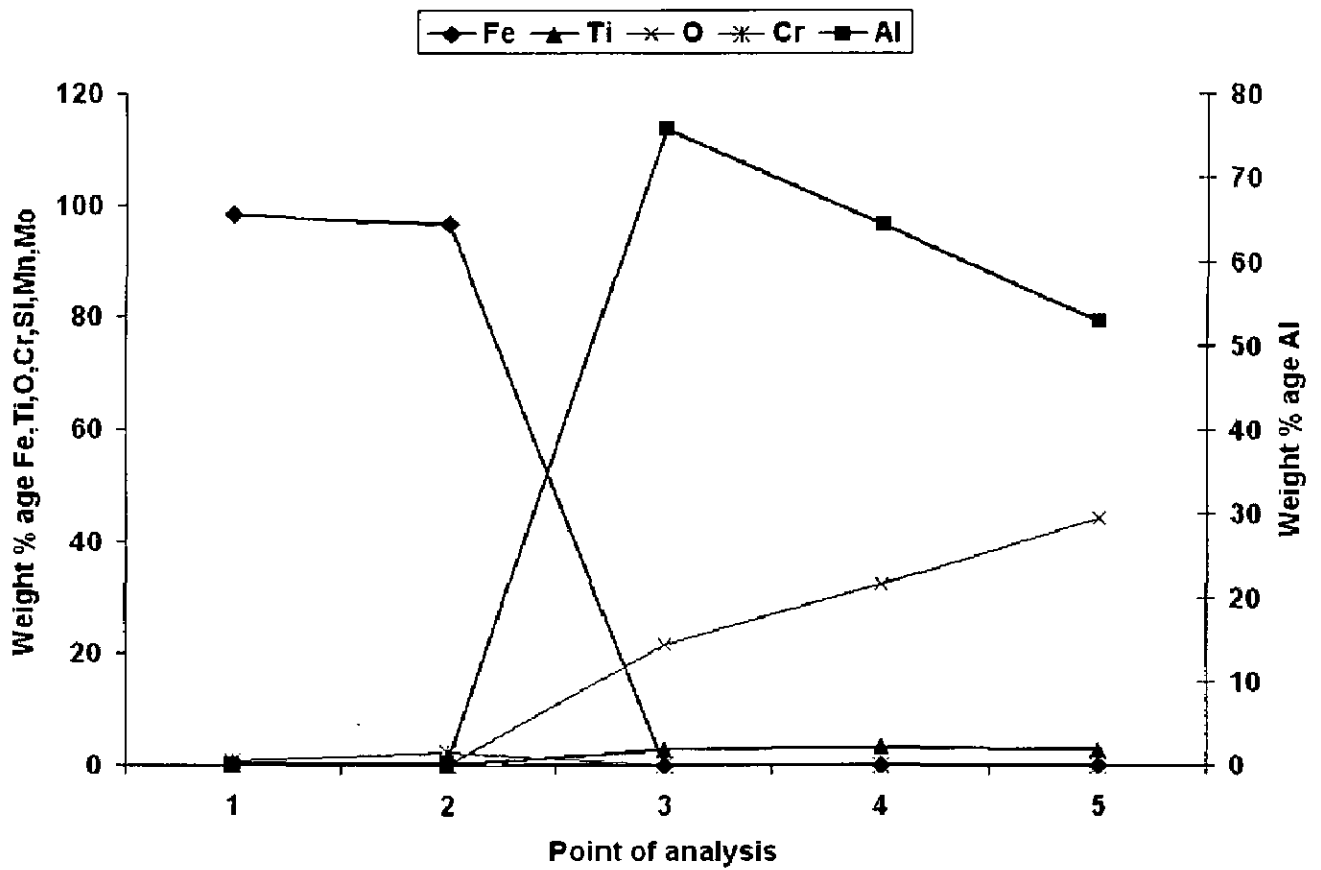


Fig. 4.19: Cross sectional morphology and elemental composition variation across the cross-section of Al_2O_3 -3 wt% TiO_2 coated T22 boiler steels

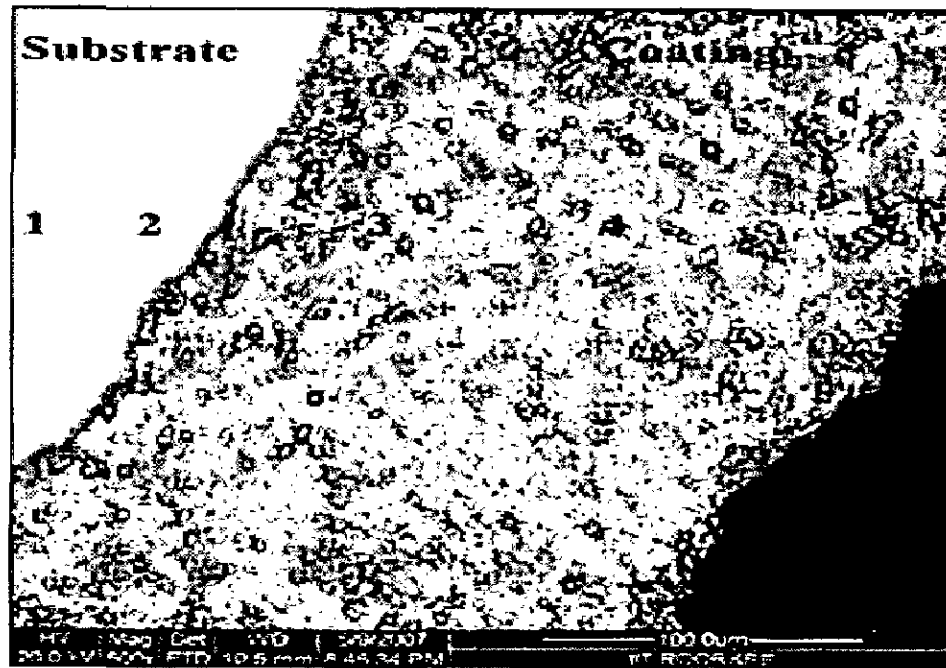
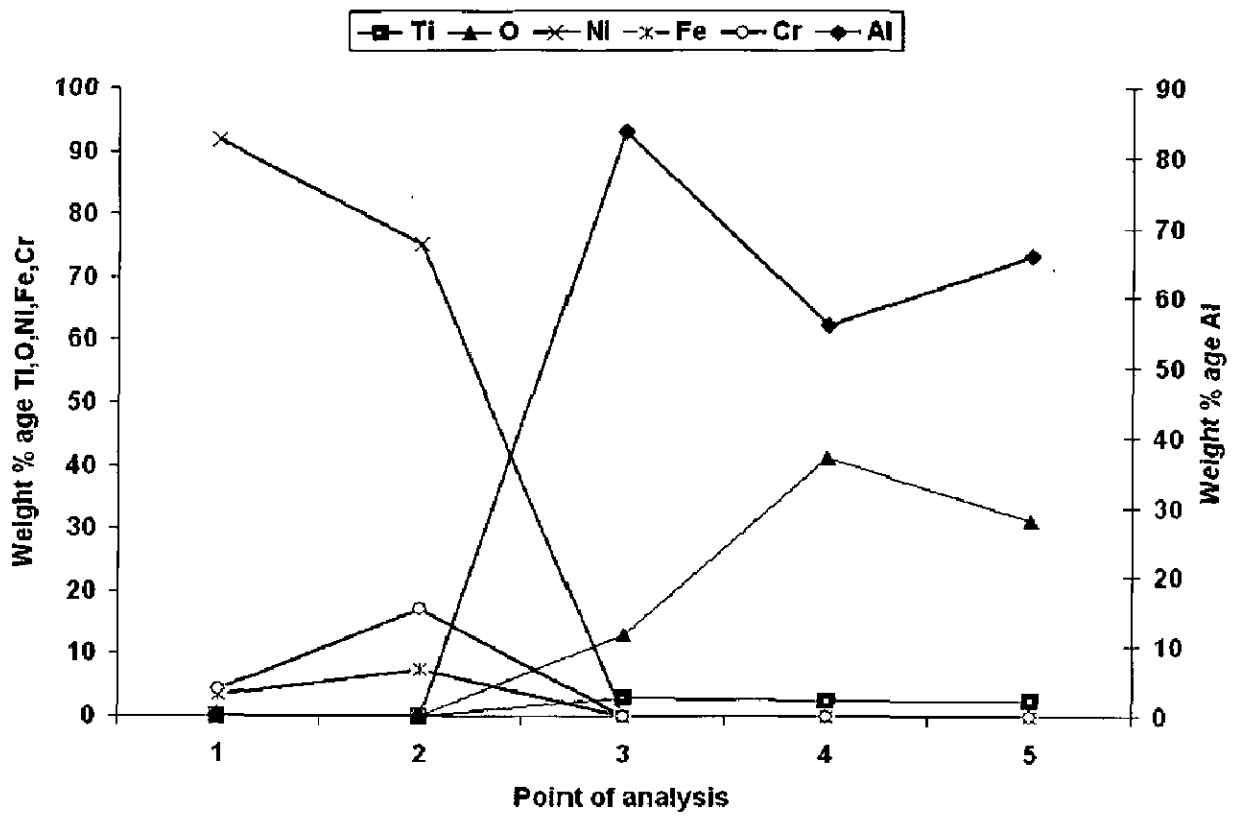


Fig. 4.20: Cross sectional morphology and elemental composition variation across the cross-section of Al₂O₃-3 wt% TiO₂ coated superalloy Superni 600.

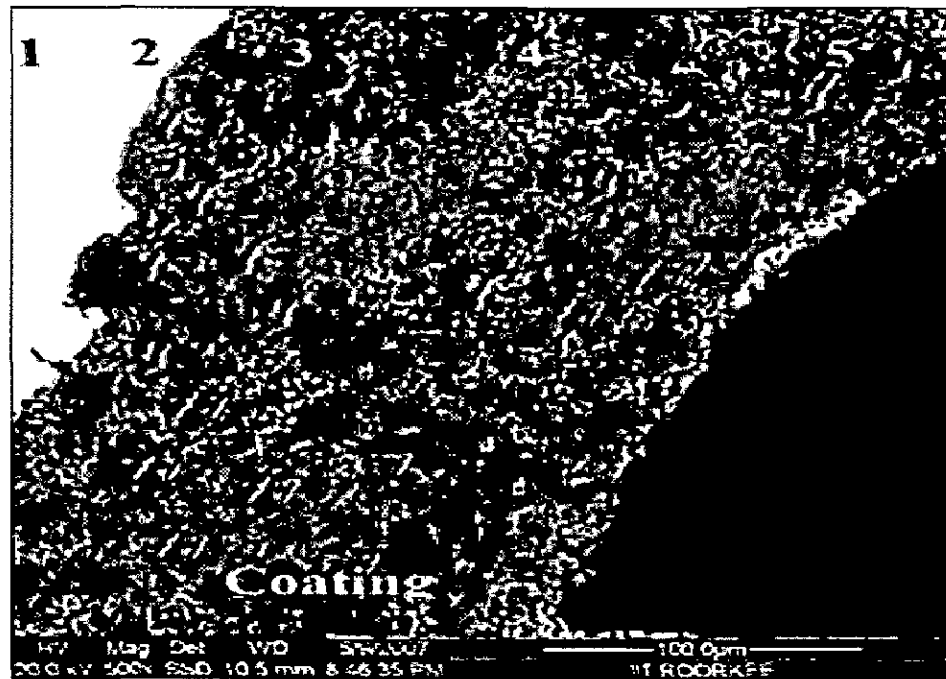
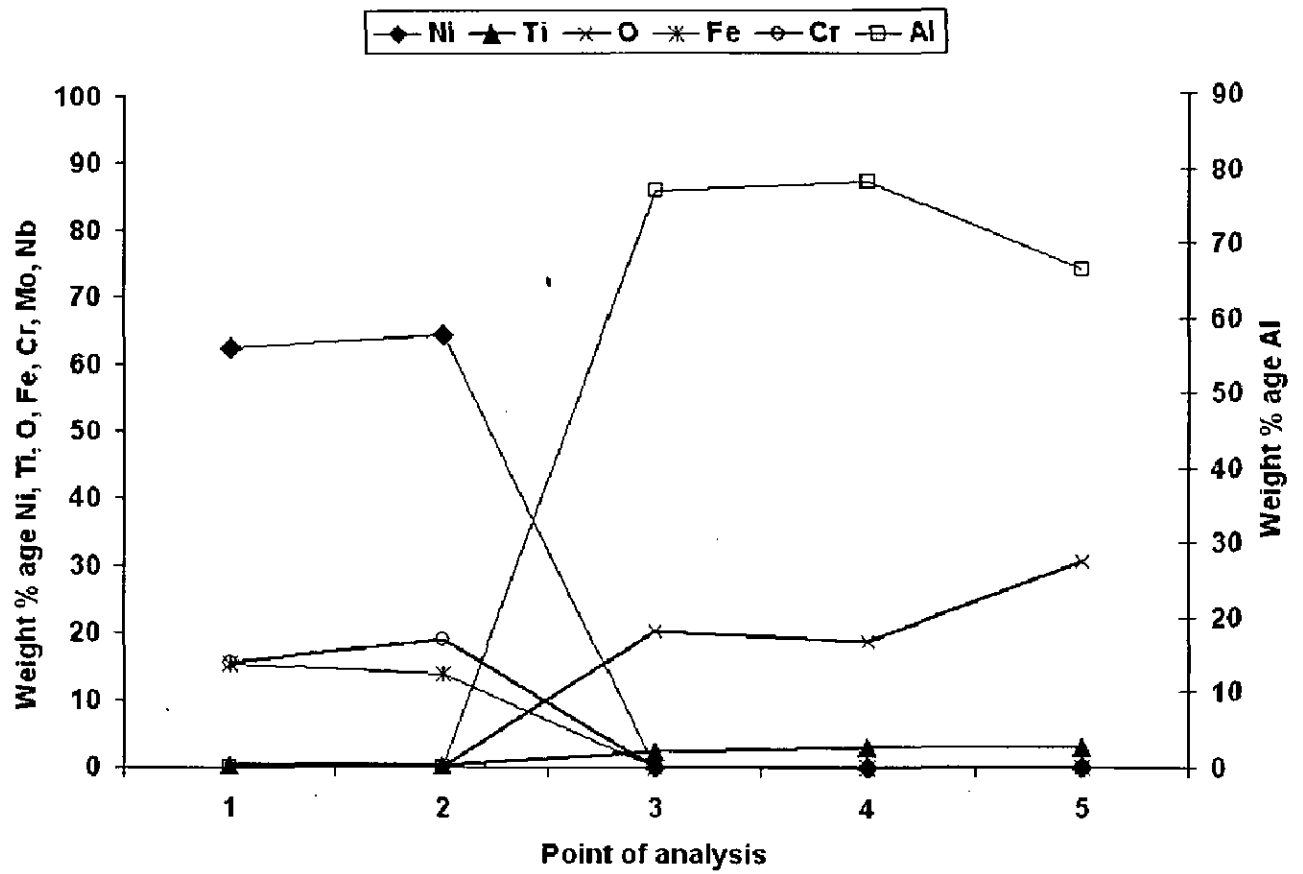


Fig. 4.21: Cross sectional morphology and elemental composition variation across the cross-section of Al_2O_3 -3 wt% TiO_2 coated superalloy Superni 718.

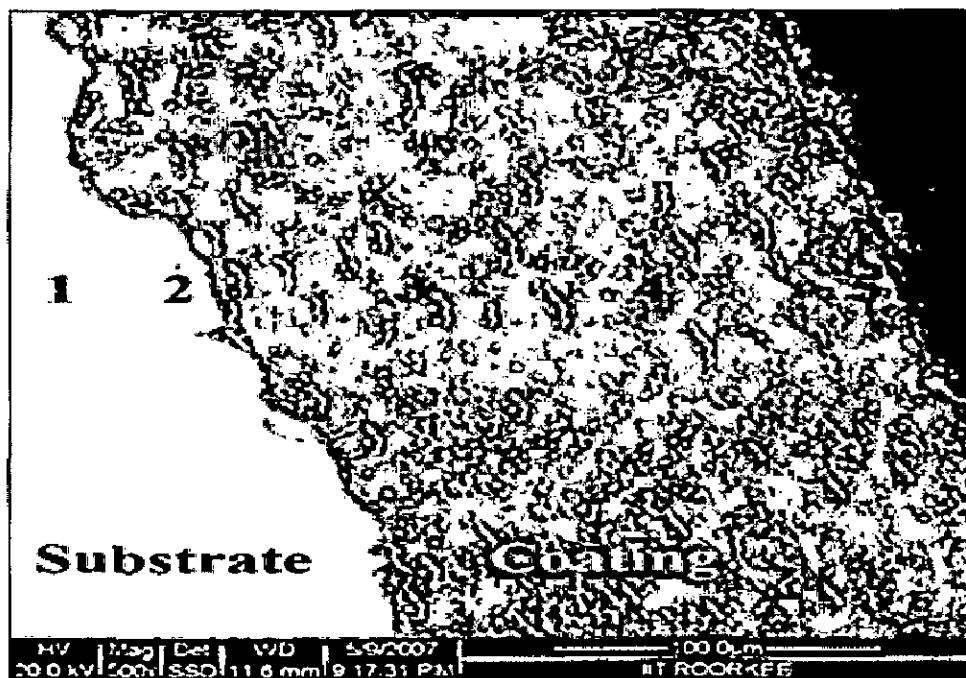
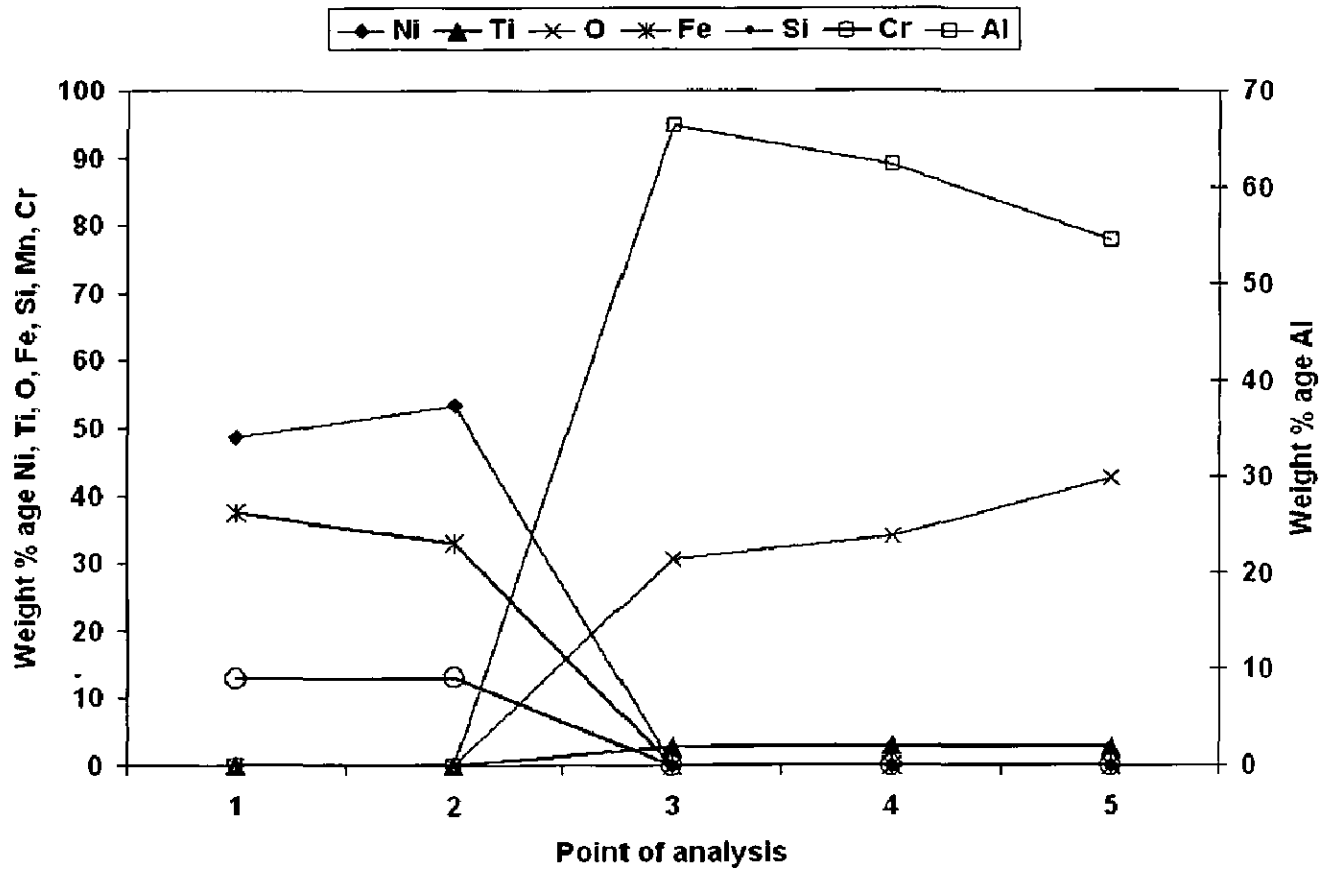


Fig.4.22: Cross sectional morphology and elemental composition variation across the cross-section of Al_2O_3 -3 wt% TiO_2 coated superalloy Superfer 800.

layers are TiO_2 and the grey ones correspond to Al_2O_3 . Fig. shows the section view and surface appearance of D-gun sprayed alumina coating in the ground condition. Coating was dense with low porosity (<1%) and free of interface cracks.

BSE images were obtained at the cross-section of the coated alloys and EDX analysis was performed at some selected areas of interest to ascertain elemental composition (weight %) at different points across the coatings. In the Figs showing cross sectional morphology and the corresponding elemental composition variation across the cross-section of Al_2O_3 -3 wt% TiO_2 coated alloys, it is clear that the coating portion contains Alumina and Titania along with oxygen while analysis at the points on the substrate has shown the presence of constituent elements of the substrate alloys.

4.3.8.3 X-Ray Mapping

The X-ray mappings for the D-gun sprayed Al_2O_3 -3Wt% TiO_2 coatings are shown in Fig. 4.23 to 4.27, which indicate the presence of basic elements of the feedstock powder. The elemental mappings for all the coated alloys show that the basic elements of the alloy powder viz. Alumina and Titania are present in the coated region. The elemental mapping for the coating shows that the main phase in coatings is alumina. Titania is present at the splat boundaries as thin discontinuous streaks. Cross-sectional BSE image of the as-sprayed Al_2O_3 -3Wt% TiO_2 coating shows a typical lamellar structure consisting of mainly Al-rich splats with titanium mainly present at the splat boundaries.

4.4 DISCUSSION

The Microstructural studies of Boiler steels ASTM SA 213 T11 and T22 have revealed the presence of ferrite and pearlite which is as per the grade of this steel (ASM Handbook 2001) and that the matrix for all the superalloys under study is a solid solution. The microstructures of these superalloys are compared with the standard microstructures from Metals Handbook (1975) and ASM Handbook (2001). The formation of carbides in case of superalloy has been revealed invariably, which could again be characterised with reference to the data available in the said handbooks. Basically strength of the Ni-base superalloys depends on the mechanism of solid solution hardening and precipitation hardening, singly and in combination. The main carbides which have the possibility of their formation by precipitation in the Ni- and Co- based superalloys under study are MC, M_7C_3 and M_{23}C_6 , keeping in view the role of various alloying elements towards formation of particular carbide.

Heath et al., 1997 has suggested that the thick coatings have better corrosion resistance. But thicknesses more than certain limit leads to self disintegration of coatings. Higher thickness may lead to cracks due to accumulation of residual stresses in the splat layers during spraying and solidification. It was aimed to produce coatings with thickness of 200 to 250 microns. In the present study it was possible to obtain a thickness in the range of 200-230 μm . After spraying the coating thickness was measured along the cross-section for some randomly selected samples as has been reported in Table 4.1. The porosity of the coatings influence the behavior of the coatings as pores form an interconnected network through which the corrosive species could reach the coating substrate interface which may ultimately result in reduced mechanical strength. The Porosity of the coatings has a great impact on the erosion corrosion behavior of the coatings.

The coatings produced by D-gun spraying has limited or no porosity. The porosity measurements for the D-gun sprayed coatings are also summarised in Table 4.1. The lower value of porosity may be attributed to the higher kinetic energy of the powder particles. The high velocity involved in the D-gun spraying process have shown elimination of much of the porosity as Air entrapped between the individual splats is markedly reduced in this technique, thus reducing the porosity. The values of porosity are in close agreement with the findings of Sobiecki et al., 2004, Saravanan et al., (2000). The lack of defects and porosity at the particle/particle and particle/substrate interface suggest an adequate particle kinetic energy during deposition that was able to generate above the alloy critical velocity and thus creating an intimate bonding at the interfaces.

A slight increase in the values of microhardness values for the substrate superalloys has been observed near the interface between the coating and the substrate in all the cases. The hardening of the substrates as observed may be attributed to the high speed impact of the coating particles during D-gun spray deposition. This increase in microhardness effect has also been reported by (Higuera et al., 1998; Hidalgo et al, 1997, 1999 and 2000; Sidhu 2003; Mishra 2006; and Sidhu 2006).

The detonation gun process hardens the coatings due to its higher velocity of particle impact. There is a variation in the microhardness with the distance from the coating substrate interface. The observed non-uniformity in the hardness values along the thickness of the coatings may be due to the microstructural changes along the cross section of the coatings. The observed microhardness values for the coatings have been compared with those reported by Wang et al., (2006), Ramachandran et al., (1998), , Saravanan et al., (2000) and are

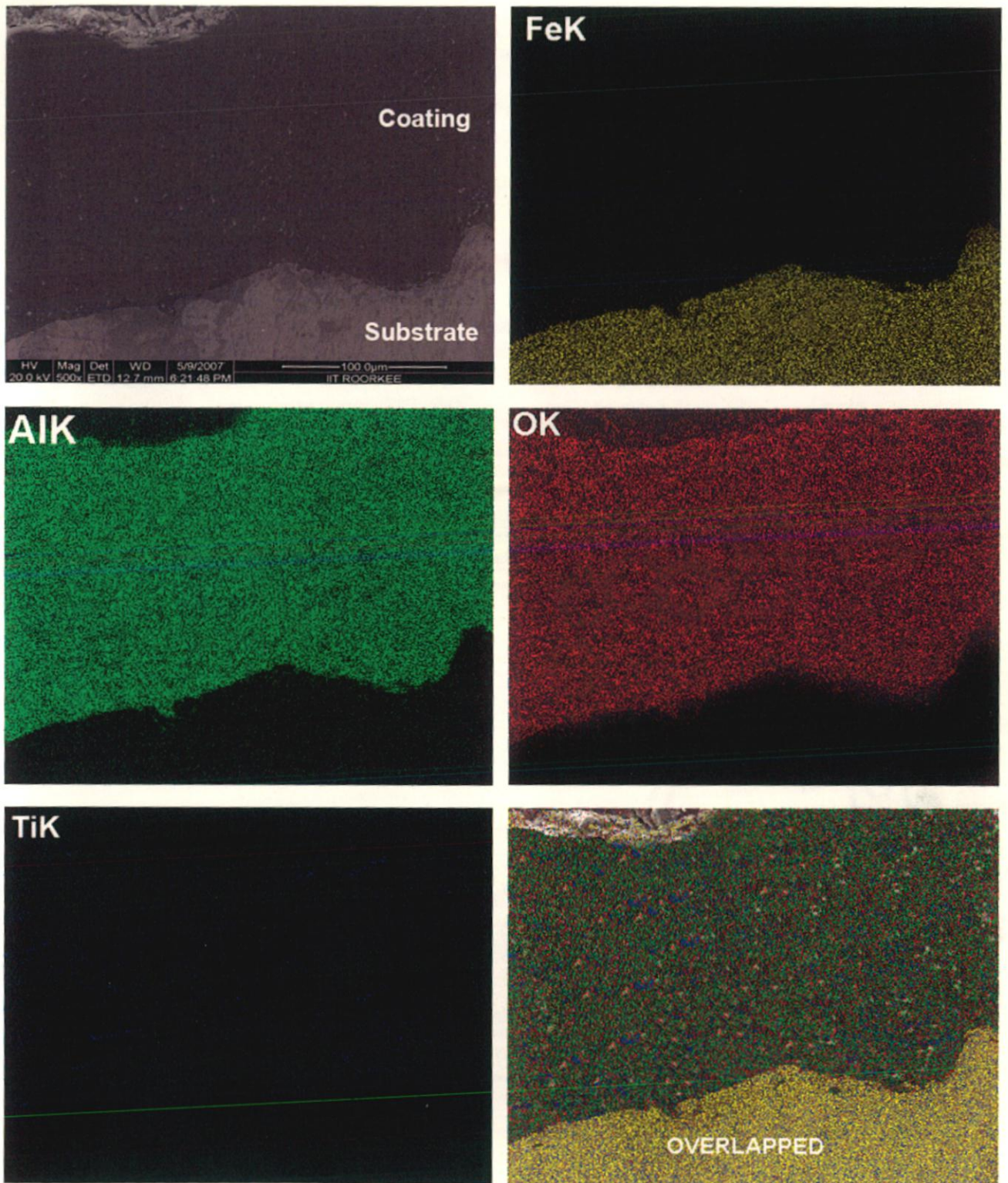


Fig.4.23: BSEI and elemental X-ray mappings of the cross-section of D-gun sprayed Al_2O_3 -3 Wt% TiO_2 coating on the boiler steel T11, 500X.

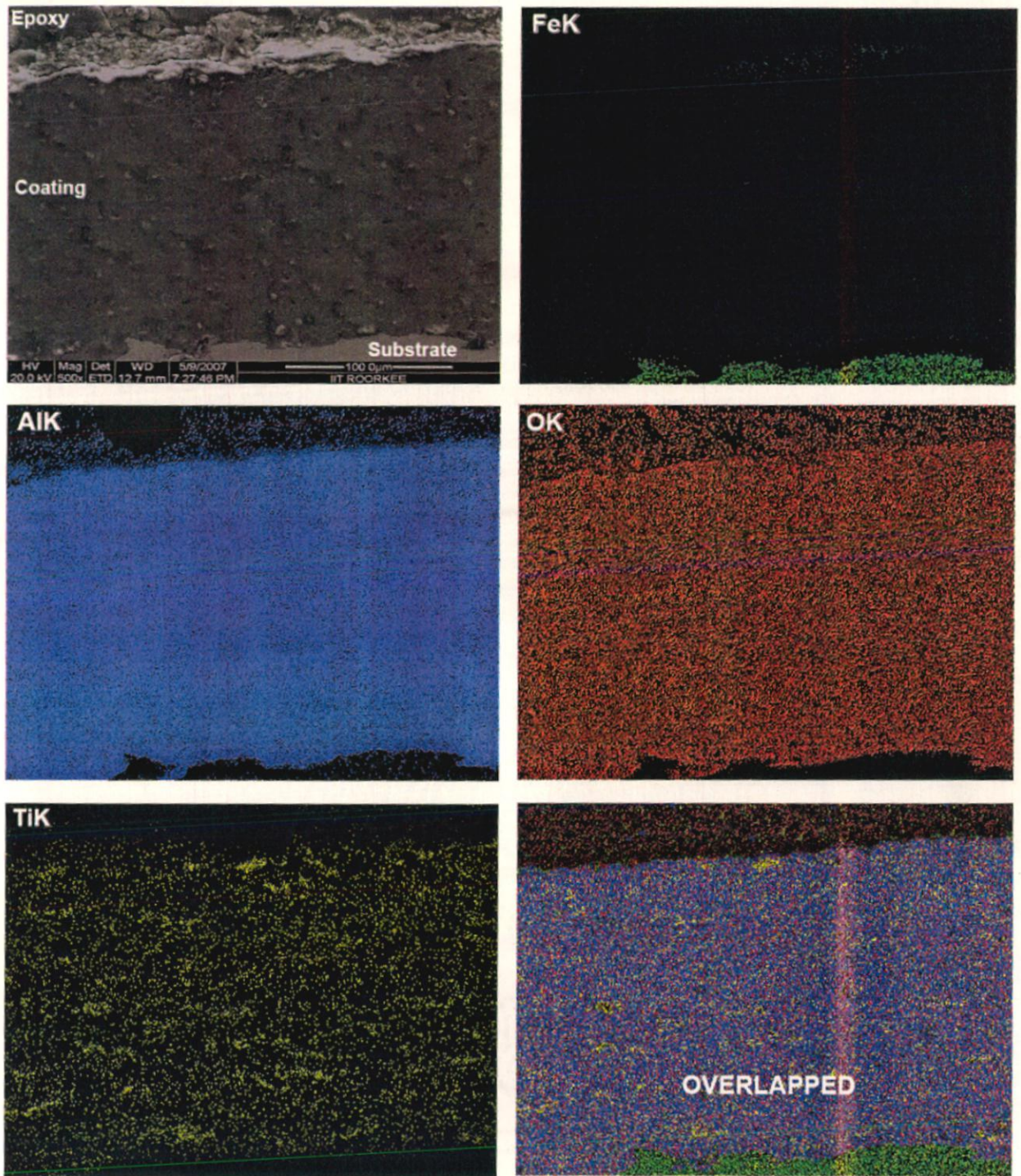


Fig.4.24: BSEI and elemental X-ray mappings of the cross-section of D-gun sprayed Al_2O_3 -3 Wt% TiO_2 coating on the boiler steel T22, 500X.

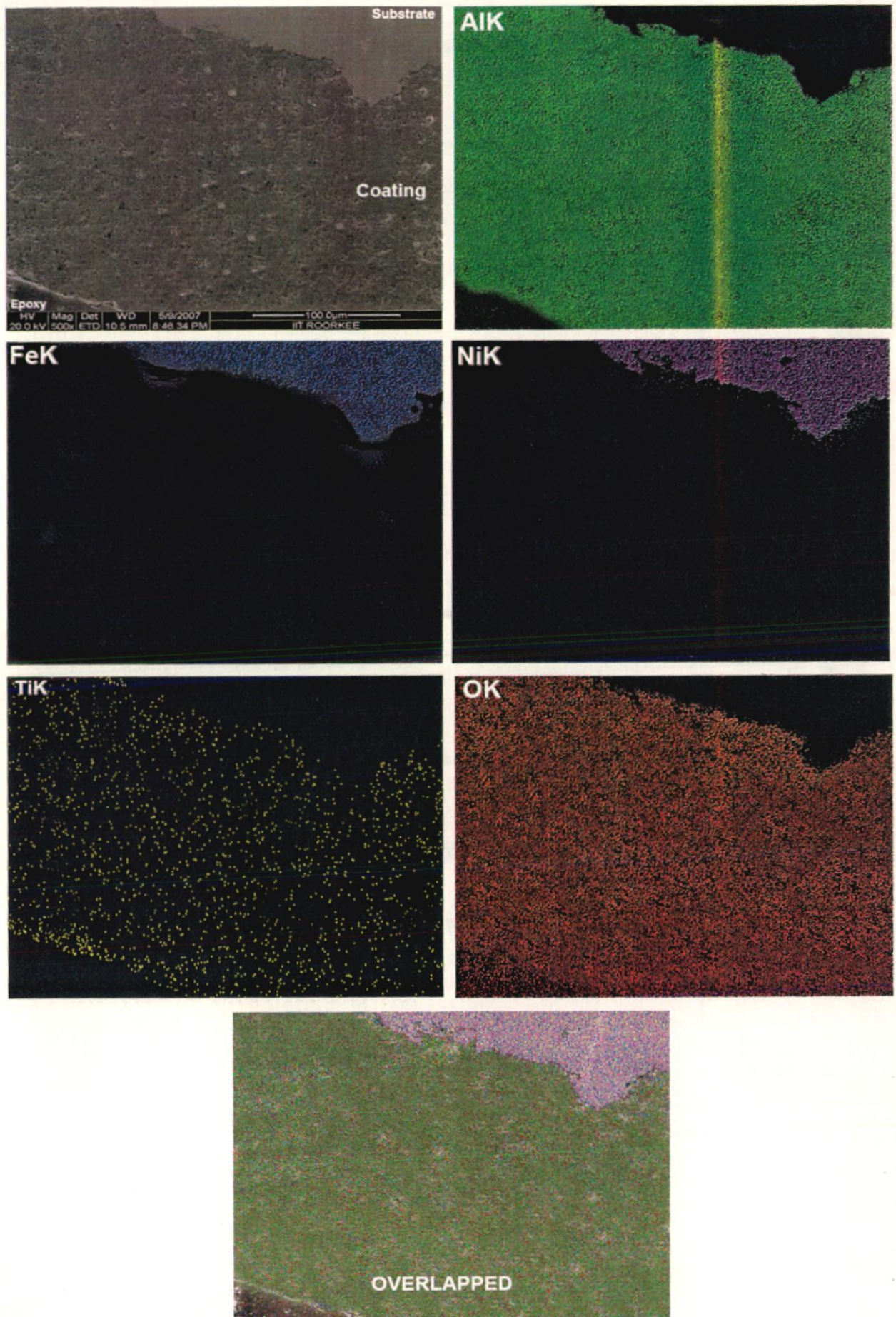


Fig.4.25: BSEI and elemental X-ray mappings of the cross-section of D-gun sprayed Al_2O_3 -3 Wt% TiO_2 coating on the superalloy Superni 600, 500X

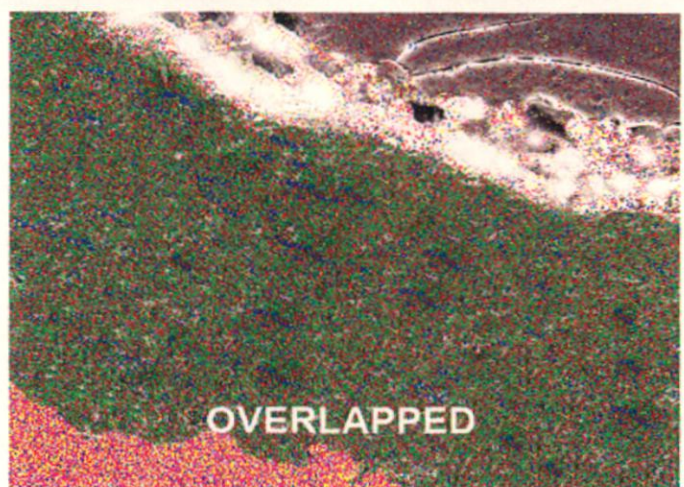
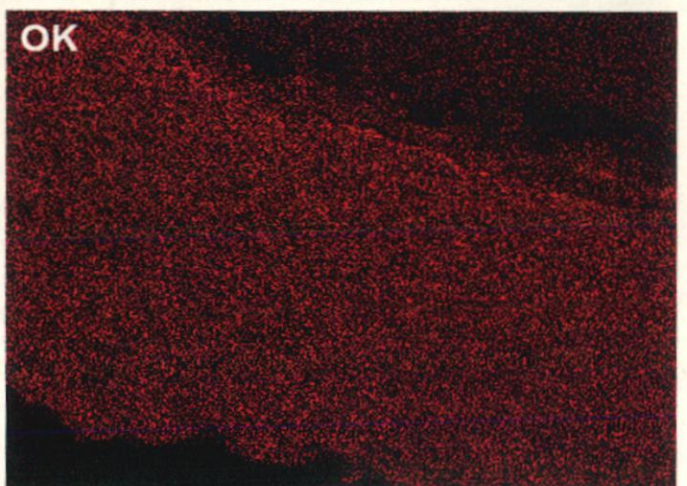
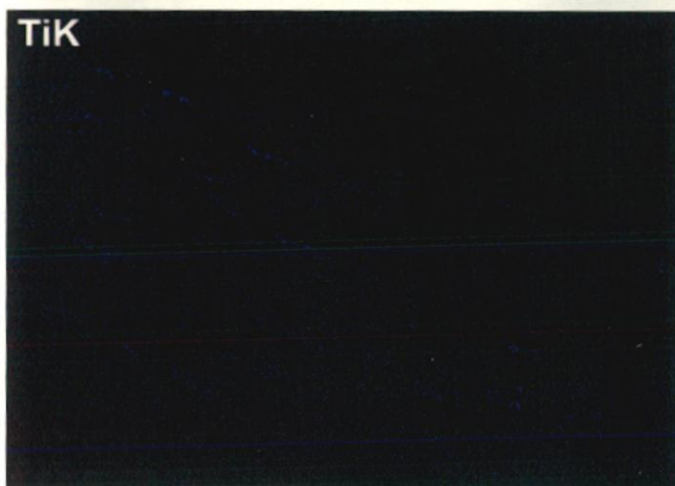
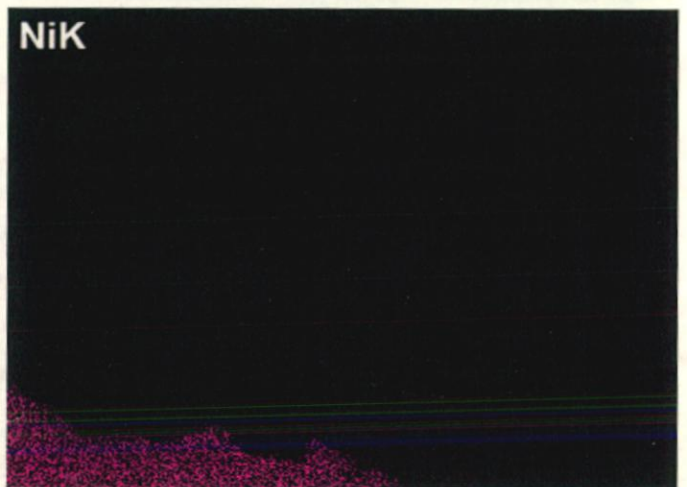
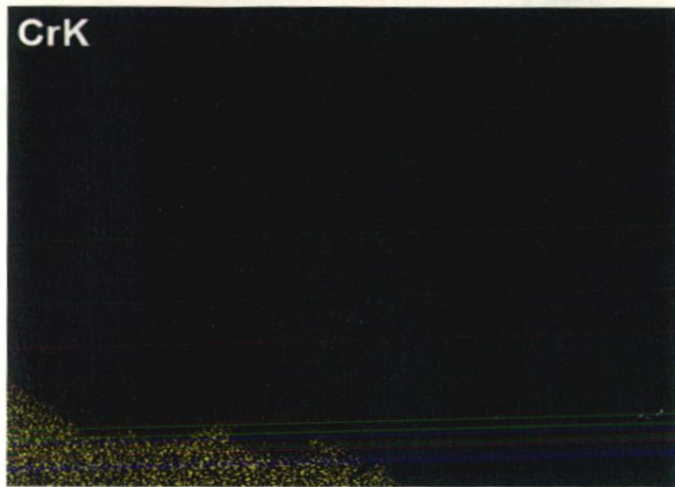
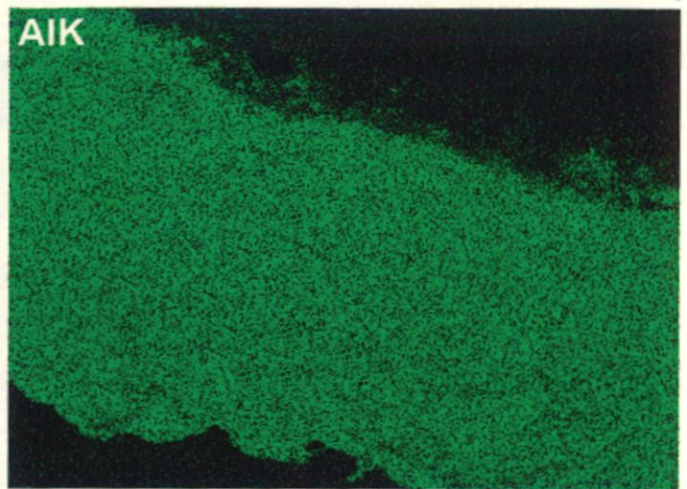
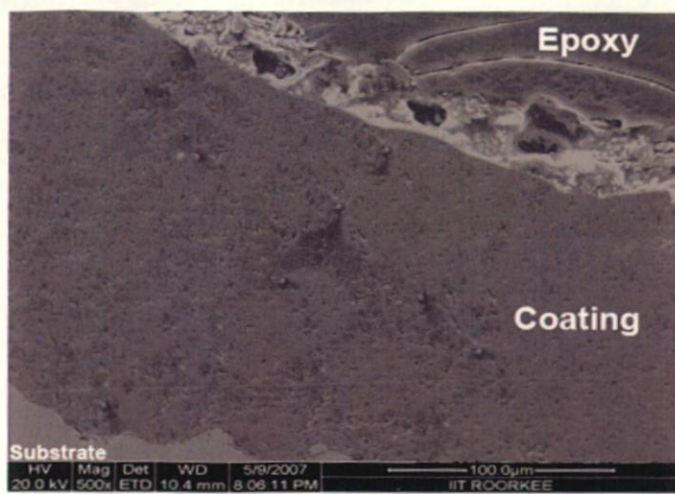


Fig.4.26: BSEI and elemental X-ray mappings of the cross-section of D-gun sprayed Al_2O_3 -3 Wt% TiO_2 coating on the superalloy Superni718, 500X

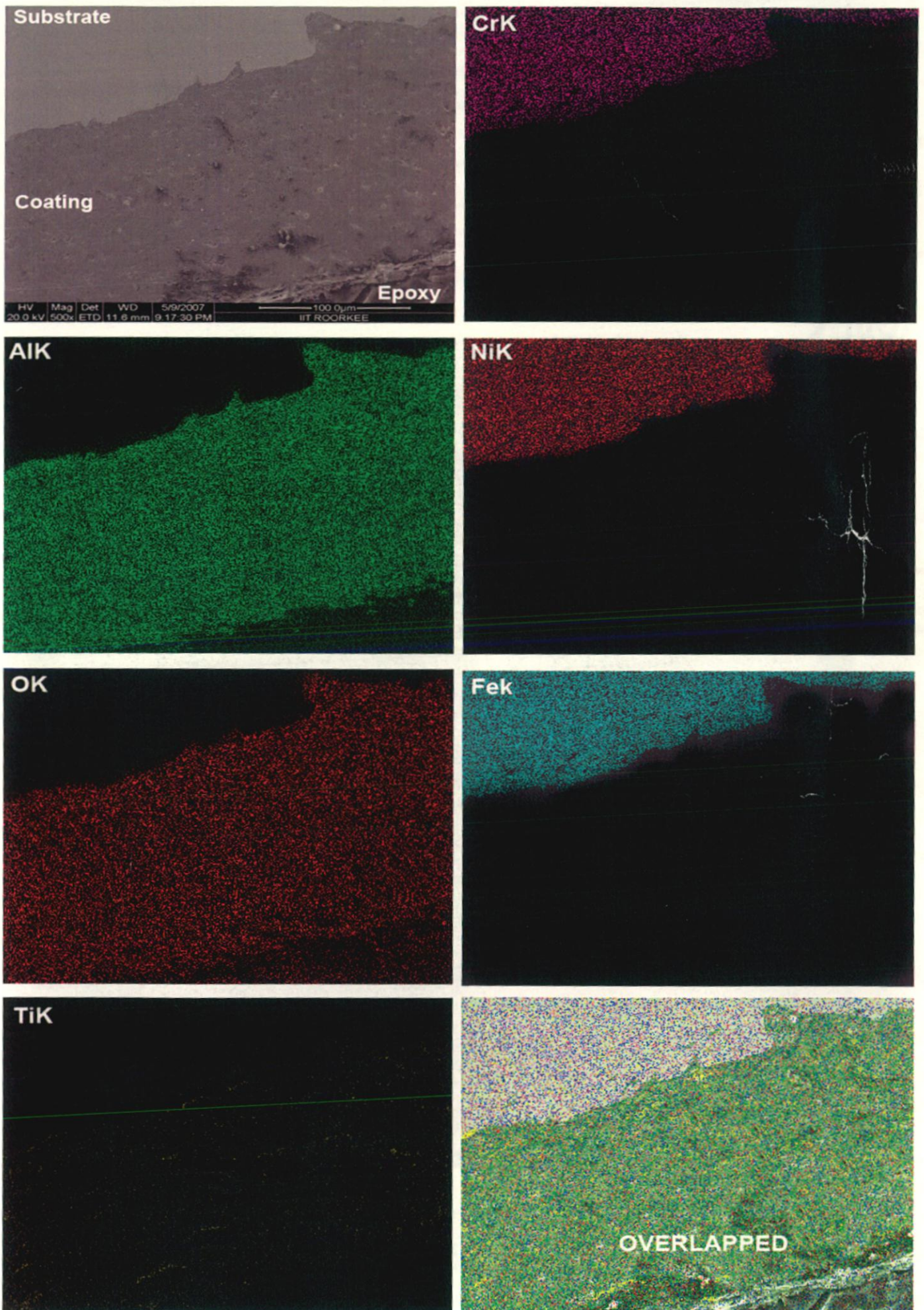


Fig.4.27: BSEI and elemental X-ray mappings of the cross-section of D-gun sprayed Al_2O_3 -3 Wt% TiO_2 coating on the superalloy Superfer 800, 500X

found to be in similar range. During the spraying, the solidification rate varies with subsequent layer deposition. The layer produced by the first impact has the highest solidification rate and the solidification rate decreases with the further deposition due to decrease in heat transfer rate from molten material to substrate (Normand et al., 2000 and Niemi et al., 1994)

The coatings obtained did not undergo any significant phase transformation except that of γ - Al_2O_3 phase formation. This is due to the fact that in detonation gun process the powder is allowed to react with high energy explosive gases inside a chamber of size about 22-25 mm internal diameter and about 1.5 m long tube closed at one end (Scott et al., 1991; Smith 1974B). The powder is usually carried by N_2 gas into the chamber and at regular intervals a spark plug detonates the gases such as O_2 and C_2H_2 . These highly combustible gases on detonation expand inside the reaction chamber drastically with very large amount of thermal and kinetic energy. This causes the powder inside to melt and expand with the explosive gases thus transferring its momentum to the molten plume. Hence, in the detonation gun process the powder interacts closely with explosive gases with an inert or reducing atmosphere made of N_2 , CO , C_2H_2 . Since most of the reaction is confined to inside the barrel the molten plume is nearly of the same composition as the start powder when it gets projected on to the substrate placed just outside the detonation gun barrel. As mentioned by researchers, (Normand et al., 2000; Lin et al., 2003) the coatings consist of γ - Al_2O_3 and little amount of α - Al_2O_3 . Actually, the powder used in the coating contains α - Al_2O_3 . During the spraying, α - Al_2O_3 transforms in to γ - Al_2O_3 due to fact that γ - Al_2O_3 has lower nucleation energy and therefore, metastable α - Al_2O_3 occurs through the melting and later rapid solidification. (Luo et al., 2003) Also upon impingement onto the cold substrate surface, the droplets lose their kinetic and thermal energies and thus experience ultrarapid solidification (Yin et al., 2008)

Under the given spray condition, D-gun sprayed coatings deposited on superalloys have a uniform microstructure. It is seen that the microstructures of D-gun coatings are much finer, i.e. the splats are much thinner. A fine structure is expected with this process since the molten particle velocities are very high in the process. Coating possessed homogeneous structure, with distinct layered structure, i.e. aluminum-rich regions (gray)

separated from titanium regions (white). The Al_2O_3 -3 wt.% TiO_2 coating exhibited a typical lamellar structure. The microstructure across the cross-section of the coatings is in good agreement with the literature. (Bluni and Mardar, 1996; Erickson et al., 1998; Westergard et al., 1998; Margadant et al., 2001 and Sidhu et al., 2004 and 2005). The EDX compositional analysis across the coating cross-section (Fig. 4.18-4.22) shows the homogeneous elemental concentration.

EROSION STUDIES IN AN AIR JET EROSION TEST RIG

Erosion studies were carried out on uncoated and coated samples at room temperature and elevated temperature. Erosion behaviour of the bare samples (superalloys and Boiler steels) as well as detonation gun sprayed coatings on the substrates, investigated in the present study has been described in this chapter. The erosion studies were carried out using a high temperature air-jet erosion test rig at a velocity of 35 ms^{-1} and impingement angles of 30° and 90° . The tests were carried out at ambient and high temperatures.

The two temperatures were taken for each test, sample temperature 400°C & air temperature 900°C and sample temperature 600°C & air temperature 900°C simulated to service conditions of boiler tubes in which sample temperature and flow gas temperature correspond to the inner and outer temperature of water wall pipes. The alumina particles of average size $50 \mu\text{m}$ were used as erodent. The specimens were visually examined at the end of each cycle during the course of study.

Erosion rates in terms of volumetric loss (mm^3/g) for different uncoated and coated alloys are compared. The eroded samples were analysed with SEM/EDX and optical profilometer. The erosion rate data for each coated alloy has been plotted along with uncoated alloy in order to assess the coating performance. Efforts have been made to understand the mode of erosion.

5.1 RESULTS

5.1.1 Uncoated alloys

5.1.1.1 Visual Examination

The Surface macrographs showing the erosion scar produced on the top surface of the uncoated boiler steels namely T11, T22 and superalloys namely Superni 600, Superni 718, and Superfer 800 superalloys eroded at 30° and 90° impact angles at room temperature and at elevated temperature are shown in Figs 5.1.-5.3

After Condition 1 Tests

When samples were tested at condition 1 i.e. at room temperature, the visual inspection of each sample showed roughing of the upper surface and the formation of scars on the surface exposed to the erosion. The samples after testing at room temperature are shown in Fig. 5.1.

After Condition 2 Tests

When the substrate temperature was increased to 400°C and the surrounding temperature to 900°C, the effects of corrosion along with the erosion were also evident. At this temperature, the alloys showed a thin scale. The erosion seems to clean the scale off the surface in the eroded/corroded region especially in boiler steels. In boiler steels, the impact of erodent removes the scale down to the substrate-scale interface as shown in Fig. 5.2. Away from this eroded region a thin layer of scale was observed on the surface and the eroded/corroded region showed rust colored discoloration. The superalloys were generally free of scale or were having very thin scale. The Superni 600 and Superni 718 showed just a thin discoloration of the metallic surface.

After Condition 3 Tests

Generally a scale is formed on the sample surface as the temperature is raised. The character of this scale depends on the test material, test temperature, and whether the scale was being struck by the alumina erodent particles. In both boiler steels there was formation of thick scale as compared to scale formed on superalloys and the scale sloughed off even from the surrounding area as can be seen in Fig. 5.3.

5.1.1.2 Erosion Rate

The erosion loss has been calculated by volume change method. The volume loss occurred after erosion testing was measured by using non contact optical profilometry as explained in chapter 3. The erosion depth was measured at six random locations to obtain the average erosion depth of an eroded scar. At each location (including eroded and uneroded area) surface profiles were taken.

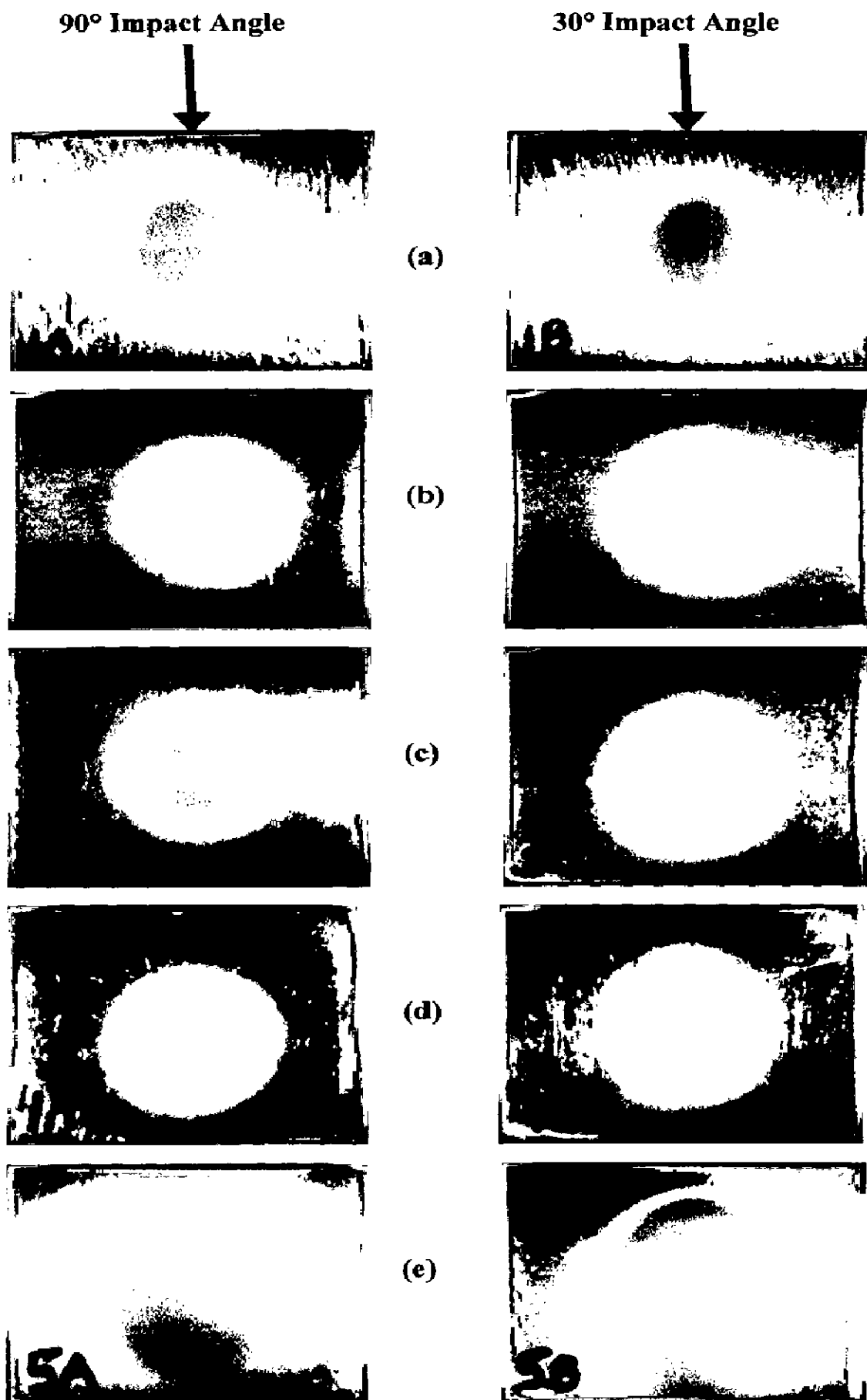


Fig. 5.1

Macrographs of Uncoated alloys eroded at condition 1 and impact angles of 90° and 30°

(a) Boiler Steel T11 (b) Boiler Steel T22 (c) Superni 600 (d) Superni 718
 (e) Superfer 800

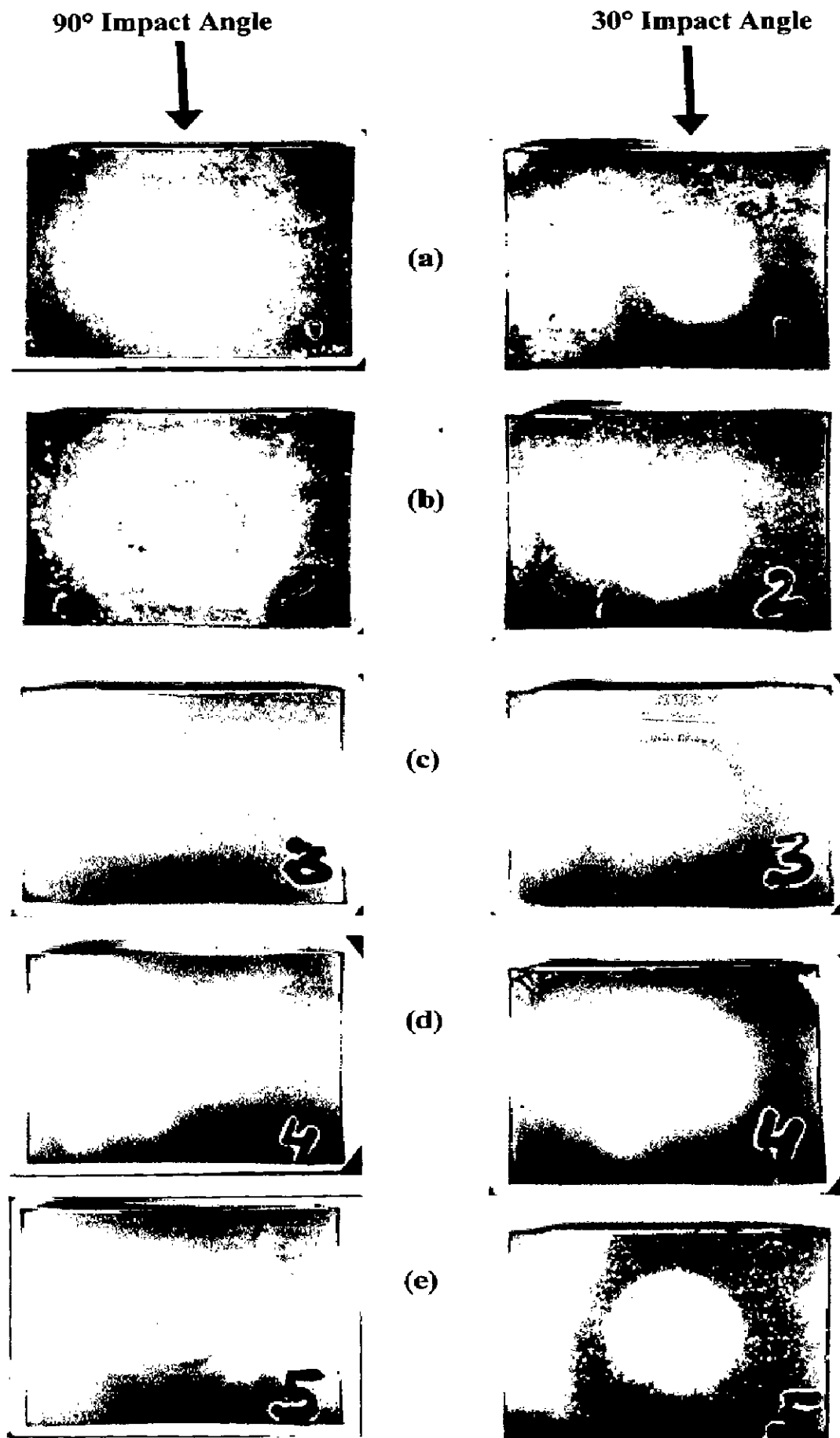


Fig. 5.2: Macrographs of Uncoated alloys eroded at condition 2 and impact angles of 90° and 30°
 (a) Boiler Steel T11 (b) Boiler Steel T22 (c) Superni 600 (d) Superni 718
 (e) Superfer 800

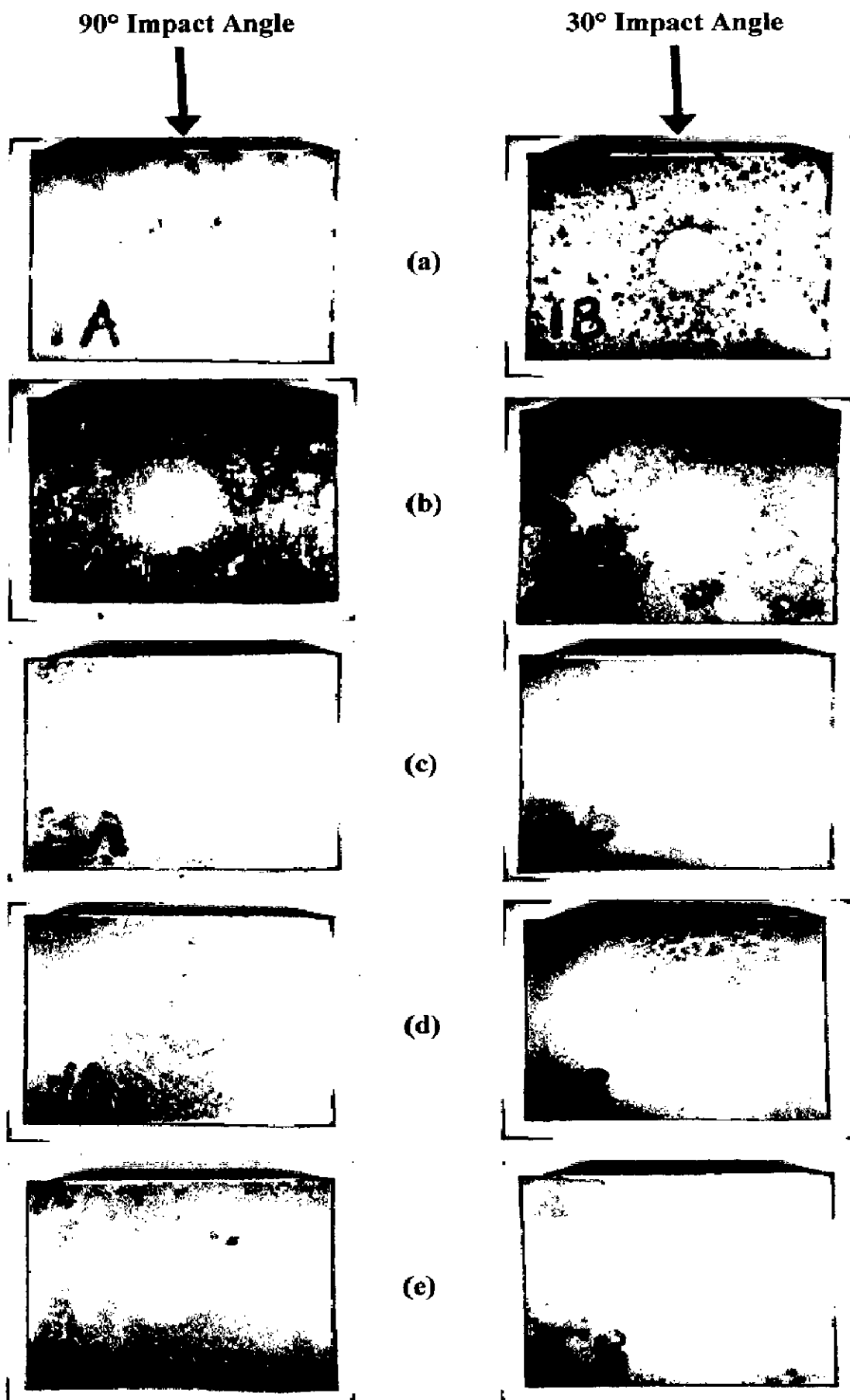


Fig. 5.3: Macrographs of Uncoated alloys eroded at condition 3 and impact angles of 90° and 30°
 (a) Boiler Steel T11 (b) Boiler Steel T22 (c) Superni 600 (d) Superni 718
 (e) Superfer 800

Representative three dimensional optical profiles of the uncoated specimens eroded at room temperature as well as high temperature at both impact angles are shown in Figs 5.4 to 5.6.

The erosion rate of the uncoated boiler steels namely T11, T22 and superalloys namely Superni 600, Superni 718, and Superfer 800 superalloys at an impact velocity of 35 ms^{-1} and impingement angle of 30° and 90° at room temperature (condition 1) is shown in Fig. 5.7. From the graph, it can be inferred that the erosion rate of Boiler steels is comparatively higher than the superalloys at both the impact angles. Volume erosion rate of Superfer 800 superalloy is marginally higher than that for the other superalloys, whereas erosion rate of Superni 600 and 718 are lowest amongst all the superalloys tested at both the impact angles. The volume erosion rate for Boiler steels T11 and T22 is $3.419 \times 10^{-3} \text{ mm}^3/\text{gm}$ & $3.586 \times 10^{-3} \text{ mm}^3/\text{gm}$ and for superalloys Superni 600, Superni 718 and Superfer 800 is $1.086 \times 10^{-3} \text{ mm}^3/\text{gm}$, $0.975 \times 10^{-3} \text{ mm}^3/\text{gm}$ and $1.352 \times 10^{-3} \text{ mm}^3/\text{gm}$ respectively at 90° impact angle. While at 30° impact, the volume erosion rate for Boiler steels T11 and T22 is $7.052 \times 10^{-3} \text{ mm}^3/\text{gm}$ & $6.452 \times 10^{-3} \text{ mm}^3/\text{gm}$ and for superalloys Superni 600, Superni 718 and Superfer 800 is $1.211 \times 10^{-3} \text{ mm}^3/\text{gm}$, $1.281 \times 10^{-3} \text{ mm}^3/\text{gm}$ and $1.947 \times 10^{-3} \text{ mm}^3/\text{gm}$ respectively.

At condition 2 i.e. when substrate temperature was 400°C and surrounding air at 900°C , there is substantial increase in volume erosion rate of all the alloys under testing as shown in Fig. 5.8. The volume erosion rate for Boiler steels T11 and T22 is $3.831 \times 10^{-3} \text{ mm}^3/\text{gm}$ & $3.975 \times 10^{-3} \text{ mm}^3/\text{gm}$ and for superalloys Superni 600, Superni 718 and Superfer 800 is $1.225 \times 10^{-3} \text{ mm}^3/\text{gm}$, $1.494 \times 10^{-3} \text{ mm}^3/\text{gm}$ and $1.608 \times 10^{-3} \text{ mm}^3/\text{gm}$ respectively at 90° impact angle. While at 30° impact, the volume erosion rate for Boiler steels T11 and T22 is $9.947 \times 10^{-3} \text{ mm}^3/\text{gm}$ & $9.127 \times 10^{-3} \text{ mm}^3/\text{gm}$ and for superalloys Superni 600, Superni 718 and Superfer 800 is $1.727 \times 10^{-3} \text{ mm}^3/\text{gm}$, $1.711 \times 10^{-3} \text{ mm}^3/\text{gm}$ and $1.977 \times 10^{-3} \text{ mm}^3/\text{gm}$ respectively.

On further increasing the substrate temperature to 600°C and surrounding temperature of 900°C , volume erosion rate is also increased as shown in Fig. 5.9. From the Fig. it is

apparent that the volume erosion rate is pretty much higher for the boiler steels. The volume erosion rate for Boiler steels T11 and T22 is $5.708 \times 10^{-3} \text{ mm}^3/\text{gm}$ & $6.025 \times 10^{-3} \text{ mm}^3/\text{gm}$ and for superalloys Superni 600, Superni 718 and Superfer 800 is $1.381 \times 10^{-3} \text{ mm}^3/\text{gm}$, $1.633 \times 10^{-3} \text{ mm}^3/\text{gm}$ and $1.663 \times 10^{-3} \text{ mm}^3/\text{gm}$ respectively at 90° impact angle. While at 30° impact, the volume erosion rate for Boiler steels T11 and T22 is $12.425 \times 10^{-3} \text{ mm}^3/\text{gm}$ & $13.486 \times 10^{-3} \text{ mm}^3/\text{gm}$ and for superalloys Superni 600, Superni 718 and Superfer 800 is $2.483 \times 10^{-3} \text{ mm}^3/\text{gm}$, $2.466 \times 10^{-3} \text{ mm}^3/\text{gm}$ and $2.622 \times 10^{-3} \text{ mm}^3/\text{gm}$ respectively.

In case of superalloys, the low volume erosion rate may be attributed to the formation of martensitic phases and chromium carbide precipitates. Similar behavior of superalloys especially with Cr more than 12% has been observed by Fernandes et al. 2008. Addition of Cr reduces the oxidation rate of materials by facilitating the formation of Cr_2O_3 (Stack et al. 1993).

Fig. 5.10 Fig. 5.11 shows the variation in volume erosion rates of substrate alloys at 30° and 90° impact angles with change in test temperature. A tendency for increase in erosion rate with temperature has been observed in all alloys. So the temperature effect can be demonstrated on the basis of the observation that the erosion rate at acute impingement angle increases significantly with temperature, suggesting that alloys tends to show behaviour more typical of a ductile material at elevated temperatures.

5.1.1.3 SEM/EDX Analysis

From SEM/EDX analysis of alloys is shown in Fig. 5.12 and 5.13 at condition 1 i.e. after erosion testing at room temperature. Scanning electron micrographs were used to examine the surface features of the eroded samples. The SEM observations were made on the eroded surface of all the alloys at both the impact angles i.e. at 30° and 90° at condition 1. Scanning electron microscopy (SEM) revealed various erosion mechanisms like metal removal, oxide chipping, fracture and spalling within the oxide layer and at the scale/metal interface etc both at room temperature and at elevated temperature. The micrographs have

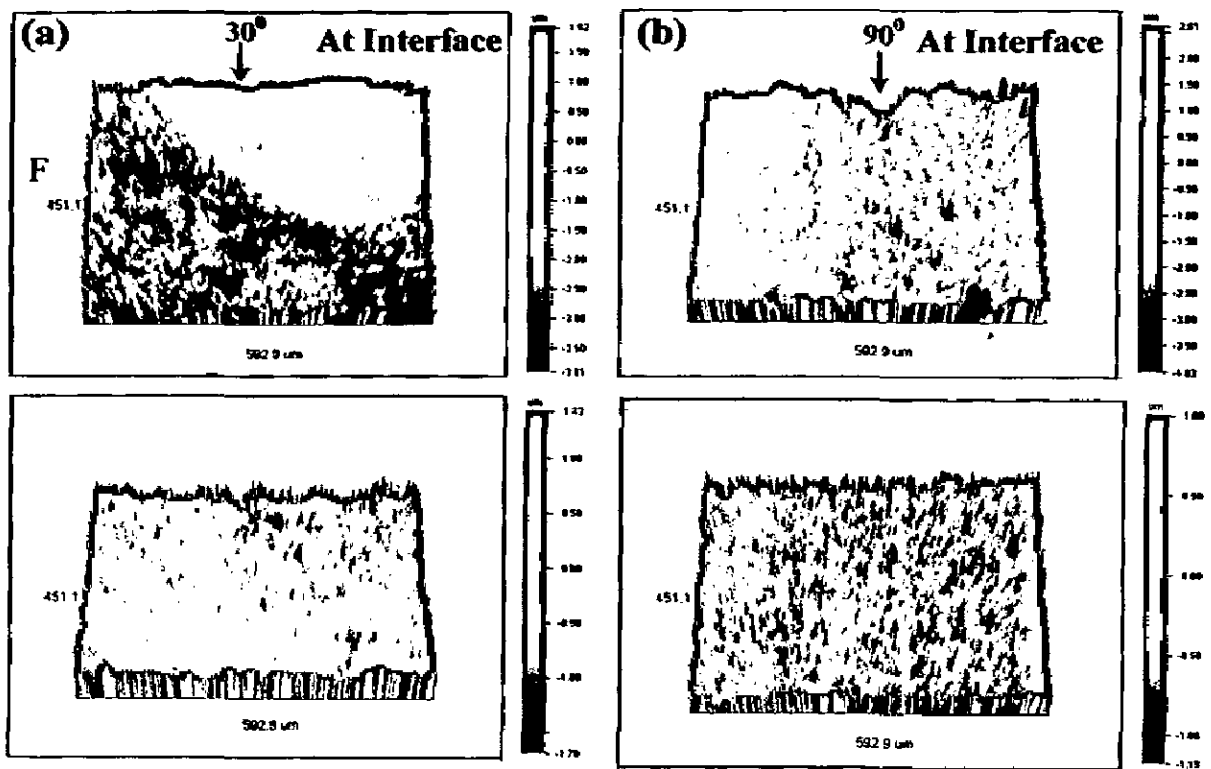


Fig. 5.4: 3D Optical Profile of the Specimen eroded at condition 1 showing depth profiles at interface and at eroded zone
 (a) Eroded at 30° impact angle (b) Eroded at 90° impact angle

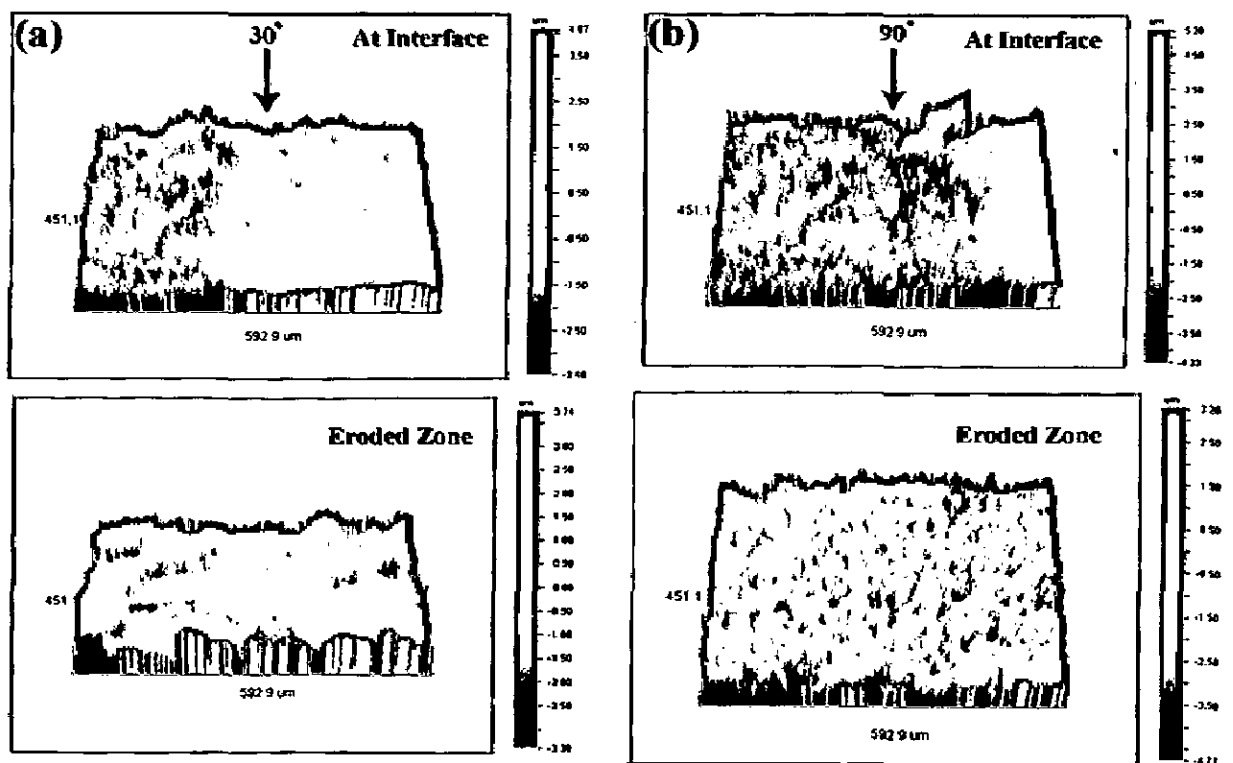


Fig. 5.5: 3D Optical Profile of the Specimen eroded at condition 2 showing depth profiles at interface and at eroded zone.
 (a) Eroded at 30° impact angle (b) Eroded at 90° impact angle

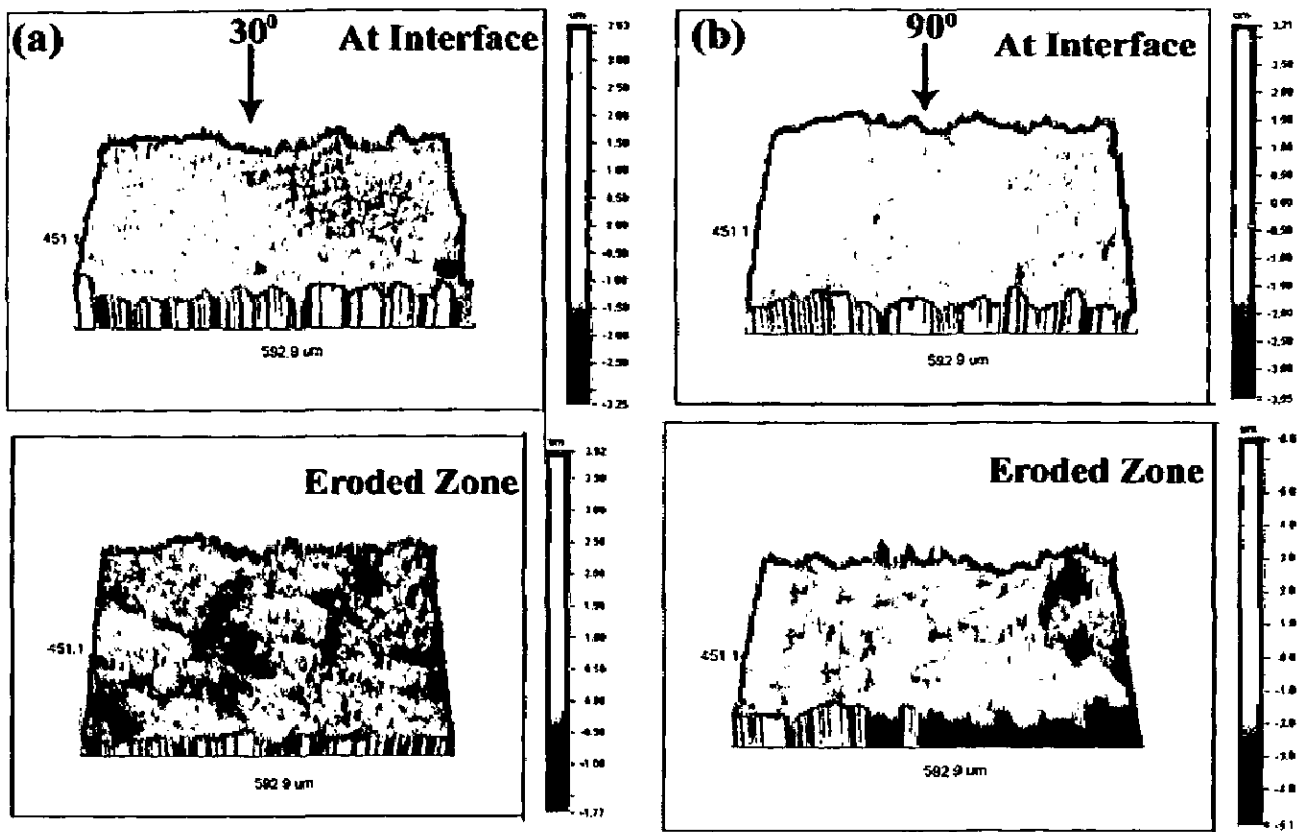


Fig. 5.6: 3D Optical Profile of the Specimen eroded at condition 3 showing depth profiles at interface and at eroded zone.
 (a) Eroded at 30° impact angle (b) Eroded at 90° impact angle

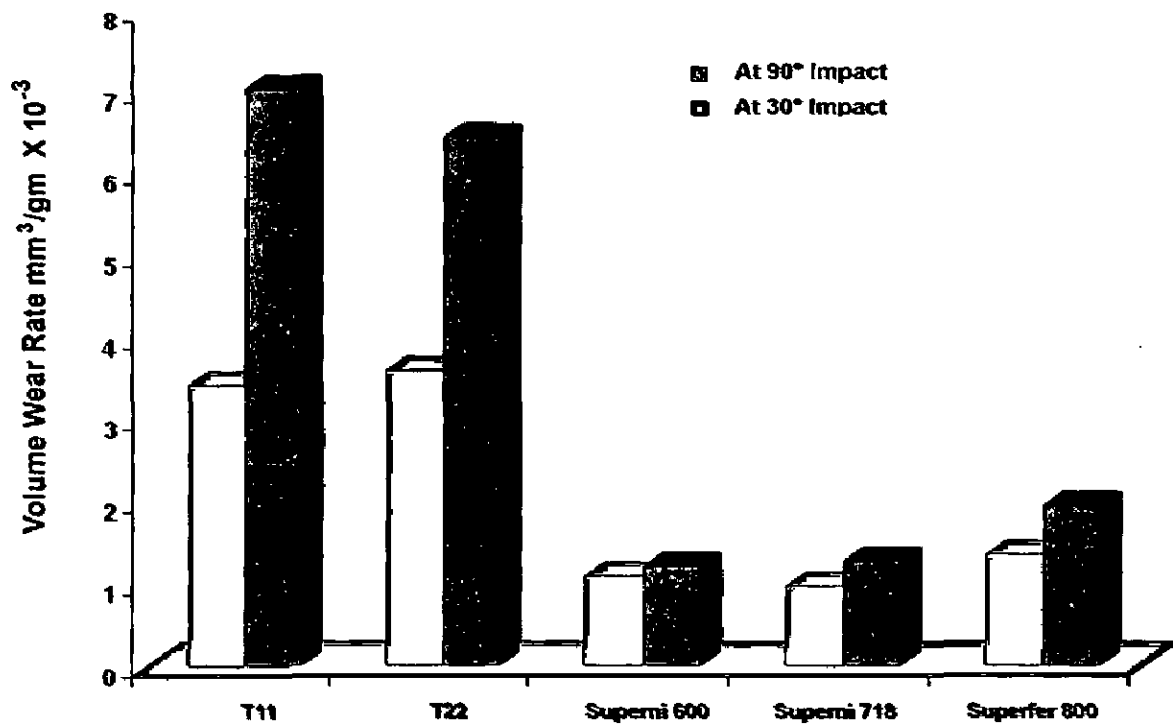


Fig. 5.7: Bar diagram showing the Volume erosion rates of substrate alloys under oblique and normal impact at condition 1.

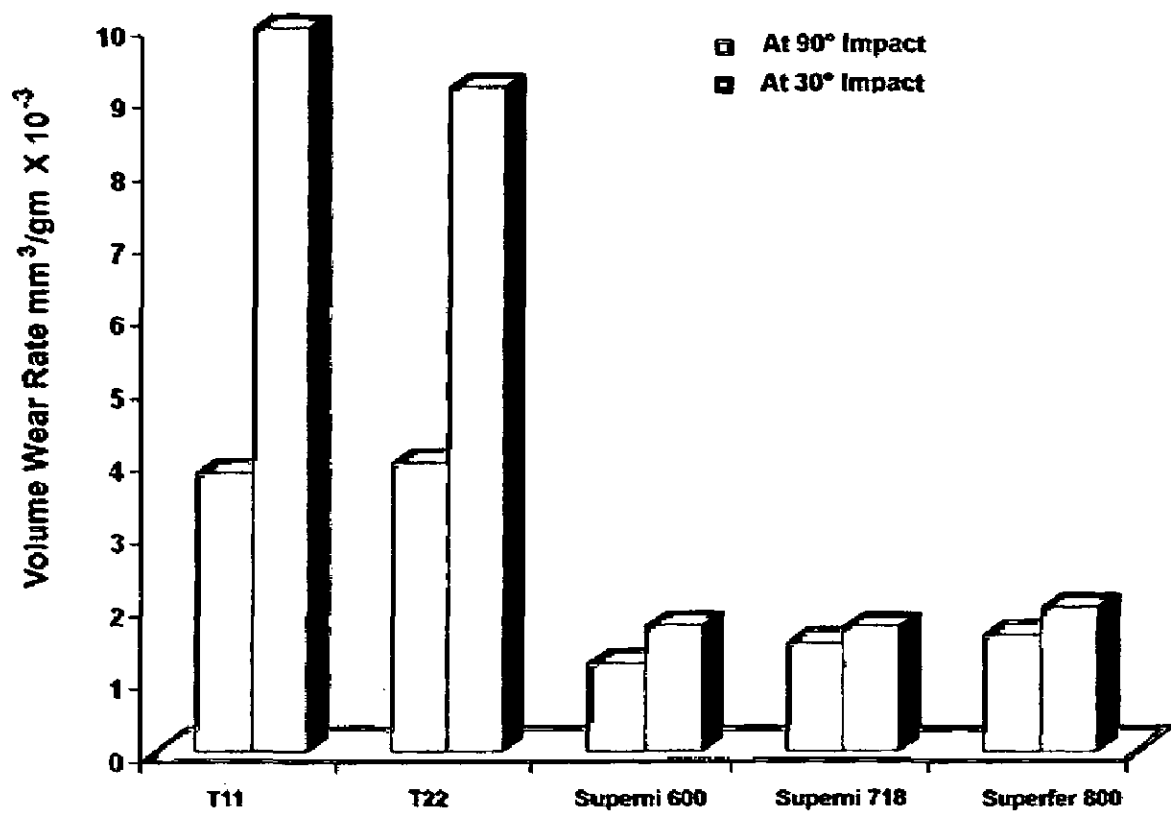


Fig. 5.8: Bar diagram showing the Volume erosion rates of substrate alloys under oblique and normal impact at condition 2.

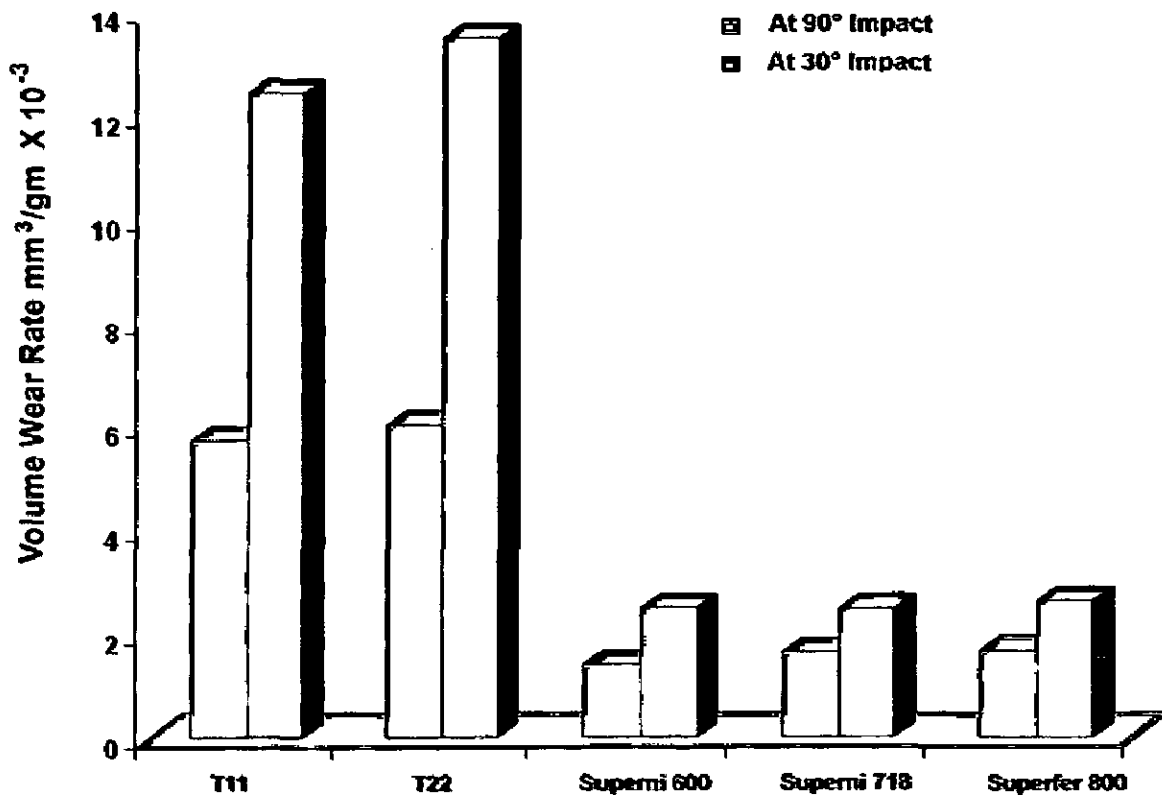


Fig. 5.9: Bar diagram showing the Volume erosion rates of substrate alloys under oblique and normal impact at condition 3.

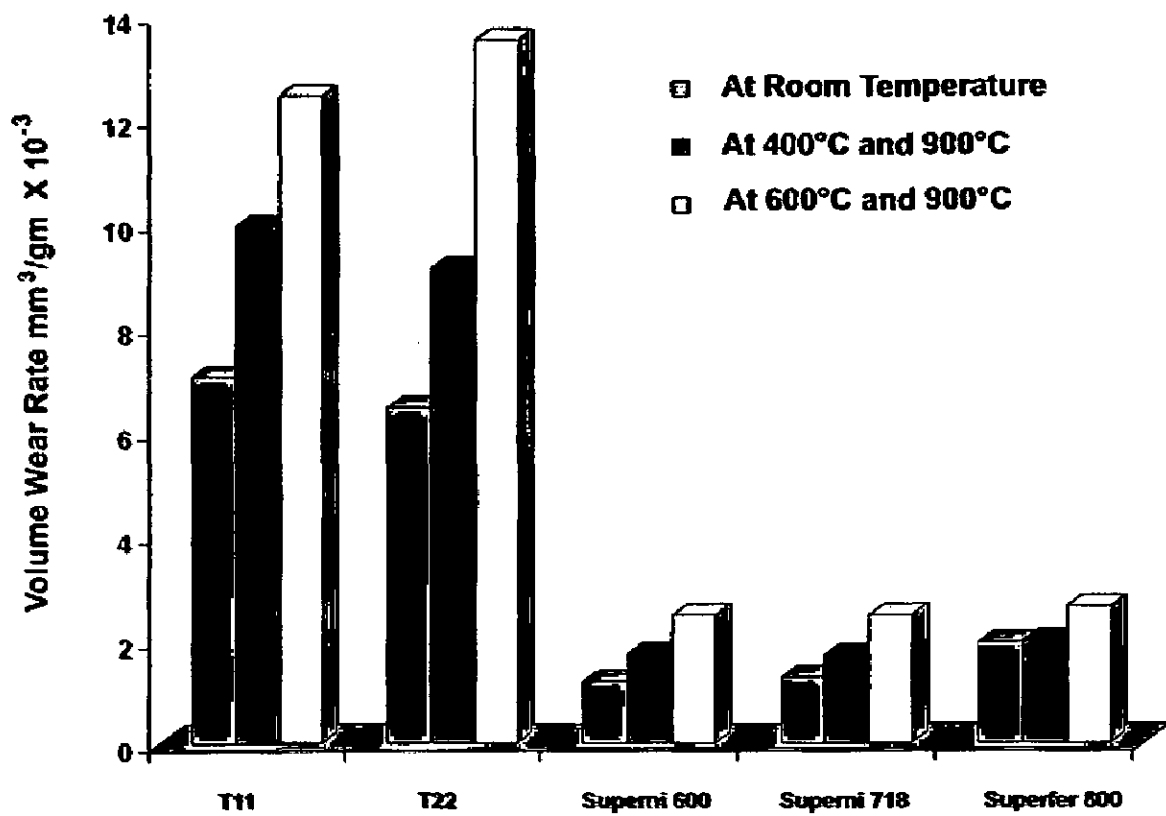


Fig. 5.10: Bar diagram showing the variation in Volume erosion rates of substrate alloys at 30° impact angle with change in test temperature

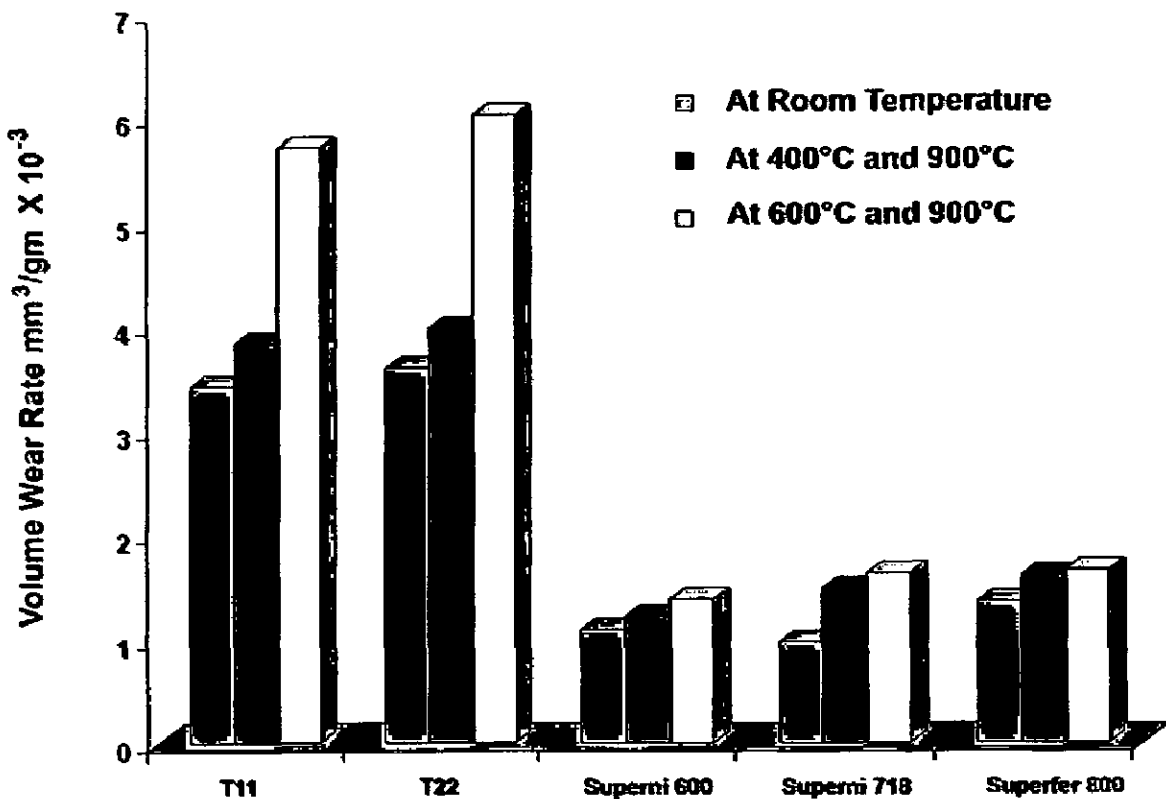


Fig. 5.11: Bar diagram showing the variation in Volume erosion rates of substrate alloys at 90° impact angle with change in test temperature.

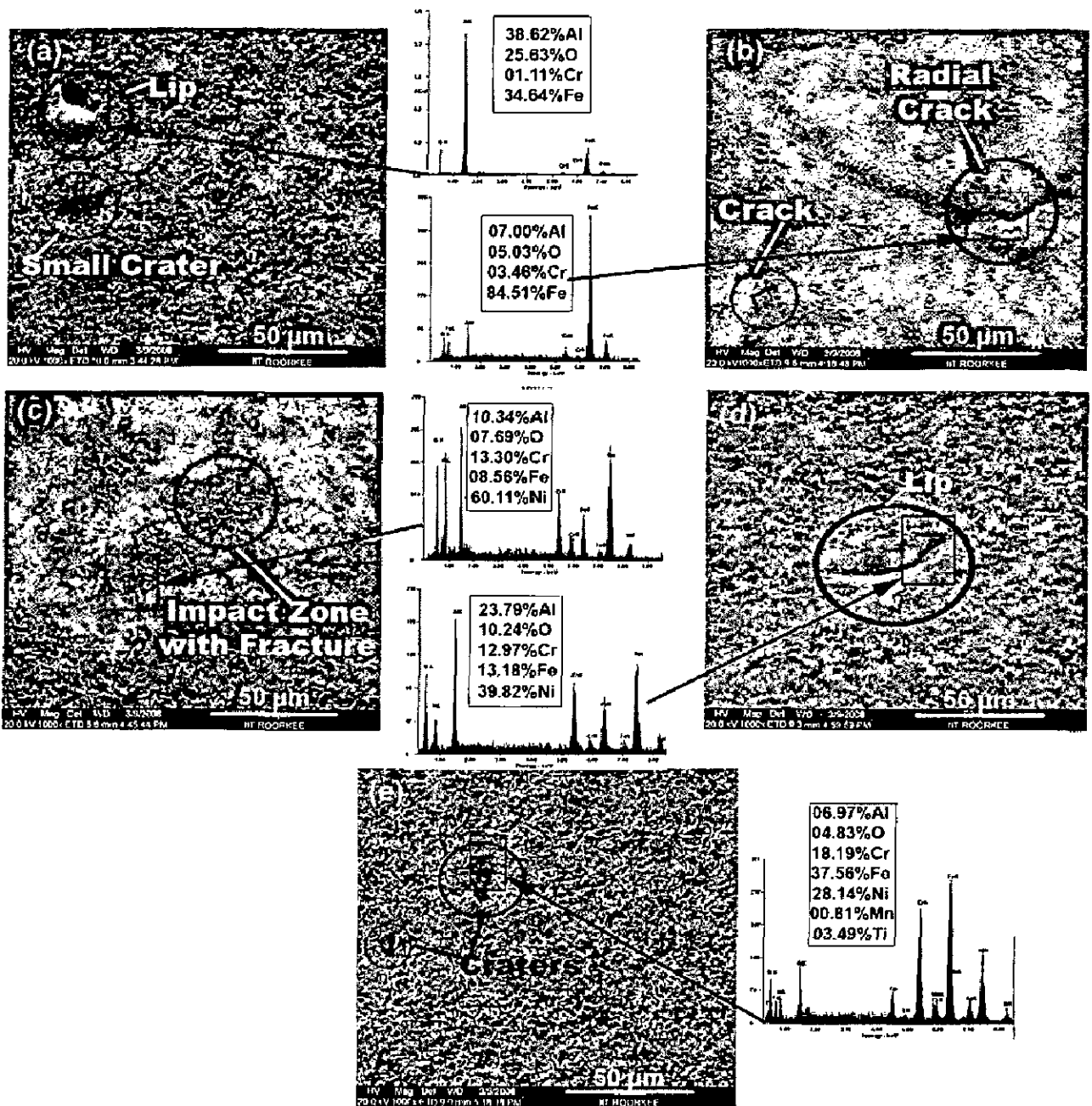


Fig. 5.12: Scanning Electron Macrographs and EDX analysis of uncoated alloys eroded at condition 1 and impact angle of 30°
 (a) Boiler Steel T11 (b) Boiler Steel T22 (c) Superni 600 (d) Superni 718 (e) Superfer 800

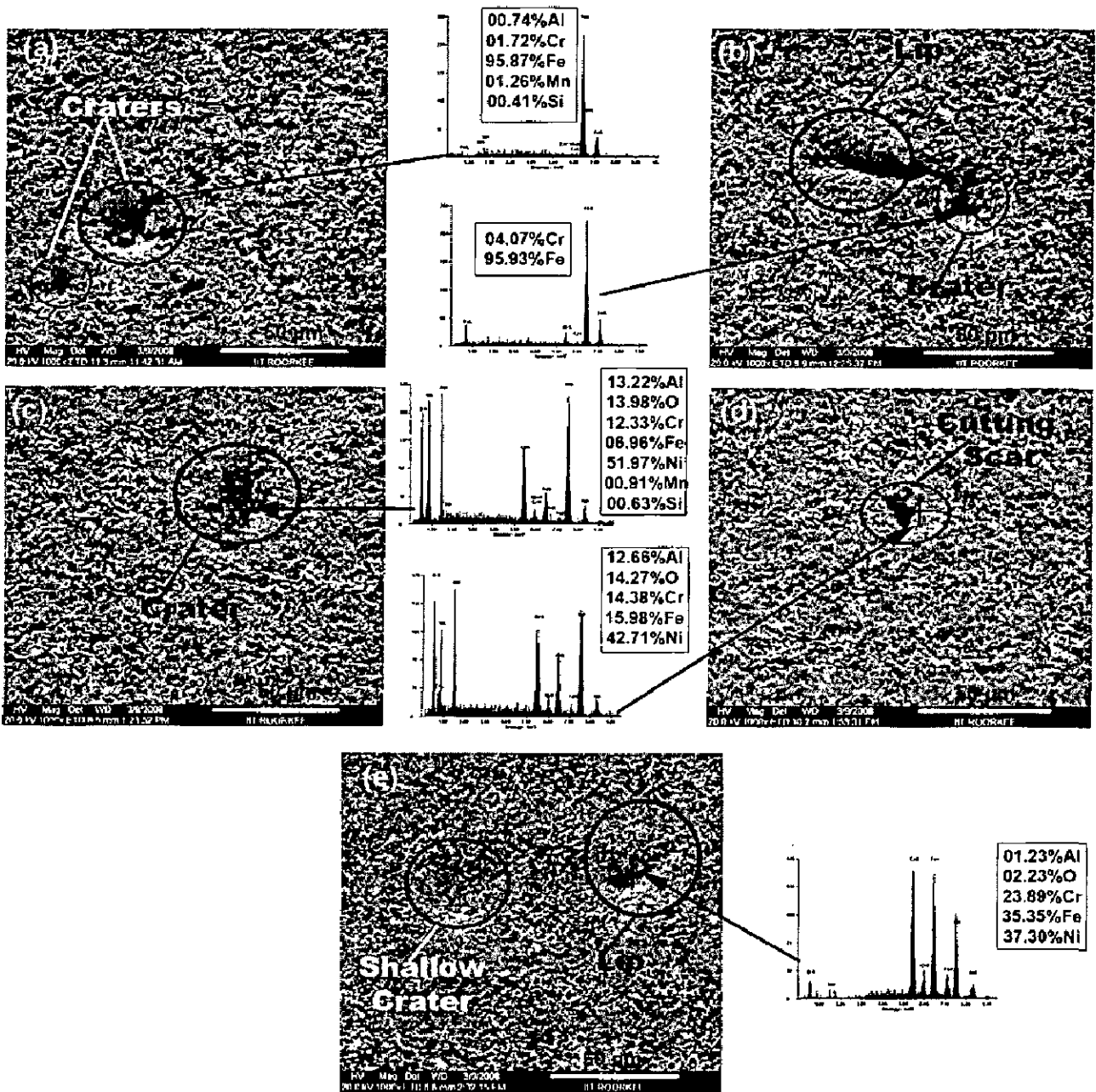


Fig. 5.13 Scanning Electron Macrographs and EDX analysis of uncoated alloys eroded at condition 1 and impact angle of 90°
 (a) Boiler Steel T11 (b) Boiler Steel T22 (c) Superni 600 (d) Superni 718 (e) Superfer 800

revealed severe deformation at the surfaces resulting in formation of craters with minor cracks. It is observed from the SEM of the eroded surfaces of alloys at 30° impact angle at condition 1 i.e. at room temperature, that the material gets removed due to cutting and plastic deformation mainly. In case of boiler steel T11 shown in Fig. 5.12(a), there is indication of lip formation and crater formation while in boiler steel T22, cracks are clearly visible on the surface as shown in Fig. 5.12 (b). In case of Superni 600 superalloy, fracture with clear impact

zone is visible Fig. 5.12(c) and in Superni 718 lip formation is there shown in Fig. 5.12(d). In case of Superfer 800, there are visible craters Fig. 5.12(e).

In case of 90° impact, wider craters and platelets formed on the surfaces of alloys with plastic deformation (Fig. 5.13). It is observed from micrographs of the eroded surface that the erodent particles deform the exposed surface by ploughing, displacing material to the side and in front of the particle in form of lip due to severe plastic flow. With the subsequent erodent impacts these highly strained lips are vulnerable to be removed as micro platelets. In boiler steel T11 shown in Fig. 5.13 (a), craters are formed along with cutting scar on the eroded surface and on T22 surface wide lip along with crater is visible Fig. 5.13 (b). In superalloy Superni 600, crater is formed Fig. 5.13 (c) and in Superni 718 cutting scar is visible Fig. 5.13 (d).and in Superfer 800 shallow crater and lip formation are visible on eroded surface Fig. 5.13 (e)..

The EDX spectra and compositions at selected points of the eroded alloys at room temperature at both angles are also shown in Fig. 5.12 and 5.13. Along with alloy composition, there is detection of major peaks of Al and O in some cases. This may be due to the presence of erodent particles which might have got embedded in the substrate during subsequent impacts. At 30° impact and room temperature conditions testing, in boiler steel T11 shown in Fig. 5.12 (a) when analysed at selected region in the proximity of a lip shown in Fig., there is 38.62% of Al along with 25.63%O which again indicates embedment of erodent particle. Similar erodent particle embedments have also been

observed in other substrate alloys along with substrate alloy composition at the selected regions Fig. 5.12 (b-e).

EDX spectra along with composition at selected points in the surfaces eroded at 90° are shown in Fig. 5.13. In boiler steels the EDX spectra, Fig. 5.13 (a, b), inside craters have indicated constituent composition of both the steels and there is no detection of other elements while in superalloys especially in Superni 600 and Superni 718, the Al and O have been detected in substantial amounts indicating the presence of erodent presence in the eroded region Fig. 5.13 (c, d).

In Condition 2 erosion tests, it is observed from the SEM of the eroded surfaces of alloys at 30° impact angle that the material gets removed due to cutting and plastic deformation as shown in Fig. 5.14. The micrographs have revealed very severe deformation at the surfaces with formation of craters and hills with cracks. The impacting particle removes material by chip formation, essentially scraping material off the surface of the solid in a manner similar to machining (Finnie 1960). In boiler steels T11 clear crack network is visible on the surface Fig. 5.14 (a) and in boiler steel T22 Fig. 5.14 (b) crater formation along with sever plastic deformation is visible. In superalloys Superni 600 and Superni 718, there is visible plastic deformation on the eroded surface Fig. 5.14 (c, d) and in case of Superfer 800; lip is visible on the eroded surface. The EDX analysis boiler steels T11 and T22, eroded at condition 2 at 30° impact angle has indicated the presence of O with Fe, Cr and Al and in case of superalloys the analysis has indicated the presence of O and Al along with the other constituents of superalloy composition.

In case of 90° impact, there is clear indication of formation of cracks on the surface of boiler steels T11 and T22 as is revealed from the SEM shown in Fig.5.15 (a,b) and also oxide fracture and removal are visible on the surface. While in case of superalloys small cracks are visible. In Superni 600 shown in Fig. 5.15 (c) chip formation along with cracks are visible and in Superni 718 small cracks are visible along with craters as shown in Fig. 5.15(d). In case of Superfer 800 severe plastic deformations along with craters formations were observed

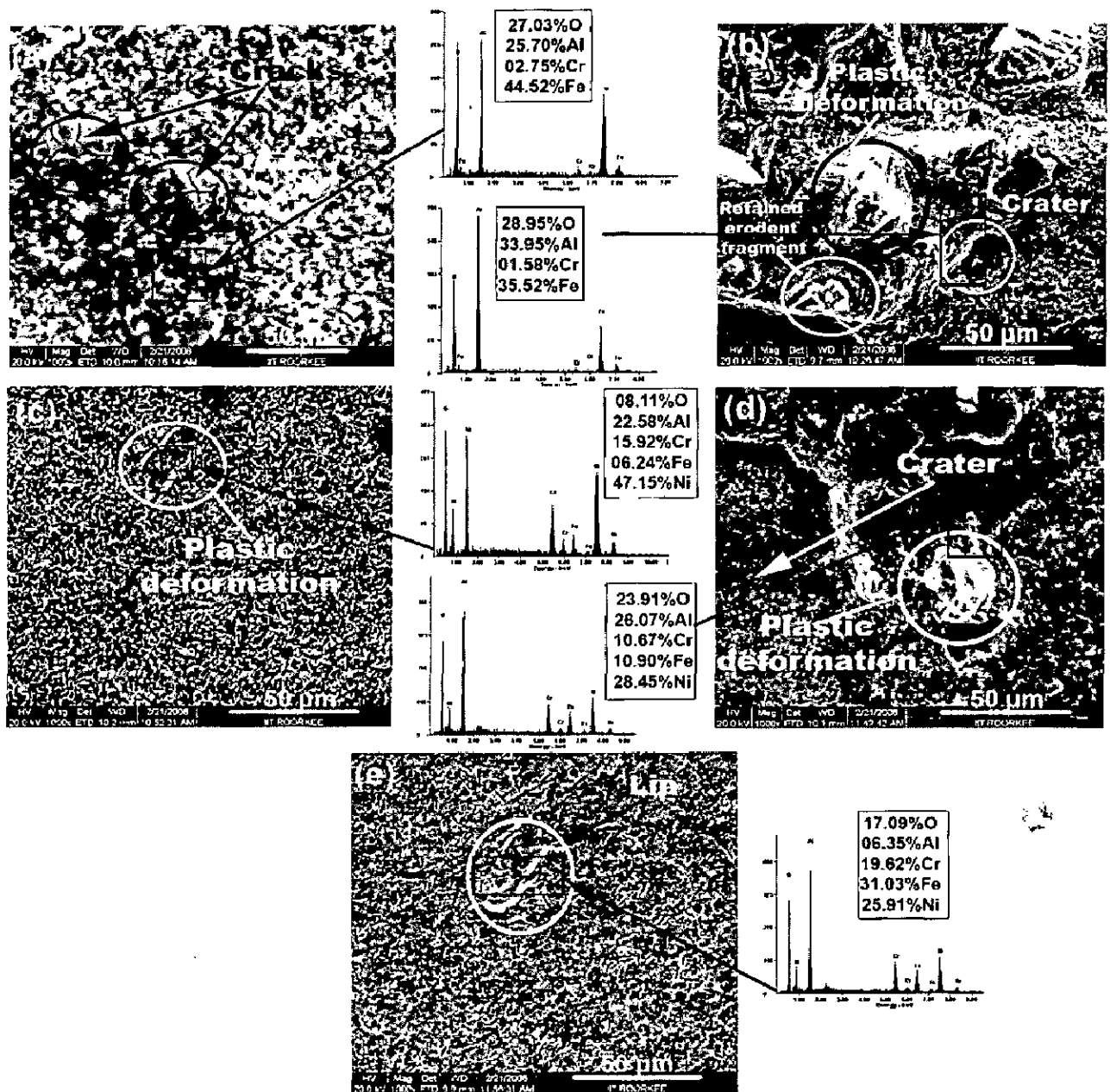


Fig. 5.14: Scanning Electron Macrographs and EDX analysis of uncoated alloys eroded at condition 2 and impact angle of 30°
 (a) Boiler Steel T11 (b) Boiler Steel T22 (c) Superni 600 (d) Superni 718 (e) Superfer 800

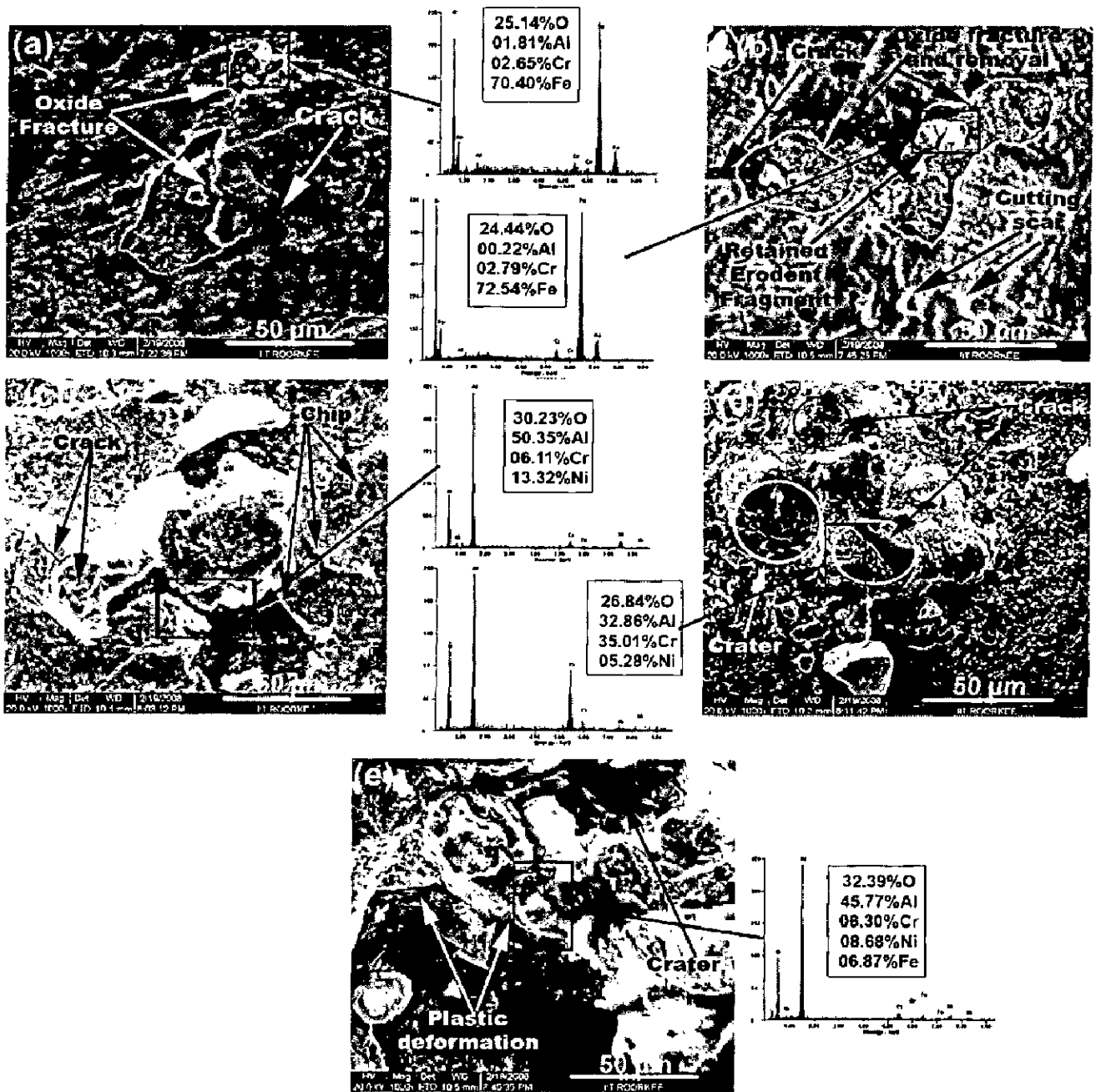


Fig. 5.15: Scanning Electron Macrographs and EDX analysis of uncoated alloys eroded at condition 2 and impact angle of 90°
 (a) Boiler Steel T11 (b) Boiler Steel T22 (c) Superni 600 (d) Superni 718 (e) Superfer 800

as shown in Fig. 5.15 (e). EDX analysis of boiler steels have revealed presence of Fe and Cr along with O indicating the formation of iron oxide Fig.5.15 (a,b) while in case of superalloy there is substantial presence of Al indicating the presence of erodent fragments on the eroded surface as is clear from Fig. 5.15 (c,d and e).

Also in Condition 3 erosion tests, it is observed from the SEM of the eroded surfaces of alloys at 30° impact angle that the material gets removed by cutting and plastic deformation mechanism as shown in Fig. 5.16. Cracks are visible on the eroded surfaces. The micrographs have revealed very severe deformation at the surfaces with formation of craters and hills. The material removal is by chip formation like in machining and by the process of extrusion. The impacting particle has removed the material by chip formation, essentially scraping material off the surface of the solid and exposing a new surface in a manner similar to machining. In boiler steel T11, micrograph has indicated oxide removal and crack propagation on the eroded surface shown in Fig.5.16 (a). While in case of T22 steel shallow crater is visible on the eroded surface and it appears that the upper surface layer could have been removed with particle impacts Fig.5.16 (b). In case of super alloy Superni 600, small crater along with cracks on the eroded surface and chip formation is visible shown in Fig.5.16 (c) and in Superni 718, cutting scar and shallow crater is visible Fig.5.16 (d). Cracks and shallow craters are visible on the eroded surface of Superfer 800 Fig.5.16 (e).

The EDX analysis boiler steels T11 has indicated the presence of Fe and Cr with negligible amount of Al and O as shown in Fig. 5.16(a) and T22 steel has shown presence of 8.35% of Al along with 13.99%O with 73.47% Fe and 4.19% Cr as shown in Fig. 5.16(b). While in case of superalloys (Fig. 5.16 c, d and e) the analysis has indicated the presence of O and Al along with the other constituents of superalloy composition indicating alumina particles embedded in the material.

In case of 90° impact, there is clear indication of formation of cracks on the surface of eroded samples as shown in Fig. 5.17. Under high temperature erosion conditions, a thick scale is formed on the target material during erosion and the deformed zone formed due to

impact is confined within the scale. The continuous erodent impacts subsequently results in deformation, extrusion and work hardening, until fracture occurs and the material is completely lost from the surface. In case of boiler steel T11oxide fracture and removal is clearly visible on the surface micrograph and there is indication of crack propagation along the fractured surface as shown in Fig. 5.17(a). In case of Boiler steel T22, the eroded surface showed flake chipped off from the surface and cracks on the eroded surface Fig. 5.17(b).

In superalloy Superni 600, cracks are visible on the eroded surface and some shallow crater as can be seen shown in Fig. 5.17(c). In Superni 718, plastic deformation along with cracks is visible in Fig. 5.17(d) while in Superfer 800, there is crack network and lip formation shown in Fig. 5.17(e). The micrographs have indicated that the cavities are developed as a result of impact of erodent particles. Surface hillocks are also observed at various places which represent the portion of the alloy being partly removed from the surface of the specimens. EDX analysis at selected area of boiler steel T11 have shown presence of O along with Fe, Cr and Al indicating oxide formation at this condition. Presence of Al is indicating some erodent particles have been retained on the surface as shown in Fig. 5.17 (a). In case of Boiler steel T22, EDX analysis had revealed 11.07 % Al along with 9.09% O and 76.10% Fe and 3.74% Cr. In Superni 600, 35.15% Al along with Cr, Fe, Ni and O have been detected at the selected region. In Superni 718, 12.88% Al with Fe, Ni, Cr and O have been detected at the selected area. In Superfer 800, at the selected region, 51.68 % of Al with 30.35 % O has been detected clearly revealing the erodent particle embedment.

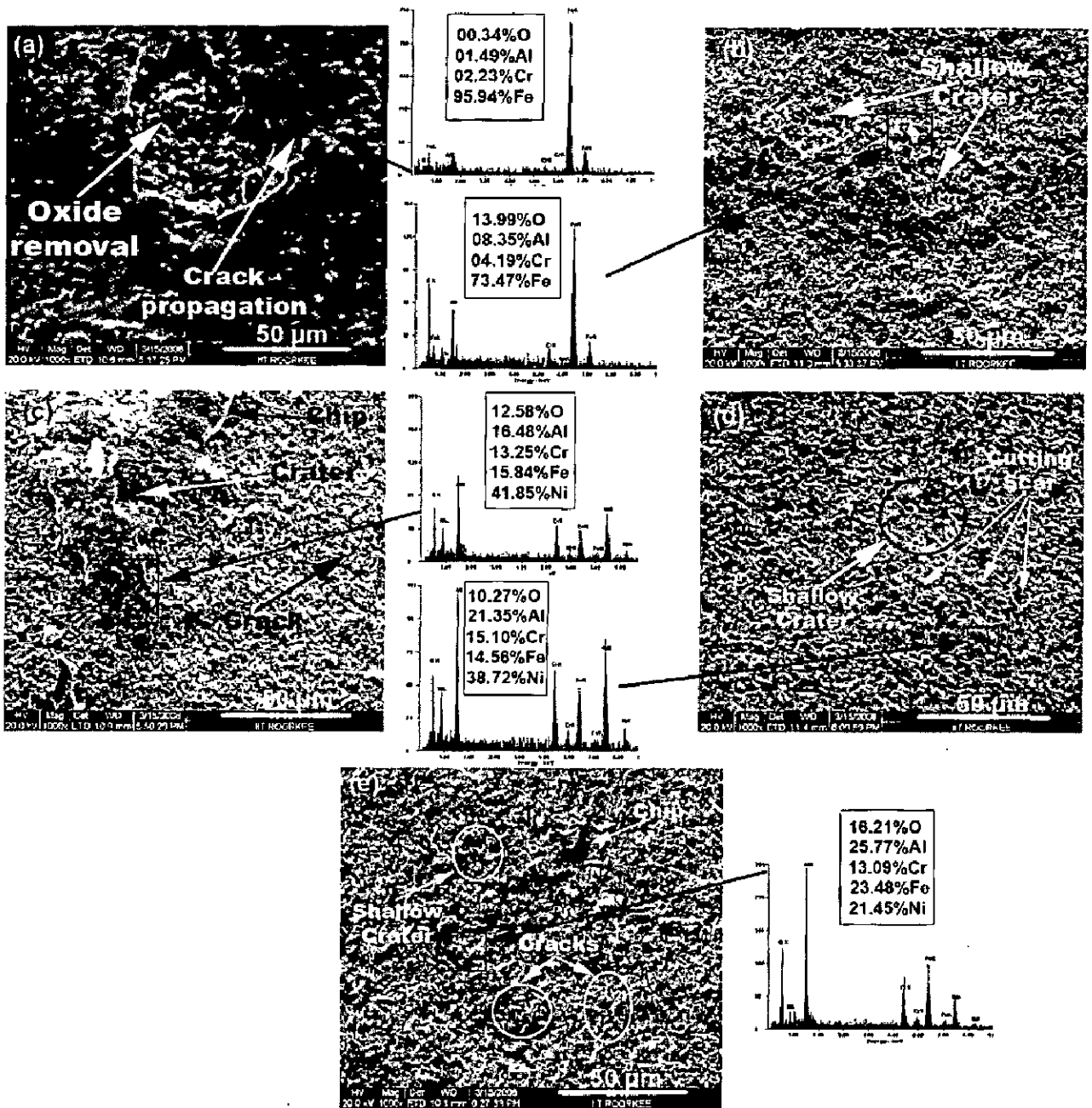


Fig. 5.16: Scanning Electron Macrographs and EDX analysis of uncoated alloys eroded at condition 3 and impact angle of 30°
 (a) Boiler Steel T11 (b) Boiler Steel T22 (c) Superni 600 (d) Superni 718 (e) Superfer 800

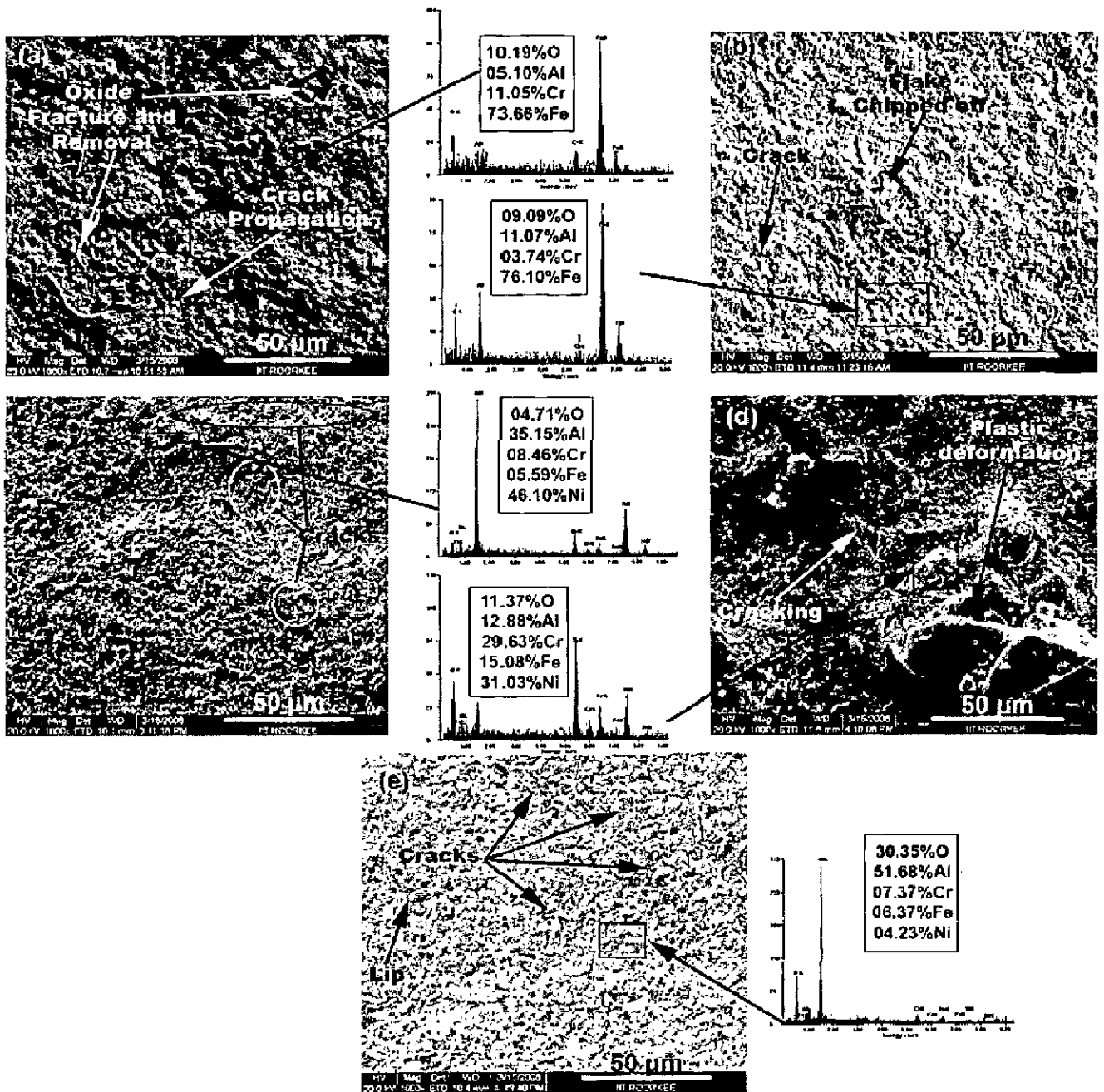


Fig. 5.17: Scanning Electron Macrographs and EDX analysis of uncoated alloys eroded at condition 3 and impact angle of 90°
 (a) Boiler Steel T11 (b) Boiler Steel T22 (c) Superni 600 (d) Superni 718 (e) Superfer 800

5.1.2 Al₂O₃-3wt%TiO₂ coated alloys

5.1.2.1 Visual Examination

The Surface macrographs showing the erosion scar produced on the top surface of the Al₂O₃-3wt%TiO₂ coated boiler steels namely T11, T22 and superalloys namely Superni 600, Superni 718, and Superfer 800 superalloys eroded at 30° and 90° impact angles at room temperature and at elevated temperature are shown in Figs 5.18-5.20

After Condition 1 Tests

The samples after testing at Condition 1 are shown in Fig. 5.18. The visual inspection of each sample showed slight discolouration at the impact zone. Also the roughening of the upper surface and the formation of scars in the eroded area were observed.

After Condition 2 Tests

The macrographs of the coated samples after testing at Condition 2 are shown in Fig. 5.19. The change in colour of the samples from original grey to cream due to thin scale formation was observed. The erosion seems to have cleaned the scale off the surface in the eroded region. The eroded region showed discoloration at the impact site.

After Condition 3 Tests

The macrographs of the coated samples after testing at Condition 3 are shown in Fig. 5.20. The change in colour of the samples from grey to cream was observed and the impact zone showed a brighter zone than the surrounding area.

5.1.2.2 Erosion Rate

The erosion loss has been calculated by volume change method. The volume loss occurred after erosion testing was measured by using non contact optical profilometry as explained in chapter 3. At normal impact, ceramic materials are characterized by erosive wear being maximal at the impact angle of 90°. The volume erosion loss at 90° impact angle is higher than that of erosion loss at 30° impact angle. Representative three dimensional optical profiles of the uncoated specimens eroded at room temperature as well as high temperature at both impact angles are shown in Figs 5.21 to 5.23.

The erosion rate of the Al₂O₃-3 wt% TiO₂ coated boiler steels namely T11, T22 and superalloys namely Superni 600, Superni 718, and Superfer 800 superalloys at an impact velocity of 35ms-1 and impingement angle of 30° and 90° at room temperature (condition 1) is shown in Fig. 5.24. From the graph, it can be inferred that the erosion rate of coated alloys eroded at 90° impact angle is higher than the erosion rate at 30° impact angle. Volume wear rate of coated Supreni 718 superalloy is marginally higher than the other coated substrates at 90° impact angle while at 30° impact angle erosion rate of coated Superni 600 is marginally high.

At 90° impact angle, the volume erosion rate for Al₂O₃-3 wt% TiO₂ coated boiler steels T11 and T22 is 1.447 x10⁻³ mm³/gm & 1.513 x10⁻³ mm³/gm and for Al₂O₃-3 wt% TiO₂ coated superalloys Superni 600, Superni 718 and Superfer 800 is 1.513 x10⁻³ mm³/gm, 1.55 x10⁻³ mm³/gm and 1.502 x10⁻³ mm³/gm respectively.

While at 30° impact, the volume erosion rate for Al₂O₃-3 wt% TiO₂ coated Boiler steels T11 and T22 is 0.883 x10⁻³ mm³/gm & 0.933 x10⁻³ mm³/gm and for Al₂O₃-3 wt% TiO₂ coated superalloys Superni 600, Superni 718 and Superfer 800 is 1.041 x10⁻³ mm³/gm, 1.025 x10⁻³ mm³/gm and 1.022 x10⁻³ mm³/gm respectively.

At condition 2 i.e. when substrate temperature was 400°C and surrounding air at 900°C, there is substantial increase in volume erosion rate as shown in Fig. 5.25. The volume erosion rate for Al₂O₃-3 wt% TiO₂ coated Boiler steels T11 and T22 is 1.836 x10⁻³ mm³/gm & 1.858 x10⁻³ mm³/gm and for Al₂O₃-3 wt% TiO₂ coated superalloys Superni 600, Superni 718 and Superfer 800 is 1.788 x10⁻³ mm³/gm, 1.742 x10⁻³ mm³/gm and 1.653 x10⁻³ mm³/gm respectively at 90° impact angle. While at 30° impact, the volume erosion rate for coated Boiler steels T11 and T22 is 1.077 x10⁻³ mm³/gm & 1.064 x10⁻³ mm³/gm and for coated superalloys Superni 600, Superni 718 and Superfer 800 is 1.141 x10⁻³ mm³/gm, 1.153 x10⁻³ mm³/gm and 1.075 x10⁻³ mm³/gm respectively.

On further increasing the substrate temperature to 600°C and surrounding temperature of 900°C, volume erosion rate is also increased as shown in Fig. 5.26. From the Fig. it is apparent that the volume erosion rate is higher than the erosion rate at condition 1 and condition 2. The volume erosion rate for Al₂O₃-3 wt% TiO₂ coated Boiler steels T11 and T22 is 2.486 x10⁻³ mm³/gm & 2.4 x10⁻³ mm³/gm and for Al₂O₃-3 wt% TiO₂ coated superalloys Superni 600, Superni 718 and Superfer 800 is 2.188 x10⁻³ mm³/gm, 2.108 x10⁻³ mm³/gm and 2.292 x10⁻³ mm³/gm respectively at 90° impact angle. While at 30° impact, the volume erosion rate for Boiler steels T11 and T22 is 1.266 x10⁻³ mm³/gm and 1.316 x10⁻³ mm³/gm and for superalloys Superni 600, Superni 718 and Superfer 800 is 1.286 x10⁻³ mm³/gm, 1.253 x10⁻³ mm³/gm and 1.53 x10⁻³ mm³/gm respectively.

Fig. 5.27 and Fig. 5.28 shows the variation in volume erosion rates of coated substrate alloys at 30° and 90° impact angles with change in test temperature. A tendency for increase in erosion rate with temperature has been observed in all the coated alloys. The erosion rate at normal impact i.e. at 90° impingement angle is more as compared to erosion rate at 30° impact thus showing the typical behavior of brittle materials.

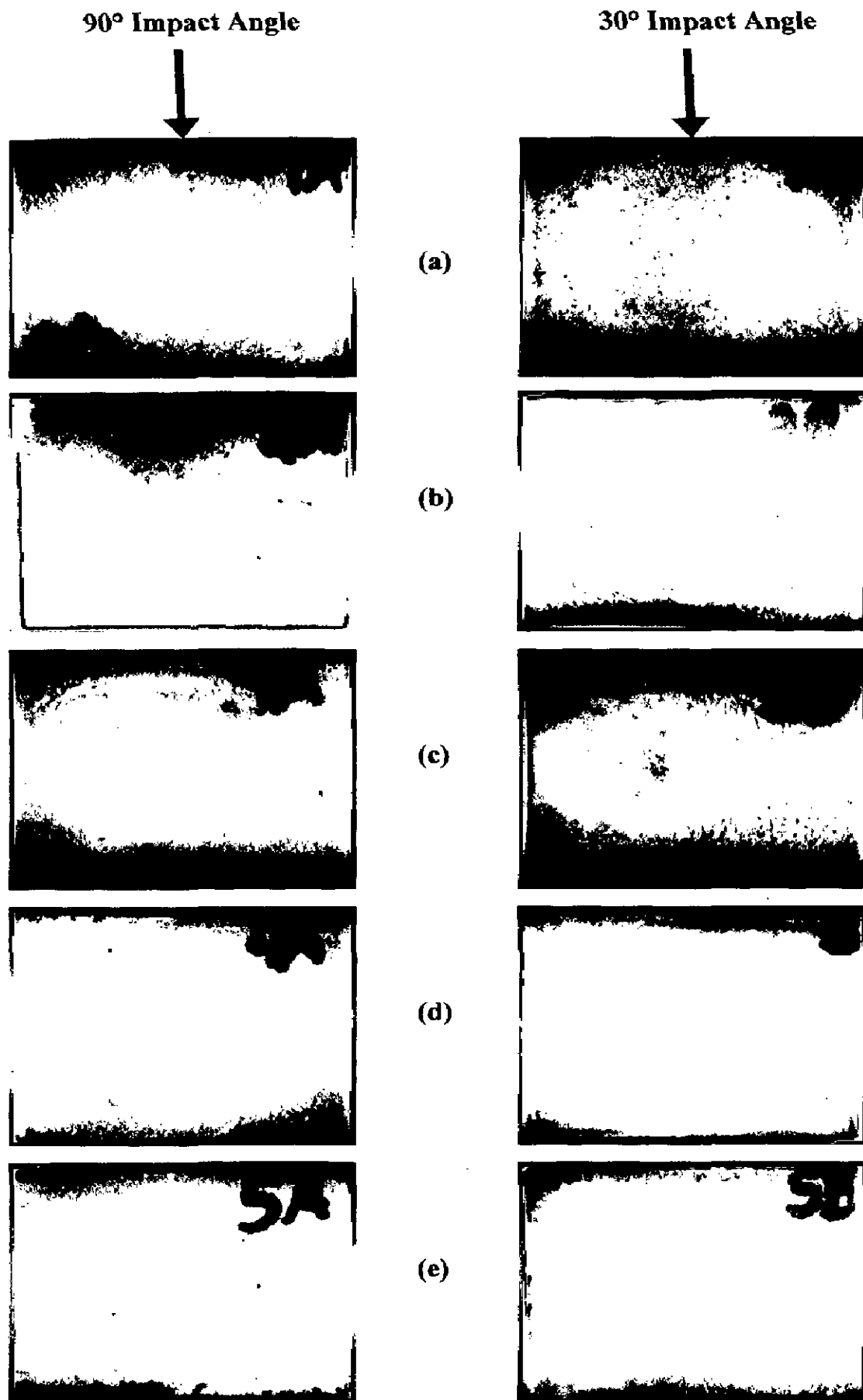


Fig. 5.18: Macrographs of Al_2O_3 -3 wt% TiO_2 coated alloys eroded at condition 1 and at impact angles of 90° and 30°
 (a) Boiler Steel T11 (b) Boiler Steel T22 (c) Superni 600 (d) Superni 718
 (e) Superfer 800

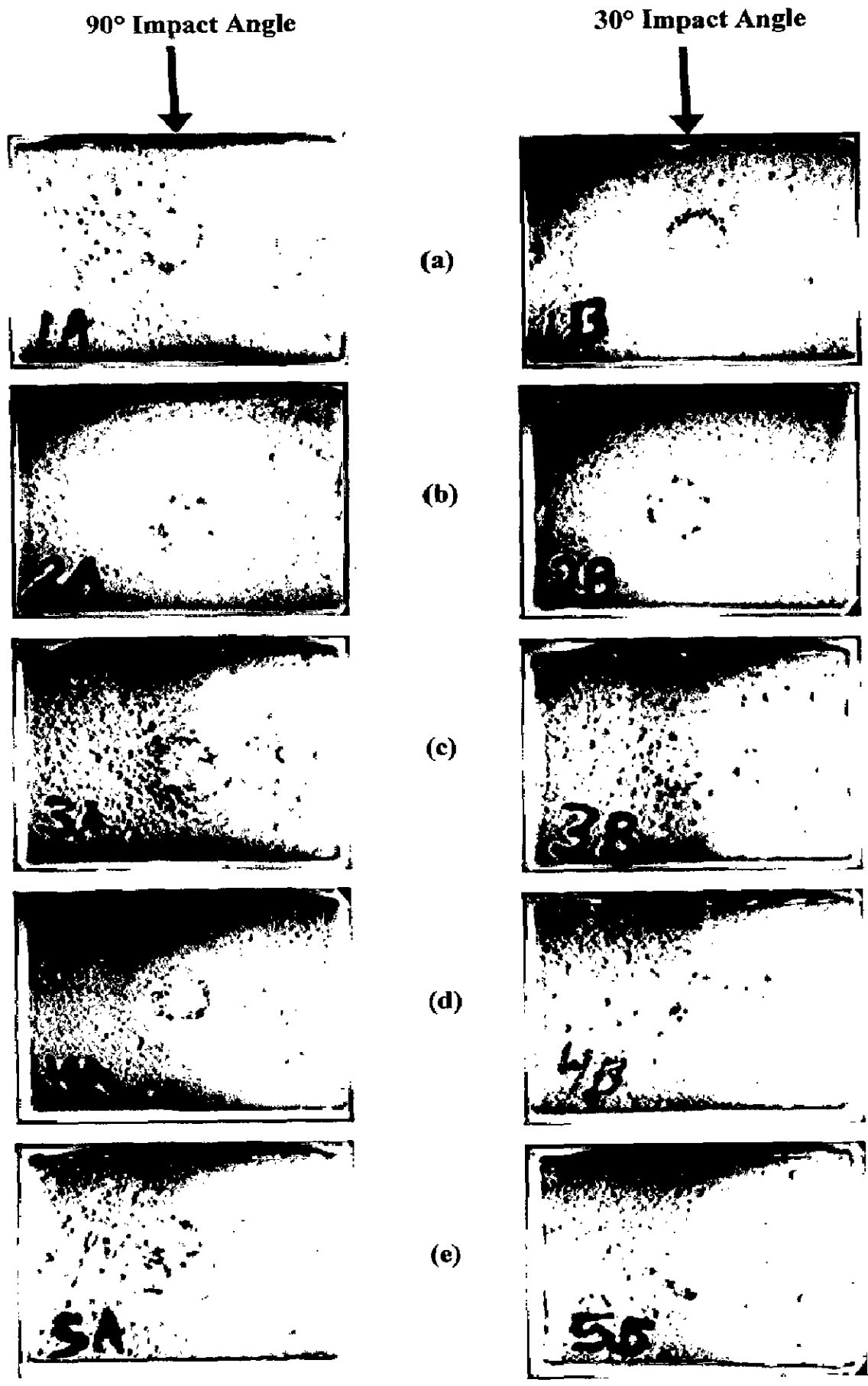


Fig. 5.19: Macrographs of Al_2O_3 -3 wt% TiO_2 coated alloys eroded at condition 2 and at impact angles of 90° and 30°
 (a) Boiler Steel T11 (b) Boiler Steel T22 (c) Superni 600 (d) Superni 718
 (e) Superfer 800

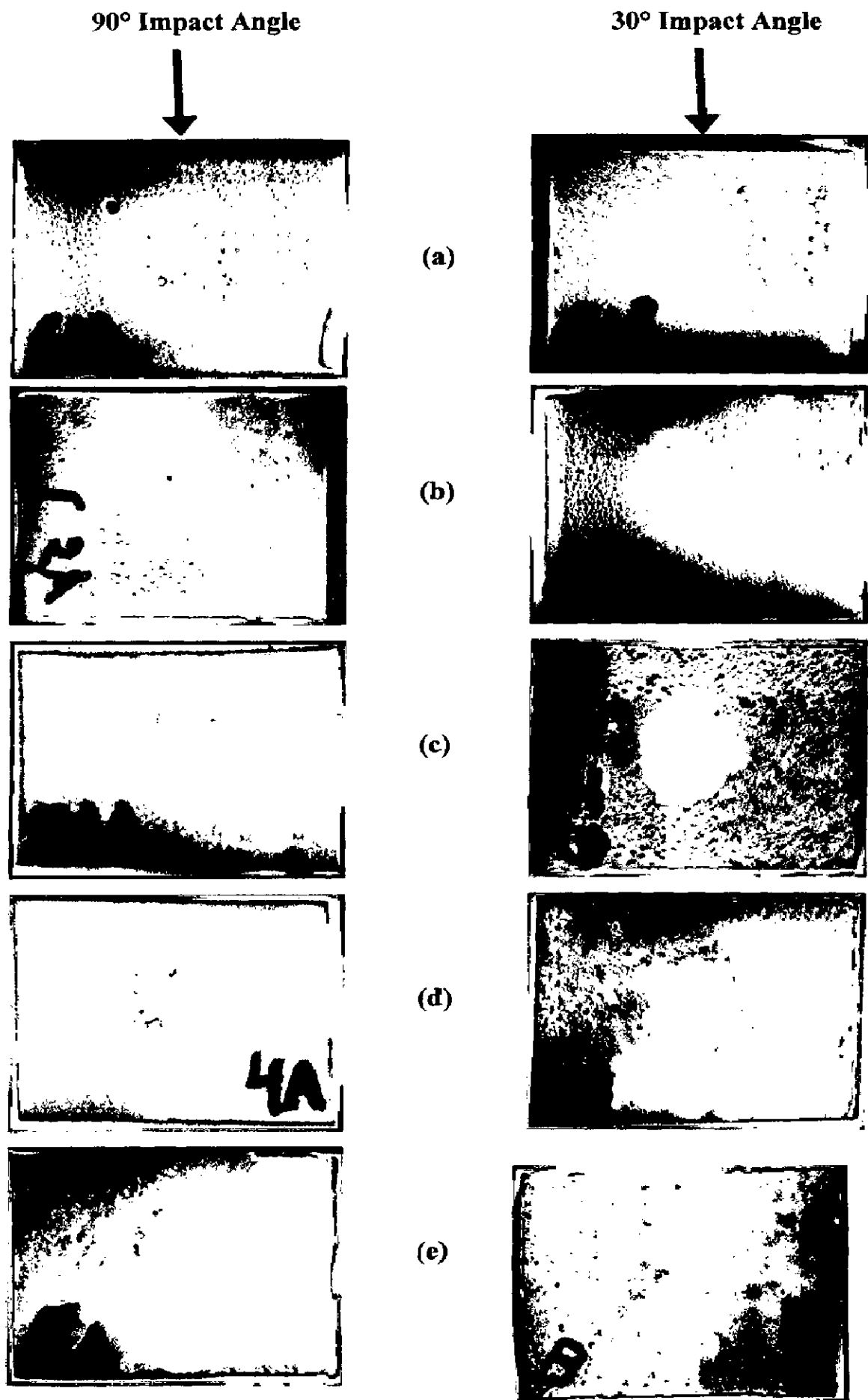


Fig. 5.20: Macrographs of Al_2O_3 -3 wt% TiO_2 coated alloys eroded at condition 3 and at impact angles of 90° and 30°
 (a) Boiler Steel T11 (b) Boiler Steel T22 (c) Superni 600 (d) Superni 718
 (e) Superfer 800

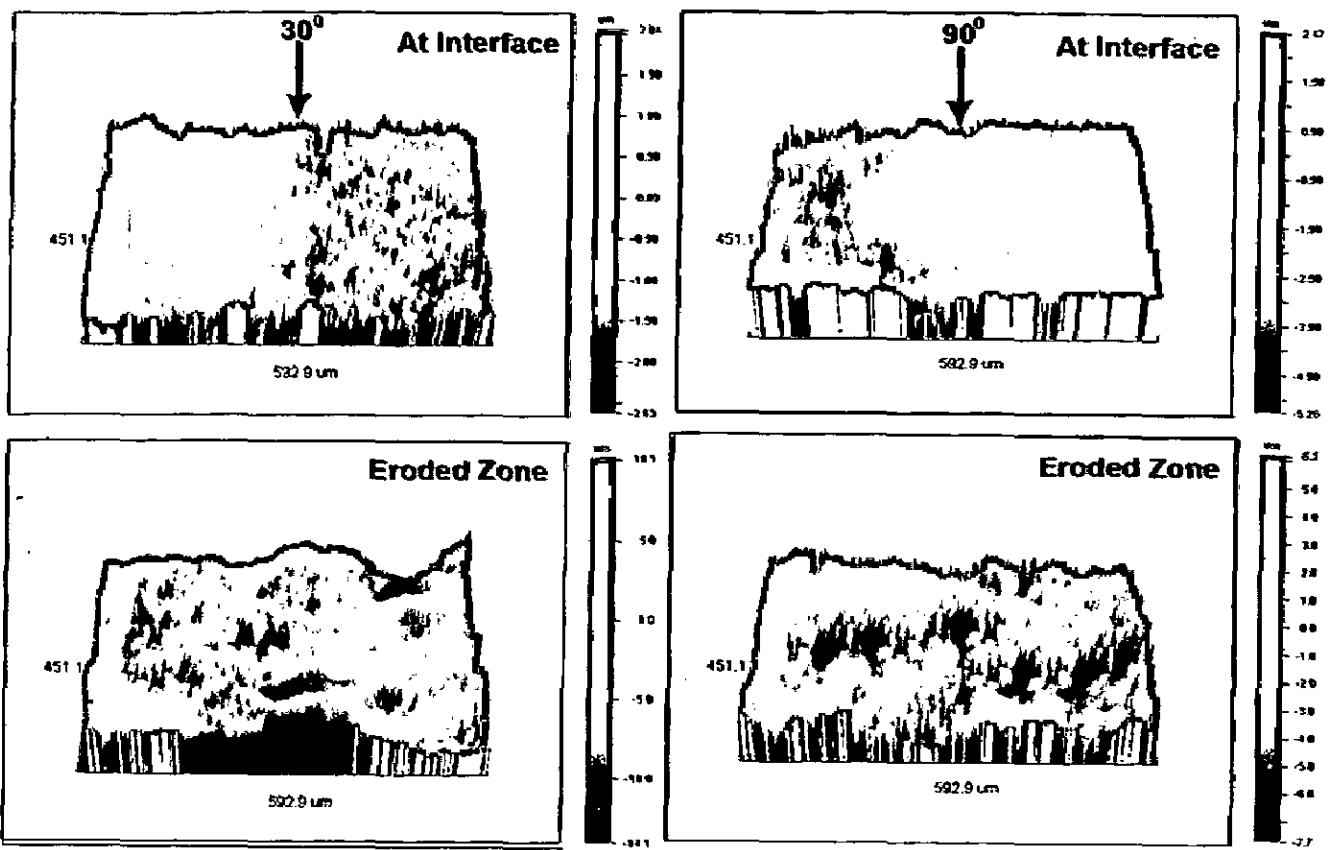


Fig. 5.21: 3D Optical Profile of Al_2O_3 -3 wt% TiO_2 coated specimen eroded at condition 1 showing depth profiles at interface and at eroded zone
 (a) Eroded at 30° impact angle (b) Eroded at 90° impact angle

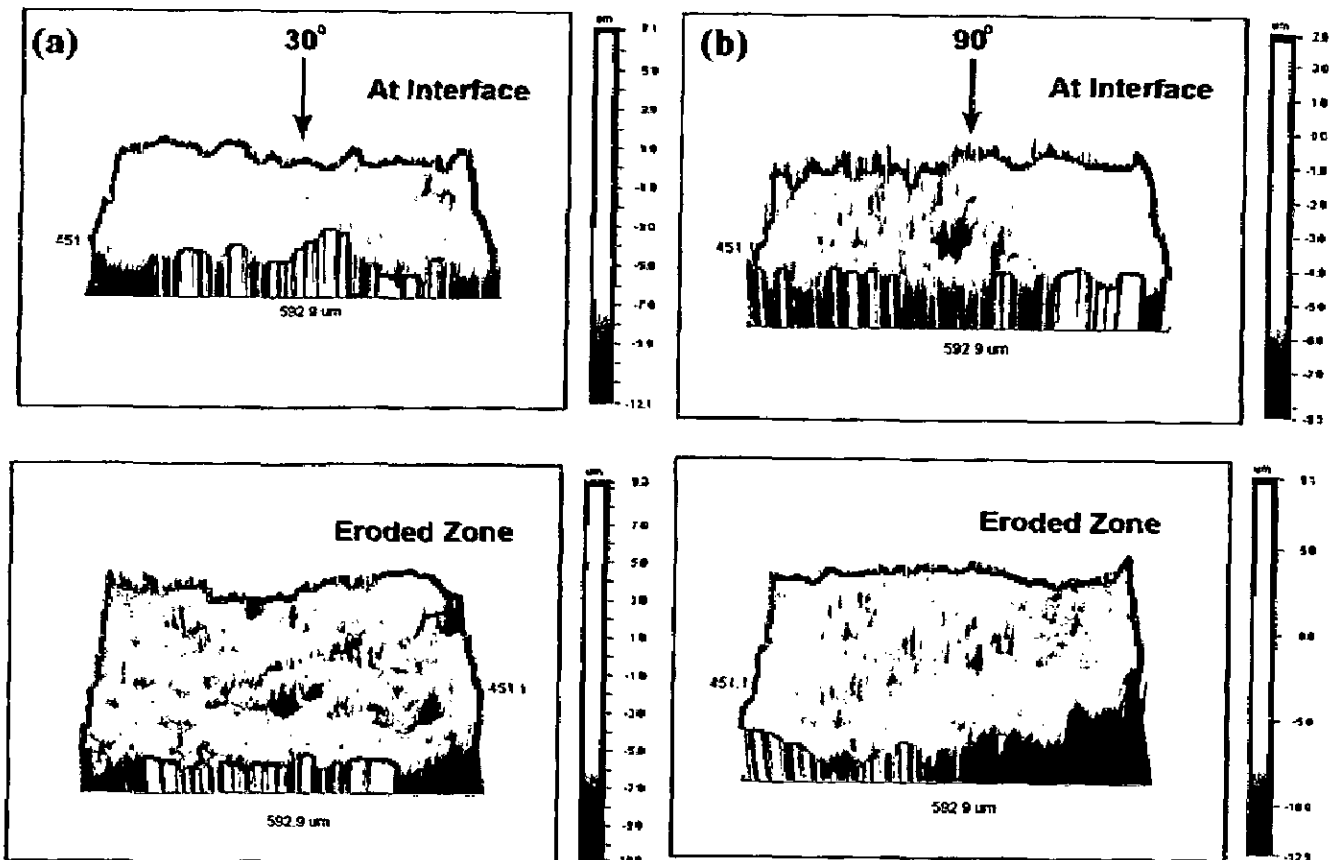


Fig. 5.22: 3D Optical Profile of Al_2O_3 -3 wt% TiO_2 coated specimen eroded at condition 2 showing depth profiles at interface and at eroded zone
 (a) Eroded at 30° impact angle (b) Eroded at 90° impact angle

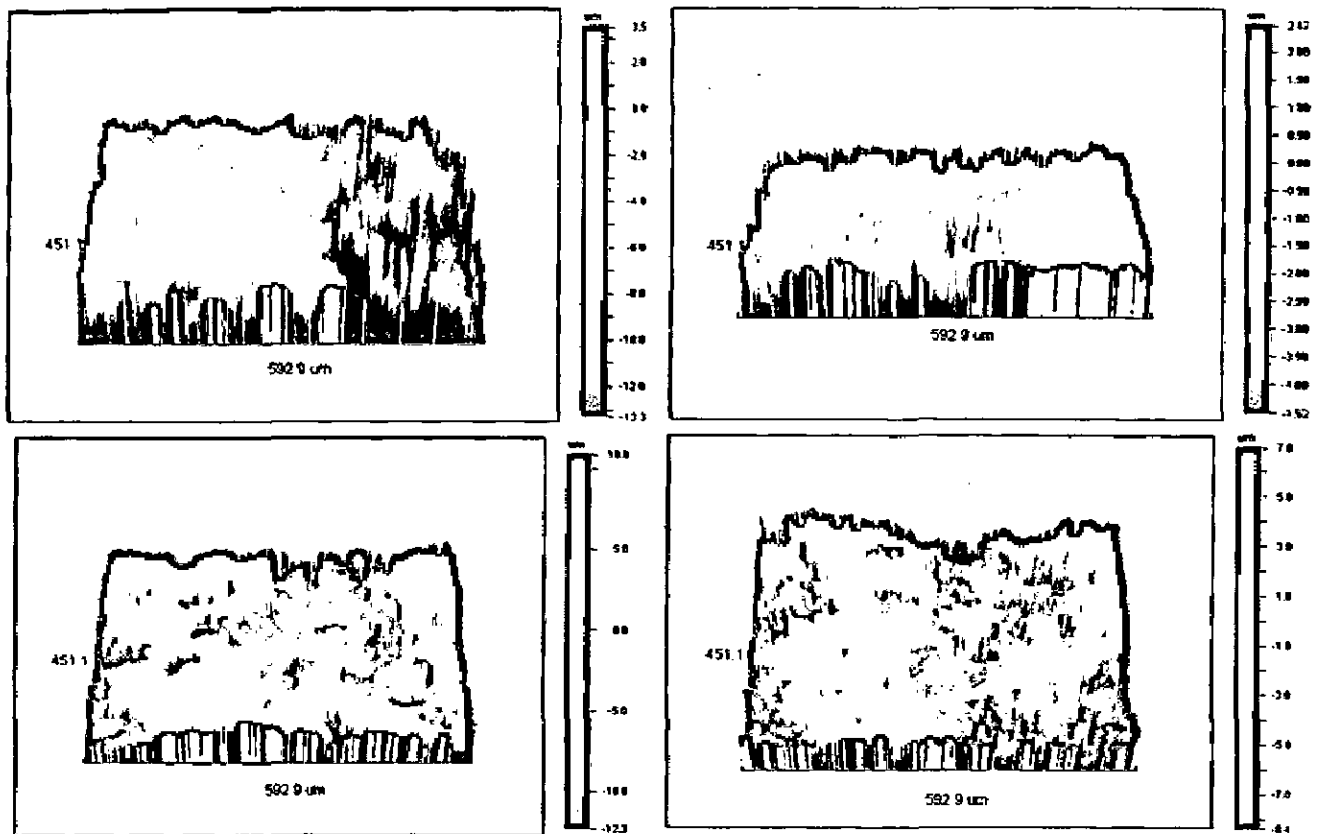


Fig. 5.23: 3D Optical Profile of Al_2O_3 -3 wt% TiO_2 coated specimen eroded at condition 3 showing depth profiles at interface and at eroded zone.
 (a) Eroded at 30° impact angle (b) Eroded at 90° impact angle

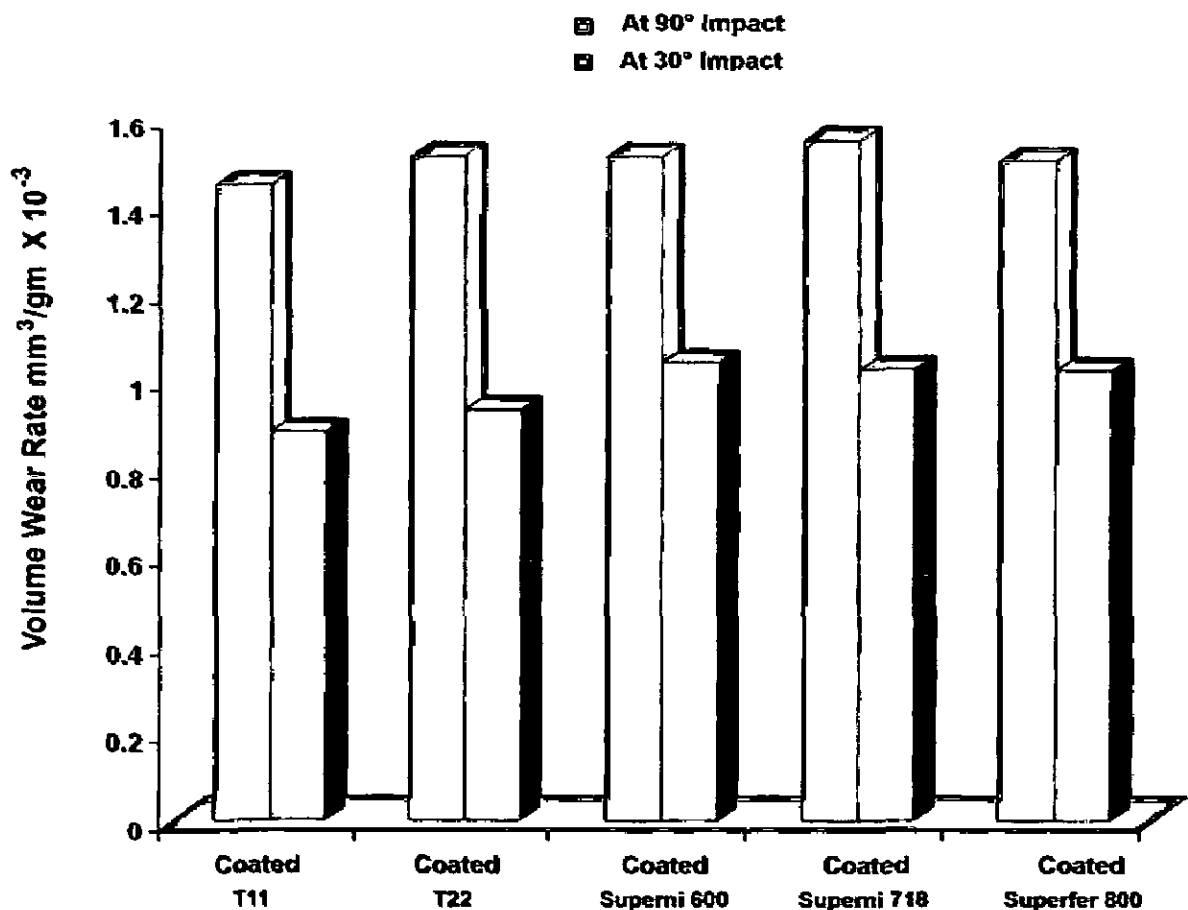


Fig. 5.24: Bar diagram showing the volume erosion rates of coated alloys under oblique and normal impact at condition 1

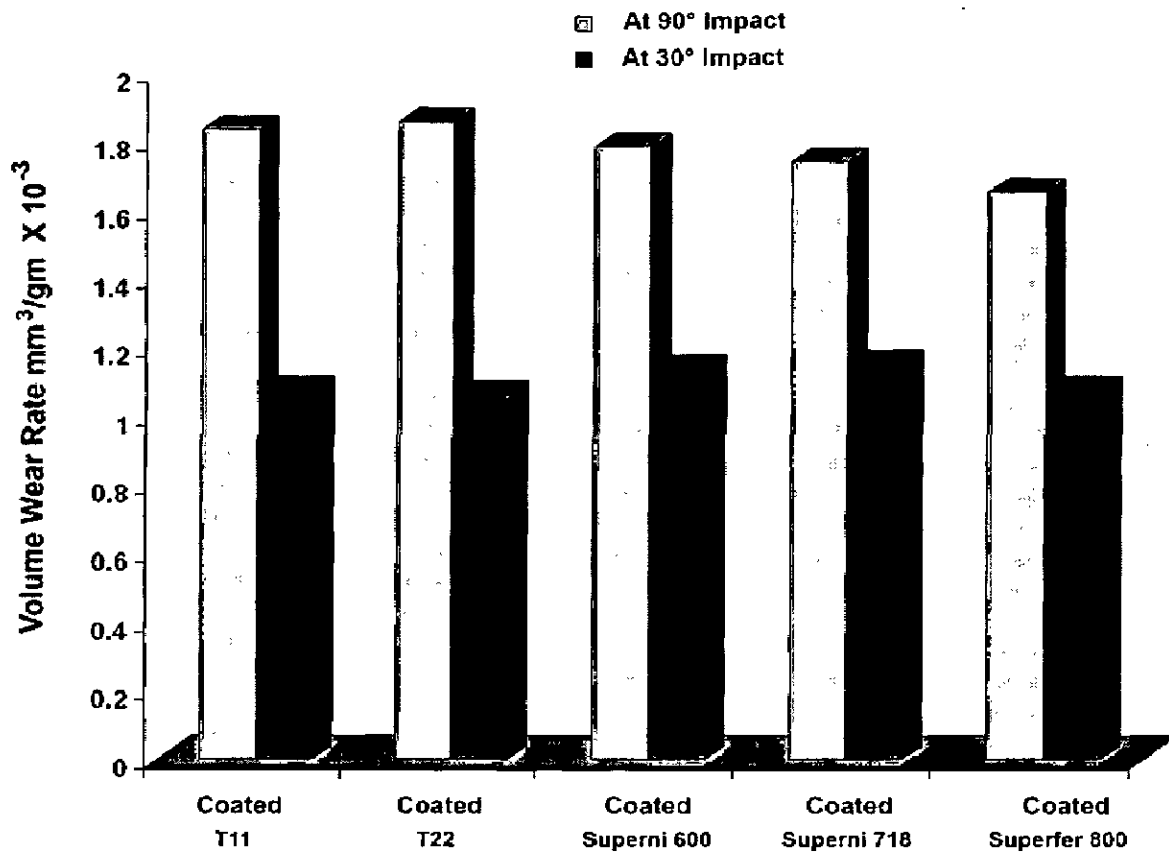


Fig. 5.25: Bar diagram showing the Volume erosion rates of coated alloys under oblique and normal impact at condition 2.

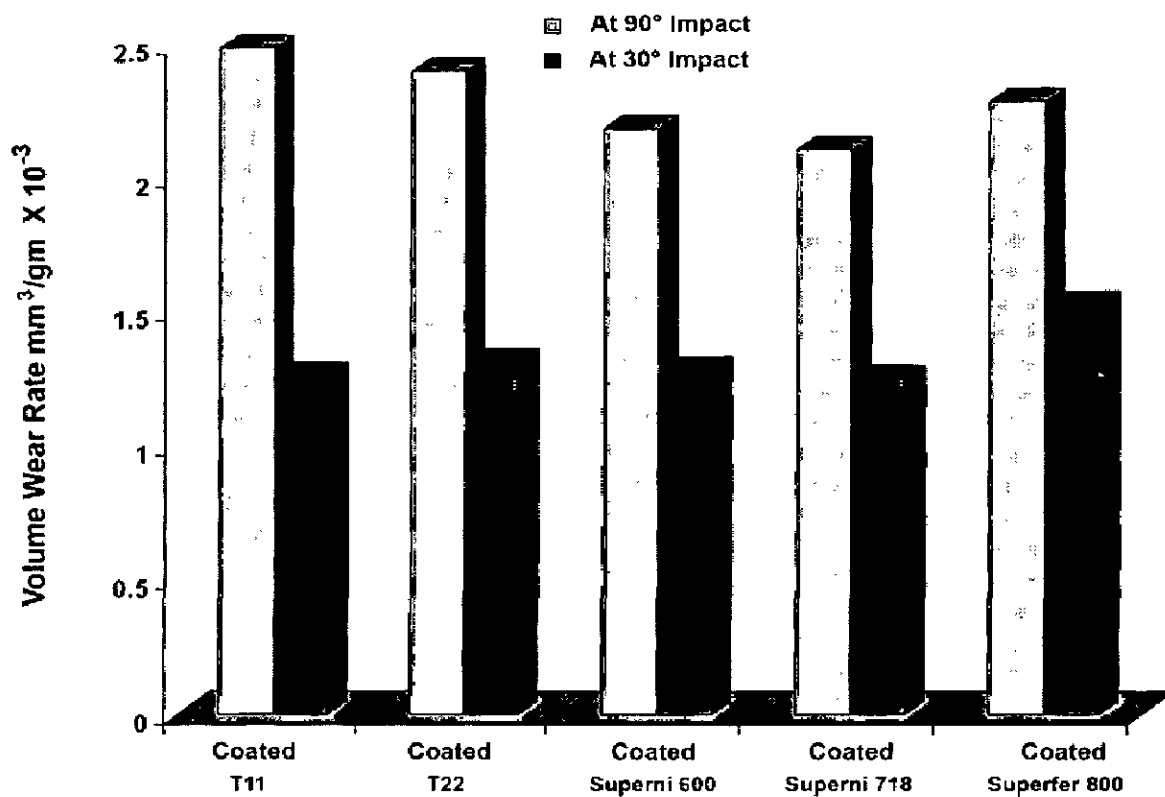


Fig. 5.26: Bar diagram showing the Volume erosion rates of coated alloys under oblique and normal impact at condition 3.

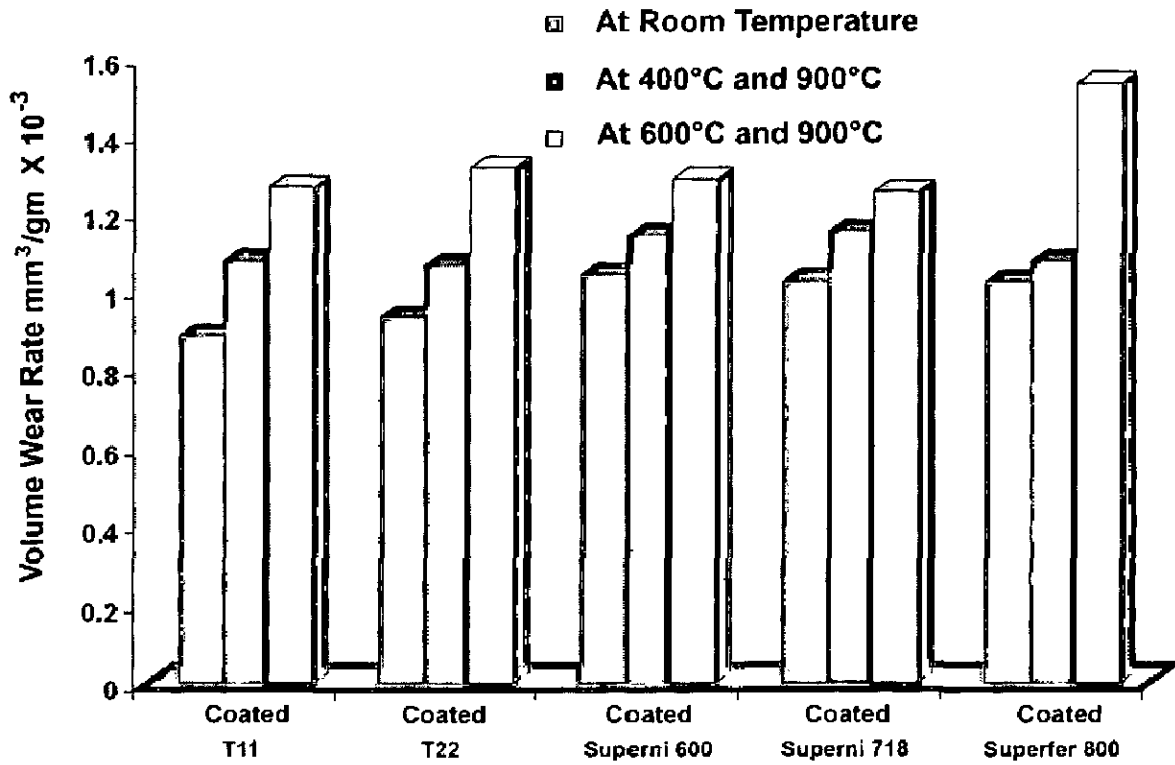


Fig. 5.27: Bar diagram showing the variation in Volume erosion rates of coated alloys at 30° impact angle with change in test temperature

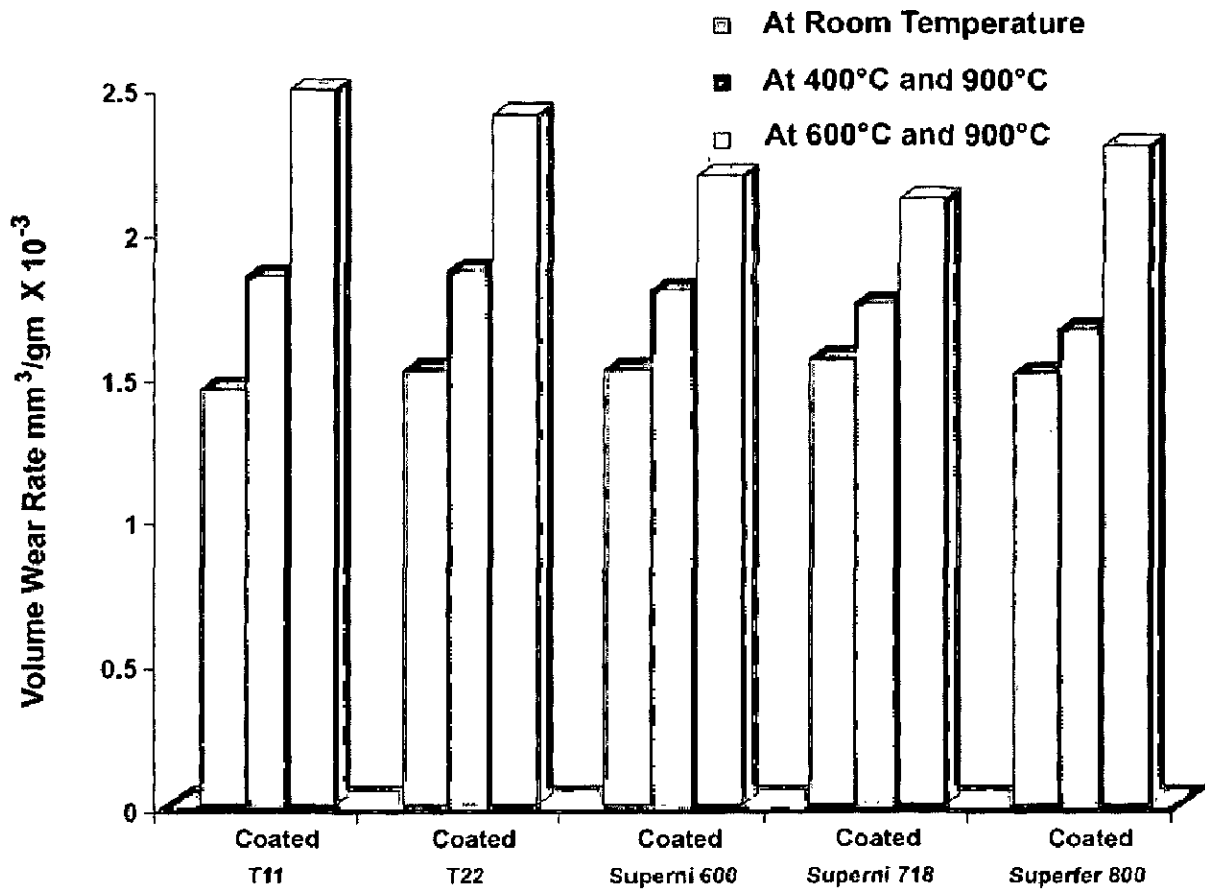


Fig. 5.28: Bar diagram showing the variation in Volume erosion rates of coated alloys at 90° impact angle with change in test temperature

5.1.2.3 SEM/EDX Analysis

SEM/EDX analysis of Al_2O_3 -3 wt% TiO_2 coated alloys is shown in Fig. 5.29 to Fig. 5.34 at condition 1, 2 and 3 respectively. The observations were made on the eroded surface of all the coated alloys at both the impact angles i.e. at 30° and 90° . Scanning electron microscopy (SEM) revealed various erosion mechanisms like chipping, flake formation with brittle fracture, splat debonding and spalling within the coating layer. The micrographs have revealed fracture at the surfaces with impressions of formation of craters with crack network. Fig. 5.29 and Fig. 5.30 shows the scanning electron micrographs with EDX analysis of coated samples after testing at room temperature i.e. at condition 1 at 30° impact and 90° impact respectively. The SEM of each sample revealed cracks, craters and retained erodent fragments on the exposed surface. The cracks propagated with fracture resulting in craters on the surface. Splat debonding is also observed in few cases. Few retained erodent fragments in the exposed coatings can also be seen. In Fig. 5.29 (a), a big crater formed on the eroded surface of coated boiler steel T11 is shown. In case of coated boiler steel T22, there are small craters and chipping is also observed as shown in Fig. 5.29 (b). In coated Superni 600, a big crater is observed with retained erodent fragment as shown in Fig. 5.29 (c). In case of coated Superni 718, small craters and some cracking can be observed from the eroded surface Fig. 5.29 (d). In case of coated Superfer 800, craters were formed on the eroded surface and also splat debonding can also be seen as shown in Fig. 5.29 (e). It is observed from the SEM of the eroded surfaces of coated alloys at 30° impact angle that the material gets removed due to crater formation with brittle fracture as can be observed in Fig. 5.29. The craters formed along with cracks on the surfaces of the coated alloys eroded at 30° impact angle are clearly visible in these micrographs.

While in case of higher impact angles i.e. at 90° , when the eroding particle strikes the surface of a coating at 90° the material is severely damaged and fractured as shown in Fig. 5.30. The subsequent erodent particle impacts cause further cracking and fracture. Brittle fracture at the exposed surface can be seen. In case of coated boiler steel T11, splat debonding and crater formation can be observed as shown in Fig. 5.30 (a) and in case of boiler steel T22 shown in Fig. 5.30 (b), craters and fractured splats were observed.

Brittle fracture on the eroded surface and crack propagation was observed on coated Superni 600 surface after erosion testing as shown in Fig. 5.30 (c). In coated Superni 718, fracture along with crack propagation and craters can be seen on eroded surface shown in Fig. 5.30 (d). Also in case of coated Superfer 800, crater formation and brittle fracture can be seen as indicated in Fig. 5.30 (e).

EDX spectra along with composition at selected points in the surfaces eroded at 90° are shown in Fig. 5.29 and 5.30. The EDX analysis has not detected any elemental peak of substrate alloy i.e. there is no detection of external element except that of powder constituents. In coated Superni 600, Superni 718 and Superfer 800, when analysed at selected points shown in above Fig.s, there is indication of presence of erodent particle in the eroded region.

When the coated substrate temperature was increased to 400°C and the surrounding temperature to 900°C i.e. at condition 2, the SEM/EDX analysis is shown in Fig. 5.31 and Fig. 5.32. At this temperature, the coated alloys showed a clear impact zone from where material has been removed away with the impact of erodent. In coated boiler steel T11, a clear erodent impact zone with crater is visible on the eroded surface as shown in Fig. 5.31(a). In coated boiler steel T22, flakes chipping can be observed as shown in Fig. 5.31 (b). In coated Superni 600, impact zone with cracks and craters can be seen shown in Fig. 5.31 (c) and in coated Superni 718, craters can be observed as shown in Fig. 5.31 (d). In case of coated Superfer 800, some splat debonding and chipping off of the coating can be observed as shown in Fig. 5.31 (e). Presence of more visible fractured splats might be resulting in brittle fracture. In condition 2 erosion tests, it is observed from the SEM of the eroded surfaces of alloys at 30° impact angle Fig. 5.31 that the material removal is less. The micrographs have revealed deformation at the surfaces with formation of shallow craters and flake formation. Splat debonding is also observed in few micrographs. The impacting particle removes material by chip formation, essentially scraping material off the surface of the solid in a manner similar to machining. While in case of 90° impact, there is clear indication of formation of cracks on the surface and impact zone is wider as shown in Fig. 5.32 than that observed at 30° impact. The continuous subsequent impacts of erodent particles caused formation of wide craters. In coated boiler steel T11, crater formation and scale chipping off can be observed on the eroded surface as shown in Fig. 5.32(a). In coated boiler steel T22, an impact zone with wide crater can be seen as shown in Fig. 5.32 (b). In coated Superni 600, impact zone with brittle fracture can be seen shown in Fig. 5.32 (c) and in coated Superni 718, brittle fracture and some fractured splats can be observed as shown in Fig. 5.32 (d). In case of coated Superfer 800, fractured splats can be observed as shown in Fig. 5.32 (e).

EDX spectra along with composition of the condition 2 eroded surfaces at selected regions on are shown in Fig. 5.31 and 5.32. Only coating powder composition has been detected thus indicating the protective nature and integrity of the coating after condition 2 erosion testing.

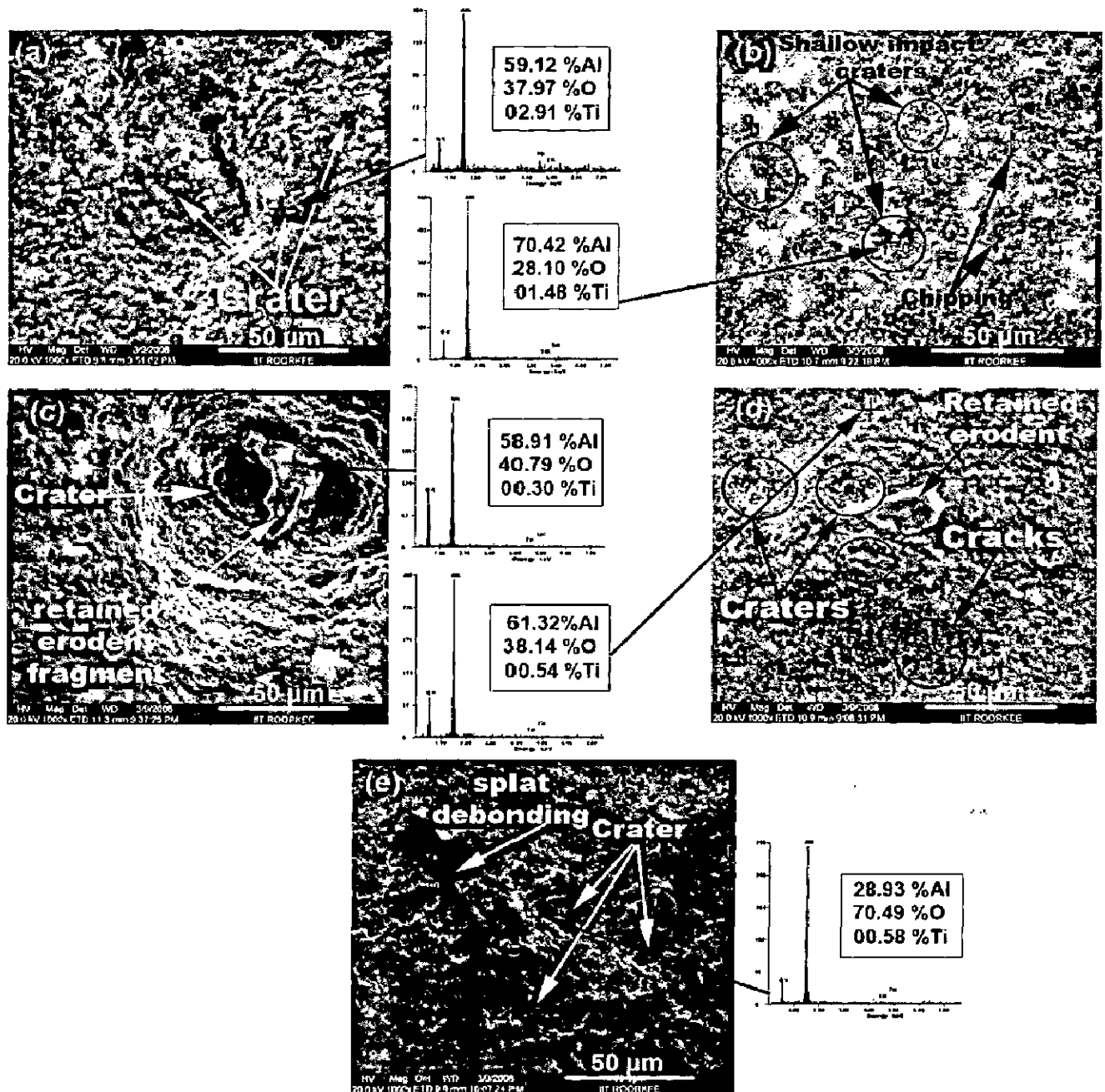


Fig. 5.29: Scanning Electron Macrographs and EDX analysis of Al_2O_3 -3 wt% TiO_2 coated alloys eroded at condition 1 and impact angle of 30°
 (a) Boiler Steel T11 (b) Boiler Steel T22 (c) Superni 600 (d) Superni 718
 (e) Superfer 800

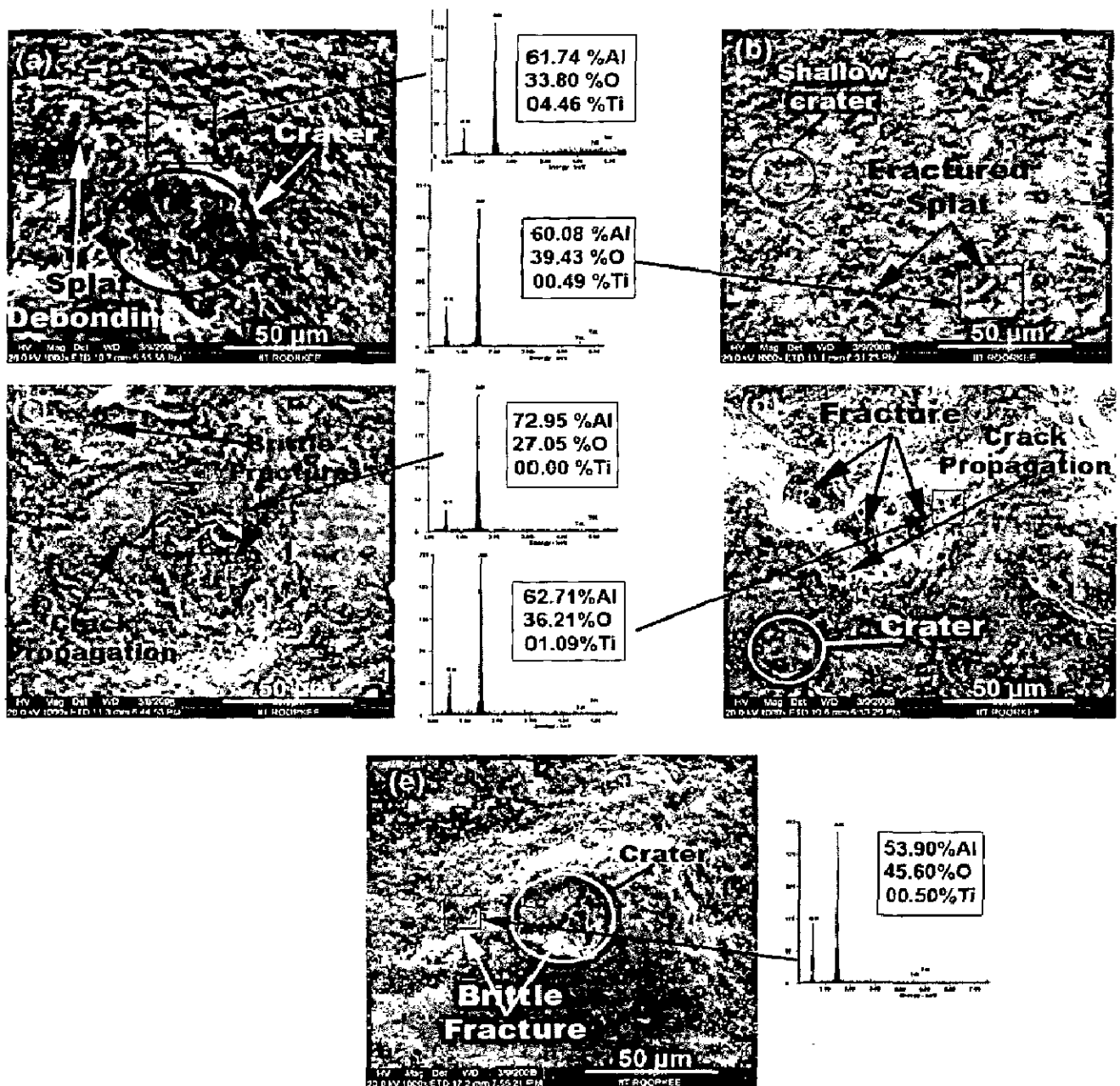


Fig. 5.30: Scanning Electron Macrographs and EDX analysis of Al_2O_3 -3 wt% TiO_2 coated alloys eroded at condition 1 and impact angle of 90°
 (a) Boiler Steel T11 (b) Boiler Steel T22 (c) Superni 600 (d) Superni 718
 (e) Superfer 800

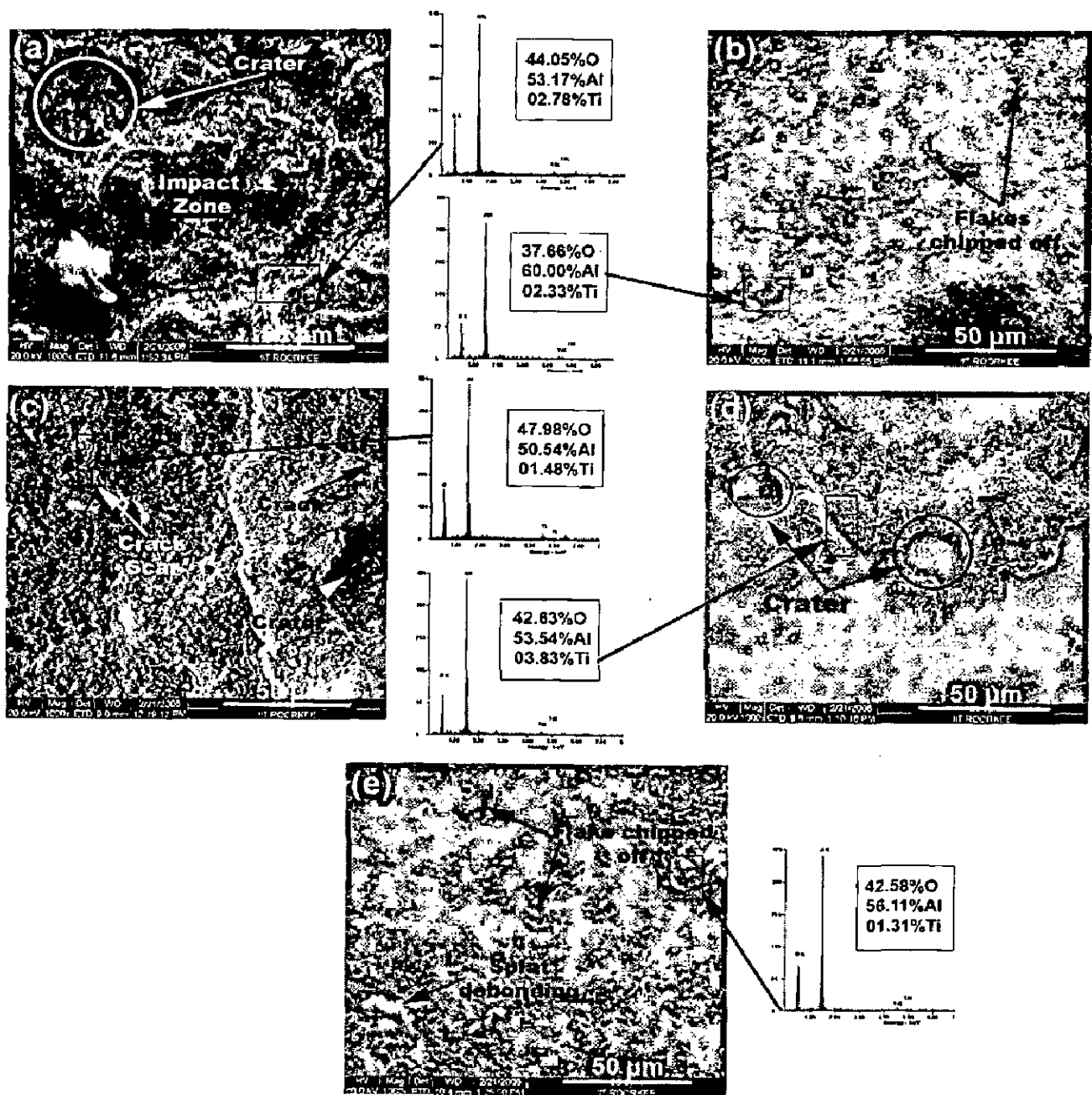


Fig. 5.31: Scanning Electron Macrographs and EDX analysis of Al₂O₃-3 wt% TiO₂ coated alloys eroded at condition 2 and impact angle of 30°
 (a) Boiler Steel T11 (b) Boiler Steel T22 (c) Superni 600 (d) Superni 718
 (e) Superfer 800

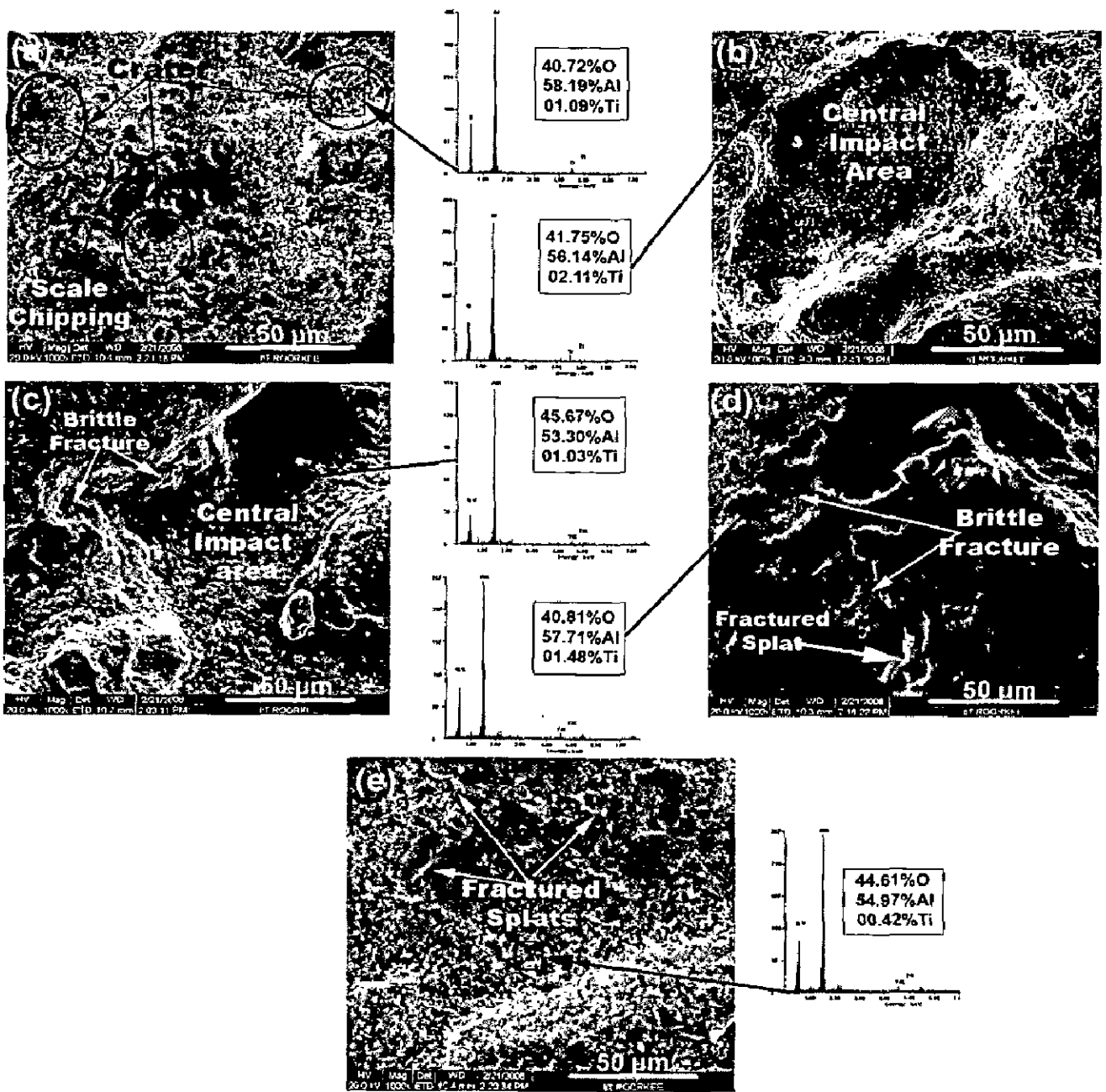


Fig. 5.32: Scanning Electron Macrographs and EDX analysis of Al_2O_3 -3 wt% TiO_2 coated alloys eroded at condition 2 and impact angle of 90°
 (a) Boiler Steel T11 (b) Boiler Steel T22 (c) Superni 600 (d) Superni 718
 (e) Superfer 800

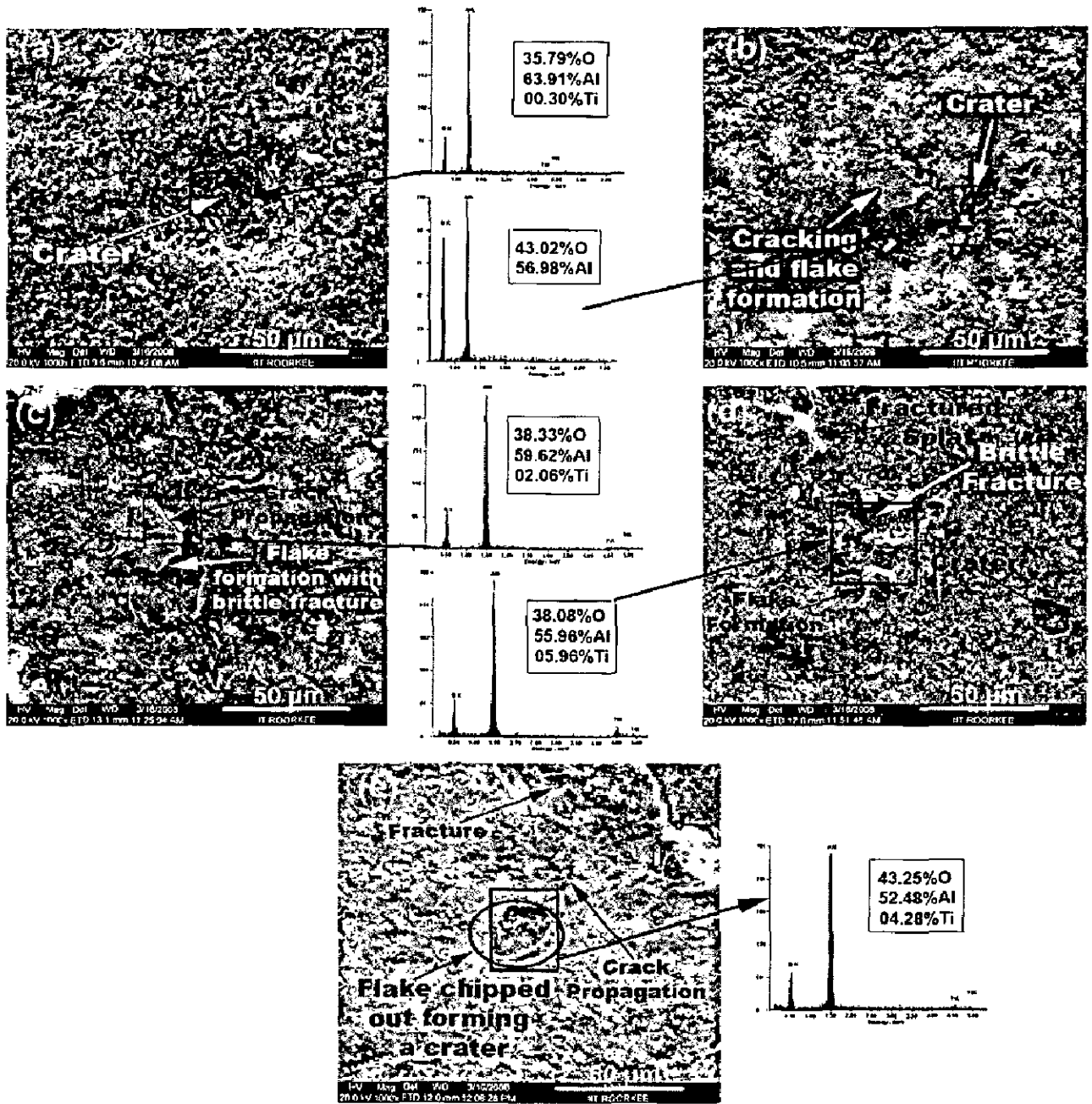


Fig. 5.33: Scanning Electron Macrographs and EDX analysis of Al_2O_3 -3 wt% TiO_2 coated alloys eroded at condition 3 and impact angle of 30°
 (a) Boiler Steel T11 (b) Boiler Steel T22 (c) Superni 600 (d) Superni 718
 (e) Superfer 800

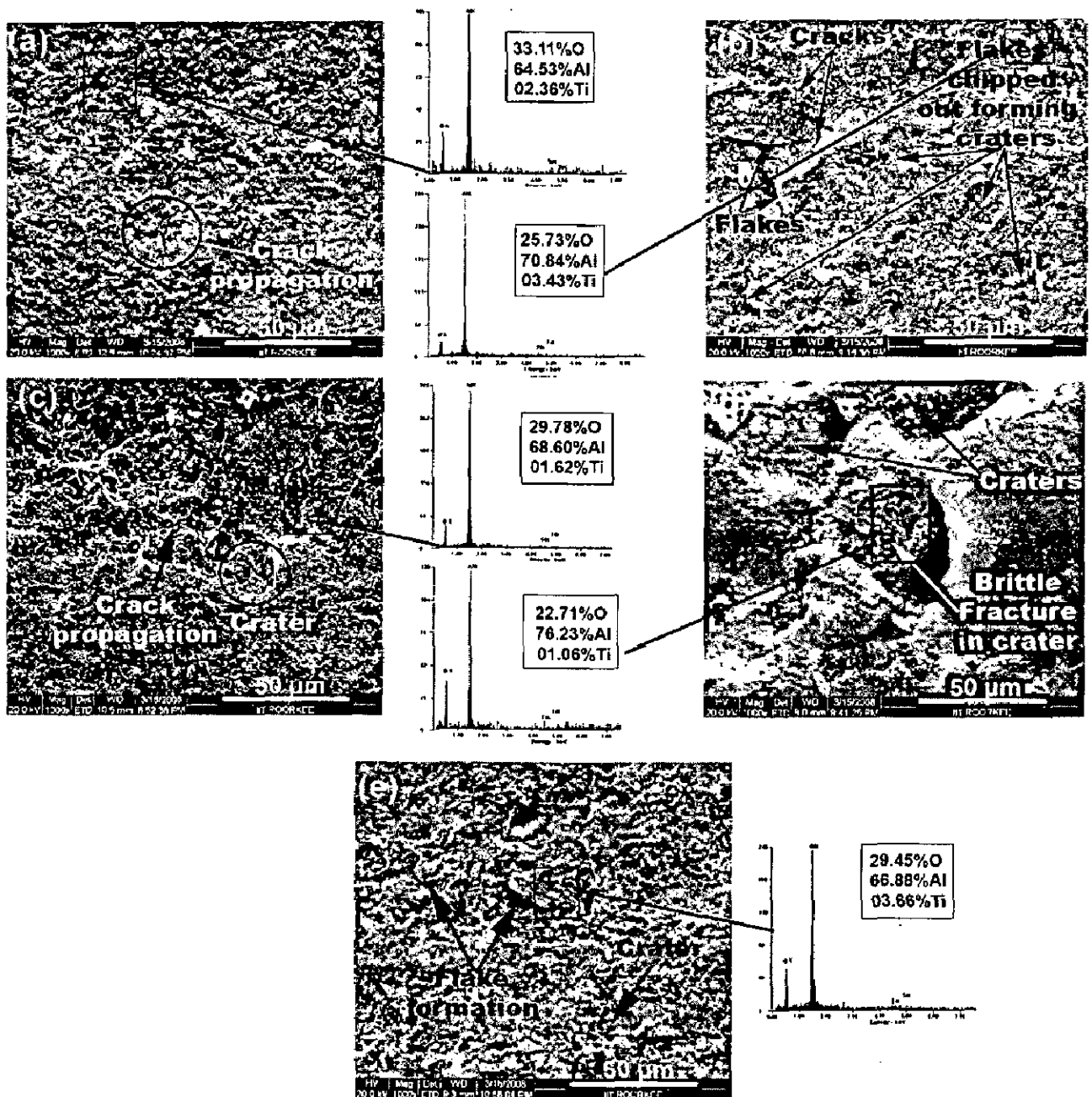


Fig. 5.34: Scanning Electron Macrographs and EDX analysis of Al_2O_3 -3 wt% TiO_2 coated alloys eroded at condition 3 and impact angle of 90°
 (a) Boiler Steel T11 (b) Boiler Steel T22 (c) Superni 600 (d) Superni 718
 (e) Superfer 800

Fig. 5.33 and Fig. 5.34 shows the SEM/EDX analysis of samples after testing at condition 3. There was formation of crack network. In all the coated alloys, there was formation of thick flakes which were removed with the subsequent impacts as the cracks propagated. There is clear indication of severe fracture on the surfaces.

In condition 3 erosion tests, it is observed from the SEM of the eroded surfaces of coated alloys at 30° impact angle that the material gets removed due severe brittle fracture. Brittle fracture zone with cracks are visible on the eroded surfaces as shown in Fig. 5.33.

In coated boiler steel T11, crater with brittle fracture is visible on the eroded surface as shown in Fig. 5.33(a). In coated boiler steel T22, cracking and flake formation can be observed as shown in Fig. 5.33 (b). In coated Superni 600, flake formation with brittle fracture and with cracks and crack propagation can be seen shown in Fig. 5.33 (c) and in coated Superni 718; craters, brittle fracture, flake formation and fractured splats can be observed on eroded surface as shown in Fig. 5.33 (d). In case of coated Superfer 800, flake chipped out resulting in formation of crater and fracture and crack propagation can be observed as shown in Fig. 5.33 (e)

In case of 90° impact, there is clear indication of formation of cracks on the surface as shown in Fig. 5.34. The propagation of cracks leads to surface chipping and ultimately surface fracture. The micrographs have indicated that the craters are developed as a result of impact by erodent particles and severe brittle fracture along with flake formation and subsequent crack propagation.

In coated boiler steel T11, crack propagation can be observed on the eroded surface as shown in Fig. 5.34(a). In coated boiler steel T22, cracks and flakes can be observed and crater formed by chipping out of flakes as shown in Fig. 5.34 (b). In coated Superni 600, crack propagation and crater formation can be seen shown in Fig. 5.34 (c) and in coated Superni 718, crater formation and brittle fracture inside crater can be observed as can be observed from Fig. 5.34 (d). In case of coated Superfer 800, flake formation, craters and fracture on the eroded surface can be observed as shown in Fig. 5.34 (e)

Fig. 5.33 and Fig. 5.34 shows the EDX analysis of the eroded samples at condition 3 and impact angles 30° and 90° respectively. The EDX analysis of coated alloys eroded at both angles has indicated the compositions of the coating powder. The peaks of Al and Ti along with O have been detected. There is no indication of the elemental peaks of the substrate alloy confirming the protective nature of the alumina titania coatings. The erosion phenomenon is only confined to surface of the coatings and has not penetrated into the coating in any case. At certain selected eroded regions only Al, Ti and O have been detected indicating that coating has protected the substrate alloys very well.

5.1.3 Discussion

In erosion testing, the material is eroded by continuous impact of erodent particles, the erosion starts at the centre first, and then proceeds towards the edges of the samples. The shape of developed scar depends on the angle of impact. The erosion scar produced, in general, on all the surfaces of the tested samples at both the impact angles have been schematically illustrated in Fig. 5.35. When erodent strikes the surface at an impact angle of 30° , material is eroded creating an elliptical shape depression; while at a 90° impact angle, material is eroded forming a circular depression. It has been observed that all the coated alloys have maintained adherence with the substrates under study during the erosion testing at all the temperatures.

5.1.3.1 Uncoated alloys

At room temperature testing, the boiler steels under study have shown higher erosion rate than the superalloys. The erosion rate in terms of volume loss for the substrate boiler steels T11 and T22 is $7.052 \times 10^{-3} \text{mm}^3/\text{gm}$ and $6.452 \times 10^{-3} \text{mm}^3/\text{gm}$ while superalloys have given very low erosion rates and lie in a narrow range of $1.211-1.947 \times 10^{-3} \text{mm}^3/\text{gm}$. The generalized erosion behaviour of the all the alloys was ductile in nature as observed from their scanning electron micrographs. Based on the present data the erosion rates for 30° impact angle at room temperature can be arranged in following order:

T11>T22>Superfer 800 > Superni 718 > Superni 600

From the above it can be inferred that the relative erosion resistance of Superfer 800 at oblique impact angle is least among the superalloys under study, while Superni 600 has shown maximum erosion resistance and boiler steels in comparison have shown very inferior resistance. The erosion rates for superalloys at 30° impact angle are low as compared to boiler steels but the Superfer 800 superalloy has shown greater erosion rate than the other superalloys.

In case of normal impact, the erosion rate is less as compared to the erosion rate at 30° impact and the sequence of erosion rate of alloys based on the data at normal impact angle is:

T22>T11>Superfer 800 > Superni 600 > Superni 718

From the present study, it can be inferred that, the erosion rates of alloys were greatest at 30° impact angle, which is the characteristic erosion behaviour of ductile material. From this sequence, it can be inferred that the relative erosion resistance of Superfer 800 is minimum among the superalloys under study, while Superni 718 has shown maximum erosion resistance at normal impact angle and T22 has got more erosion rate than T11.

Tabakoff (1995) also reported the similar behaviour for cobalt-based alloy X-40. He reported the ductile erosion behaviour of the cobalt-based alloy with maximum erosion at 45°

impact angle. From SEM observations of all the eroded alloys at 30° impact angle, it can be inferred that the cutting and ploughing play the dominant role in erosion of materials. Lips and cutting scars are visible in most of the micrographs of the eroded alloys at 30° impact angle, thus indicating that the cutting mechanism is predominant in material removal. At room temperature, there is no formation of oxide scale so erosion phenomenon is purely metallic or substrate dominated. Schematic metallic erosion is shown in Fig. 5.36

Similar erosion behavior of ductile materials has been reported by Hutchings (1992), Sidhu et al., (2007) and Kumar et al., (2008). When erodent particles strike the surface continuously, it results in formation of craters. Further particle impact causes plastic deformation of the new crater being formed on the unsupported surface of the already existing crater.

Tilly, (1973) and Levy (1986) has explained that when the eroding particle strikes the surface of a ductile material at or near 90° the material is extruded to the edge of the damage zone to form lips that will then be vulnerable to subsequent impacts. These subsequent impacts will cause further deformation, extrusion and work hardening, until fracture occurs and the material is completely lost from the surface. A secondary stage can also occur when the impacting particles are brittle and fracture on impact, resulting in further secondary impact damage at a reduced velocity and lower impact angles. At normal impact angle, the erosion occurred by the platelet mechanism in all the alloys in general, similar to that described by Hutchings and Levy (1989). They reported that in the steady state condition, the three phases occur simultaneously at different locations over the surface. In the initial phase the impacting particle forms a crater, and material is extruded or displaced from the crater to form a raised lip or mound. In the second phase the displaced metal is deformed by subsequent impacts; this may lead to lateral displacement of the material, and can be accompanied by some ductile fracture in heavily strained regions. Finally, after a relatively few impacts, the displaced material becomes so severely strained that it is detached from the surface by ductile fracture. The craters and lips formed by the impact of erodent particles on the surface of alloys are clearly visible in Fig. 5.13. The general erosion mechanism is thus similar to one defined by Hutchings and Winter (1974) in which material is raised above the mean surface, followed by deformation during subsequent impacts and ultimate removal of the deformed material.

Most of the metallic materials, irrespective of temperature of erosion, exhibit a ductile behaviour, i.e. a maximum erosion rate at oblique impact angles (Tabakoff W and Vittal, 1983) The erosion of soft, tough materials is predominantly ductile and material loss can occur in the ways like: cutting wear due to impact at low angles (Finnie, 1960), and extrusion at high angles. Erosion of ductile materials is essentially a combination of the two processes,

with one being dominant over the other depending on impact angle and material properties and particle properties and shape. So in solid particle erosion, material removal by impacting particles takes place by:

- (i) material removal due to cutting wear,
- (ii) material removal due to repeated plastic deformation

It has been observed by that for low values of impingement angle, the erosion rate increases with an increase in the impingement angle, and the maximum erosion rate occurs with impingement angle between 20°- 40°. Thereafter, the erosion rate decreases (Mbabazi et al., 2004 and Das et al., 2006)

In Plastic deformation wear, during particle impact, loss of material because of particle erosion may occur by a combined extrusion-forging mechanism. Platelets are initially extruded from shallow craters made by the impacting particle. Once formed, the platelets are forged into a strained condition, in which they are vulnerable to being knocked off the surface in one or several pieces. Owing to the high strain rates, adiabatic shear heating occurs in the surface region immediate to the impact site. Beneath the immediate surface region, a work hardened zone forms, as the kinetic energy of the impacting particles is enough to result in a considerably greater force being imparted to the metal than is required to generate platelets at the surface. When the surface is completely converted to platelets and craters and the work-hardened zone reaches its stable hardness and thickness, steady state erosion begins. The reason why the steady state erosion rate is the highest is because the subsurface cold-worked zone acts as an anvil, thereby increasing the efficiency of the impacting particles to extrude-forge platelets in the now highly strained and most deformable surface region. This cross-section of material moves down through the metal as erosion loss occurs. In the platelet mechanism of erosion, there is a localised sequential extrusion and forging of metal in a ductile manner, leading to removal of the micro segments thus formed (Das et al., 2006)

When erosion testing temperature was raised to 400°C and surrounding atmosphere to 900°C i.e. at condition 2, the erosion rate has shown an increase. The erosion rate in terms of volume loss per unit of erodent for the substrate boiler steels T11 and T22 is $9.947 \times 10^{-3} \text{mm}^3/\text{gm}$ and $9.127 \times 10^{-3} \text{mm}^3/\text{gm}$ while in case of superalloys erosion rates are found to be in a range of $1.711\text{-}1.977 \times 10^{-3} \text{mm}^3/\text{gm}$. Based on the present data the erosion rates for 30° impact angle at condition 2 temperature can be arranged in following order:

T11>T22>Superfer 800 > Superni 718 > Superni 600

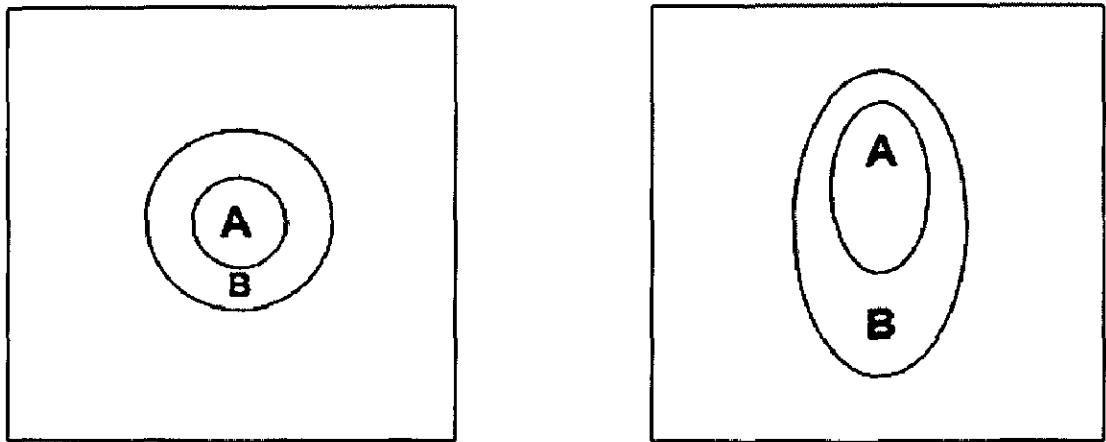


Fig. 5.35: Schematic diagram showing the erosion scar produced in general on the eroded surface at an impact angle of 90° and 30° ; Mark "A" represents a localized region of material removal and Mark "B" represents the peripheral region of the elastically loaded material

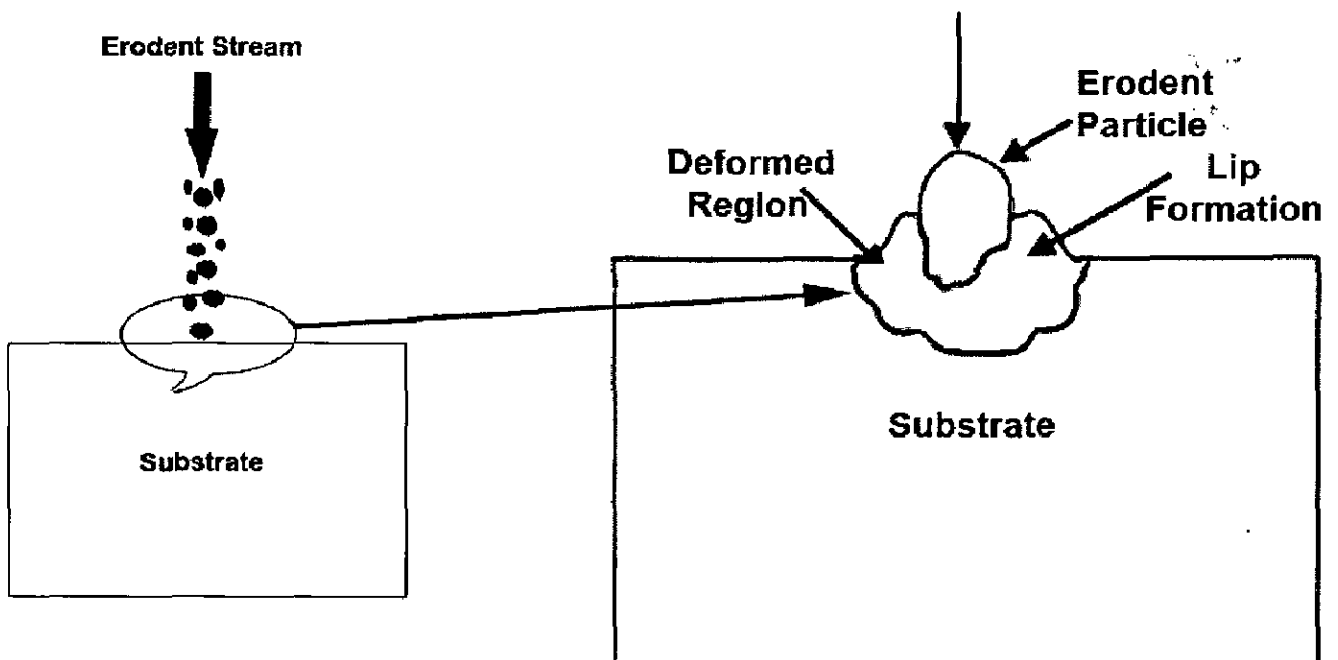


Fig. 5.36: Schematic diagram showing the metallic erosion

Here also from the above data, it can be inferred that the relative erosion resistance of Superfer 800 at oblique impact angle is least among the superalloys under study, while Superni 600 has shown maximum erosion resistance. Here at this temperature, erosion rate of all the alloys have increased substantially except that of Superfer 800 superalloy where there is only marginal increase in erosion rate.

In case of normal impact, the erosion rate is less as compared to the erosion rate at 30° impact and the sequence of erosion rate of alloys based on the data at normal impact angle is:

T22>T11>Superfer 800 > Superni 600 > Superni 718

The erosion rates of alloys were greatest at 30° impact angle, which is the characteristic erosion behaviour of ductile material. From this sequence, it can be inferred that the relative erosion resistance of Superfer 800 is minimum among the superalloys under study, while Superni 718 has shown maximum erosion resistance at normal impact angle.

At low erosion temperatures, at high impact velocities and feed rates, there is no oxide scale. Even if there is any oxide scale, it will be very thin and it will be able to deform in the same manner as that of the substrate target. The works of Shida and Fujikawa (1985), Singh and Sundararajan (1990) Levy et al., (1986) can be considered elevated temperature erosion of metals with minimum or negligible oxidation. Under such circumstances, erosion takes place from the metallic surface and this mechanism of erosion is called metal erosion. The erosion behaviour in this regime is similar to the ambient temperature erosion behaviour of metallic materials. The erosion response in the metal erosion regime is ductile.

The probable erosion mechanism at low metallic temperature is schematically shown in Fig. 5.37. It is almost similar to metallic erosion at room temperature. In the metal erosion regime, there are two modes by which materials can be removed. These modes are ploughing and cutting. In general, when a particle is in contact with a target at positive rake angle, the cutting mode operates. On the other hand, the ploughing mechanism operates at negative rake angle. Cutting mechanisms result in generation of new surfaces while the ploughing mechanism involves the displacement and extrusion of the material with no new surface generation. In addition, the cutting mode is more efficient than the ploughing mode when considered in terms of energy consumed per unit volume removal of the target material.

In metals and alloys, during erosion, once the lip is formed, it is fractured by several modes. In the case of ductile metals like copper, brass, aluminium and iron, the lip fracture occurs by necking, and the resulting fracture is ductile (Quadir and Schewmon 1981; Christman and Schewmon, 1979). This mode of lip fracture is shown schematically in Fig. 5.38. The two modes of material removal considered above involve the fracture of pre-existing lips.

When erosion testing temperature was raised to 600°C and surrounding atmosphere to 900°C i.e. at condition 3, the erosion rate has shown further increase. The erosion rate in terms of volume loss for the substrate boiler steels T11 and T22 is $12.245 \times 10^{-3} \text{mm}^3/\text{gm}$ and $13.486 \times 10^{-3} \text{mm}^3/\text{gm}$ while superalloys have given erosion rates in a range of $2.466\text{-}2.622 \times 10^{-3} \text{mm}^3/\text{gm}$. Based on the present data the erosion rates for 30° impact angle at condition 3 can be arranged in following order:

T11>T22>Superfer 800 > Superni 718 > Superni 600

At condition 3, the volume erosion loss has increased almost double as that at room temperature. Here also from the above data, it can be inferred that the relative erosion resistance of Superfer 800 at oblique impact angle is least among the superalloys under study, while Superni 600 has shown maximum erosion resistance. Here at this temperature, erosion rate of all the alloys have increased substantially except that of Superfer 800 superalloy where there is only marginal increase in erosion rate.

In case of normal impact, the erosion rate is less as compared to the erosion rate at 30° impact and the sequence of erosion rate of alloys based on the data at normal impact angle is:

T11>T22 >Superfer 800 > Superni 718 > Superni 600

From the present study, it can be inferred that, the erosion rates of alloys at condition 3 were greatest at 30° impact angle, which is the characteristic erosion behaviour of ductile material. From this sequence, it can be inferred that the relative erosion resistance of Superfer 800 is minimum among the superalloys under study, while Superni 600 has shown maximum erosion resistance at normal impact angle and T22 has got more erosion rate than T11.

At high temperature erosion is affected by oxidation. Each erodent impact event removes the scale down to the substrate-scale interface. The scale thickness is typically of the same order of magnitude as the depth of indentation, while the cross-sectional area of the oxide chip is of a similar size to the cross-section of the impacting erodent particle. Fig. 5.39 shows schematically oxide removal from the exposed surface at high temperature. Erosive impact induces stresses in the scale layer, reducing the critical thickness for spallation and thereby accelerating the oxidative attack.

At this temperature, erosion takes place from oxide scale only. Under such conditions, a thick oxide scale is formed on the target material during erosion and the deformed zone formed due to impact is confined within the oxide scale. The erosion behaviour from the oxide scale is characterized by a brittle erosion response, strong velocity dependence and particle feed rate independent of the erosion rate. This erosion mechanism is termed oxide erosion. In oxide erosion, material removal occurs with the formation of intersecting cones and radial cracks, which nucleate from pre-existing flaws once a critical tensile stress is exceeded. At an

intermediate temperature, impact velocity and particle feed rate, an oxide scale of intermediate thickness is formed. However, the depth of the deformed zone extends to the metallic substrate beyond the oxide scale. Consequently, the oxide scale beneath the eroding particle tends to crack, gets pushed down into much softer base material and in the process the softer base material gets squeezed out onto the top surface through the cracks in the oxide scale. Over a period of time, the repetition of such a process during each impact causes the formation of a composite layer comprising the bulk metal and broken pieces of oxide scale. Erosion takes place from this composite layer. This probable erosion mechanism is presented schematically in Fig. 5.40 and is termed as oxidation affected erosion. The interesting aspect of oxidation affected erosion is that the volume fraction of the oxide in the composite layer is a function of erosion conditions such as temperature, impact velocity and particle feed rate. As a result, the erosion behaviour in the oxidation affected erosion regime can vary from a ductile to a brittle response depending on the amount of oxide scale present in the composite layer. Further, unlike in the case of metal erosion or oxide erosion, the oxidation affected erosion rate depends strongly on the test temperature and particle feed rate (Roy, 2006).

Fig. 5.10 shows the variation in volume erosion rates of substrate alloys at 30° impact angle with change in test temperature. There is clear dependence of erosion rate on the temperature. As the testing temperature increases from room temperature at 30° impact, the erosion rate increases very fast and is almost double when calculated at 600°C. While in case of 90° impact, erosion volume rate has increased but not to the extent as observed in 30° impact angle as shown in Fig. 5.11. It has been observed that erosion rates of substrate alloys impacted at low angles increases steeply as the temperature increases. So the temperature effect can be demonstrated on the basis of the observation that the erosion rate at acute impingement angle increases significantly with temperature, suggesting that alloys tends to show behaviour more typical of a ductile material at elevated temperatures. A tendency for erosion rate to increase with temperature has been observed in all alloys. Thus, it may be concluded that the erosion rate of alloys impacted at all angles definitely increases as the temperature is increased but effect at acute angles is dominant. Also, the rate of erosion depends upon the type of alloy and its composition. The erosion behaviour of metallic materials at elevated temperature is governed by the nature of interaction between erosion and oxidation. The nature of interaction between erosion and oxidation in turn depends on the thickness, morphology, adherence and the toughness of the oxide scales that form in these materials. It has been observed that erosion rates of steels impacted at low angles increase as the temperature of the steel increases. Also, Hutchings & Winter (1974) concluded that the mechanism of material removal was one of shearing of the top layers of the target surface in

the direction of motion of the projectiles. They carried out experimental investigations to determine the effect of erosion owing to particle orientation during oblique impact of angular particles on lead and mild steel targets. They noted that for particle incidence angles close to 90°, erosion occurred by plastic deformation of the target surface.

It is observed that a severe plastic deformation occurs in the zone around the point of impact of each particle in the form of lip and platelets which are detached on further impacts resulting in mass loss in both the oblique and normal impacts. Similar mechanism of material removal has also been observed by Levy et al., (1984). Levy described it in terms of three distinct phases that occur sequentially in ductile erosion mechanism. In first phase, an erodent particle impact forms a crater and material is extruded from crater to form a raised lip. In next phase, the displaced metal or lip is deformed by subsequent impacts and finally after few impacts, the displaced metal becomes so severely strained that it is detached from the surface by ductile fracture.

It is noted that erosion rates at low impingement angles increase significantly with increasing temperature, but at high impingement angles the effect of temperature is less insignificant. The exposure temperature, 400°C and 600°C with surrounding air temperature of 900°C of this study was chosen because it is a target temperature for eroded parts in new and future combustion plants, e.g. superheater tubes positioned within the loop seal of a circulating fluidized bed combustor (Norling and Olefjord 2003). It has been suggested by Hjörnhede et al., (2000) and Norling and Olefjord (2000) that the eroding particles cause crack formation in the oxide and that oxygen or other oxidising gases are transported via these cracks through the oxide towards the metal.

As the temperature is raised to 400°C substrate and 600°C surrounding, there is formation of thin oxide scale which plays little role in erosion rate increase. However, as the temperature is further increased to 600°C substrate and 900°C surroundings, the erosion rate increases due to the formation and easy removal of the oxide scale - oxide modified erosion. Especially in this region, the erosion rate is dependent on the properties of the composite oxide/substrate, the ease with which the scale is removed and the oxidation kinetics. The third regime is where the oxide forms sufficiently quickly and is thick enough that the impact of particles does not expose the base metal. Thus only oxide is removed during impacts - oxide dominated erosion. The temperatures at which these various regimes operate depend on a number of factors, which include particle size, velocity and flux as well as the composition of the alloy, which influences oxidation rates.

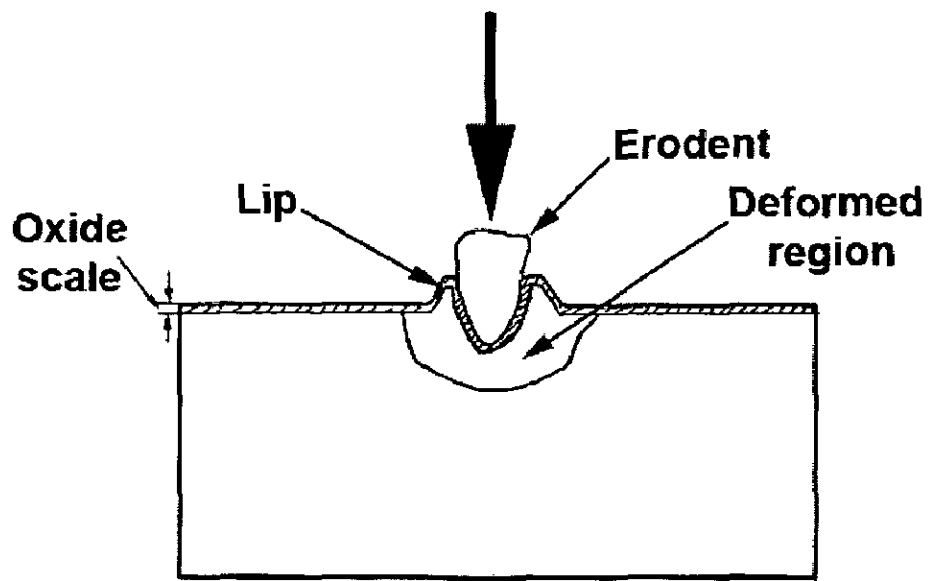


Fig. 5.37: Schematic diagram showing probable erosion mechanism at low temperature.

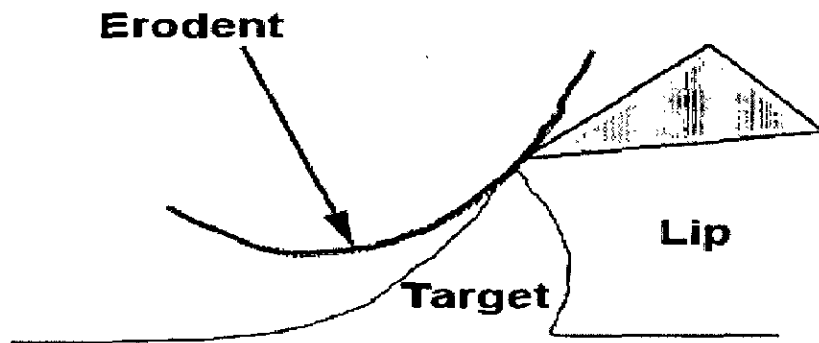


Fig. 5.38: Lip fracture mode in metallic erosion

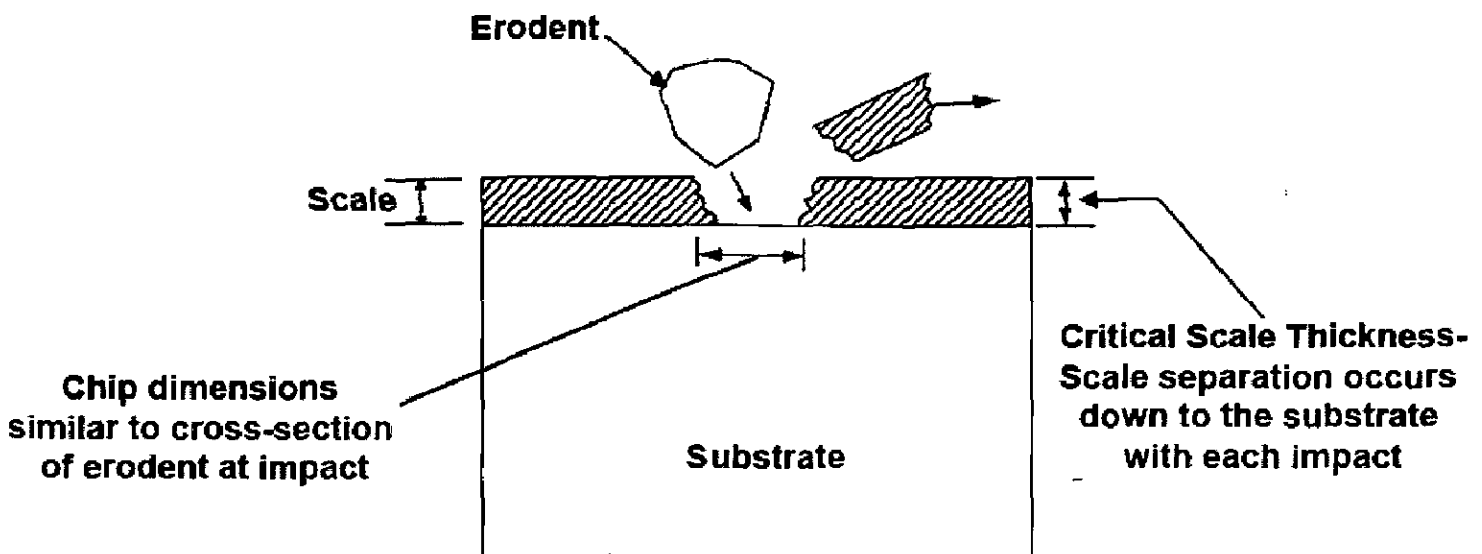


Fig. 5.39: Schematic oxide removal from the exposed surface at high temperature

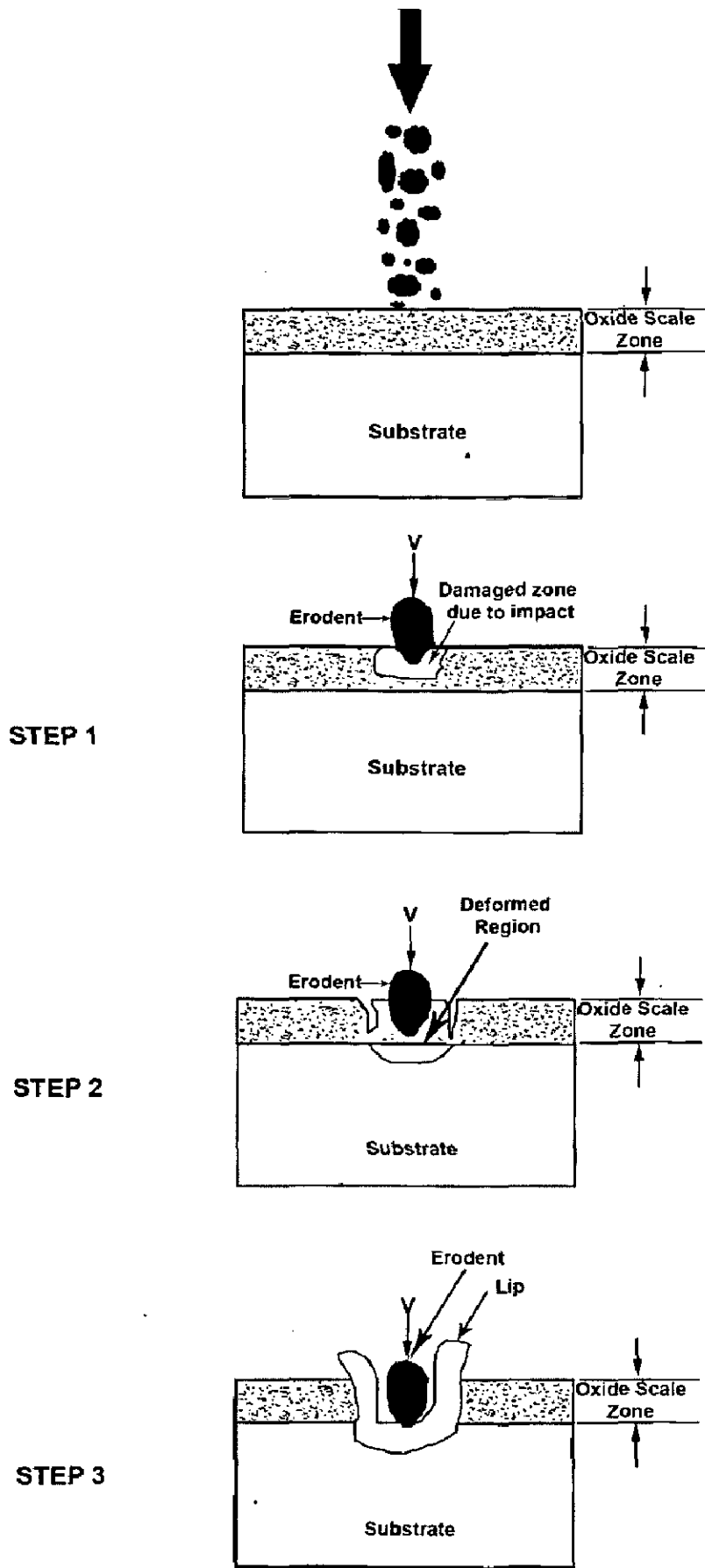


Fig. 5.40: Schematic diagram showing probable mechanism of oxidation affected Erosion showing deformed zone formed due to erodent impact.

5.1.3.2 Al_2O_3 -3wt% TiO_2 coated alloys

As ceramics are brittle in nature so erosion of ceramics is identified as a complex mechanism in which different stages like tribochemical reaction, microfracture etc. operate. In case of Ceramics (Brittle Materials) material loss in solid particle erosion occurs predominantly through the formation and interaction of a subsurface micro crack network (Guessasma et al., 2006). The material removal is related to the formation and propagation of cracks. For the ceramic coatings the fracture occurs at interface between flattened ceramic particles i.e. splats. The cracks develop on the surface when the surface stresses reach a critical value to initiate microcracking. When these cracks propagate and intersect with the surface, material is lost. Hence for a brittle material the erosion resistance is a function of its resistance to crack.

A good number of reports are available on erosion behaviour of alumina coatings. The resistance to erosion of such coatings depends upon shape, size, and hardness of erodent particles, particle velocity, angle of impact and the presence of cracks and pores (He et al., 1993; Ajayi and Ludema, 1991; Mcpherson, 1989; Wang, 1996; Hawthorne et al., 1997).

Zhang et al. 1997 examined room temperature solid particle erosion of Alumina coatings and observed that erosion rate is maximum for an impact angle of 90° . The failure is by the progressive removal of splats and can be attributed to the presence of defects and pores in the inter-splat regions.

Representative erosion scar on coating is shown schematically in Fig. 5.41 in which various erosion phenomenon like chipping; cracking occurring in coating can be visualized. The coating erosion is dependent on angle of impingement; Fig. 5.42 shows schematically the fracture of coatings dependent on impact angle. It is shown schematically how an impinging solid particle can damage coating surfaces. The mechanism of erosion of brittle materials is quite different from that of ductile materials. Brittle erosion is due to the crack formation in the surface and the resultant chipping of the material. The material is removed by the intersection of cracks, which radiate out from the point of impact of the eroding particle. During particle impact upon a ceramic surface, median and radial cracks develop at the impact site. Upon rebound of the particle i.e. unloading of the impact site, lateral cracks develop parallel to the surface and finally curve and propagate towards the surface, leading to chipping and loss of material. Erosion in plasma sprayed ceramics has been attributed to the failure of individual splat boundaries. Although surface cracks have been seen to form in VPS coatings, similar to behaviour in sintered ceramics, propagation from one splat to another is limited. Subsurface damage of VPS alumina involves neither radial nor median cracks.

Instead, cracks more similar to lateral fractures develop around impressions, in which a consolidated region immediately beneath the fracture is attributed to splat debonding. As inter-splat bonding is increased, the damage mechanisms start to resemble those observed in bulk ceramics. (Ramm et al., 1993)

The modes of deformation and fracture depend on the particle velocity, shape, and its mechanical properties relative to those of the target material. Blunt particles traveling at low velocities set up hertzian stress fields in the target, which initiate cone cracking, while angular particles traveling at high velocities produce inelastic deformation zones and initiate median and lateral cracking (Wiederhorn and Hockey 1983).

In the present investigation, the specimens showed brittle erosion morphology as indicated by their cracked and chipped surfaces. Brittle erosion occurred by a cracking and chipping of fractured and loosened pieces. Cracks form in the intermediate surface region of brittle materials on an erodent impact. Crack formed in bulk of a brittle coating due to particle impingement is shown schematically in Fig. 5.43.

Cracking or plastic deformation initiates near the splat boundary, generating small chips of material. Schematic splat edge chipping mechanism is shown in Fig. 5.44. Continued erosion leads to crack propagation into the splat and chipping or plastic deformation of the exposed splat edge. Alternatively repeated impact may lead to subsurface inter-splat crack propagation.

It is clear from SEM shown in Fig. 5.29 that there were some radial and lateral cracks as well as the fractured, loosened pieces on the eroded specimens' surfaces. Some erodent particles were also deposited on these surfaces. Cracking is thought to be initiated at the "splat boundary" during impact of erosive particles. Under continual impacting of particles, the radial and lateral cracks were developed, and then fractured and loosened pieces were chipped off. Finally, many small voids and pits formed. Similar observations have been reported by Lin et al., (2004), Habib et al., (2006) and Branco et al., (2004).

At room temperature testing i.e. at condition 1, scanning electron micrographs of the eroded samples as seen in Fig. 5.30 Al_2O_3 -3 wt % TiO_2 coating showed evidence of splat removal with small fragmented particles, and no plastic deformation was observed which explains the high resistance to wear.

The subsurface cracks produced by erosion tend to propagate along the boundary between material that has been completely molten during thermal spraying, i.e., the outer regions of the particle, and the inner core.

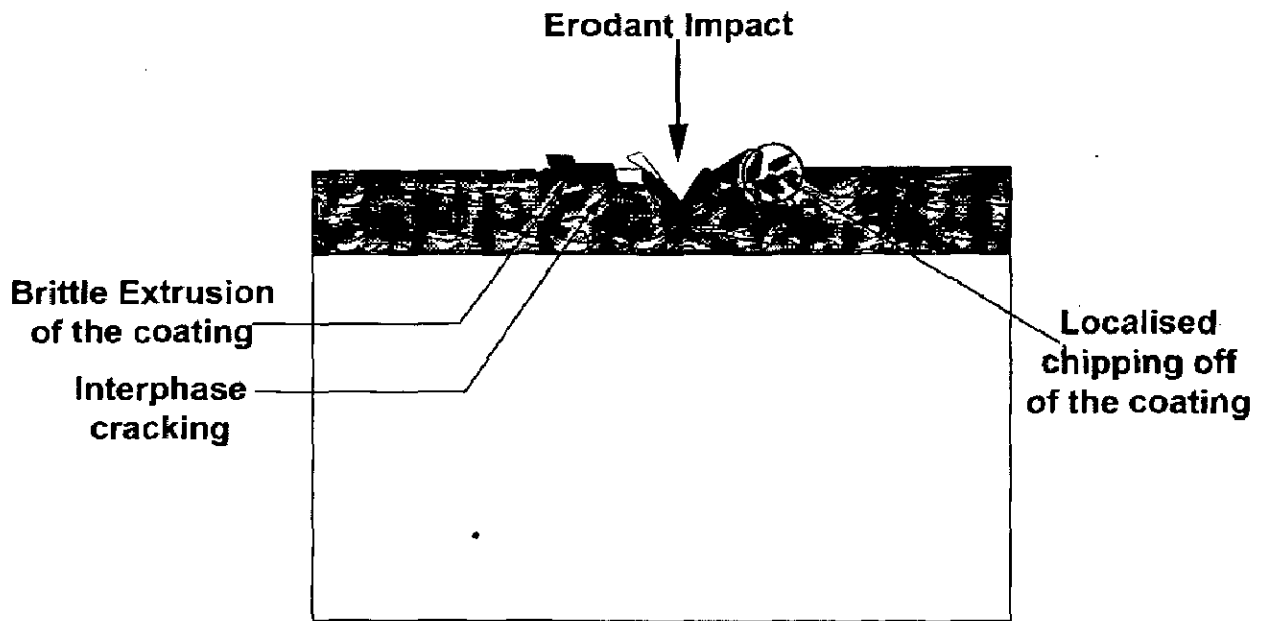


Fig. 5.41: Schematic representative erosion scar on coating showing different modes of erosion in coating

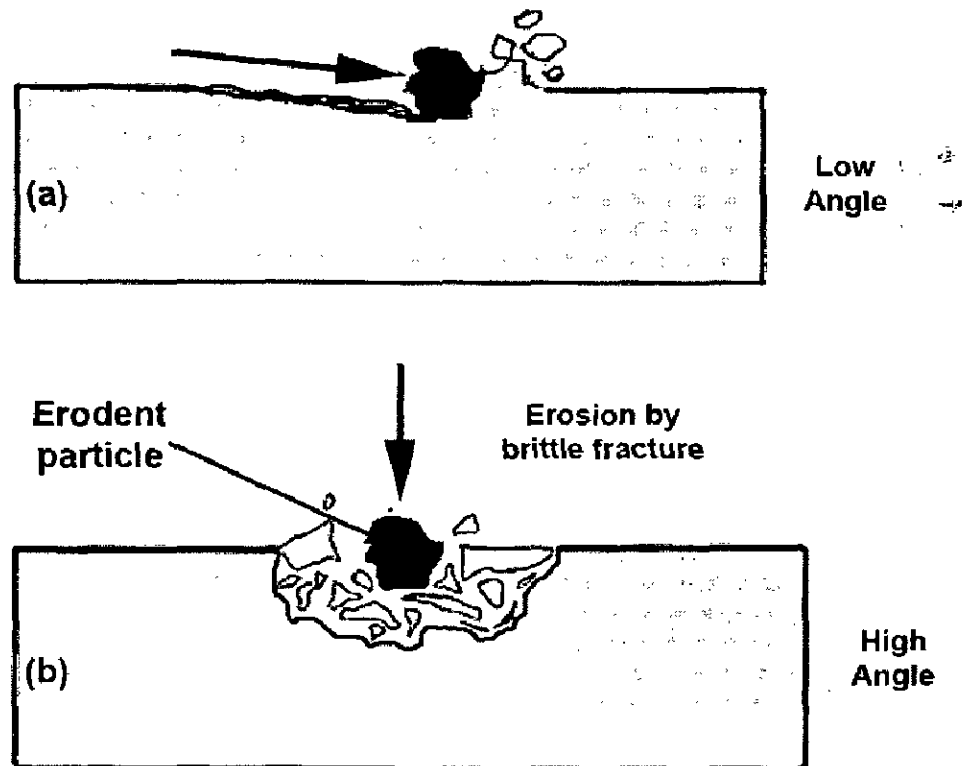


Fig. 5.42: Schematic representation of coating fracture dependent on impact angle (a) Low angle (b) High angle

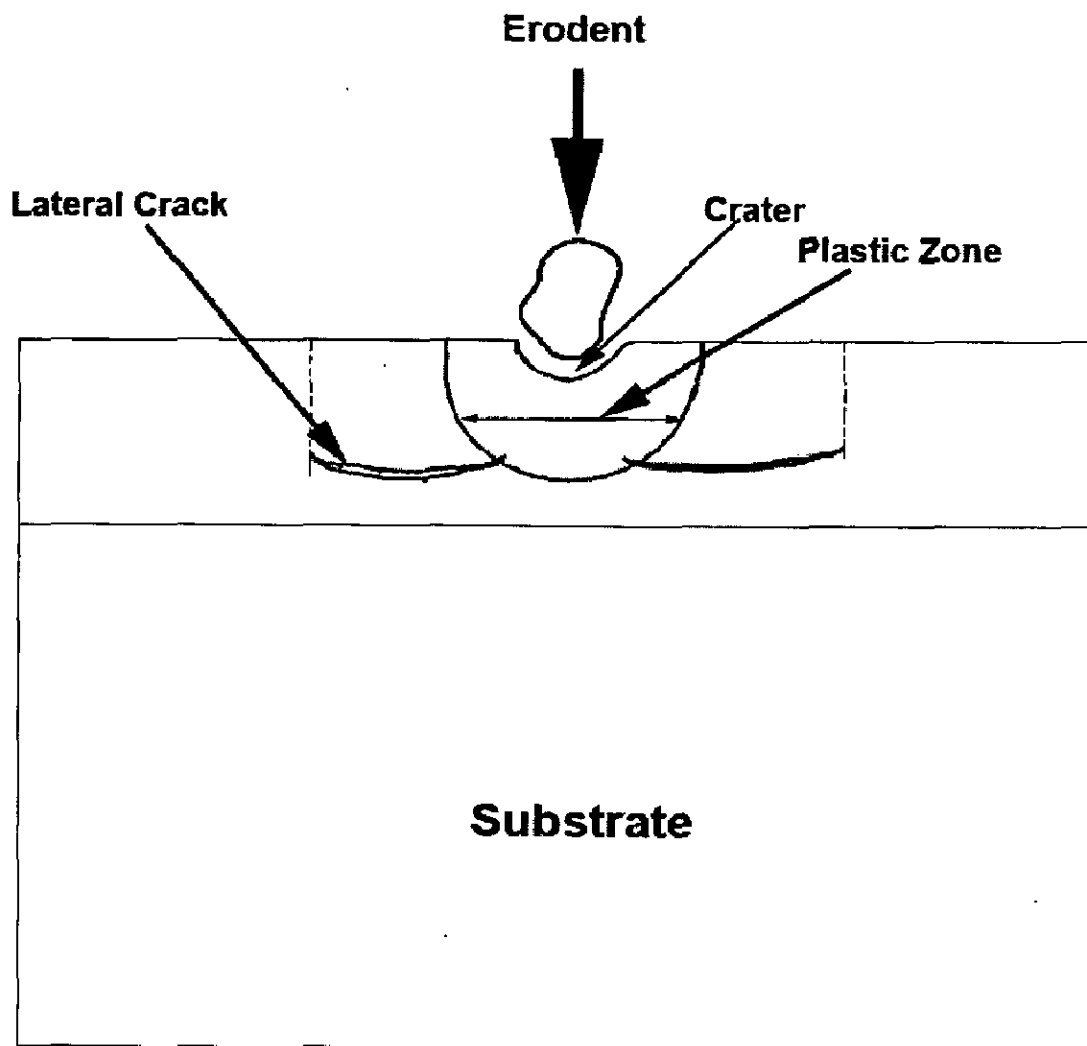


Fig. 5.43: Crack formed in bulk of a coating due to particle impingement

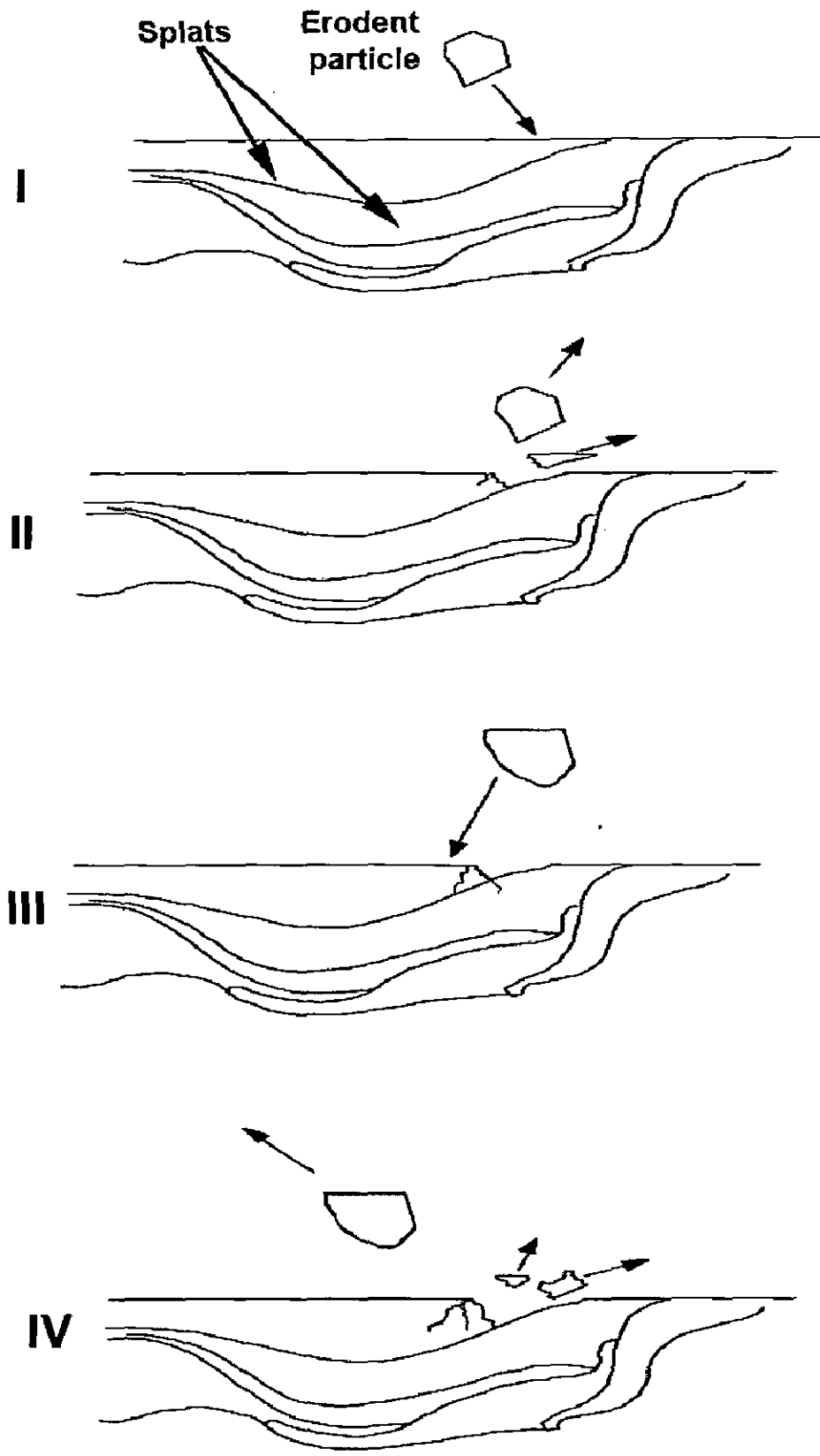


Fig. 5.44: Schematic of splat edge chipping mechanism due to particle impingement.

The material removal mechanism for coated specimens at 90° impact was removal of fractured splats. Generally, only minor parts of individual splats were removed at each impact resulting in splat debonding with subsequent impacts. At higher temperature, the erosion mechanisms featured larger wear fragments, consisting of entire splats or clusters of splats. Erosion of coatings at low impact angles can be seen schematically in Fig. 5.45. At lower impact angle i.e. at 30° impact, the coatings showed a large amount of plastic deformation with little or no signs of splat debonding see Fig. 5.29. At higher temperature testing, especially at condition 3, number of cracks had developed in eroded surfaces. The link up of these cracks forms chips of material that are readily ejected by subsequent impacts in a manner similar to that of bulk brittle materials. Splat chip ejection is shown schematically in Fig. 5.46.

Schematic of the mechanism of “flake” formation during particle impact as observed in the coatings eroded at high temperature is shown in Fig. 5.47. As seen from the Fig. 5.30, at some areas of the surface of the coating, flakes are formed resulting in removal of the upper layer. The wear debris from the coating gets plastified and then becomes strongly adhered strongly to surface of the coating. The SEM examination of eroded surfaces revealed that the erosion characteristics of coating at elevated temperatures were significantly different from those at ambient temperature. There was plastic deformation occurring on the eroded surfaces at high temperatures and low impingement angles. Similar behavior has been observed by Westergard et al., (1998). Plastic deformation on the surfaces of the coating might have occurred due to the pressure and temperature increase during the test. This is consistent with the earlier study (Fervel et al., 1999).

At relatively higher temperatures and lower particle feed rates and impact velocities, the oxide scale that forms during erosion is brittle and non-adherent. In such cases, the oxide scale gets removed after it attains a critical thickness. The erosion behaviour in this regime exhibits a brittle erosion response (Roy, 2006).

Impact zones showed signs of significant plastic deformation, particularly in the matrix phase. Outside these features, brittle interphase cracking was evident, the combined effect of multiple impacts generating extensive interphase crack networks in the regions between indentations. Localised mass loss occurred through fracture of the plastically deformed material around the indent peripheries, as well as through the ejection of chips of material formed by the linkup of the crack networks surrounding each impact site. Gross mass loss an order of magnitude greater than these mechanisms occurred through extensive

chip formation generated by fracture of inter-indent regions of material laterally displaced by multiple erodent impacts in an apparent low cycle fatigue mechanism, Fig. 5.48.

In this process an initial erodent impact indents several microns into the surface, generating a homogeneous plastically deformed indentation zone surrounded by an extensive brittle interphase crack network, Fig. 5.48. When a nearby erodent impact occurs, the localised damage mechanisms occur in the same manner, however, the material between the two indents is no longer well supported and is susceptible to being displaced laterally towards the initial indentation. This region of material is expected to be less tough than the undeformed surrounding material, due to the extensive cold work and brittle interphase cracking induced by the multiple impacts. The combination of these factors makes this inter-indent material prone to fracture and ejection from the surface.

So in Al_2O_3 -3wt% TiO_2 coated alloys; the erosion rate was high at normal impact and low at oblique impact. The difference in erosion rates for shallow and normal impact angles can be attributed to the different material removal mechanisms in these two cases. SEM examination of the eroded surfaces provides some insight into the material removal process. A comparison between the morphological features in completely eroded surfaces of material subjected to solid particle erosion at 30° and 90° impacts, shows two different methods of materials removal. In the case of the low angle eroded surface, the dominant material removal mechanism was splat edge chipping and plastic deformation, while in the case of the high angle eroded surface, the material removal mechanism was mainly splat chip ejection only. Splat ejection is caused by splat boundary microcracking while plastic deformation is believed to be the result of the smearing of the deformed materials. These differences may be explained as follows.

Low Angle Impact

At low angle impact, the kinetic energy of the erodent particles contributes mainly to the ploughing mechanism and very little to normal repeated impact. The ploughing mechanism is associated with the plastic smearing and cutting of the materials, while the repeated impact mechanism is responsible for initiating and propagating the grain boundary microcracks. Ceramics have high hardness, and thus they are not easily plastically deformed. Hence the material removal rate is low.

High Angle Impact

At high angle impact, the kinetic energy of the impinging particles contributes mainly to repeated impact. Ceramics have low fracture toughness, and therefore cracks readily propagate to form a crack network. Brittle nature of the ceramics allows the cracks readily to

propagate to form crack networks. The subsequent impacts will easily remove the surface material via the ejection of the upper layer grains. Hence the material removal rate is high. This is in good agreement with previous studies (Xu and Jahanmir, 1996; Wang et al., 2000) the mechanism of the materials removal for the $\text{Al}_2\text{O}_3 \cdot \text{TiO}_2$ coating consists of grain dislodgement due to grain boundary fracture; and lateral crack chipping.

At room temperature testing, the erosion rate in terms of volume loss for the Al_2O_3 -3wt% TiO_2 coated substrate alloys is between 0.883 to $1.041 \times 10^{-3} \text{ mm}^3/\text{ gm}$ at 30° impact. While in case of normal impact, the erosion rate is more as compared to the erosion rate at 30° impact and lies between 1.447 to $1.550 \times 10^{-3} \text{ mm}^3/\text{ gm}$. The generalized behaviour of the all the coated alloys was brittle in nature as observed from their scanning electron micrographs.

From the present study, it can be inferred that, the erosion rates of alloys were greatest at 90° impact angle, which is the characteristic erosion behaviour of brittle materials. The Al_2O_3 -3wt% TiO_2 coated alloys eroded at 30° impact angle has shown a surface morphology as shown in Fig. 5.29 consisting of small grooves, craters and scars which indicated material removal by crack propagation leading to surface chipping and forming craters. The small cracks in the surface acts as failure initiating sites which ultimately results in brittle fracture. Here an erosion crater was formed by the loss of couple of grains due to intergranular cracking or chipping. The propagation of cracks leads to surface chipping which is dominant materials removal mechanism

Alman et al. (1999, 2002) analyzed the erosion of WC-Co hard metals. It was found that the erosive wear rate of the WC-6Co materials increases steadily with an increase in the test temperature up to 700°C . The measured erosion rate at 700°C was more than double the rate at room temperature.

Erosive wear behaviour of titanium and chromium carbide cermets at elevated temperatures (up to 800°C) was studied by Kübarsepp et al., (2002) and Hussainova et al. (2003). TiC-base cermets (TiC content 50-80 wt %) bonded with Ni-Mo alloys (Mo content

20 and 33 wt %), Ni-steels (Ni content 5-14 wt %) and Cr-Ni-steels (1% Cr, 1% Ni) were investigated. Tests at elevated temperatures were performed at 400, 600 and 800°C, impact angles 70-90° and jet velocity 40 m/s. To compare the erosion resistance of TiC-base cermets with that of WC-base hard metals, WC- 25Co hard metal was used as a reference material. The results of experiments have indicated that erosive wear resistance of WC-Co hard metal and TiC-based cermets depends on the testing temperature.

At condition 1, from the Fig. 5.27 and 5.28, it can be inferred that the erosion rate of all the coated alloys is almost same with small deviations. Volume wear rate of coated Superni 600 superalloy is marginally higher than that for the other coated alloys at impact angle of 30° while at impact angle of 90° volume wear rate of coated Superni 718 superalloy is marginally higher than that for the other alloys. As the temperature of testing increased to 400°C of coated substrate and 900°C of surrounding atmosphere, there is substantial increase in volume erosion rate of all the alloys under testing as shown in Fig. 5.28 at 90° impact while there is small increment in volume erosion rate at 30° impact as is clear from Fig. 5.27. At oblique impact (at small and medium impact angles), with the mechanism of microcutting dominating, hardness characteristics are important, while at normal impact, with the direct or low-cycle fracture mechanism dominating, toughness and fatigue characteristics are important. On further increasing the substrate temperature to 600°C, volume erosion rate is also increased substantially as shown in Fig. 5.27.

Fig. 5.27 shows the variation in volume erosion rates of coated alloys at 30° impact angle with change in test temperature. As the testing temperature increases from room temperature to 400°C of substrate and 600°C of surroundings at 30° impact, the erosion rate has shown an increase. While in case of 90° impact, erosion volume rate has increased substantially as shown in Fig. 5.28. It has been observed that erosion rates of coated alloys impacted at low angles do not increase rapidly as the temperature increases, suggesting that alloys tend to show typically brittle behaviour at elevated temperatures. A tendency for erosion rate to increase with temperature has been observed in coated alloys. The erosion rate is less at 30° impact angle as compared to one at 90° impact angle. Similar behavior dependent on temperature has been observed by Mishra et al., (2008) and Lin et al., (2004).

Also with the increase in Temperature there is increase in erosion rate. At 30° impact angle, at room temperature erosion rate is (0.883 to 1.041 $\times 10^{-3}$ mm³/gm) and as the temperature is increased to 400°C of substrate and 900°C of the surrounding air, erosion rate has increased and varies between 1.064 $\times 10^{-3}$ mm³/gm and 1.153 $\times 10^{-3}$ mm³/gm on further increase in temperature erosion has increased to 1.253 $\times 10^{-3}$ mm³/gm to 1.53 $\times 10^{-3}$ mm³/gm as shown in Fig. 5.27.

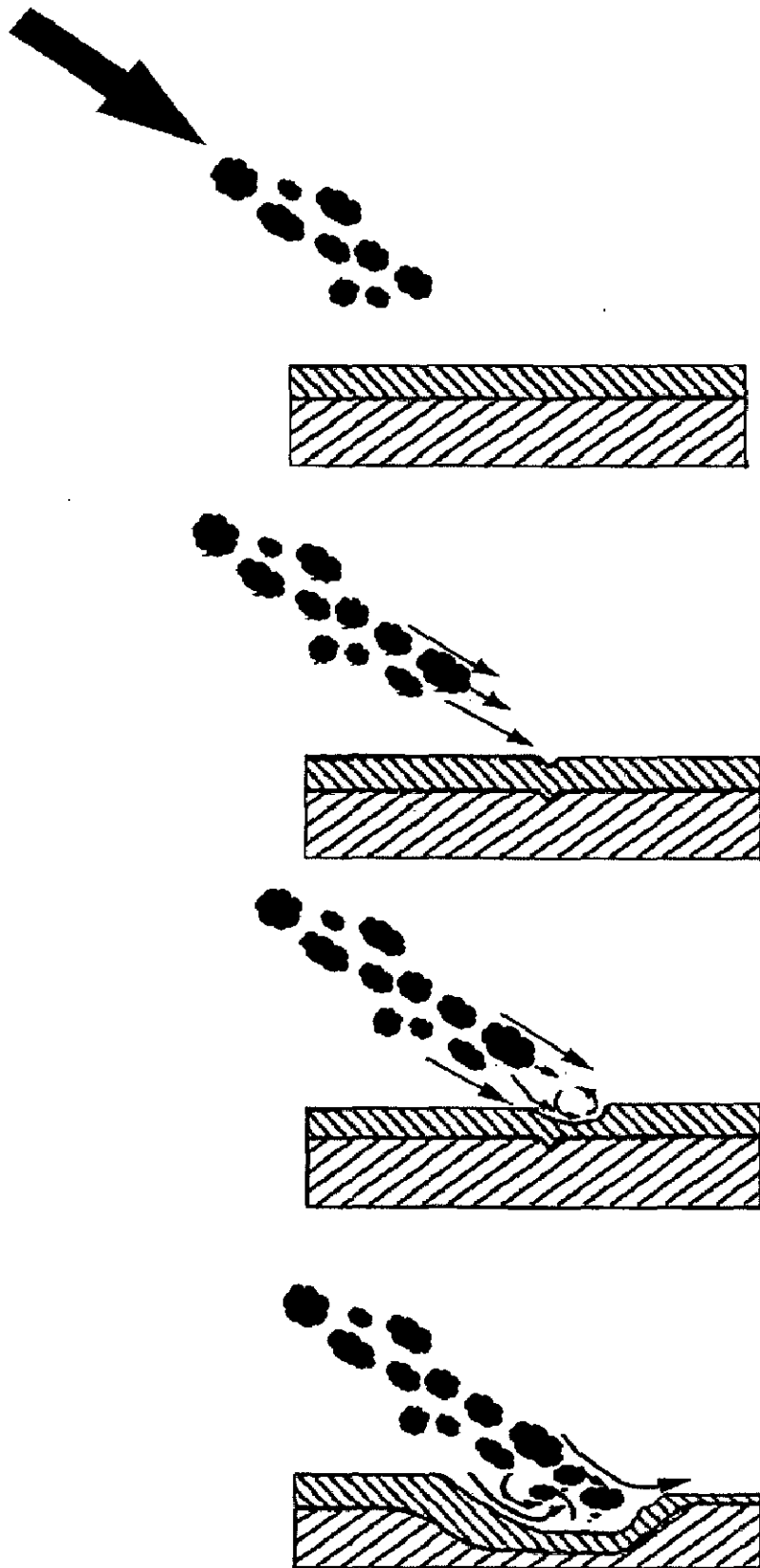


Fig. 5.45: Schematic diagram showing probable erosion mechanism of detonation gun sprayed Al_2O_3 -3 Wt% TiO_2 coatings at low impact angles due to particle impingement.

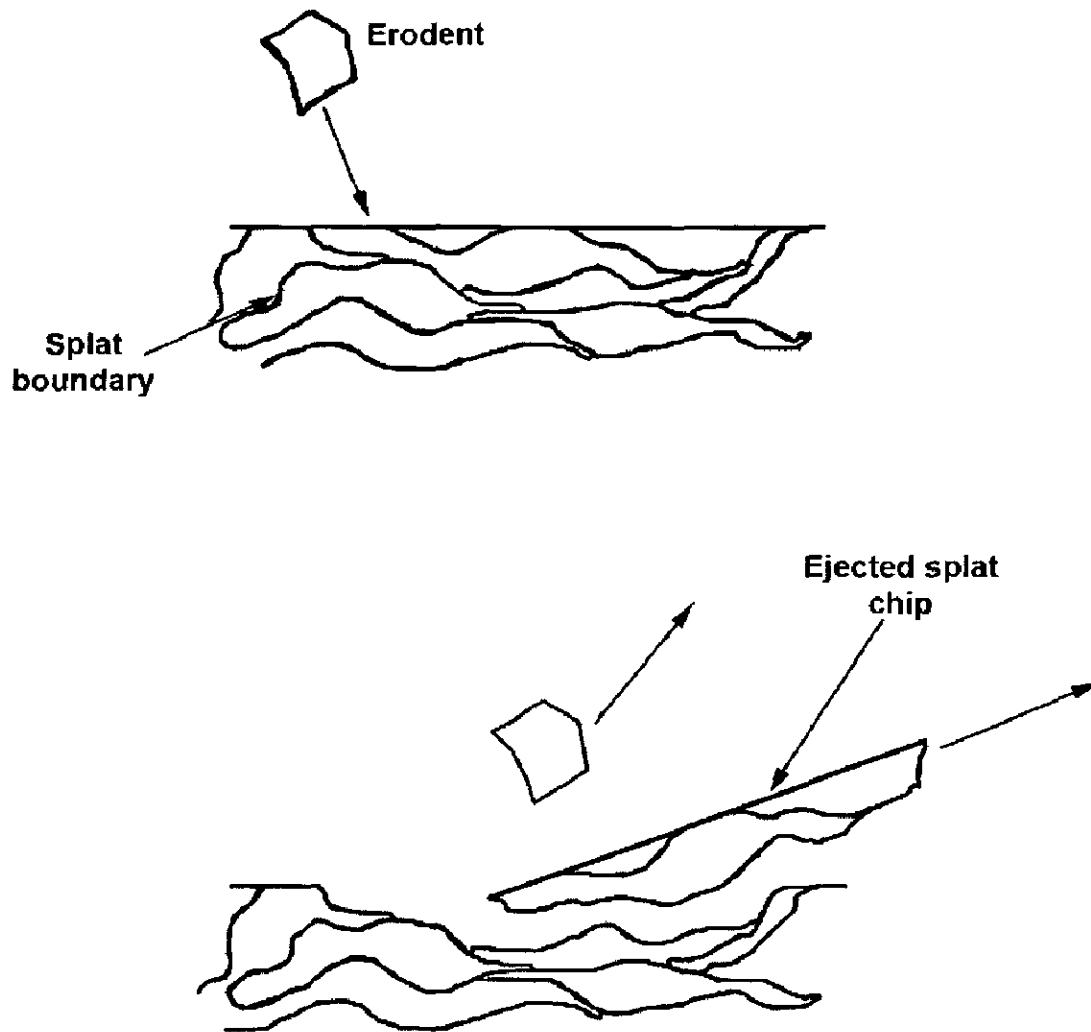


Fig. 5.46: Schematic illustrating the mechanism of gross splat chip formation during erosive impact as a result of low inter-splat adhesion.

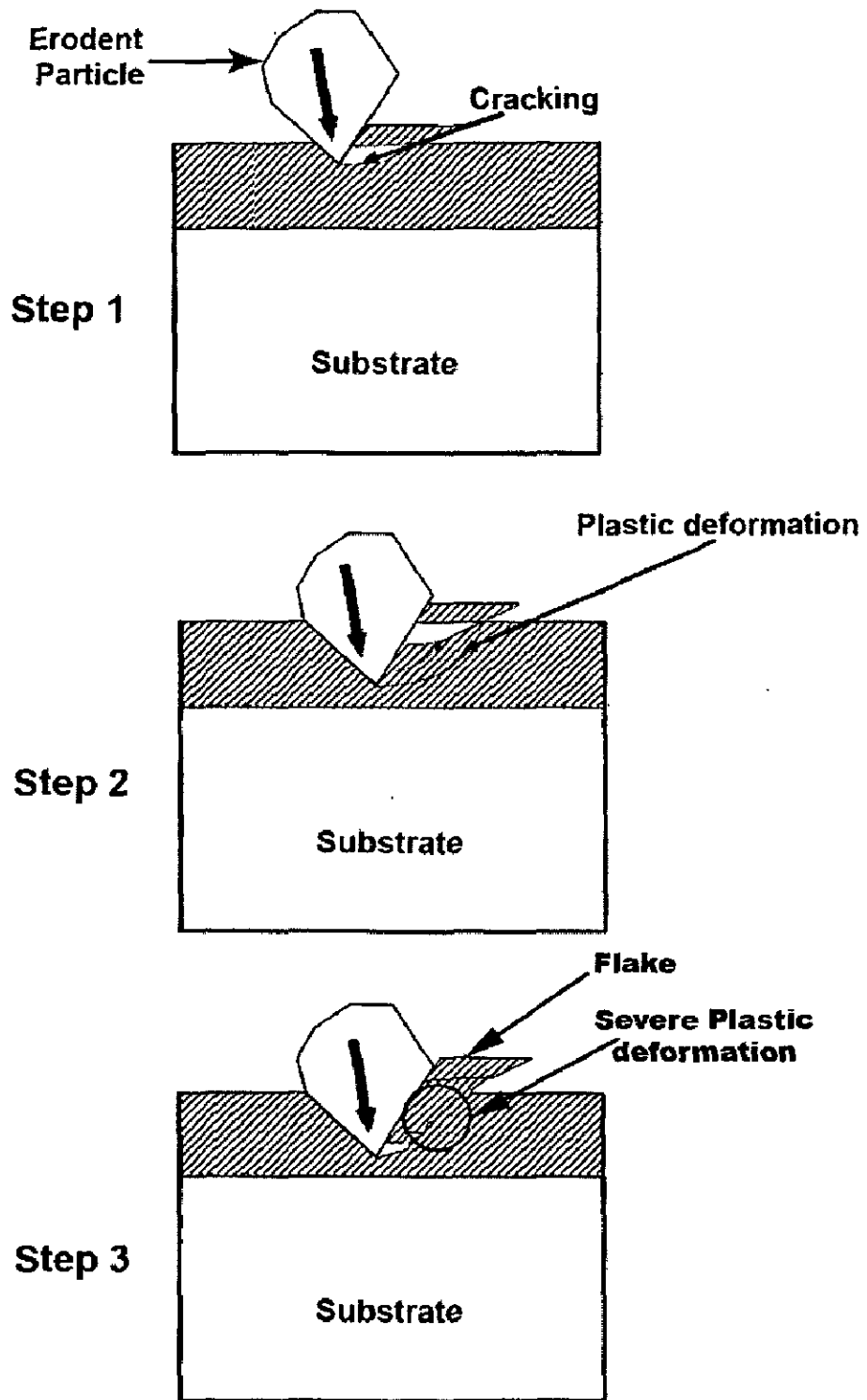


Fig. 5.47: Schematic illustrating the mechanism of flake formation during particle impact

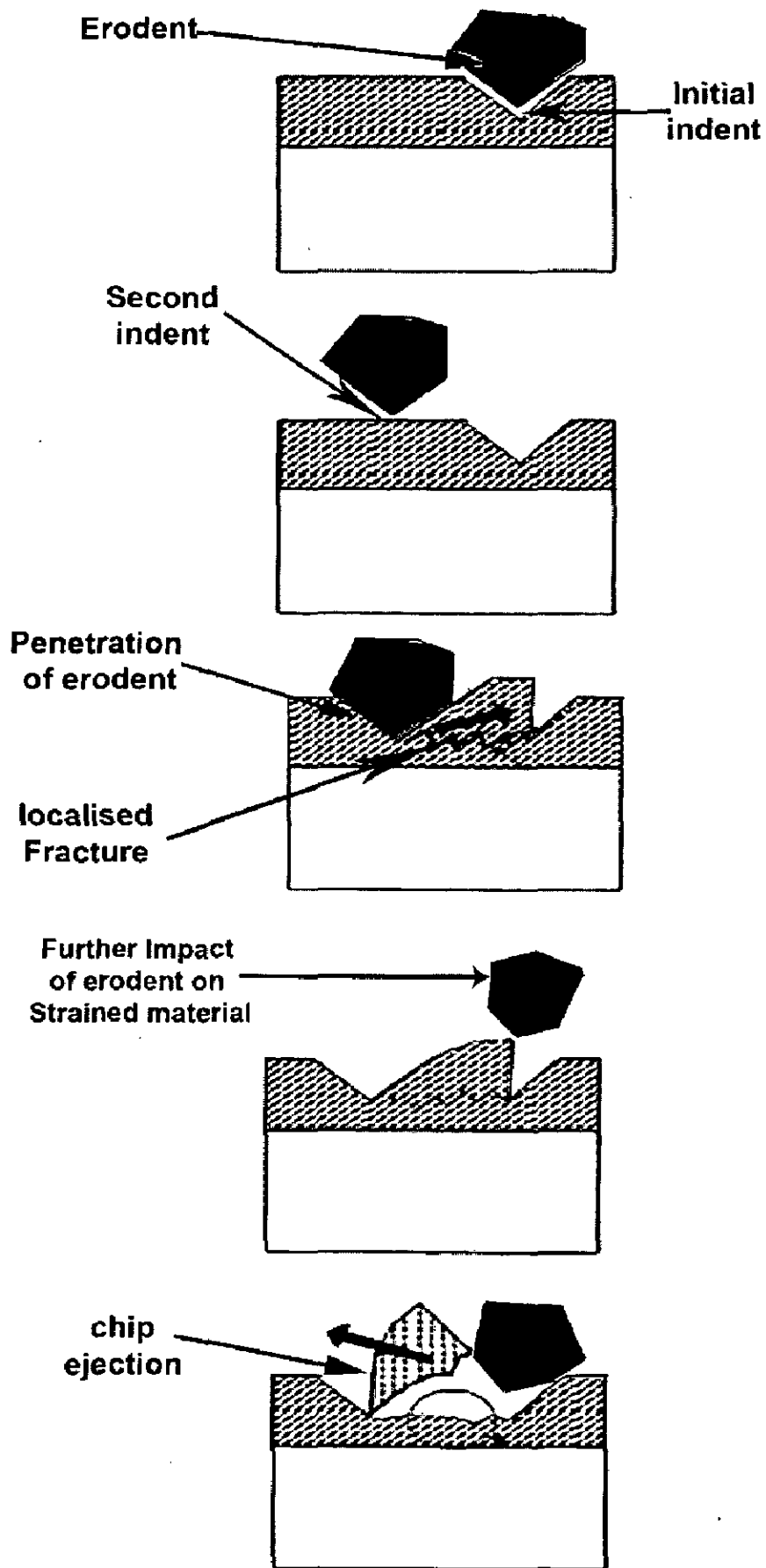


Fig. 5.48: Schematic representation of gross chip formation in the region between neighbouring indents, resulting from the large depth of erodent penetration.

While at 90° impact, the rise in erosion rate is much higher for given increase in temperature. At room temperature erosion rate lies between $1.447-155 \times 10^{-3} \text{mm}^3/\text{gm}$ and at condition 2, erosion rate lies between $1.653-1.858 \times 10^{-3} \text{mm}^3/\text{gm}$ and on further increase in temperature i.e at condition 3, erosion rate increases in the range of $2.108-2.486 \times 10^{-3} \text{mm}^3/\text{gm}$ as shown in Fig. 5.28.

The effect of temperature on the erosion rate has been studied by Zhou and Bahadur (1995) and they have reported that the effect of temperature on erosion is significant above 400 °C and the rate of increase in erosion rate is greater at higher temperatures. They have also reported that for the three aluminas containing silicate glassy phase, there is a slight drop in erosion rate at 200°C. In general, it can be concluded that erosion rate increases with increasing temperature.

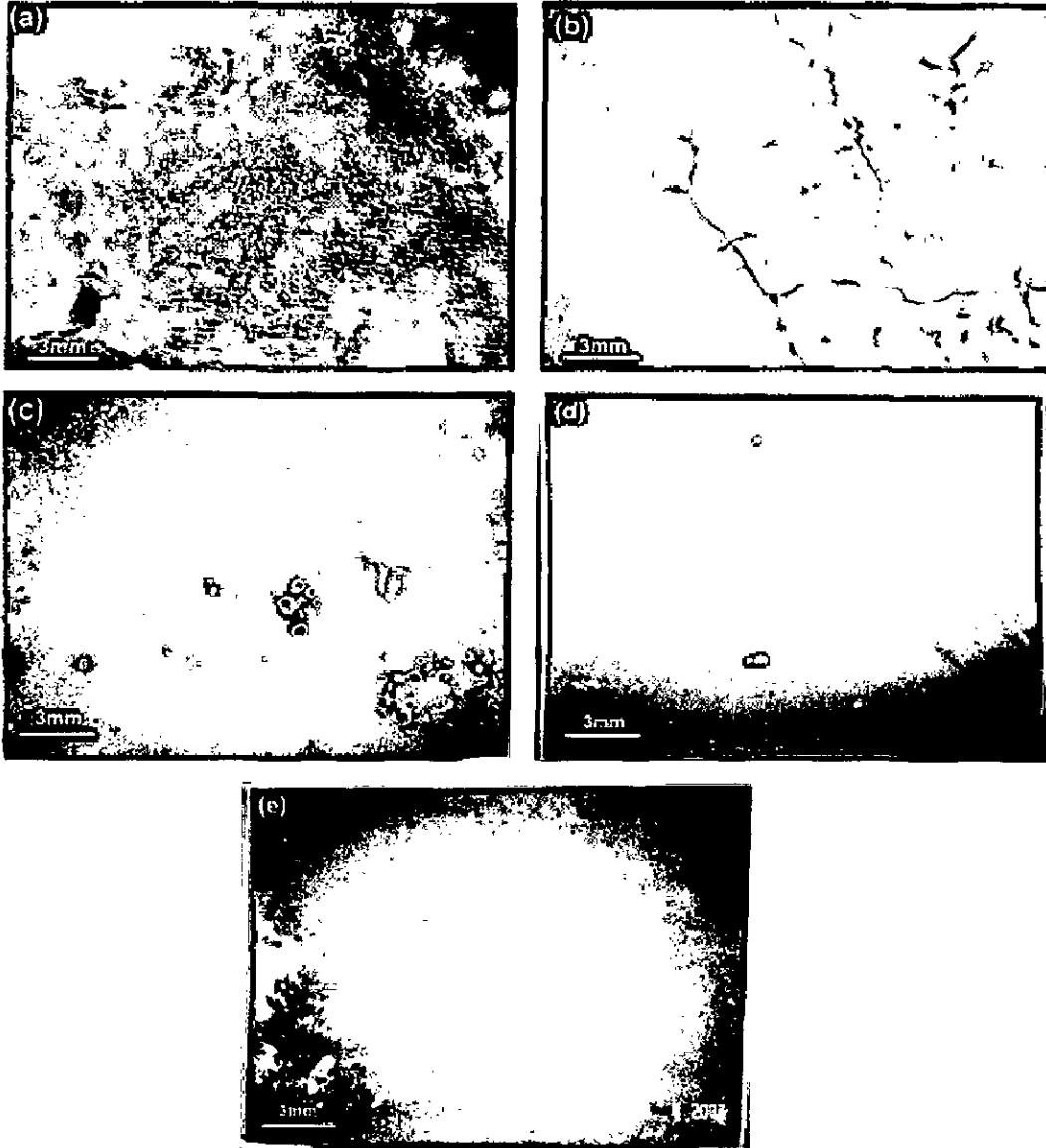


Fig. 6.1: Macrographs of substrate alloys after cyclic oxidation in air at 900°C for 50 cycles.
(a) T11 (b) T22 (c) Superni 600 (d) Superni718 (e) Superfer 800

HIGH TEMPERATURE OXIDATION AND HOT CORROSION STUDIES

This chapter describes the critical examination of corrosion products and the behaviour of uncoated and D-gun coated alloys when subjected to high temperature cyclic oxidation in air at 900°C for 50 cycles and the hot corrosion behaviour of uncoated and D-gun coated alloys in an aggressive environment of molten salt (Na_2SO_4 -60% V_2O_5) at 900°C under cyclic conditions. The samples were visually examined at the end of each cycle during the course of study. Weight change technique was used to study reaction rate and to understand the kinetics of oxidation. The different phases and their distribution in the studied specimens were analysed with the help of XRD, SEM/EDX and X ray mapping.

6.1 RESULTS

6.1.1 Oxidation studies of uncoated and coated alloys in air

6.1.1.1 Uncoated alloys

6.1.1.1.1 Visual Examination

The macrographs for substrate alloys T11, T22, Superni 600, superni 718 and Superfer 800 after oxidation at 900°C for 50 cycles in air environment are shown in Fig. 6.1. T11 steel turned to bluish grey after first cycle. After 3rd cycle spalling and sputtering was observed. The colour of scale was shining grey. After 7th cycle there was a clear formation of crack network on the scale which subsequently broke away. Then with further passing of cycles these cracks became deep and ultimately after 13th cycle, thin layers like flakes from the scale started separating out from the top surface and side surfaces. Layers continued to separate out for few cycles until a uniform and clear integrated surface appeared. Then again spalling and crack formation started and again layers were peeled off and it continued in the same manner. In case of T22 boiler steel, the colour of the sample turned to grey colour after first cycle. Then after 2nd cycle, small spots appeared on the surface. The spalling and sputtering started just after 4th cycle. There was appearance of minor cracks like grain boundaries in the oxide scale of T22 steel after 7th cycle. After 11th cycle, the scale turned black at the edges and started

cracking from the edges of the surface. Then thin scale layer peeled off from the surface beneath which surface with black patches appeared. Then again spalling of the surface was visible and crack network appeared on the surface. Morphology of the oxide scale for steels after 50 cycles of oxidation is shown in Fig. 6.2. The scale formed on T22 steel is irregular and fragile and has dull grey appearance.

In case of superalloys colour of oxide scale formed on the Ni-base superalloys Superni 600 and superni 718 after air oxidation for 50 cycles at 900°C was dark grey with some brownish spots. In case of Superni 600 in the early cycles of study there is no visible change. Few white spots could be seen on the thin scale of Superni 600 from 26th cycle onwards which turned into some white coloured powder which vanished towards the end of cycles. In Superni 718, after first cycle the colour of specimen became grey. After 8th cycle, some minor brown spots were visible on the surface. There was no visible change in coming cycles till 45th cycle. Then there was some formation of light green colour on the surface scale layer. In case of Superfer 800, brownish black spots appeared after 7th cycle and the scale for oxidised Superfer 800 showed increasing dominance of the brownish spots on the dark grey background with the progress of the study.

Lustrous scales was formed on superni 600 and superni 718 in early cycles of study, which eventually became dull with coming number of cycles. The scales of the Superni 600, Superni 718 and Superfer 800 showed no spalling and remained intact with the substrates. The oxide scale morphology of the oxidized superalloys has been shown in Fig. 6.3, which indicate continuous scales without any crack formation.

6.1.1.1.2 Weight Change Data

Weight gain per unit area expressed in mg/cm² is plotted as a function of time expressed in number of cycles for oxidized T11, T22 boiler steels is shown in Fig. 6.4 and for superalloys Superni 600, superni 718 and Superfer 800 superalloys is shown in Fig. 6.6.

Boiler steels showed extensive spalling. T22 steel showed more weight gain than T11 steels. The total weight gain at the end of 50 cycles for T11 and T22 steels is 102.88 and 119.12 mg/cm² respectively.

Weight gain square (mg²/cm⁴) plotted as a function of time (number of cycles) in Fig. 6.5, from where it can be inferred that the boiler steels followed almost parabolic behaviour. The parabolic rate constants, K_p for T11 and T22 steels are 6.33 and 8.28 X10⁻⁸ g² cm⁻⁴ s⁻¹ respectively.

In case of superalloys, superfer 800 showed maximum weight gain as compared to other two superalloys Superni 600 and Superni 718. In all the superalloys the weight gain upto 10th cycle is almost similar and after 10th cycle in case of superfer 800, it has shown a fast increase in weight gain upto 40th cycle and afterwards it is almost constant. In case of other oxidised superalloys viz. Superni 600 and Superni 718, rapid oxidation rate has not been observed and very small weight gains have been observed and steady state with the progress of exposure time, in spite of the fact that some minor deviations are observed. The total weight gain at the end of 50 cycles for the superalloys Superni 600, 718 and Superfer 800 is 0.28, 0.97 and 4.03, mg/cm² respectively. This shows that the weight gain in case of oxidised Superni 600 is lowest, whereas it is highest in case of Superfer 800.

In Fig. 6.7, the (weight gain/unit area)² versus number of cycles for all the superalloys are plotted to determine the conformance with the parabolic rate law. Although some scatter in the data can be observed in the plots, but it is apparent that these data can be approximated by a parabolic relationship. If the scatter in the measurements is not considered, the values of parabolic rate constant (K_p) for the superalloys Superni 600, 718 and Superfer 800 are calculated as 2.22×10^{-13} , 5.19×10^{-12} and 1.13×10^{-10} g² cm⁻⁴ s⁻¹ respectively. Superfer 800 has not followed the parabolic rate law.

6.1.1.1.3 X-ray Diffraction Analysis

The X-ray diffractograms of the scale for T11 and T22 boiler steels after exposure to air at 900°C for 50 cycles are shown in Fig. 6.8. Both boiler steels have Fe₂O₃ as the main constituent of scale. During the oxidation process continuous and intense spalling was observed. Also some peaks of Cr₂O₃ along with Fe₂O₃ are indicated in the oxide scale of both the boiler steels T11 and T22.

The X-ray diffractograms for the uncoated superalloys after exposure to air at 900°C for 50 cycles is shown in Figs. 6.9 and 6.10. Fe₂O₃, NiFe₂O₄, NiCr₂O₄ and Al₂Fe₂O₆ phases are found to be present in all the oxidised superalloys. The formation of NiO has been indicated in the scales of Superni 600 and Superfer 800.

6.1.1.1.4 SEM/EDX Analysis

(a) Surface Morphology

SEM/EDX analysis was used for the detection of presence of corrosion products and corrosion-inhibiting species and their concentrations. The surface scale morphology and the EDX analysis for substrate alloys exposed at 900°C for 50 cycles in air environment is shown in Fig. 6.2 and Fig. 6.3. From SEM/EDX analysis of T11 and T22 boiler steels, it has been revealed that the main constituent of scale is Fe, with minor concentrations of S, Mn, Cr, and Mo along with O. The oxide scale consisting mainly of Fe₂O₃ was loose and porous. The micrograph indicates presence of pits and cracks in scale. Rapid growth of Iron Oxide in the matrix region of the boiler steels led to much thicker scale formation. The appearance of scale in case of boiler steels is highly bulky and porous and there is a continuous network of cracks along the scale. Frequent spalling was observed throughout the study.

In case of superalloys exposed to air at 900°C for 50 cycles, a fine surface scale mainly consisted of Ni, Fe and Cr along with O as shown in Fig.6.3. The scale on the matrix regions was significantly flatter and no spallation of the scale has been observed. A well adherent corrosion scale is formed which mainly consists of Cr, Fe and Ni along with O. SEM/EDX micrograph of the scale formed after oxidation for Superni 600 superalloy indicates mainly Ni along with O rich phase, Fig. 6.3 (a). There is no indication of cracks on the surface of the scale in case of Superni 600 and scale mainly consisted of Cr, Ni, Fe and Mn along with O. The scale matrix consisted of Ni (42.69%) and Cr (7.33%) at point 1 and Ni (23.07%) and Cr (32.20%) at point 2 as indicated by EDX analysis shown in Fig. 6.3 (a). The morphology of scale for the oxidised Superni 718, Fig. 6.3 (b) is having Cr rich matrix 40.41 % and 45.11 % at point 1 and point 2. The other constituent of scale were Fe and Ni with small amount of Mn along with O. In case of superfer 800, the scale mainly consisted of Fe and Cr along with O as shown in 6.3 (c).

(b) Cross-Sectional Analysis and X ray mapping

The BSE image and the EDX analysis across the cross section on uncoated alloys are shown in Fig.6.11 to Fig. 6.15. Throughout the scale higher percentage of Fe oxide is

there and also chromium oxide is present throughout the scale thickness though in small quantity. The results of oxide scale analysis across the cross-section for oxidised T11 and T22 boiler steels are plotted and shown in Fig. 6.11 and 6.12 along with micrographs. The scale was quite fragile and porous and was continuously peeled off from the surface. In Fig. 6.11, there is clear indication of internal oxidation. Also in case of T11 steel traces of Mn and Si have been revealed while in case of T22 steel traces of Mo have been revealed along with Mn and Si.

In case of superalloys, EDX analysis has revealed that the scale mainly consisted of Ni and Cr oxides with iron oxide. Oxides of Chromium are present throughout the scale in all the superalloys. Oxide scale morphology along with variation of elemental composition across the cross-section of superalloy Superni 600 subjected to cyclic oxidation in air at 900°C after 50 cycles has been depicted in Fig. 6.13. The plots of elemental composition variation show that the scale mainly consists of iron, nickel and chromium along with oxygen. As one moves from substrate towards scale, the concentration of oxygen is found to increase while the nickel content in the scale decreases as one moves away from the alloy-scale interface, while iron has shown no significant variation in its concentration. In Superni 718, a very thin scale consisting mainly of nickel and chromium with some iron is observed as shown in Fig. 6.14. Small traces of Nb and Ti were also observed. Chromium percentage has increased while Ni percentage has decreased as one moves towards scale. In superfer 800, Fig. 6.15, scale has major portion of iron oxide and there is decrease of chromium percentage at the edges of the scale which may be depletion of Chromium.

Back Scattered Electron Image of cross-section of uncoated substrate alloys (T11, T22, superni 600, superni 718 and Superfer 800) and corresponding X-ray mapping after oxidation in air at 900°C after 50 cycles is shown in Fig.6.16 to 6.20 respectively. In boiler steels, there is a severe internal attack as the oxide scale is penetrating into the substrate. Iron from the substrate is forming iron oxide by combining with oxygen. There is continuous spalling of scale layer by layer. In boiler steel T11 (Fig.6.16), main constituent is iron oxide with presence of minor concentration of Mn and Cr. Scale has already spalled and in remaining visible scale Chromium is present in pockets especially where iron is not present and at the lower part of the scale surface chromium is present

with oxygen indicating the formation of chromium oxide. In T22 boiler steel, chromium band formation is visible in the scale and the scale mainly consisted of iron oxide as is clear from Fig. 6.17. There is irregular layer of Cr_2O_3 above which there is a thin layer in which oxygen is present in large amount. There is clear indication of internal oxidation.

While in all the superalloys there is a thin scale formation and the top layer of scale is iron oxide. In superni 600, Fig.6.18 scale is thin and internal attack is visible. Thin scale might have formed as per the EDX but in the cross section scale is not observed. At point 1 no Oxygen is detected, as we move through the points 2, 3, 4 and 5 there is presence of small amount of oxygen as per point analysis on the cross-section. In superni 718, Fig.6.19 attack is confined and thin scale is formed. From x ray mapping, higher concentration of Cr along with Oxygen is visible in scale. The formation of Cr_2O_3 at the scale substrate interface has further restricted the oxidation by acting as a protective layer. In Superfer 800, Fig.6.20, internal attack is visible and thin scale is formed. At point 3 and 4 Oxygen is present along with iron and Nickel thus confirming the formation of oxides of iron and Nickel. At the extreme end of scale, in maps (overlapped) it is visible that major proportion of the scale is of iron oxide. The scale mainly contains iron along with oxygen which indicates the formation of Fe_2O_3 .

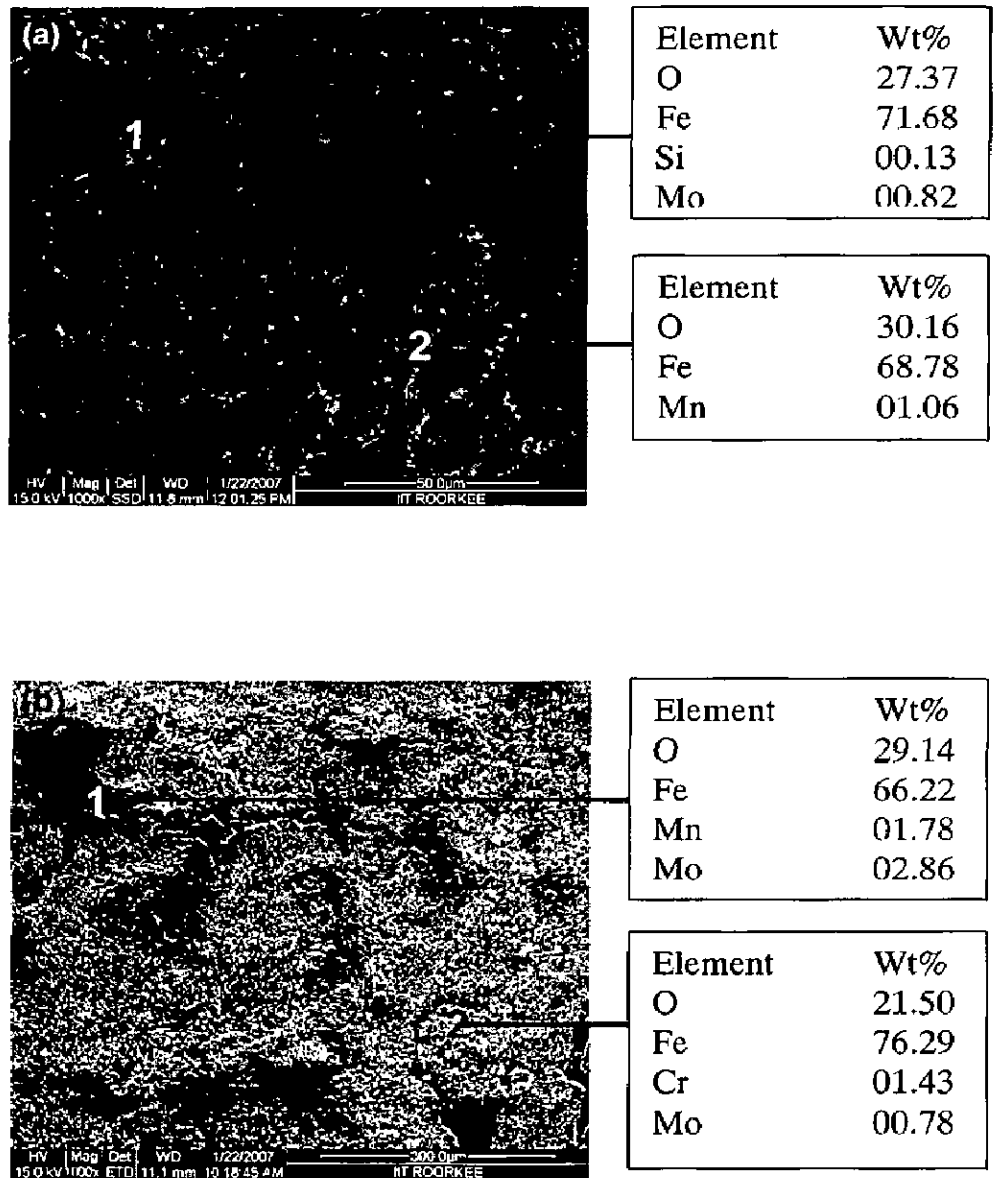


Fig. 6.2: Surface scale morphology and EDX analysis for boiler steels oxidised in air at 900°C for 50 cycles (a) T11, 1000 X and (b) T22, 1000 X.

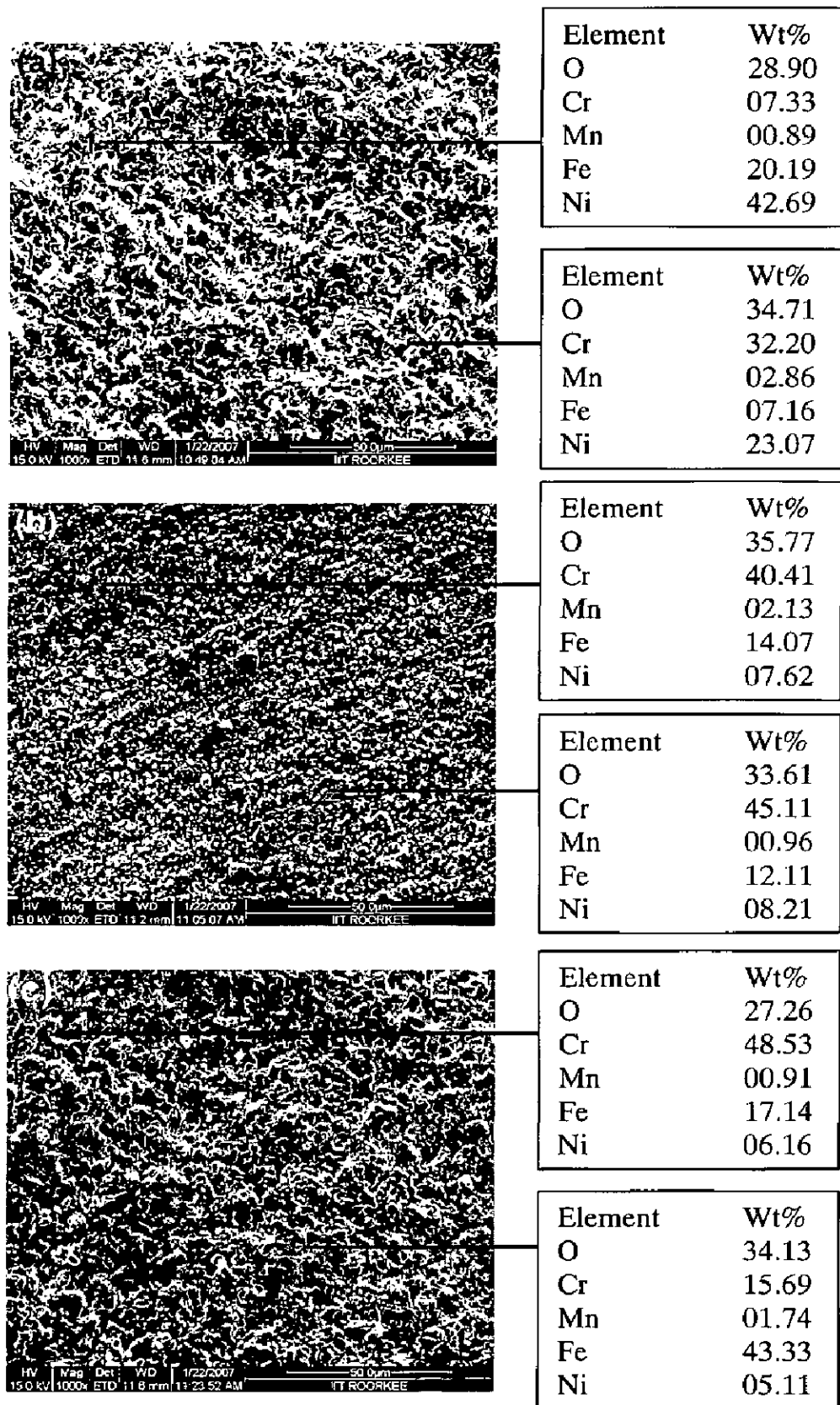


Fig. 6.3: Surface scale morphology and EDX analysis for superalloys oxidised in air at 900°C for 50 cycles (a) Superni 600, 1000 X (b) Superni 718, 1000 X. and (c) Superfer 800, 1000X.

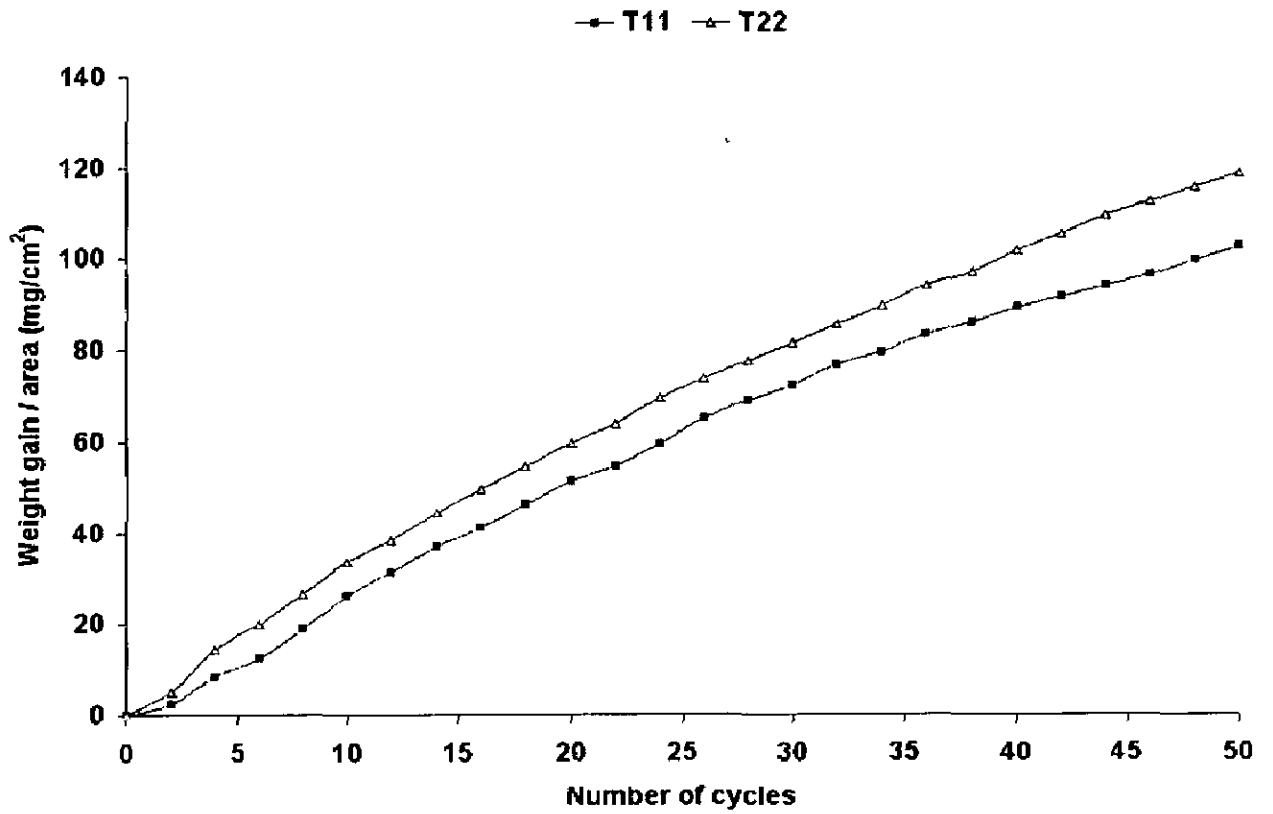


Fig. 6.4: Weight gain plot for uncoated steels exposed to air at 900°C for 50 cycles.

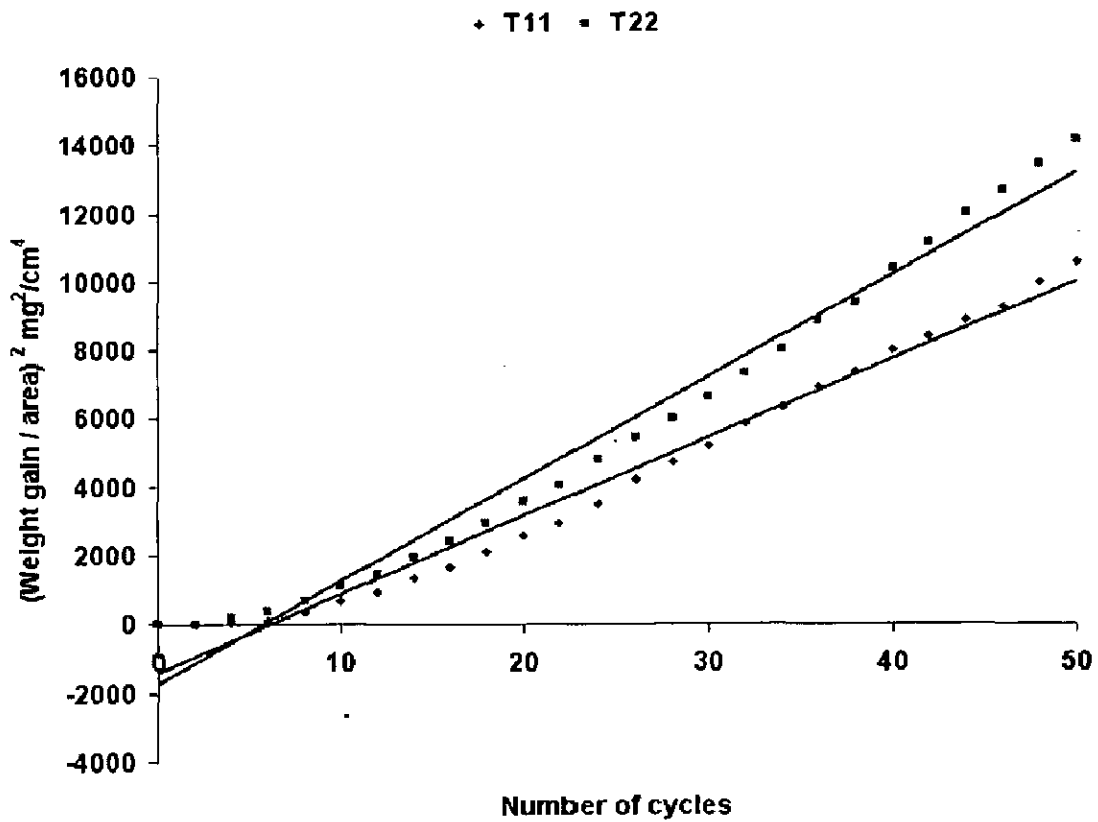


Fig. 6.5: Weight gain square (mg^2/cm^4) plot for uncoated steels exposed to air at 900°C for 50 cycles.

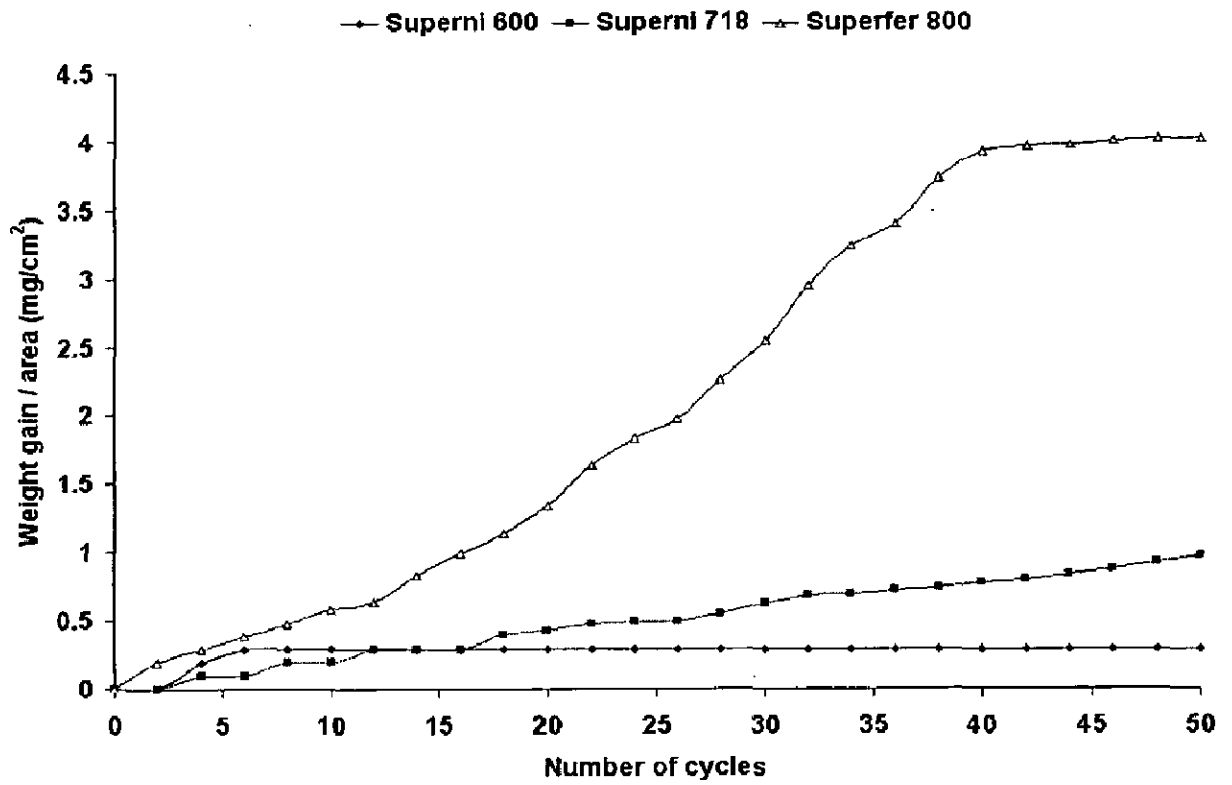


Fig. 6.6: Weight gain plot for uncoated superalloys exposed to air at 900°C for 50 cycles.

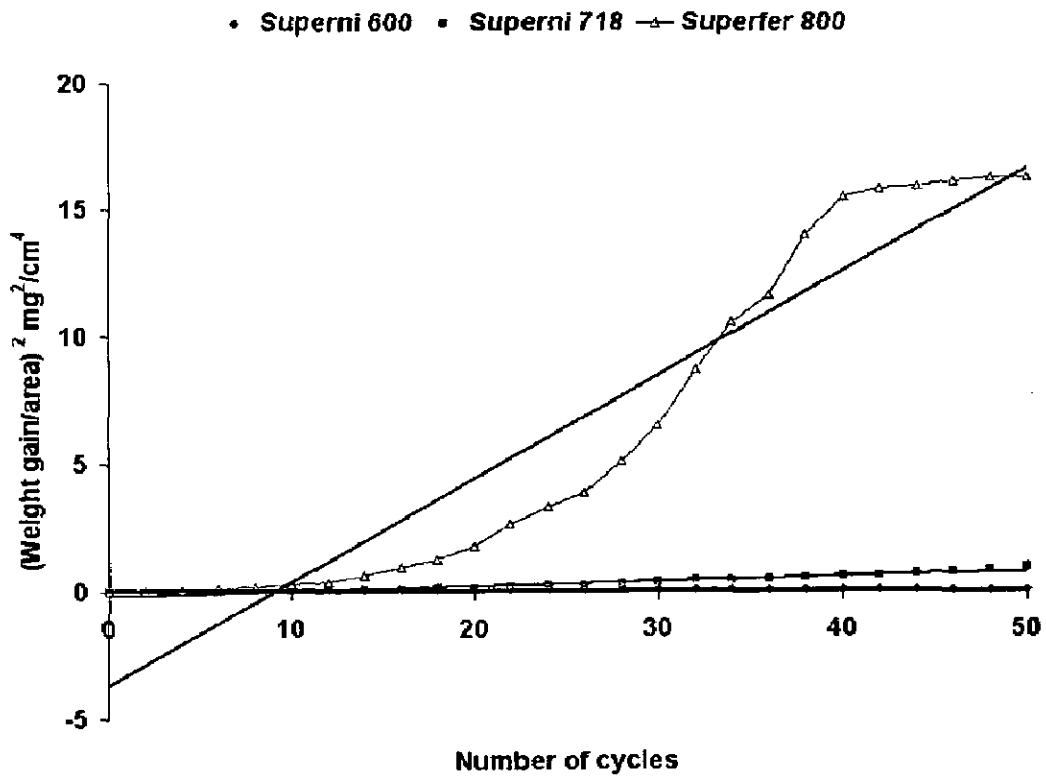
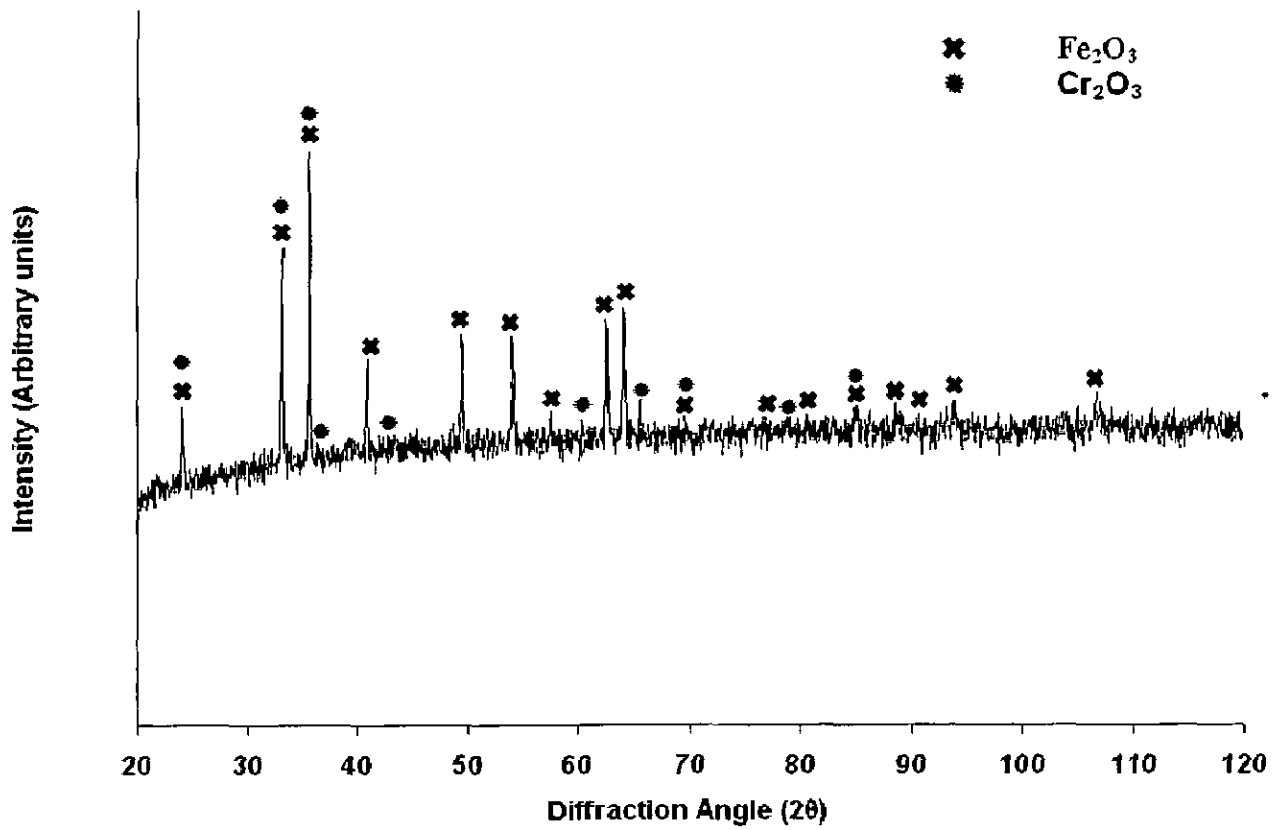
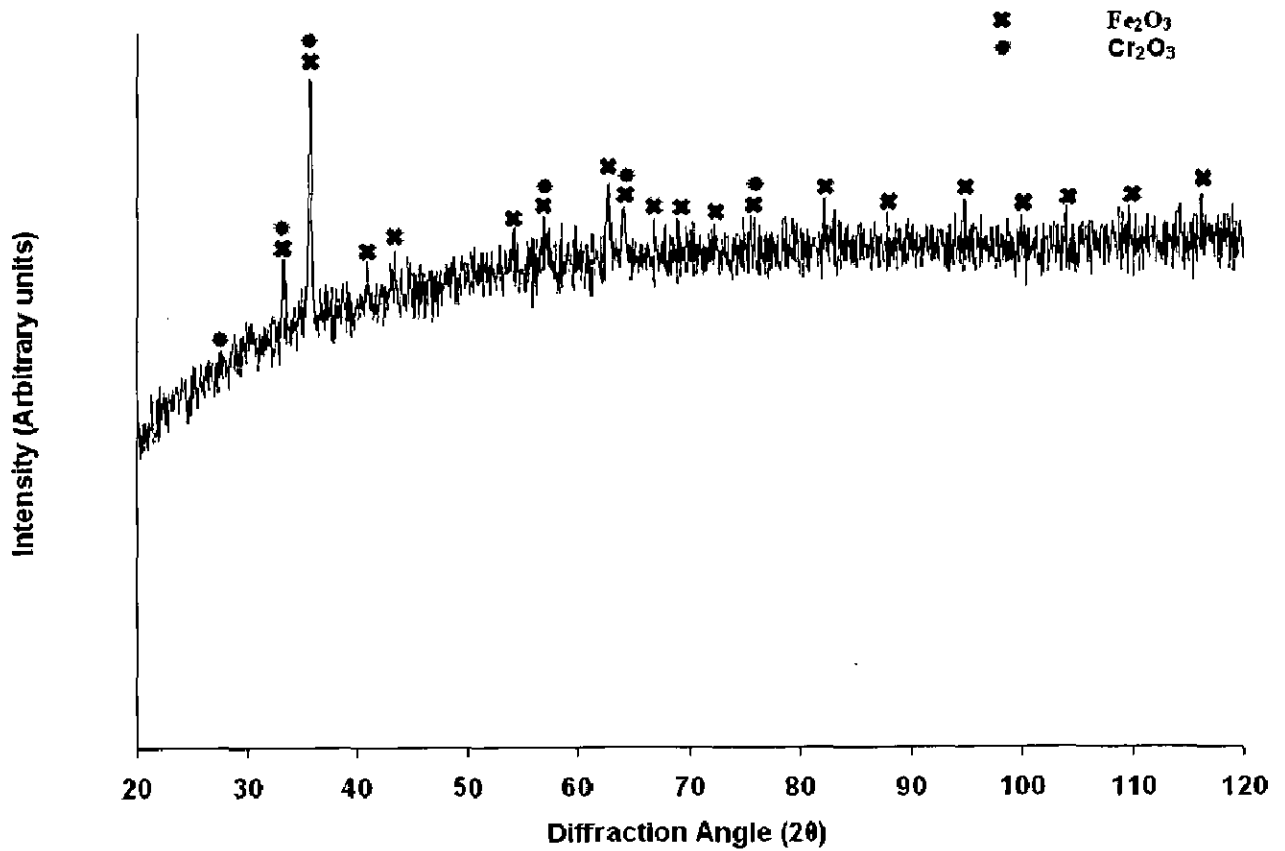


Fig.6.7: Weight gain square (mg^2/cm^4) plot for uncoated superalloys exposed to air at 900°C for 50 cycles.



(a)



(b)

Fig. 6.8: X-ray diffraction profiles for T11 and T22 boiler steels subjected to cyclic oxidation in air at 900°C for 50 cycles.
 (a) T11 (b) T22

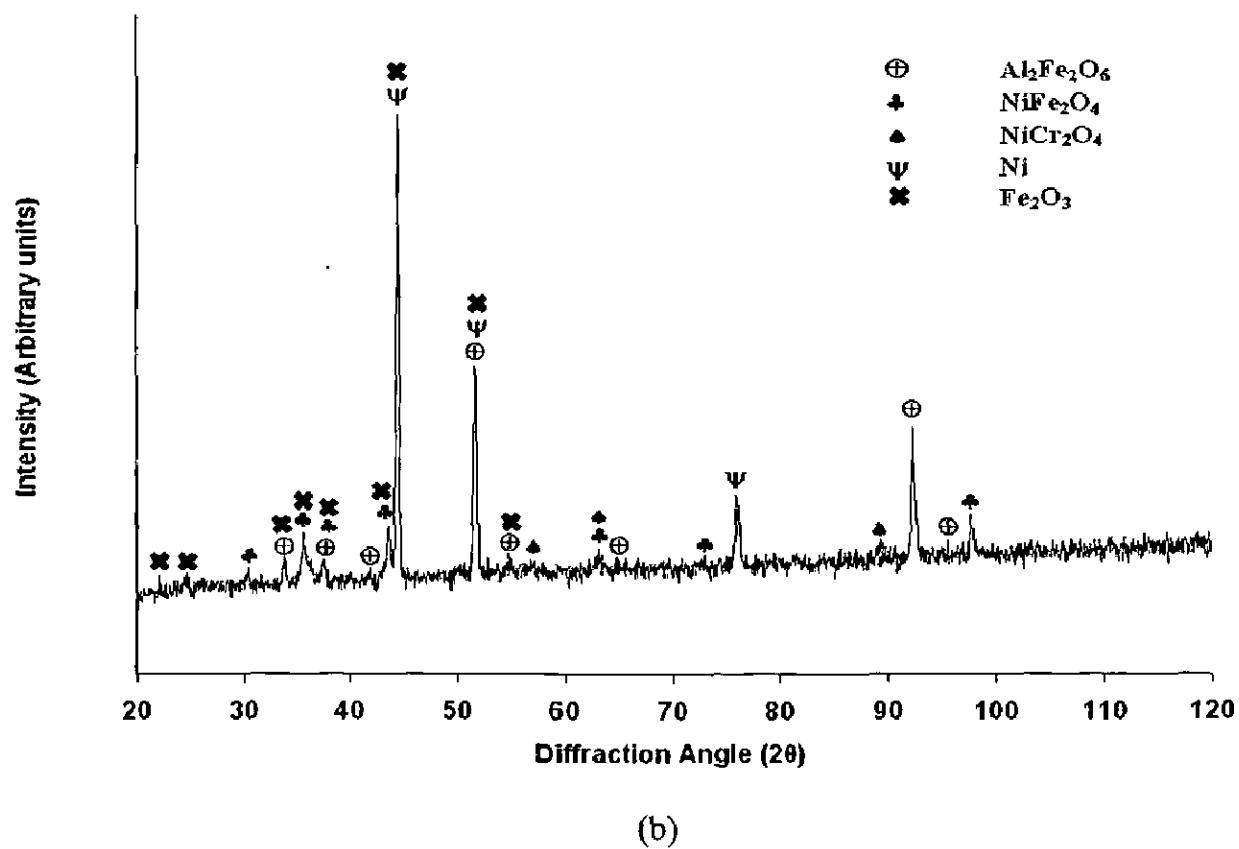
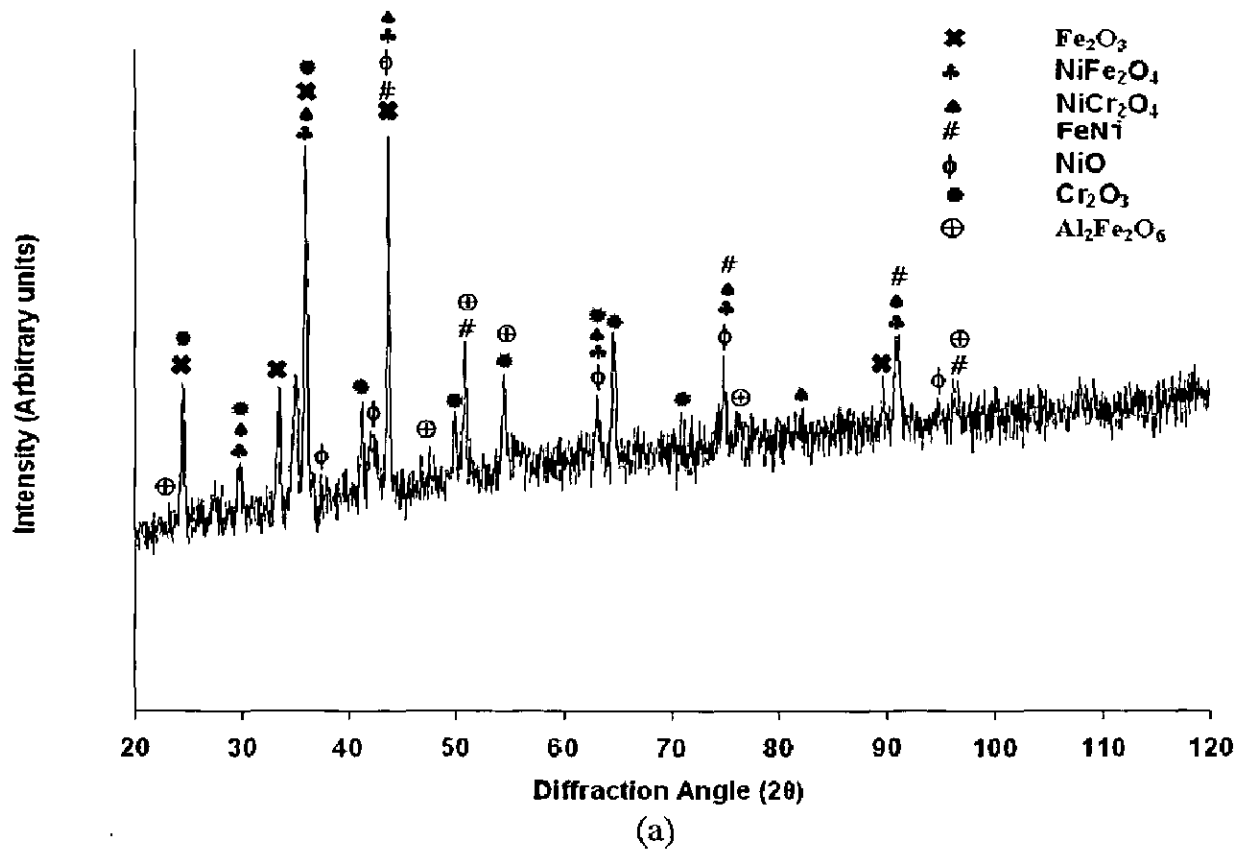


Fig.6.9: X-ray diffraction profiles for superalloys superni 600 and superni 718 subjected to cyclic oxidation in air at 900°C for 50 cycles.
 (a) Superni 600 (b) Superni 718

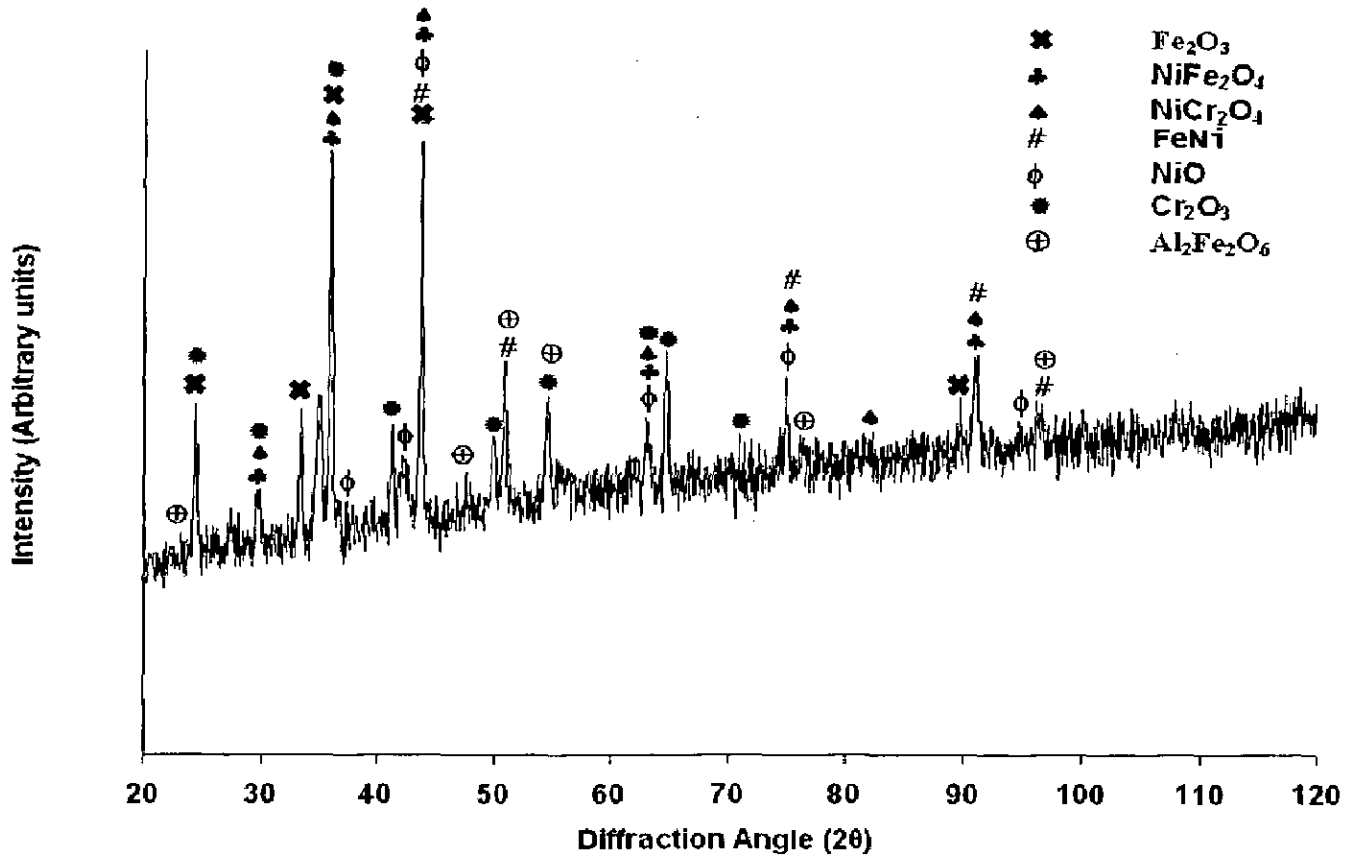


Fig. 6.10: X-ray diffraction profiles for superalloy Superfer 800 subjected to cyclic oxidation in air at 900°C for 50 cycles.

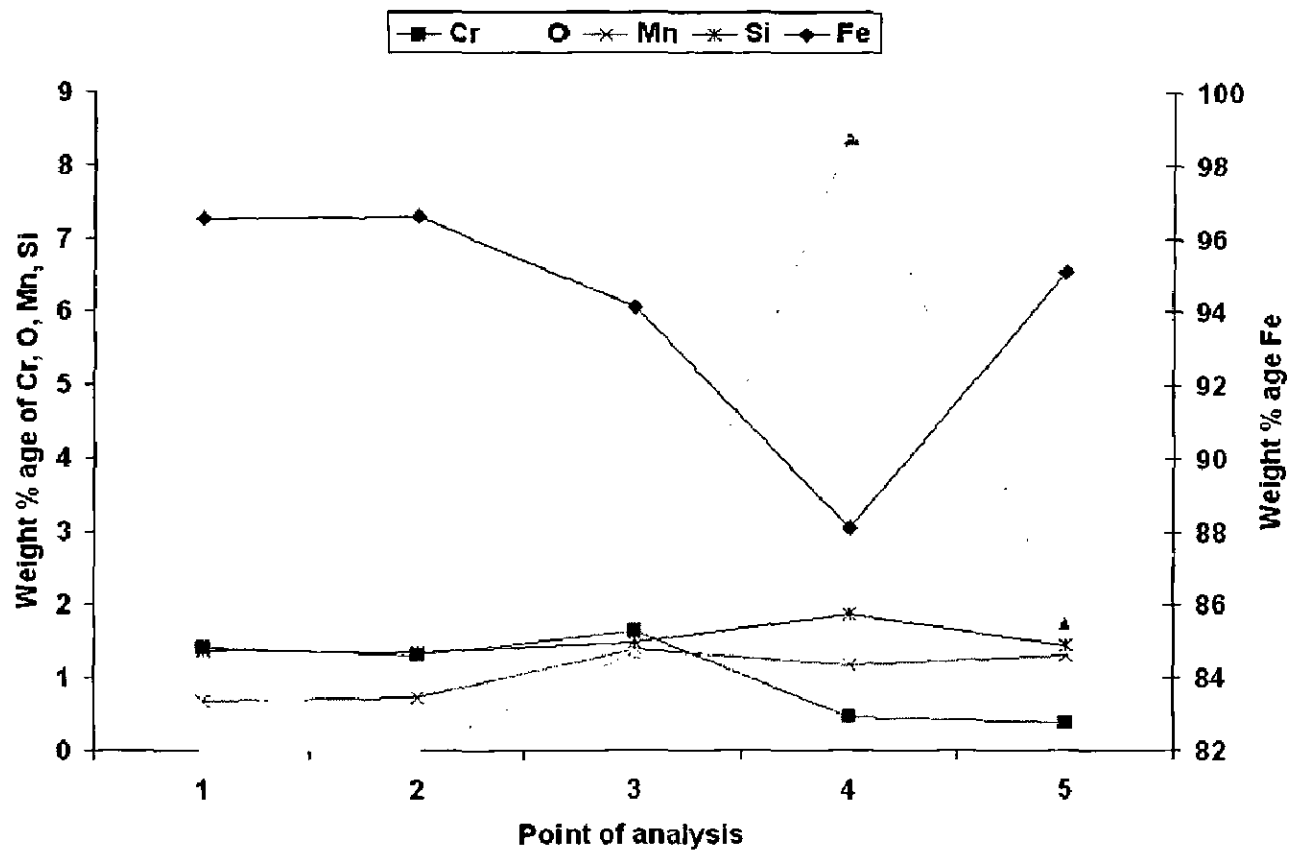


Fig.6.11: Cross sectional morphology and elemental composition variation across the cross-section of boiler steel T11 exposed air at 900°C for 50 cycles, 1000 X.

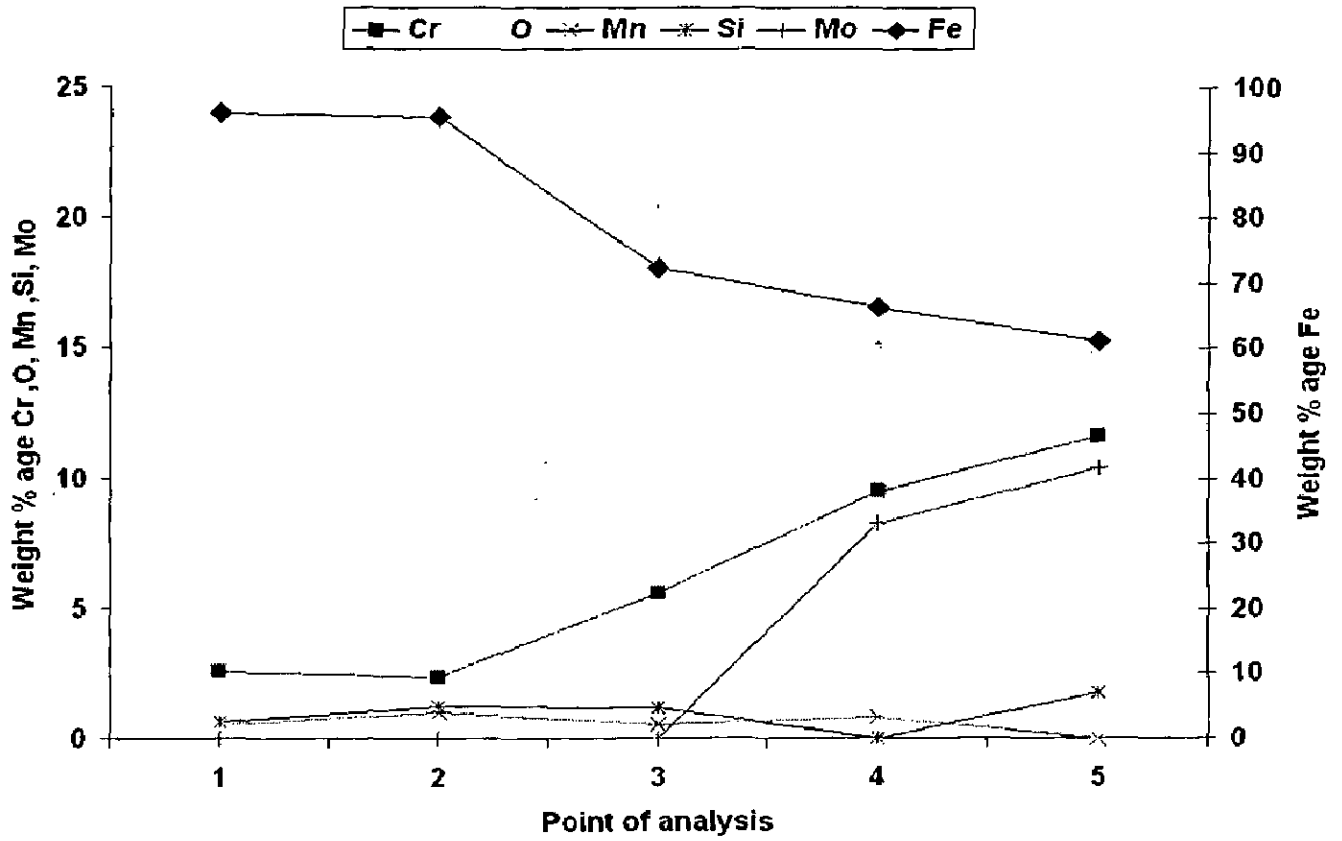


Fig.6.12: Cross sectional morphology and elemental composition variation across the cross-section of boiler steel T22 exposed air at 900°C for 50 cycles, 1000 X.

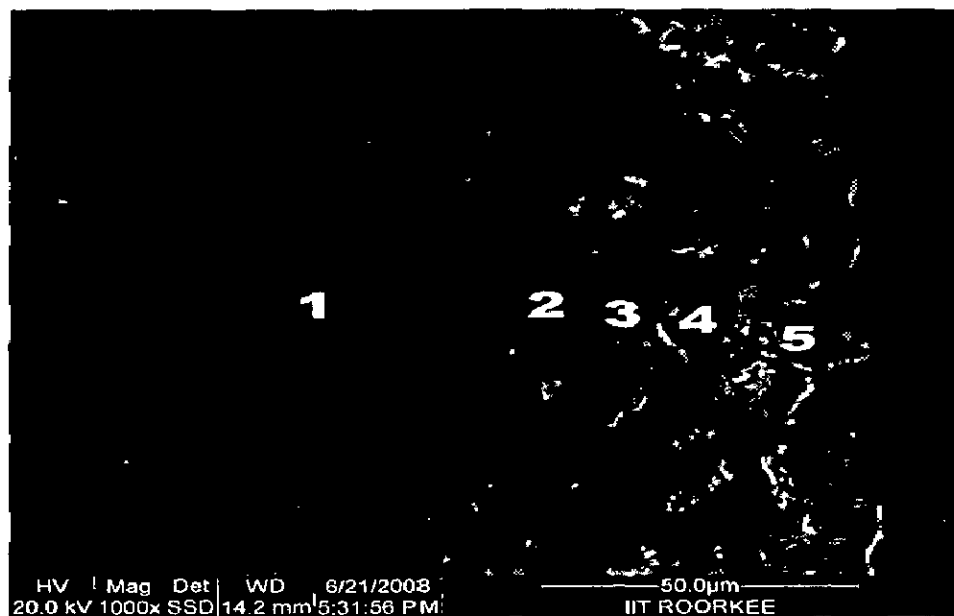
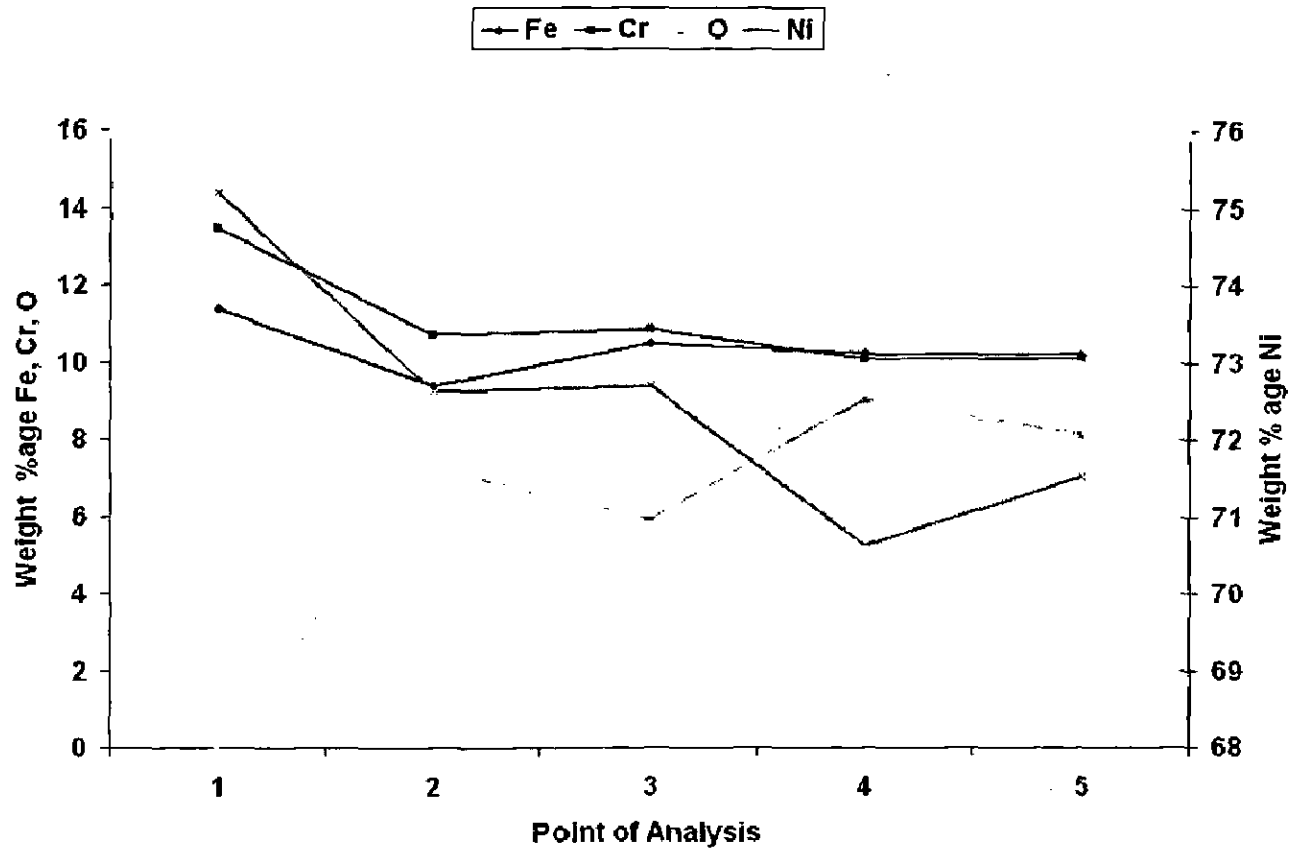


Fig 6.13: Cross sectional morphology and elemental composition variation across the cross-section of superalloy Superni 600 exposed air at 900°C for 50 cycles, 1000 X.

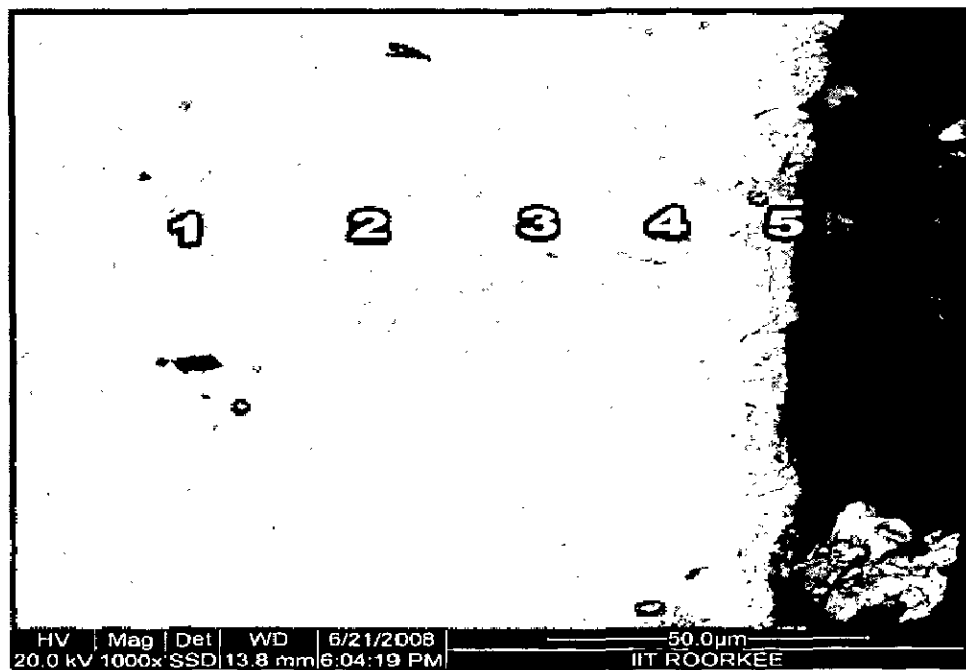
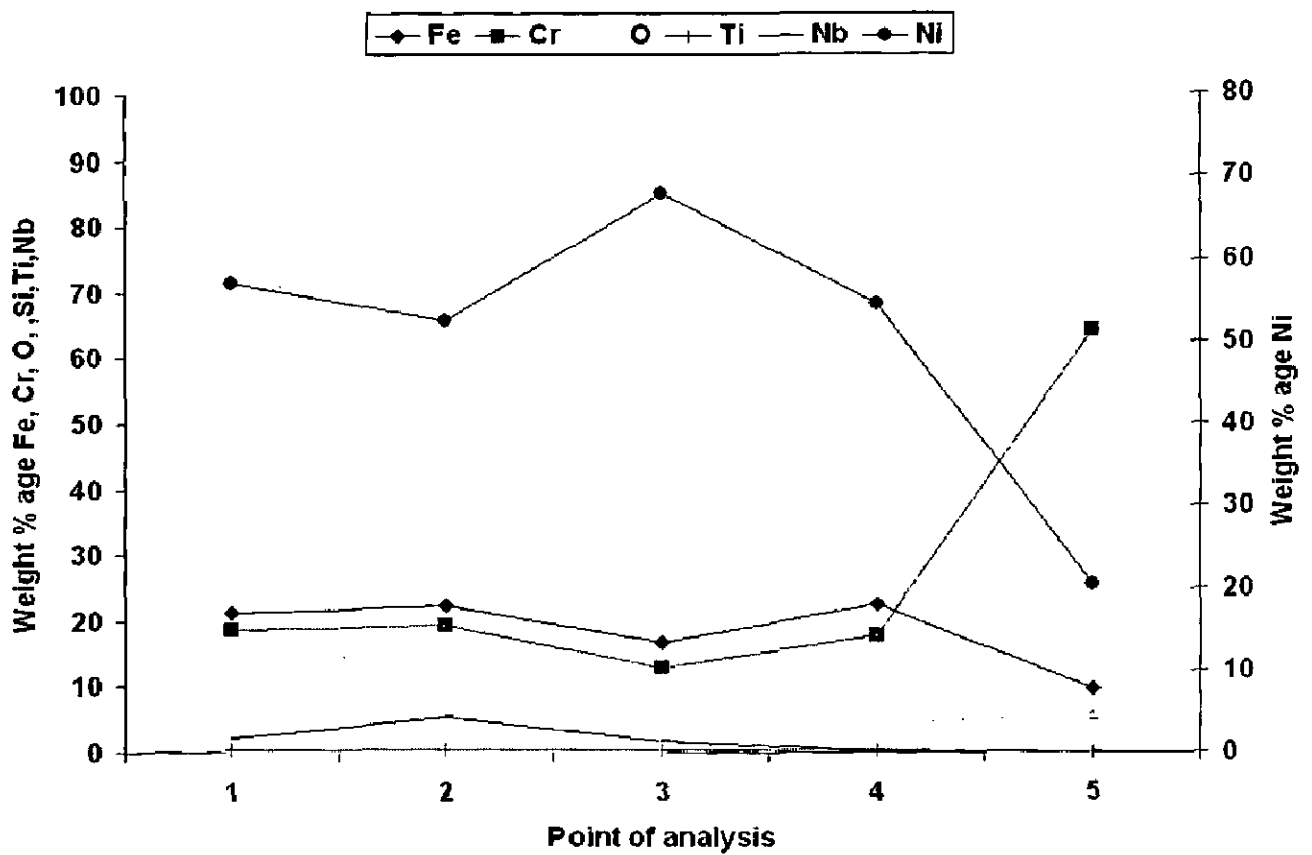


Fig 6.14: Cross sectional morphology and elemental composition variation across the cross-section of superalloy Superni 718 exposed air at 900°C for 50 cycles, 1000 X.

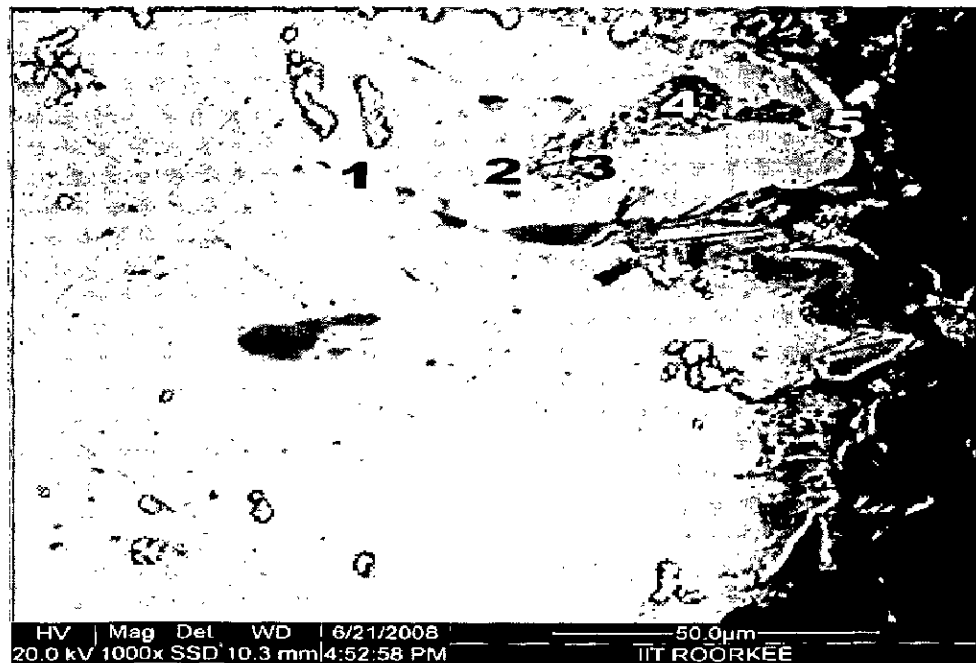
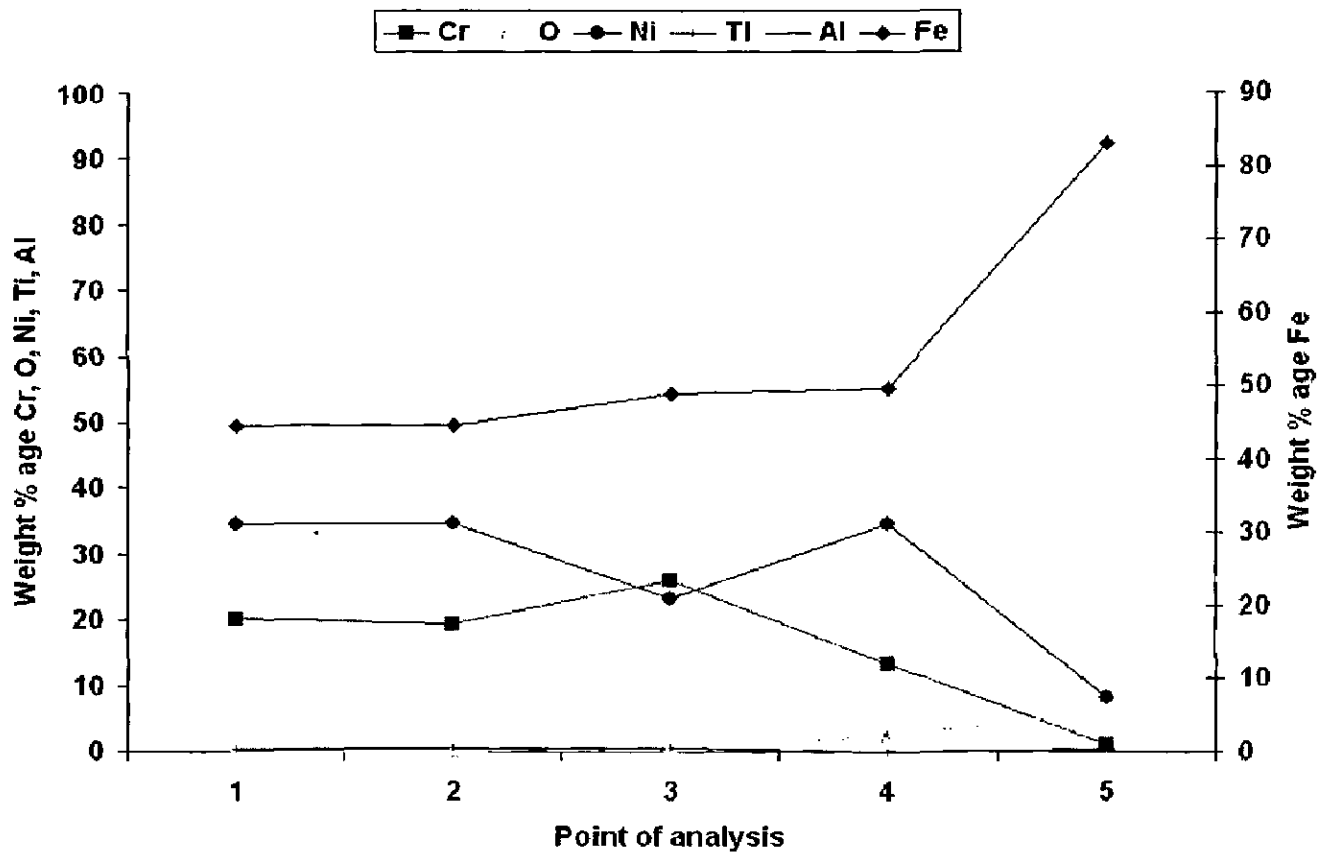


Fig.6.15: Cross sectional morphology and elemental composition variation across the cross-section of superalloy Superfer 800 exposed air at 900°C for 50 cycles, 1000 X.

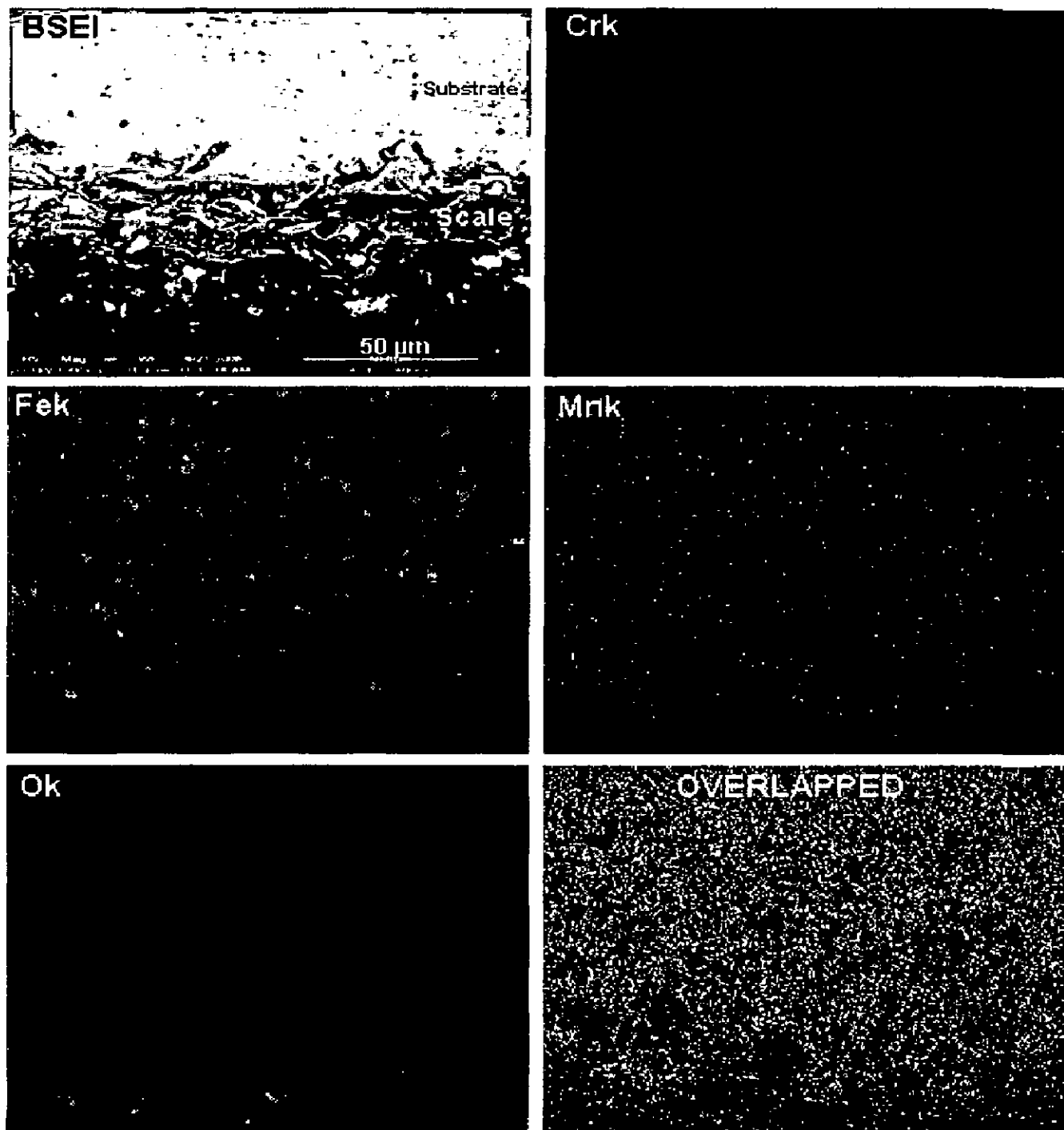


Fig. 6.16: BSEI and X-ray mapping of the cross-section of boiler steel T11 subjected to cyclic oxidation in air at 900°C for 50 cycles.

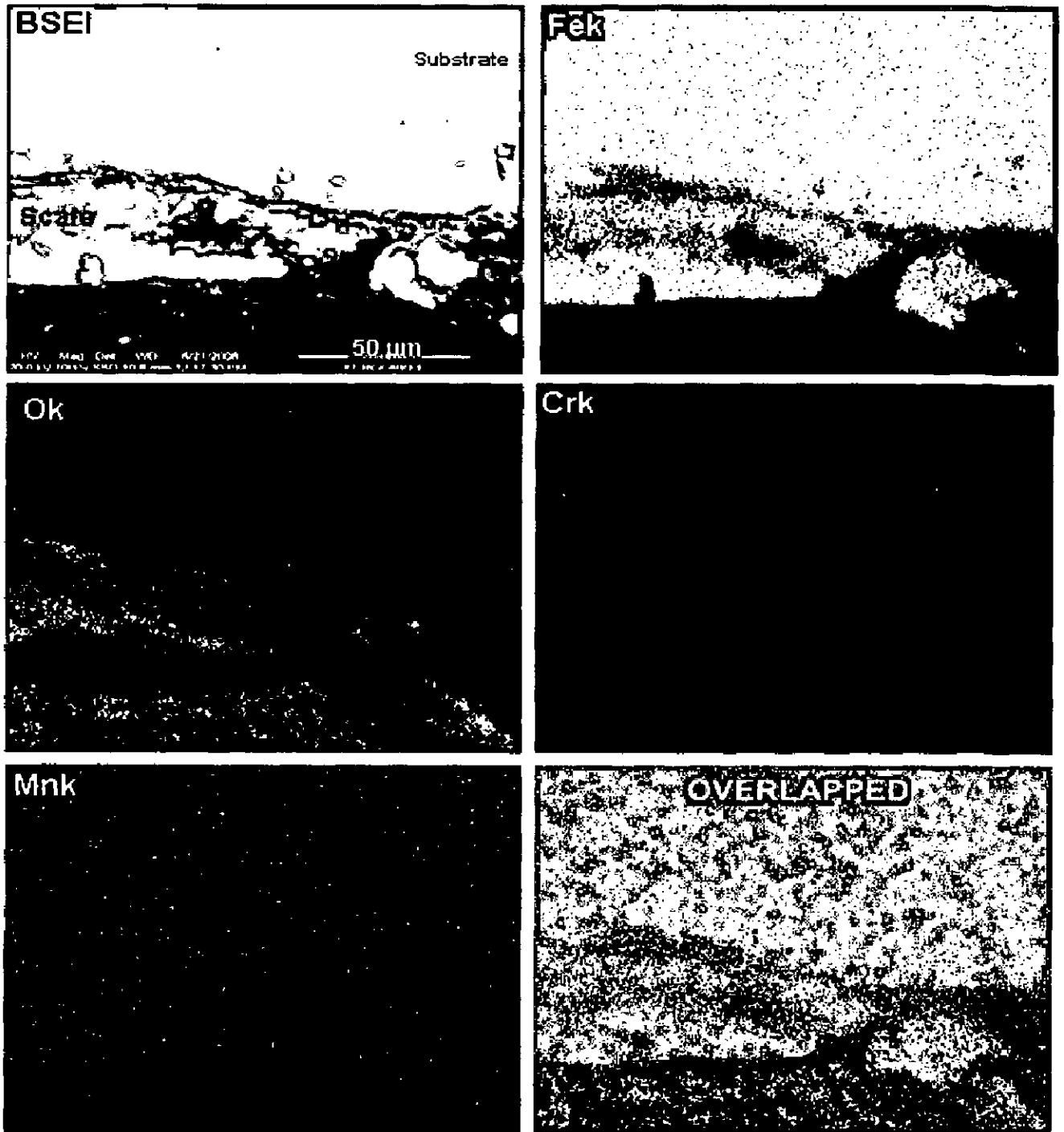


Fig. 6.17: BSEI and X-ray mapping of the cross-section of boiler steel T22 subjected to cyclic oxidation in air at 900°C for 50 cycles.

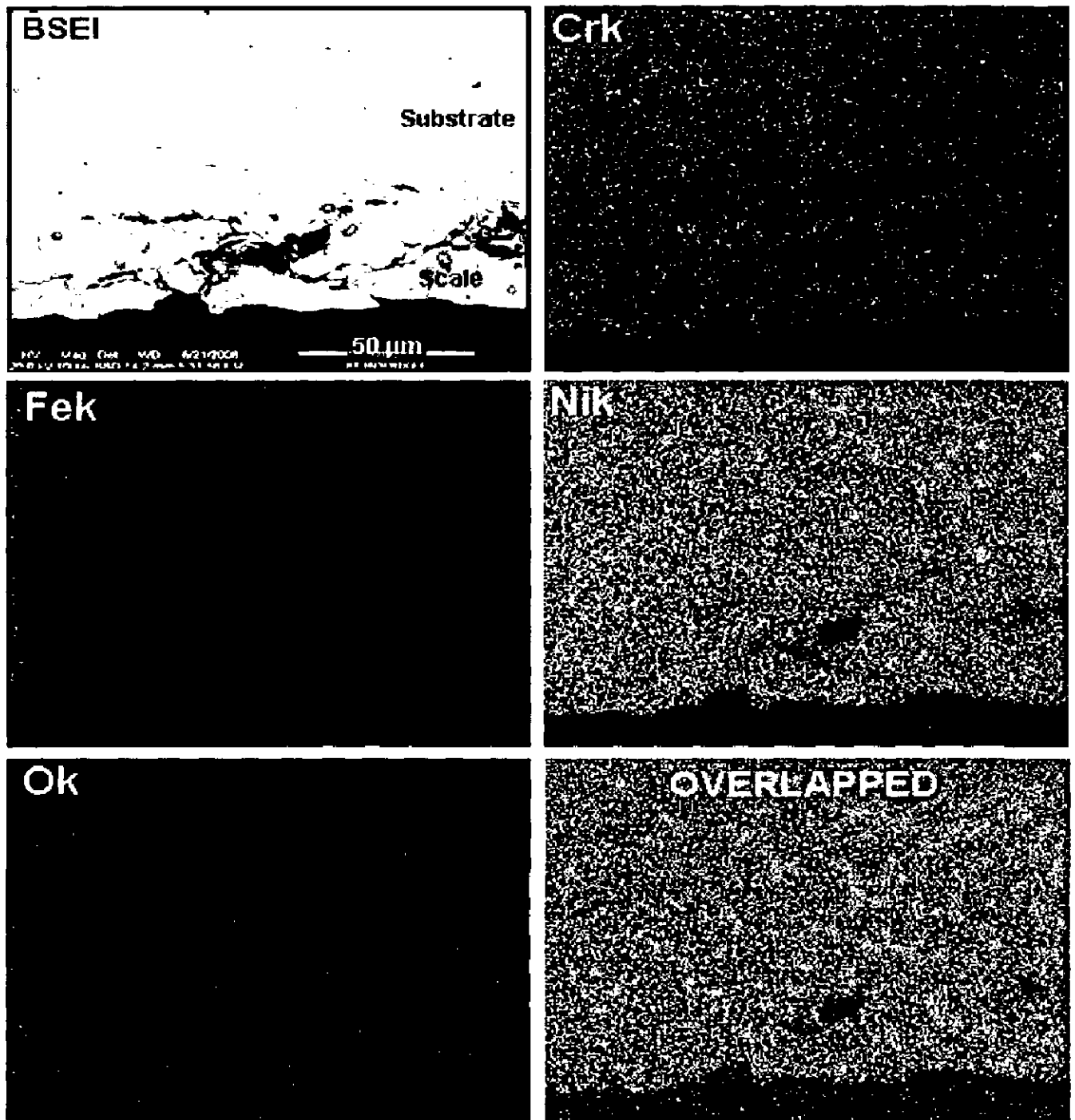


Fig.6.18: BSEI and X-ray mapping of the cross-section of superalloy Superni 600 subjected to cyclic oxidation in air at 900°C for 50 cycles.

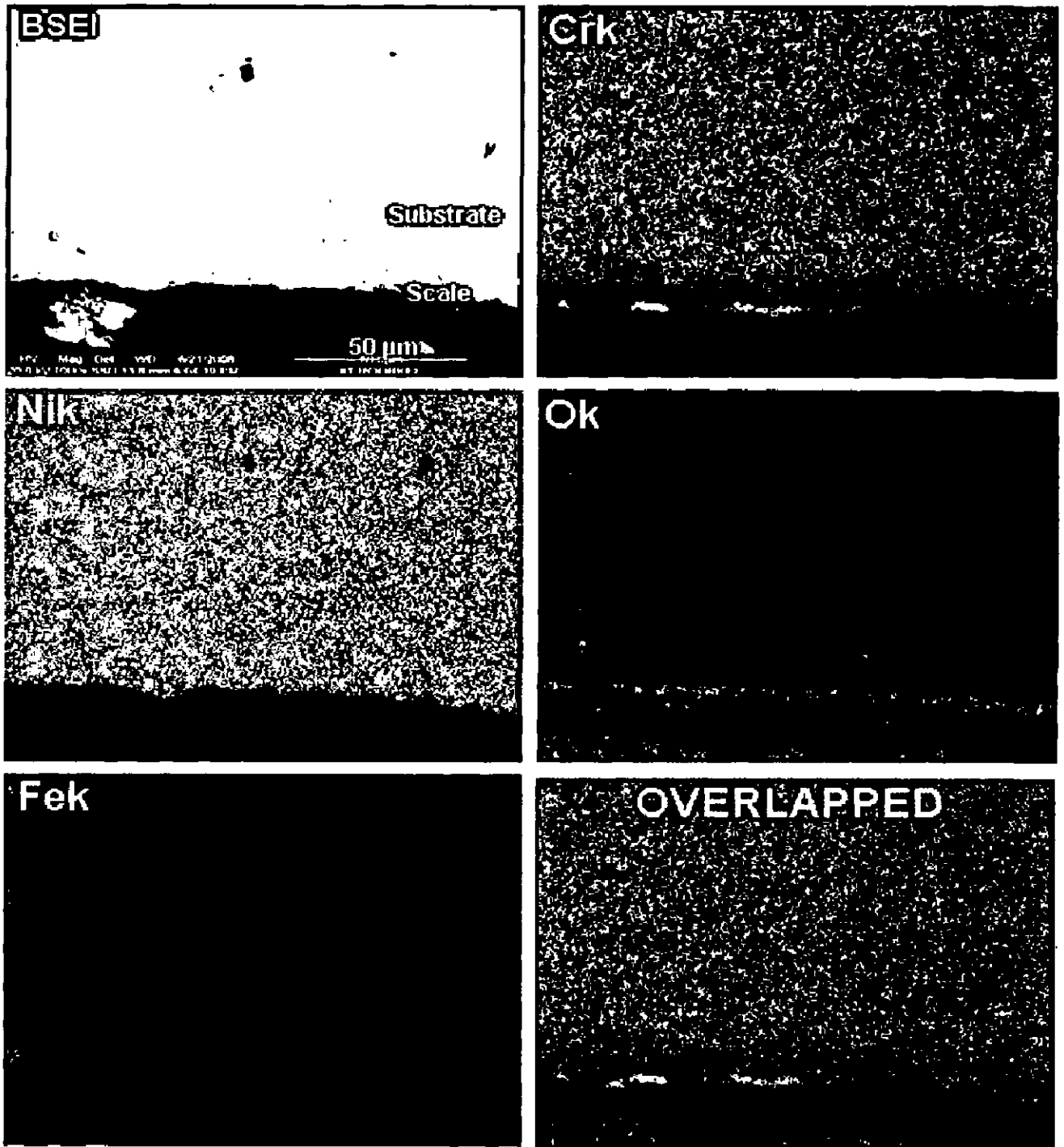


Fig.6.19: BSEI and X-ray mapping of the cross-section of superalloy Superni 718 subjected to cyclic oxidation in air at 900°C for 50 cycles.

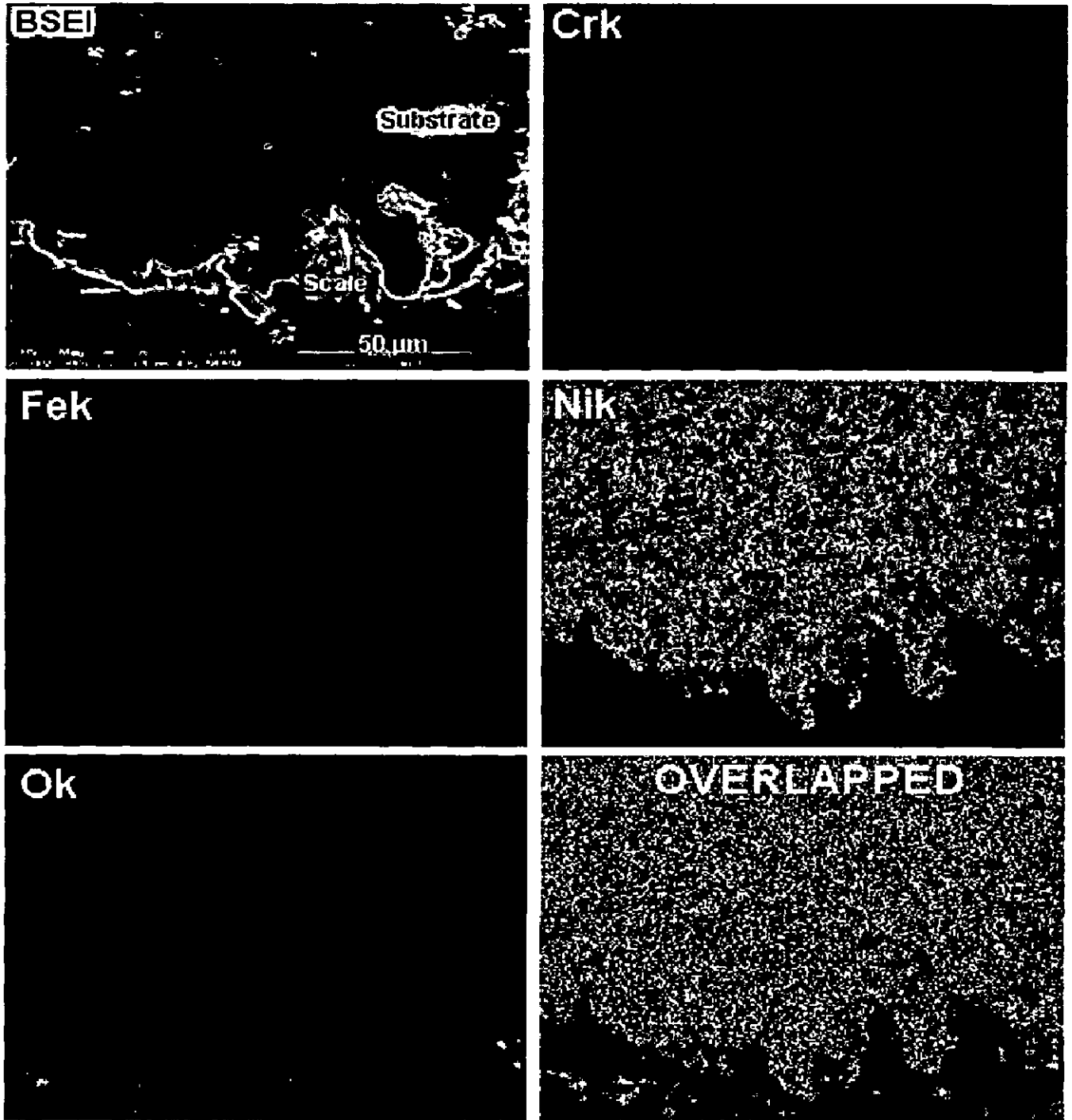


Fig. 6.20: BSEI and X-ray mapping of the cross-section of superalloy Superfer 800 subjected to cyclic oxidation in air at 900°C for 50 cycles.

6.1.1.2 Coated alloys

6.1.1.2.1 Visual examination

The macrographs of $\text{Al}_2\text{O}_3 - 3 \text{ wt}\% \text{ TiO}_2$ coated T11, T22, Superni 600, Superni 718 and Superfer 800 substrate alloys after oxidation at 900°C for 50 cycles in air environment are shown in Fig. 6.21. In the visual examination, it was observed that the colour of samples started changing from grey to cream (pale white) and in the subsequent cycles it turned to reddish cream colour. During the whole oxidation exposure, coating remained intact and there was no spalling or sputtering of the coating unlike bare specimens.

6.1.1.2.2 Weight Change Data

Weight gain per unit area expressed in mg/cm^2 is plotted as a function of time expressed in number of cycles for oxidized $\text{Al}_2\text{O}_3 - 3 \text{ wt}\% \text{ TiO}_2$ coated T11, T22 boiler steels is shown in Fig. 6.22 and for superalloys Superni 600, superni 718 and Superfer 800 superalloys is shown in Fig. 6.24.

The coated alloys showed less weight gain than uncoated alloys, the total weight gain at the end of 50 cycles for coated T11 and T22 steels is 2.874 and 1.853 mg/cm^2 and for coated superalloys i.e. $\text{Al}_2\text{O}_3 - 3 \text{ wt}\% \text{ TiO}_2$ coated Superni 600, Superni 718 and Superfer 800 is 1.1597, 0.3472 and 1.702 mg/cm^2 respectively.

Weight gain square (mg^2/cm^4) plotted as a function of time (number of cycles) in Fig. 6.23, from where it can be inferred that there is a scatter in the data as observed in the plots and the data can not be approximated by a parabolic relationship. If the scatter in the measurements is not considered, the values of parabolic rate constant (K_p) for the coated boiler steels T11 and T22 are 4.747×10^{-11} and $2.28 \times 10^{-11} \text{ g}^2 \text{ cm}^{-4} \text{ s}^{-1}$ respectively.

In case of $\text{Al}_2\text{O}_3 - 3 \text{ wt}\% \text{ TiO}_2$ coated superalloys; coated superfer 800 (Fig. 6.24) showed maximum weight gain as compared to other two coated superalloys Superni 600 and superni 718. In coated superfer 800, initially there is rapid weight gain upto 14th cycle, and then there is some constant weight gain for two cycles and then again there is weight gain upto 24th cycle and afterwards it is constant. In superni 600, upto 20th cycle there is weight gain and afterwards it is almost constant. In case of coated superni 718, weight gain is very small. Initially for first two cycles there is no weight gain and then there is small weight gain from 2nd to 4th cycle and then again it has become constant upto 8th cycle, afterwards there is some weight gain upto 12th cycle. Then it remained constant upto 16th cycle. Then there is small weight gain upto 18th cycle and afterwards it has become constant. In case of coated superalloys viz. Superni 600 and superni 718, rapid oxidation rate has not been observed and very small weight gains have been observed and

steady state has been reached with the progress of exposure time, in spite of the fact that some minor deviations are observed in between. The total weight gain at the end of 50 cycles for the superalloys Superni 600, 718 and Superfer 800 is 1.16, 0.35 and 1.71 mg/cm² respectively. This shows that the weight gain in case of oxidised Al₂O₃-3wt% TiO₂ coated Superni 718 is lowest, whereas it is highest in case of Al₂O₃-3 wt% TiO₂ coated Superfer 800.

In Fig. 6.25, the (weight gain/unit area)² versus number of cycles for all the coated superalloys are plotted to determine the conformance with the parabolic rate law. The curve for coated Superni 718 is parabolic. While in case of superni 600 and superfer 800, scatter in the data can be observed in the plots and the data can not be approximated by a parabolic relationship. If the scatter in the measurements is not considered, the values of parabolic rate constant (K_p) for the superalloys Superni 600, 718 and Superfer 800 are calculated as 8.19 X 10⁻¹², 7.22X10⁻¹³ and 1.65x10⁻¹¹ g² cm⁻⁴ s⁻¹ respectively.

6.1.1.2.3 X-ray Diffraction Analysis

X-ray diffraction profiles for Al₂O₃-3 wt% TiO₂ coated boiler steels subjected to cyclic oxidation in air at 900⁰C for 50 cycles are shown in Fig. 6.26. Both the coated boiler steels have Al₂O₃ and TiO₂ as the main constituent. After the oxidation process some peaks Al₂TiO₇O₁₅ of were observed in coated T11 and Al₂TiO₅ was observed in coated T22 steel. The X-ray diffractograms for the coated superalloys after exposure to air at 900⁰C for 50 cycles is shown in Figs. 6.27 and 6.28. Al₂O₃ and TiO₂ along with minor phases of Al₂TiO₅ and Al₂TiO₇O₁₅ were found to be present in all the oxidised coated superalloys.

6.1.1.2.4 SEM/EDX Analysis

(a) Surface Morphology

The SEM micrograph showing the morphology of the Al₂O₃ - 3 wt% TiO₂ coated samples and the EDX analysis after exposure to air at 900⁰C for 50 cycles is shown in Figs. 6.29 and 6.30. From SEM/EDX analysis of T11 and T22 boiler steels, it has been revealed that the constituent of scale is Al and Ti along with O. The oxide scale is intact and firm. No spalling was observed throughout the study.

Also in case of Al₂O₃ - 3 wt% TiO₂ coated superalloys exposed to air at 900⁰C for 50 cycles, a fine surface scale is observed mainly consisted of Al and Ti with O as shown in Fig.6.30. No spallation of the scale has been observed. A well adherent scale is formed which mainly consists of Al₂O₃ and TiO₂. The matrix of the scale of all the coated substrates has dominance of Al₂O₃ and is evident from EDX analysis.

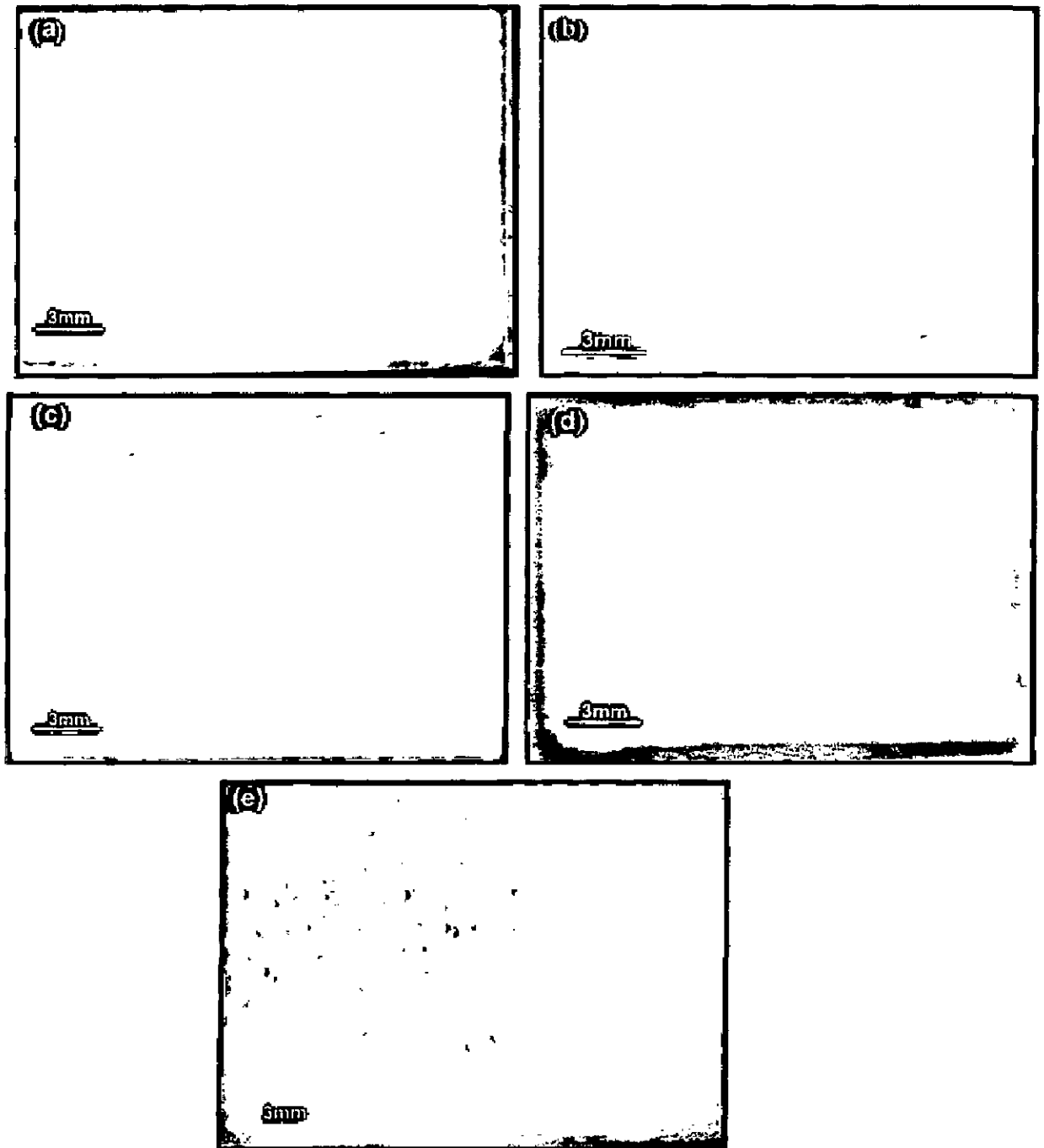


Fig.6.21: Macrographs of $\text{Al}_2\text{O}_3\text{-3wt\%TiO}_2$ coated substrate alloys after cyclic oxidation in air at 900°C for 50 cycles.
(a) T11 (b) T22 (c) Superni 600 (d) Superni718 (e) Superfer 800

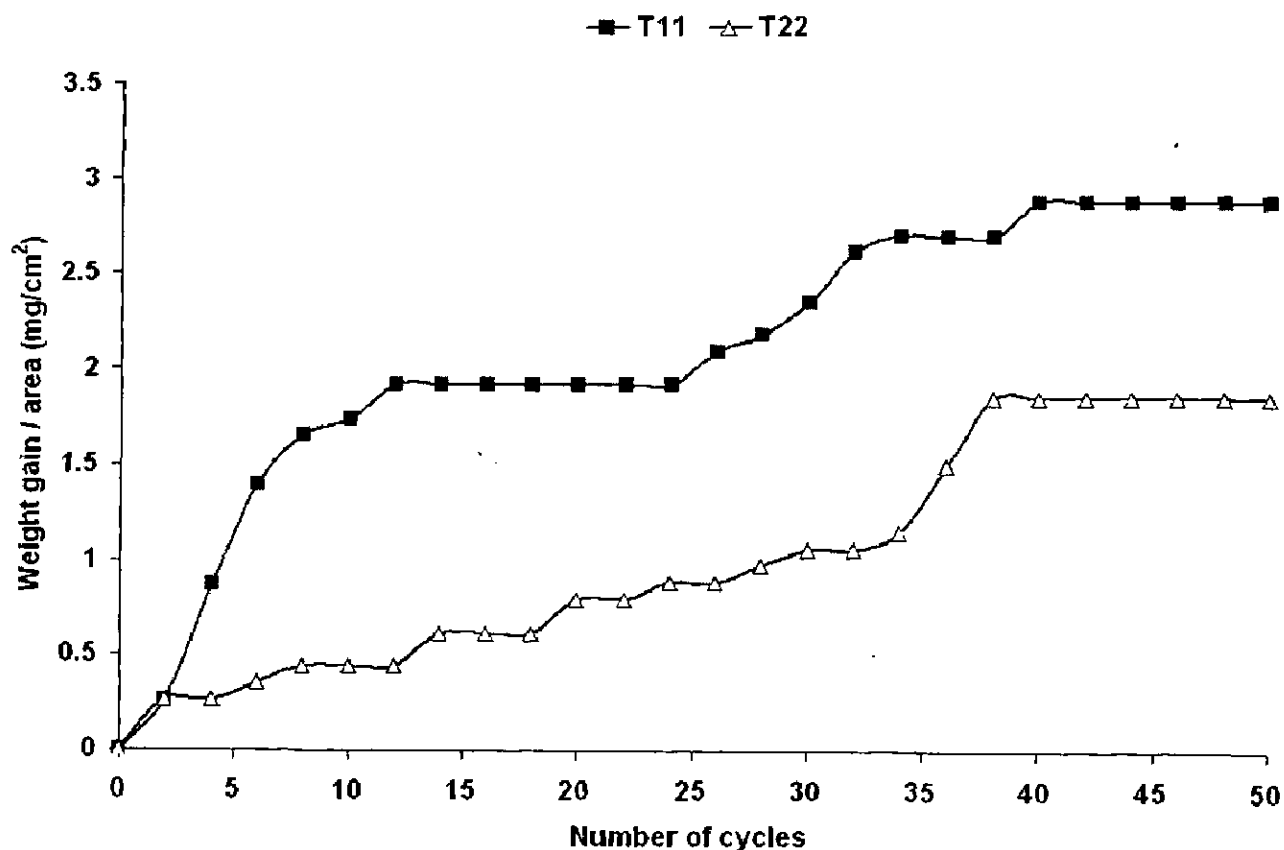


Fig. 6.22: Weight gain plot for Al_2O_3 - 3 wt% TiO_2 coated boiler steels T11 and T22 exposed to air at 900°C for 50 cycles.

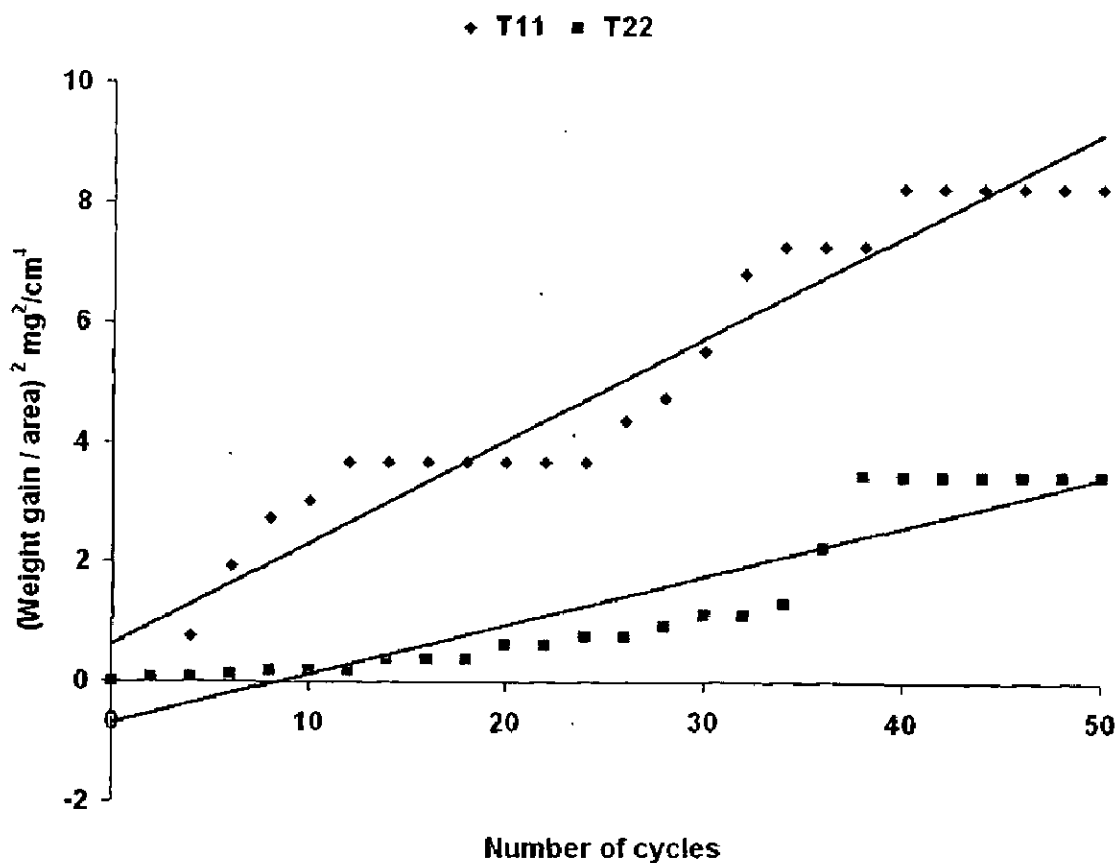


Fig.6.23: Weight gain square (mg^2/cm^4) plot for Al_2O_3 - 3 wt% TiO_2 coated boiler steels T11 and T22 exposed to air at 900°C for 50 cycles.

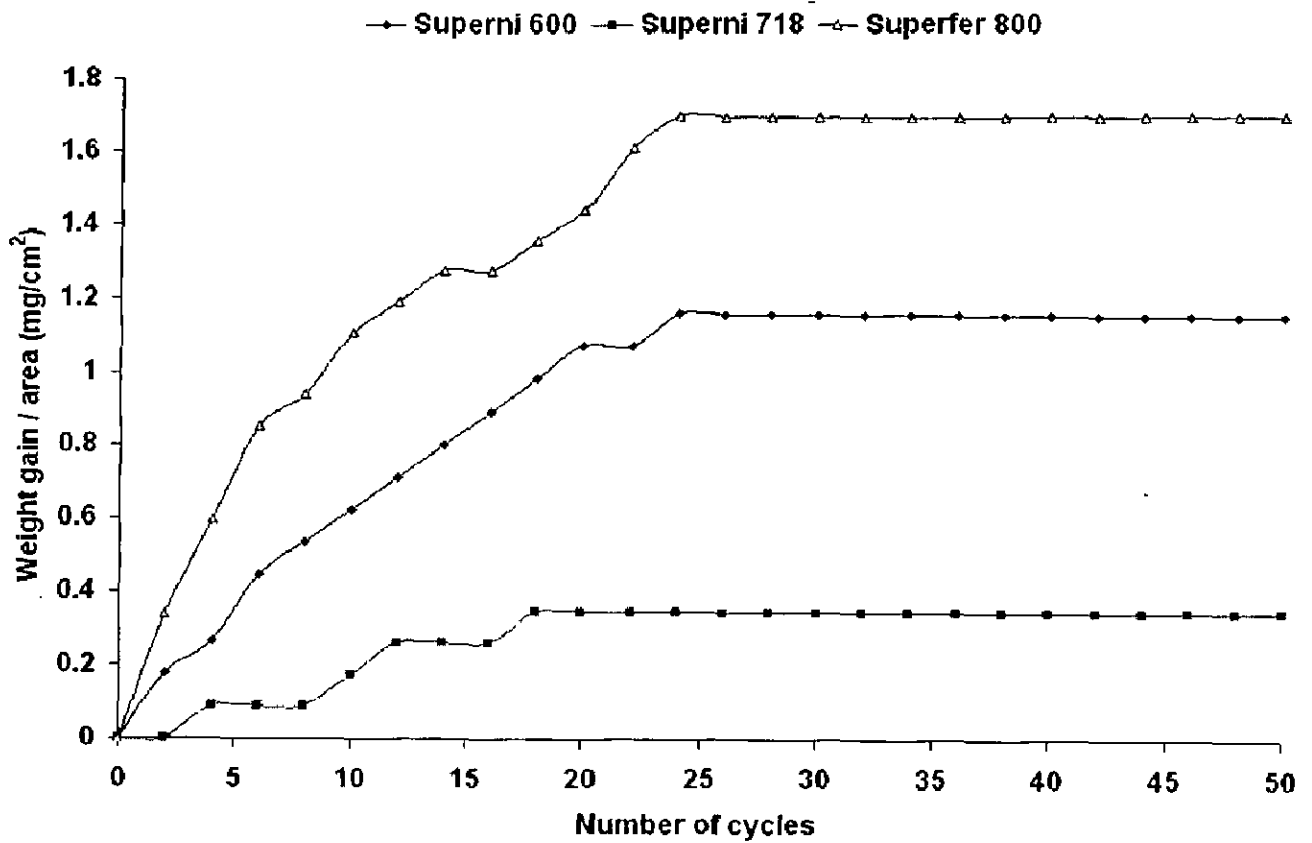


Fig. 6.24: Weight gain plot for Al_2O_3 - 3 wt% TiO_2 coated superalloys Superni 600, Superni 718, Superfer 800 exposed to air at 900°C for 50 cycles.

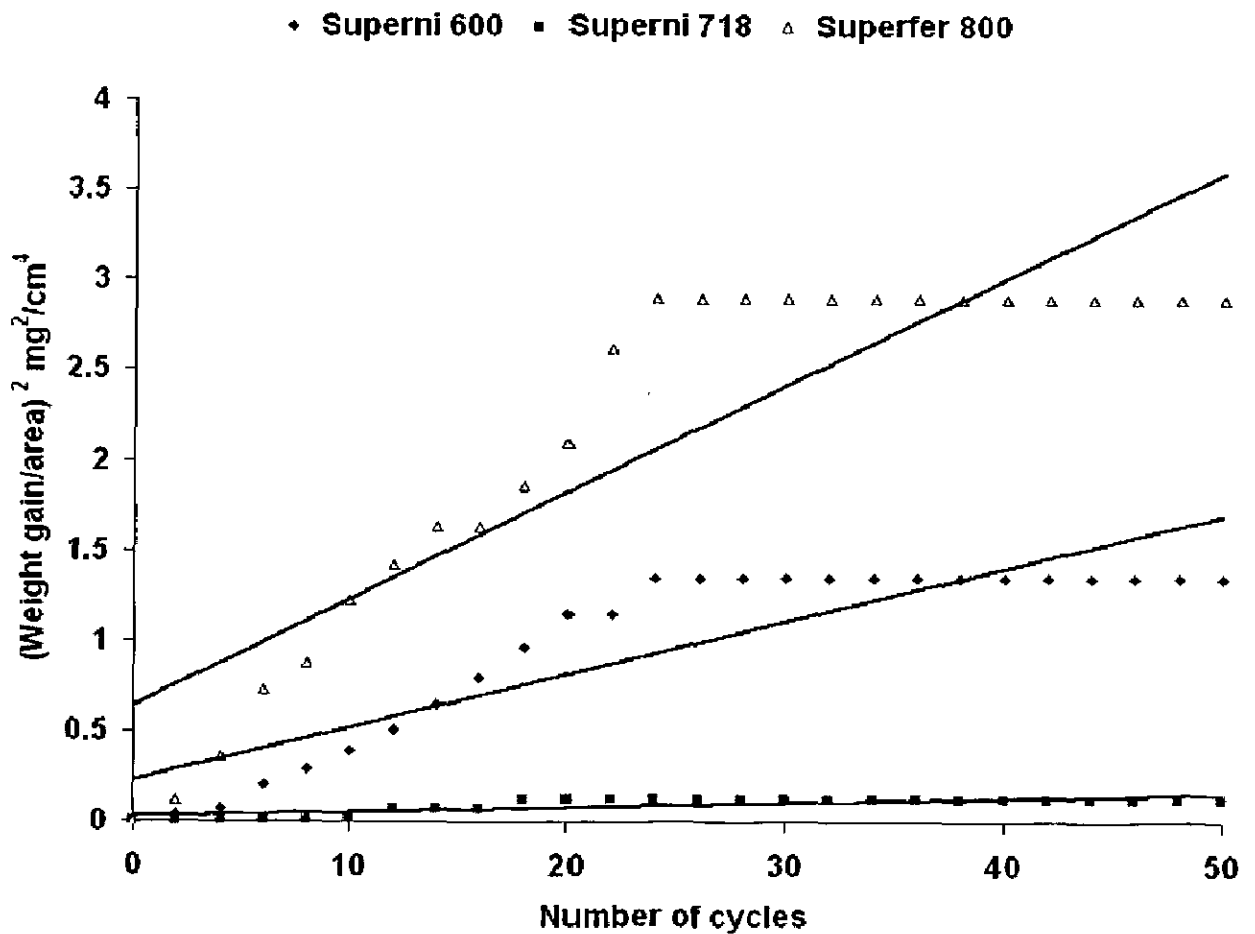
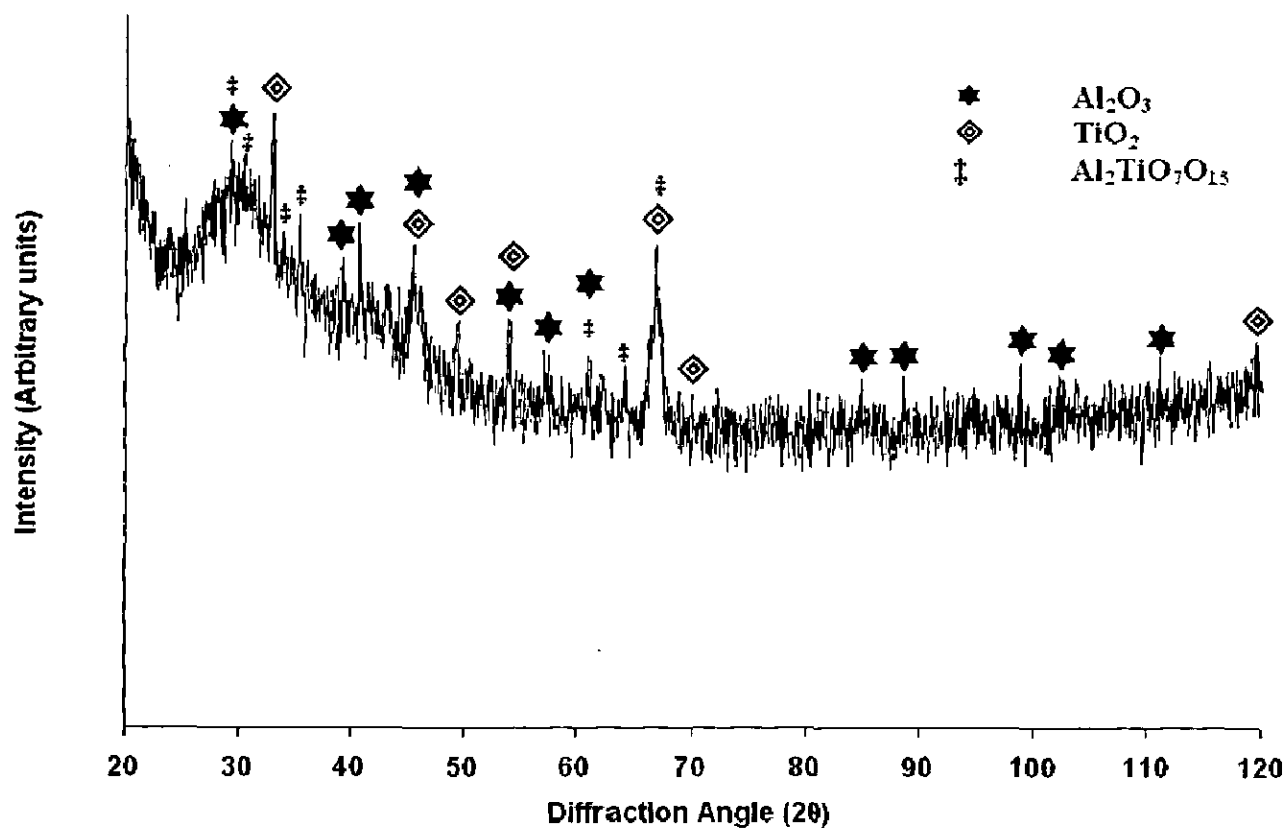
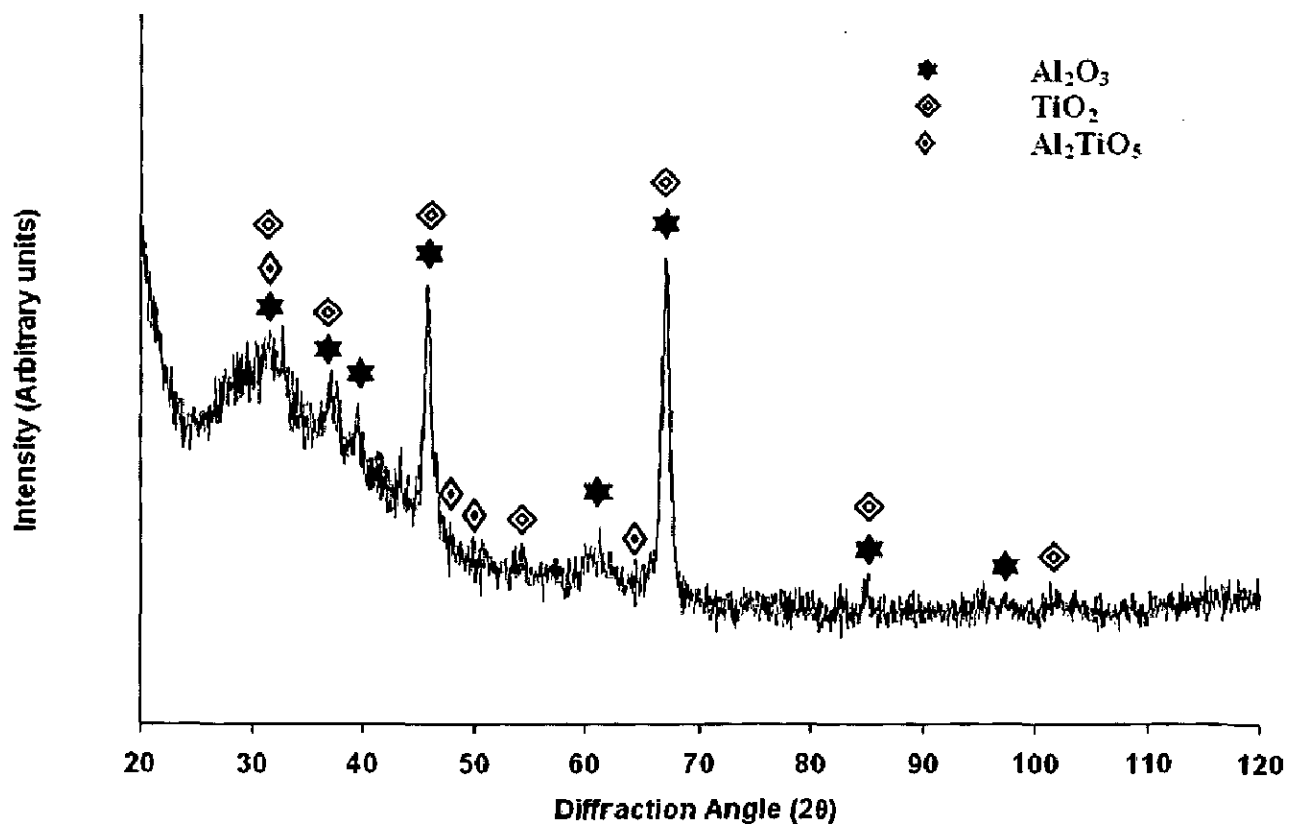


Fig. 6.25: Weight gain square (mg^2/cm^4) plot for Al_2O_3 - 3 wt% TiO_2 coated superalloys Superni 600, Superni 718, Superfer 800 exposed to air at 900°C for 50 cycles.



(a)

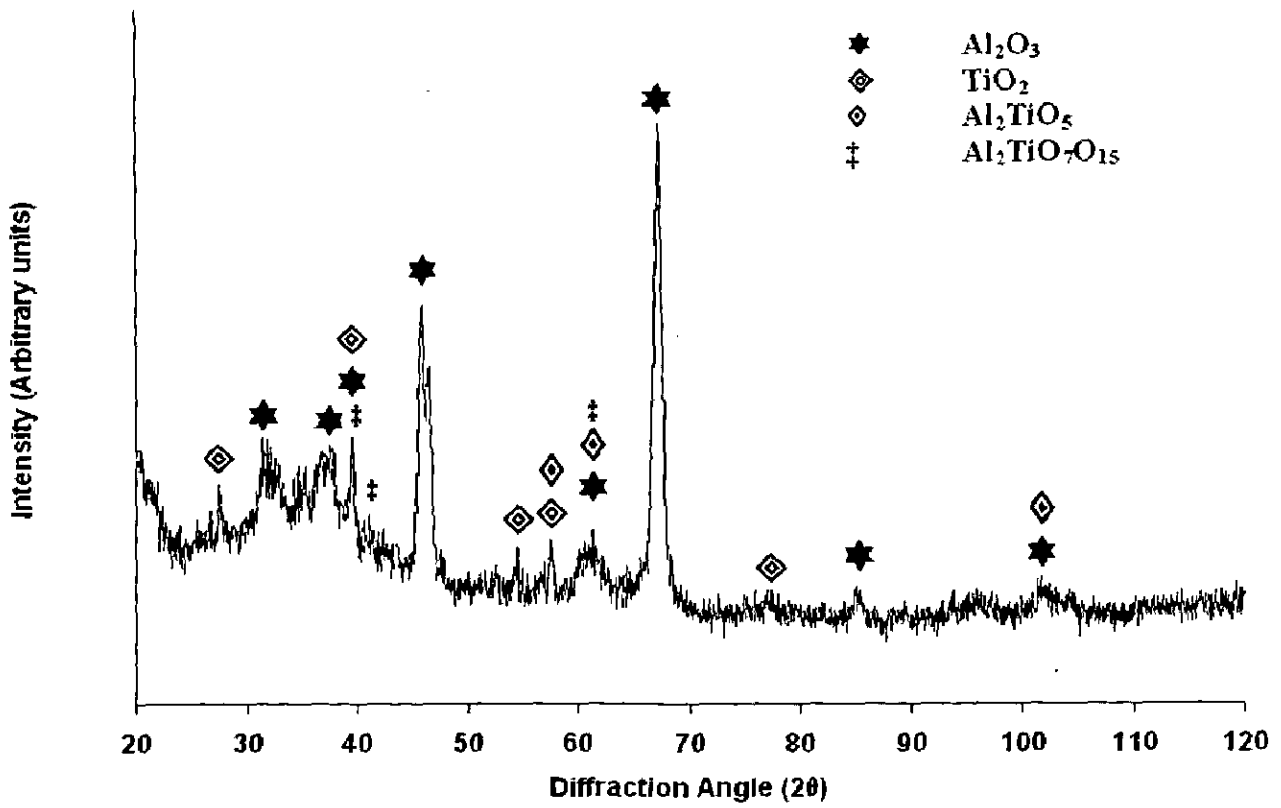


(b)

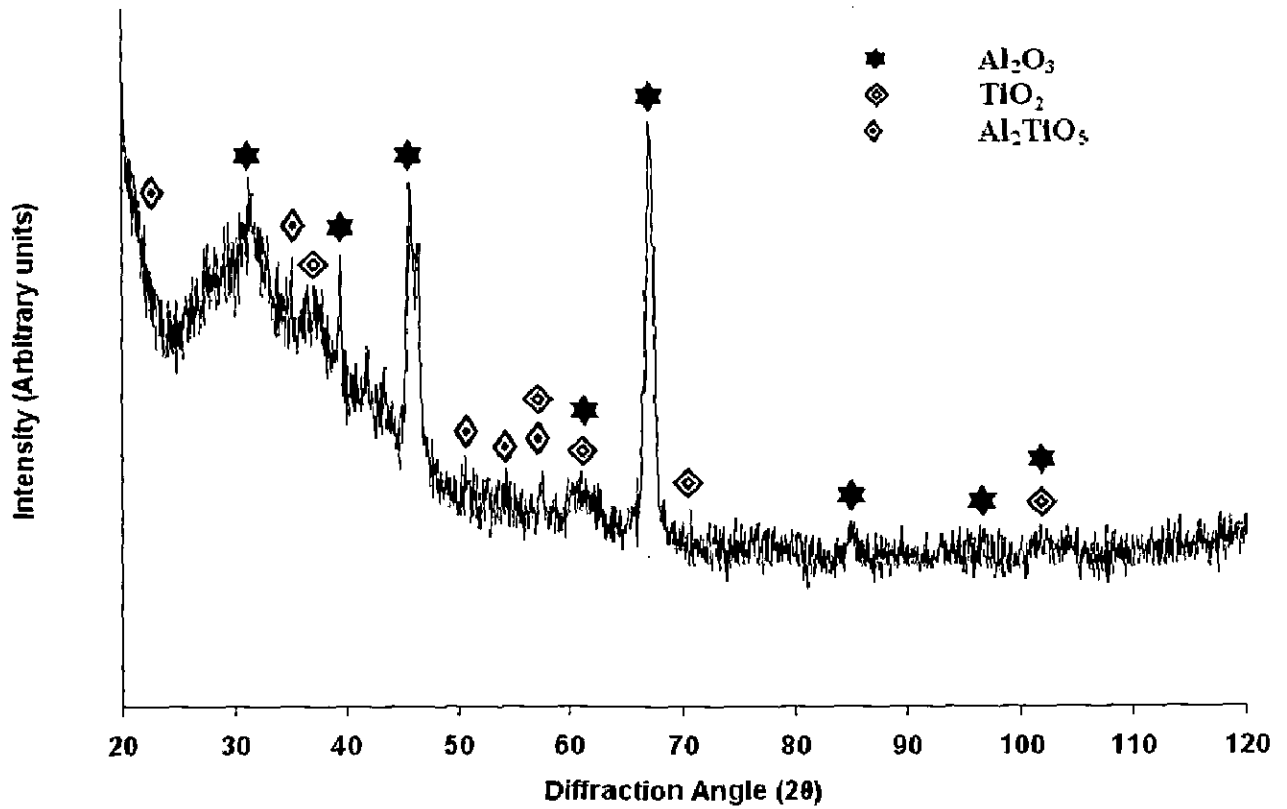
Fig. 6.26: X-ray diffraction profiles for Al_2O_3 -3 wt% TiO_2 coated boiler steels subjected to cyclic oxidation in air at 900°C for 50 cycles.

(a) T11

(b) T22



(a)



(b)

Fig. 6.27: X-ray diffraction profiles for Al_2O_3 -3 wt% TiO_2 coated superalloys subjected to cyclic oxidation in air at 900°C for 50 cycles.
 (a) Superni 600 (b) Superni 718

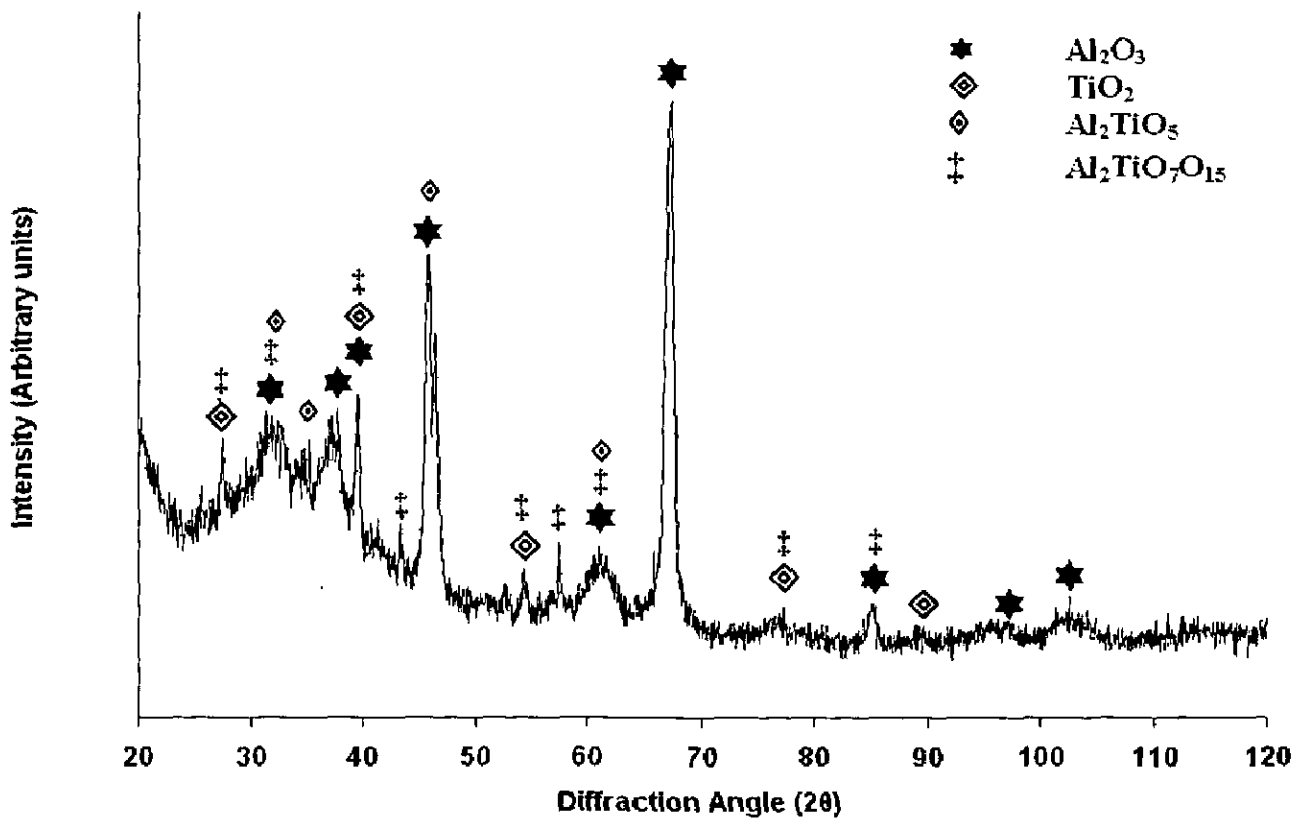


Fig. 6.28: X-ray diffraction profiles for Al₂O₃-3 wt% TiO₂ coated superalloy Superfer 800 subjected to cyclic oxidation in air at 900°C for 50 cycles.

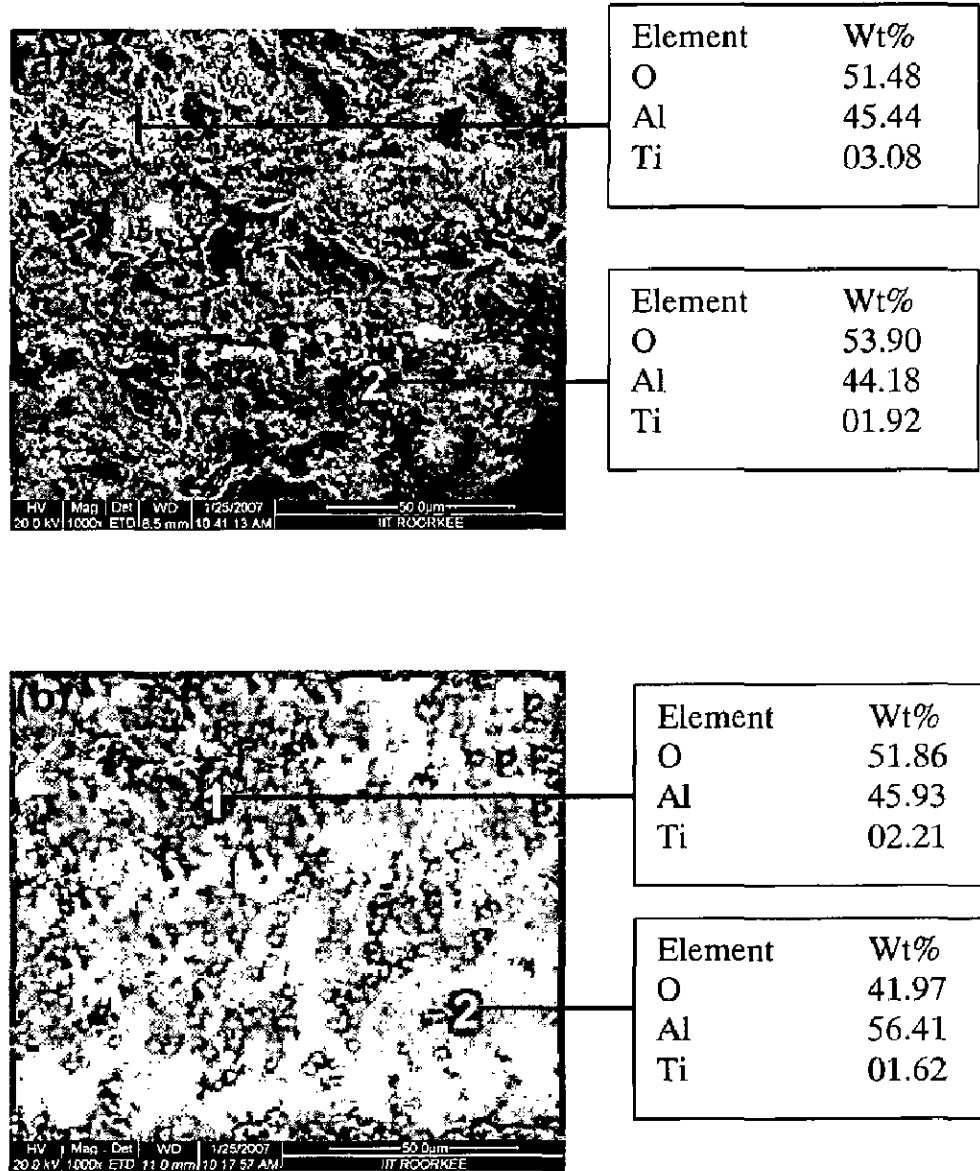


Fig. 6.29: Surface scale morphology and EDX analysis for Al_2O_3 -3wt% TiO_2 coated steels oxidized in air at 900°C for 50 cycles
 (a) T11, 1000 X (b) T22, 1000 X.

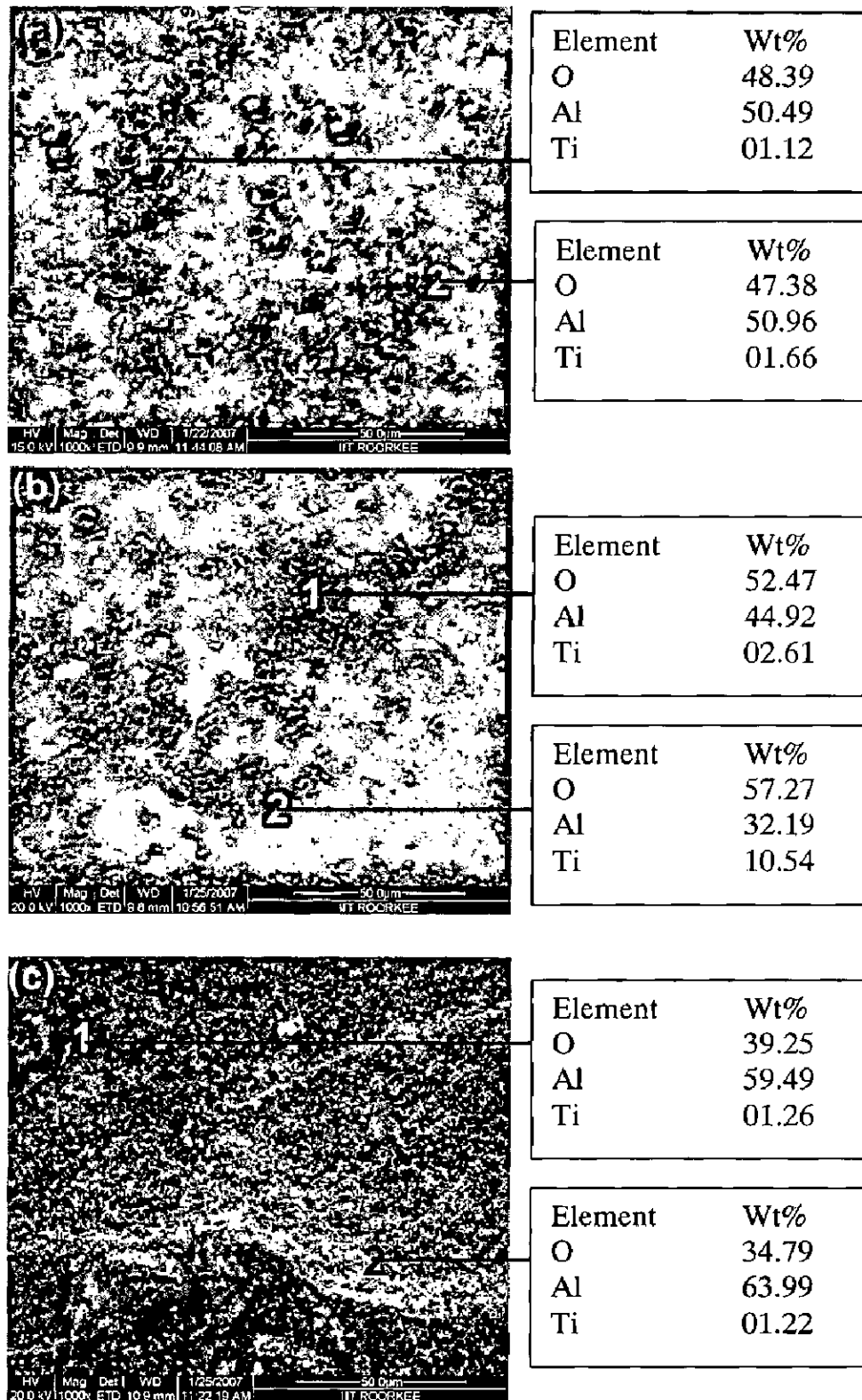


Fig. 6.30: Surface scale morphology and EDX analysis for $\text{Al}_2\text{O}_3\text{-3wt\%TiO}_2$ coated superalloys oxidized in air at 900°C for 50 cycles (a) Superni 600, 1000 X (b) Superni 718, 1000 X. (c) Superfer 800, 1000X.

(b) Cross-Sectional Analysis and X ray mapping

The BSE image and the EDX analysis across the cross section on Al_2O_3 -3 wt% TiO_2 coated alloys are shown in Fig.6.31 to Fig. 6.35. The results of the cross-section analysis for oxidised T11 and T22 boiler steels are plotted and shown in Fig. 6.31 and 6.32 along with micrographs. By viewing the cross sectional micrograph and the corresponding EDX analysis of coated T11, it is quite clear that coating is firm and intact and there is no deterioration of coating and hence coating has protected the surface very well. There is no penetration of oxygen in the substrate during the entire exposure of the coated specimen. As we approach from substrate to coating, at point 4 and point 5 there is no indication of presence of elements other than present in the coating and same is in case of coated T22.

Also in case of coated superalloys, EDX analysis has revealed that the scale mainly consisted of Al and Ti oxides. Oxide scale morphology along with variation of elemental composition across the cross-section of superalloy coated Superni 600 subjected to cyclic oxidation in air at 900°C after 50 cycles has been depicted in Fig. 6.33. The plots of elemental composition variation show that the scale mainly consists of aluminum and titanium along with oxygen. There is no penetration of oxygen into the substrate through the coating. In coated Superni 718, (Fig. 6.34) coating is intact and adherent and there is no oxidation of substrate beneath the coating. In coated Superfer 800, Fig. 6.35, the coating has major portion of aluminium oxide

Back Scattered Electron Image of cross-section of Al_2O_3 -3 wt% TiO_2 coated substrate alloys (T11, T22, Superni 600, Superni 718 and Superfer 800) and corresponding X-ray mapping after oxidation in air at 900°C after 50 cycles is shown in Fig. 6.36 to 6.40 respectively. In all the coated alloys coatings has acted as a barrier and thus have prevented oxidation of substrate by inhibiting the penetration of oxygen. There is no spalling of coating throughout the testing. In coated boiler steels T11 and T22 (Fig.6.36 and 6.37), main constituent is aluminium oxide and there is no inward

penetration of any element into the substrate. In coated T22 steel very thin layer of Fe_2O_3 is seen at the outer edge of the coating (Fig.6.37)

In coated Superni 600, Fig.6.38 coating remained intact. TiO_2 is seen concentrated as a streak at the interface and is also dispersed throughout the coating. Iron and Nickel have diffused into the coating but are not oxidised. In coated Superni 718, Fig.6.39 coating is intact and iron from substrate has diffused into the coating. A clear titanium rich band is seen along the interface and also a parallel band of titanium is present in the coating. TiO_2 is also seen at the top surface of the coating. In coated Superfer 800, Fig.6.40 Iron, Nickel and chromium have diffused from substrate into the coating and is present around Al_2O_3 grain. Some Cr has diffused from base alloy to the interface of the coating as is visible from the overlapped maps. Cr_2O_3 band has been formed at the coating substrate interface. The coating is intact and has prevented the penetration of oxygen from the atmosphere into the substrate. Thin streak of iron is also visible in the exposed coating

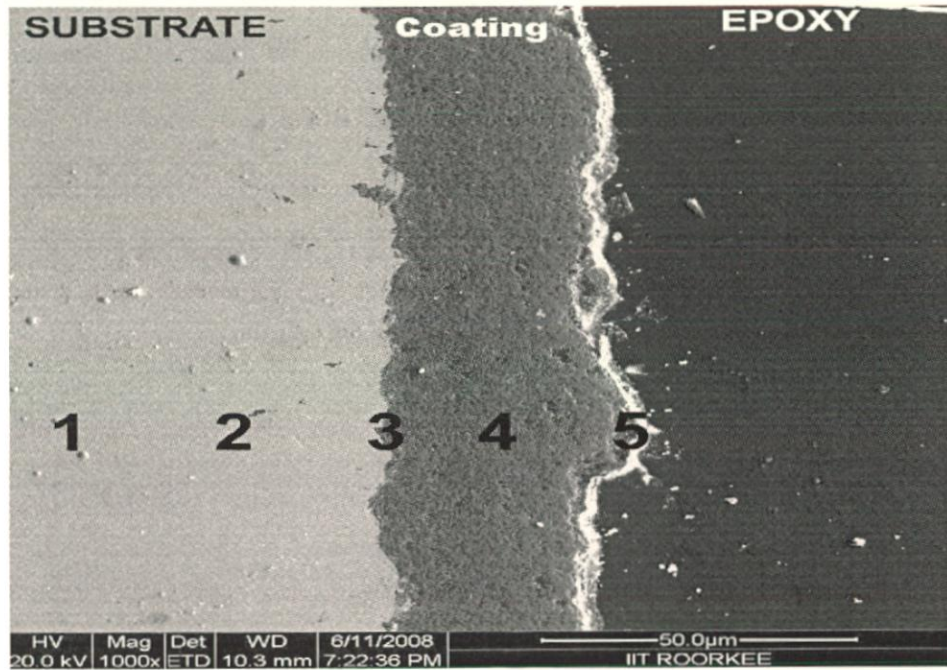
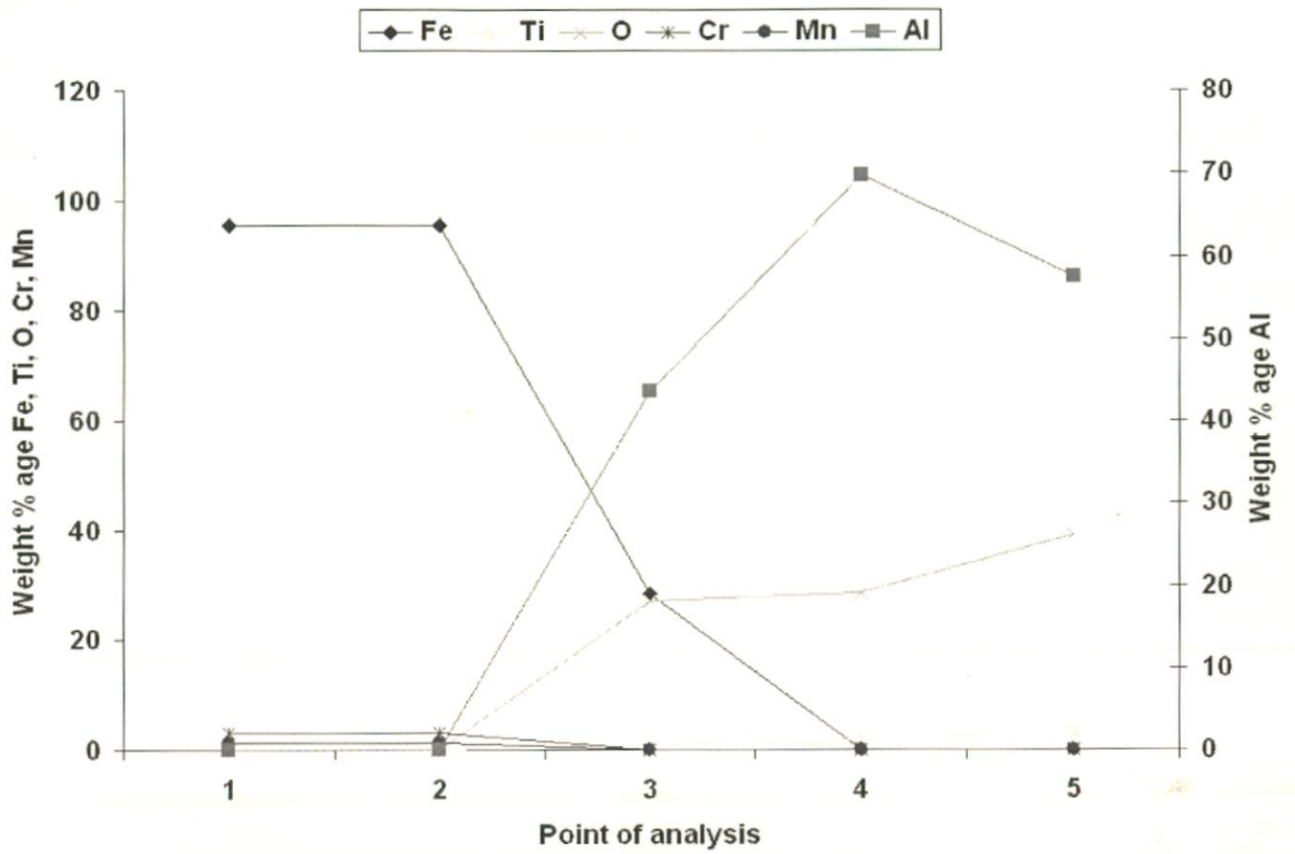


Fig. 6.31: Cross sectional morphology and elemental composition variation across the cross-section of $\text{Al}_2\text{O}_3\text{-3wt\%TiO}_2$ coated boiler steel T11 exposed to air at 900°C for 50 cycles, 1000 X.

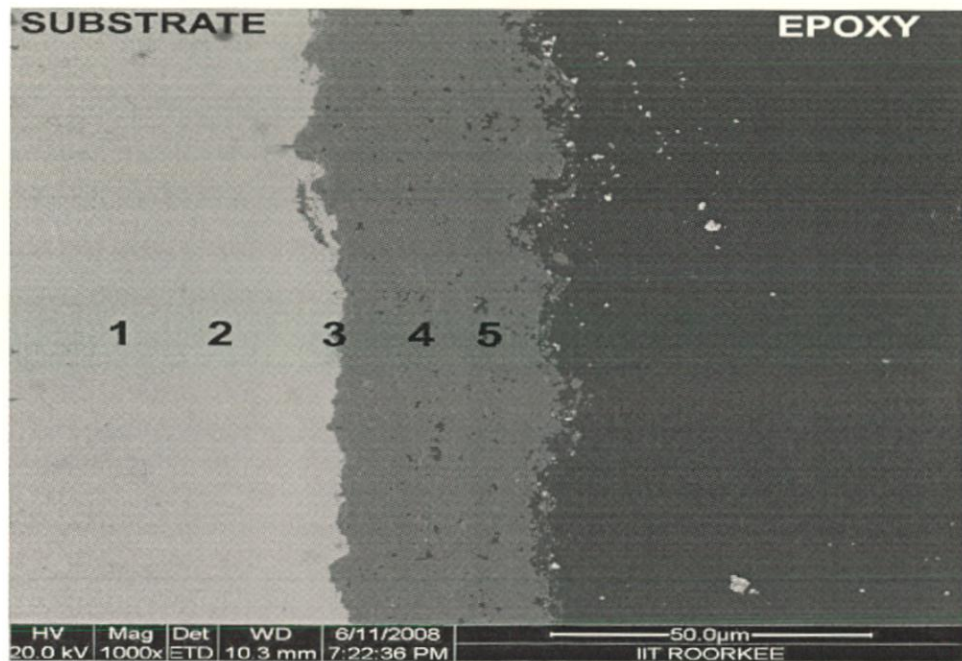
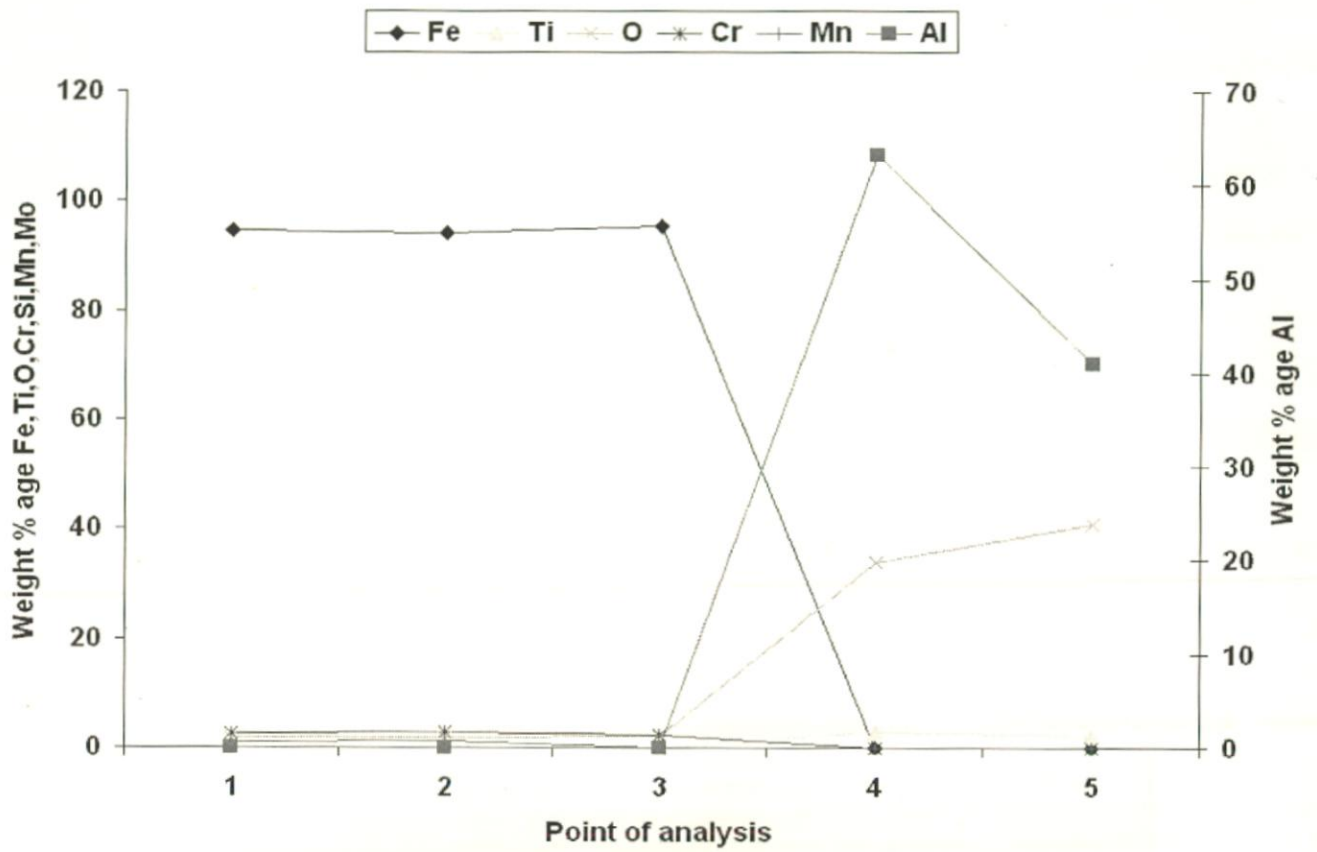


Fig 6.32: Cross sectional morphology and elemental composition variation across the cross-section of $\text{Al}_2\text{O}_3\text{-3wt\%TiO}_2$ coated boiler steel T22 exposed to air at 900°C for 50 cycles, 1000 X.

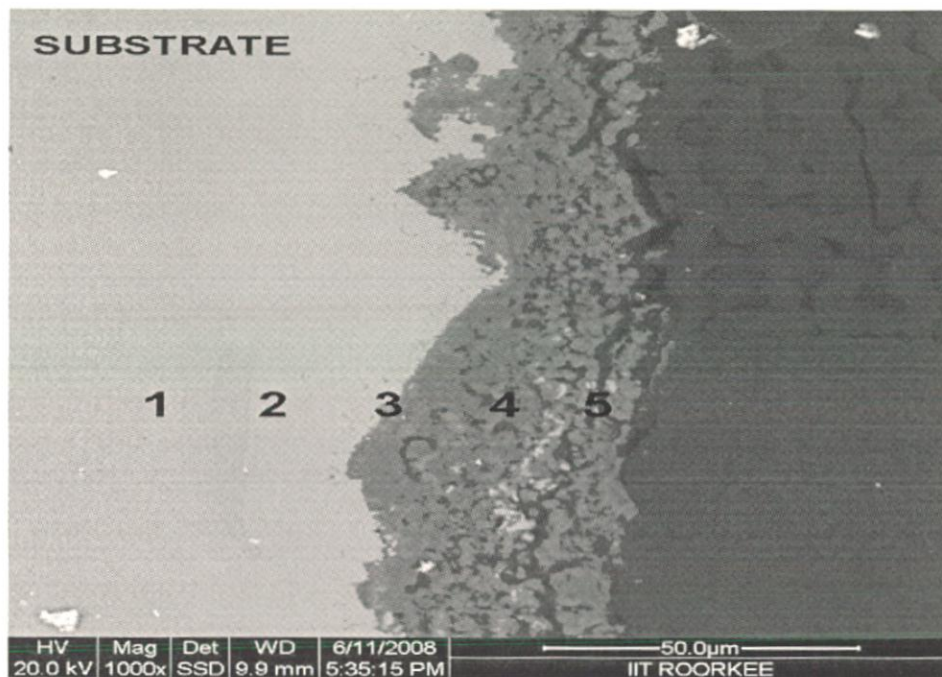
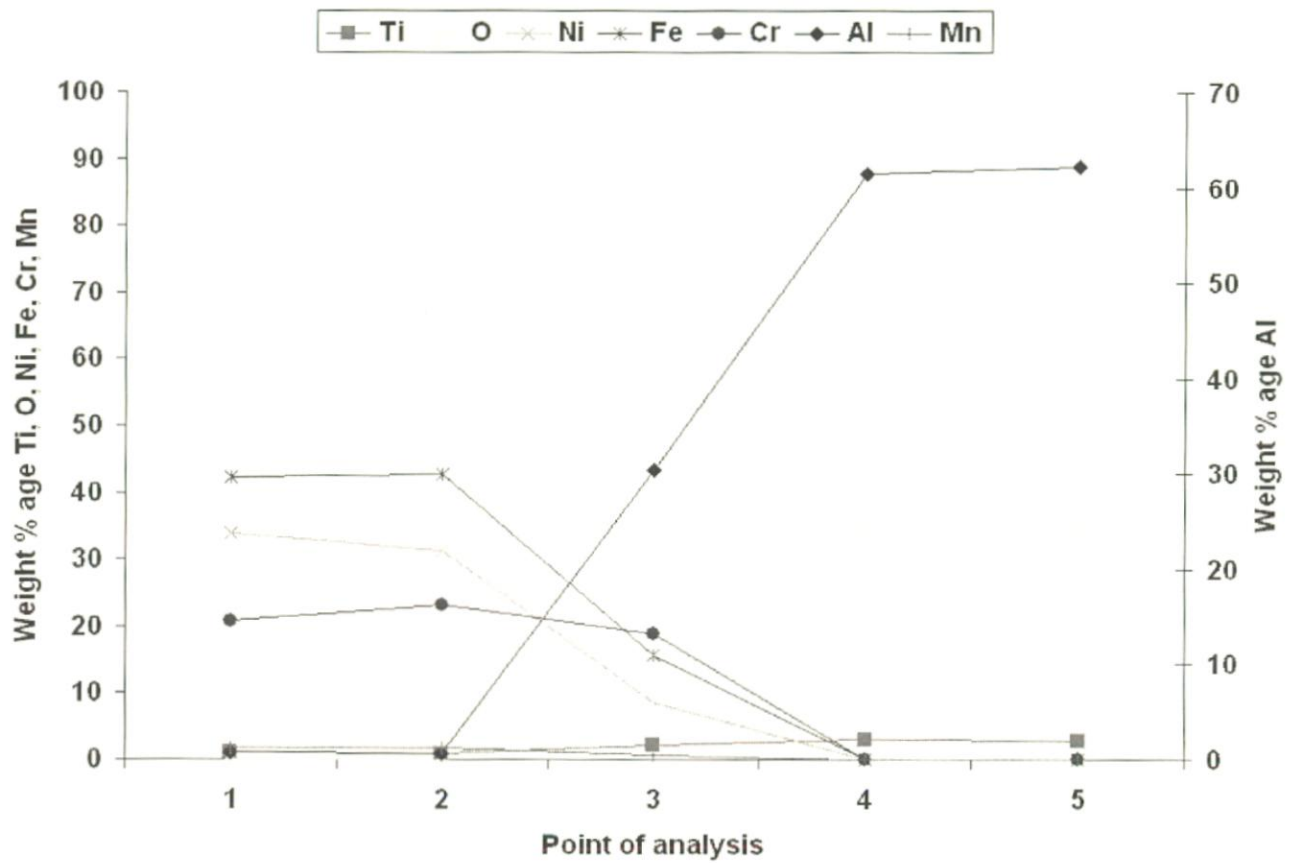


Fig. 6.33: Cross sectional morphology and elemental composition variation across the cross-section of $\text{Al}_2\text{O}_3\text{-3wt\%TiO}_2$ coated superalloy Superni 600 exposed to air at 900°C for 50 cycles, 1000 X.

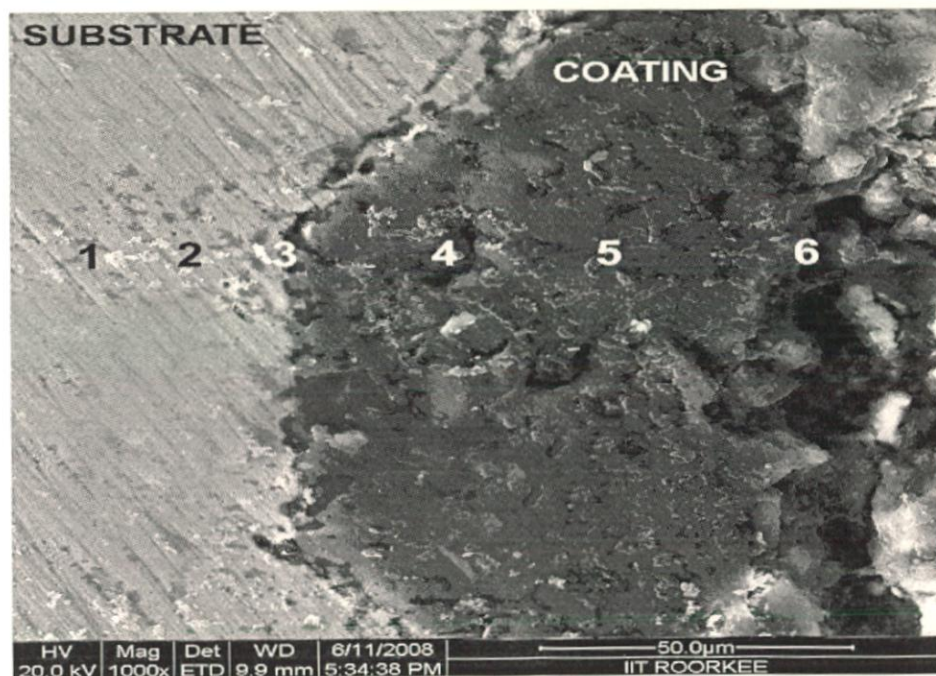
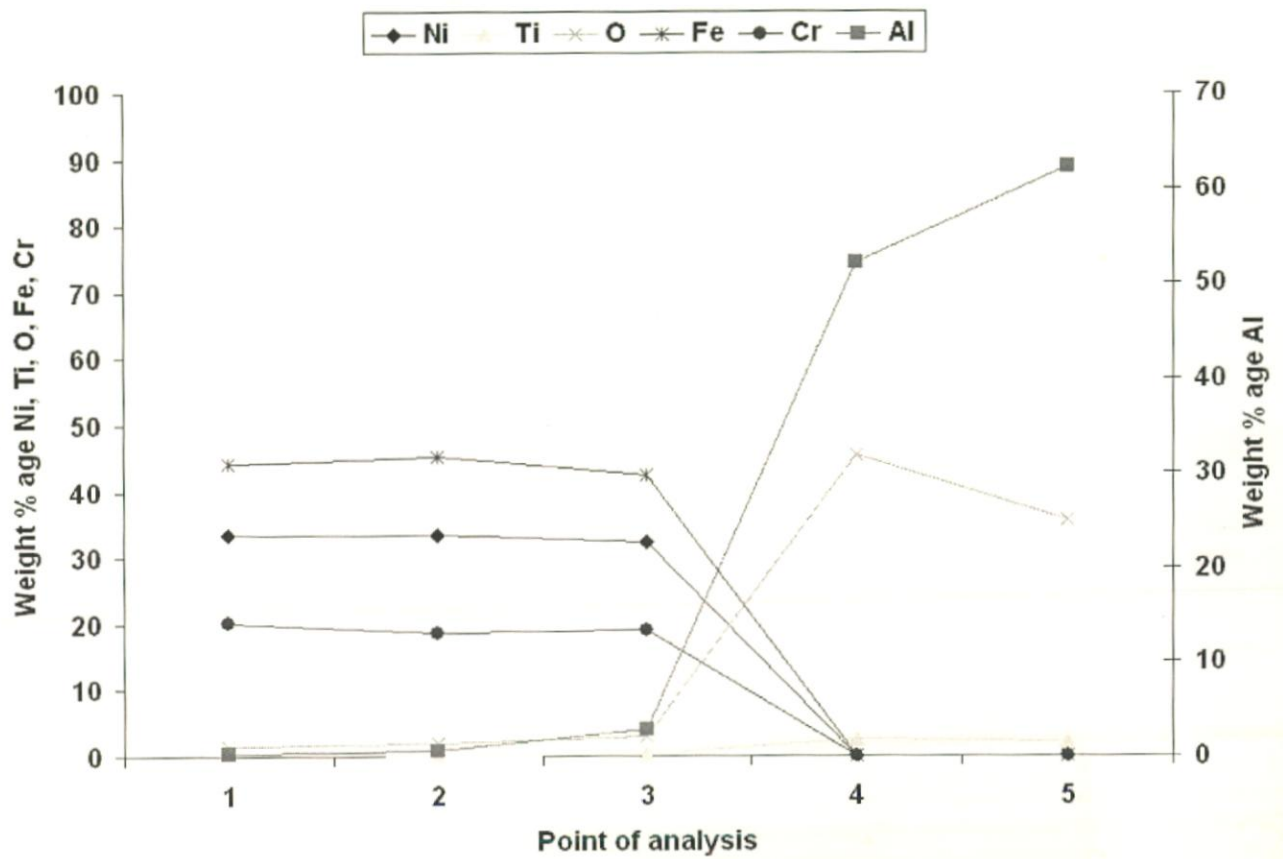


Fig. 6.34: Cross sectional morphology and elemental composition variation across the cross-section of $\text{Al}_2\text{O}_3\text{-3wt\%TiO}_2$ coated superalloy Superni 718 exposed to air at 900°C for 50 cycles, 1000 X.

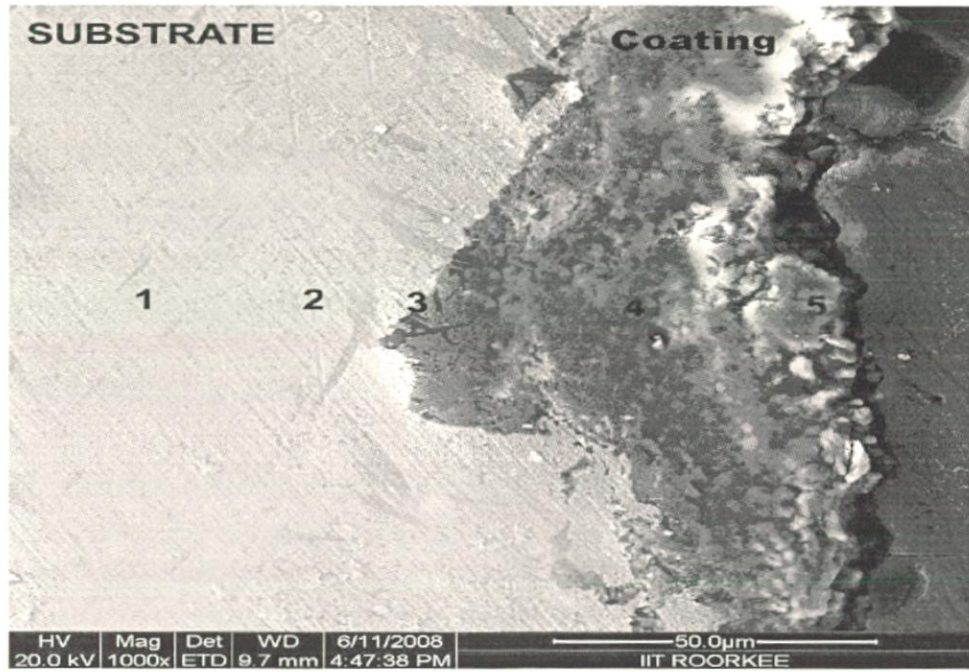
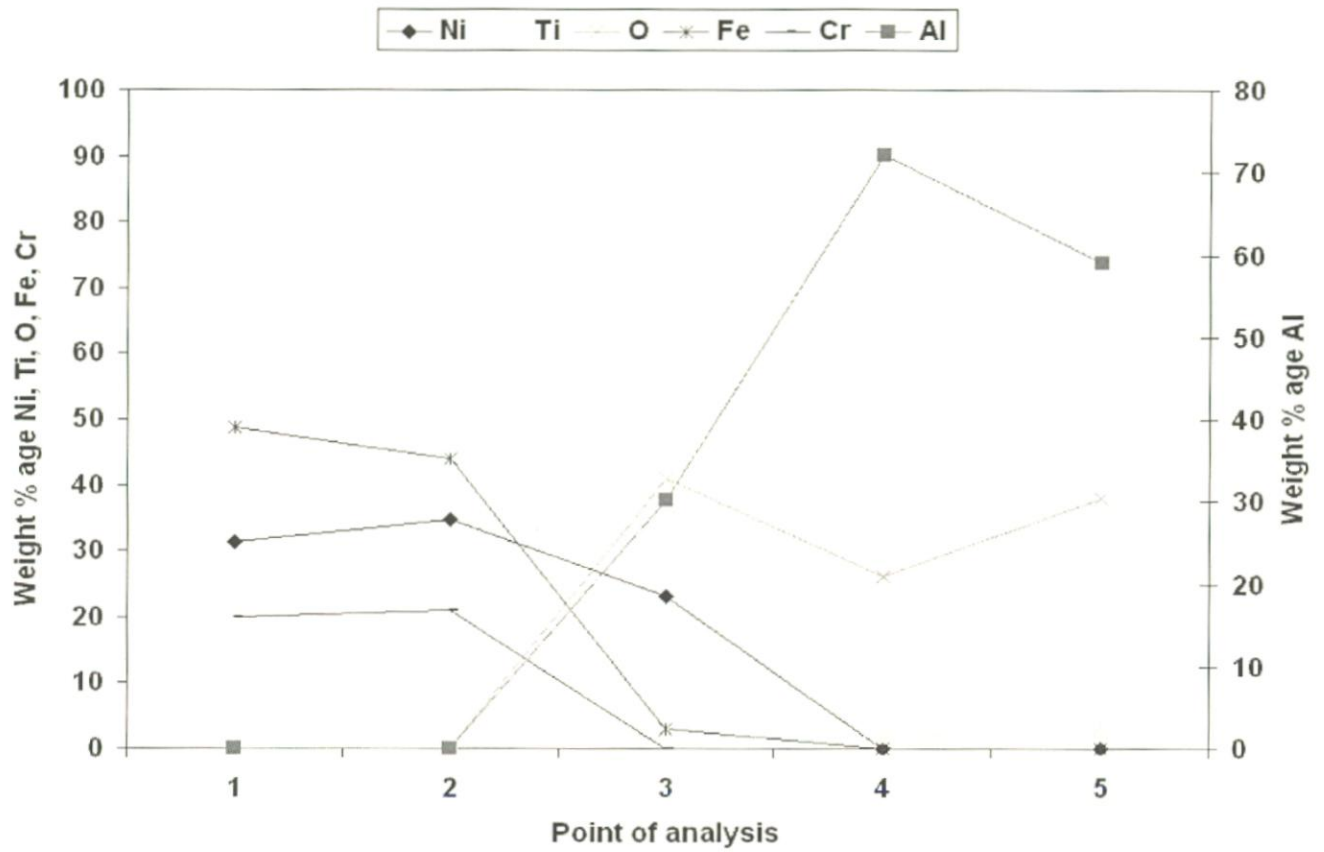


Fig. 6.35: Cross sectional morphology and elemental composition variation across the cross-section of $\text{Al}_2\text{O}_3\text{-3wt\%TiO}_2$ Coated superalloy Superfer 800 exposed to air at 900°C for 50 cycles, 1000 X.

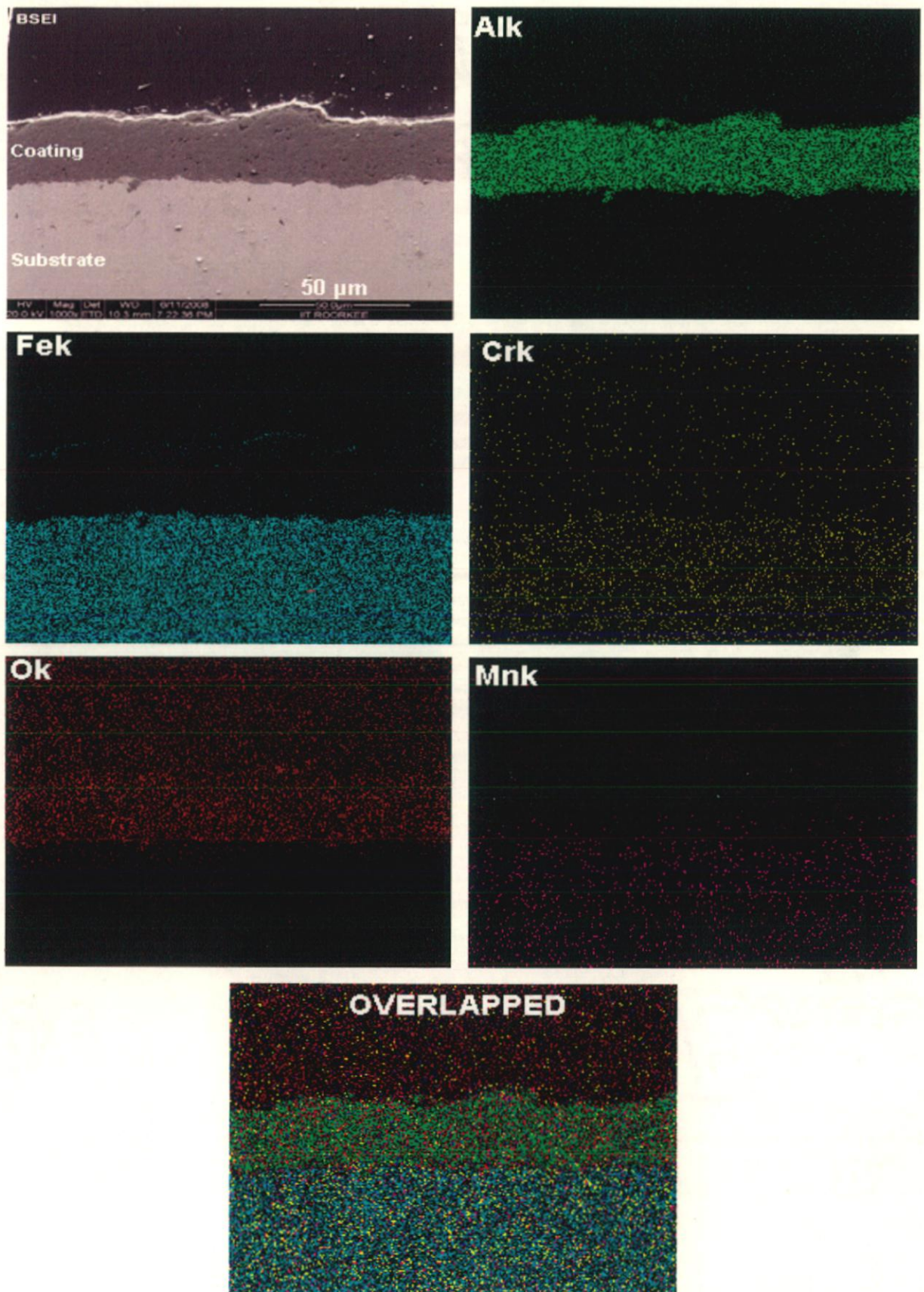


Fig.6.36: BSEI and X-ray mapping of the cross-section of Al_2O_3 -3 wt% TiO_2 coated boiler steel T11 subjected to cyclic oxidation in air at 900°C for 50 cycles.

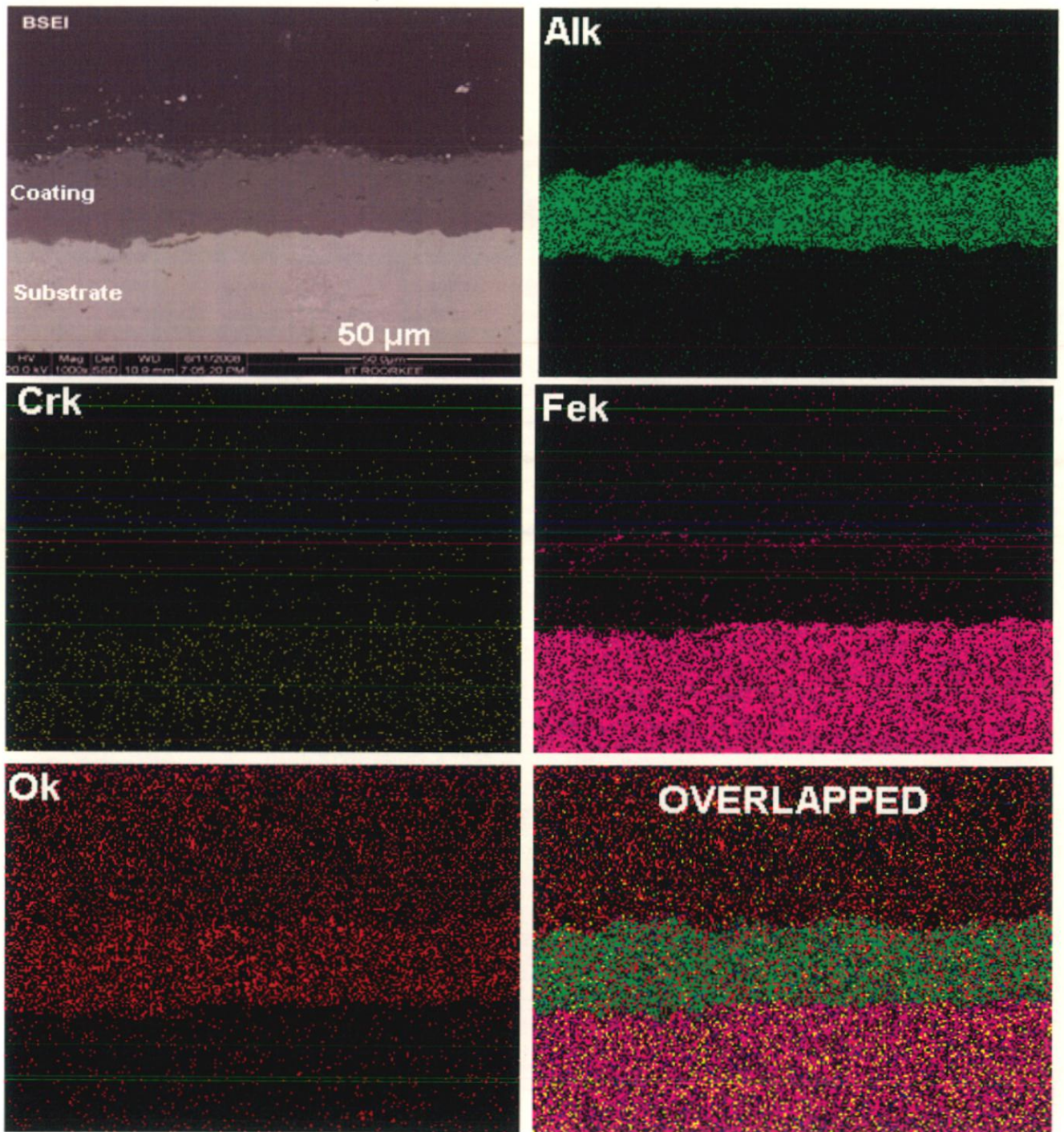


Fig. 6.37: BSEI and X-ray mapping of the cross-section of Al_2O_3 -3 wt% TiO_2 coated boiler steel T22 subjected to cyclic oxidation in air at 900°C for 50 cycles.

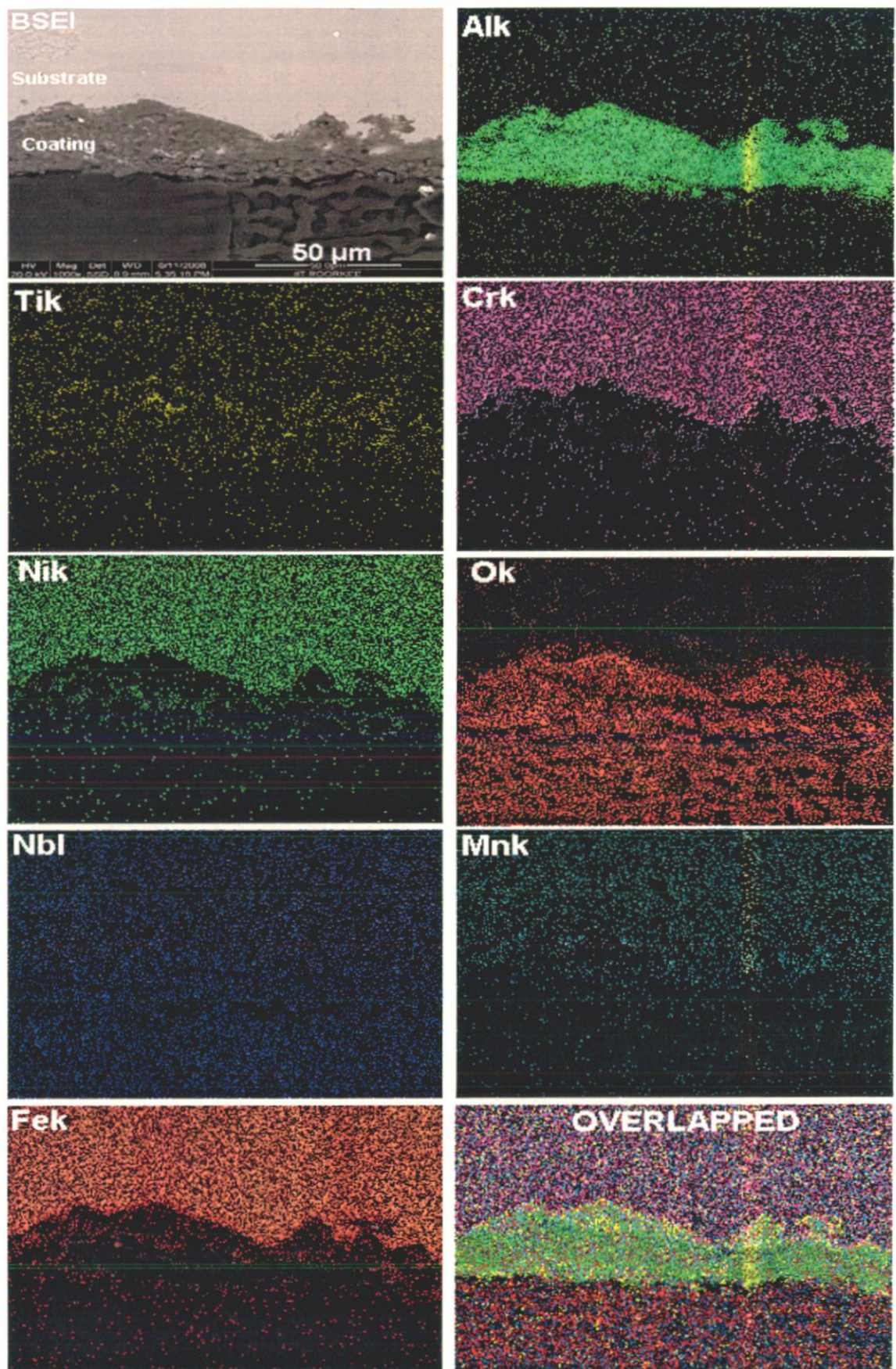


Fig.6.38: BSEI and X-ray mapping of the cross-section of Al_2O_3 -3 wt% TiO_2 coated superalloy Superni 600 subjected to cyclic oxidation in air at 900°C for 50 cycles.

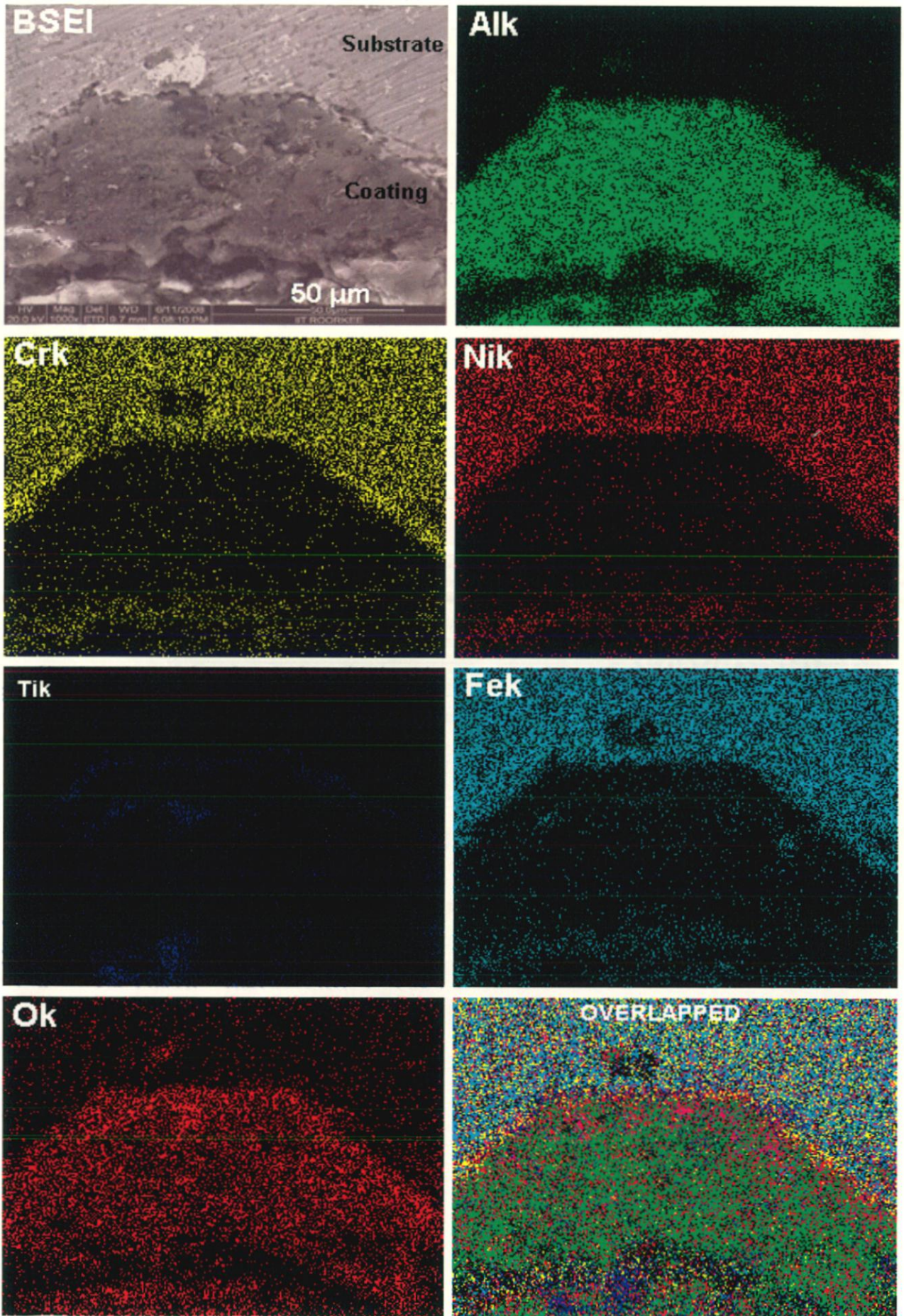


Fig. 6.39: BSEI and X-ray mapping of the cross-section of Al_2O_3 -3 wt% TiO_2 coated superalloy Superni 718 subjected to cyclic oxidation in air at 900°C for 50 cycles.

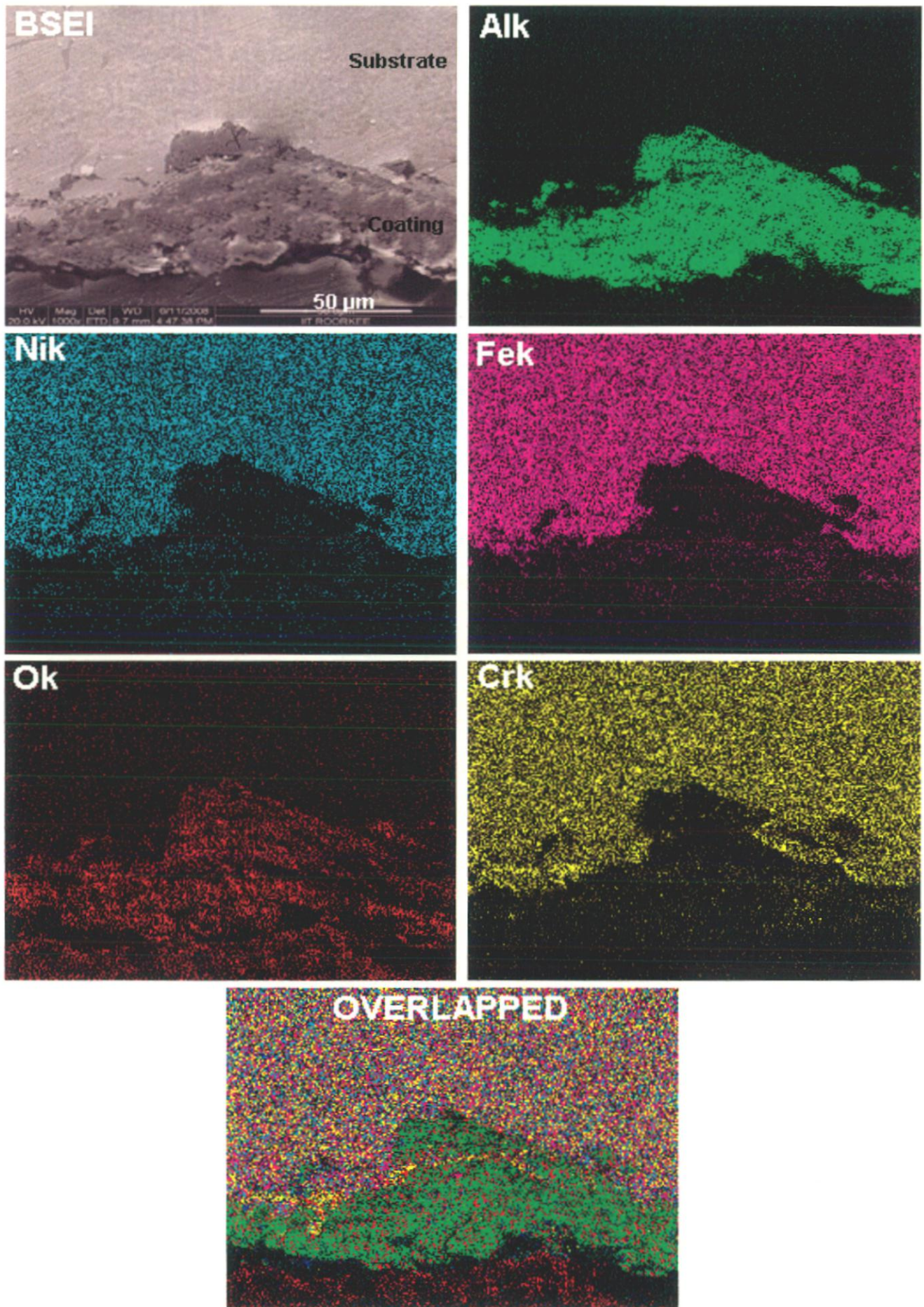


Fig. 6.40: BSEI and X-ray mapping of the cross-section of Al_2O_3 -3 wt% TiO_2 coated superalloy Superfer 800 subjected to cyclic oxidation in air at 900°C for 50 cycles.

6.1.2 Hot Corrosion Studies of Uncoated and Coated Alloys in Molten Salt Environment

6.1.2.1 Uncoated alloys

6.1.2.1.1 Visual Examination

The macrographs of base alloys T11, T22, Superni 600, superni 718 and Superfer 800 after hot corrosion in an aggressive environment of molten salt (Na_2SO_4 -60% V_2O_5) at 900°C under cyclic conditions for 50 cycles are shown in Fig. 6.41. It can be seen from the macrograph that intense spalling has occurred for T11 and T22 steels. The scales formed are massive and have cracked.

In case of T11 steel, exposed to molten salt environment, light grey scale appeared during first few cycles which turned to grayish black as the cycles progressed. After first cycle the sample started turning grey and with passing cycles, some black spots appeared in the centre of the specimen. Spalling of the scale was observed with each passing cycle. After 5th cycle, outer edges of the specimen were shining grey while the interior was black. Spalling started from the central position after 6th cycle. Then the grayish appearance moved from edges towards the centre. Then appearance of the scale was dual colour in nature i.e. it got dark grey in center and light grey at the edges. The dark coloured region in the centre then turned to black and spalled. After 21st cycle, the surface seemed to be composed of three regions; shining grey at edges, dull grey and black at the centre. After 22nd cycle, grain boundary like structure appeared on the surface. Then thick layer formed on the edges. After 32nd cycle, cracking of top layer of scale started in centre. After 2 cycles, cracks became wide and deep and extremely black surface beneath cracks is visible. After 35th cycle the top scale broke away exposing the internal surface.

In T22 steel, surface became grey after first cycle followed by formation of black spots further exposure it became shining grey. Needle like structure was formed on the surface while edges became dull grey with black spots. After 7th cycle, thin layers from all the surface started peeling off. After 10th cycle, severe spalling resulted in multi layered cracking which continued throughout the study. Spalling was so severe that thick layers were formed and separated out after each cycle.

The scale was fragile and started spalling in the early cycles in both boiler steels. Once there was formation of the cracks then there was gradual increase in the width of cracks for every subsequent cycle.

In case of T11 base steel, the scale was lustrous dark black. Whereas fragile and dark grey colour scale was there for T22 base steel. Intense spalling was observed through out the experimentation. As soon as subscale forms the top layer of scale breaks away from it and the separated multiple layers overlapping each other were seen.

In superalloys, a very thin scale appeared on the surfaces from 1st cycle onwards. In superni 600, after first cycle, the surface turned brown and light brownish grey coloured scale appeared after 5th cycle. Then onwards a fragile scale could be seen on the surfaces of the specimen with tiny cracks at the edges. The fragile scale separated out from the surfaces in the form of small and thin flakes and by the end of 17th cycle detachment of scale was observed followed by intensive spalling. After 21st cycle small cracks were clearly visible on the surface and very rough and uneven surface appeared. Then spalling and crack formation continued throughout the study. After 46th cycle there was a severe cracking and visible deterioration of the surface.

In superni 718, surface became totally black after first cycle. After 2nd cycle there was appearance of brown and rusty patches throughout the surface and the size of the patches increased in the subsequent cycles and afterwards surface became rough. After 19th cycle there was appearance of some powder precipitates black in colour on the surface. The colour of the scale became jet black in the coming cycles with spalling and minor sputtering (disintegration of the scale accompanied by cracking sound during cooling). Minor spalling and sputtering went on till the end of the 50th cycle.

In Superfer 800 specimen, after first cycle, carbon black coloured scale appeared on the surface and patch formation in the scale started. There was sputtering of small particles after 2nd cycle. The spalling and sputtering intensified as the period of study progressed with lot of corrosion products collected in the boat. After 11th cycle, small cracks were visible on the scale but not much of disintegration was observed. After 34th cycle some shining pits appeared on the surface of scale followed by separating out of small particles. After 42nd cycle, the scale had lustrous appearance with chip like structure in a grey matrix. Then there was surface disintegration in the form of tiny flakes coming out of the surface. The surfaces of the scale become uneven and pits were observed at places from where spalling had taken place.

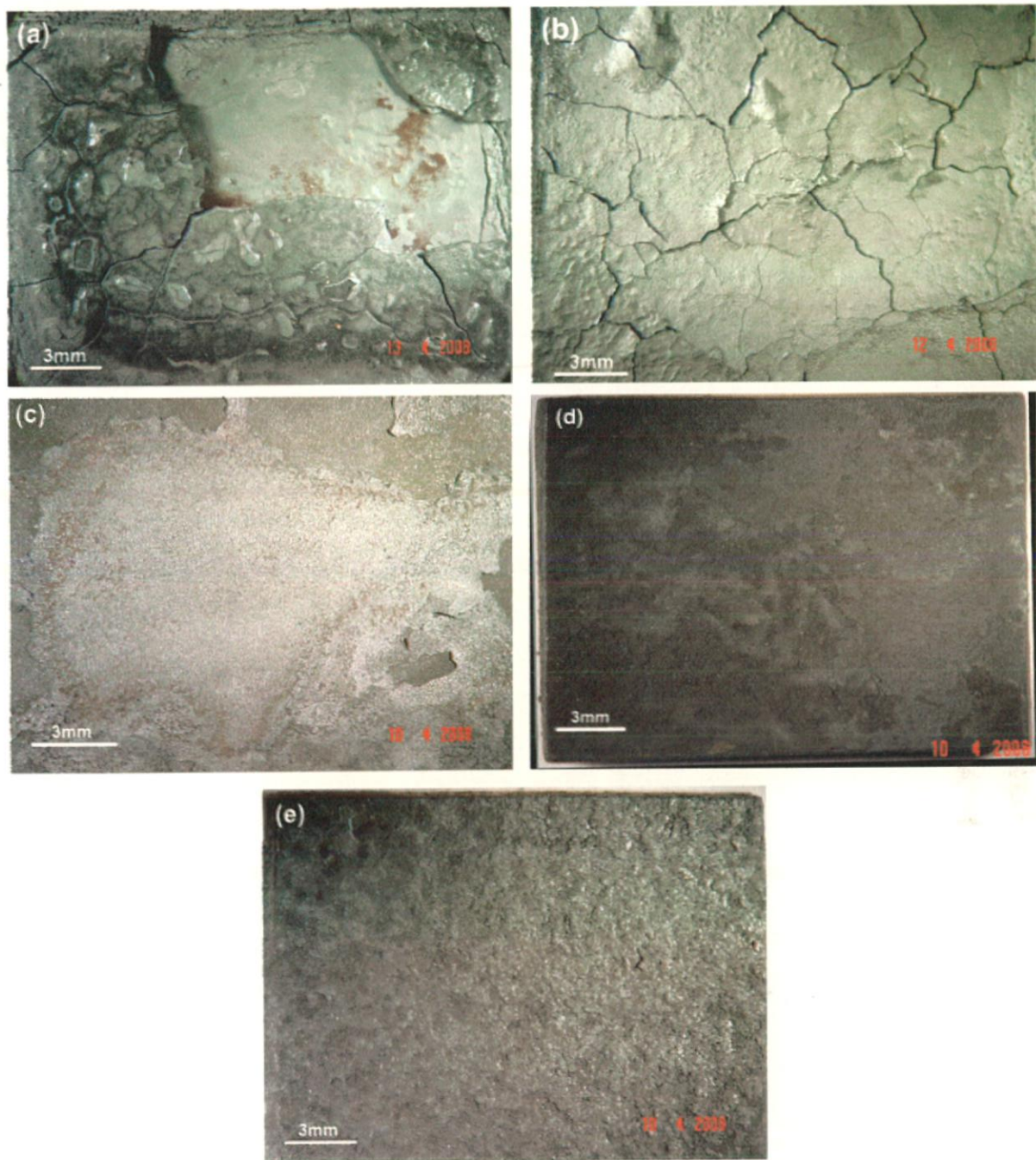


Fig.6.41: Macrographs of substrate alloys after cyclic hot corrosion in $\text{Na}_2\text{SO}_4\text{-60\%V}_2\text{O}_5$ at 900°C for 50 cycles
 (a) T11 (b) T22 (c) Superni 600 (d) Superni 718 (e) Superfer 800

during the exposure to molten salt environment, vigorous and intense spalling was observed. Peaks of Cr_2O_3 along with FeS_2 have also been observed in the oxide scale of both the boiler steels T11 and T22.

The X-ray diffractograms of the scales for superalloys are reported in Fig. 6.47 and 6.48 after exposure to molten salt ($\text{Na}_2\text{SO}_4\text{-60\%V}_2\text{O}_5$) at 900°C for 50 cycles. It is evident from the diffraction patterns that Superni 600 and Superni 718 have shown formation of similar phases after hot corrosion in the given environment. For these two superalloys NiO , Fe_2O_3 , Cr_2O_3 , FeV_2O_4 and $\text{Ni}(\text{VO}_3)_2$ are common phases while NiCr_2O_4 is extra phase revealed in superni 600. Further in case of hot corroded Superfer 800 phases identified are Fe_2O_3 , NiO , NiCr_2O_4 , and FeV_2O_4 .

6.1.2.1.4 SEM/EDX Analysis

(a) Surface Morphology

SEM/EDX analysis was used for the detection of presence of corrosion products and corrosion-inhibiting species and their approximate concentrations. The SEM micrograph along with EDX analysis of the T11 and T22 boiler steel exposed to $\text{Na}_2\text{SO}_4\text{-60\%V}_2\text{O}_5$ environment at 900°C given in Fig. 6.49. EDX analysis indicates the formation of predominantly Fe oxide scale in both the steels after exposure to molten salt environment. Cr and Mn along with O are the other two phase detected by EDX analysis. The top scale indicates spalling and cracking.

SEM micrographs along with EDX analysis for Superni 600, superni 718 and superfer 800 base superalloys after exposure to $\text{Na}_2\text{SO}_4\text{-60\%V}_2\text{O}_5$ environment at 900°C are shown in Fig. 6.50. Surface scale mainly consisted of Ni, Fe and Cr along with O in case of all the superalloys. Minor spallation of the scale could be observed in superni 600 and Superni 718 while in case of superfer 800, it was relatively more. SEM/EDX micrograph of the scale formed after hot corrosion for Superni 600 superalloy indicates mainly Cr and Ni rich phases. At point 1, the scale matrix consisted of Ni (23.31%), Fe (10.80) Cr (29.52%) and O (32.11%) and Ni (20.47%), Fe (9.24) Cr (29.95%) and O (36.79%) at point 2 as indicated by EDX analysis shown in Fig. 6.50 (a). Also some other minor constituents like Mn, Si, Na and V are also present in the scale. In case of Superni 718, Fig. 6.50 (b) there is a outer surface scale i.e. point 2, having Ni rich matrix where main composition is 76.12 % Ni, 6.39 % Cr and 8.58 % Fe with 8.91 % O. At point 1, there is a spalled region i.e. subscale with 33.92 % Ni, 14.87 % Cr and 16.05 % Fe along with 31.64 % O. The other minor constituents of scale were Mn, Al and V. In case of superfer 800, there was intense spalling of scale and scale was disintegrated in the form of thin flakes. In this case the final scale mainly consisted of Fe, Ni and Cr along with O as shown in Fig. 6.50(c).

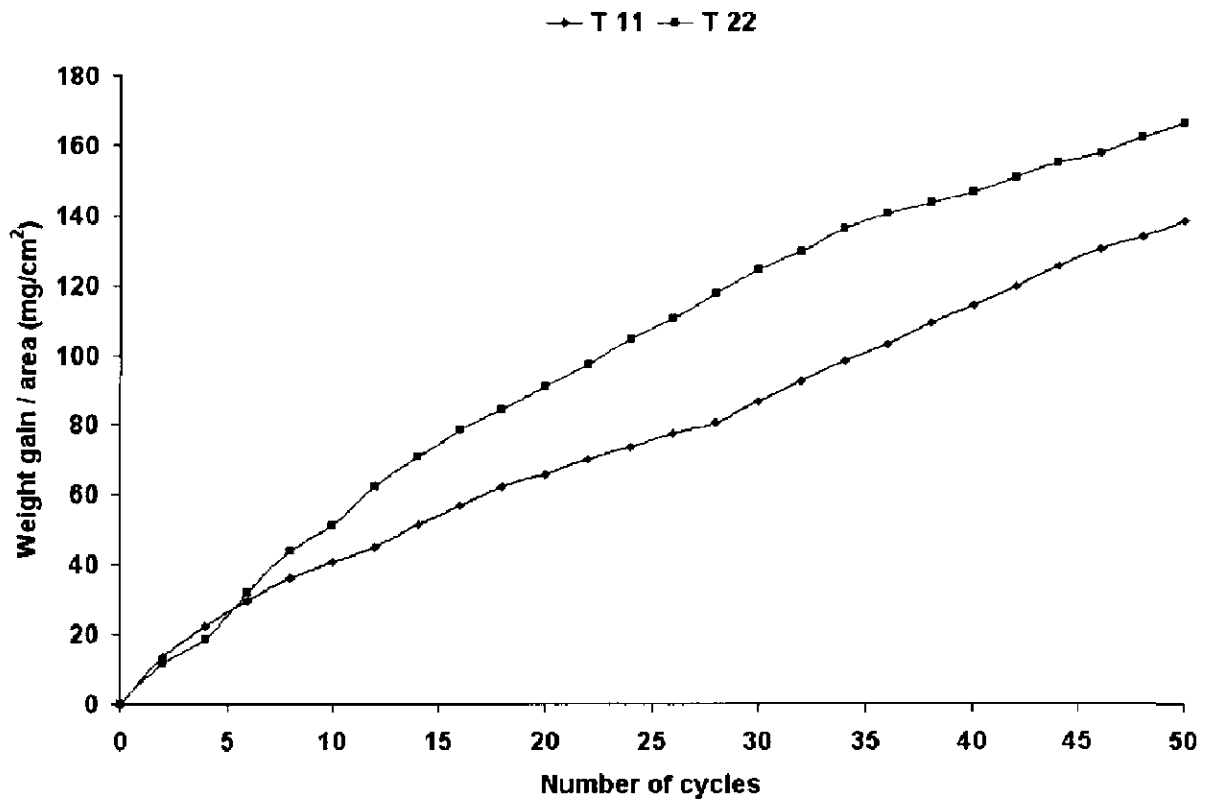


Fig. 6.42: Weight gain plot for uncoated boiler steels T11 and T22 subjected to cyclic hot corrosion in Na₂SO₄-60%V₂O₅ at 900°C for 50 cycles.

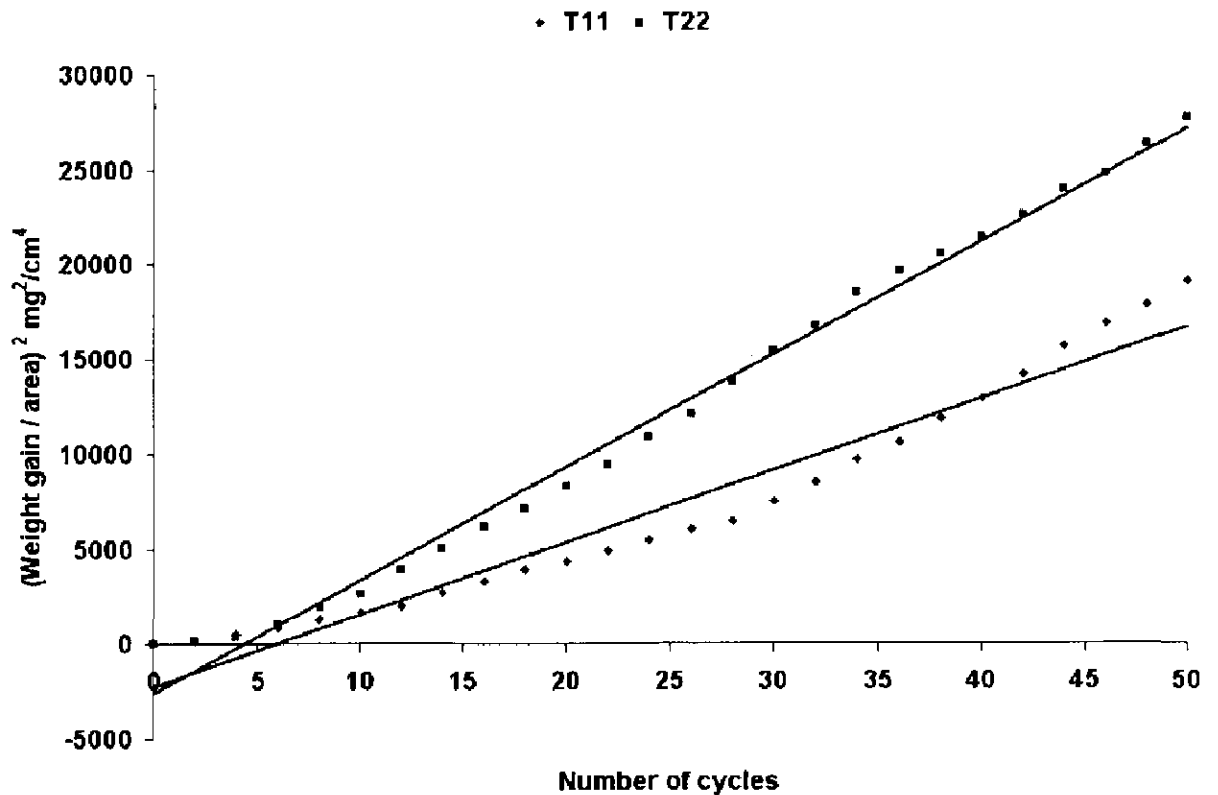


Fig.6.43: Weight gain square (mg²/cm⁴) plot for uncoated boiler steels T11 and T22 subjected to cyclic hot corrosion in Na₂SO₄-60%V₂O₅ at 900°C for 50 cycles.

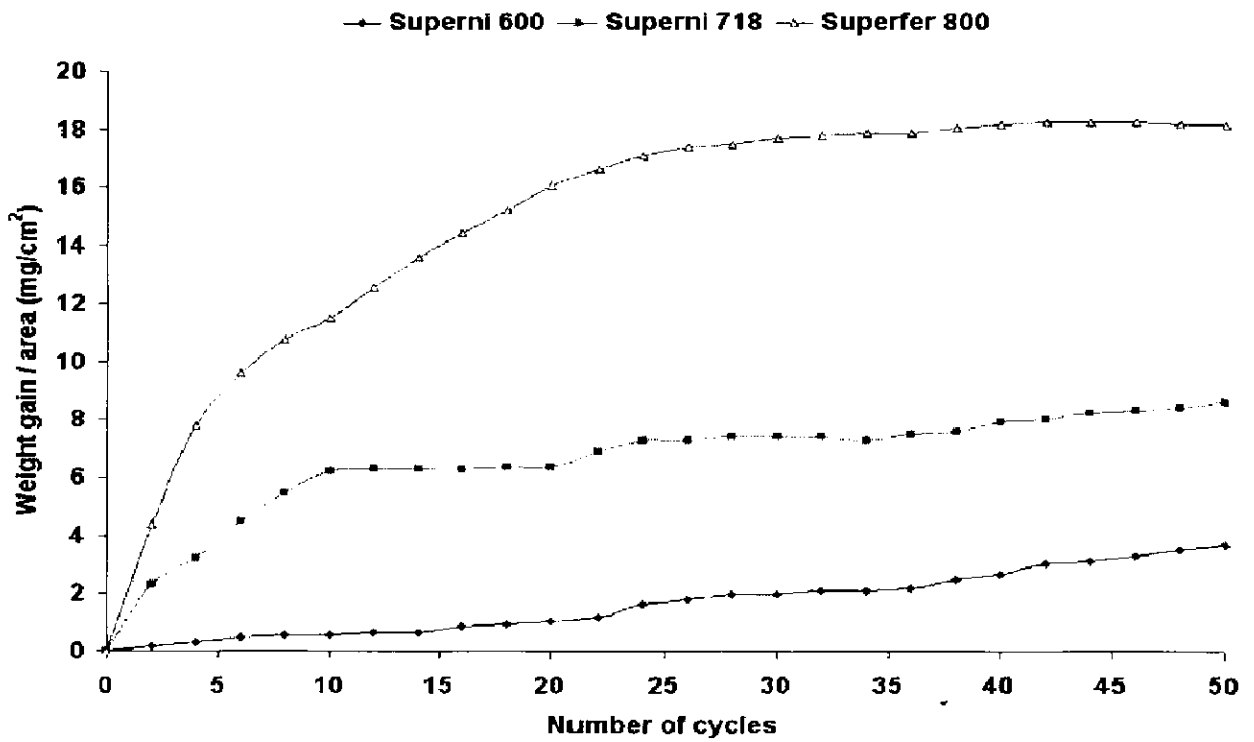


Fig. 6.44: Weight gain plot for uncoated superalloys Superni 600, Superni 718, Superfer 800 subjected to cyclic hot corrosion in $\text{Na}_2\text{SO}_4\text{-60\%V}_2\text{O}_5$ at 900°C for 50 cycles.

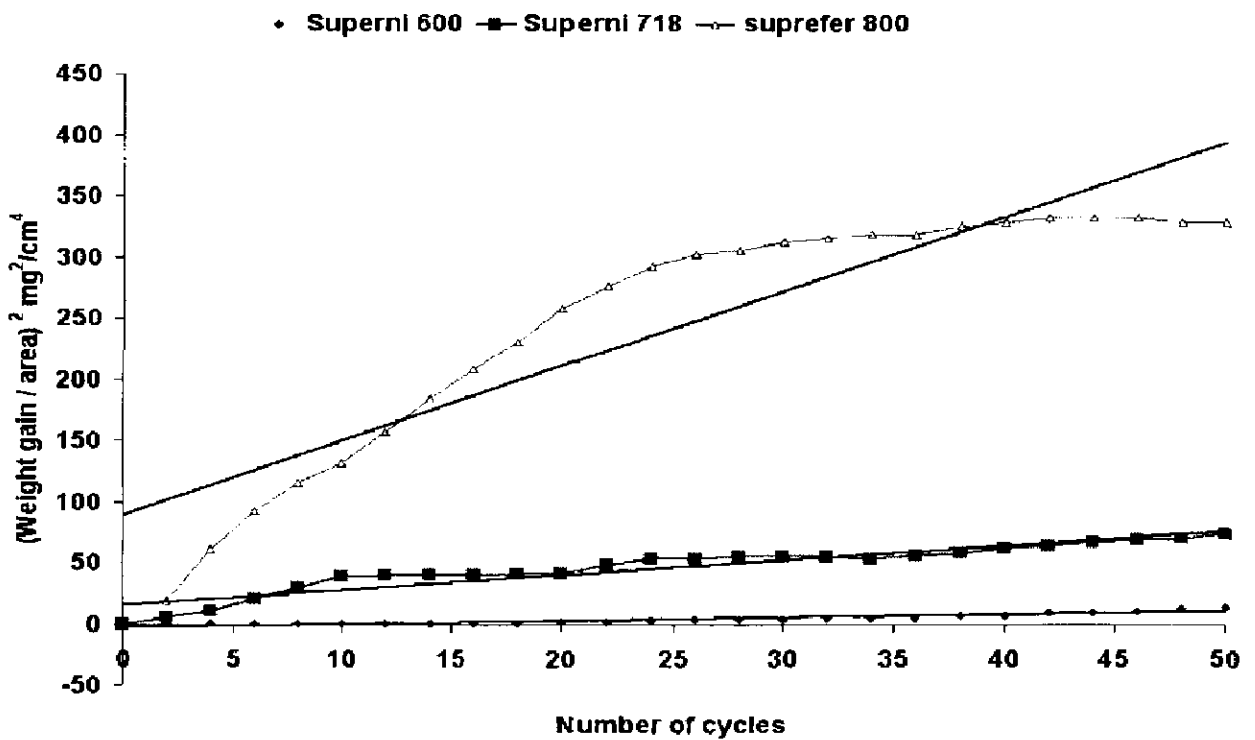


Fig.6.45: Weight gain square (mg^2/cm^4) plot for uncoated Superni 600, Superni 718, Superfer 800 subjected to cyclic hot corrosion in $\text{Na}_2\text{SO}_4\text{-60\%V}_2\text{O}_5$ at 900°C for 50 cycles

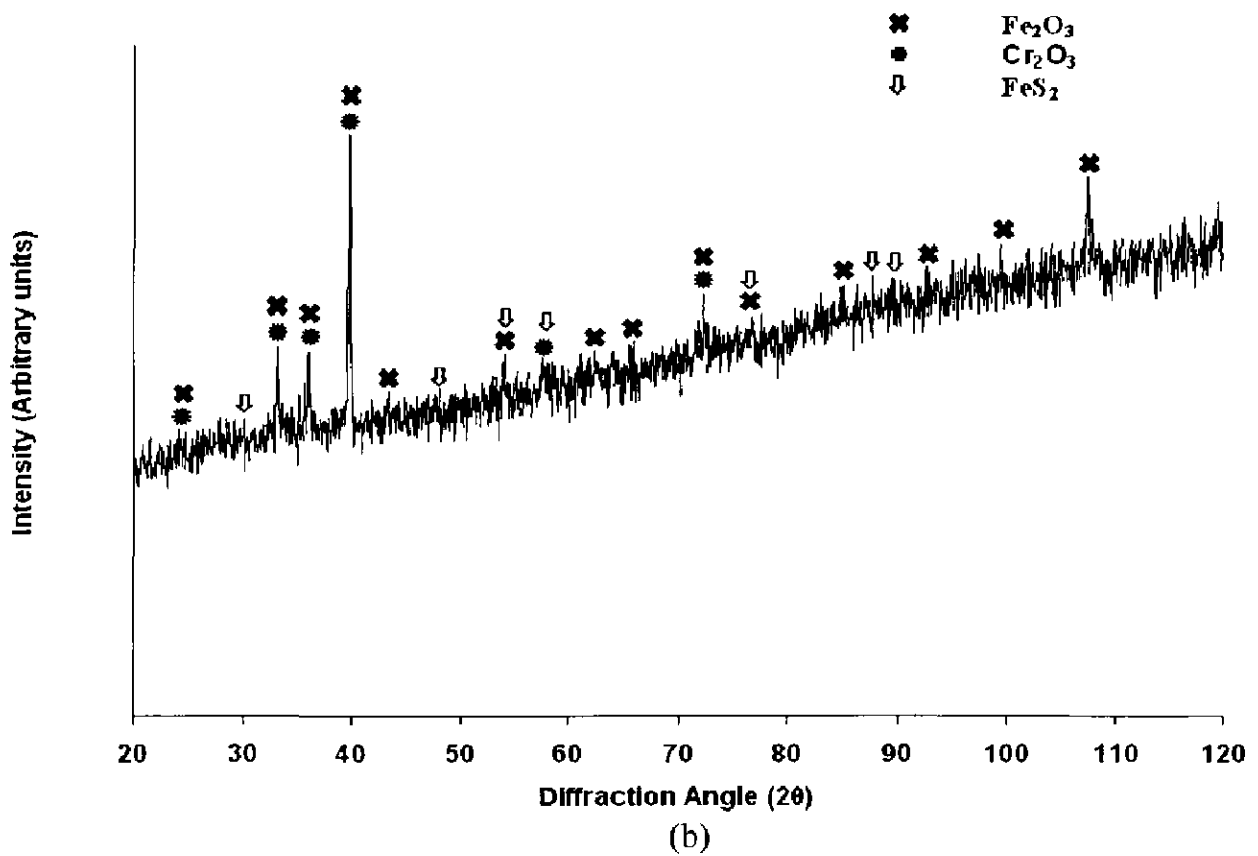
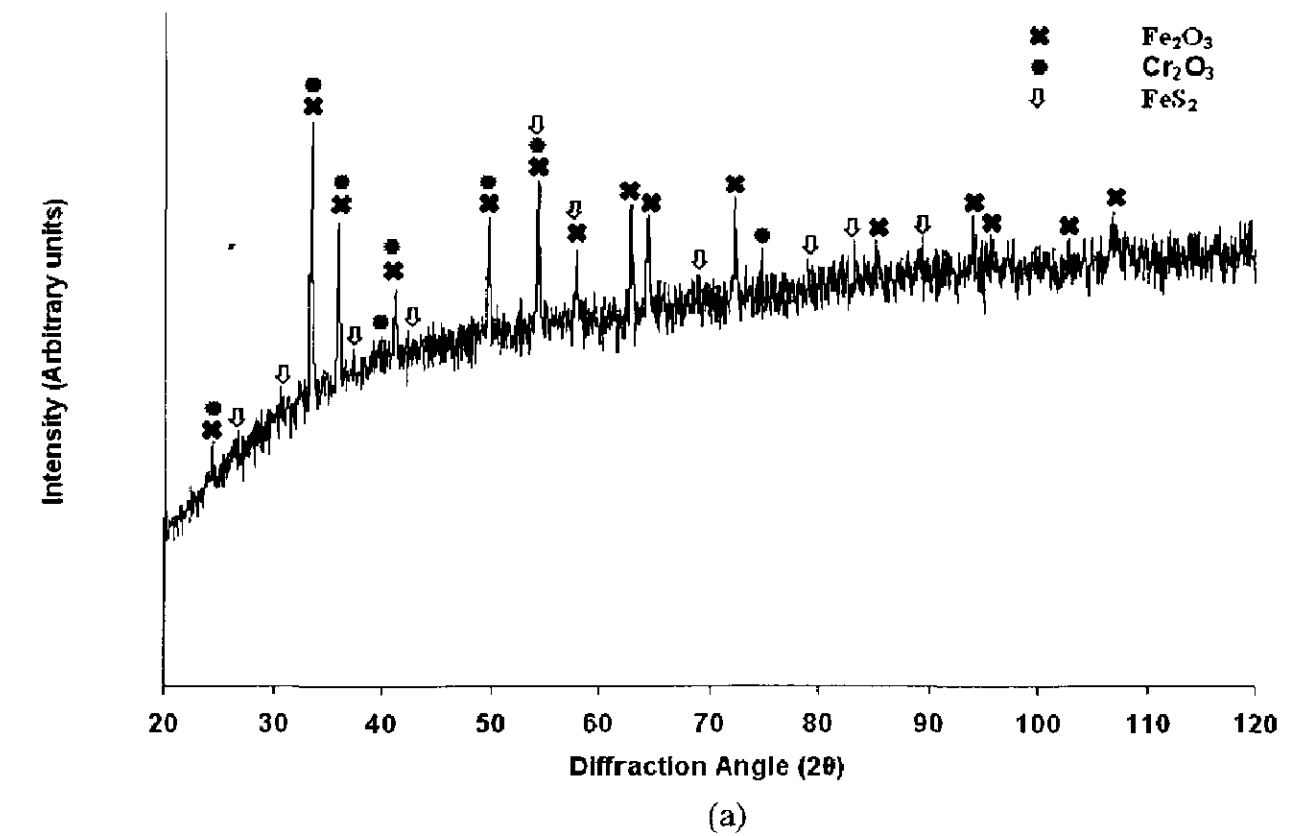
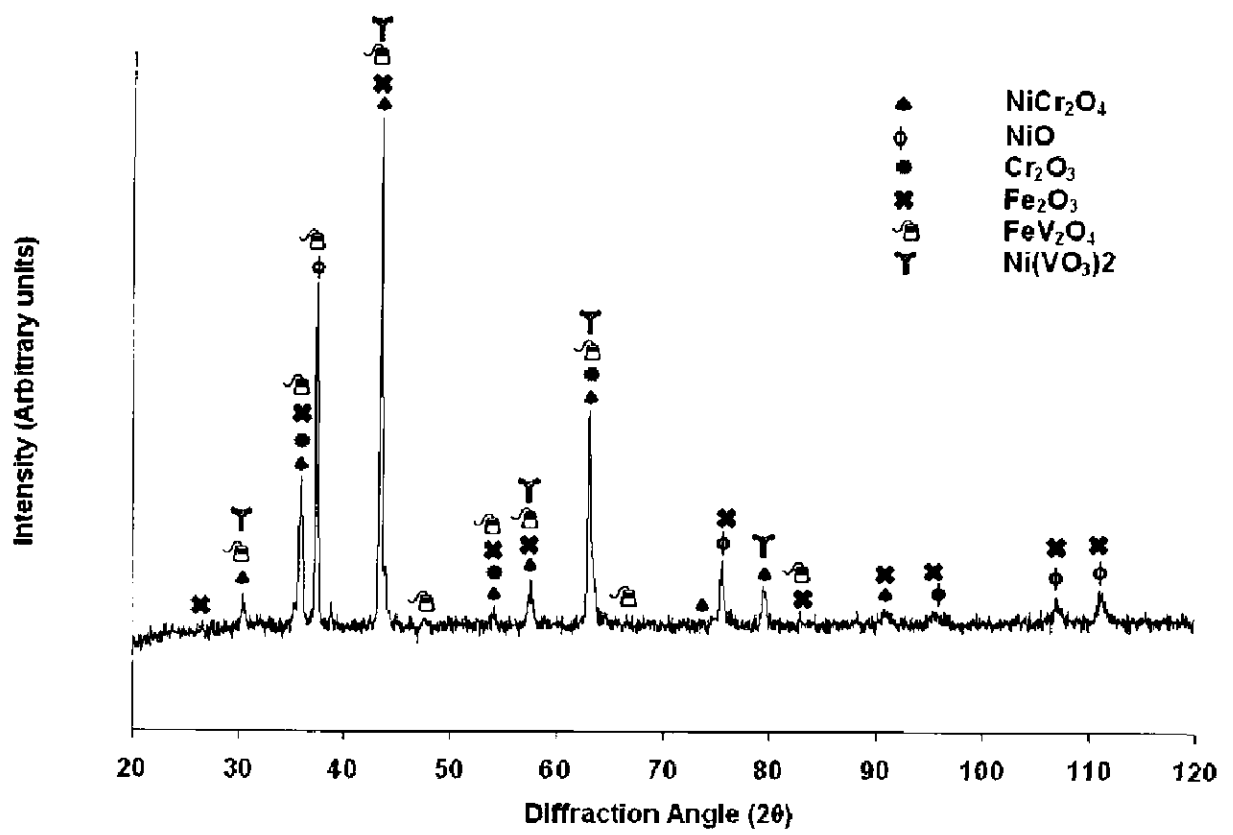
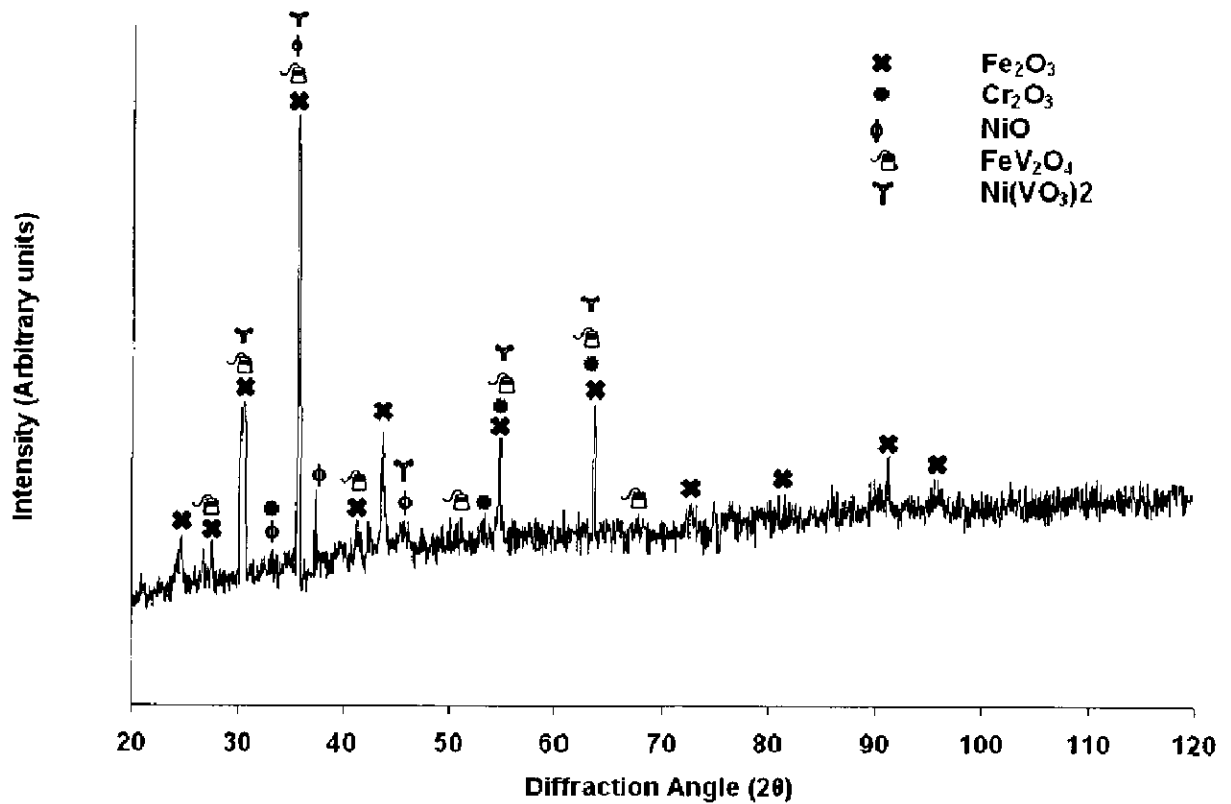


Fig.6.46: X-ray diffraction profiles for boiler steels subjected to cyclic hot corrosion in Na_2SO_4 -60% V_2O_5 at 900°C for 50 cycles.
 (a) T11 (b) T22



(a)



(b)

Fig. 6.47: X-ray diffraction profiles for superalloys Superni 600 and Superni 718 subjected to cyclic hot corrosion in $\text{Na}_2\text{SO}_4\text{-60\%V}_2\text{O}_5$ at 900°C for 50 cycles.
 (a) Superni 600 (b) Superni 718

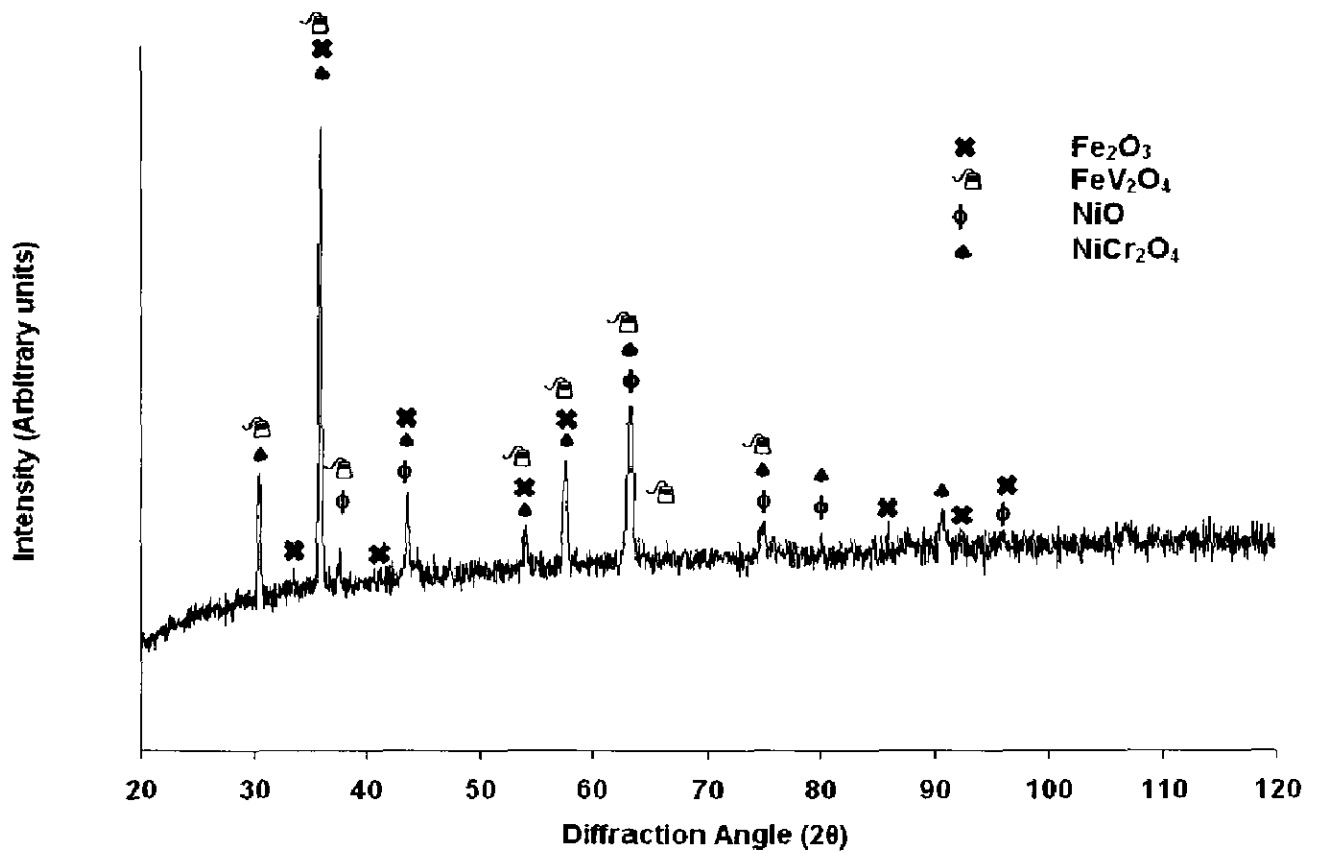


Fig. 6.48: X-ray diffraction profile for superalloy Superfer 800 subjected to cyclic hot corrosion in Na₂SO₄-60%V₂O₅ at 900°C for 50 cycles.

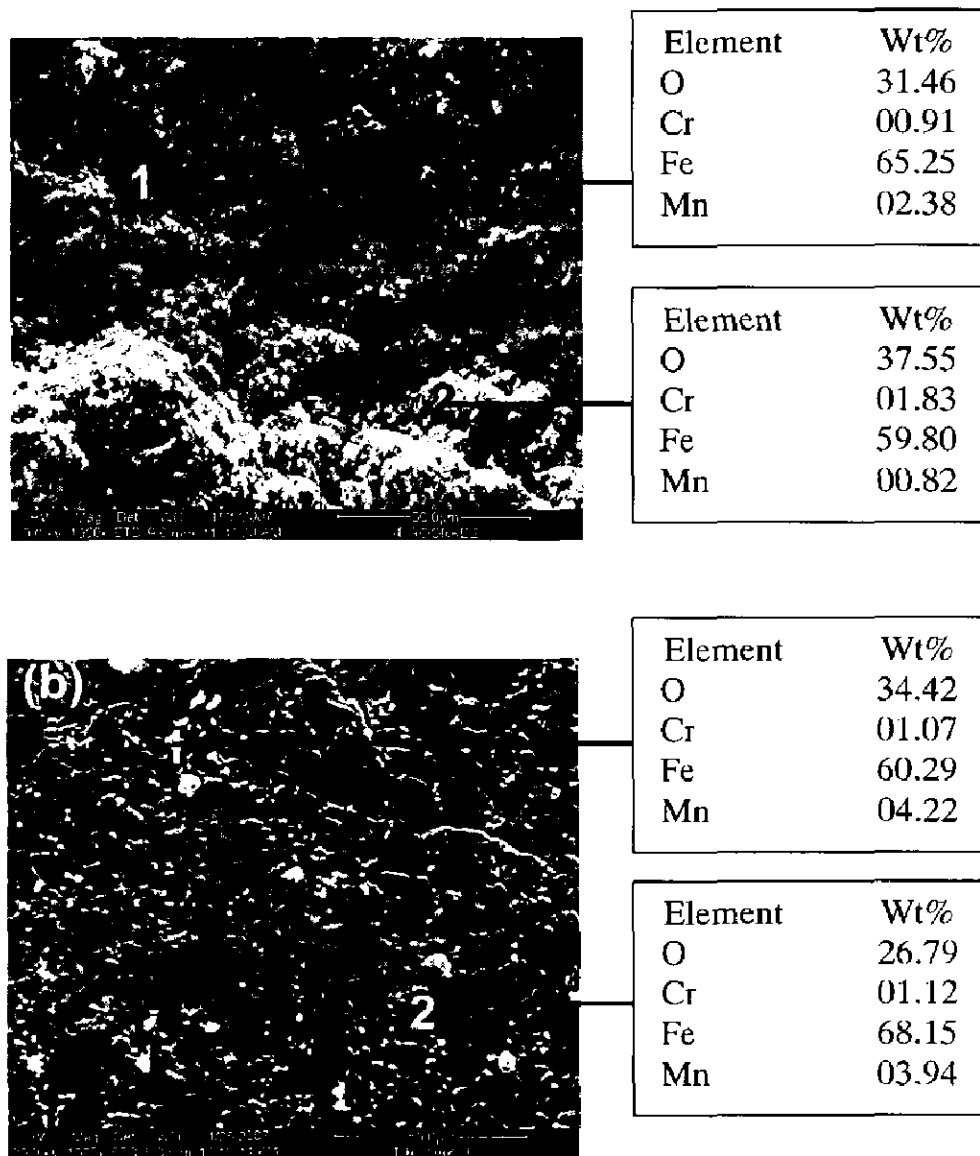


Fig. 6.49: Surface scale morphology and EDX analysis for boiler steels subjected to cyclic hot corrosion in Na_2SO_4 -60% V_2O_5 at 900°C for 50 cycles (a) T11, 1000 X and (b) T22, 1000 X.

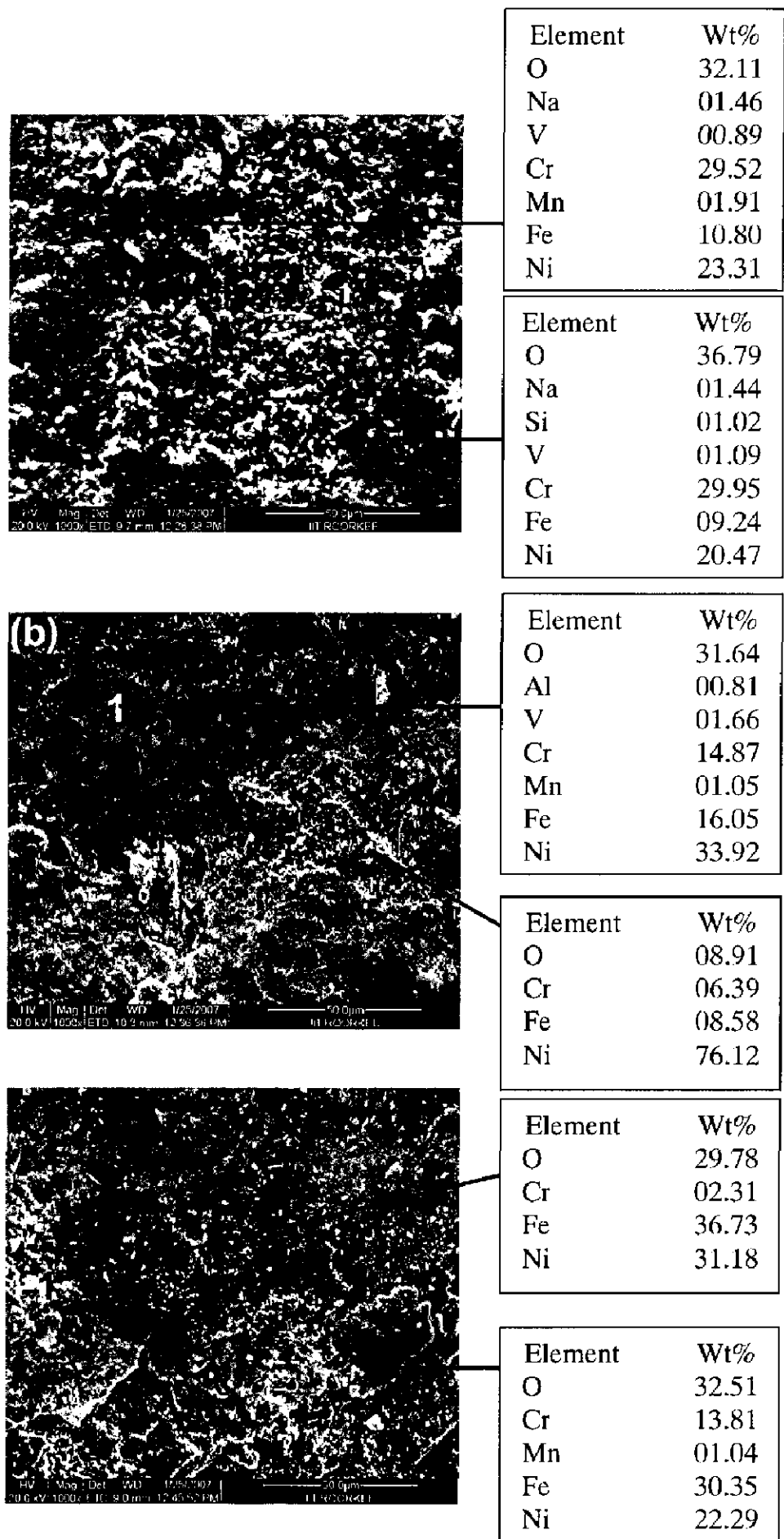


Fig. 6.50: Surface scale morphology and EDX analysis for superalloys subjected to cyclic hot corrosion in Na_2SO_4 -60% V_2O_5 at 900°C for 50 cycles (a) Superni 600, 1000 X and (b) Superni 718, 1000 X., (c) Superfer 800, 1000 X.

(b) Cross-Sectional Analysis and X ray mapping

Cross sectional morphology and elemental composition variation across the cross-section of substrate alloys exposed to $\text{Na}_2\text{SO}_4\text{-60\%V}_2\text{O}_5$ at 900°C for 50 cycles is shown in Fig. 6.51-6.55. The results of oxide scale analysis across the cross-section for corroded T11 and T22 boiler steels are plotted and shown in Fig. 6.51 and 6.52 along with micrographs. In boiler steel T11 after exposure to molten salt, throughout the scale Fe oxide percentage is high and also considerable amount of chromium oxide is present throughout the scale thickness. Whereas in case of T22 steel, scale was thick. Considerable amount of chromium along with oxygen was present in the scale. Traces of S and V have been revealed in the scale.

In case of corroded superalloys, EDX analysis has revealed that the scale mainly consisted of Ni, Cr and Fe along with oxygen. Oxide scale morphology along with variation of elemental composition across the cross-section of superalloy Superni 600 subjected to cyclic hot corrosion in $\text{Na}_2\text{SO}_4\text{-60\%V}_2\text{O}_5$ at 900°C for 50 cycles has been depicted in Fig. 6.53. EDX analysis presents a comparative estimate of elemental compositions at some points in the substrate as well as in the scale. The plots of elemental composition variation show that the scale mainly consisted of iron, nickel and chromium along with oxygen. Oxygen is found to be absent at point 1, i.e. in substrate but is present in small percentage at point 2 and has shown scatterness as one moves into the scale. From this it can be concluded that the oxygen has penetrated into the substrate. Oxygen is present in little higher amount at point 4 and further it has increased at point 5. As one moves from substrate towards scale, the concentration of oxygen is found to increase, also iron has shown small variation in its concentration. In superni 718, a thin scale consisting of iron, nickel and chromium is observed as shown in Fig. 6.54. Considerable amount of chromium oxide is present in the scale. At point 1 there is no oxygen and at interface of substrate and scale i.e. at point 2, there is presence of oxygen indicating the oxidation, Ni percentage has decreased and Cr percentage has increased. At point 4, Cr_2O_3 is more and NiO is less while at point 5, NiO is more and Cr_2O_3 is less. Small traces of V and S were also observed. There is no deep penetration of oxygen into the

substrate but it has penetrated locally i.e. near the surface only. In superfer 800, Fig. 6.55. , scale is relatively thicker and has iron oxide as major constituent. Just at interface i.e. at point 2, it is rich in Ni with little bit of iron and little bit of Cr. Iron and Chromium have oxidised to form the scale. At point 3 the amount of Ni has decreased and iron has increased and oxygen is present thereby indicating the formation of Fe_2O_3 and Cr_2O_3 and at point 4 similar composition is there and top of the scale again contains Fe, Ni and Cr oxides. As one moves into the scale, there is decrease of Nickel percentage.

Back Scattered Electron Image of cross-section of uncoated substrate alloys (T11, T22, superni 600, superni 718 and Superfer 800) and corresponding X-ray mapping after exposure to Na_2SO_4 -60% V_2O_5 environment at 900°C are shown in Fig.6.56 to 6.60 respectively. In boiler steels, there is a severe internal attack as the scale is penetrating deep into the substrate. The scale is porous and quite fragile. Iron from the substrate is forming iron oxide. Continuous spalling of scale layer by layer was observed. In boiler steel T11 (Fig.6.56), main constituent is iron oxide with presence of minor concentration of Mn, Cr, S and V. Sulphur has penetrated into the substrate. Also a very thin Cr_2O_3 band is visible at the scale substrate interface. Alternate bands of Cr_2O_3 and Fe_2O_3 are visible in the scale. In T22 boiler steel, the scale is thick and porous and it mainly consisted of iron oxide as is clear from Fig. 6.57. Cr_2O_3 is also present throughout the scale. Sulphur and vanadium has penetrated into the substrate. A thick flake of iron is visible at the outer edge of the scale but is not continuous this may be a substrate chip which has been impinged into the epoxy interface.

In superalloy, superni 600, (Fig. 6.58) there is severe internal attack, and scale is quite porous. In scale there is formation of Cr rich band in combination with oxygen. In scale, where Ni is absent, Cr and Fe are present along with oxygen. Through cracks internal penetration has occurred with thick scale formation. Severe internal attack is also visible. As oxygen is present throughout the scale, it can be inferred that there is formation of iron oxide, nickel oxide and chromium oxide throughout the scale.

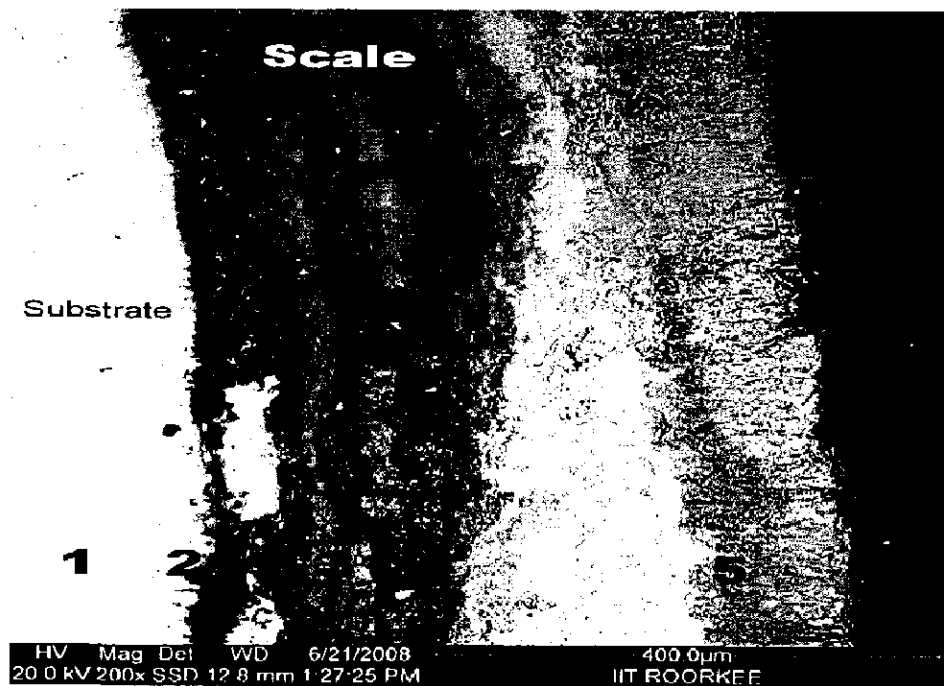
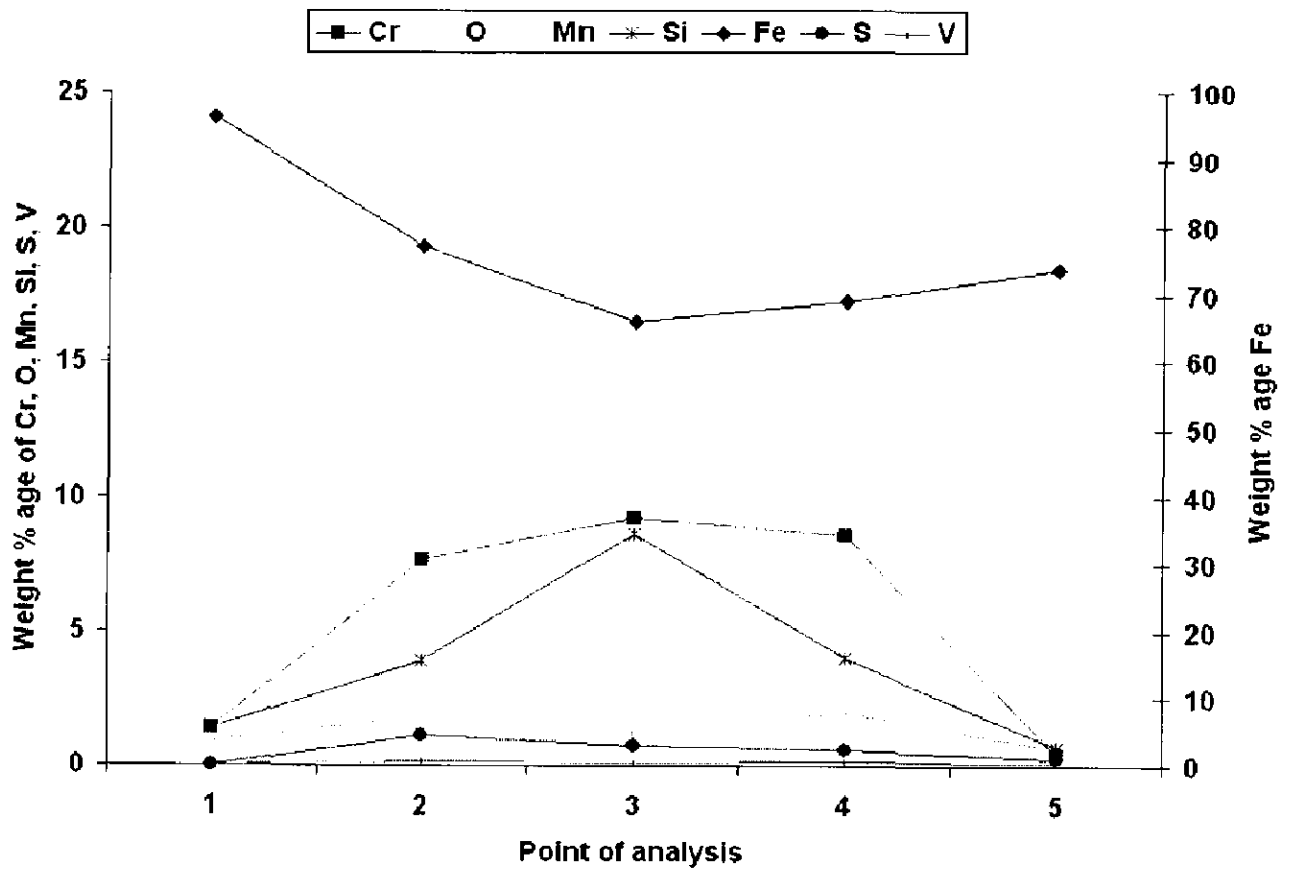


Fig. 6.51: Cross sectional morphology and elemental composition variation across the cross-section of boiler steel T11 exposed to Na_2SO_4 -60% V_2O_5 at 900°C for 50 cycles, 200 X.

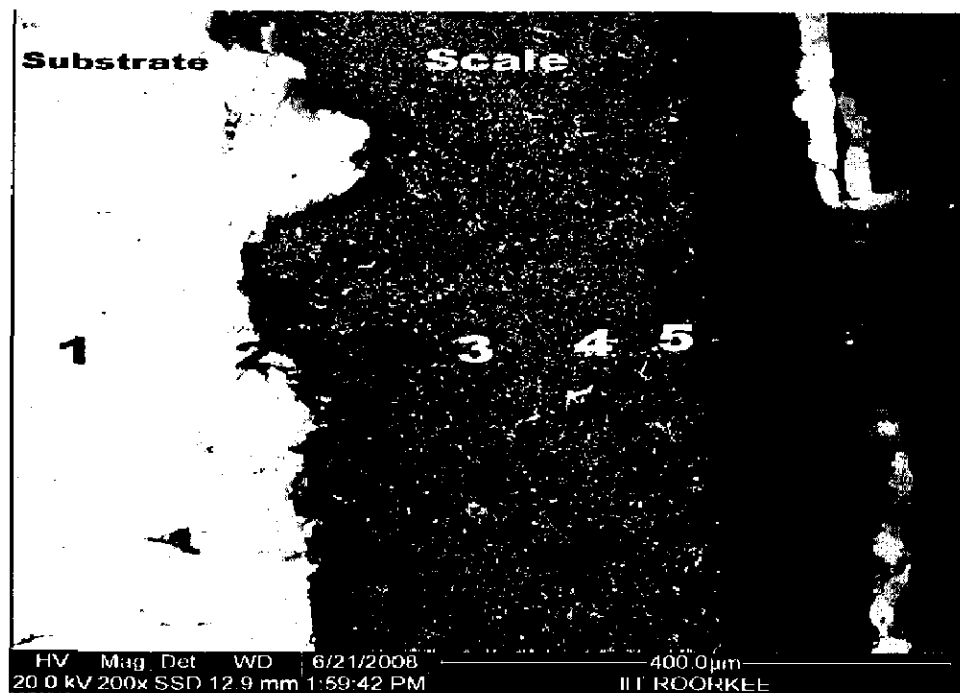
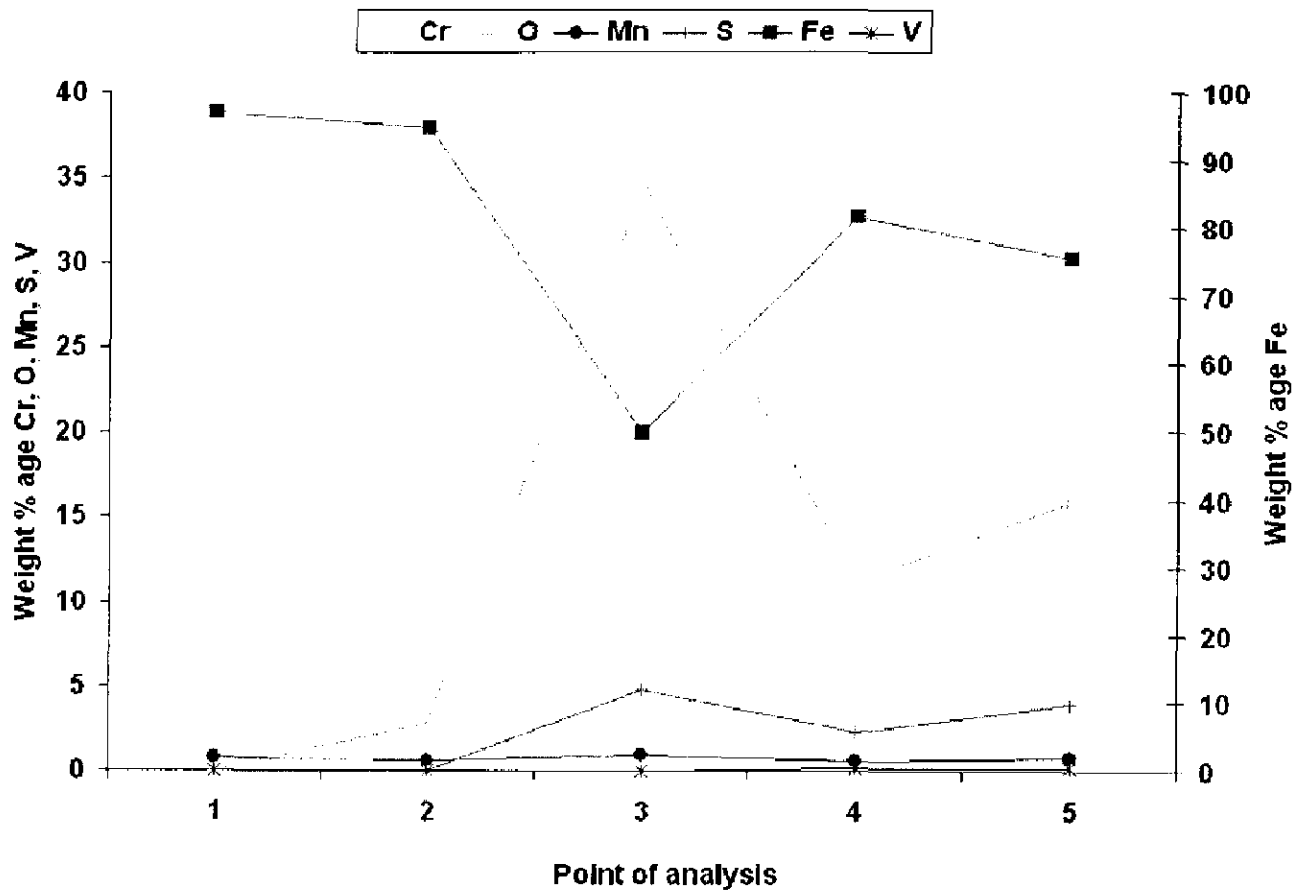


Fig. 6.52: Cross sectional morphology and elemental composition variation across the cross-section of boiler steel T22 exposed to Na_2SO_4 -60% V_2O_5 at 900°C for 50 cycles, 200X.

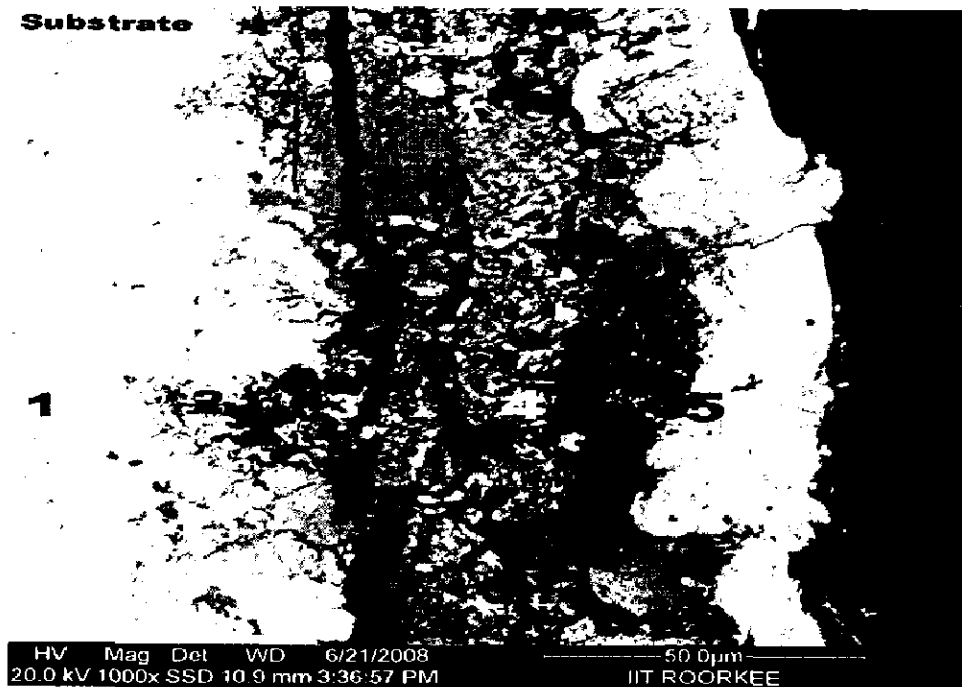
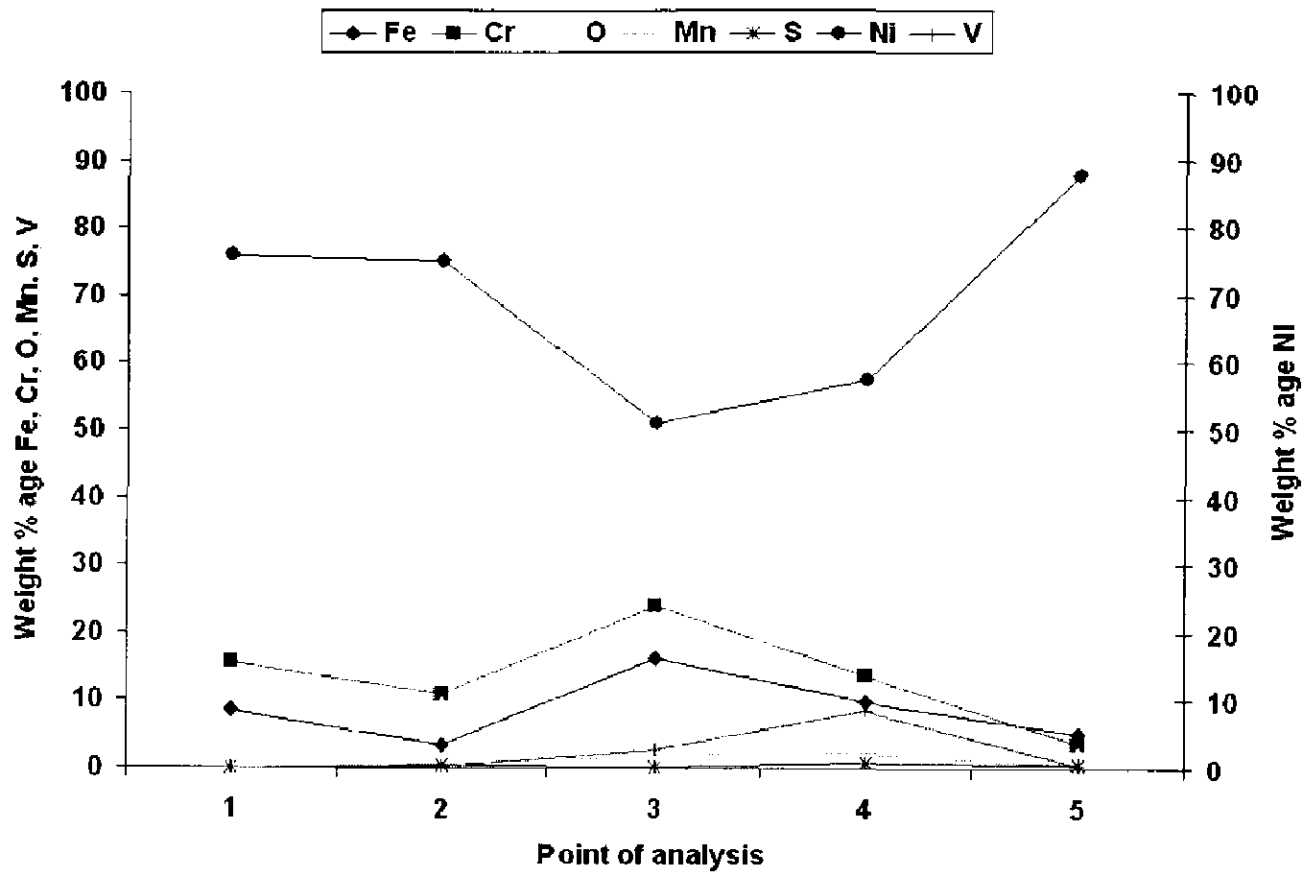


Fig.6.53: Cross sectional morphology and elemental composition variation across the cross-section of superalloy Superni 600 exposed to $\text{Na}_2\text{SO}_4\text{-60\%V}_2\text{O}_5$ at 900°C for 50 cycles, 1000 X.

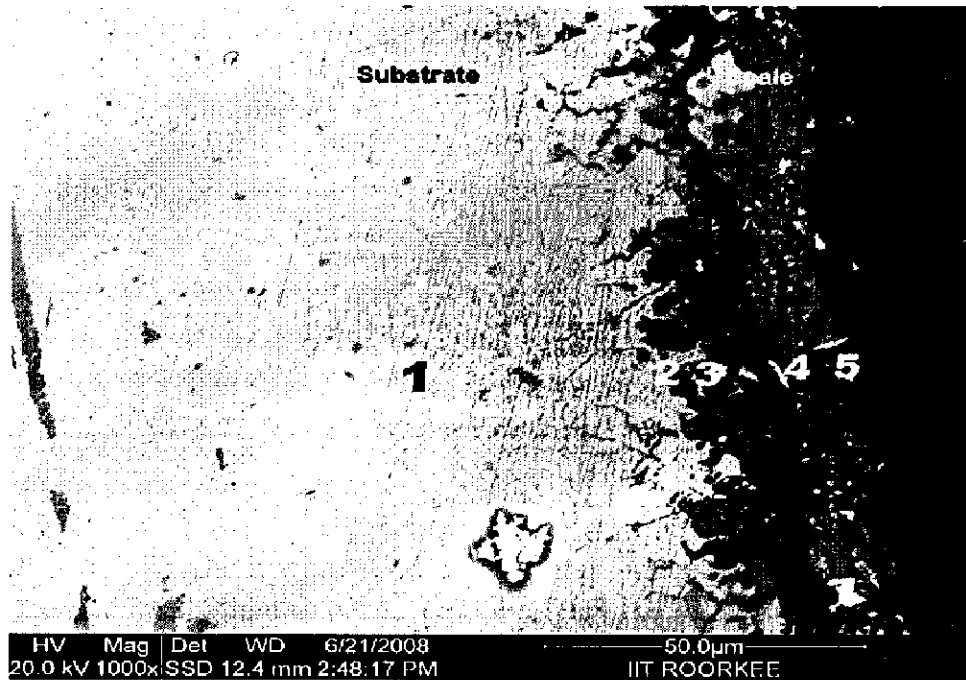
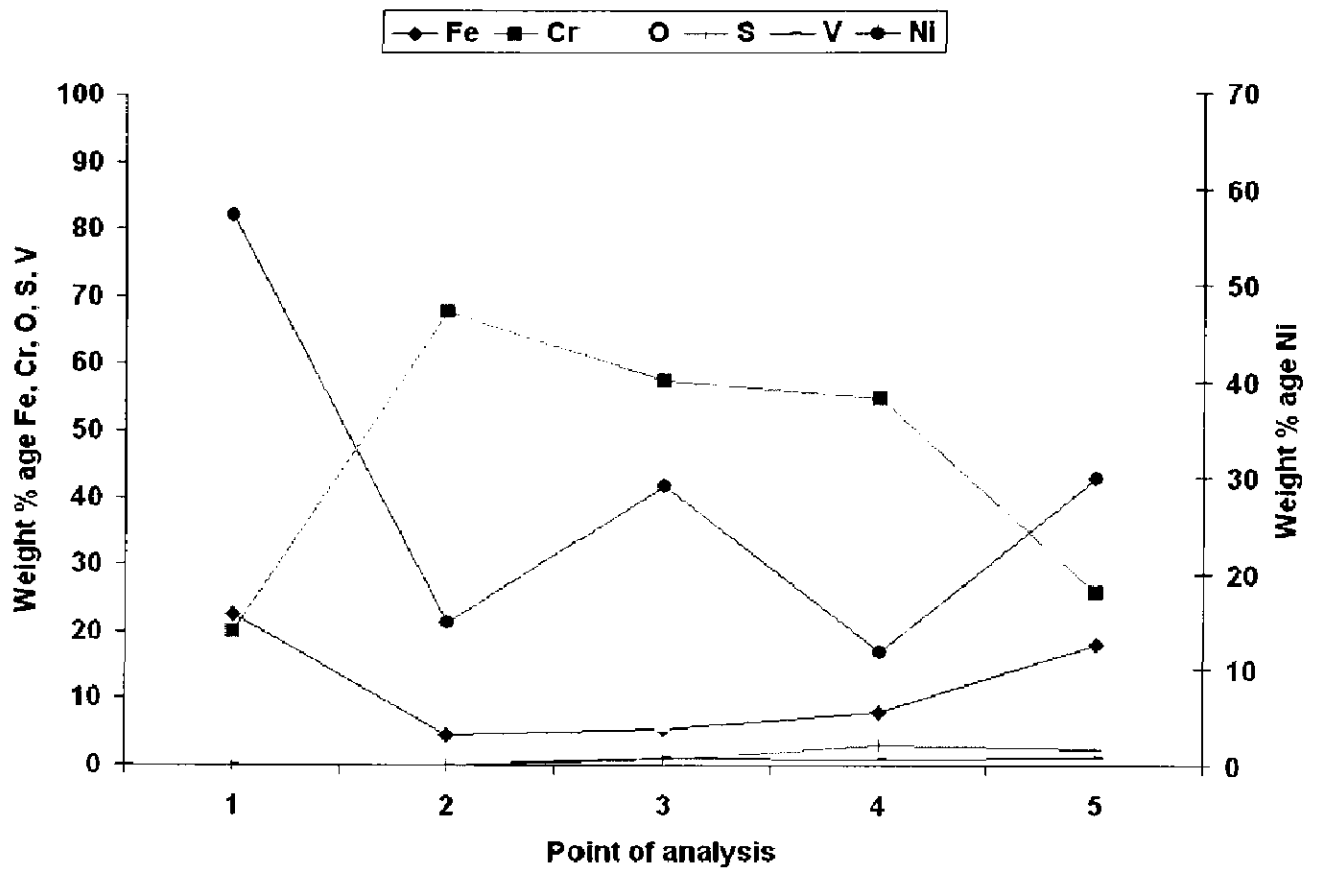


Fig.6.54: Cross sectional morphology and elemental composition variation across the cross-section of superalloy Superni 718 exposed to Na_2SO_4 -60% V_2O_5 at 900°C for 50 cycles, 1000 X.

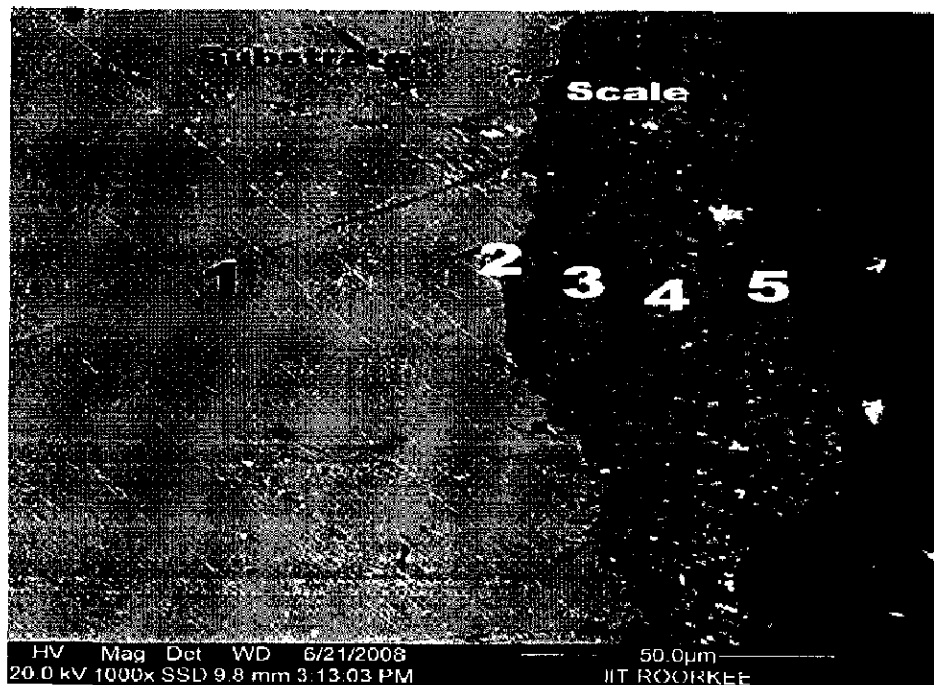
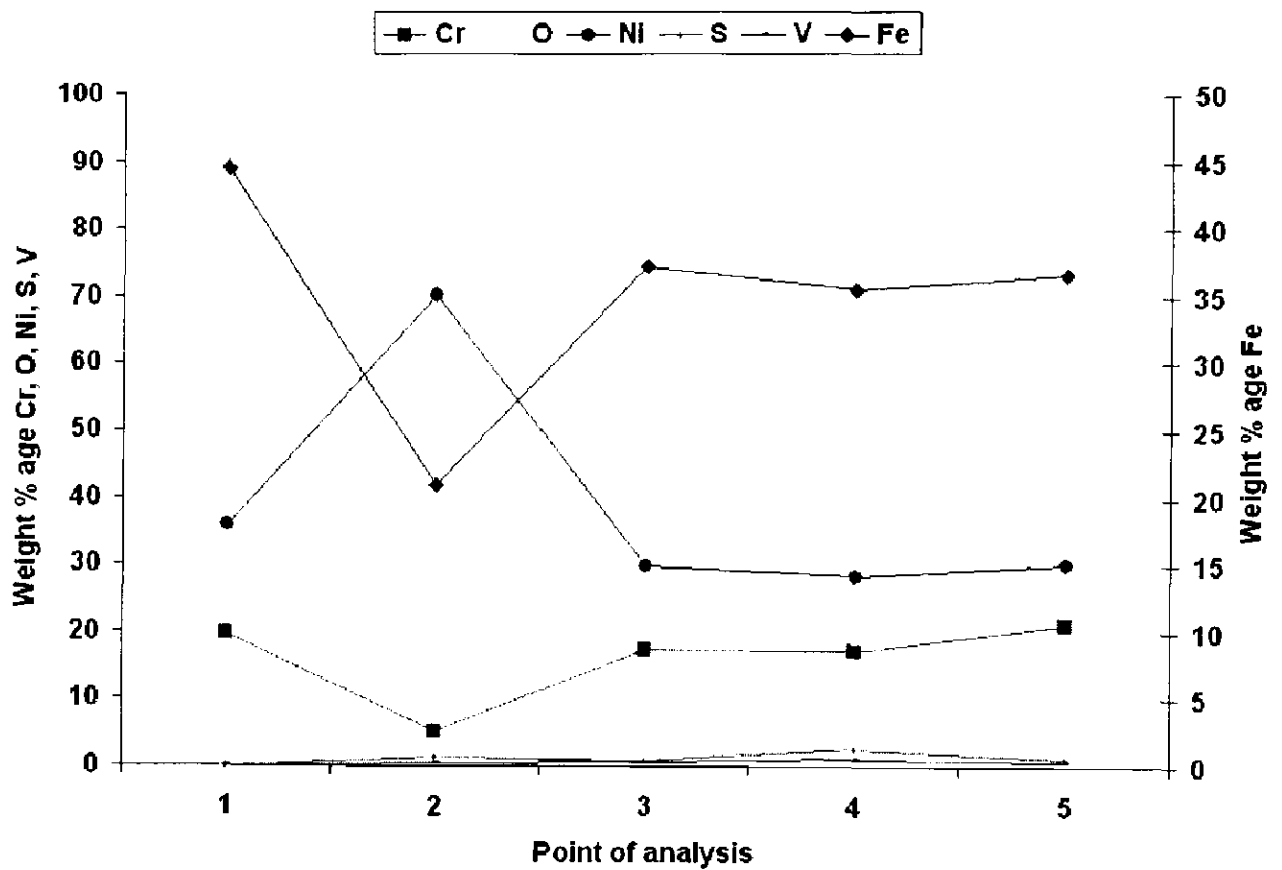


Fig.6.55: Cross sectional morphology and elemental composition variation across the cross-section of superalloy Superfer 800 exposed to $\text{Na}_2\text{SO}_4\text{-60\%V}_2\text{O}_5$ at 900°C for 50 cycles, 1000X.

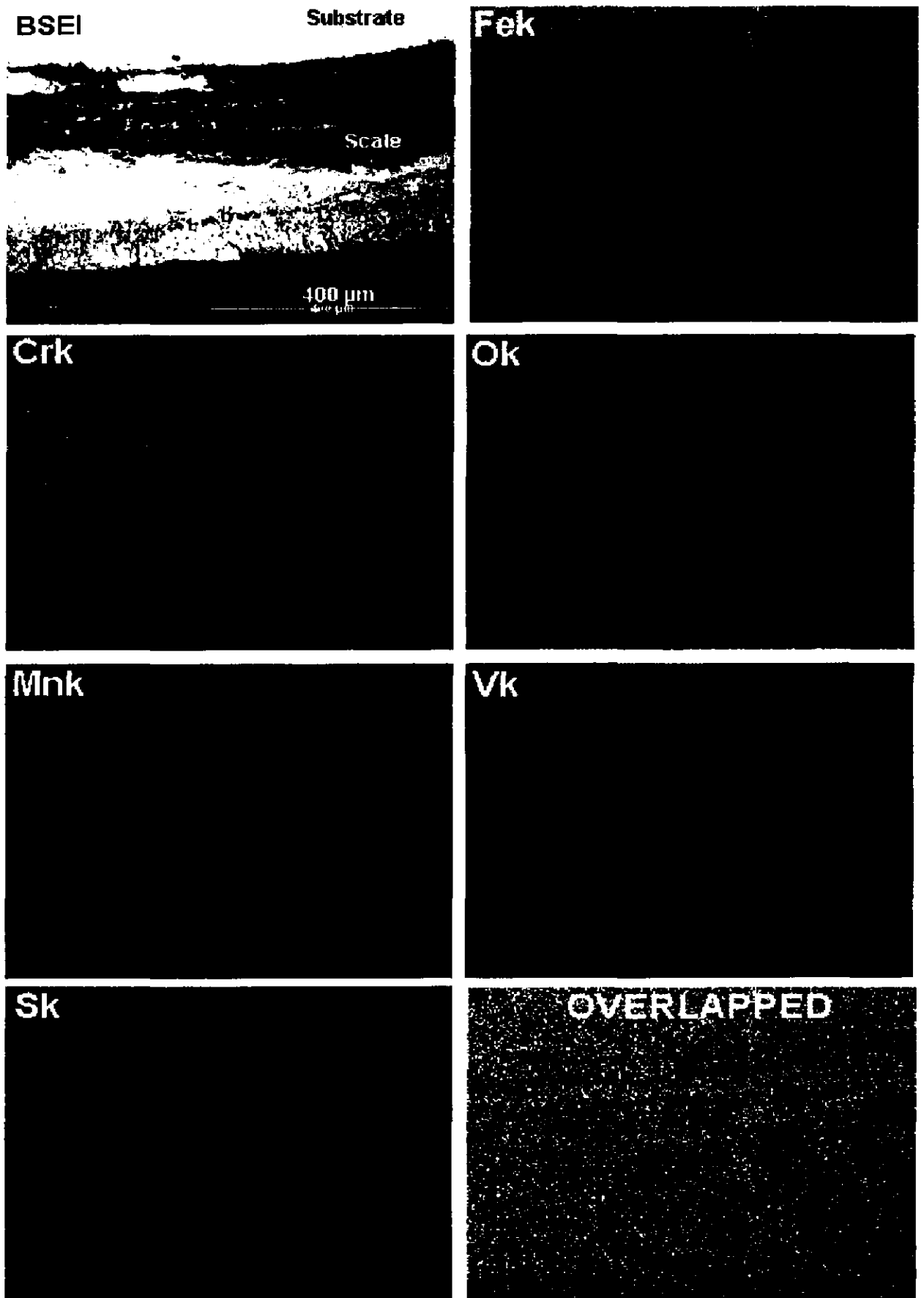


Fig. 6.56: BSEI and X-ray mapping of the cross-section of boiler steel T11 subjected to cyclic hot corrosion in $\text{Na}_2\text{SO}_4\text{-60\%V}_2\text{O}_5$ at 900°C for 50 cycles, 200 X.

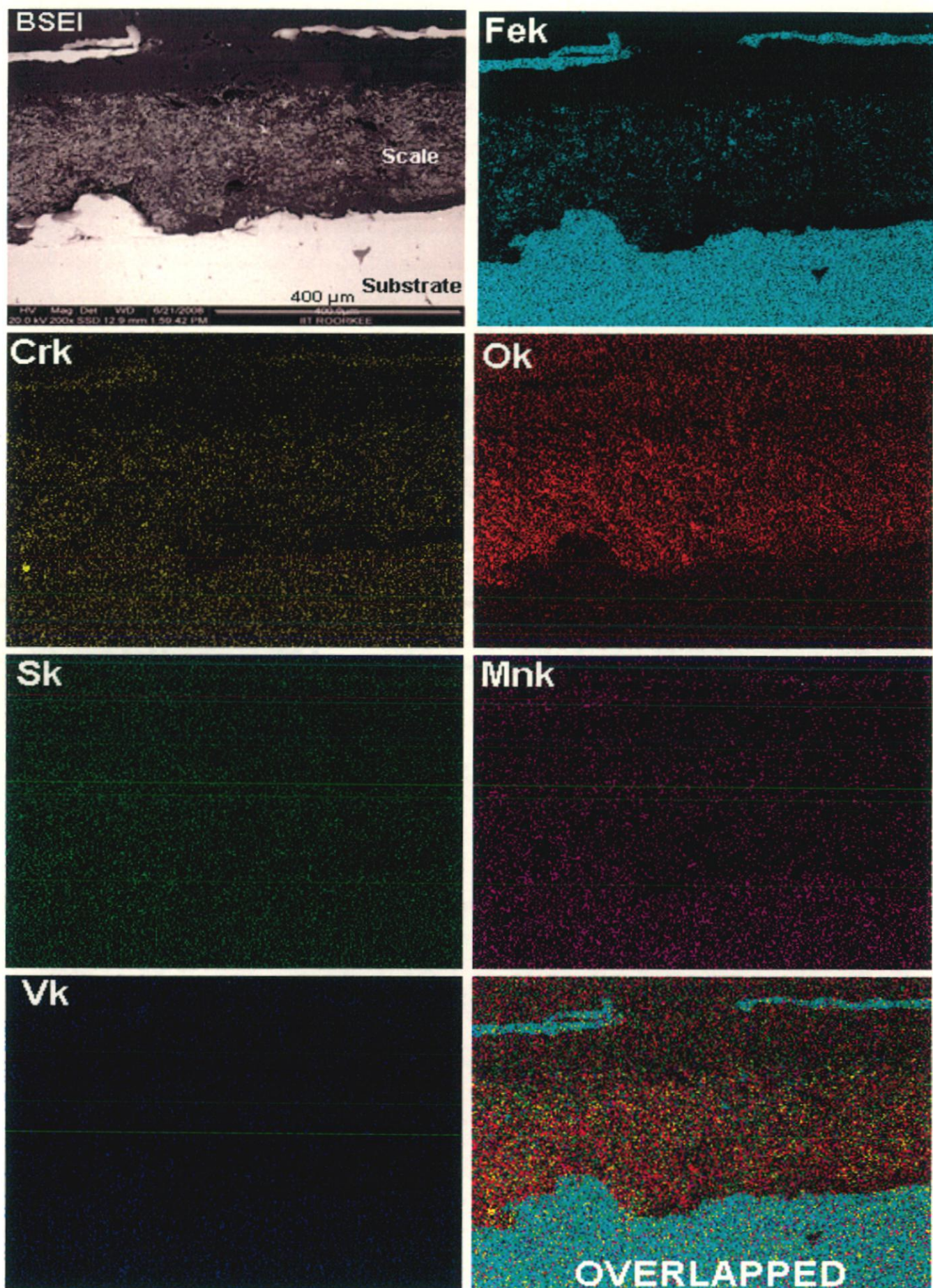


Fig. 6.57: BSEI and X-ray mapping of the cross-section of boiler steel T22 subjected to cyclic hot corrosion in $\text{Na}_2\text{SO}_4\text{-60\%V}_2\text{O}_5$ at 900°C for 50 cycles, 200X.

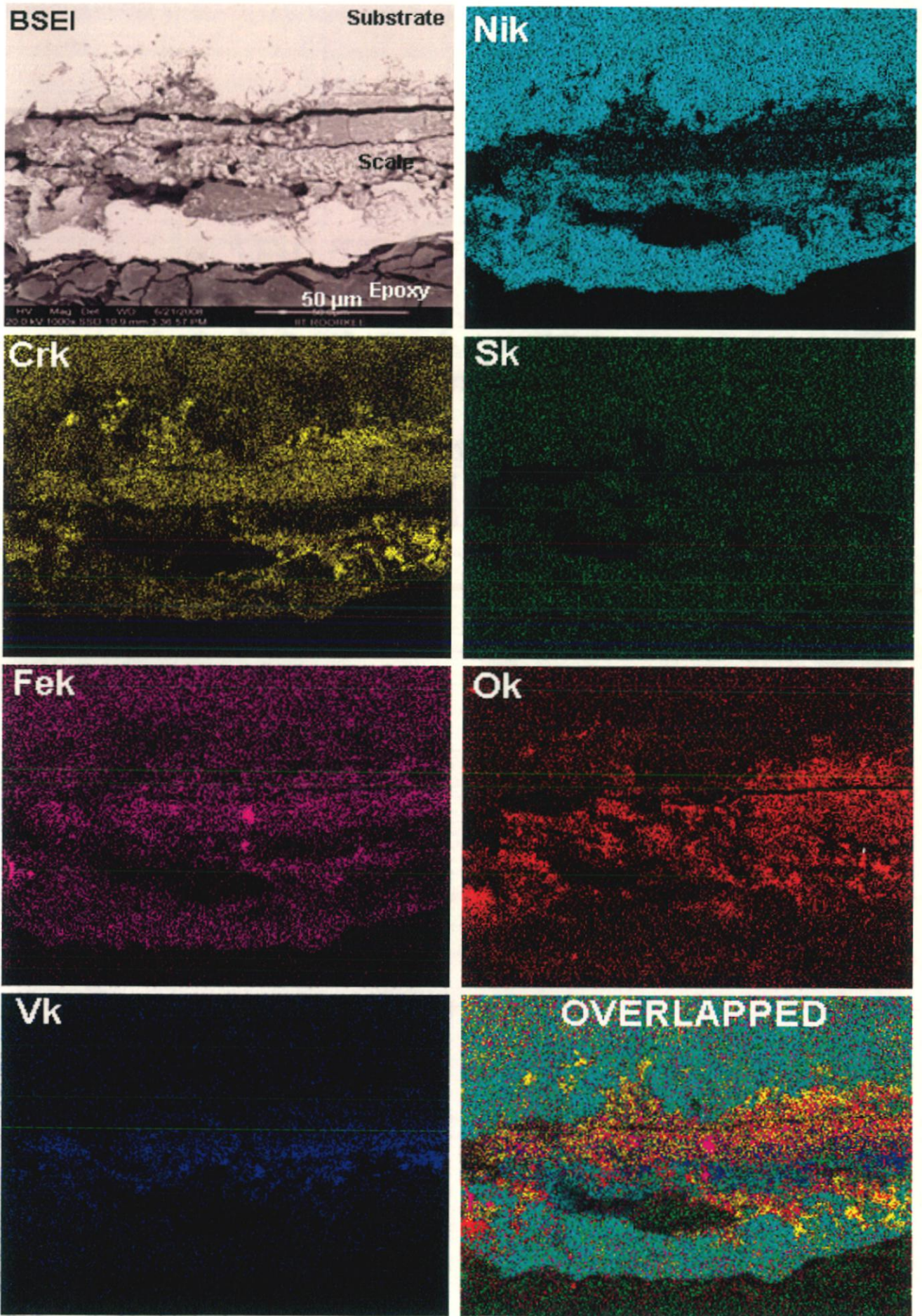


Fig. 6.58: BSEI and X-ray mapping of the cross-section of superalloy Superni 600 subjected to cyclic hot corrosion in $\text{Na}_2\text{SO}_4\text{-60}\%\text{V}_2\text{O}_5$ at 900°C for 50 cycles, 200X.

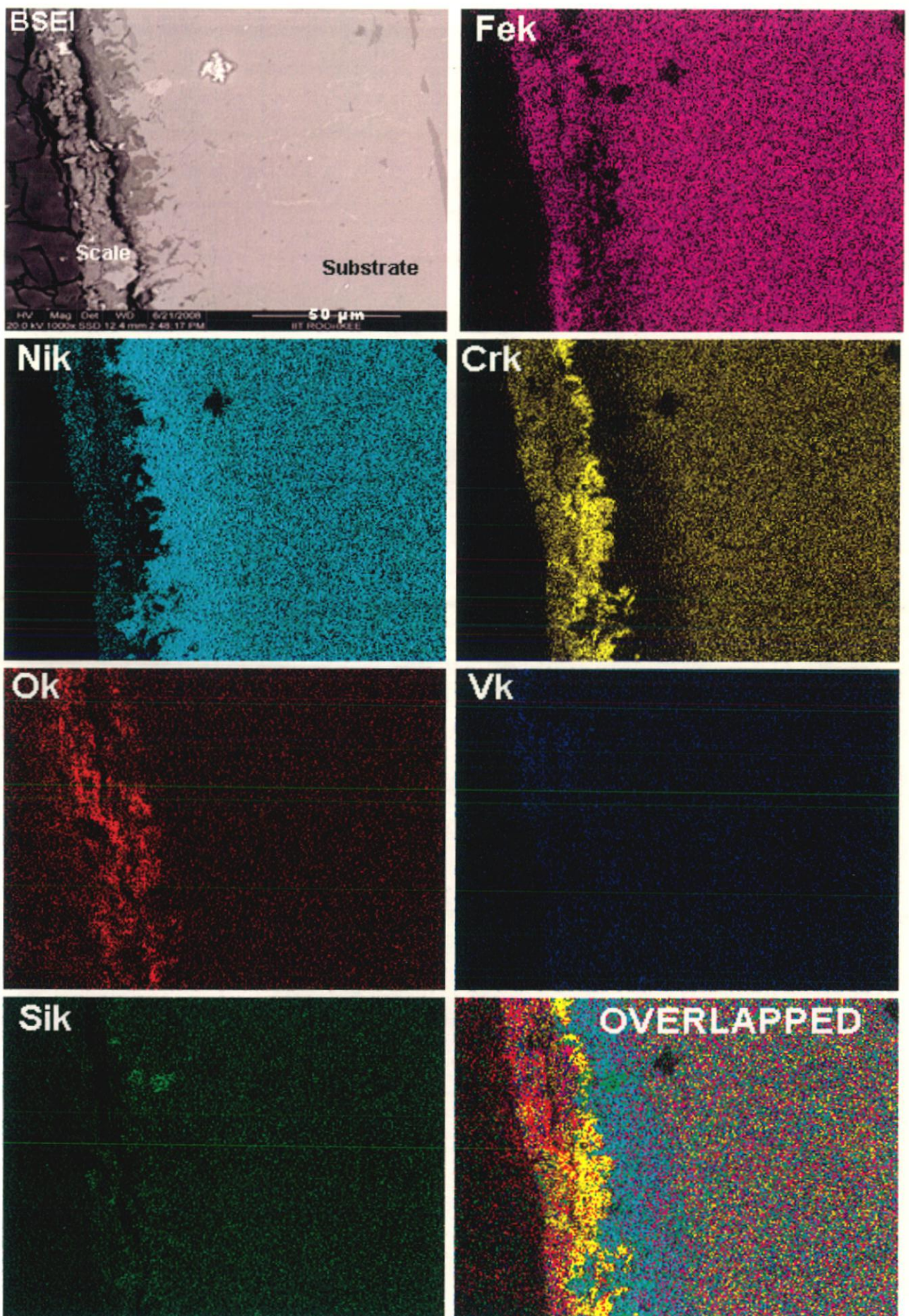


Fig.6.59: BSEI and X-ray mapping of the cross-section of superalloy Superni 718 subjected to cyclic hot corrosion in Na_2SO_4 -60% V_2O_5 at 900°C for 50 cycles, 1000 X.

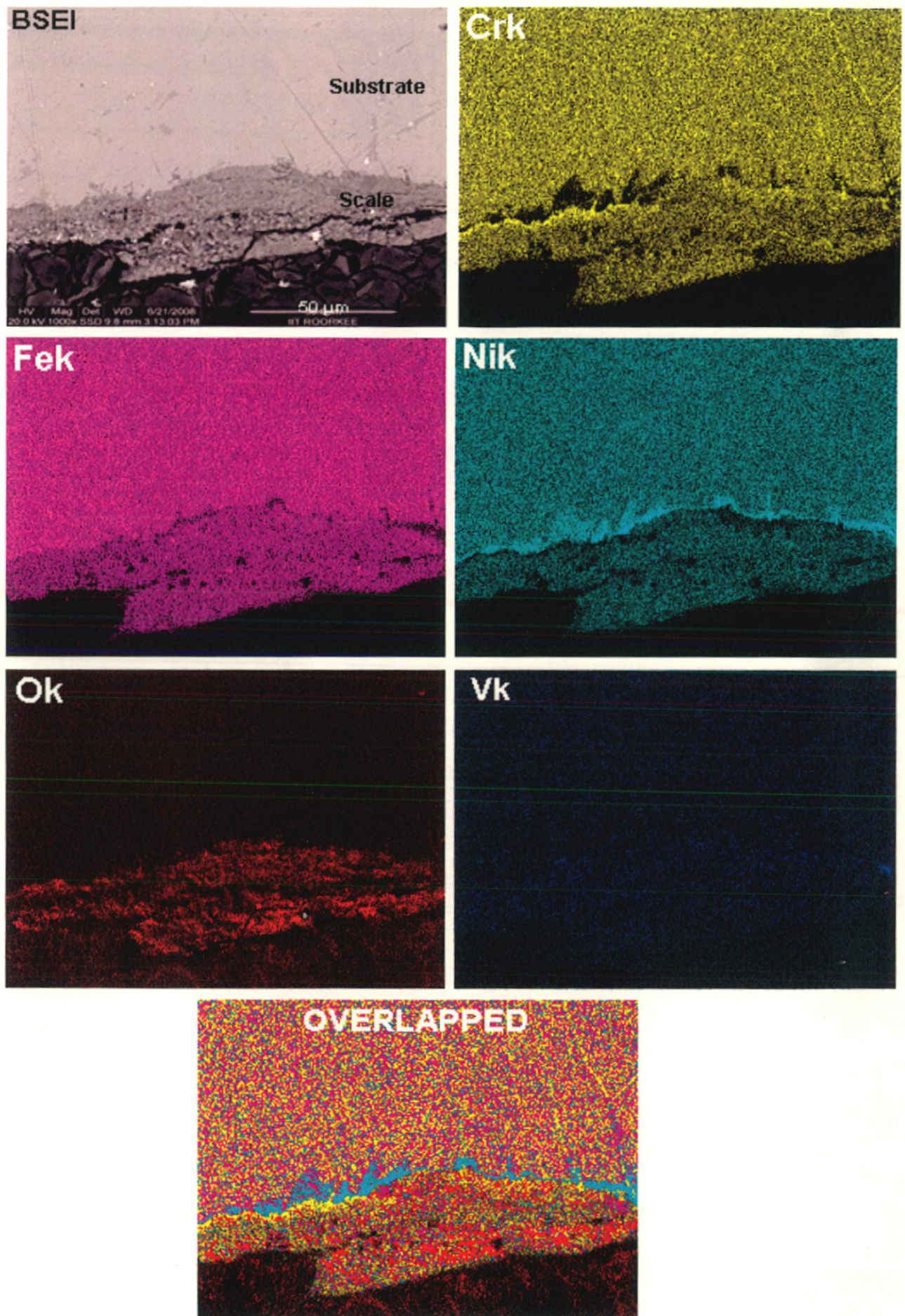


Fig. 6.60: BSEI and X-ray mapping of the cross-section of superalloy superfer 800 subjected to cyclic hot corrosion in $\text{Na}_2\text{SO}_4\text{-60\%V}_2\text{O}_5$ at 900°C for 50 cycles, 1000 X.

Cr_2O_3 formed is providing protection for further oxidation. Vanadium band is also visible in the scale in between the substrate and top metallic layer. The oxygen is co-existing with Fe and Cr. Internal oxidation has taken place and outer substrate layer has prevented further oxidation. In Superni 718, Fig.6.59 attack is confined and thin scale is formed. Ni has diffused from the substrate and is concentrated along the substrate scale boundary. At the top of the scale Ni and Cr are present and chromium rich band is clearly visible in the scale. It can be inferred that chromium is coming out from the substrate and forming chromium oxide in the scale. Also Ni rich portion is seen at the scale substrate interface. In Superfer 800, Fig.6.60 scale formed is porous and fragile. In scale higher percentage of Fe_2O_3 is present with some amount of Chromium oxide and Nickel oxide. Nickel concentration has increased in the substrate along substrate scale interface in the shape of thin band which has prevented the further oxidation as Cr has migrated to form the Cr_2O_3 scale. At the interface of substrate and scale, there is thin nickel rich band. Cr_2O_3 is present above this Ni band in the scale. Cr has come from substrate to form irregular Cr_2O_3 band leaving a Ni rich band in the substrate which is clearly visible in the overlapped map. The scale mainly contains iron, nickel, chromium along with oxygen which indicates the formation of Fe_2O_3 , Cr_2O_3 , NiO. Percentage of Fe_2O_3 is higher as compared to other oxides.

6.1.2.2 Coated alloys

6.1.2.2.1 Visual examination

The macrographs of Al_2O_3 - 3 wt% TiO_2 coated T11, T22, Superni 600, Superni 718 and Superfer 800 substrate alloys after hot corrosion in an aggressive environment of molten salt (Na_2SO_4 -60% V_2O_5) at 900°C under cyclic conditions for 50 cycles are shown in Fig. 6.61. In the visual examination, it was observed that the colour of samples started changing from grey to cream (pale yellow) and in the subsequent cycles it turned to reddish cream. During the whole molten salt exposure, coating remained intact and there was no spalling or sputtering of the coating unlike uncoated specimens. In case of coated boiler steel T11, some dark patches were observed on the surface whereas on coated T22 some shining was observed.

6.1.2.2.2 Weight Change Data

Weight gain per unit area expressed in mg/cm^2 is plotted as a function of time expressed in number of cycles for molten salt exposed Al_2O_3 - 3 wt% TiO_2 coated T11, T22 boiler steels is shown in Fig. 6.62 and for superalloys Superni 600, superni 718 and

Superfer 800 superalloys is shown in Fig. 6.64. The total weight gain at the end of 50 cycles for coated boiler steels T11 and T22 is 3.787 and 3.594, mg/cm² respectively. Weight gain square (mg²/cm⁴) plotted as a function of time (number of cycles) or boiler steels is shown in Fig.6.63. There is scatter in data, if the scatter in the measurements is not considered, the values of parabolic rate constant (K_p) for coated boiler steels T11 and T22 are calculated as 8.19×10^{-11} and 7.57×10^{-11} g² cm⁻⁴ s⁻¹ respectively.

While in case of coated superalloys, coated superfer 800 showed maximum weight gain as compared to other two superalloys superni 600 and superni 718. In superfer 800, initially there is rapid weight gain upto 6th cycle, and then there is a gradual weight gain upto 20th cycle and then again there is rapid weight gain upto 26th cycle and afterwards it is constant. Superni 600 has almost followed the same trend. In case of coated superni 718, weight gain is almost negligible for the initial 10 cycles, then there is slight increase upto 18th cycle, and there is rapid increase upto 26th cycle and afterwards it has become constant. The total weight gain at the end of 50 cycles for Al₂O₃ - 3 wt% TiO₂ coated superalloys Superni 600, 718 and Superfer 800 are 2.22, 0.88 and 2.68 mg/cm² respectively. This shows that the weight gain in case of Al₂O₃ - 3 wt% TiO₂ coated Superni 718 is lowest, whereas it is highest in case of Al₂O₃ - 3 wt% TiO₂ coated Superfer 800. The weight gains are very small as compared to uncoated or bare alloys

In Fig. 6.65, the (weight gain/unit area)² versus number of cycles for all the coated superalloys are plotted to determine the conformance with the parabolic rate law. The curve for Superni 718 is parabolic. While in case of superni 600 and superfer 800, scatter in the data can be observed in the plots and the data can not be approximated by a parabolic relationship. If the scatter in the measurements is not considered, the values of parabolic rate constant (K_p) for the superalloys Superni 600, 718 and Superfer 800 are calculated as 2.91×10^{-11} , 5.91×10^{-12} and 4.03×10^{-11} g² cm⁻⁴ s⁻¹ respectively.

6.1.2.2.3 X-ray Diffraction Analysis

X-ray diffraction profiles for Al₂O₃-3 wt% TiO₂ coated boiler steels subjected to cyclic hot corrosion in Na₂SO₄-60%V₂O₅ at 900°C for 50 cycles are shown in Fig. 6.66. Both coated boiler steels T11 and T22 have Al₂O₃ and TiO₂ as the main constituent with minor peak of Al₂TiO₇O₁₅. The X-ray diffractograms for the coated superalloys after exposure to molten salt at 900°C for 50 cycles is shown in Figs. 6.67 and 6.68. Major peaks of Al₂O₃ and TiO₂ along with minor peaks of Al₂TiO₅ were observed in all the coated superalloys under study.

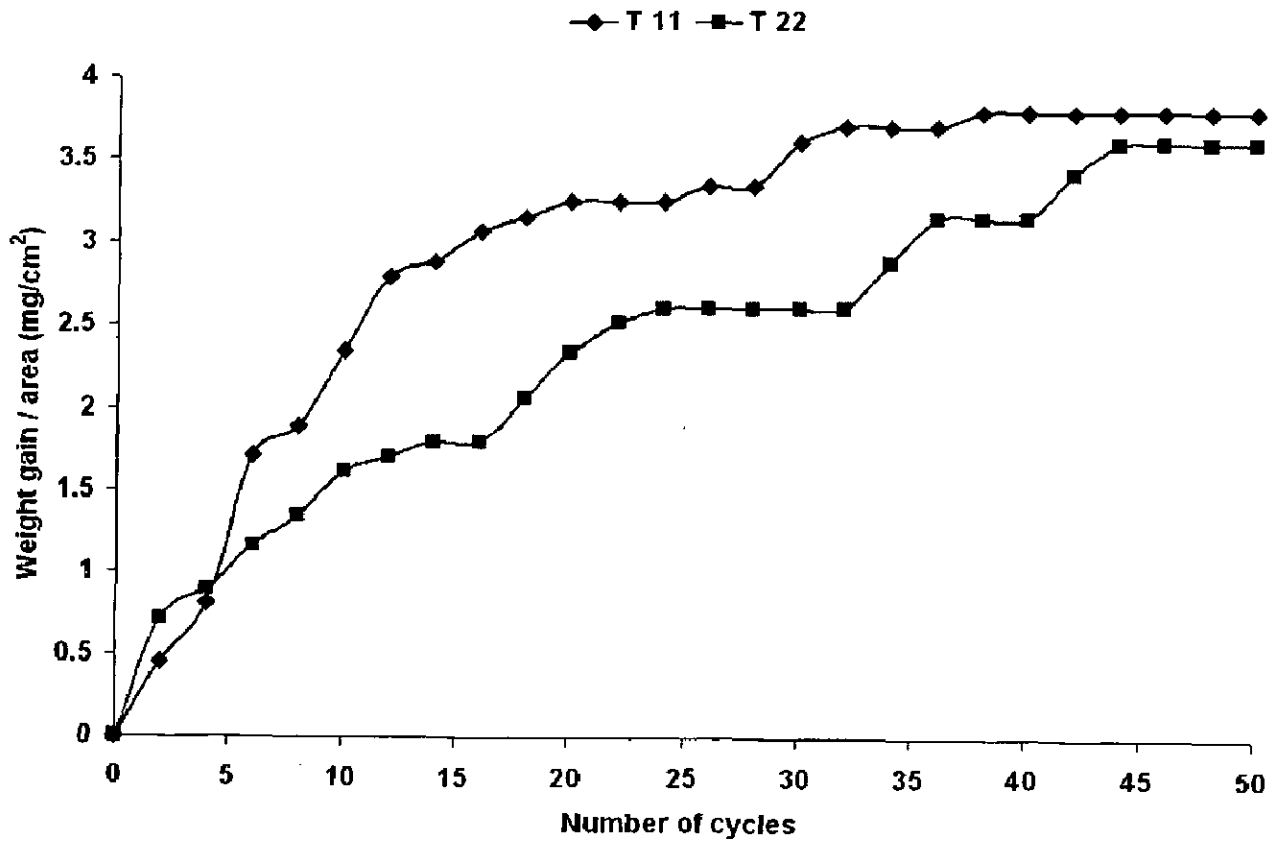


Fig. 6.62: Weight gain plot for Al_2O_3 - 3 wt% TiO_2 coated boiler steels T11 and T22 subjected to cyclic hot corrosion in Na_2SO_4 -60% V_2O_5 at 900°C for 50 cycles.

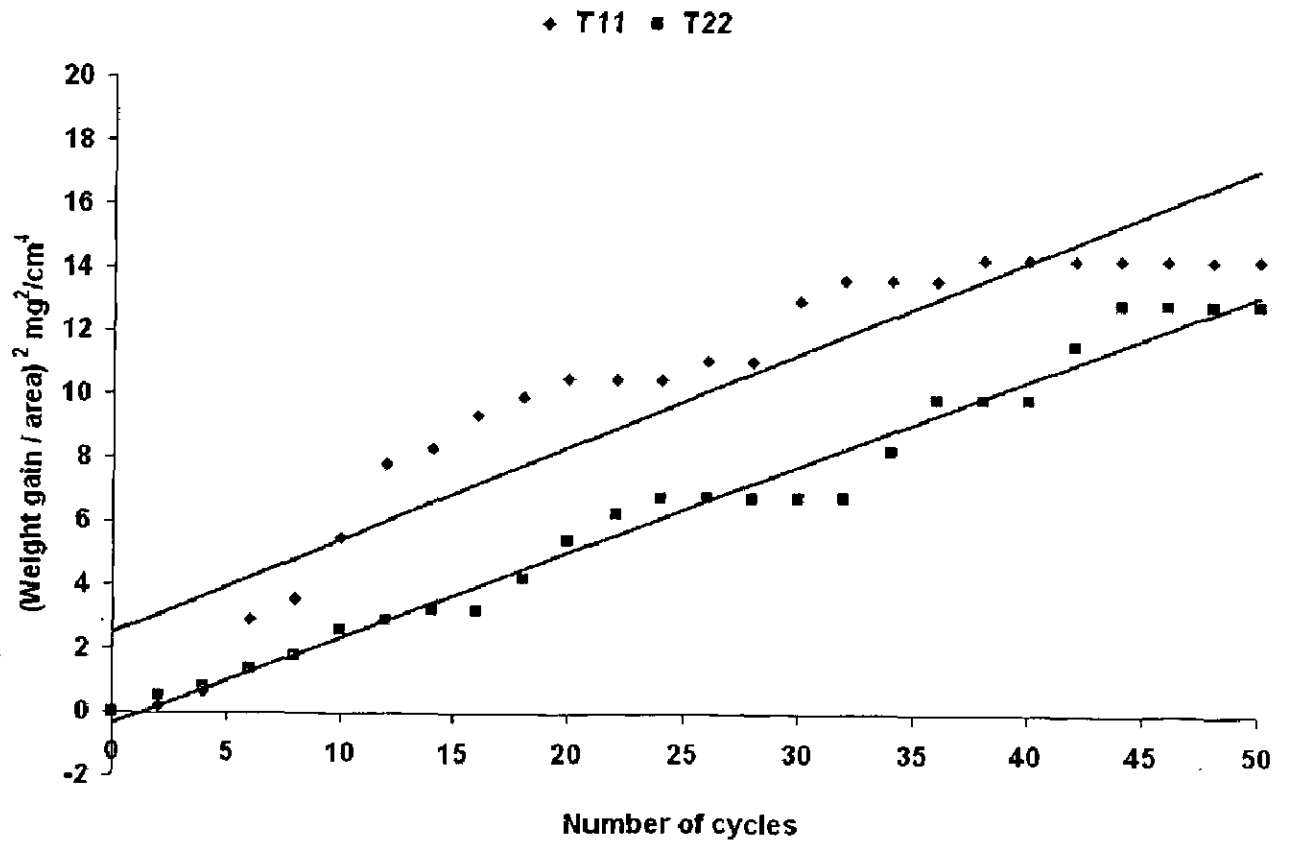


Fig.6.63: Weight gain square (mg^2/cm^4) plot for Al_2O_3 - 3 wt% TiO_2 coated boiler steels T11 and T22 subjected to cyclic hot corrosion in Na_2SO_4 -60% V_2O_5 at 900°C for 50 cycles.

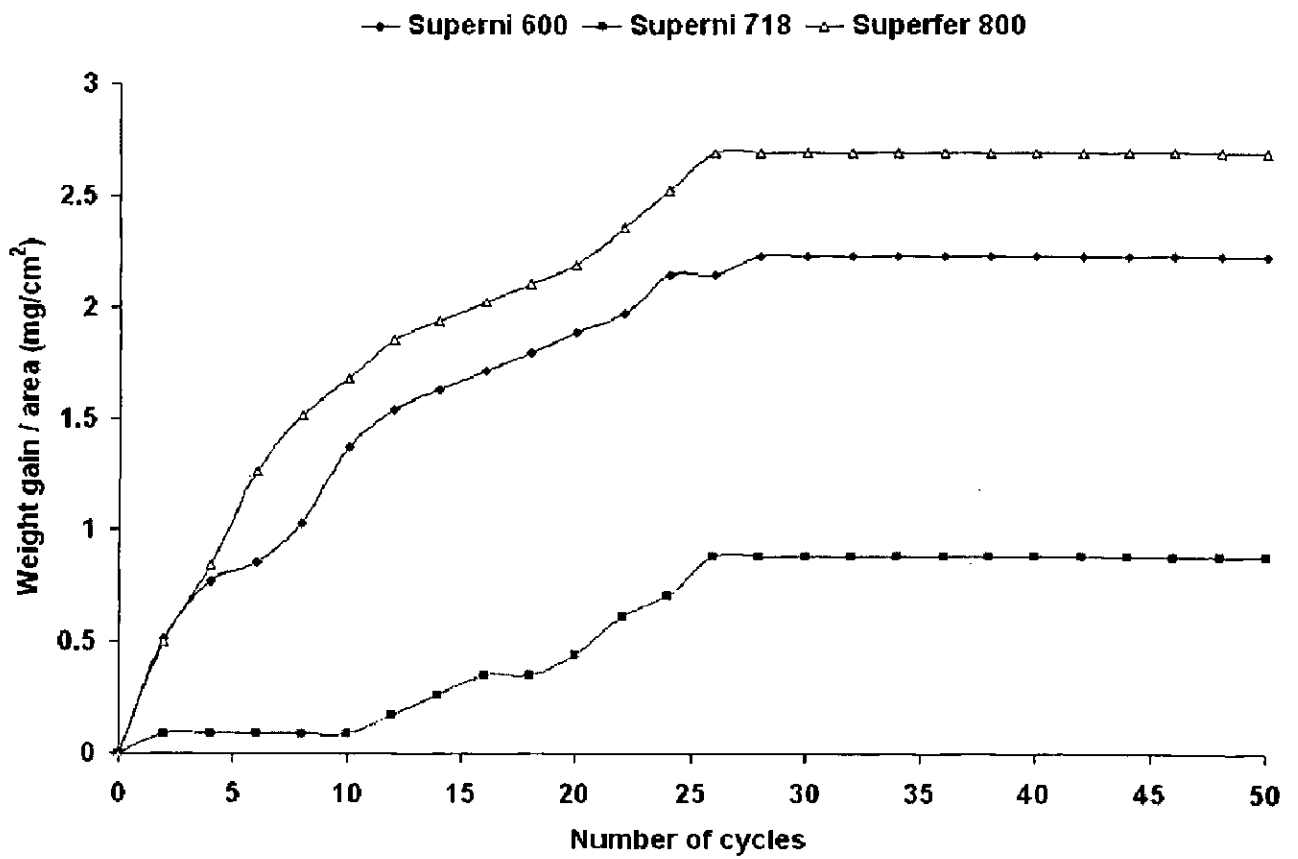


Fig. 6.64: Weight gain plot for Al_2O_3 - 3 wt% TiO_2 coated superalloys Superni 600, Superni 718, Superfer 800 subjected to cyclic hot corrosion in Na_2SO_4 -60% V_2O_5 at 900°C for 50 cycles.

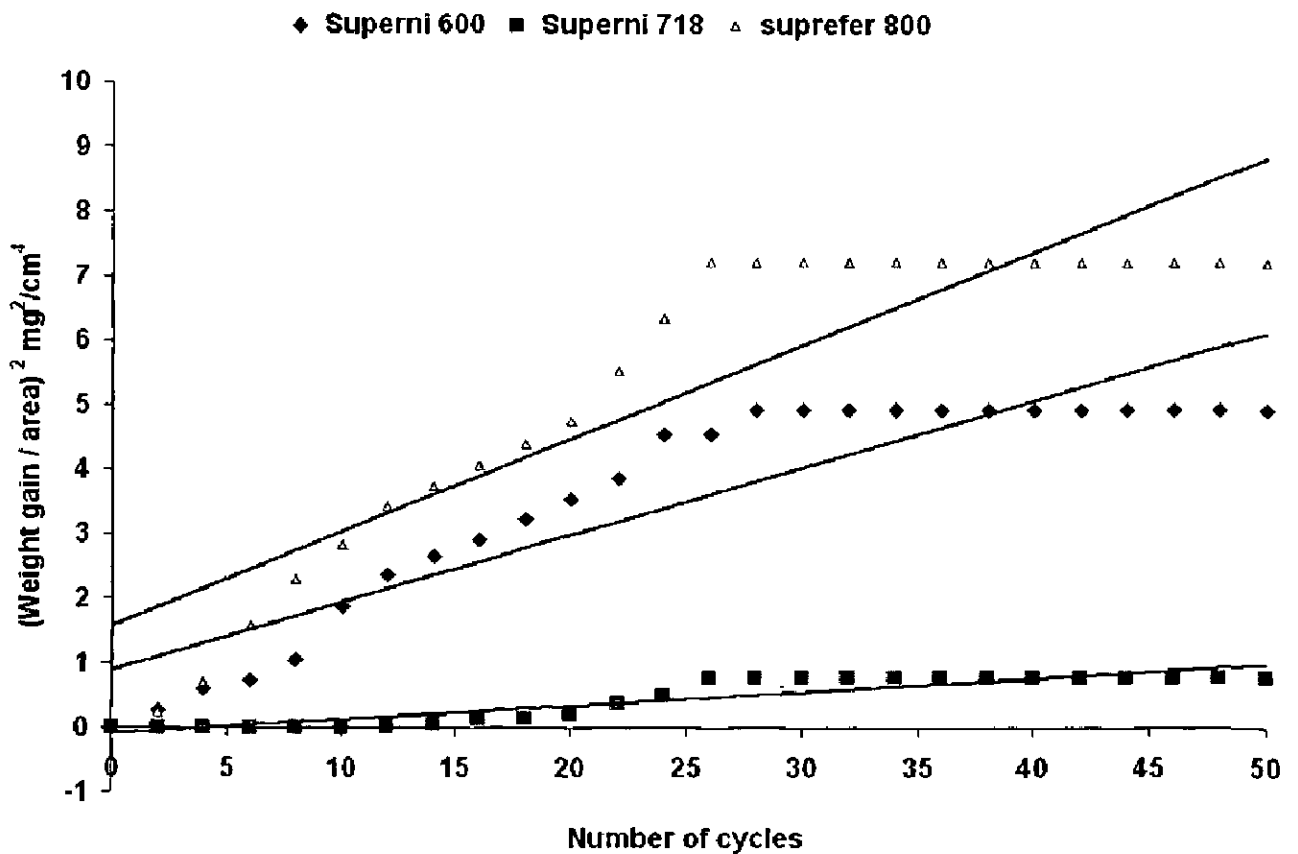
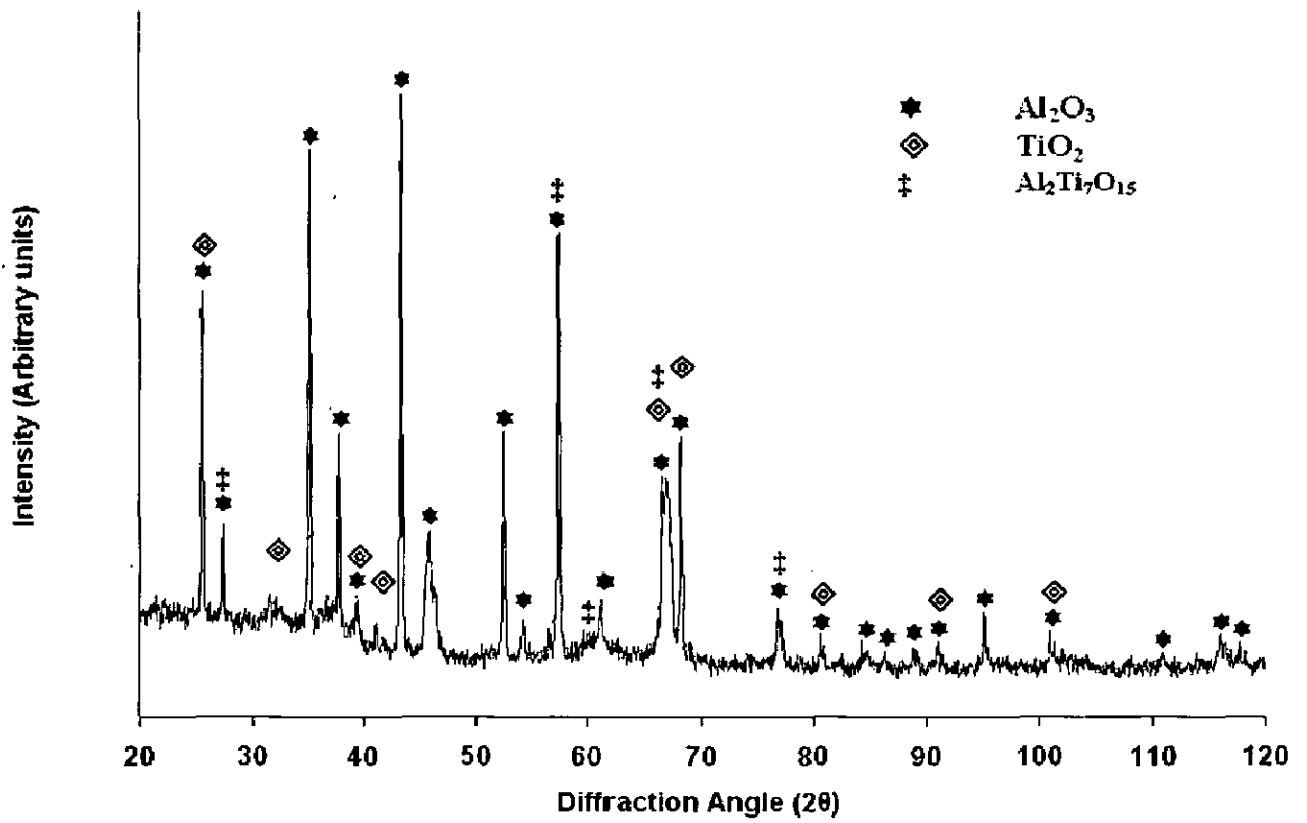
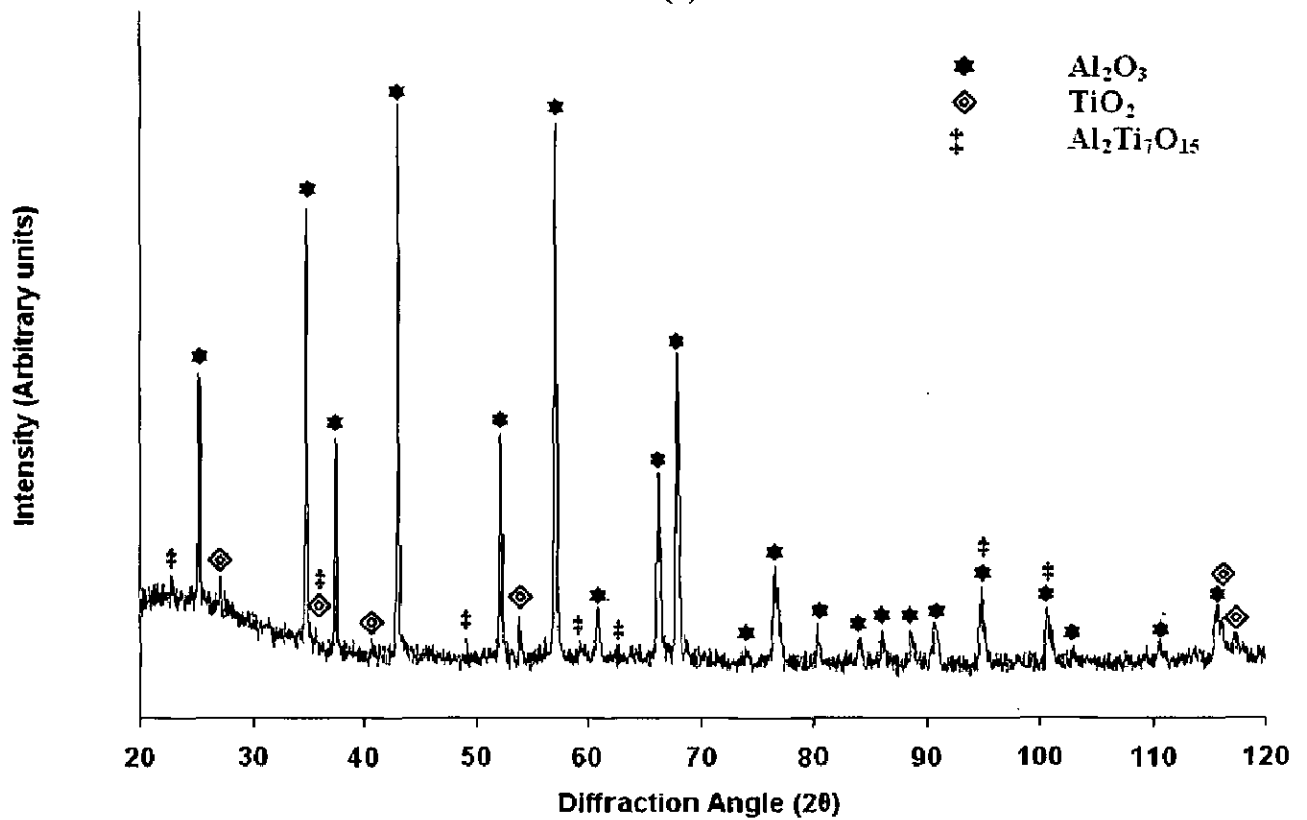


Fig.6.65: Weight gain square (mg^2/cm^4) plot for Al_2O_3 - 3 wt% TiO_2 coated superalloys Superni 600, Superni 718, Superfer 800 subjected to cyclic hot corrosion in Na_2SO_4 -60% V_2O_5 at 900°C for 50 cycles.

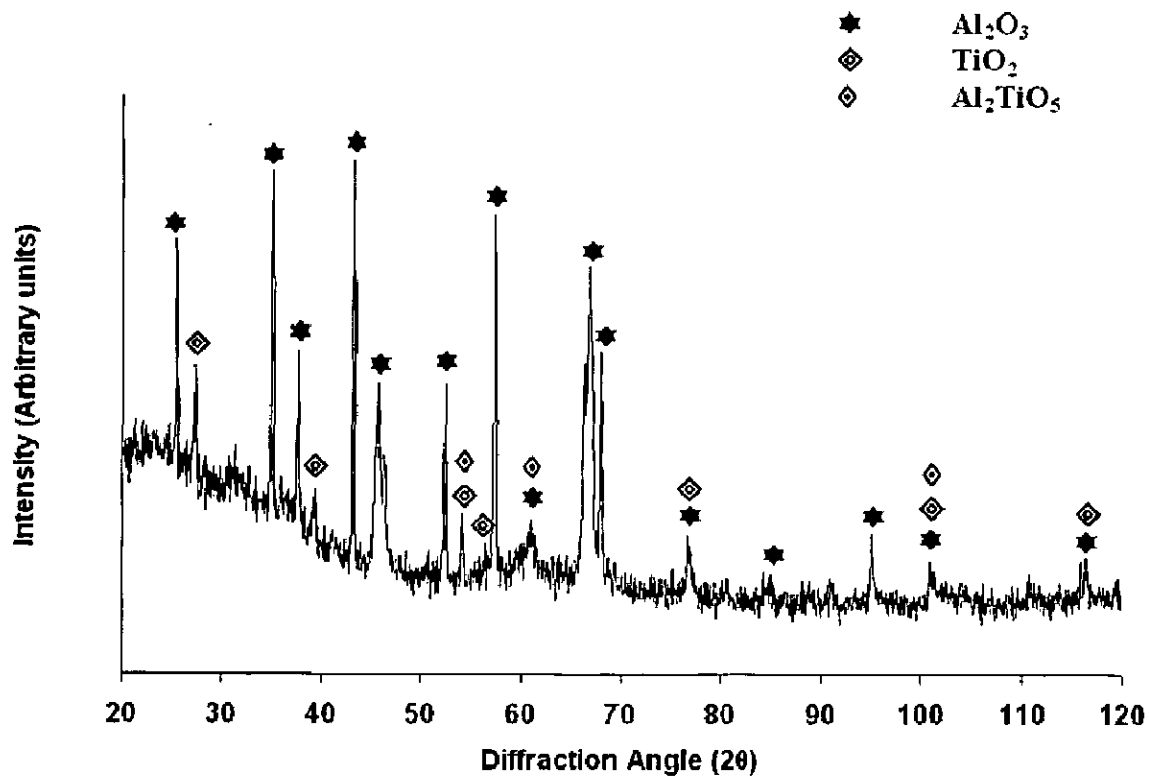


(a)

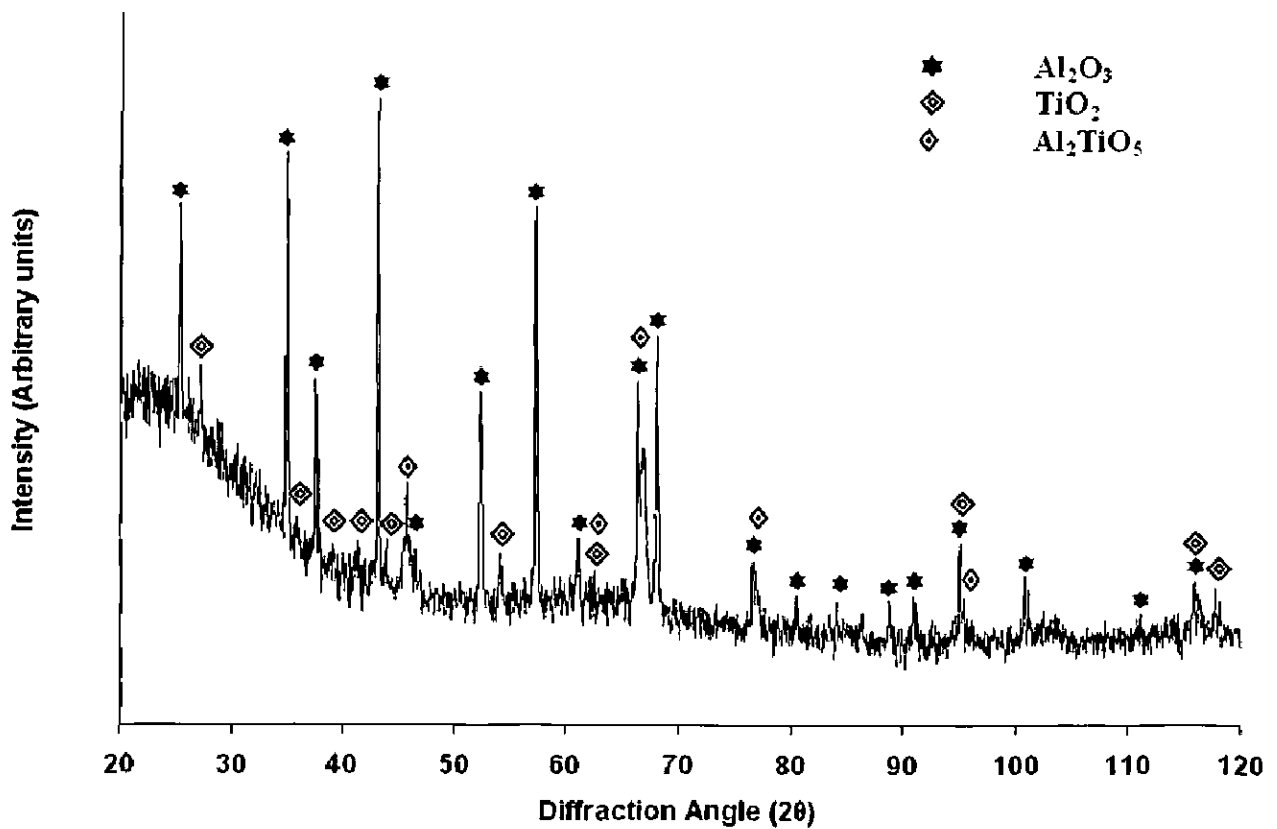


(b)

Fig. 6.66: X-ray diffraction profiles for Al_2O_3 -3 wt% TiO_2 coated boiler steels subjected to cyclic hot corrosion in Na_2SO_4 -60% V_2O_5 at 900°C for 50 cycles.
 (a) T11 (b) T22



(a)



(b)

Fig. 6.67: X-ray diffraction profiles for Al_2O_3 -3 wt% TiO_2 coated superalloys subjected to cyclic hot corrosion in Na_2SO_4 -60% V_2O_5 at 900°C for 50 cycles.

(a) Superni 600

(b) Superni 718

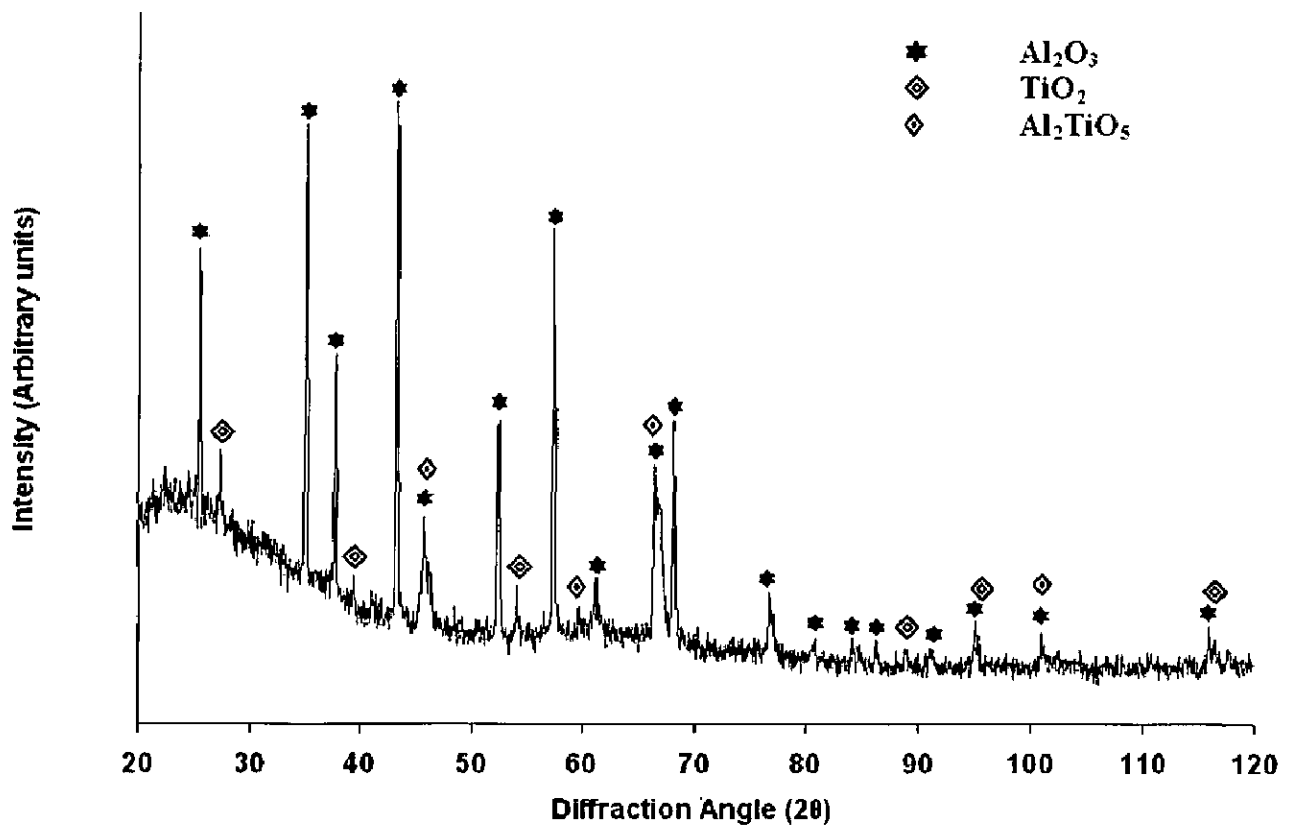


Fig. 6.68: X-ray diffraction profiles for Al₂O₃-3 wt% TiO₂ coated superalloy Superfer 800 subjected to cyclic hot corrosion in Na₂SO₄-60% V₂O₅ at 900°C for 50 cycles.

6.1.2.2.4 SEM/EDX Analysis

(a) Surface Morphology

The SEM micrograph showing the morphology of the Al_2O_3 - 3 wt% TiO_2 coated samples and the EDX analysis after exposure to Na_2SO_4 -60% V_2O_5 environment at 900°C for 50 cycles is shown in Figs. 6.69 and 6.70. From SEM/EDX analysis, it has been revealed that the constituent of scale are Al and Ti along with O. The oxide scale is intact and firm. No spalling was observed throughout the study.

In T11 steel, small percentage of Fe is observed (1.13%) at point 1 and (2.44%) at point 2 along with oxygen. Also in case of Al_2O_3 - 3 wt% TiO_2 coated superalloys exposed to molten salt at 900°C for 50 cycles, a surface scale mainly consisted of Al and Ti with oxygen as shown in Fig.6.70. No spallation of the scale has been observed. Coating after the cyclic exposure to molten salt is well adherent. The matrix of the scale of all the coated substrates has dominance of Al and is evident from EDX analysis.

(b) Cross-Sectional Analysis and X ray mapping

The BSE image and the EDX analysis across the cross section on Al_2O_3 -3 wt% TiO_2 coated alloys after exposure to Na_2SO_4 -60% V_2O_5 environment at 900°C for 50 cycles is shown in Fig.6.71 to Fig. 6.75. The results of the cross-section analysis of T11 and T22 boiler steels after molten salt exposure are plotted and shown in Fig. 6.71 and 6.72 along with micrographs. By viewing the cross sectional micrograph and the corresponding EDX analysis of coated T11, it is quite clear that coating is firm and intact and there is no deterioration of coating and hence coating has protected the surface very well. There is no penetration of oxygen in the substrate during the entire exposure of the coated specimen. As we approach from substrate to coating, at point 3, 4 and point 5 there is no indication of presence of elements other than present in the coating and same is in case of T22.

Also in case of superalloys, EDX analysis has revealed that the scale mainly consisted of Al and Ti along with oxygen. Oxide scale morphology along with variation of elemental

composition across the cross-section of superalloy Superni 600 subjected to cyclic oxidation in air at 900°C after 50 cycles has been depicted in Fig. 6.73. The plots of elemental composition variation show that the scale mainly consists of aluminum and Titanium along with oxygen. There is no penetration of oxygen into the substrate through the coating. In superni 718, (Fig. 6.74) coating is intact and adherent and there is no oxidation of substrate beneath the coating. In superfer 800, Fig. 6.75, the coating has major portion of aluminium oxide

Back Scattered Electron Image of cross-section of Al_2O_3 -3 wt% TiO_2 coated substrate alloys (T11, T22, superni 600, superni 718 and Superfer 800) exposed to molten salt at 900°C and corresponding X-ray mapping after oxidation in air at 900°C after 50 cycles is shown in Fig. 6.76 to 6.80 respectively. In all the Al_2O_3 -3 wt% TiO_2 coated alloys coating has acted as a barrier and thus have prevented oxidation of substrate by inhibiting the penetration of oxygen. There is no spalling of coating throughout the testing. In boiler steels T11 and T22 (Fig.6.76 and 6.77), main constituent is aluminium oxide and there is no inward penetration of any element into the substrate but in maps of boiler steel T22 , iron is visible at the interface of epoxy and coating which could have been impinged into the epoxy during polishing of the specimen. In coated superni 600, Fe_2O_3 is visible at the right edge of the coating adjoining to epoxy depicted in Fig. 6.78. In case of coated superni 718, (Fig. 6.79) major phase of coating Al_2O_3 and TiO_2 band is visible in the coating and there is no penetration of oxygen into the substrate through the coating. Fig. 6.80 shows the mapping for coated superfer 800, in which coating is intact and there is no inward penetration of oxygen or any other element.

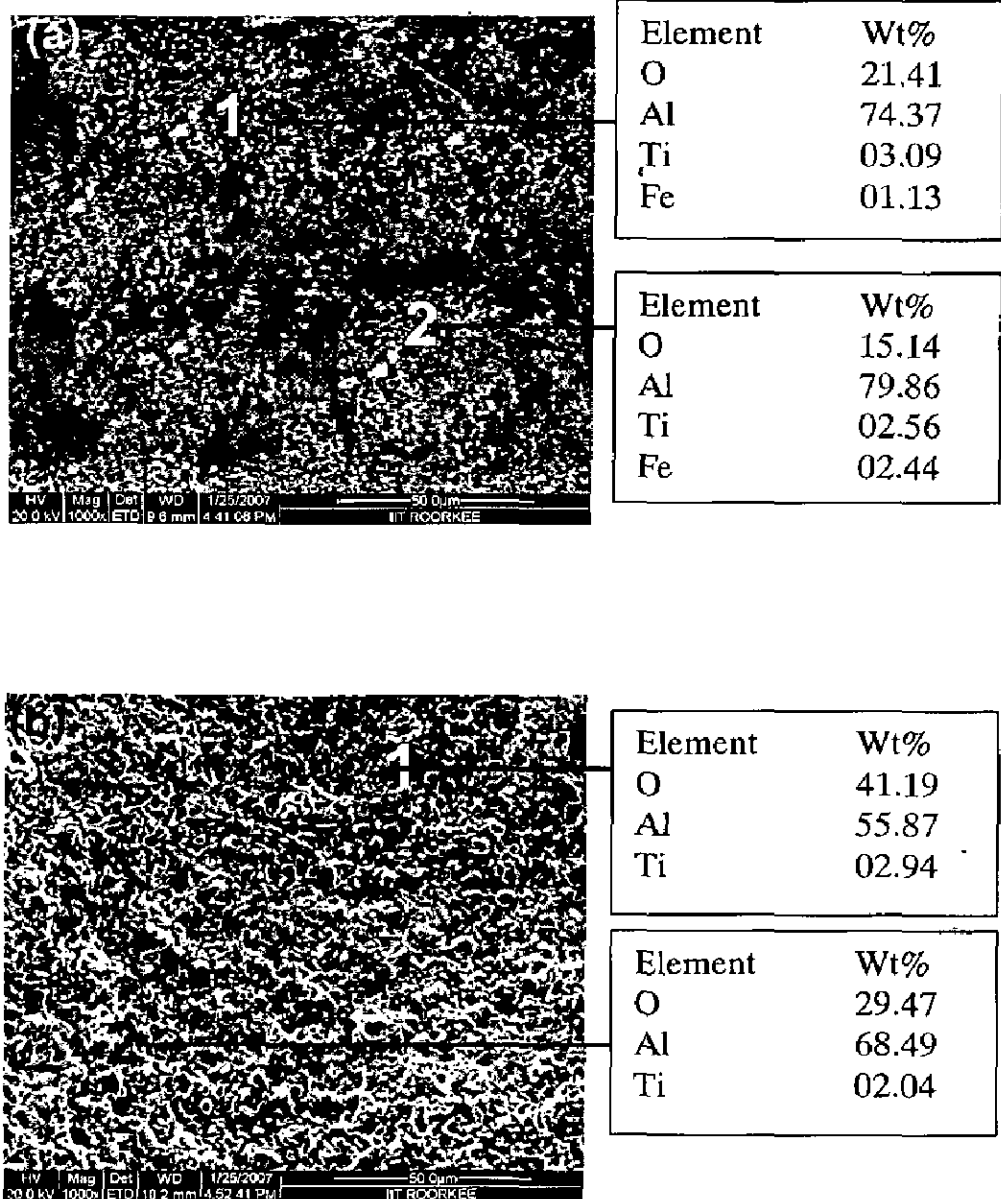


Fig. 6.69: Surface scale morphology and EDX analysis for $\text{Al}_2\text{O}_3\text{-3wt\%TiO}_2$ coated steels corroded in $\text{Na}_2\text{SO}_4\text{-60\%V}_2\text{O}_5$ at 900°C for 50 cycles (a) T11, 1000 X (b) T22, 1000 X.

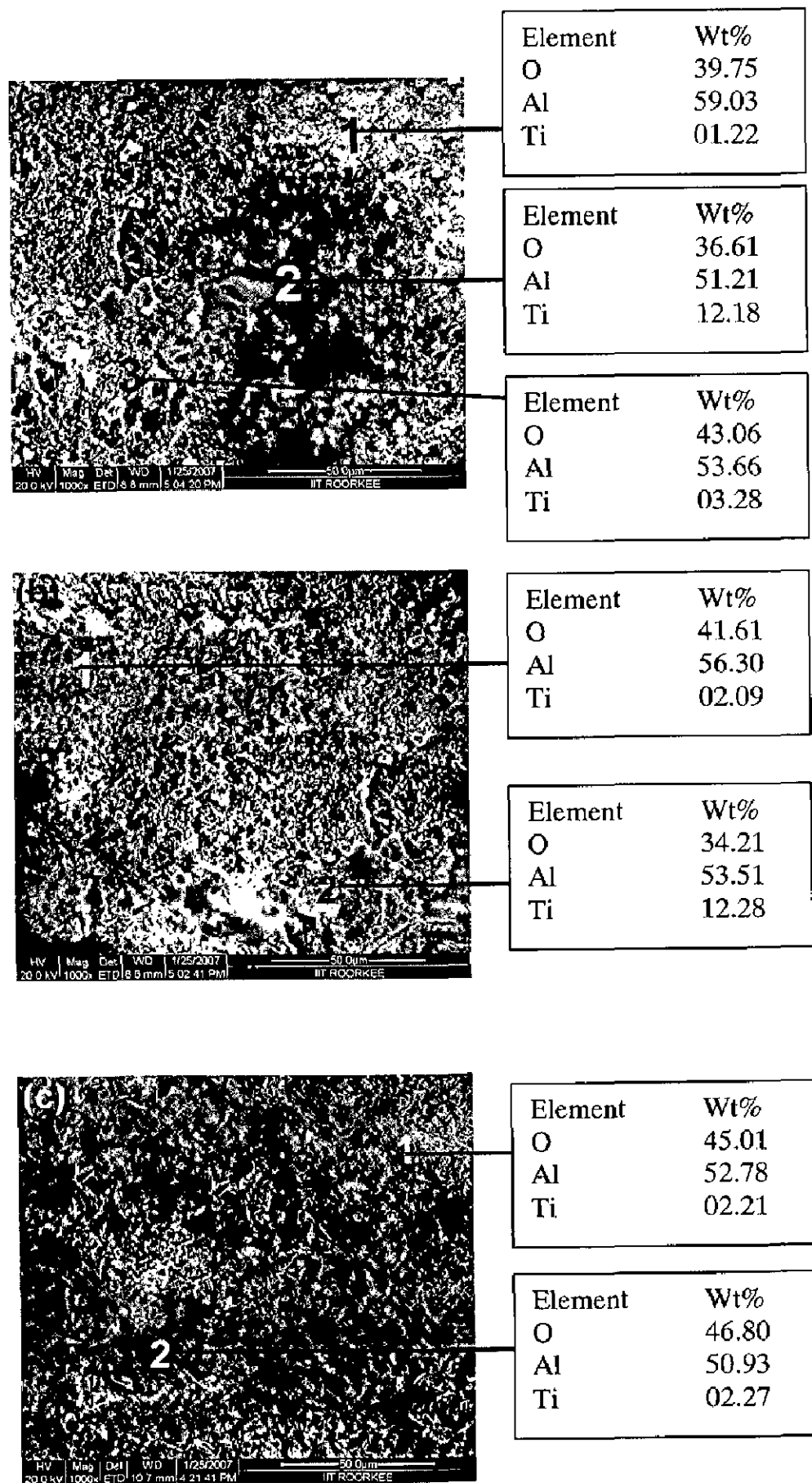


Fig. 6.70: Surface scale morphology and EDX analysis for $\text{Al}_2\text{O}_3\text{-3wt\%TiO}_2$ coated superalloys corroded in $\text{Na}_2\text{SO}_4\text{-60\%V}_2\text{O}_5$ at 900°C for 50 cycles (a) Superni 600, 1000 X (b) Superni 718, 1000 X. (c) Superfer 800, 1000X

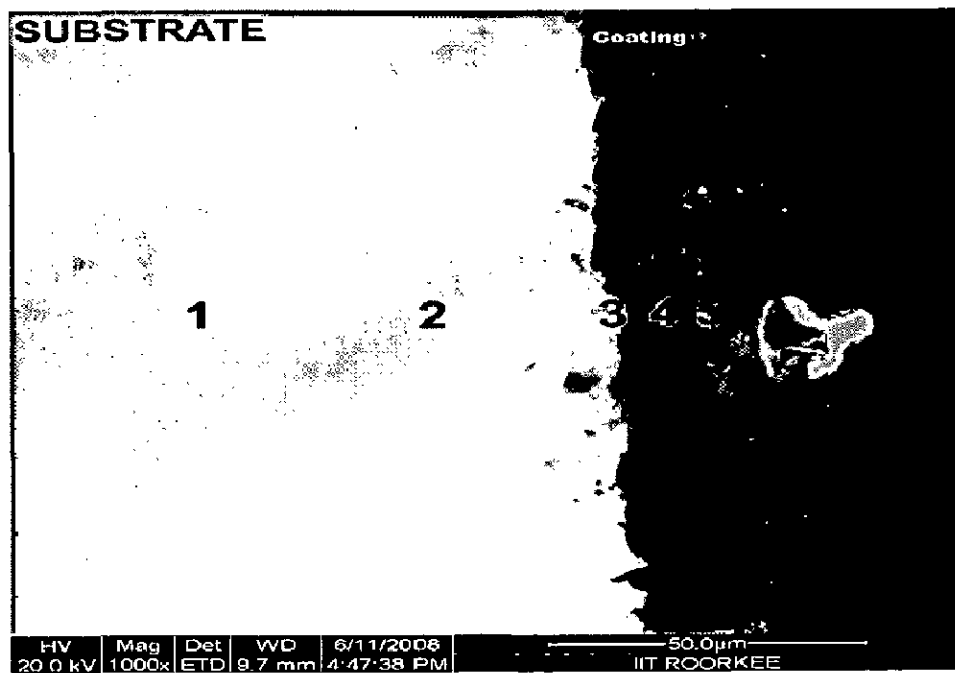
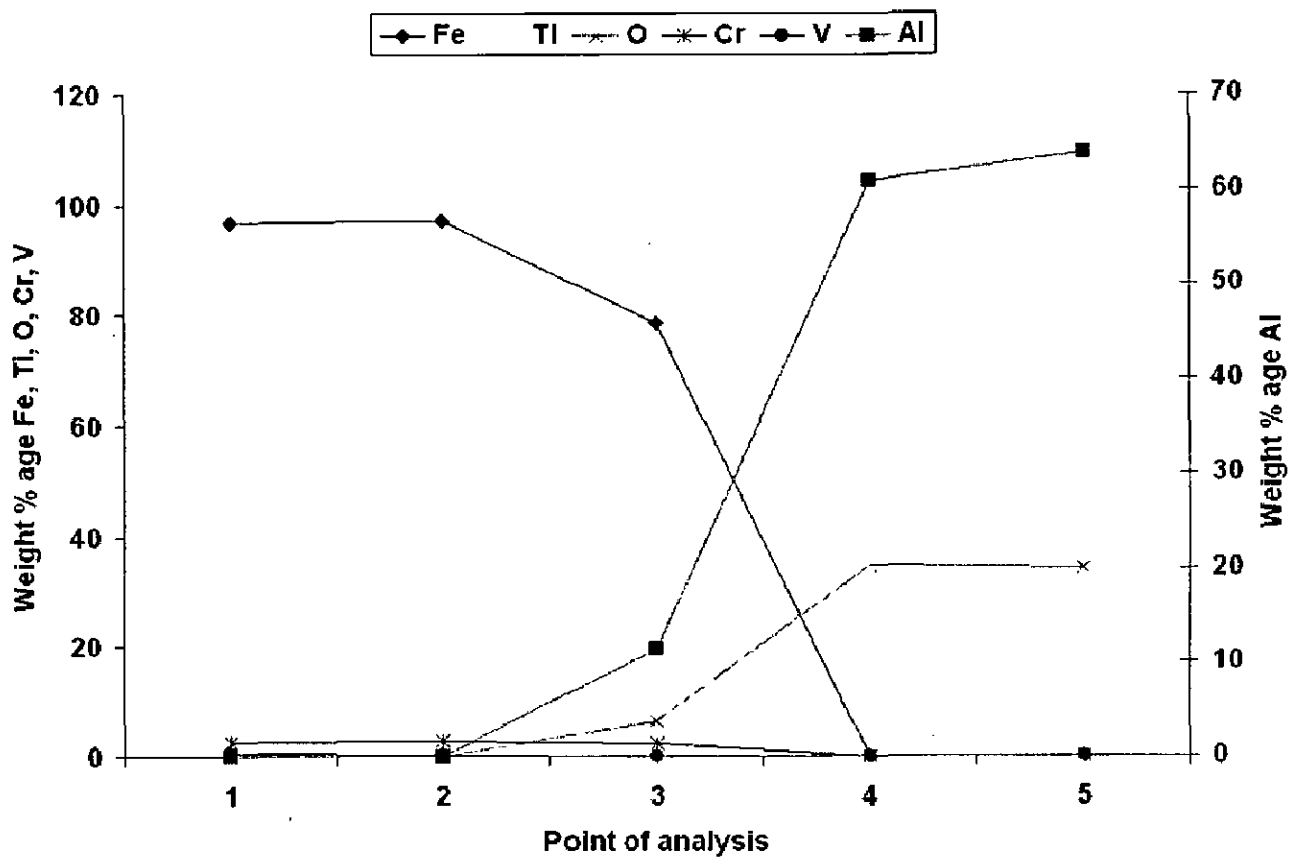


Fig.6.71: Cross sectional morphology and elemental composition variation across the cross-section of $\text{Al}_2\text{O}_3\text{-3wt\%TiO}_2$ coated boiler steel T11 exposed to $\text{Na}_2\text{SO}_4\text{-60\%V}_2\text{O}_5$ at 900°C for 50 cycles, 1000 X.

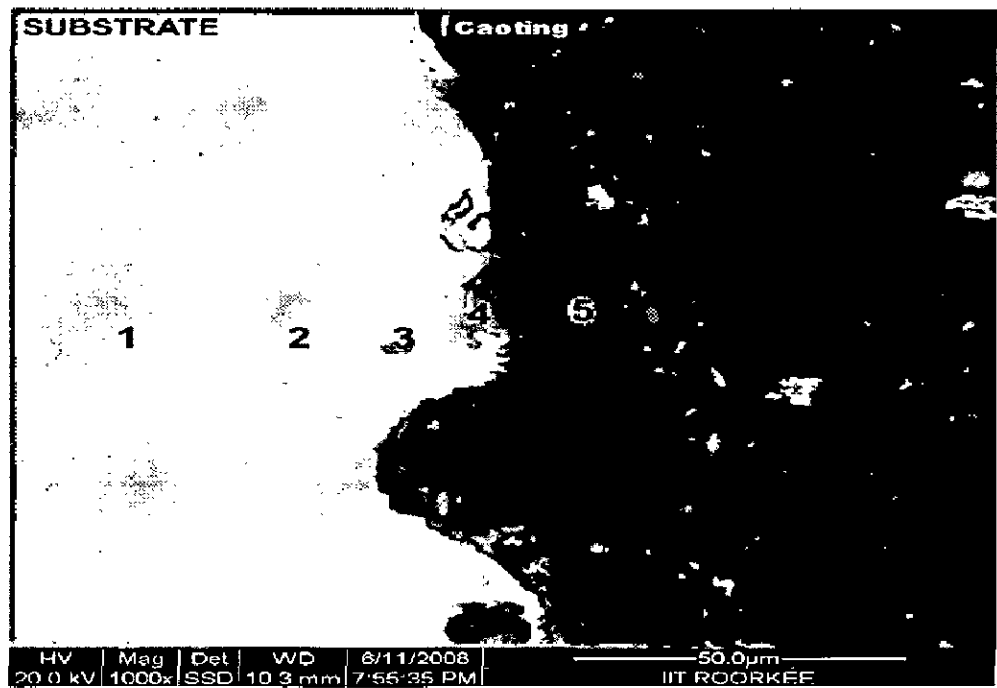
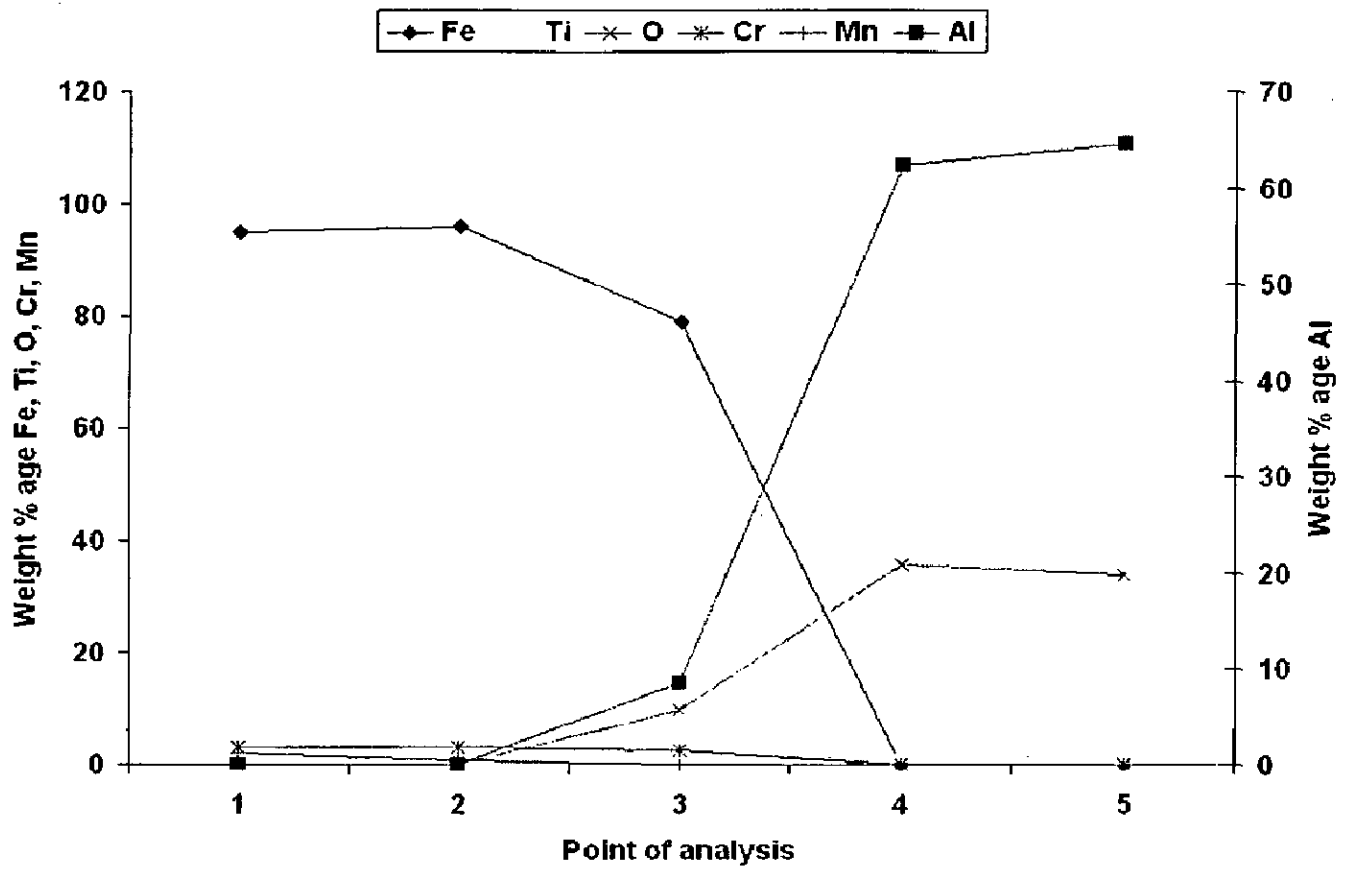


Fig.6.72: Cross sectional morphology and elemental composition variation across the cross-section of $\text{Al}_2\text{O}_3\text{-3wt\%TiO}_2$ Coated boiler steel T22 exposed to $\text{Na}_2\text{SO}_4\text{-60\%V}_2\text{O}_5$ at 900°C for 50 cycles, 1000 X.

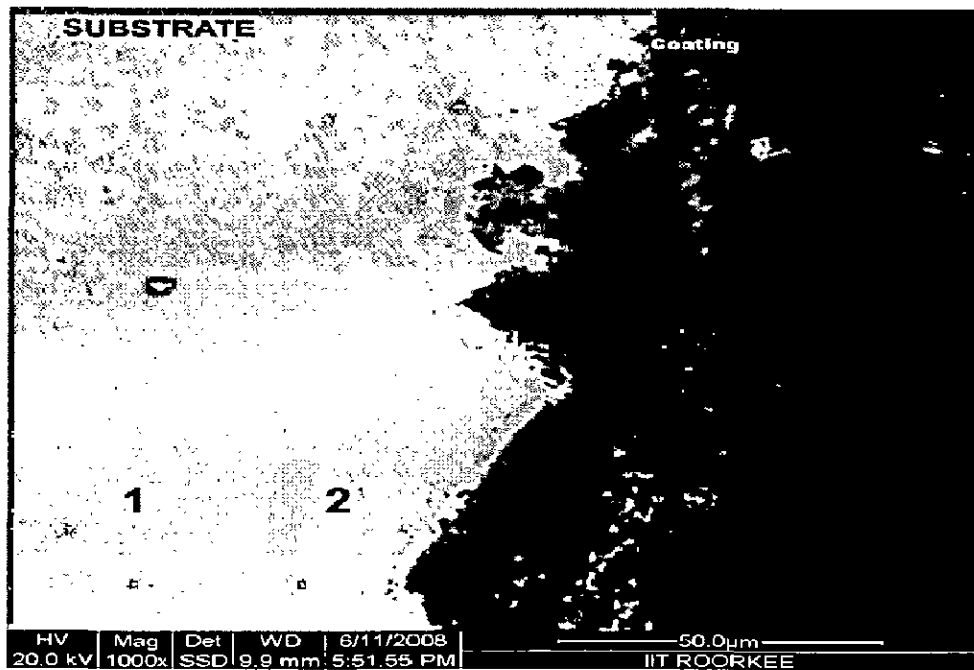
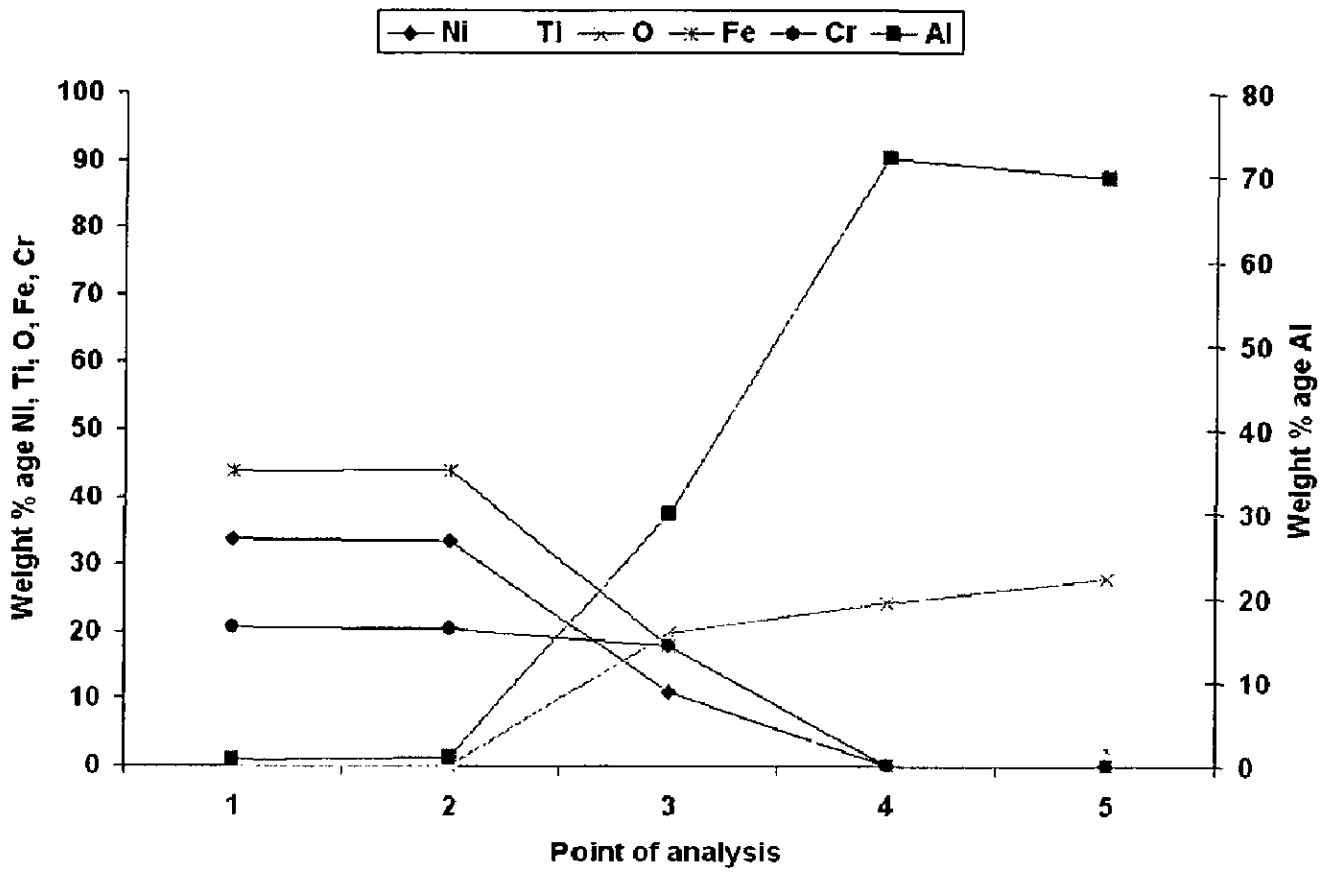


Fig.6.73: Cross sectional morphology and elemental composition variation across the cross-section of $\text{Al}_2\text{O}_3\text{-3wt\%TiO}_2$ Coated superalloy Superni 718 exposed to $\text{Na}_2\text{SO}_4\text{-60\%V}_2\text{O}_5$ at 900°C for 50 cycles, 1000X.

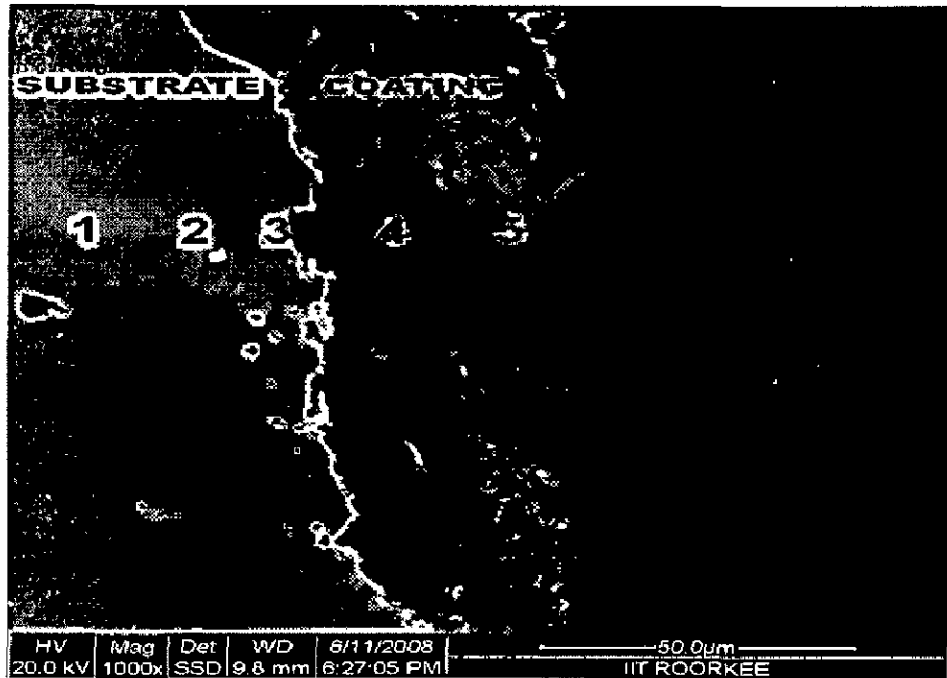
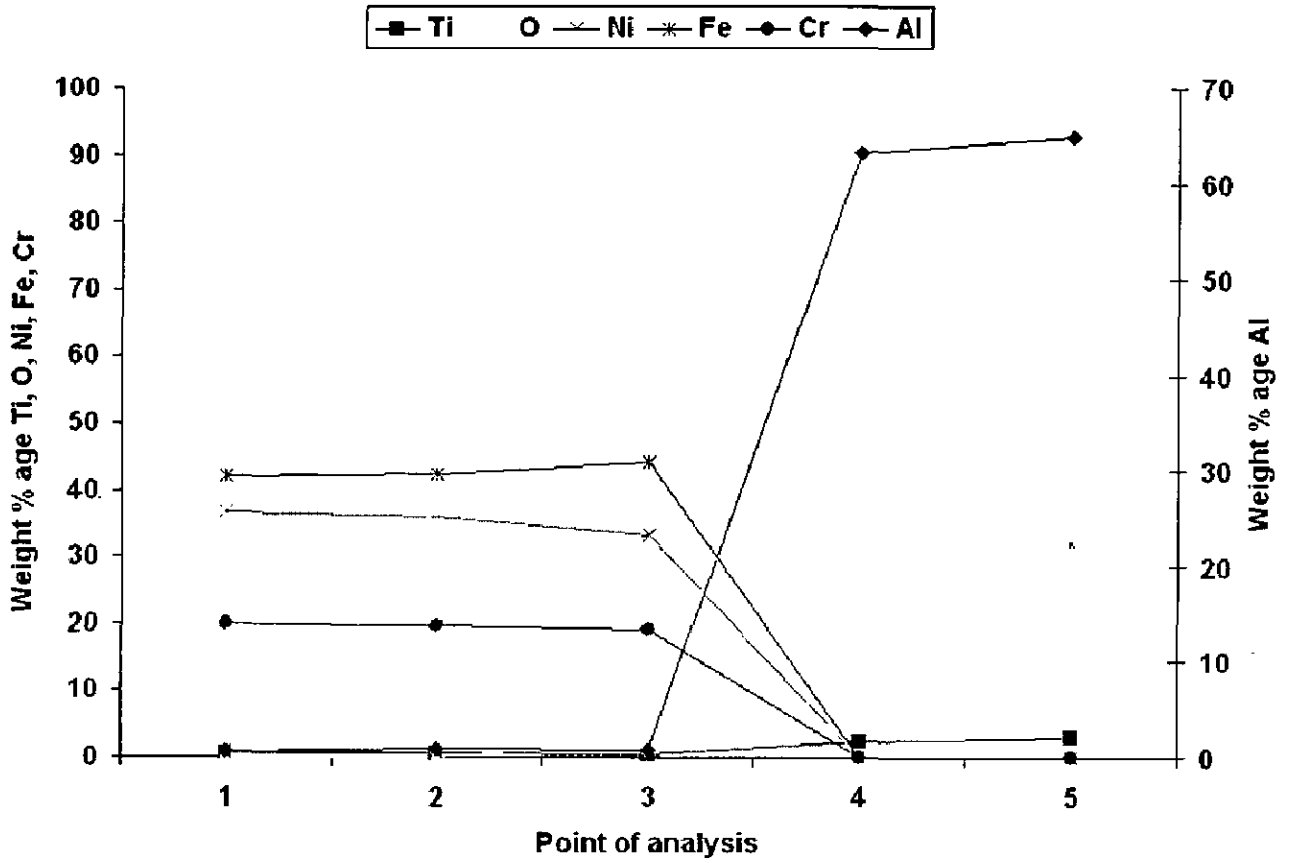


Fig.6.74: Cross sectional morphology and elemental composition variation across the cross-section of $\text{Al}_2\text{O}_3\text{-3wt\%TiO}_2$ Coated superalloy Superni 600 exposed to $\text{Na}_2\text{SO}_4\text{-60\%V}_2\text{O}_5$ at 900°C for 50 cycles, 1000 X.

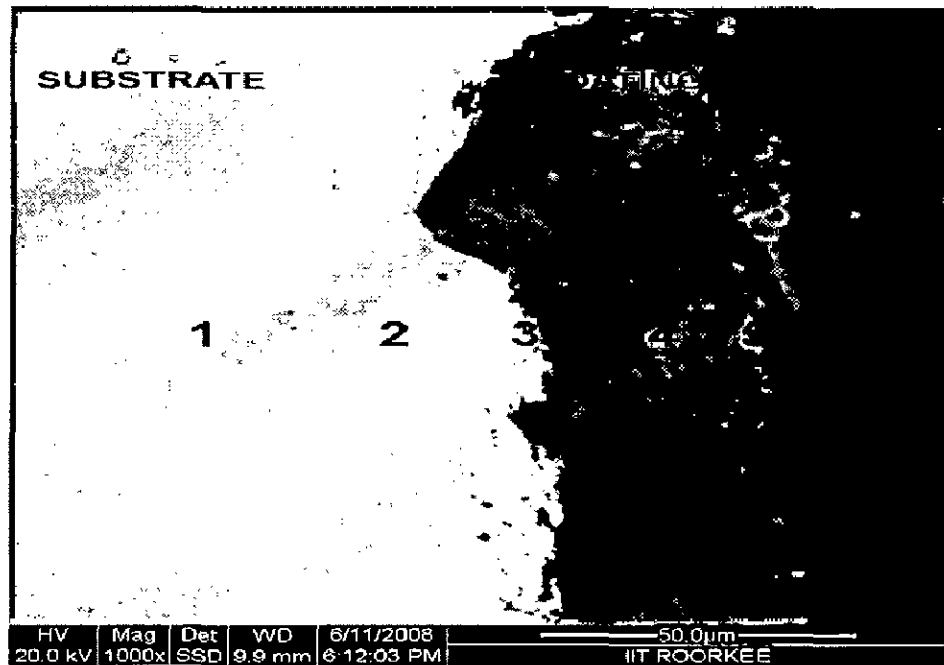
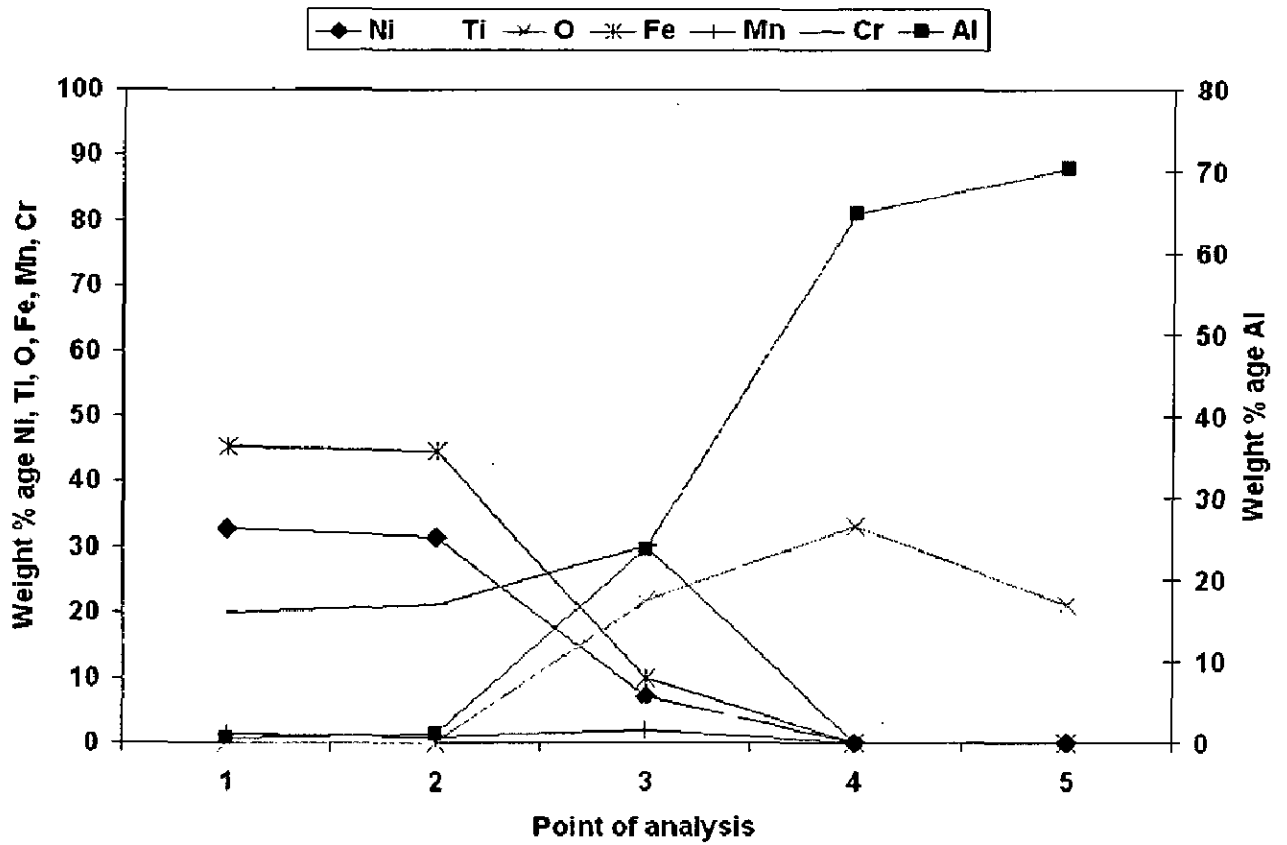


Fig.6.75: Cross sectional morphology and elemental composition variation across the cross-section of $\text{Al}_2\text{O}_3\text{-3wt\%TiO}_2$ coated superalloy Superfer 800 exposed to $\text{Na}_2\text{SO}_4\text{-60\%V}_2\text{O}_5$ at 900°C for 50 cycles, 1000 X.

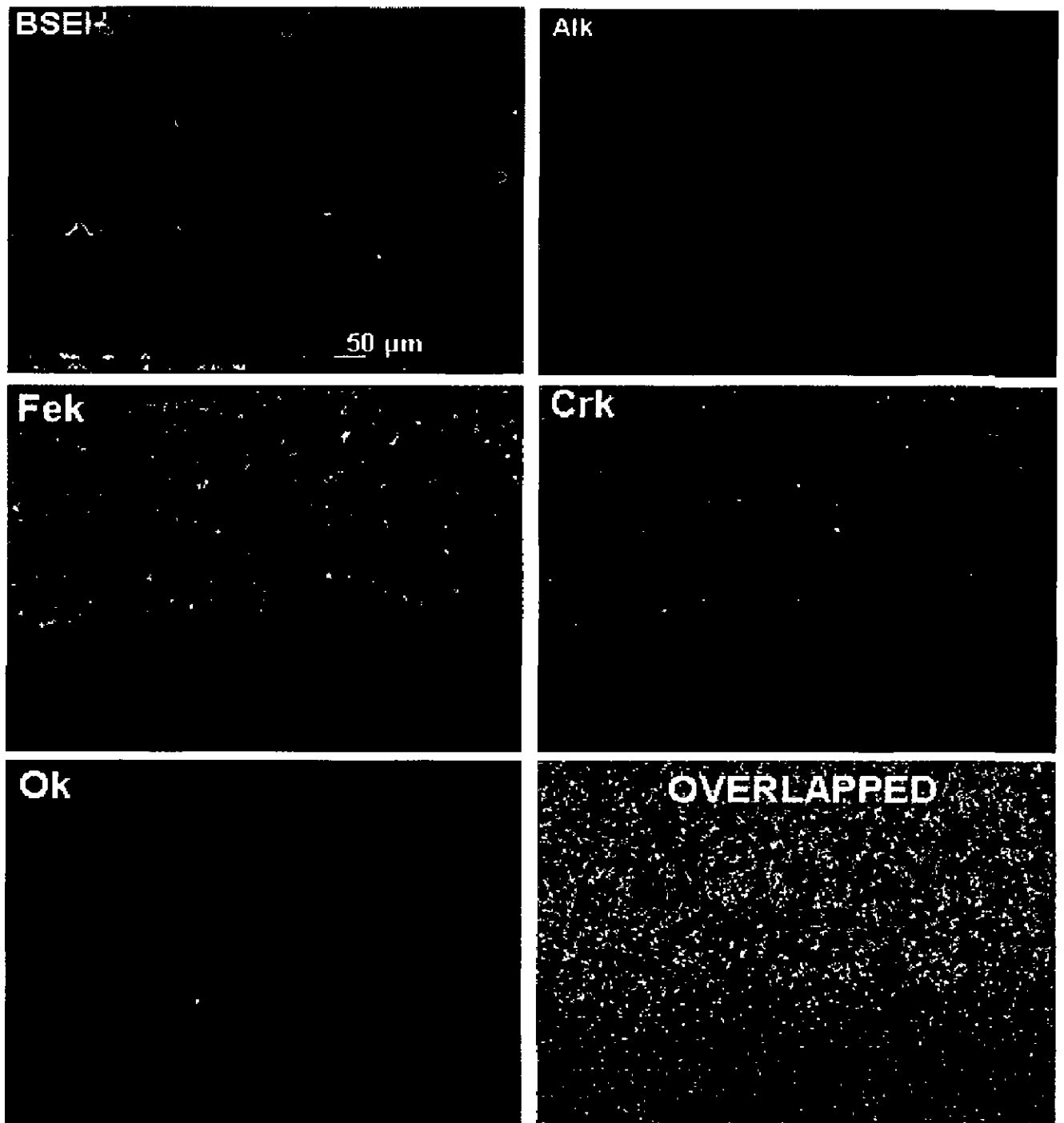


Fig. 6.76: BSEI and X-ray mapping of the cross-section of Al_2O_3 -3 wt% TiO_2 coated boiler steel T11 subjected to cyclic hot corrosion in Na_2SO_4 -60% V_2O_5 at 900°C for 50 cycles, 1000 X.

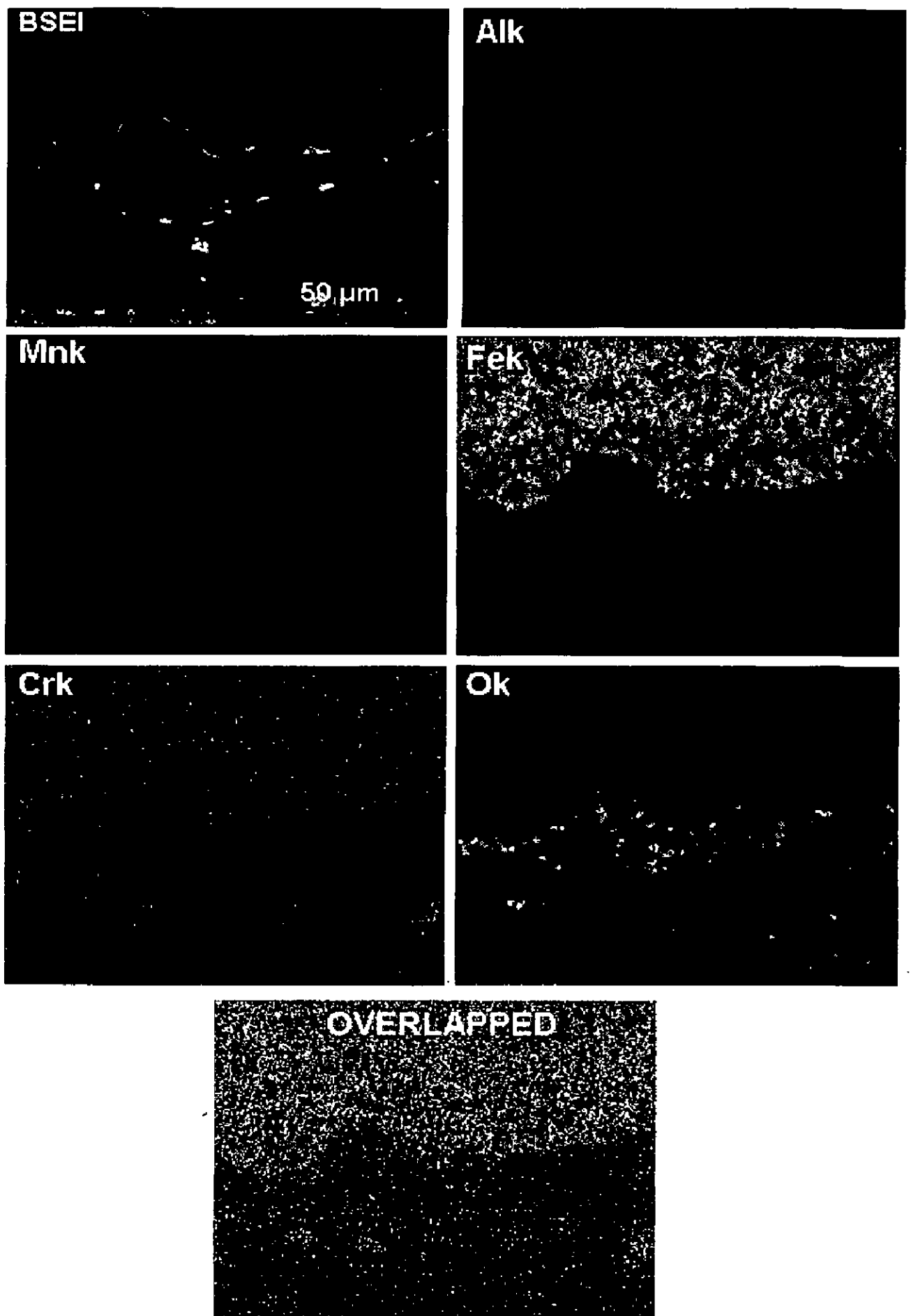


Fig. 6.77: BSEI and X-ray mapping of the cross-section of Al_2O_3 -3 wt% TiO_2 coated boiler steel T22 subjected to cyclic hot corrosion in Na_2SO_4 -60% V_2O_5 at 900°C for 50 cycles, 1000 X.

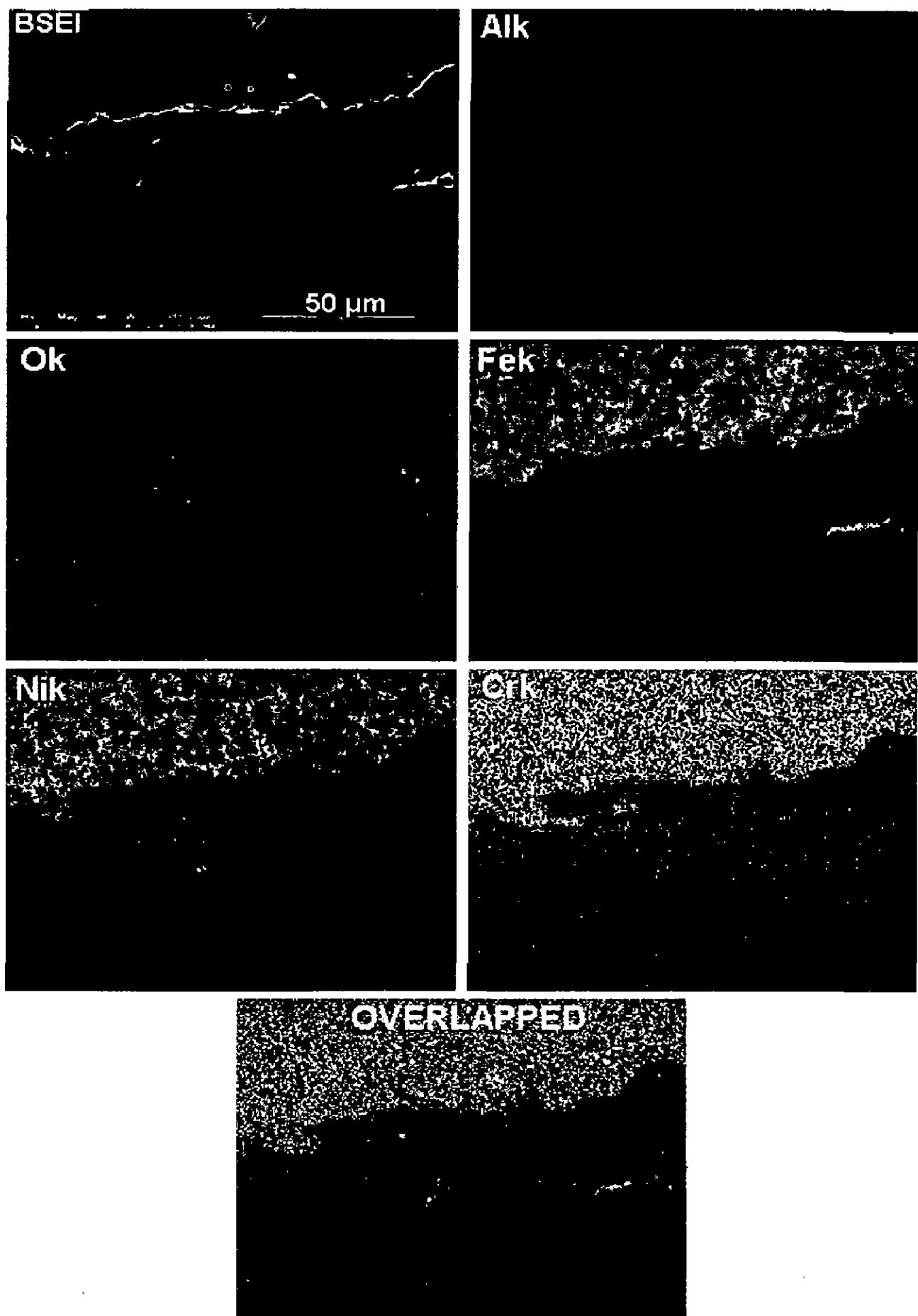


Fig. 6.78: BSEI and X-ray mapping of the cross-section of $\text{Al}_2\text{O}_3\text{-3 wt\%TiO}_2$ coated superalloy Superni 600 subjected to cyclic hot corrosion in $\text{Na}_2\text{SO}_4\text{-60\%V}_2\text{O}_5$ at 900°C for 50 cycles, 1000 X.

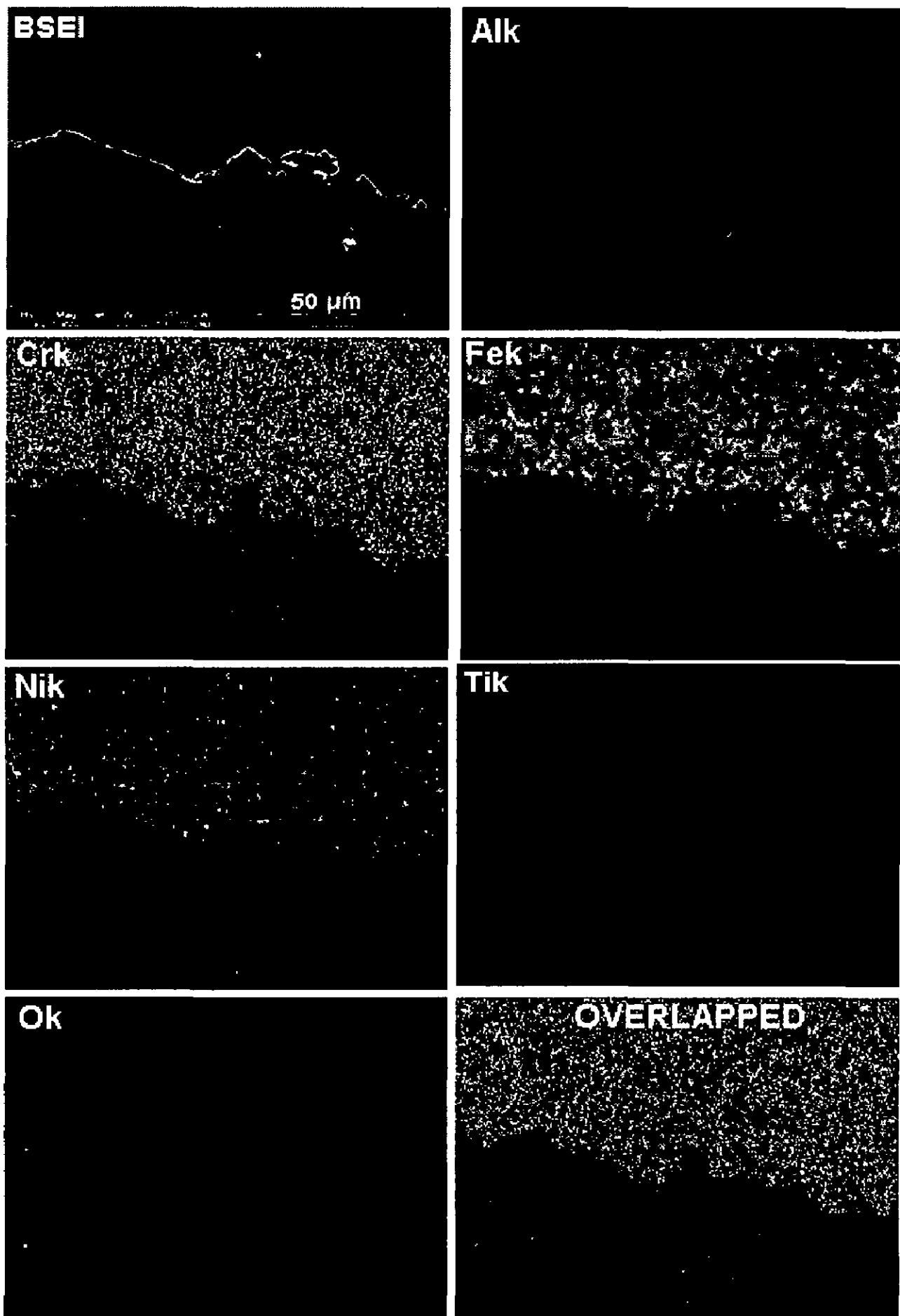


Fig. 6.79: BSEI and X-ray mapping of the cross-section of Al_2O_3 -3 wt% TiO_2 coated superalloy Superni 718 subjected to cyclic hot corrosion in Na_2SO_4 -60% V_2O_5 at 900°C for 50 cycles, 1000 X.

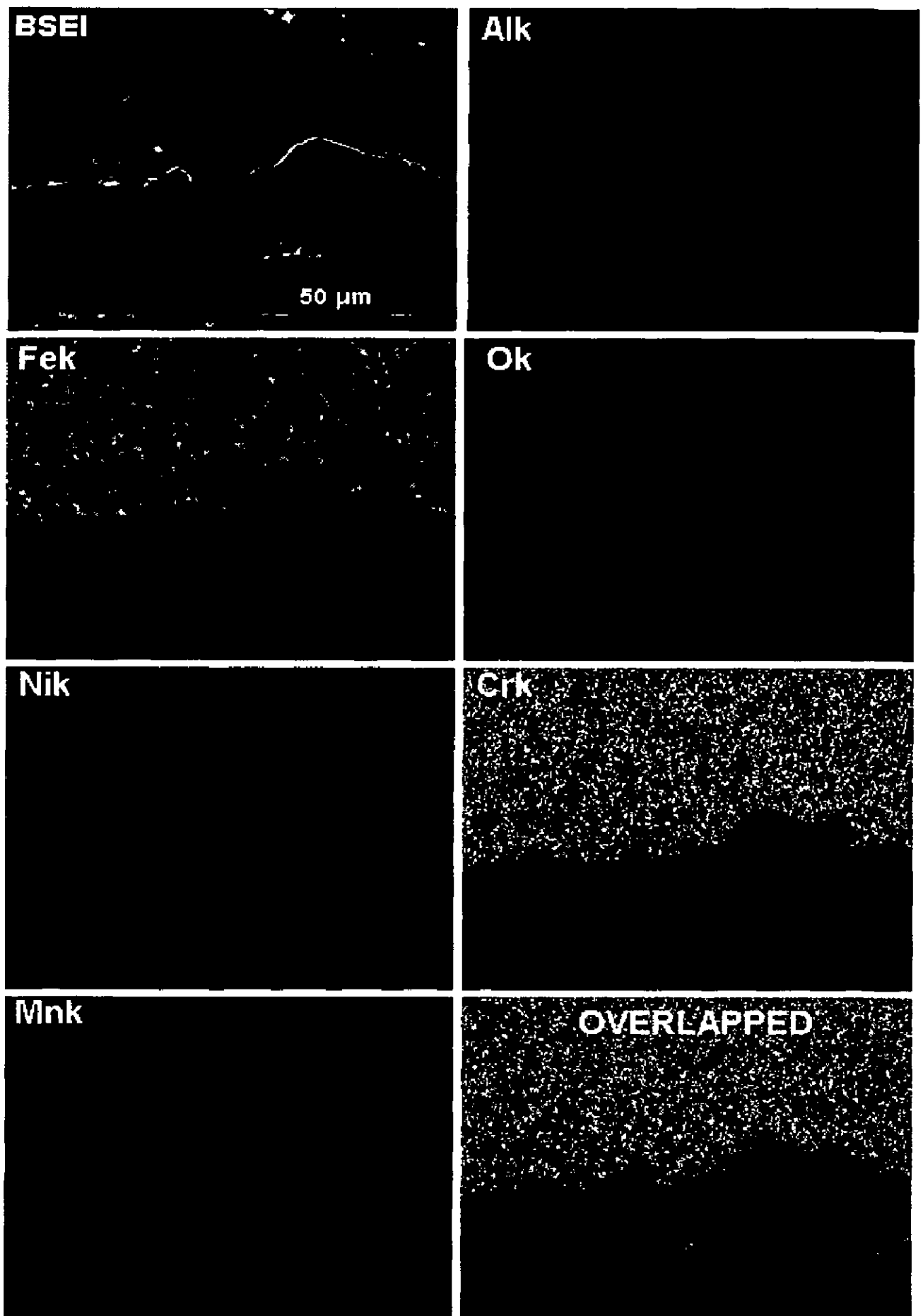


Fig.6.80: BSEI and X-ray mapping of the cross-section of Al_2O_3 -3 wt% TiO_2 coated superalloy Superfer 800 subjected to cyclic hot corrosion in Na_2SO_4 -60% V_2O_5 at 900°C for 50 cycles, 1000 X.

6.2 SUMMARY OF RESULTS

The results of air oxidation and molten salt studies for uncoated and coated alloys are summarised in Table 6.1 and 6.2. These tabulated results are ready reference to compare the oxidation and hot corrosion behaviour of uncoated and coated alloys.

Table 6.1: Summary of the results for uncoated and coated alloys after high temperature cyclic oxidation in air at 900°C for 50 cycles.

Base Alloy	Coating	Weight Change (mg/cm ²)	Parabolic Rate Constant Kp (g ² cm ⁻⁴ s ⁻¹)	XRD Phases	Remarks
T11	Uncoated	102.88	6.33 X 10 ⁻⁸	Fe ₂ O ₃ , Cr ₂ O ₃	Bulky and porous scale. Along with continuous network of cracks. Intense spalling of oxide scale observed
	Al ₂ O ₃ -3wt%TiO ₂	2.87	4.75 X 10 ⁻¹¹	Al ₂ O ₃ , TiO ₂ , Al ₂ TiO ₇ O ₁₅	Surface scale observed mainly consisted of Al ₂ O ₃ and TiO ₂ . No spalling or cracking of coating was observed.
T22	Uncoated	119.12	8.28 X 10 ⁻⁸	Fe ₂ O ₃ , Cr ₂ O ₃	Scale was bulky and porous. Massive spalling and sputtering initiated, almost all the scale spalled
	Al ₂ O ₃ -3wt%TiO ₂	1.85	2.28 X 10 ⁻¹¹	Al ₂ O ₃ , TiO ₂ , Al ₂ TiO ₅	The Coating and the thin oxide scale is intact and firm. Surface scale observed mainly consisted of Al ₂ O ₃ and TiO ₂ . No spalling and cracking was observed throughout the study.

Superni 600	Uncoated	0.28	2.22×10^{-13}	Fe_2O_3 , NiFe_2O_3 , NiCr_2O_4 , FeNi , NiO , Cr_2O_3 and $\text{Al}_2\text{Fe}_2\text{O}_6$	Scale was thin and internal attack visible No spalling of scale was observed and scale remained intact.
	Al_2O_3 - 3wt%TiO ₂	1.16	8.19×10^{-12}	Al_2O_3 , Al_2TiO_5 , TiO_2 , $\text{Al}_2\text{TiO}_7\text{O}_{15}$	Surface scale observed mainly consisted of Al_2O_3 and TiO_2 . No spalling and cracking. Matrix of the scale of all the coated substrates has dominance of Al_2O_3
Superni 718	Uncoated	0.97	5.19×10^{-12}	$\text{Al}_2\text{Fe}_2\text{O}_6$ NiFe_2O_3 , NiCr_2O_4 , Ni , Fe_2O_3	Attack was confined and thin scale formed with no tendency for spalling. Scale remained intact. Some internal localized cracks were observed in Cross-section indicating internal oxidation
	Al_2O_3 - 3wt%TiO ₂	0.35	7.22×10^{-13}	Al_2O_3 , Al_2TiO_5 , TiO_2 ,	No spalling and cracking of coating. Coating remained intact and iron from substrate has diffused into the coating. A clear Titanium rich band seen along the interface
Superfer 800	Uncoated	4.03	1.13×10^{-10}	Fe_2O_3 , NiFe_2O_3 , NiCr_2O_4 , FeNi , NiO , Cr_2O_3 and $\text{Al}_2\text{Fe}_2\text{O}_6$	No spalling, intact and continuous scale. Internal attack visible and thin scale formed.
	Al_2O_3 - 3wt%TiO ₂	1.71	1.65×10^{-11}	Al_2O_3 , Al_2TiO_5 , TiO_2 , $\text{Al}_2\text{TiO}_7\text{O}_{15}$	Iron, Nickel and chromium have diffused from substrate into the coating and is present around Al_2O_3 grain. No spalling and cracking observed. The coating remained intact and has prevented the penetration of oxygen from the atmosphere into the substrate

Table 6.2: Summary of the results for uncoated and coated alloys after hot corrosion in an aggressive environment of molten salt ($\text{Na}_2\text{SO}_4\text{-60\%V}_2\text{O}_5$) at 900°C under cyclic conditions for 50 cycles

Base Alloy	Coating	Weight Change (mg/cm^2)	Parabolic Rate Constant K_p ($\text{g}^2 \text{cm}^{-4} \text{s}^{-1}$)	XRD Phases	Remarks
T11	Uncoated	138.51	10.58×10^{-8}	Fe_2O_3 , Cr_2O_3 and FeS_2	Scale formed lustrous black coloured and was fragile and intense spalling was observed.
	$\text{Al}_2\text{O}_3\text{-3wt\%TiO}_2$	3.78	8.19×10^{-11}	Al_2O_3 , TiO_2 and $\text{Al}_2\text{TiO}_7\text{O}_{15}$	Coating remained intact and there was no spalling or sputtering of the coating
T22	Uncoated	166.65	16.57×10^{-8}	Fe_2O_3 , Cr_2O_3 and FeS_2	Massive Dark grey coloured Scale Intensive spalling and multilayered cracking was observed.
	$\text{Al}_2\text{O}_3\text{-3wt\%TiO}_2$	3.59	7.57×10^{-11}	Al_2O_3 , TiO_2 and $\text{Al}_2\text{TiO}_7\text{O}_{15}$	Coating remained intact and there was no spalling or sputtering of the coating
	Uncoated	3.69	7.05×10^{-11}	NiCr_2O_4 , NiO , Cr_2O_3 , Fe_2O_3 , FeV_2O_4 and $\text{Ni}(\text{VO}_3)_2$	Thin and Fragile scale was observed. Tiny Cracks developed in the scale from 6 th cycle onward, resulting in spallation. Scale separated out in the form of small and thin flakes by the end of 17 th cycle. Spalling and crack

Superni 600					formation continued throughout the study
	Al ₂ O ₃ - 3wt%TiO ₂	2.22	2.91X10 ⁻¹¹	Al ₂ O ₃ , Al ₂ TiO ₅ , TiO ₂ ,	Coating remained intact and there was no spalling or sputtering of the coating
Superni 718	Uncoated	8.61	3.39X10 ⁻¹⁰	Fe ₂ O ₃ ,Cr ₂ O ₃ , NiO, FeV ₂ O ₄ and Ni(VO ₃) ₂	Fragile and uneven scale was observed. Minor spalling and sputtering was observed after 19 th cycle and it continued till the end of the 50 th cycle
	Al ₂ O ₃ - 3wt%TiO ₂	0.88	5.91X10 ⁻¹²	Al ₂ O ₃ , Al ₂ TiO ₅ , TiO ₂ ,	Coating remained intact and there was no spalling or sputtering of the coating
Superfer 800	Uncoated	18.14	1.69X10 ⁻⁹	Fe ₂ O ₃ ,NiO, FeV ₂ O ₄ , NiCr ₂ O ₄ ,	Carbon black coloured scale appeared after the first cycle. Spalling from 2 nd cycle along with some sputtering. Uneven surface scale and pits were observed.
	Al ₂ O ₃ - 3wt%TiO ₂	2.68	4.03x10 ⁻¹¹	Al ₂ O ₃ , Al ₂ TiO ₅ , TiO ₂ ,	Coating remained intact and there was no spalling or sputtering of the coating.

6.3 DISCUSSION

In this section the results of cyclic oxidation and molten salt studies performed on uncoated and coated alloys at 900°C have been discussed.

6.3.1 Uncoated alloys

The weight gain for steels T11 and T 22 steels during oxidation studies are found to be more as compared to superalloys. It has been revealed from XRD and SEM/EDX analysis that in case of boiler steels, scale mainly consisted of Fe_2O_3 . From XRD analysis it has been revealed that Cr_2O_3 is also present in the scale. Lai (1990) has also reported Fe_2O_3 formation in his study on iron-chromium alloys. In his study, it has been reported that alloys having 2% chromium could only form the oxides of chromium along with iron oxide in the innermost layer. Similar findings are revealed by the EDX analysis in the present study where presence of chromium in the inner scale has been indicated for T22 type of boiler steels, Fig. 6.12. EDX analysis confirmed the upper scale of iron along with oxygen i.e. iron oxide for T11 and T22 steels which is followed by subscale where Fe and Cr are coexisting along with oxygen. Sadique et al. (2000) also reported chromium oxide formation in the inner scale. The spalling as observed in case of boiler steels T11 and T22 may be due to the presence of molybdenum in the steels. Chatterjee et al (2001) have suggested that during initial oxidation Fe is oxidised and the oxide scale is protective in nature. With progress of oxidation Mo becomes enriched at the alloy scale interface, leading to the formation of an inner layer of molten MoO_3 (m. p. 795°C) which penetrates along the alloy-scale interface. This liquid oxide disrupts and dissolves the protective oxide scale, causing the alloy to suffer catastrophic oxidation (Lai, 1990). During oxidation of boiler steels, volume of oxides formed was very high which lead to scale cracking and these cracks helped in internal oxidation and spalling of the scale. Similar results were observed by Khanna et al. (1982) and Ahila et.al (1994). Chatterjee et al (2001) also suggested that molybdenum is less noble than the other alloying elements, MoO_3 will be reduced to a lower oxide of

molybdenum or even to molybdenum. Simultaneously MoO_3 may exert dissolving action on other oxides, such as Fe_2O_3 and Cr_2O_3 and this fluxing may further get accelerated by the enthalpy of formation of Fe_2O_3 and Cr_2O_3 which tends to increase in the temperature at the alloy-scale interface. The mode of oxidation attack can be explained schematically as shown in Fig. 6.81 which is similar to one reported by Chatterjee et al (2001).

The superalloys have shown good oxidation resistance. The oxide scales showed no tendency towards cracking or spalling during the course of 50 cycles exposure in air at 900°C . Based on the weight change data the oxidation rates of superalloys under study can be arranged in following order:

Superfer 800 >Superni 718 > Superni 600

The relative oxidation resistance of Superfer 800 is minimum among the superalloys under study, while Superni 600 has shown maximum oxidation resistance. The chromium has formed protective layers in the respective oxide scales after 50 cycle oxidation in all the superalloys. It might have blocked the diffusion of any species through it to reach the substrate superalloys and hence provided oxidation resistance to the superalloys. The scale formed in case of Superni 600 is relatively intact, thin and uniform, and contains a continuous band of Cr just at the scale/substrate interface.

Ni-based superalloys have followed parabolic law in general with minor deviations. The small deviations from the parabolic rate law have also been observed by Levy et al (1989) and Finfrock (2001) during their studies on the oxidation and hot corrosion of some Ni-based superalloys. Superfer 800 has not followed parabolic law.

The XRD analysis for the oxidised superalloys revealed the presence of Fe_2O_3 , NiFe_2O_4 , NiCr_2O_4 and $\text{Al}_2\text{Fe}_2\text{O}_6$ phases in all the oxidised superalloys. The formation of NiO has been indicated in the scales of Superni 600 and Superfer 800, whereas NiCr_2O_4 has been identified for all the superalloys under study. Similar observations were also made by Singh

(2005) in his study on Fe and Ni based superalloys. Li et al (2003A) have observed NiCr_2O_4 phase also for a single crystal Ni-base superalloy oxidised at 900°C in air.

The probable mode of oxidation attack on Ni based superalloys is shown schematically in Fig.6.82 which is similar to mechanism suggested by Stott (1998) in his study on oxidation of alloys at elevated temperature which can be taken as a representative case for the Ni based superalloys under study. As suggested by Stott (1998), in oxidation initiation stage i.e. when the alloy surface adsorb the oxygen molecules, small impinging nuclei of all the thermodynamically stable oxides such as those of Ni, Cr, Fe and Mn develop on the surface of the alloy. These nuclei then coalesce rapidly to give a transient layer of various oxides in a very short time as the temperature of study becomes high. As Ni percentage is highest in the superalloy Superni 600, the amount of nickel oxide in this layer will be the highest, whereas chromium oxide will be the second dominating phase, followed by oxides of Fe and Mn. Oxides like NiCr_2O_4 may also form by reaction of oxides of Ni and Cr in the transient layer. This transient layer continues to grow with NiO at the top of the scale along with iron oxide, while the thermodynamically favored chromia attempt to establish a complete layer at the base of this transient layer along with MnO. Once a continuous layer Cr_2O_3 is formed at the alloy/scale interface, the rate of oxidation is then controlled by transport of reactants across this layer, which is much slower process than across the initially formed NiO-rich layer. While in case of iron based superalloy i.e Superfer 800, mainly iron oxide phase is formed. The probable mode of oxidation attack for Superfer 800 is shown schematically in Fig. 6.83. In starting stage, oxygen is adsorbed by the surface resulting in formation of iron oxide and other oxides of the constituent elements. As Fe percentage is highest in the superalloy Superfer 800, the amount of iron oxide in this layer will be the highest, oxides like NiCr_2O_4 may also form by reaction of oxides of Ni and Cr in the transient layer. This transient layer continues to grow with iron oxide at the top as well as internal oxidation is also there. Cr_2O_3 formed is not continuous and thus can not prevent internal oxidation.

The X-ray diffractograms of the scale for T11 and T22 base steels after exposure to molten salt ($\text{Na}_2\text{SO}_4\text{-60\%V}_2\text{O}_5$) at 900°C for 50 cycles has revealed that main constituent of scale is Fe_2O_3 in both the steels. Peaks of Cr_2O_3 along with FeS_2 have also been observed in the oxide scale of both the boiler steels T11 and T22. The formation of Fe_2O_3 has also been observed by Shi (1993) for the hot corrosion of iron by Na_2SO_4 at 750°C . Similar phases were also observed by Sidhu (2003) and Ramesh (2008) in their study on boiler steels. XRD results are further supported by the surface EDX analysis. The presence of some percentage of chromium in the subscale as revealed by the EDX and X ray mapping analysis across the cross-section for T11 and T22 steel is in accordance with the findings of Sadique et al. (2000). The uncoated boiler steels after cyclic molten salt testing at 900°C have shown intense spalling and higher corrosion rate with massive scale formation. The weight gain in case of boiler steel T22 is comparatively more than that of Boiler steel T11. Though T22 boiler steel has more percentage of chromium than T11 boiler steel, but it has shown higher corrosion rate which may be attributed to the presence of comparatively higher percentage of molybdenum in this steel. Molybdenum led to the formation of MoO_3 (liquid at 900°C) and MoO_3 might have further reacted with Na_2SO_4 resulting in the formation of low temperature melting phase Na_2MoO_4 . This low melting point phase might have led to the acidic fluxing of the protective oxide scale. Identical results have been reported by Fryburg et al (1982), Pettit and Meier (1984), Misra (1986) and Sidhu, (2003). Schematic representation of possible hot corrosion mode of attack on boiler steel is shown in Fig. 6.84. The presence of FeS , Fe_2O_3 etc can be explained by reaction of alkali sulphate i.e. Na_2SO_4 containing molten salt react to form Sodium pyrosulphate ($\text{Na}_2\text{S}_2\text{O}_7$) in presence of SO_3 . This pyrosulphate helps in more and more formation of SO_3 from SO_2 . Pyrosulphate reacts with metal oxide and forms alkali metal trisulphates and this alkali metal trisulphate further reacts with the iron and form Fe_3O_4 , FeS and Na_2SO_4 . On further oxidation FeS converts into Fe_3O_4 and SO_2 . This SO_2 again combines with oxygen to form SO_3 . Thereby SO_3 is available for reaction with Na_2SO_4 in form of cyclic corrosion reaction (as explained in 2.5.4.2.4 on page 60).

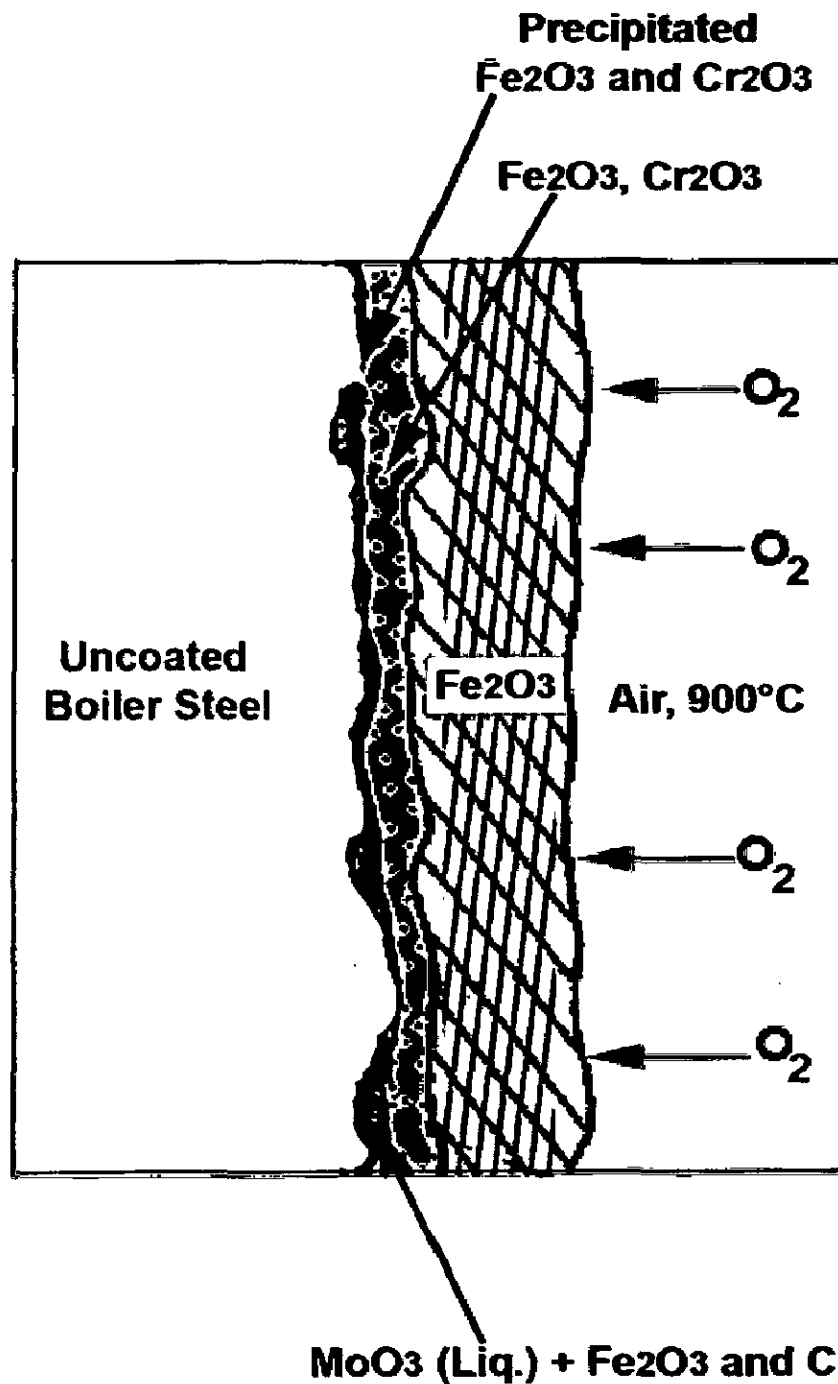


Fig. 6.81: Schematic diagram showing probable mode of oxidation attack on T22 boiler steel exposed to air at 900°C for 50 cycles.

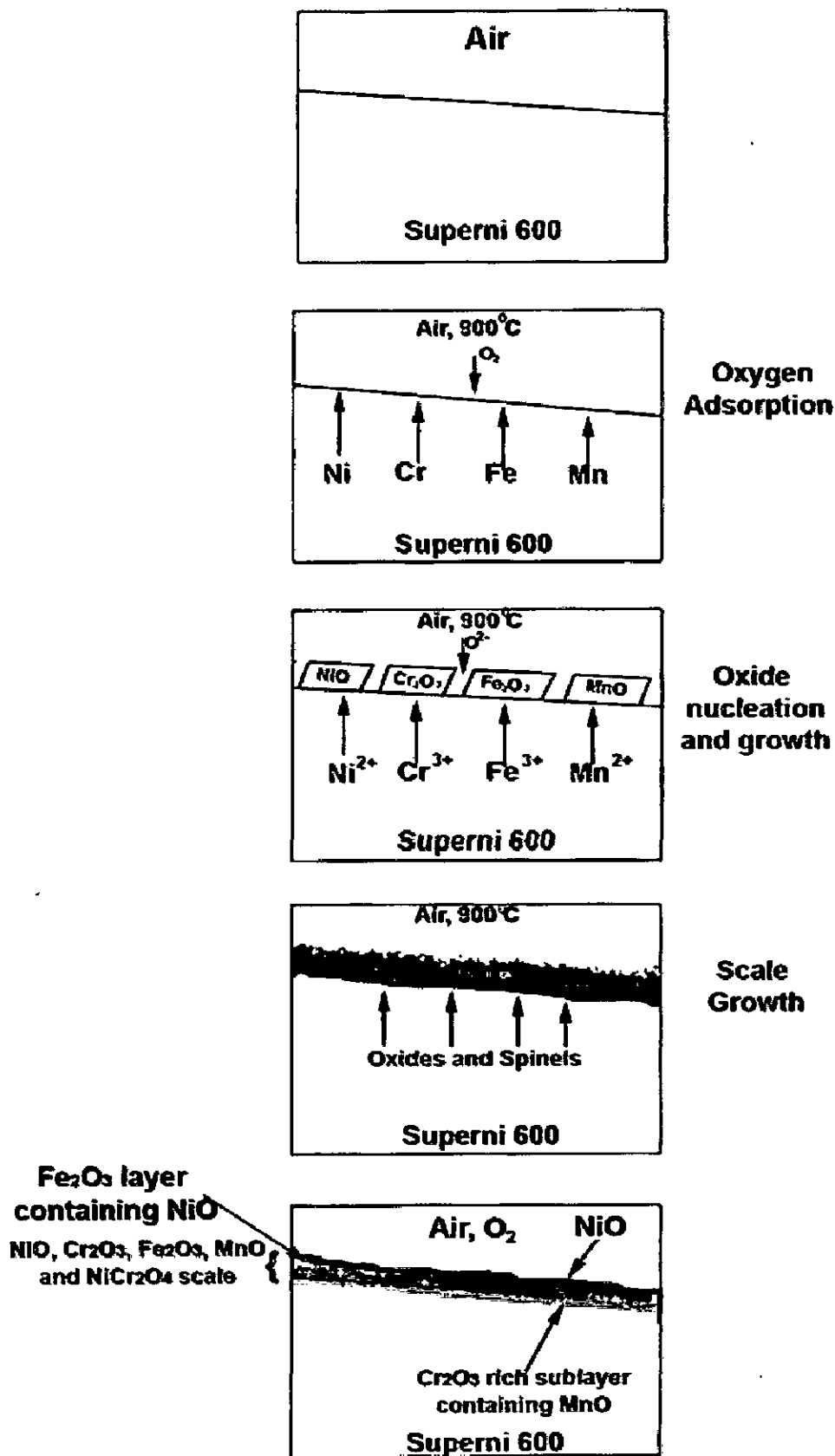


Fig. 6.82: Schematic diagram showing probable mode of oxidation attack on Ni based superalloys exposed to air at 900°C for 50 cycles.

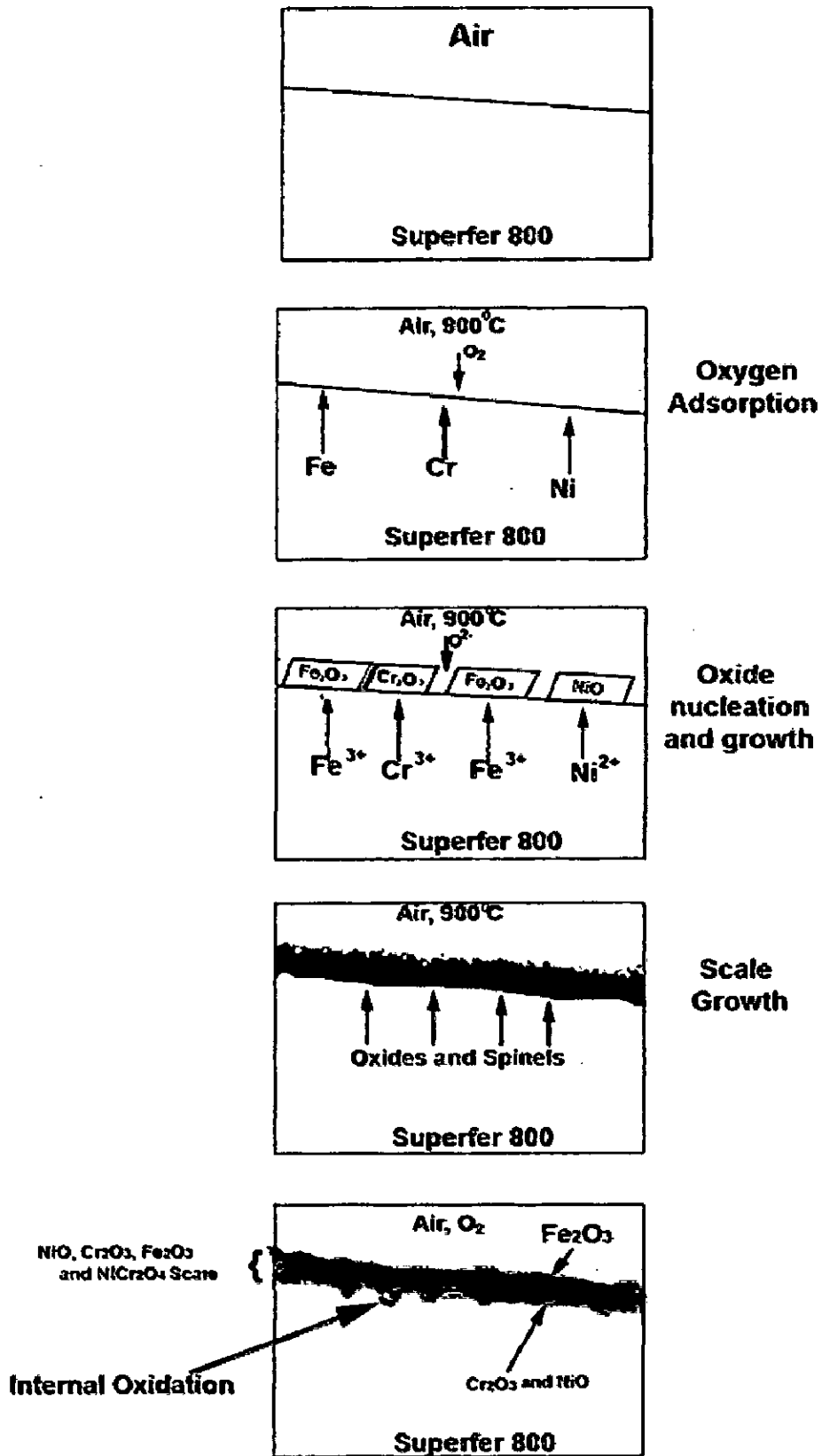


Fig. 6.83: Schematic diagram showing probable mode of oxidation attack on Fe- based superalloy Superfer 800 exposed to air at 900°C for 50 cycles.

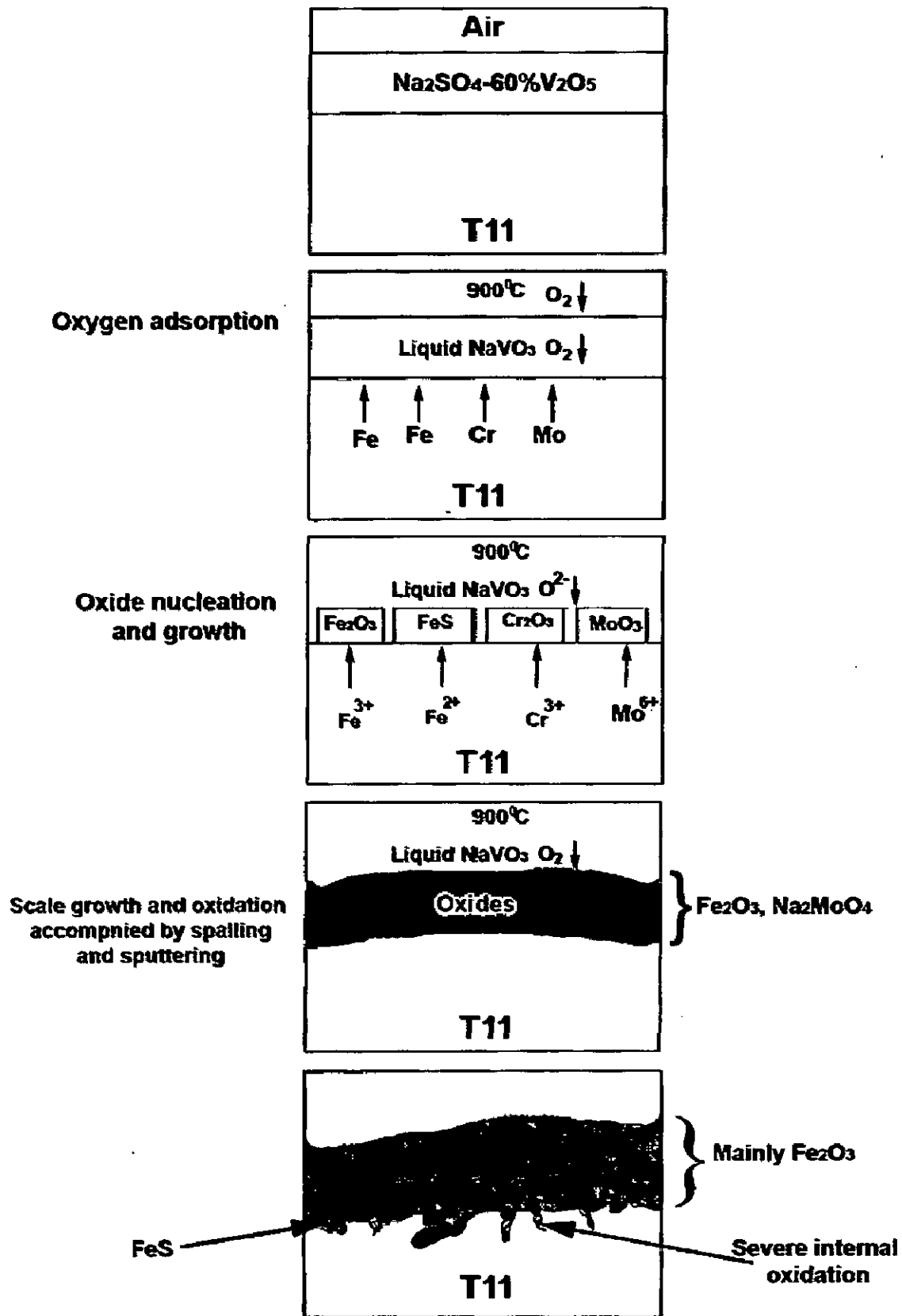


Fig. 6.84: Schematic diagram showing probable mode of hot corrosion attack on Boiler steel T11 exposed to $\text{Na}_2\text{SO}_4\text{-60\%V}_2\text{O}_5$ environment at 900°C for 50 cycles.

Misra (1986) in hot corrosion studies for molybdenum containing nickel base alloy in Na_2SO_4 environment at 750-950°C has revealed that higher the concentration of Mo, the sooner the melt would attain the MoO_3 activity necessary for the formation of solid NiMoO_4 and this would cause a decrease in the length of the period of accelerated corrosion. Lower percentage of Mo (1.081) in the concerned alloy for the present study might have increased the period of accelerating corrosion upto the end of 50 cycles. Probably this factor is responsible for the higher weight gain for this steel as compared to the other boiler steel inspite of more amount of chromium. Wang (1988) has also reported the severe spalling of scale T22 type of steel during hot corrosion in medium BTU coal gasifier environment. It has been reported that more than 70% of the scale got spalled during their test. Further Misra (1986) reported the spalling of thick external porous scale which spalled off completely on cooling for his corrosion experiments at 900°C and 950°C.

In case of superalloys, the surface XRD of Superni 600 and Superni 718 has indicated the formation of similar phases after hot corrosion in the molten salt environment. For these two superalloys NiO , Fe_2O_3 , Cr_2O_3 , FeV_2O_4 are common phases while NiCr_2O_4 and $\text{Ni}(\text{VO}_3)_2$ are other phases present in superni 718. The presence of spinel NiCr_2O_4 has been confirmed in Superni 600 and superfer 800 superalloys. Formation of nickel vanadate has been revealed in case of Superni 600 and Superni 718, while that of iron-vanadate in case of all the superalloys under study. These X-ray diffraction results are well supported by SEM/EDX results. SEM/EDX examination of the molten salt exposed samples showed the presence of cracks and indication of spallation tendency of the scale as shown in Fig. 6.50. The studies conducted by Iyer et al (1987), Swaminathan et al (1993), Tiwari (1997), Tiwari and Prakash (1996), Deb et al (1996), Tiwari and Prakash (1997) Gitanjaly (2003), Singh et al., (2005), Singh et al., 2006 and Sidhu (2006) on similar superalloys also endorse formation of identical phases. In general the uncoated superalloys have indicated accelerated oxidation in Na_2SO_4 -60% V_2O_5 environment at 900°C in comparison to that in air. The Fe-base superalloy Superfer 800 has shown least resistance to the hot corrosion amongst the Superalloys Superni 600, 718 and Superfer 800. In case of Superfer 800, oxide scale

penetrated deep into the substrate. On the basis of cumulative weight gain data for 50 cycles, corrosion rate of the superalloys under study can be arranged in the following order:



The superior corrosion resistance shown by Ni-base superalloys might be attributed to the formation of Cr_2O_3 and nickel vanadate (Kerby and Wilson, 1973 and Gitanjaly, 2003). In case of iron based superalloy i.e. Superfer 800, oxides of iron formed dominantly during the hot corrosion exposure which lead to more corrosion as compared to Ni based superalloys. Also presence of $\text{Ni}(\text{VO}_3)_2$ phase in case of Ni-based superalloys acted as a barrier for the oxidizing species (Seierstein and Kofstad, 1987 and Sidhu, 2006). Further, it has been observed that Ni based superalloys under study have obeyed parabolic rate law of oxidation upto 50 cycles. Superfer 800 has not obeyed the parabolic rate law. In superfer 800, intensive spalling and sputtering was observed. It has been observed that the rate of weight gain in case of molten salt exposure was relatively high as compared to oxidation in air. This may be due to the formation of NaVO_3 which acts as a catalyst and also serves as oxygen carrier to the base alloy, thereby leading to rapid oxidation of the basic elements of the superalloys. Simultaneously, the protective scale is destroyed or eliminated by molten salts and consequently the metal surface is exposed to direct action of aggressive environment as has been indicated in the current investigation also. Seiersten and Kofstad (1987) as well as Swaminathan et al (1993) have suggested simultaneous growth of oxides and their dissolution in molten salt as per following reaction:



After a period of high corrosion rate it has been observed that the rate of corrosion tends to be almost become uniform with the further progress of study. The formation of nickel vanadate or iron-vanadate in the scales with the progress of study might have contributed to slower oxidation rate as these vanadates are capable of decreasing the short circuit diffusion of ions as has been suggested by Swaminathan et al (1993), Tiwari and Prakash (1997), Singh (2005) and Sidhu (2006).

Fig. 6.85 shows the schematic representation of possible hot corrosion mode of attack in Na_2SO_4 -60% V_2O_5 environment on Ni based superalloys. The surface XRD has indicated

the formation of NiO, Fe₂O₃, Cr₂O₃, FeV₂O₄ and Ni (VO₃)₂ phases. The presence of spinel NiCr₂O₄ has been revealed in Superni 600 superalloy. Through cracks internal penetration has occurred. There is thick scale formation with visible severe internal attack as revealed by X-ray mapping (Fig. 6.58) of the cross-section of superalloy Superni 600 subjected to cyclic hot corrosion in Na₂SO₄-60%V₂O₅ at 900°C for 50 cycles. As oxygen is present throughout the scale, it can be inferred that there is formation of iron oxide, nickel oxide and chromium oxide throughout the scale. Cr₂O₃ formed is providing protection for further oxidation. Vanadium enriched band is present in the scale. Ni has diffused from the substrate and is concentrated along the substrate scale boundary and preventing further corrosion.

In case of hot corroded Superfer 800 phases identified are Fe₂O₃, NiO, NiCr₂O₄, and FeV₂O₄. Formation of iron vanadate has been revealed in case of Superfer 800. Scale formed is porous and fragile with higher percentage of Fe₂O₃ and some amount of Chromium oxide and Ni oxide. Nickel concentration has increased in the substrate along substrate scale interface in the shape of thin band which has prevented the further oxidation as Cr has migrated to form the Cr₂O₃ scale. Cr has come from substrate to form irregular Cr₂O₃ band leaving a Ni rich band in the substrate which is clearly visible in the overlapped map as shown in Fig. 6.60. The schematic representation of possible hot corrosion mode of attack in Na₂SO₄-60%V₂O₅ environment on Superfer 800 superalloy is shown in Fig. 6.86.

6.3.2 Coated alloys

The Al₂O₃-3 wt %TiO₂ coatings deposited on boiler steels and Ni-and Fe-based superalloys showed protective behavior in the air oxidation as well as molten salt environment at 900°C in cyclic testing. Coating remained essentially adherent to the substrate after 50 cycles of testing in both environments. The composite coating possessed very dense structure, high thermal stability and excellent cracking/spallation resistance. There was no penetration of any corrosive species into the coating as developed coating has very low porosity. Coating acted as a shield between the environment and the metallic substrate and effectively hindered the

corrosive species from migrating into substrate. Alumina-titania coated alloys have shown better spallation resistance.

The X-ray diffraction analysis has indicated Al_2O_3 and TiO_2 along with Al_2TiO_5 $\text{Al}_2\text{TiO}_7\text{O}_{15}$ phases on the surface of the coated samples after 50 cycle oxidation exposure. Minor micro cracks on the surface were detected but there was no evidence of formation of oxides from the substrate alloys. The coating has protected the surface very well. This may be due to the fact that Al_2O_3 probably hinders the grain boundary diffusion of the elements. As a consequence, there is no oxide scale growth. The compact and protective Al_2O_3 layer separated the metal substrate from the environment. As a result, the coating improved the corrosion resistance. From weight change data it can be inferred that the protection to the base metals has been provided by the coating. The oxidation and molten salt corrosion resistance provided by Al_2O_3 -3 wt % TiO_2 coatings might be attributed to the compact structure of the coatings. The Al_2O_3 -3 wt% TiO_2 composite coating was no longer oxidized and acted as an effective inert barrier to improve the isothermal and cyclic oxidation and molten salt resistance of alloys.

After molten salt studies performed on coated alloys, the coated boiler steels have shown Al_2O_3 and TiO_2 as the main constituent with minor peak of $\text{Al}_2\text{TiO}_7\text{O}_{15}$. The X-ray diffractograms for the coated superalloys after exposure to molten salt at 900°C for 50 cycles has shown peaks of Al_2O_3 and TiO_2 along with Al_2TiO_5 . EDX analysis showed that the coating was unaffected by any molten salt attack. The low value of porosity of coating never permitted any penetration into the coating and the coatings maintained their shielding capability. The coatings showed no solubility in the molten salt environment and thus excellent corrosion resistance. Coatings seem to be completely immune to corrosion attack in molten salt environment. Investigations revealed that corrosive species could not reach base material through the coatings. The coatings have shown excellent cracking and spallation resistance. The composite coating exhibited excellent high temperature oxidation resistance and hot corrosion resistance in molten sulfate salts at 900°C. The dense structure of D-gun sprayed coatings could have effectively hinder the corrosion species from migrating into substrate, and thereby remarkably improving the oxidation and hot corrosion resistance of the alloys.

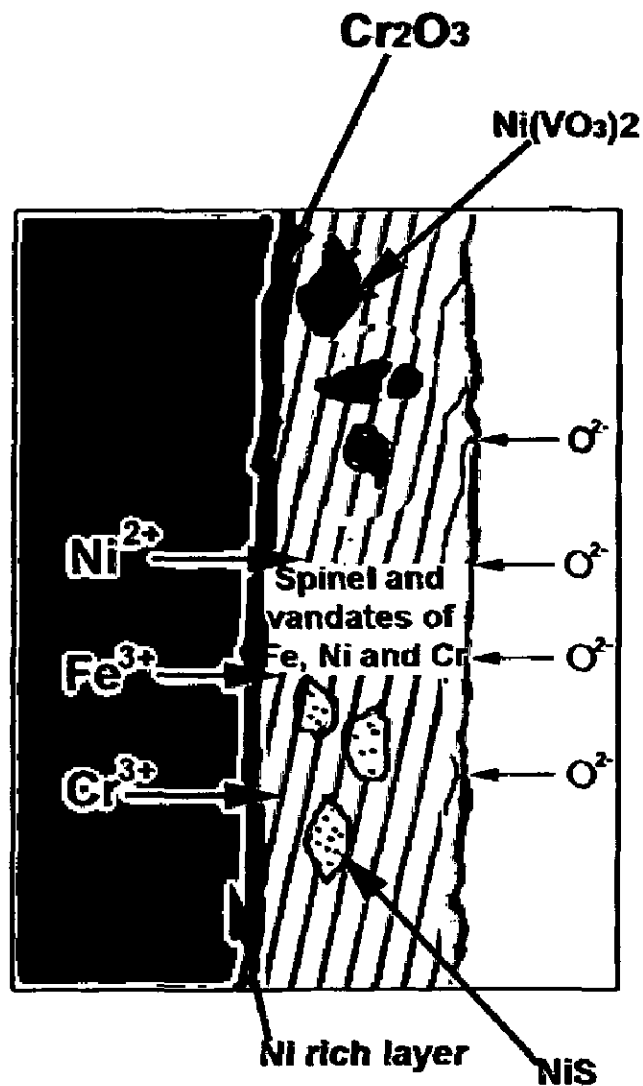


Fig. 6.85: Schematic diagram showing probable mode of hot corrosion attack on Ni based superalloy exposed to Na_2SO_4 -60% V_2O_5 environment at 900°C for 50 cycles.

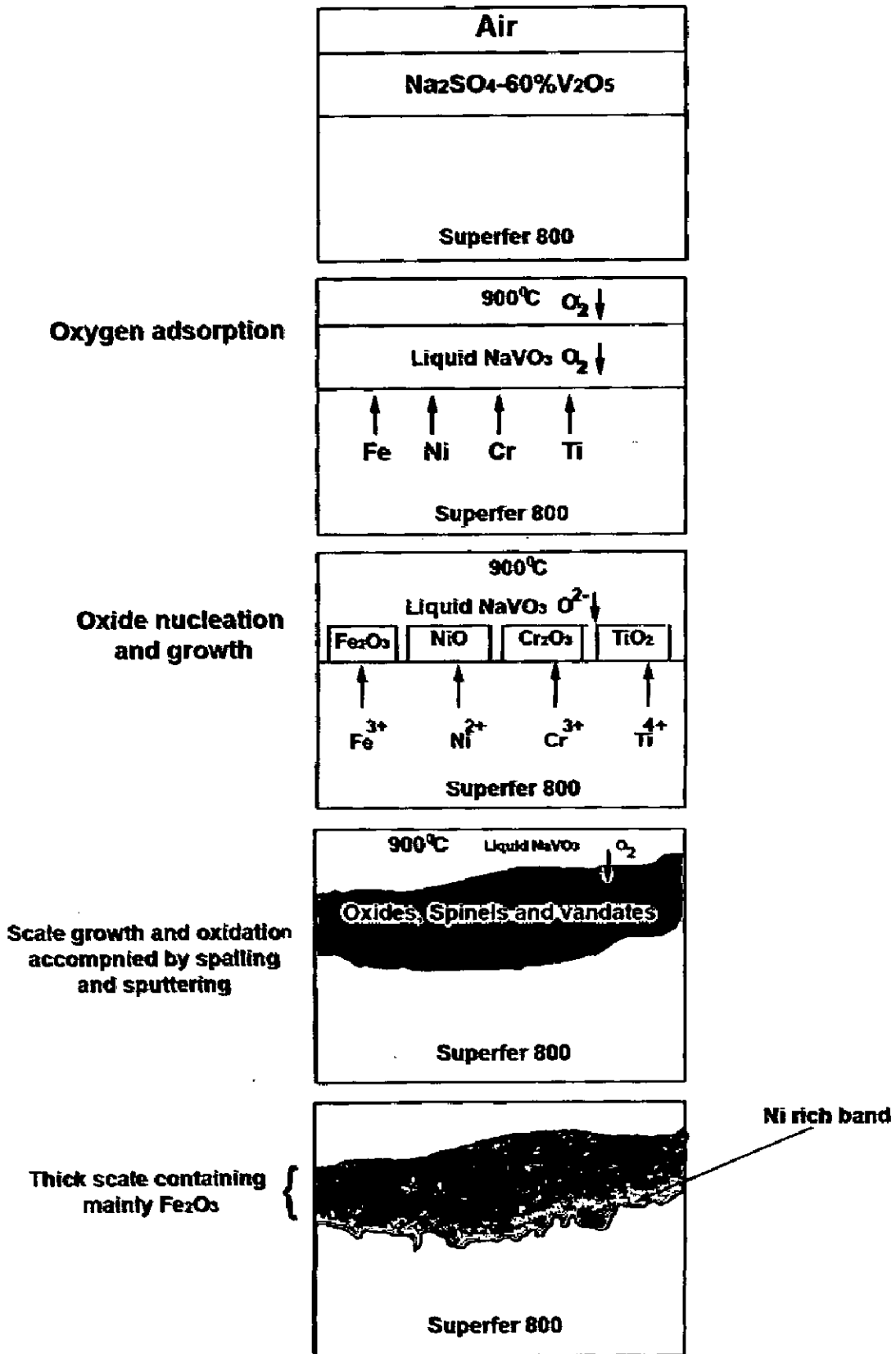


Fig. 6.86: Schematic diagram showing probable mode of hot corrosion attack on Superfer 800 superalloy exposed to Na₂SO₄-60%V₂O₅ environment at 900°C for 50 cycles.

EROSION CORROSION STUDIES IN ACTUAL INDUSTRIAL ENVIRONMENT

This chapter focuses on the study of erosion corrosion behaviour of the D-gun sprayed coated and uncoated alloys exposed to superheater zone of the coal fired boiler of Guru Gobind Singh Super Thermal Plant, Ropar, Punjab (India). Super heater zone was selected, since severe failure due to erosion-corrosion has been reported by the concerned power plant in this zone. The specimens were kept in the zone of the boiler where the gas temperature was $700^{\circ}\text{C}\pm 10^{\circ}\text{C}$. Experiments were performed for 15 cycles, each cycle consisting of 100 hours exposure followed by 1 hour cooling at ambient temperature. The specimens were visually examined at the end of each cycle for any change in the colour, luster, spalling tendency and other physical changes of the scale if any.

Weight change was measured at the end of each cycle. However in this environment the weight change data could not be of much use for predicting hot corrosion behaviour because of suspected spalling and ash deposition on the samples. Hence the extent of erosion-corrosion has been evaluated by measuring the thickness of the unreacted portion of the samples after the total exposure of 1500 hrs. The different phases and their distribution in the eroded-corroded specimens were analyzed with the help of XRD, SEM/EDX analysis.

7.1. RESULTS

7.1.1 Uncoated Alloys

7.1.1.1 Visual Examination

The macrographs of T11, T22, Superni 600, Superni 718 and Superfer 800 substrate alloys before and after 1500 hours exposure in the superheater area of coal fired boiler are shown in Fig.7.1. Grey coloured scale appeared on the surfaces of T11 and T22 steels which turned to grayish black afterwards while light brown coloured scale appeared on the surfaces of superalloys during first cycle of 100 hours and turned to black colour afterwards. In case of T11 and T22 steels, the scale was fragile and showed severe spalling. While in all the superalloys no spalling of the scale was observed and it remained intact throughout the study.

7.1.1.2 Weight Change and Thickness loss data

Assessment of the weight change was carried out after exposure at 700°C in boiler conditions on uncoated substrate alloys. The weight change consists of weight gain owing to the formation of the oxide scale and weight loss due to solid particle erosion and the suspected spalling and fluxing of the oxide scale. The net weight change of the substrate alloys in the given environment represents the combined effect of erosion and corrosion. Weight change per unit area expressed in mg/cm^2 has been plotted as a function of time expressed in hours for substrate alloys as shown in Fig.7.2. Due to severe spalling and cracking boiler steels have shown decrease in weight. Initially the weight loss is very fast due to cracking and peeling off of surface scale, then it remained almost constant for few cycles and then again weight loss was steep. While all the superalloys have shown increase in weight. The extent of erosion-corrosion has been measured in terms of metal layer lost due to scaling after 1500 hours exposure. The thickness of metal lost is 2.0782 mm and 1.7117 mm in T11 and T22 steels respectively while in case of superalloys, thickness loss is 0.2178, 0.2301 and 0.2588 mm for Superni 600, superni 718 and Superfer 800 respectively as indicated in Fig.7.3. The weight gain of the samples owes to the formation of oxide scale and deposition of fly ash and weight loss is due to continuous erosion due to fly ash and other erosive particles in the blast. Throughout the study, boiler steels suffered a weight loss. The corresponding degradation rates expressed in mils per year (mpy) and are found to be 478.13, 393.81, 50.11, 52.94 and 59.54 for T11, T 22, Superni 600, Superni 718 and Superfer 800 respectively.

7.1.1.3 X-ray Diffraction Analysis

The X-ray diffractograms for T11, T22, Superni 600, Superni 718 and Superfer 800 substrate alloys after exposure to actual boiler environment for 1500 hours are shown in Fig. 7.4-7.6 respectively. In the boiler environment, T11 and T22 steels have indicated Fe_2O_3 and Fe_3O_4 as the main constituent. FeS was also detected and minor peaks of Al_2O_3 , SiO_2 , ZnO and MnO which is indicative of deposition of fly ash on the surface of exposed steel as shown in Fig. 7.4. In case of superalloys shown in Fig. 7.5 and Fig. 7.6, Ni is main constituent in the scale with peaks of Fe_2O_3 , NiO, Al_2O_3 , SiO_2 and NiFe. In case of Superfer 800, Cr_2O_3 phase is also observed.



Samples before exposure to boiler environment

Samples after 1500 hours exposure to boiler environment

Fig. 7.1: Macrographs of uncoated substrate alloys before and after 1500 hours exposure to boiler environment:
 (a) T11 (b) T22 (c) Superni 600 (d) Superni718 (e) Superfer 800 (f) T11 after 1500 Hrs Exposure (g) T22 after 1500 Hrs Exposure (h) Superni 600 after 1500 Hrs Exposure (i) Superni 718 after 1500 Hrs Exposure (j) Superfer 800 after 1500 Hrs Exposure

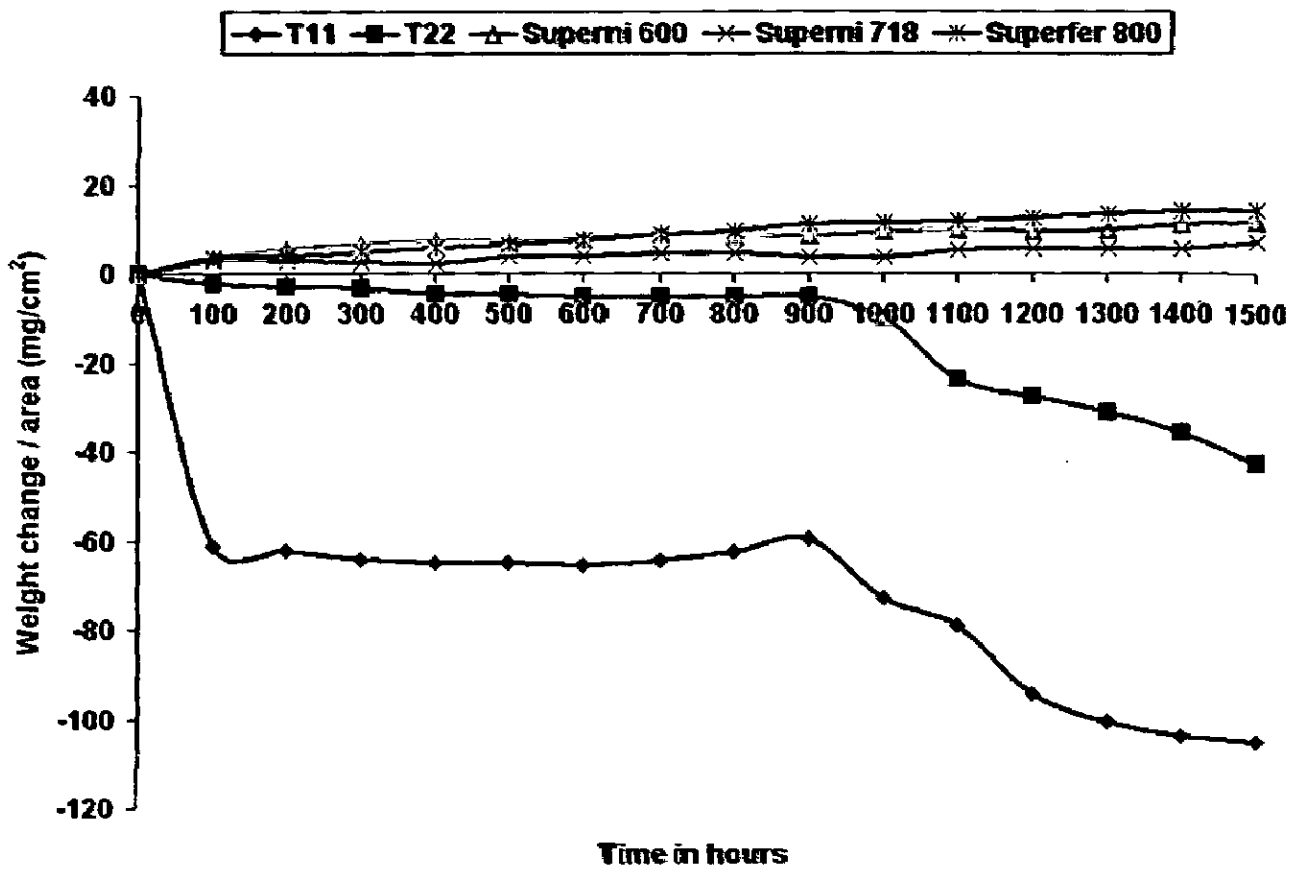


Fig. 7.2: Weight change plot for uncoated alloys exposed to superheater of the coal fired boiler for 1500 hours at 700°C.

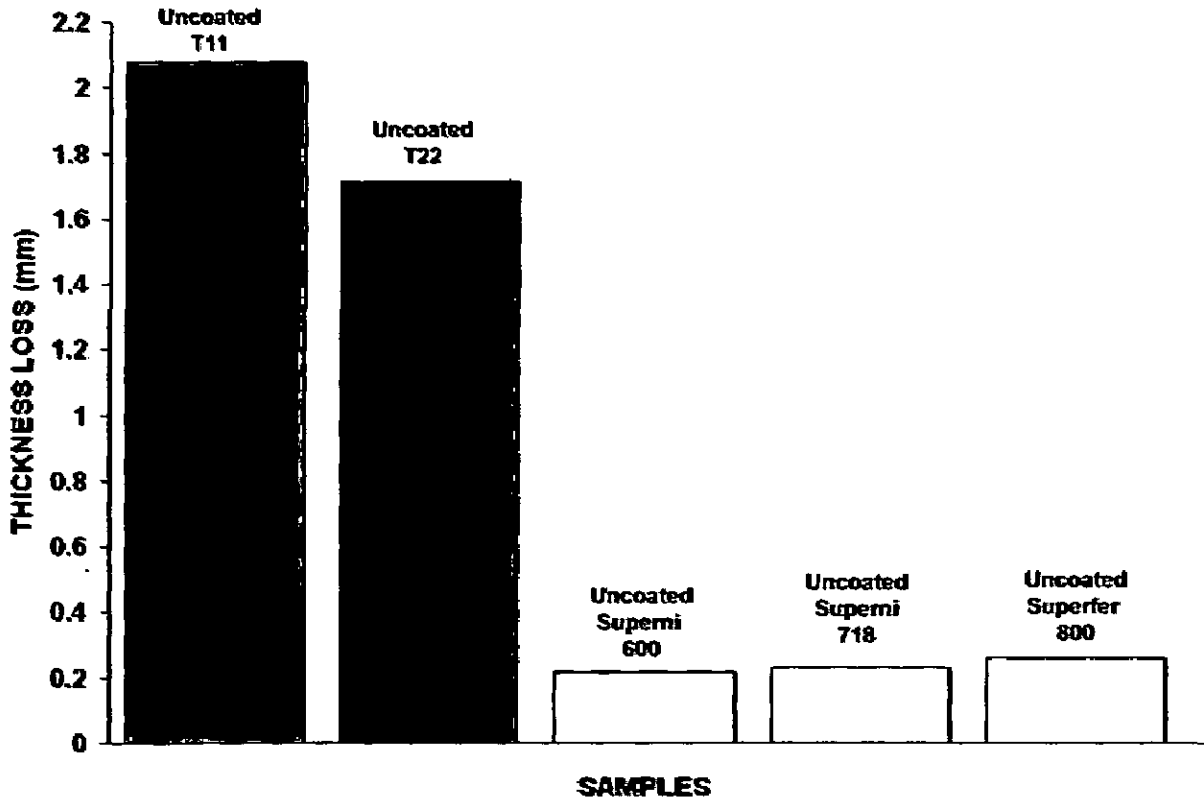


Fig. 7.3: Bar chart indicating the thickness lost in mm by the uncoated alloys after 1500 hours exposure to the coal fired boiler at 700°C.

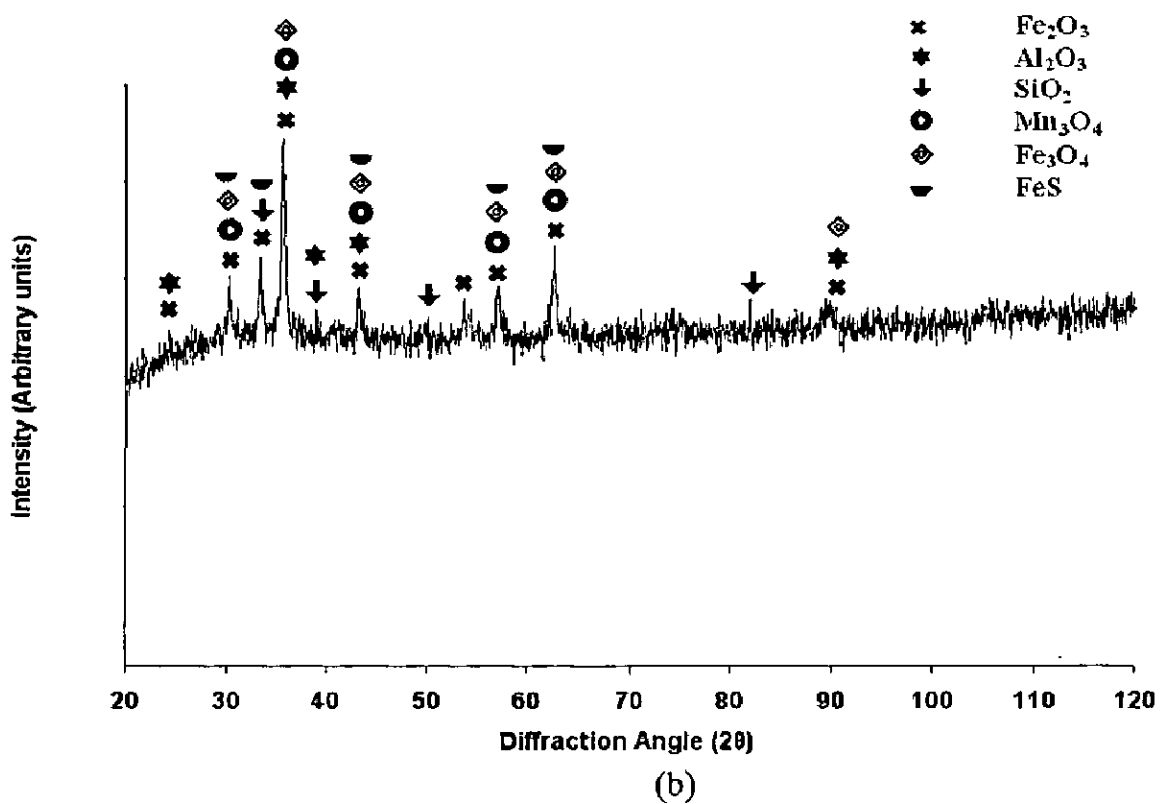
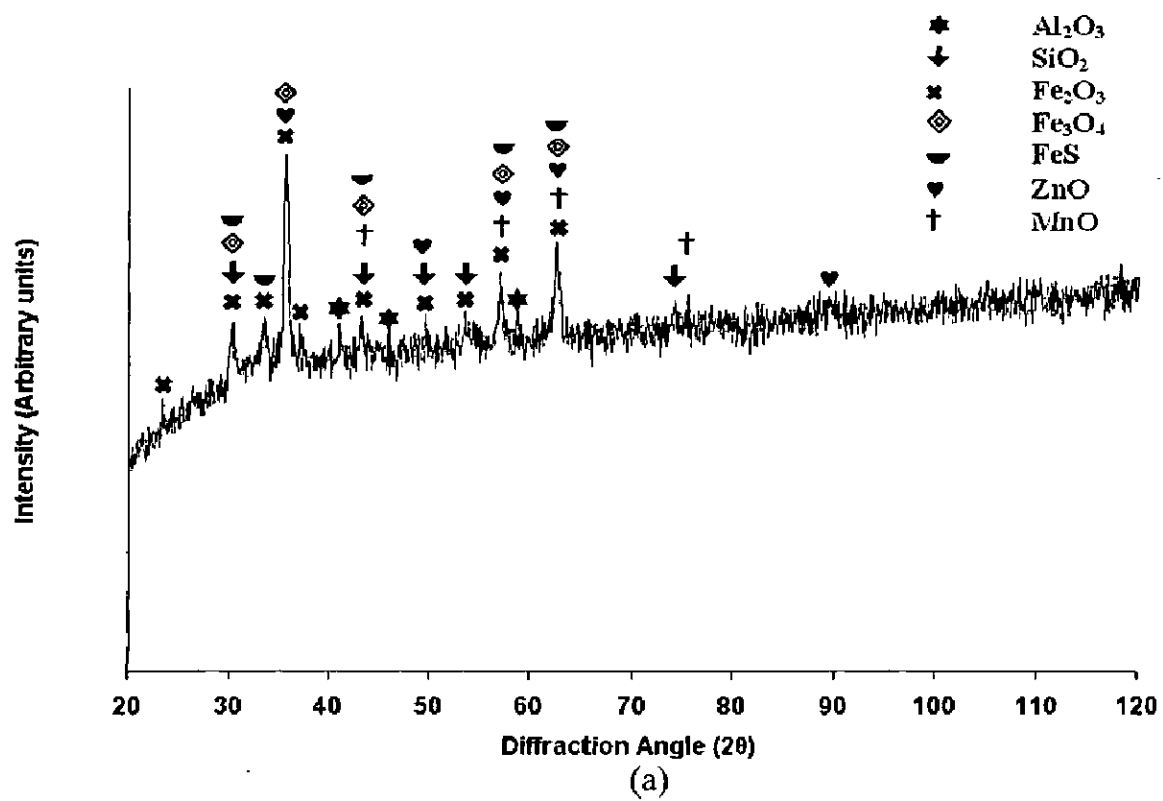
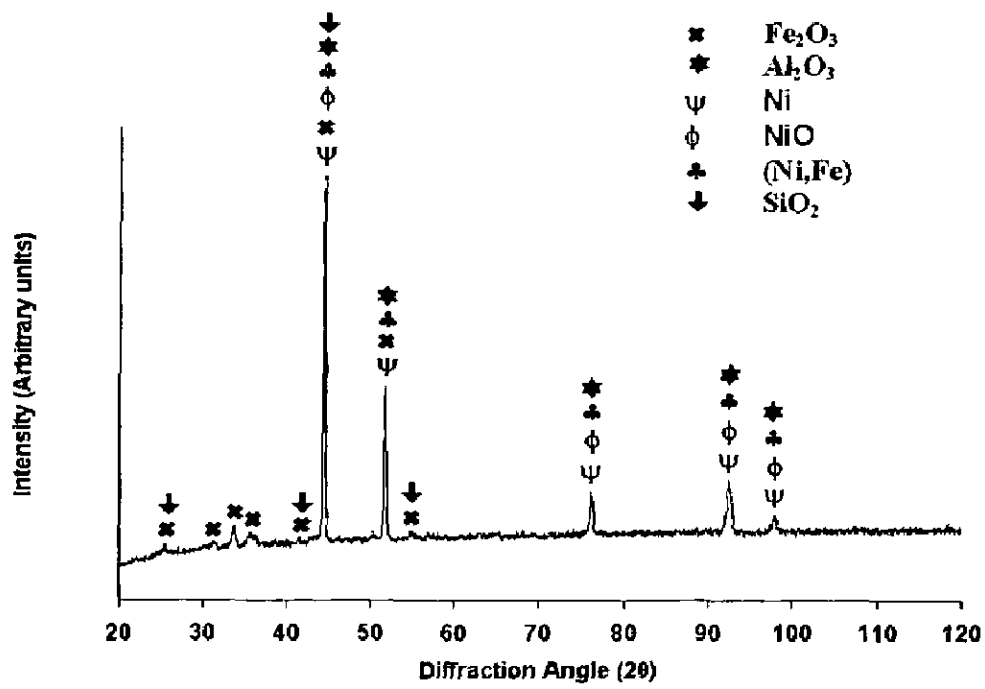
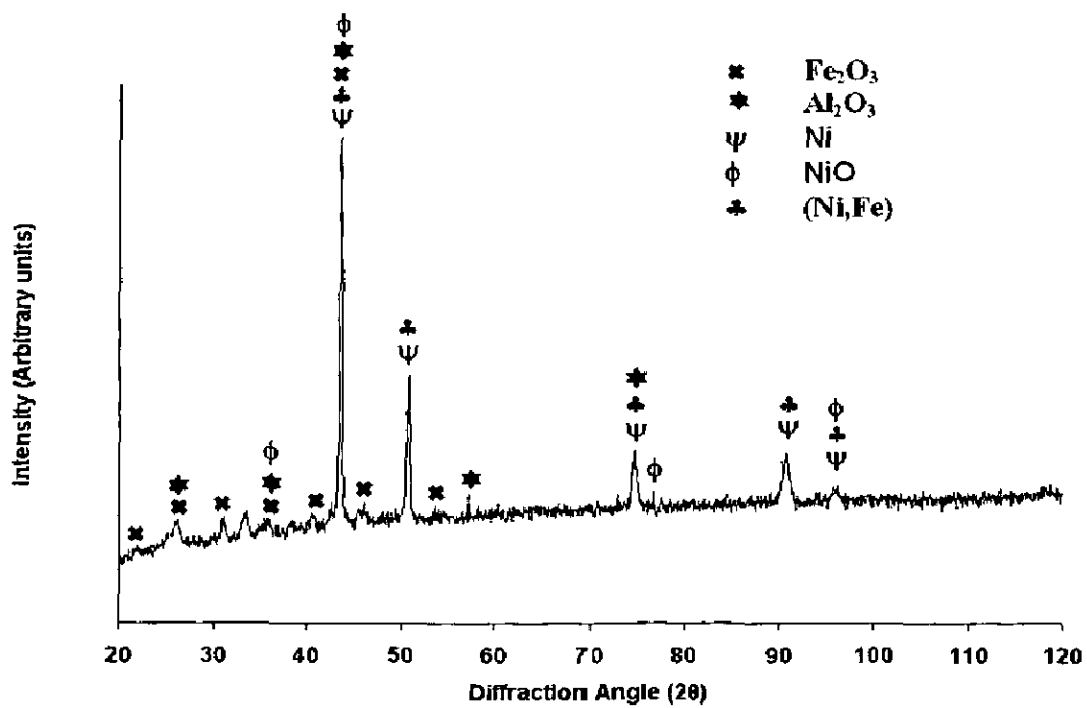


Fig. 7.4: X-ray diffraction profiles for boiler steels exposed to superheater of the coal fired boiler for 1500 hours at 700°C.
 (a) T11 (b) T22



(a)



(b)

Fig. 7.5: X-ray diffraction profiles for superalloys exposed to superheater of the coal fired boiler for 1500 hours at 700°C.
 (a) Superni 600 (b) Superni 718

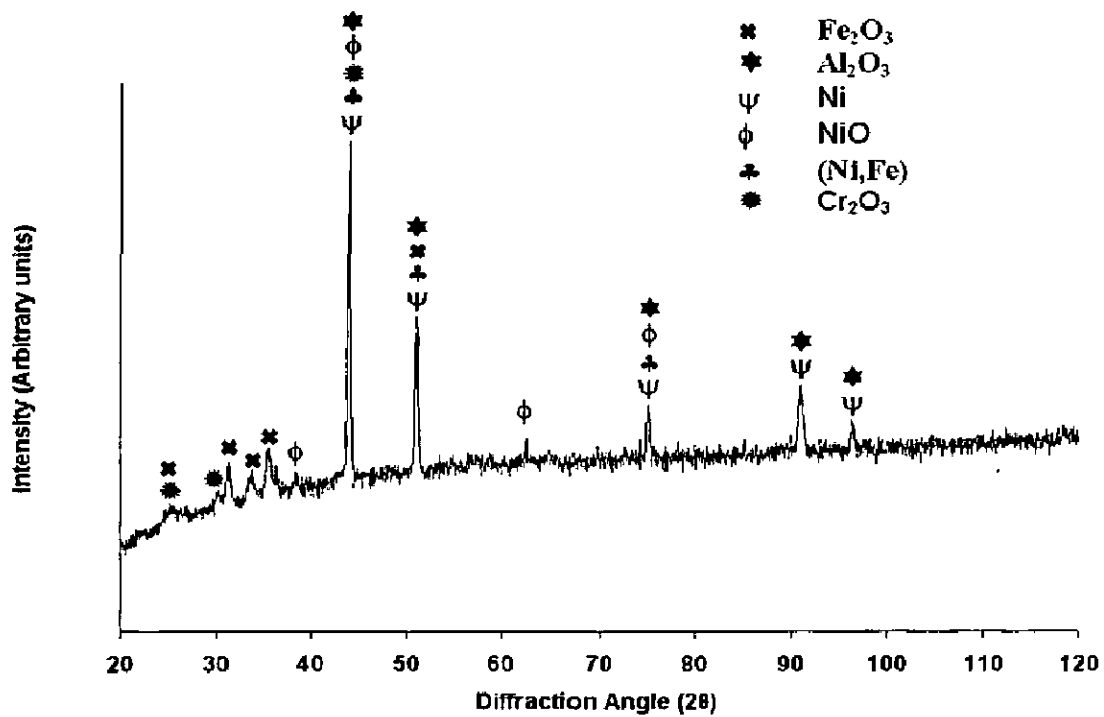


Fig. 7.6: X-ray diffraction profiles for superalloy Superfer 800 exposed to superheater of the coal fired boiler for 1500 hours at 700°C.

7.1.1.4 SEM/EDX Analysis

(a) Surface Morphology

SEM/EDX analysis was used for the detection of presence of corrosion products and corrosion-inhibiting species and their concentrations. Scale development and the effect of boiler conditions on the exposed surface was studied. The surface scale morphology and the EDX analysis for substrate alloys exposed to superheater region of coal fired boiler after 1500 hrs is shown in Fig.7.7-7.11. From SEM/EDX analysis of boiler steels T11 and T22 it has been revealed that the main constituent of scale are Fe, Al, Si and O as shown in Fig. 7.7 and 7.8. The oxide scale formed was porous and less adherent consisting mainly of iron oxide. On thin bands of the matrix phase, large bulbous oxides formed, protruding well above the surface. The micrograph indicates massive scale along with presence of embedded ash at some points and nodules are also present. There is a presence of pits and cracks in scale and also hills and craters are formed which is a clear indication of combined effect of erosion and corrosion caused by combined action of flue gases along with impact of fly ash. Rapid growth of iron oxide in the matrix region of the boiler steels led to much thicker scale formation. The EDX analysis of surface scale revealed the presence of Si, Al, Fe, Na, Ca, Mg along with O which are the constituents of fly ash. Some ash particles can be seen embedded in the scale as white colour nodules. In case of boiler steels steel exposed to boiler conditions micrographs indicates a continuous granular scale consisting mainly of Fe, Si and Al along with O. The appearance of scale in case of boiler steels is highly bulky, porous with a continuous network of cracks along the scale.

The observed corrosion mechanism was characterized by the adverse features of the corrosion behavior of the boiler steels, formation of thick oxide scales and spalling of the scale. Frequent spalling was due to the fact that the scales consisted of multi-layered

structure of oxide layers. The enhanced corrosion was mainly induced by the presence of corrosion species in the combustion products.

In case of superalloys exposed to boiler conditions, a fine surface scale mainly consisted of Al, Si, Ni, Fe and Cr along with O as shown in Fig. 7.9 -7.11. The scale on the matrix regions was significantly flatter and no spallation of the scale has been seen. At 700°C, a well adherent corrosion scale is formed which mainly consists of NiO. The formation of NiO oxide is evident in all the superalloys. There is presence of minor cracks on the surface scale and also there is an indication of erosion with the formation of hills and craters on the surface. In case of Superni 600, SEM /EDX analysis, indicates a thin scale consisting of Ni (wt% 14.72), Al (wt% 12.98) and Si (wt% 20.96) along with oxygen(37.21%) with some amount of Cr, Fe, Ca, Mn, Zn as shown in Fig. 7.9. The scale was heterogeneous and it is inferred that the composition of the elements in the scale is almost similar to ash composition along with other oxides formed from the matrix. Higher percentage of Al and Si in the scale is in indication of massive embedment of ash in the scale. In Superni 718, (Fig. 7.10) minor cracks with high Cr (wt% 24.29) content are seen with surface unevenness created by formation of hills and craters. Like in superni 600, there is also a presence of massive amount of Al and Si in the scale along with other ash constituents. Superfer 800 has shown (Fig. 7.11) some cracks along with formation of craters and hills having higher %age of Fe and Ni and some amounts of Cr, Al, Si, Cr, Ca, Mn, Ti and K on the surface.

(b) Cross-Sectional Analysis and X ray mapping

The BSE image and the EDX analysis across the cross section of uncoated alloys are shown in Fig.7.12 to Fig.7.16. In case of boiler steels, (Fig. 7.12 and 7.13) the scale was quite fragile and porous and was continuously peeled off from the surface.

Throughout the scale higher percentage of iron oxide is there and also chromium is present along with oxygen is present throughout the scale thickness though in small quantity. Mn and Si confirm the presence of ash embedment. Also in case of T22 steel traces of Ca and Mo along with Mn and Si have been revealed.

The cross sectional morphology and the corresponding EDX analysis (Fig. 7.14 to Fig. 7.16) for Superni 600, Superni 718 and Superfer 800 superalloys after 1500 hrs exposure to actual environment of coal fired boiler has revealed that the scale mainly consisted of Ni and Fe along with oxygen. Oxygen along with chromium is present throughout the scale in all the superalloys. Also minor percentage of Al and Si is present throughout the scale in all superalloys.

Back Scattered Electron Image of cross-section of uncoated substrate alloys (T11, T22, Superni 600, Superni 718 and Superfer 800) and corresponding X-ray mapping after 1500 hours exposure to boiler environment is shown in Fig.7.17 to 7.21 respectively. There is presence of ash particles indicated by presence of Al and Si with oxygen on the top surface of the scale. In boiler steels, mainly iron oxide is formed. At the top of scale Si is spread throughout the scale indicating ash embedment. Continuous spalling of scale was observed during the cyclic exposure. In case of boiler steel T11 (Fig.7.17), iron oxide remained the main constituent of the scale with presence of minor concentration of Mn, Cr and Si. In elemental maps, a thick Silica particle could be seen embedded in the scale and silica is also observed in the top of the scale. In boiler steel T22, (Fig. 7.18) main constituent is iron oxide with presence of minor concentration of Cr and Si. There is very thin Cr rich band just above the substrate scale interface.

While in all the superalloys exposed to boiler environment, a very thin scale was observed. In Superni 600, (Fig. 7.19), there is thin Ni rich band in the substrate from which Cr has depleted. This chromium is co existing with oxygen in the outer scale

thereby indicating formation of chromium oxide. There is presence of embedded silica particle which has deformed the metal. In Superni 718, (Fig. 7.20) attack is very minimal and a thin scale was observed. From X-ray mapping, streaks of silica and alumina are indicated on the top of the scale. Also Fe, Ni and Cr are coexisting with oxygen as very thin layers at the top most scale. In Superfer 800, thick scale is formed as shown in (Fig. 7.21). Ni rich layer is present in the substrate at the interface. Also Ni and Cr are coexisting with oxygen at the top of the scale. The scale by itself mainly consists of iron along with oxygen which indicates the formation of Fe_2O_3 . Si, Mg and Al particles can be seen coexisting with oxygen in the elemental maps thereby indicating embedment of ash particles.

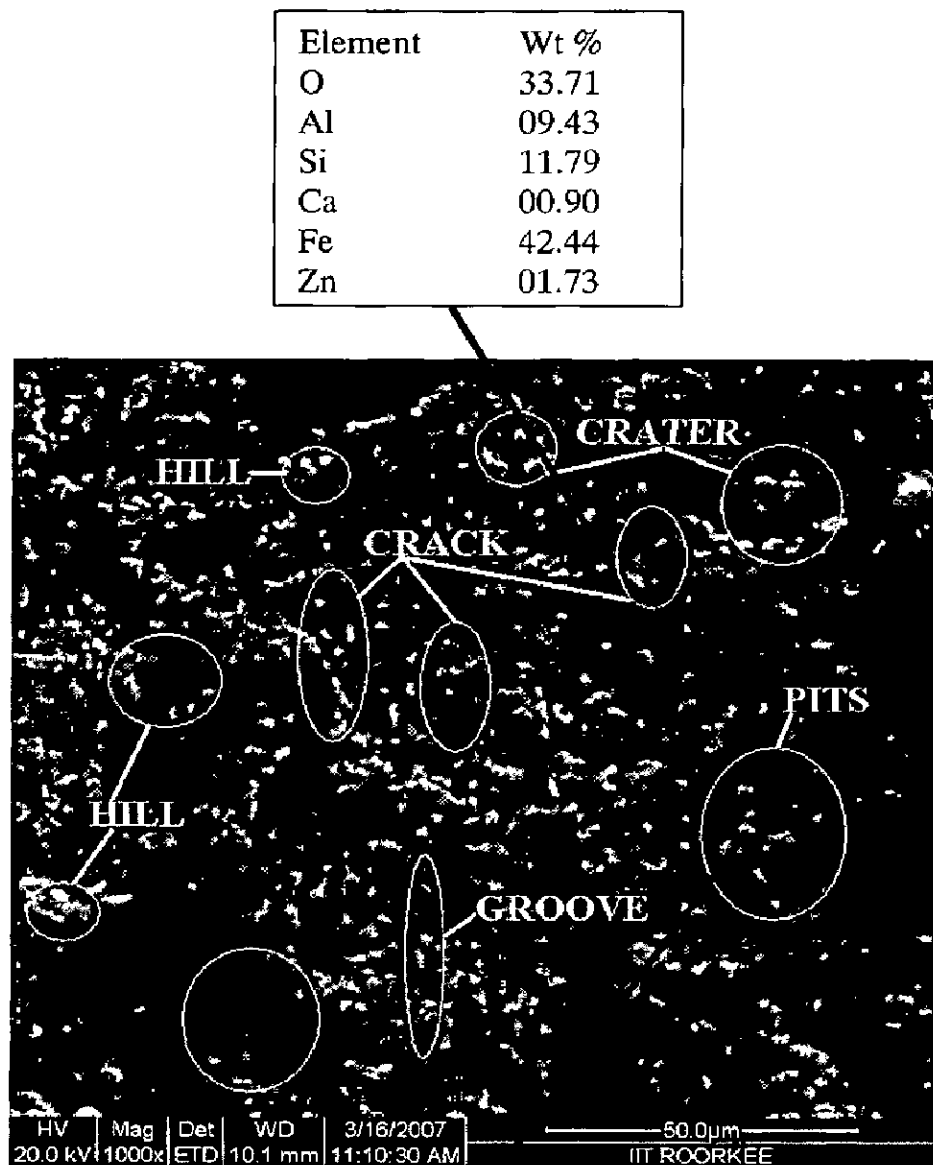
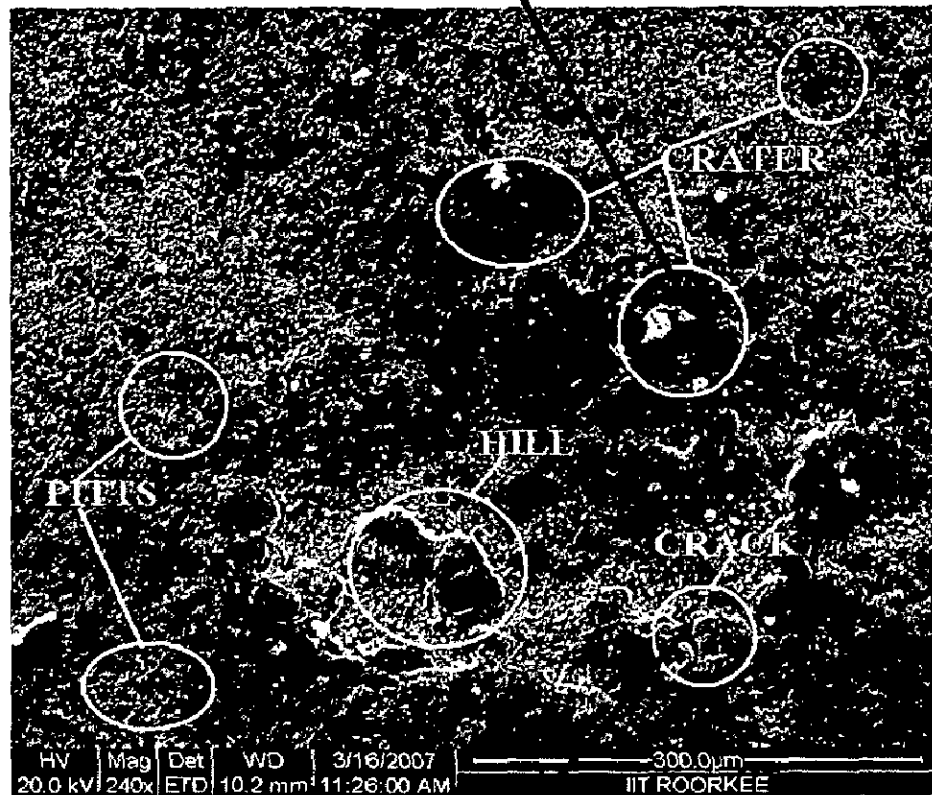


Fig.7.7: Surface scale morphology and EDX analysis for boiler steel T11 exposed to superheater of the coal fired boiler for 1500 hours at 700°C.

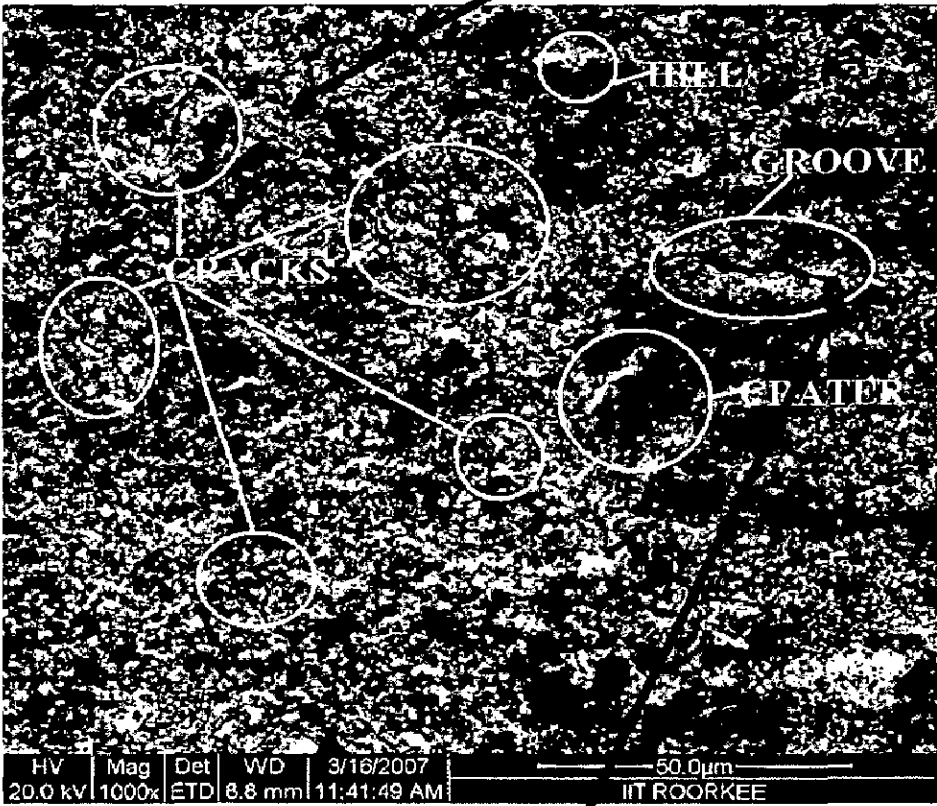
Element	Wt %
O	28.70
Al	16.46
Si	29.28
K	00.53
Ca	00.79
Ti	01.23
Fe	21.97
Na	00.96
Mg	00.08



Element	Wt %
O	31.48
Al	08.50
Si	09.28
Ca	00.58
Mg	00.09
Ti	00.98
Fe	47.14
Zn	01.95

Fig. 7.8: Surface scale morphology and EDX analysis for boiler steel T22 exposed to superheater of the coal fired boiler for 1500 hours at 700°C.

Element	Wt %
O	37.21
Al	12.98
Si	20.96
Ca	01.75
Cr	04.58
Mn	00.41
Fe	04.94
Ni	14.72
Zn	02.45



Element	Wt %
O	29.97
Al	15.42
Si	19.35
Mo	02.11
Ca	00.43
Ti	02.36
V	00.30
Cr	18.50
Mn	01.21
Fe	02.63
Ni	01.76
Zn	05.96

Fig. 7.9: Surface scale morphology and EDX analysis for superalloy Superni 600 exposed to superheater of the coal fired boiler for 1500 hours at 700°C.

Element	Wt %
O	36.72
Al	11.73
Si	18.10
Mo	01.13
K	00.71
Ca	01.11
Ti	02.84
Cr	00.65
Fe	02.24
Ni	24.77



Element	Wt %
O	37.81
Al	09.19
Si	14.25
Ag	00.02
K	00.29
Ca	00.93
Ti	01.73
Cr	24.29
Fe	02.28
Ni	09.21

Fig.7.10: Surface scale morphology and EDX analysis for superalloy Superni 718 exposed to superheater of the coal fired boiler for 1500 hours at 700°C.

Element	Wt %
O	29.17
Al	03.74
Si	12.63
Mo	01.34
K	00.32
Ca	00.89
Ti	00.72
Cr	06.86
Fe	11.49
Ni	32.84



Element	Wt %
O	28.35
Al	02.10
Si	10.46
Ca	01.51
Cr	05.16
Mn	00.33
Fe	19.98
Ni	32.11

Fig.7.11: Surface scale morphology and EDX analysis for superalloy Superfer 800 exposed to superheater of the coal fired boiler for 1500 hours at 700°C.

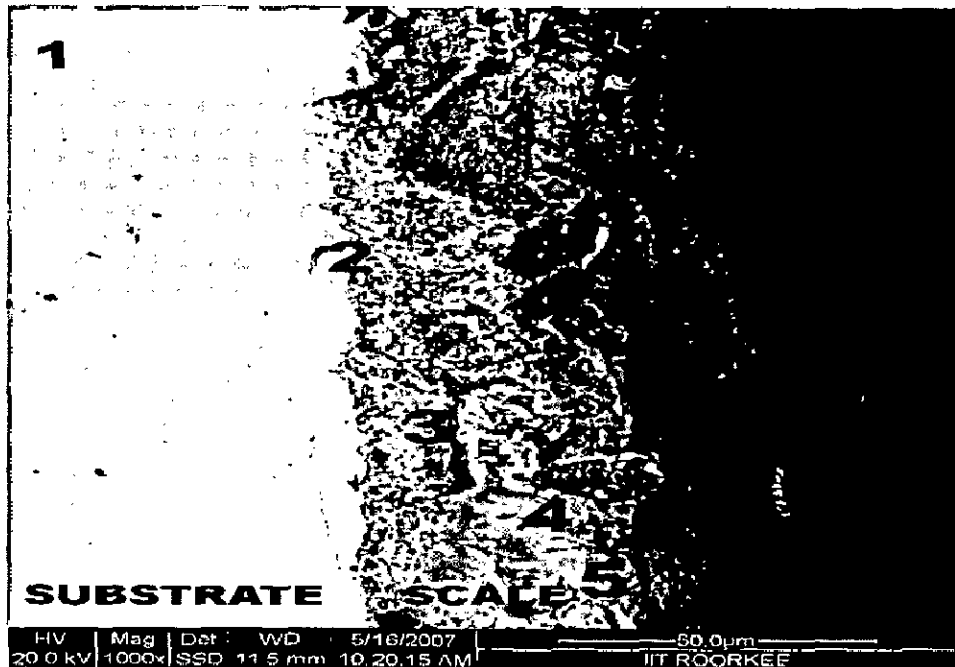
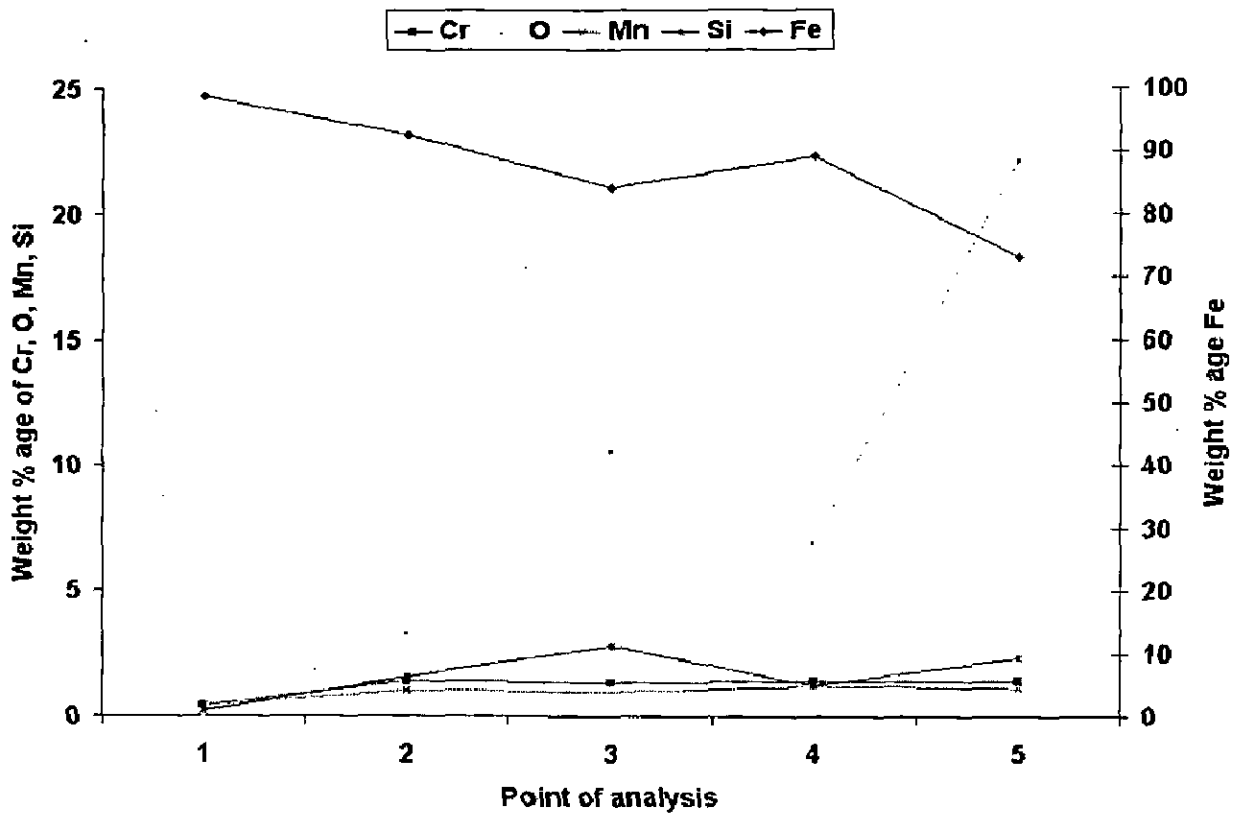


Fig. 7.12: Oxide scale morphology and elemental composition variation across the cross-section of T11 boiler steel exposed to superheater of the coal fired boiler for 1500 hours at 700°C

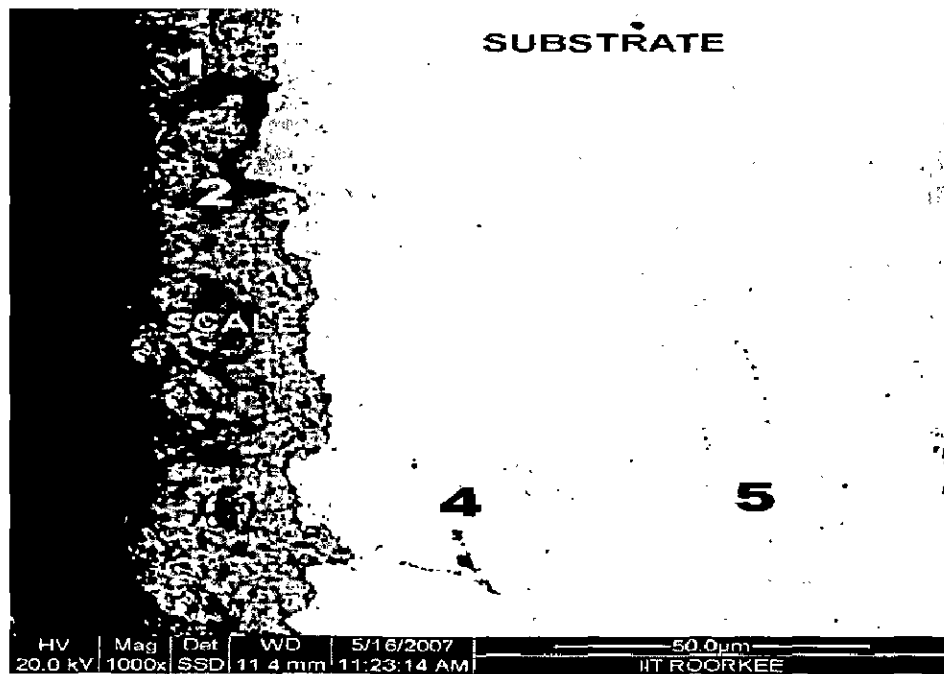
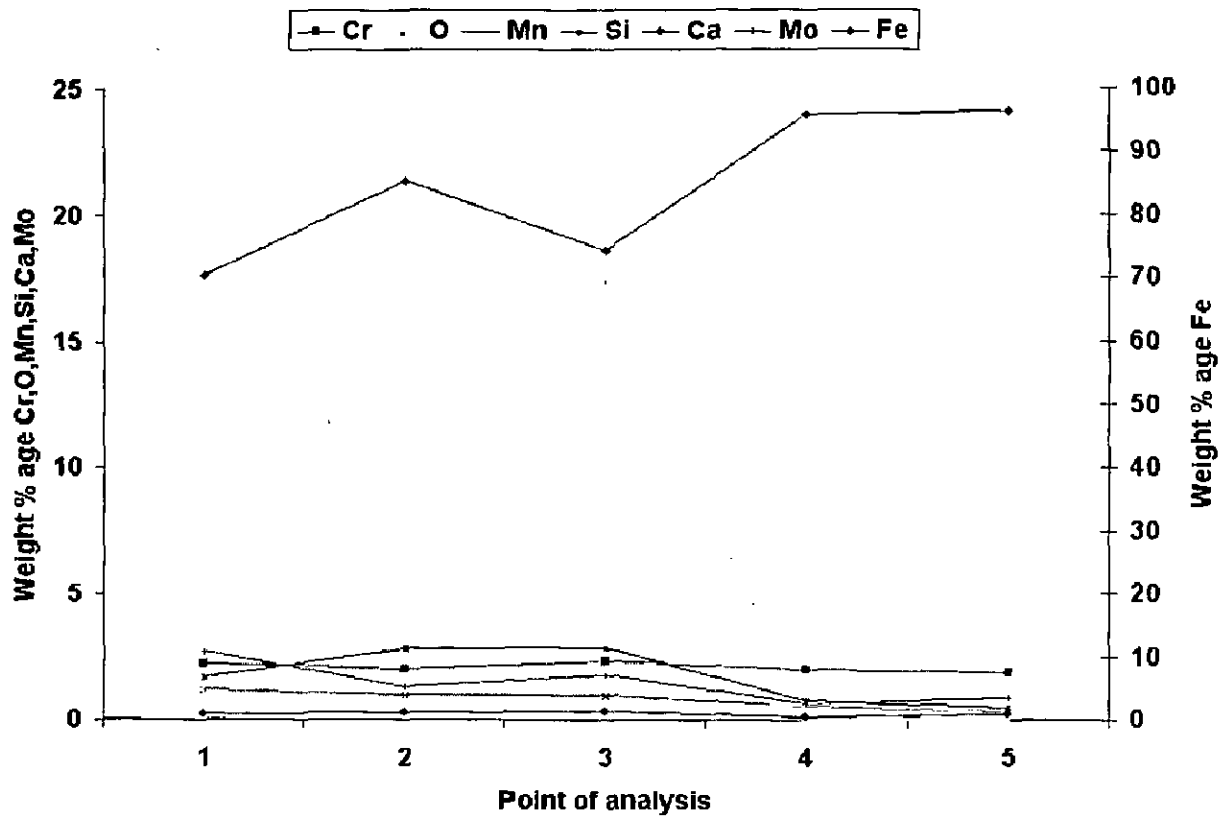


Fig. 7.13: Oxide scale morphology and elemental composition variation across the cross-section of T22 boiler steel exposed to superheater of the coal fired boiler for 1500 hours at 700°C.

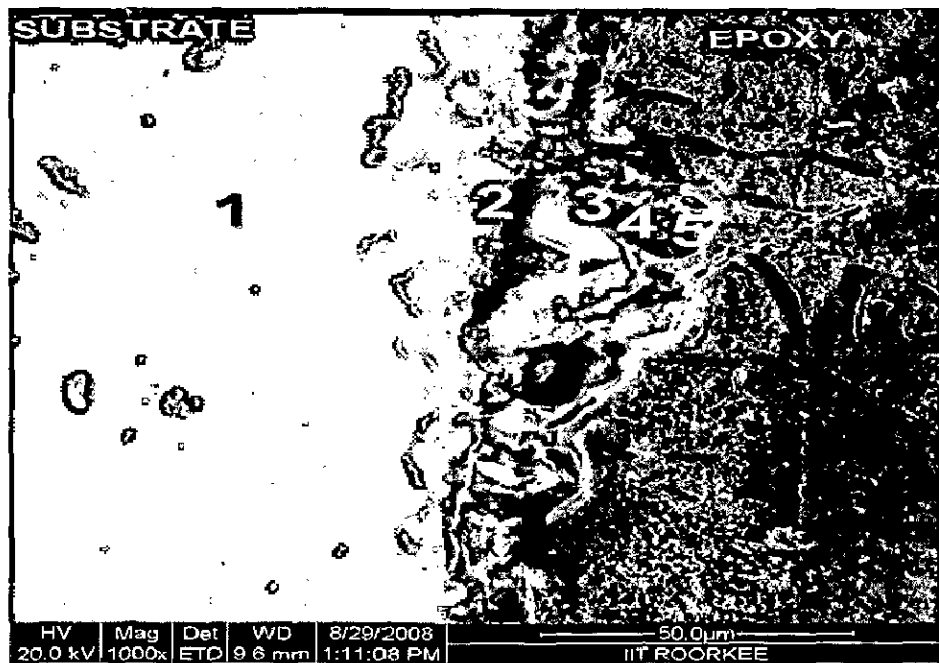
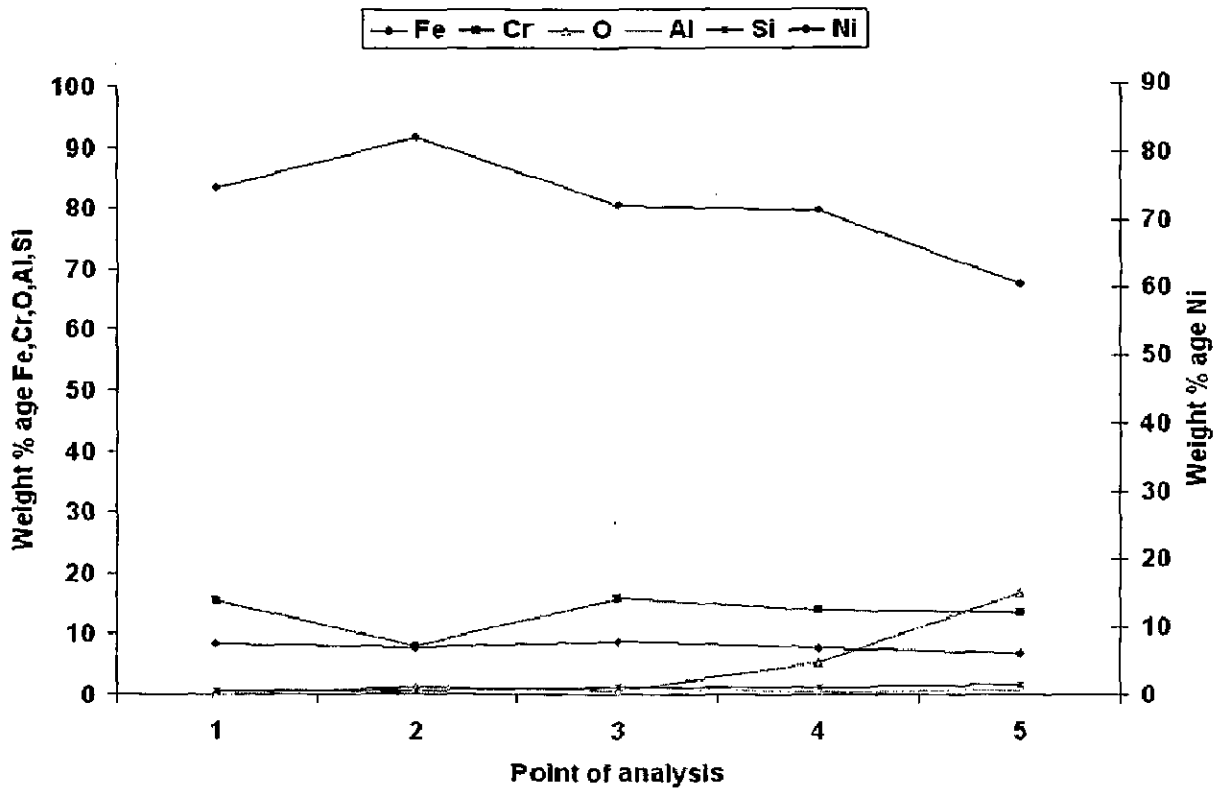


Fig. 7.14: Oxide scale morphology and elemental composition variation across the cross-section of Superni 600 superalloy exposed to superheater of the coal fired boiler for 1500 hours at 700°C.

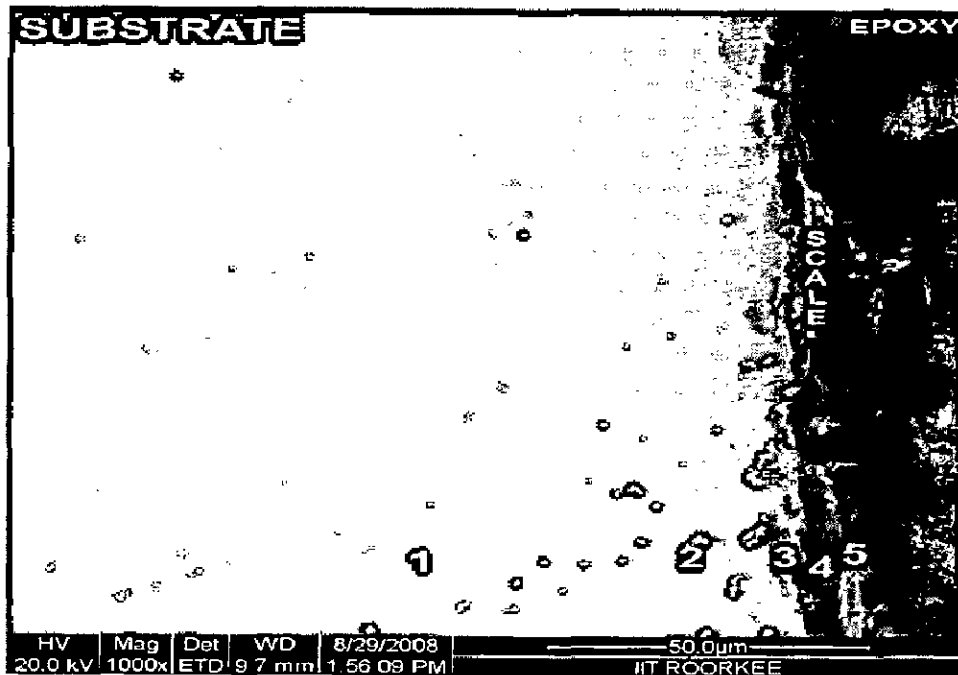
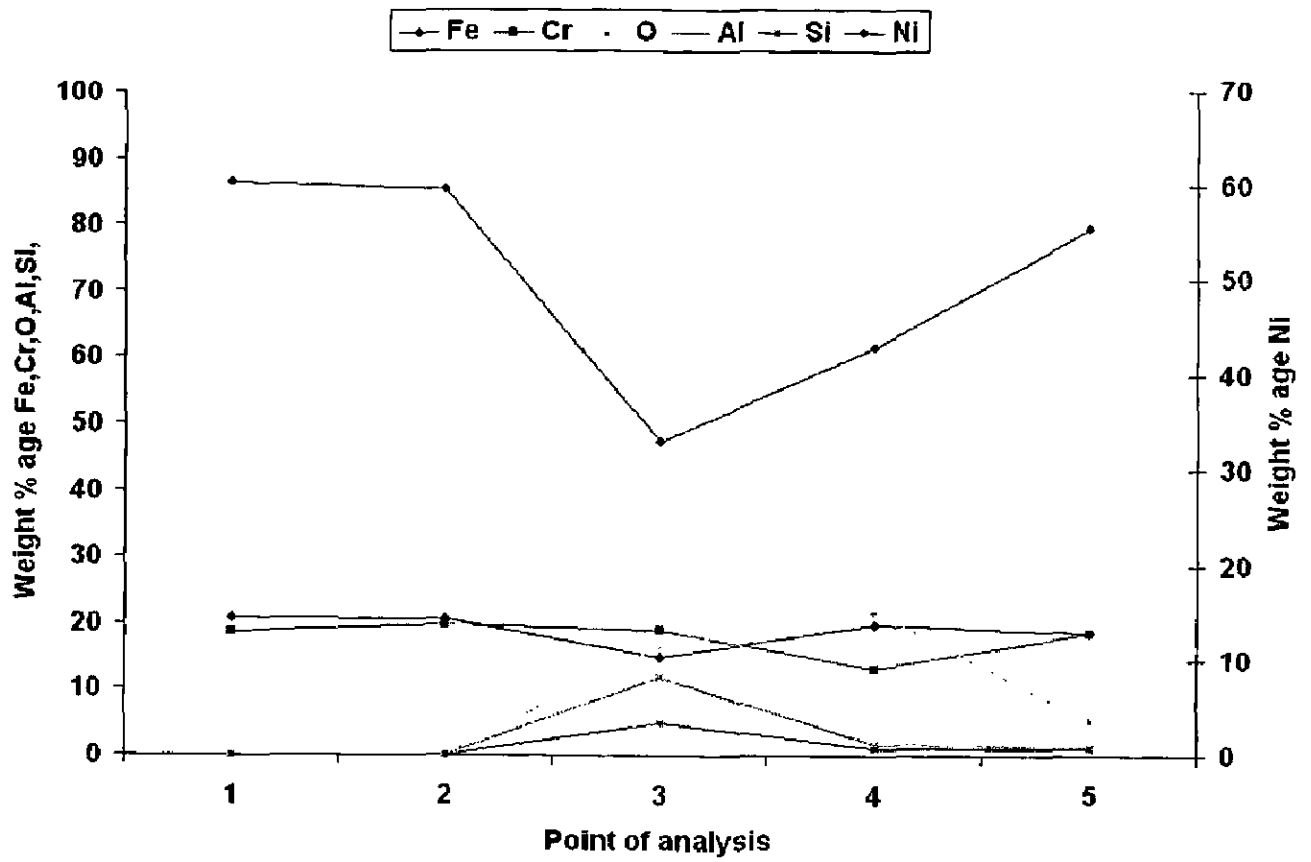


Fig. 7.15: Oxide scale morphology and elemental composition variation across the cross-section of Superni 718 superalloy exposed to superheater of the coal fired boiler for 1500 hours at 700°C

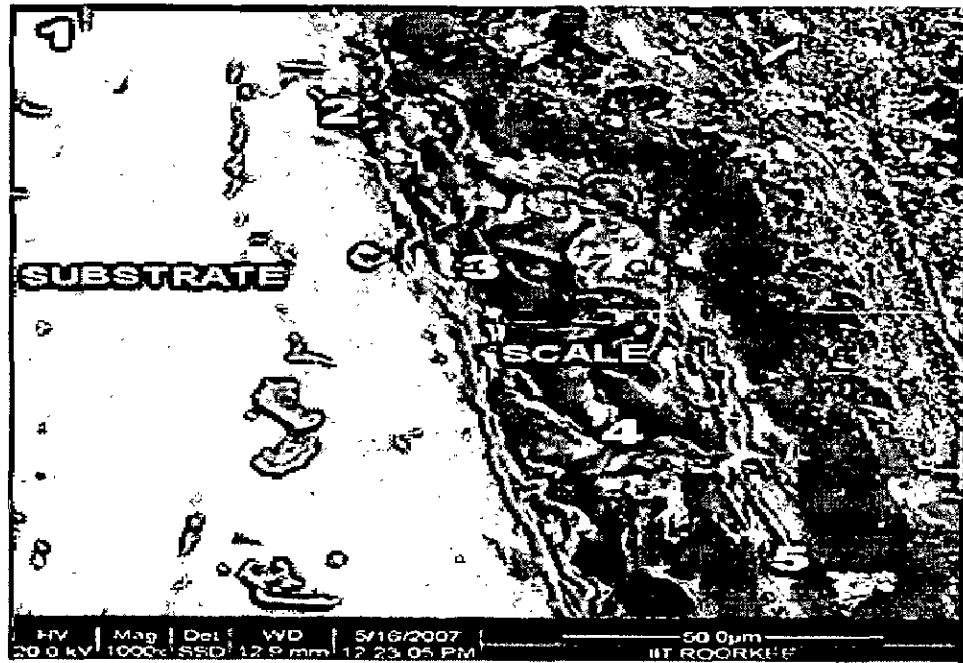
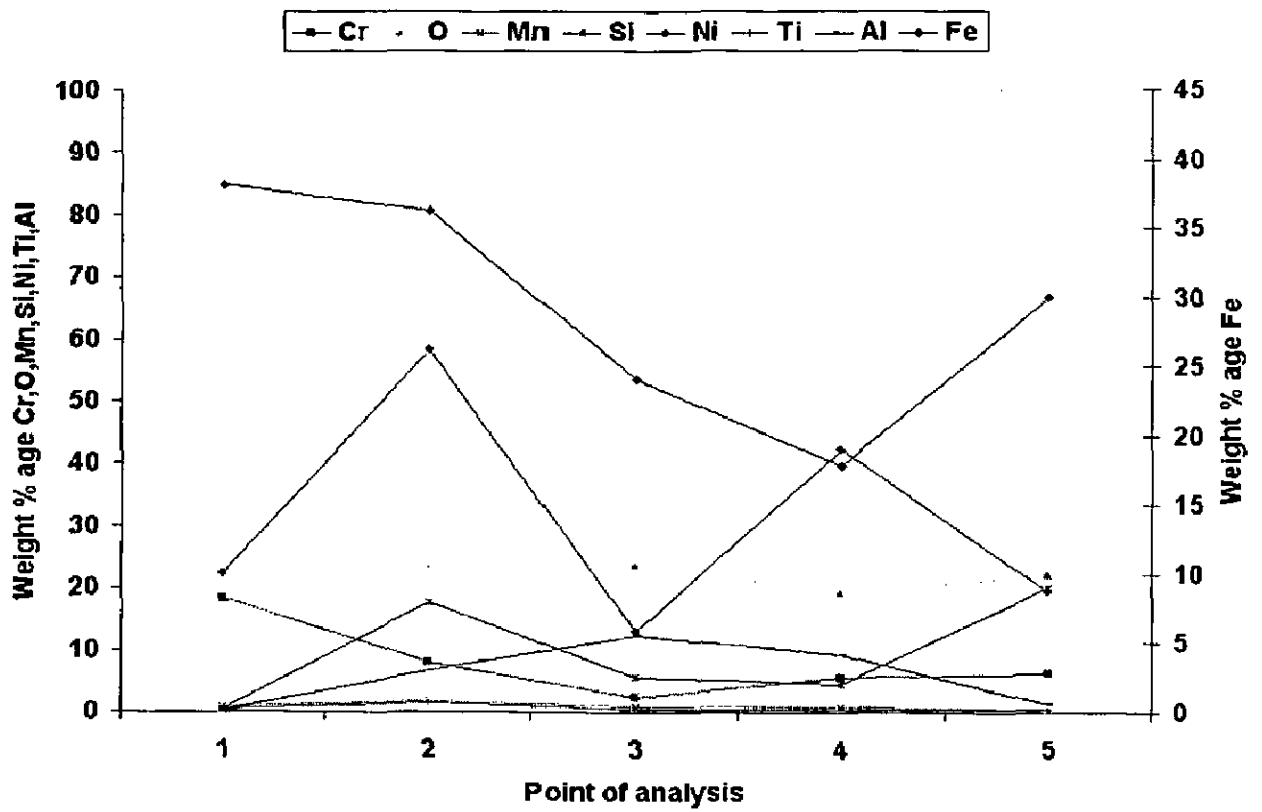


Fig. 7.16: Oxide scale morphology and elemental composition variation across the cross-section of Superfer 800 superalloy exposed to superheater of the coal fired boiler for 1500 hours at 700°C.

7. 1.2 Al₂O₃ - 3 wt% TiO₂ coated alloys

7.1.2.1 Visual Examination

The macrographs of Al₂O₃ - 3 wt% TiO₂ coated T11, T22, Superni 600, Superni 718 and Superfer 800 substrate alloys before and after 1500 hours exposure in the superheater area of coal fired boiler are shown in Fig.7.22. In the visual examination, it was observed that after the first cycle (100 hrs exposure) to the boiler environment, in Al₂O₃-3TiO₂ coated samples, the colour of the coatings changed from grey to cream as shown and with further cycles no appreciable change was observed. Coating remained intact throughout the study.

7.1.2.2 Weight Change and Thickness loss data

Weight change measurements were carried out after every cycle of 100 hrs exposure at 700°C in boiler conditions on Al₂O₃ - 3 wt% TiO₂ coated substrate alloys. The weight change consists of weight gain owing to the formation of the scale and weight loss due to solid particle erosion because of the suspected spalling and fluxing of the scale. The net weight change of the coated alloys in the given environment represents the combined effect of erosion and corrosion.

Weight change per unit area expressed in mg/cm² has been plotted as a function of time expressed in hours for Al₂O₃ - 3 wt% TiO₂ coated alloys and is shown in Fig. 7.23. All the coated alloys have shown increase in weight. The extent of erosion-corrosion has been measured in terms of thickness lost due to scaling and surface degradation after 1500 hours exposure. The thickness lost of the coating was 0.1548, 0.1279, 0.1319, 0.1361, 0.1981 mm in T11, T22, superni 600, superni 718 and superfer 800 respectively as indicated in Fig.7.24. The thickness is lost due to continuous impact of fly ash and other particles entrapped in the air blast. The corresponding degradation rates expressed in mills per year (mpy) are found to be 35.61, 29.42, 30.35, 31.31 and 45.57 for Al₂O₃ - 3 wt% TiO₂ coated T11, T 22, Superni 600, Superni 718 and Superfer 800 respectively.

7.1.2.3 X-ray Diffraction Analysis

The X-ray diffractograms for Al₂O₃ - 3 wt% TiO₂ coated T11, T22, Supemi 600, Superni 718 and Superfer 800 substrate alloys after exposure to actual boiler environment for 1500 hours are shown in Fig. 725.-7.27 respectively. The main constituent of the coated

samples are Al_2O_3 , Al_2TiO_5 , TiO_2 , SiO_2 , CaO and small fraction of Fe_2O_3 in few samples. Peaks of SiO_2 and CaO , is an indicative of fly ash on the surface of exposed alloys.

7.1.2.4 SEM/EDX Analysis

(a) Surface Morphology

Surface degradation and scale development and the effect of boiler conditions on the surface were studied using SEM/EDX analysis. The surface scale morphology and the EDX analysis for Al_2O_3 - 3 wt% TiO_2 coated alloys exposed to superheater region of coal fired boiler after 1500 hrs is shown in Fig.7.28 -7.32. From SEM/EDX analysis it has been revealed that the main constituents of scale are Al, Ti and Si along with oxygen. The presence of Si, Ca, Na, Mo and Fe along with oxygen, is an indication of embedded ash. There is a presence of pits and cracks on the surface and also hills and craters are formed which is a clear indication of combined effect of erosion and corrosion caused by combined action of flue gases and fly ash. There is no evidence of formation oxides from the substrate alloys though there is a presence of minor cracks on the surface and also there is an indication of erosion with the formation of hills and craters on the surface but these could not expose the surface of the substrate alloys and coating has protected the surface very well. This may be due to the fact that Al_2O_3 probably hinders the grain boundary diffusion of the elements. As a consequence, there is no oxide scale growth. The compact and protective Al_2O_3 layer separated the metal substrate from the boiler environment. As a result, the coating improved the hot corrosion resistance.

(b) Cross-Sectional Analysis and X ray mapping

The BSE image and the EDX analysis across the cross section on Al_2O_3 - 3 wt% TiO_2 coated alloys is shown in Fig.7.33 to Fig. 7.37. In all the coated alloys the coating was quite intact and there was no crack development in the coating. Throughout the coating thickness, the composition is entirely of Alumina and Titania.

Back scattered electron image of cross-section of coated substrate alloys (T11, T22, Superni 600, Superni 718 and Superfer 800) and corresponding X-ray mapping after 1500 hours exposure to boiler environment is shown in Fig.7.38 to 7.42 respectively. Ti is present in the form of thin streaks. Alumina coating is intact with all substrate alloys.

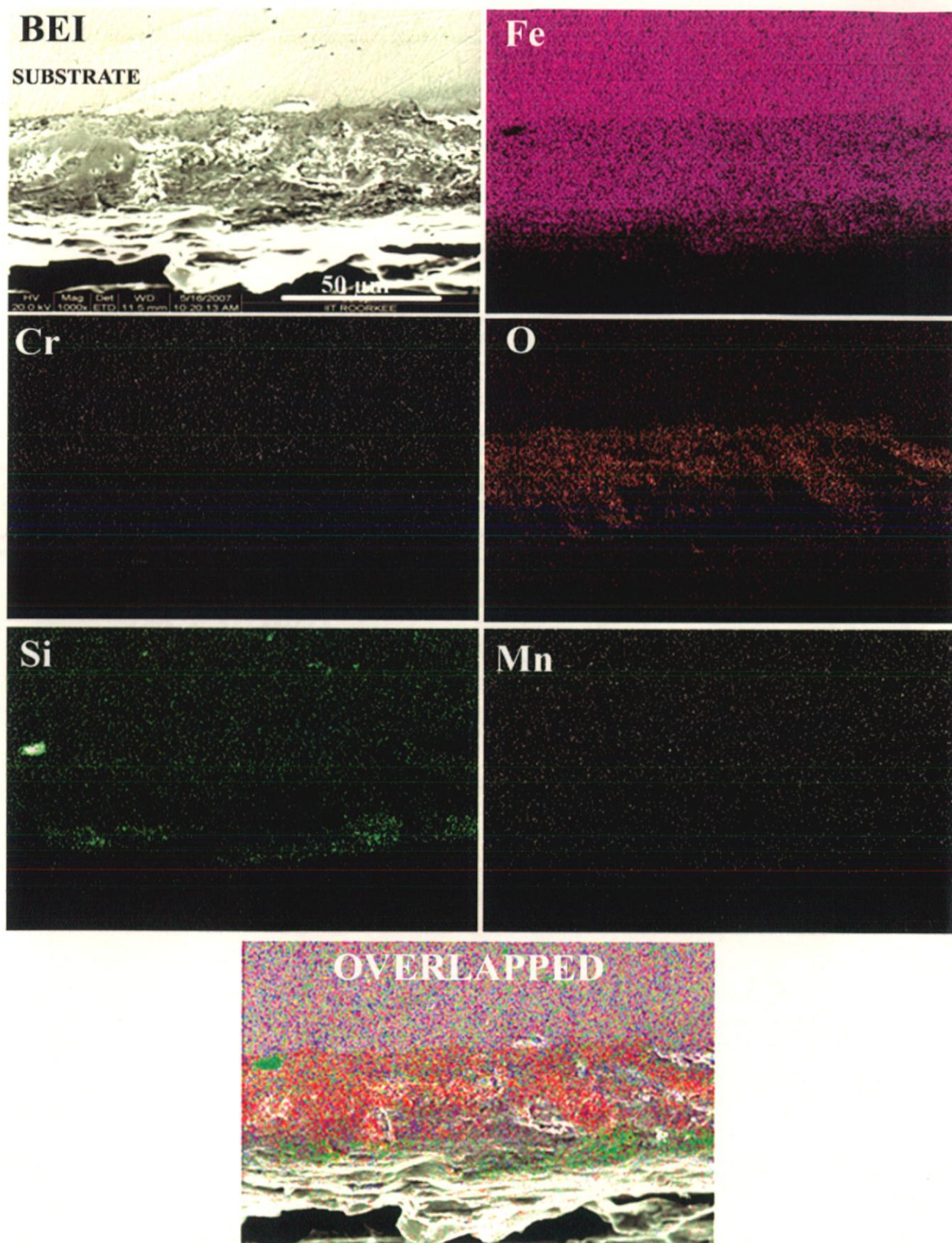


Fig. 7.17: Back scattered electron image and the corresponding x-ray mappings of cross section of uncoated T11 steel after 1500 hours exposure in boiler.

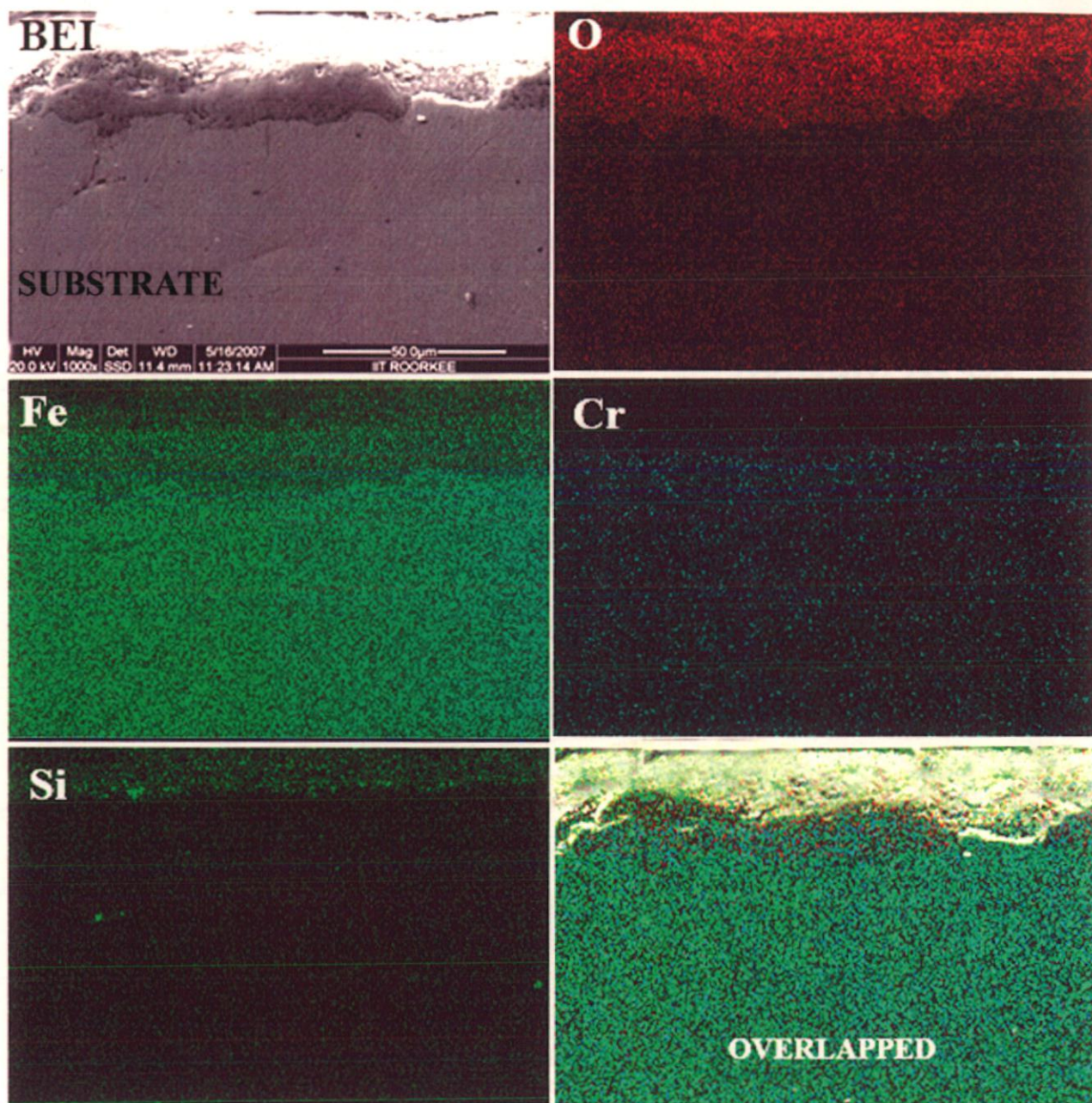


Fig. 7.18: Back scattered electron image and the corresponding x -ray mappings of cross section of uncoated T22 steel after 1500 hours exposure in boiler.

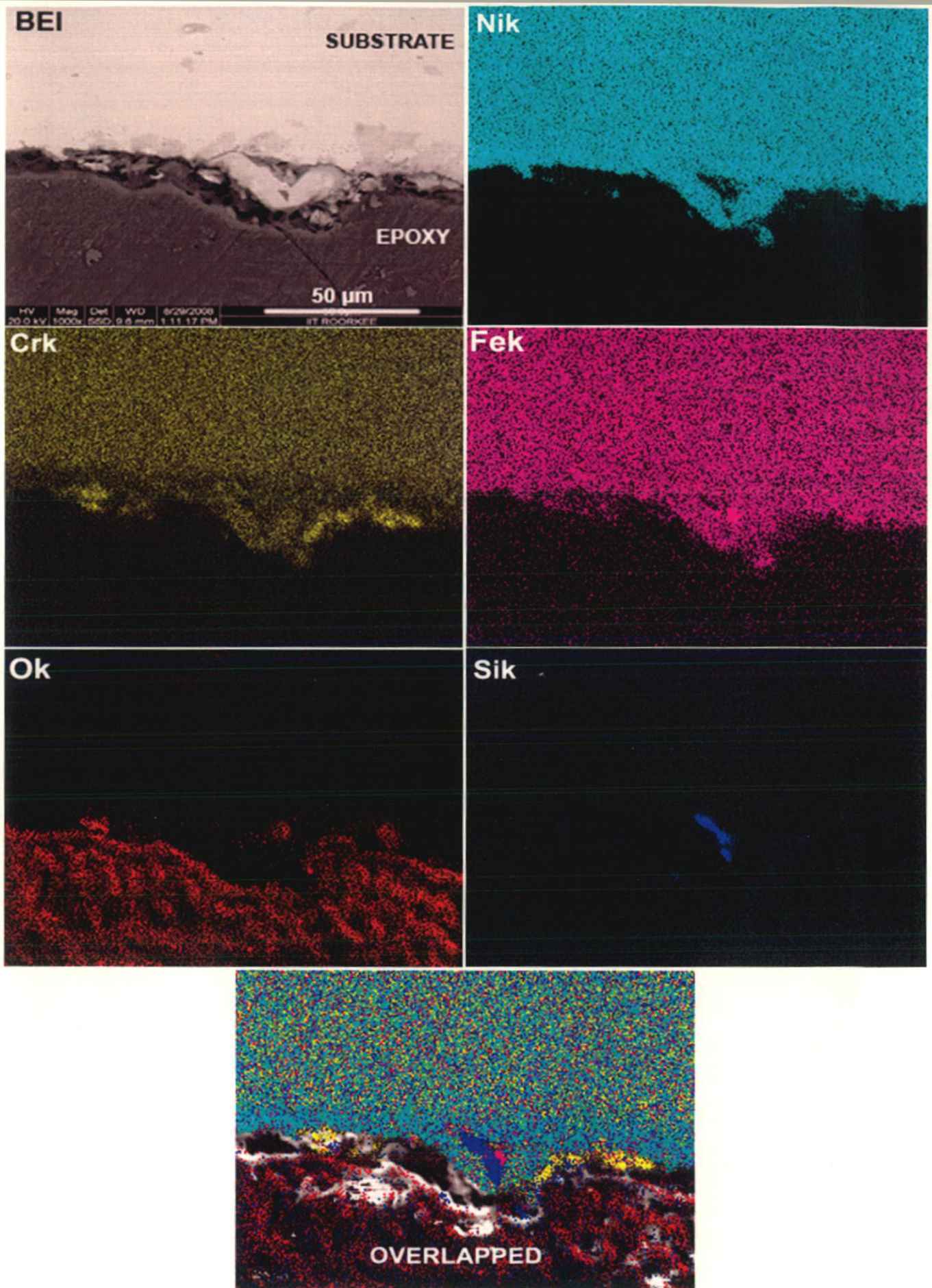


Fig. 7.19: Back scattered electron image and the corresponding x -ray mappings of cross section of uncoated superalloy Superni 600 after 1500 hours exposure in boiler.

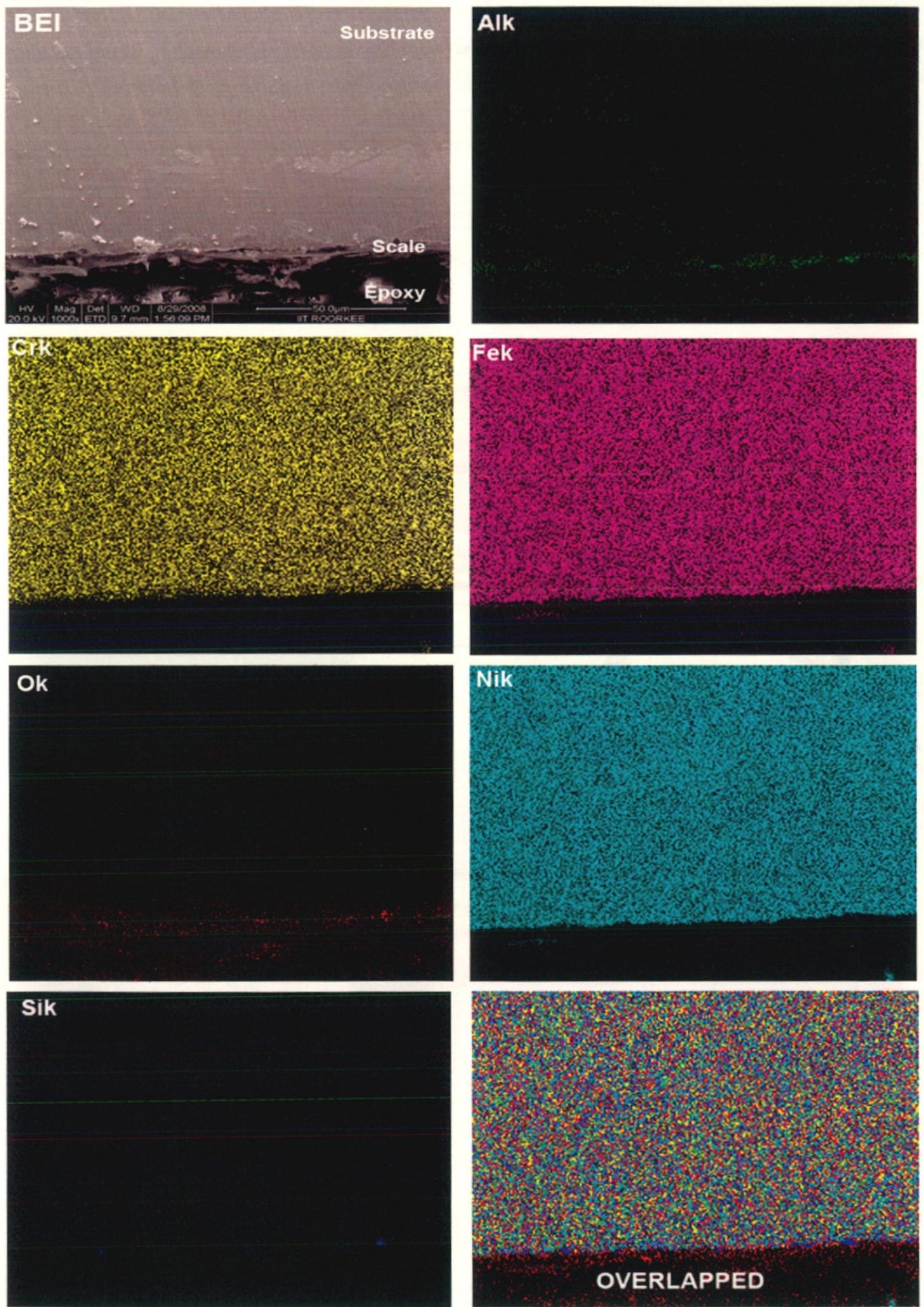


Fig. 7.20: Back scattered electron image and the corresponding x -ray mappings of cross section of uncoated superalloy Superni 718 after 1500 hours exposure in boiler.

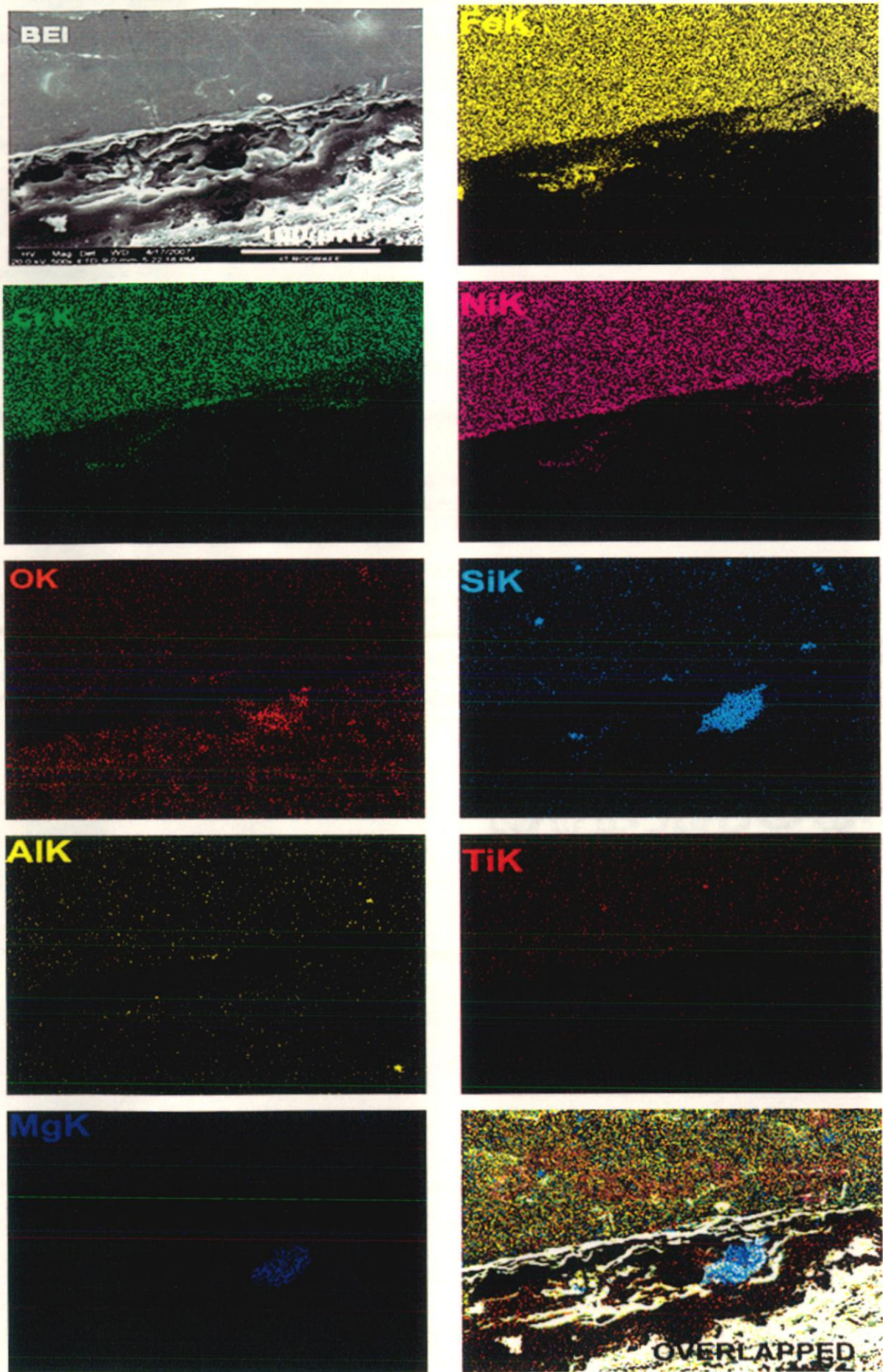
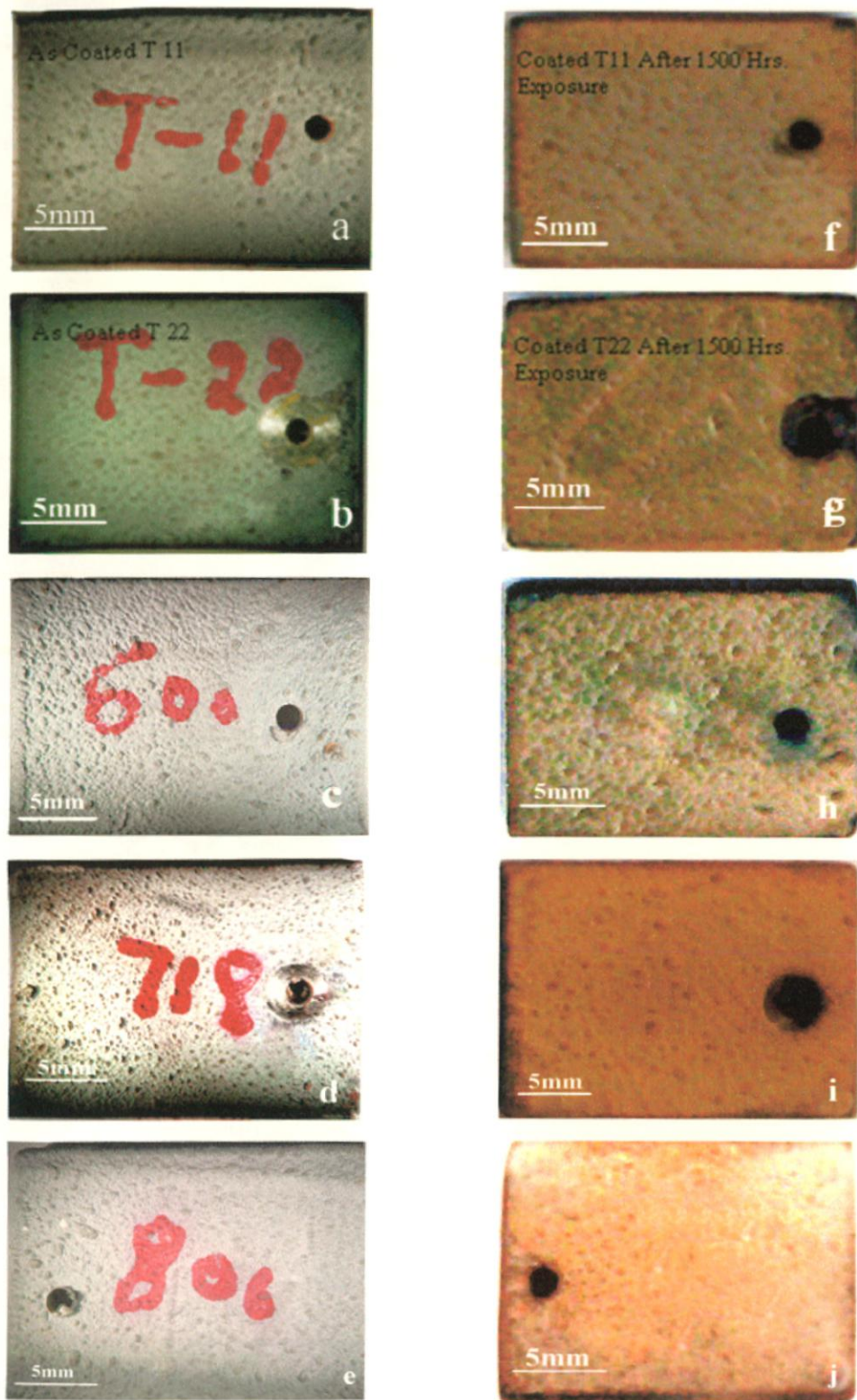


Fig. 7.21: Back scattered electron image and the corresponding x -ray mappings of cross section of uncoated superalloy Superfer 800 after 1500 hours exposure in boiler.



Samples before exposure to boiler environment

Samples after 1500 hours exposure to boiler environment

Fig.7.22: Macrographs of $\text{Al}_2\text{O}_3\text{-3wt\%TiO}_2$ coated substrate alloys before and after 1500 hours exposure to boiler environment:
 (a) T11 (b) T22 (c) Superni 600 (d) Superni718 (e) Superfer 800 (f) T11 after 1500 Hrs Exposure (g) T22 after 1500 Hrs Exposure (h) Superni 600 after 1500 Hrs Exposure (i) Superni 718 after 1500 Hrs Exposure (j) Superfer 800 after 1500 Hrs Exposure

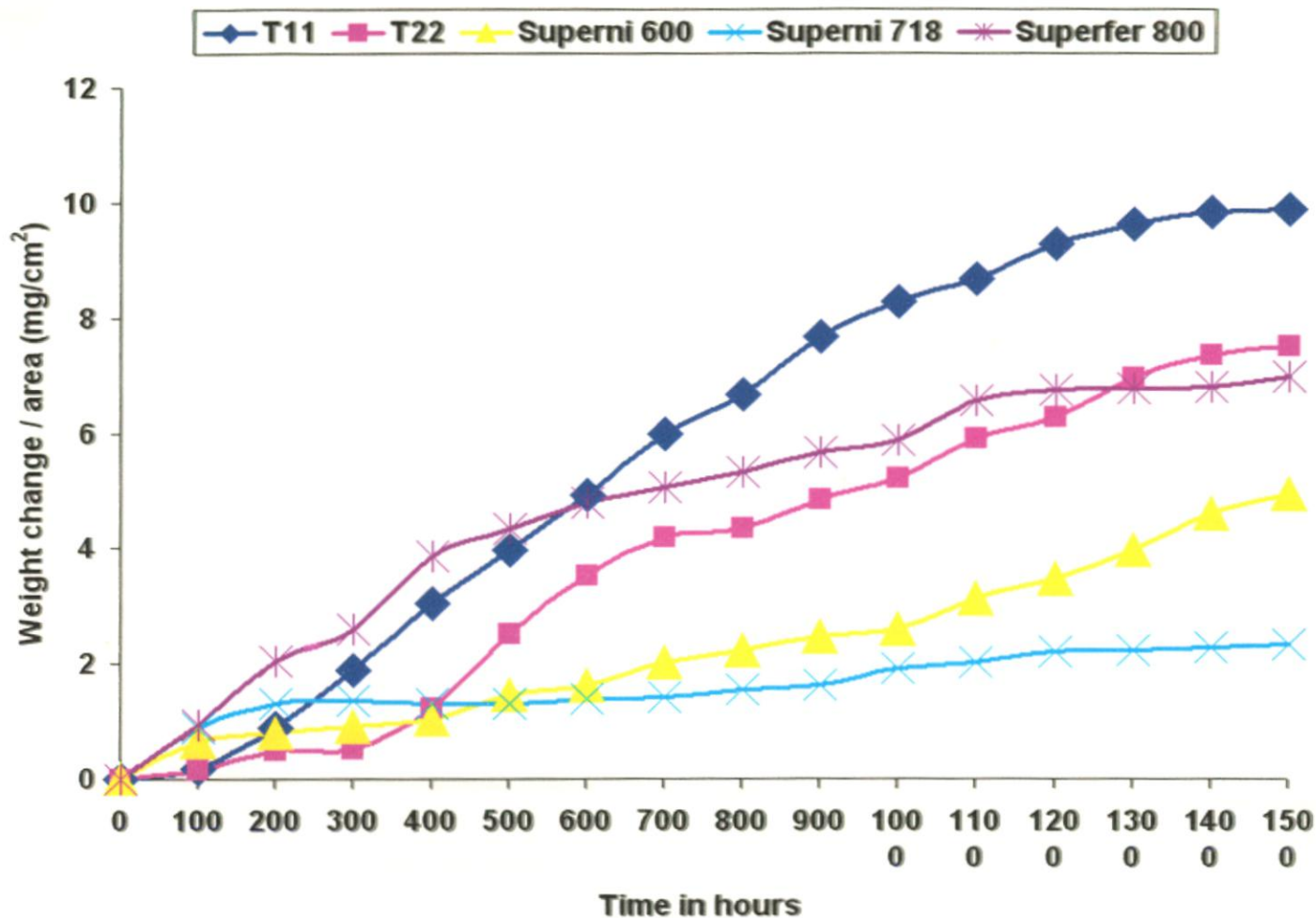


Fig.7.23: Weight change plot for $\text{Al}_2\text{O}_3\text{-3wt\%TiO}_2$ coated alloys exposed to platen superheater of the coal fired boiler for 1500 hours at 700°C .

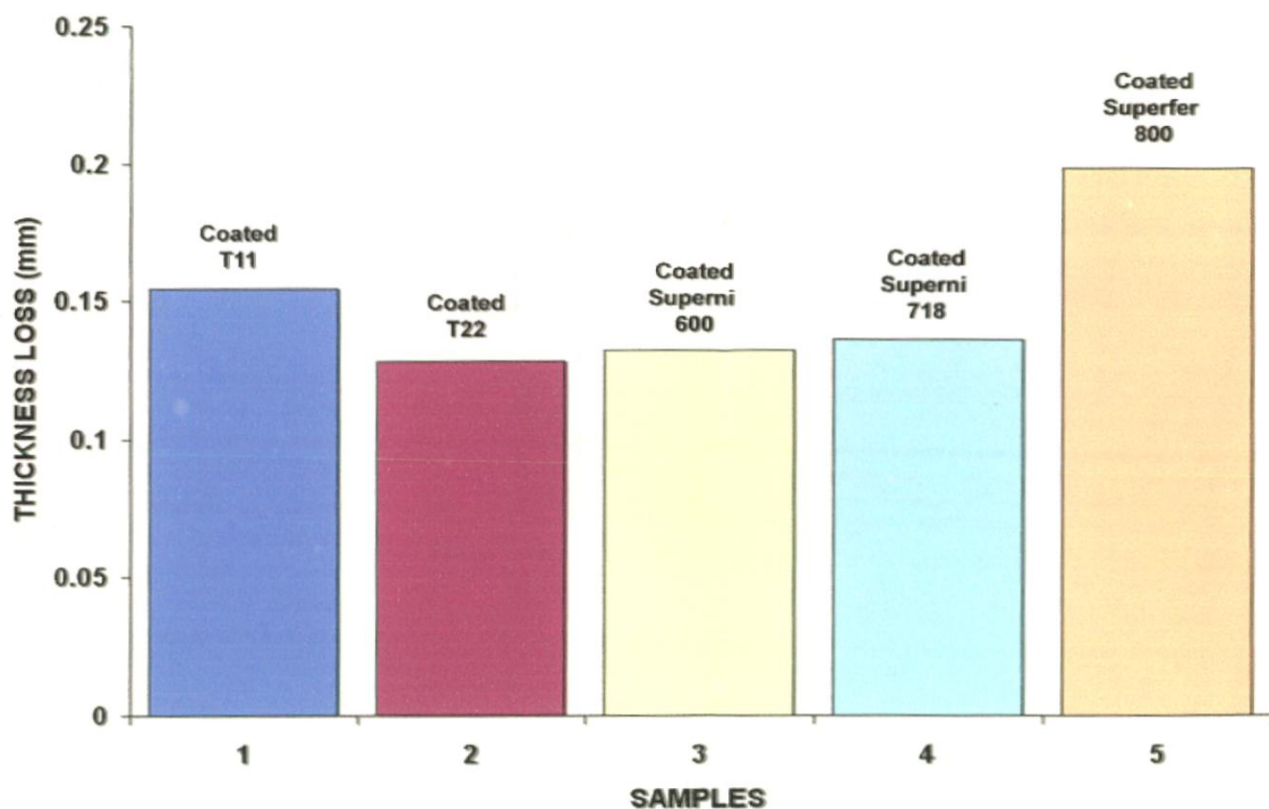
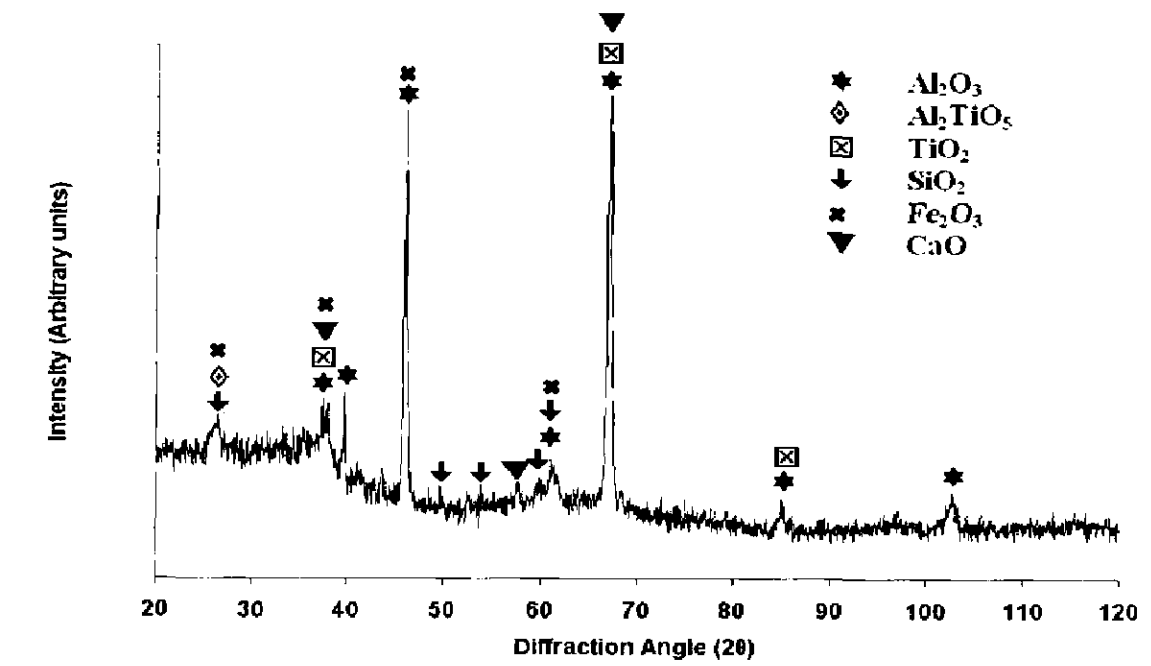
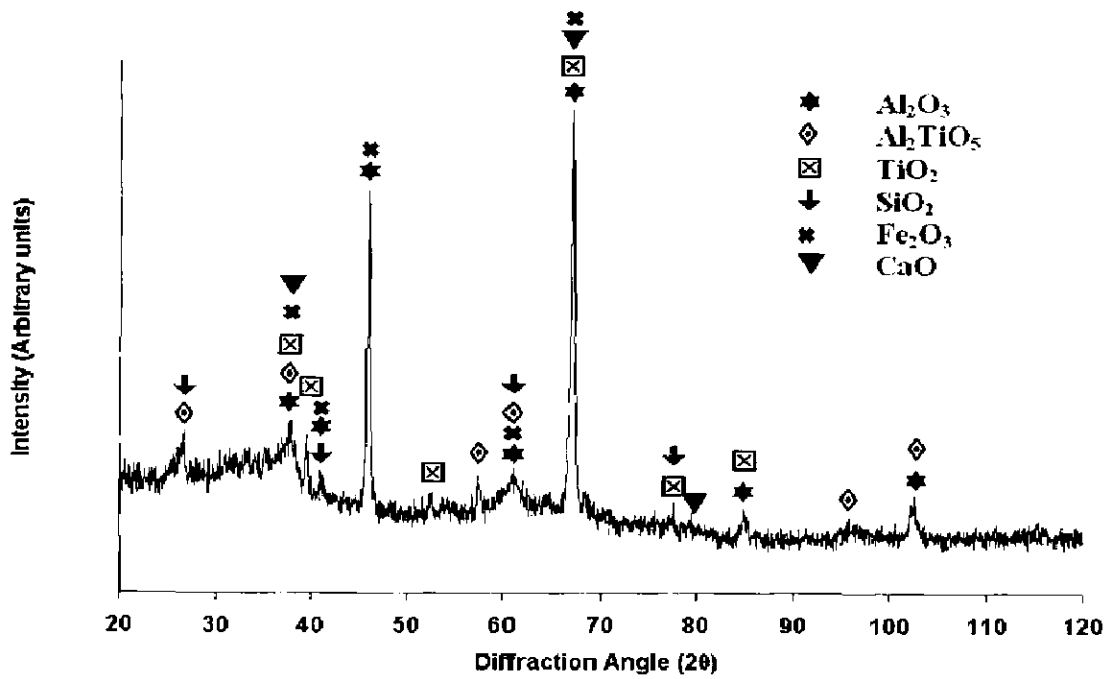


Fig.7.24: Bar chart indicating the thickness lost in mm by the $\text{Al}_2\text{O}_3\text{-3 wt\% TiO}_2$ coated alloys after 1500 hours exposure to the coal fired boiler at 700°C .

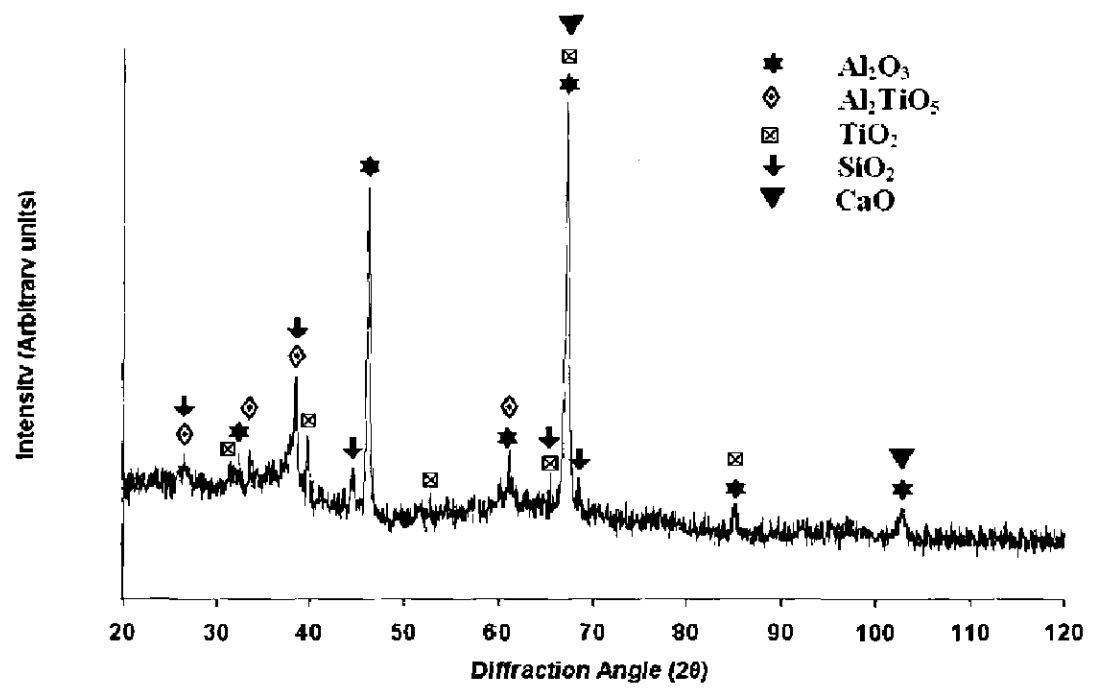


(a)

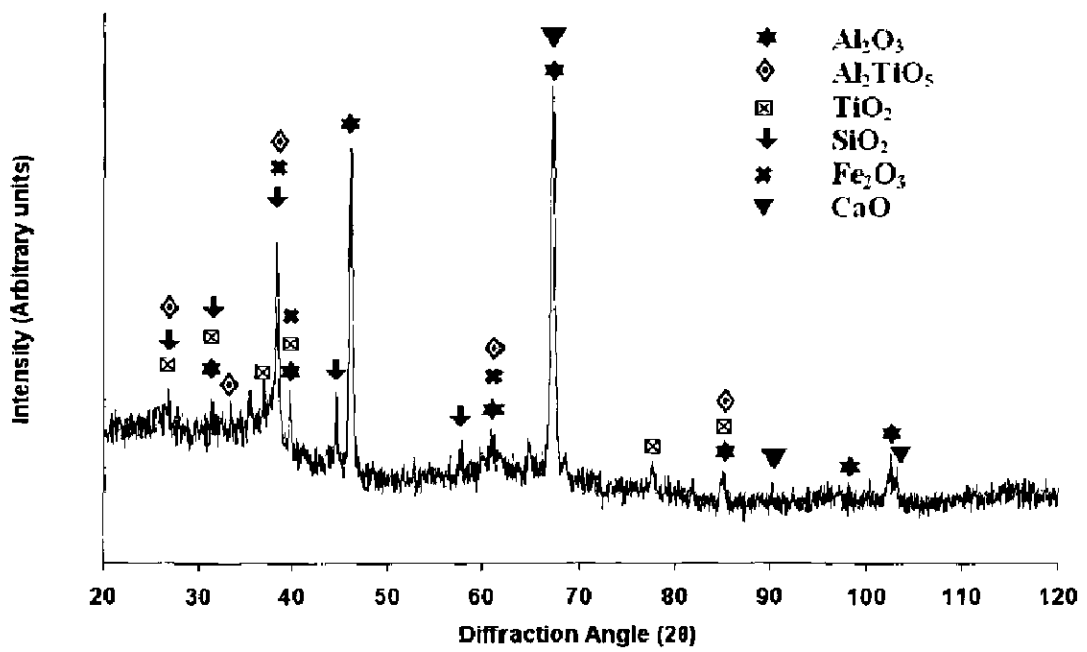


(b)

Fig. 7.25: X-ray diffraction profiles for Al_2O_3 -3 wt% TiO_2 coated boiler steels exposed to superheater of the coal fired boiler for 1500 hours at 700°C
 (a) T11 (b) T22



(a)



(b)

Fig. 7.26: X-ray diffraction profiles for Al_2O_3 -3 wt% TiO_2 coated superalloys exposed to superheater of the coal fired boiler for 1500 hours at 700°C
 (a) Superni 600 (b) Superni 718

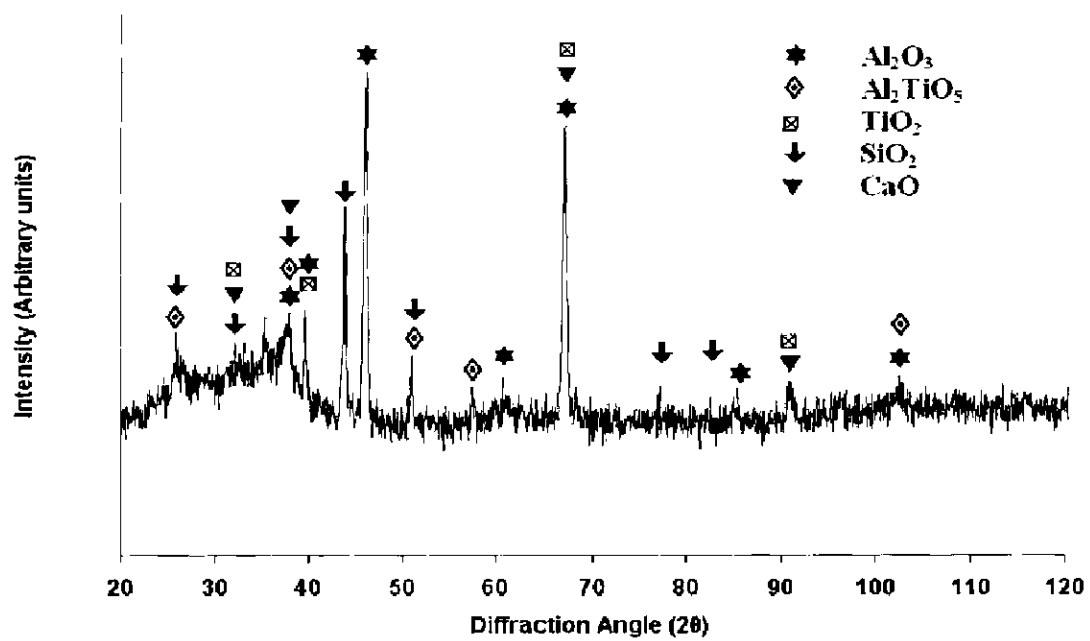
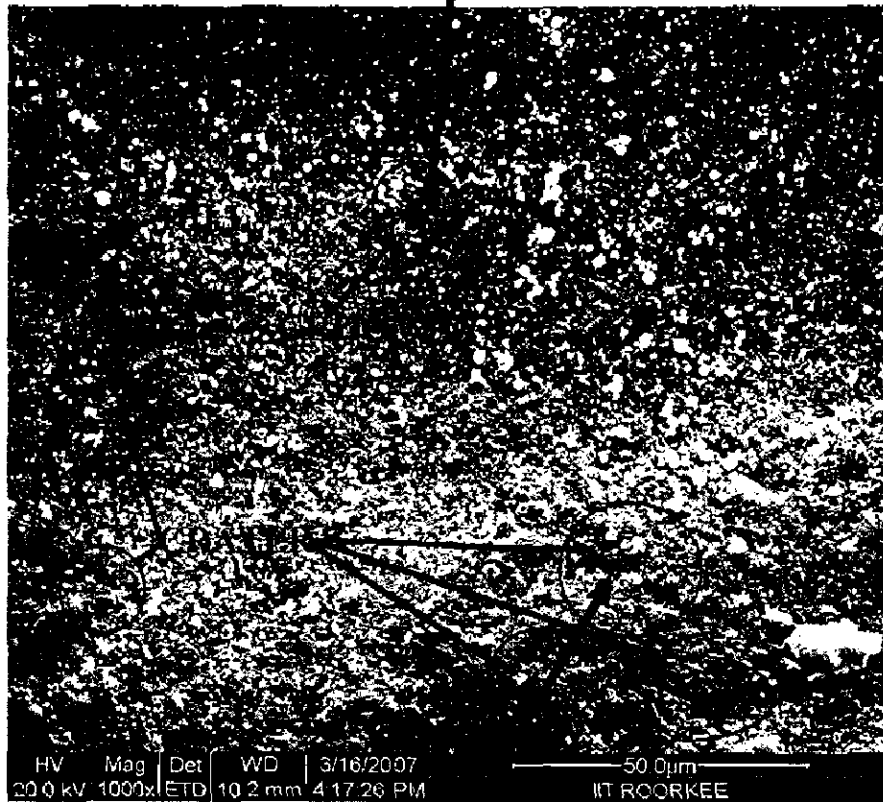


Fig. 7.27: X-ray diffraction profiles for Al₂O₃-3 wt% TiO₂ coated superalloy Superfer 800 exposed to superheater of the coal fired boiler for 1500 hours at 700°C

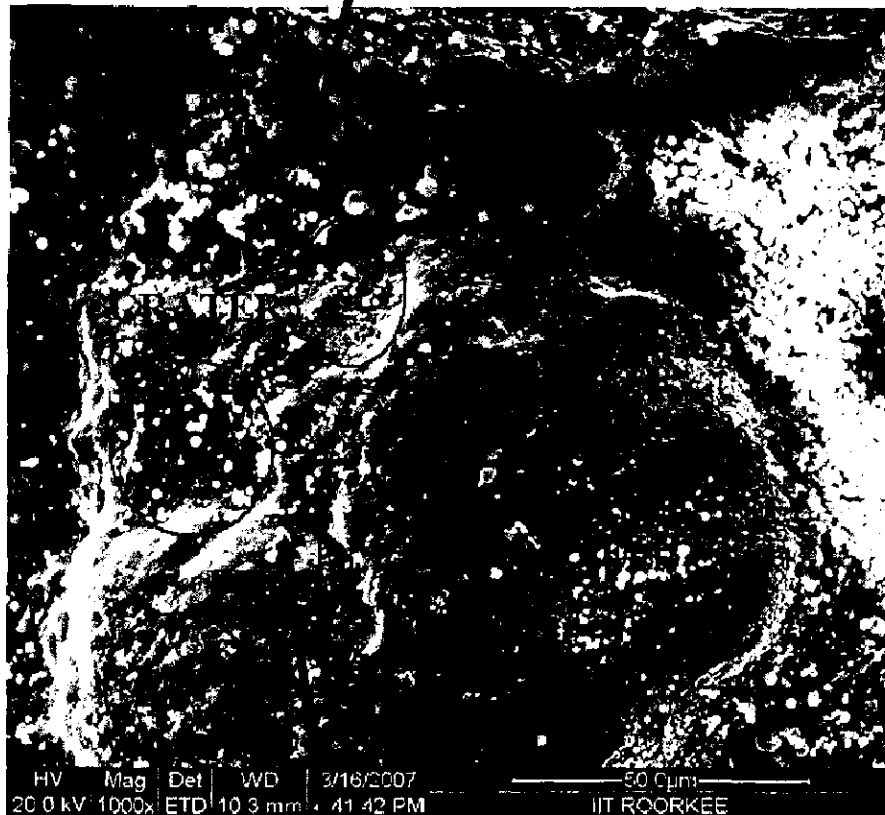
Element	Wt %
O	39.65
Zn	02.16
Al	29.97
Si	18.66
Mo	03.87
K	00.87
Sb	00.18
Ca	01.89
Ti	02.75



Element	Wt %
O	40.69
Al	26.74
Si	24.40
Ca	04.73
In	01.37
Ti	02.07

Fig.7.28: Surface scale morphology and EDX analysis for $\text{Al}_2\text{O}_3\text{-3\%TiO}_2$ coated boiler steel T11 exposed to superheater of the coal fired boiler for 1500 hours at 700°C .

Element	Wt %
O	37.33
Mg	00.83
Al	29.98
Si	27.73
K	00.74
Ti	01.72
Fe	01.67



Element	Wt %
O	36.84
Al	39.34
Na	02.22
Si	10.85
P	03.63
Nb	04.57
Ti	02.55

Fig.7.29: Surface scale morphology and EDX analysis for Al₂O₃-3%TiO₂ coated boiler steel T22 exposed to superheater of the coal fired boiler for 1500 hours at 700°C.

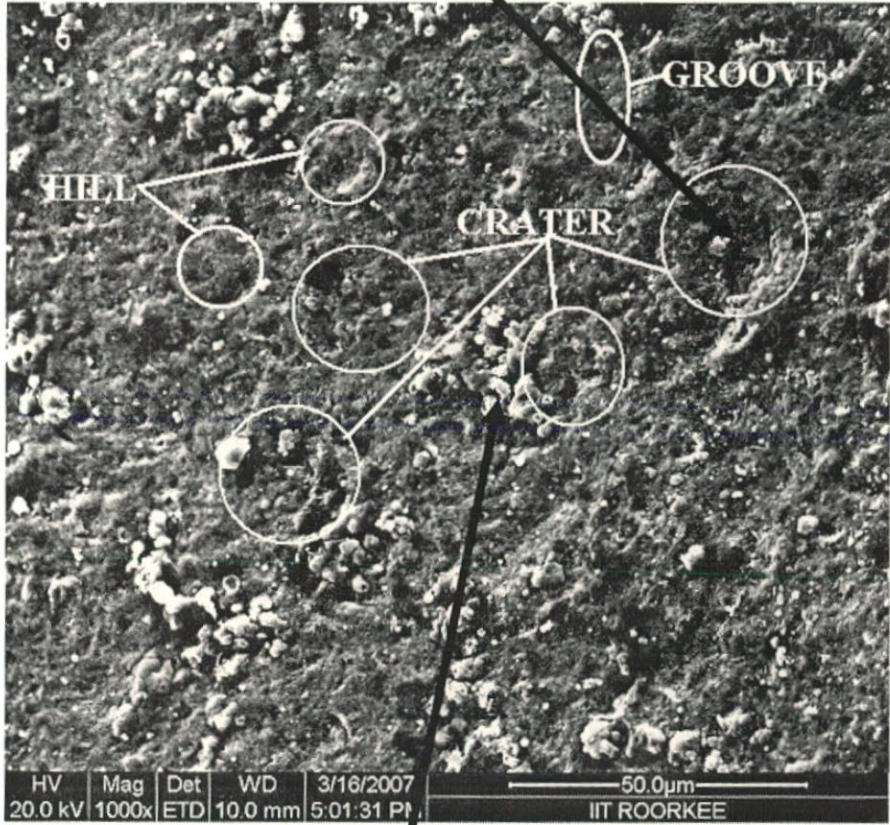
Element	Wt %
O	36.22
Al	32.13
Si	24.23
Ca	02.08
Ti	03.11
Fe	02.23



Element	Wt %
O	39.63
Al	28.81
Si	22.52
Mo	02.09
Ca	02.89
Ti	01.95
Fe	02.11

Fig.7.30: Surface scale morphology and EDX analysis for $\text{Al}_2\text{O}_3\text{-3\%TiO}_2$ coated superalloy Superni 600 exposed to superheater of the coal fired boiler for 1500 hours at 700°C.

Element	Wt %
O	29.37
Al	40.85
Si	25.58
Ca	02.47
Cr	01.08
Mn	00.24
Y	00.41



Element	Wt %
O	40.83
Al	34.73
Si	18.10
Ti	03.17
Ca	02.05
Ag	01.12

Fig.7.31: Surface scale morphology and EDX analysis for $Al_2O_3-3\%TiO_2$ coated superalloy Superni 718 exposed to superheater of the coal fired boiler for 1500 hours at 700°C.

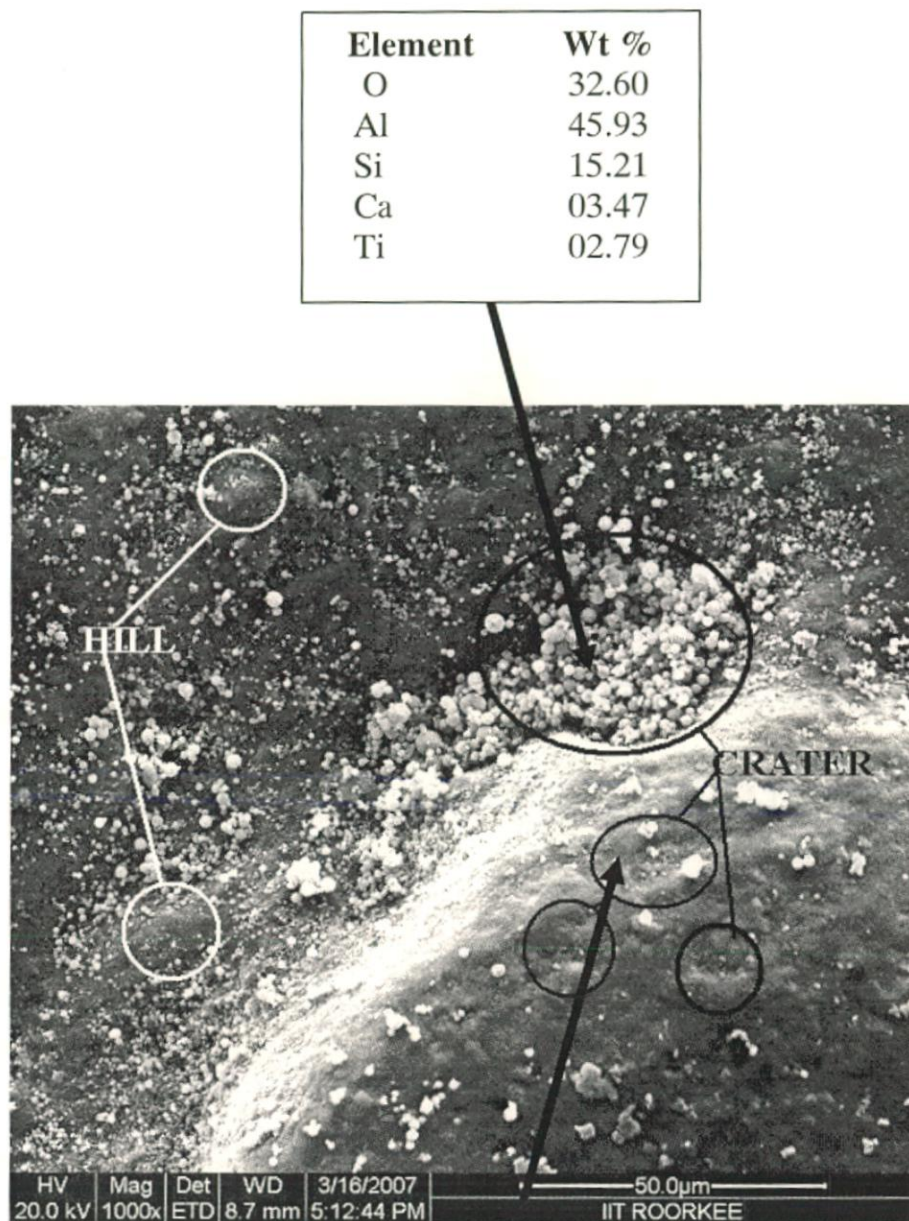


Fig.7.32: Surface scale morphology and EDX analysis for $\text{Al}_2\text{O}_3\text{-3\%TiO}_2$ coated superalloy Superfer 800 exposed to superheater of the coal fired boiler for 1500 hours at 700°C .

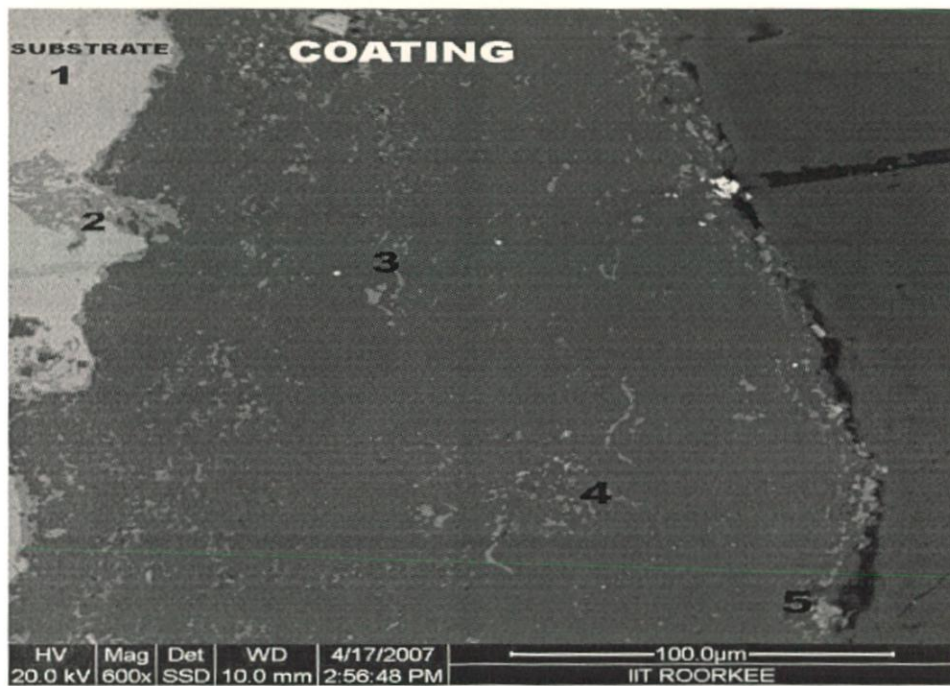
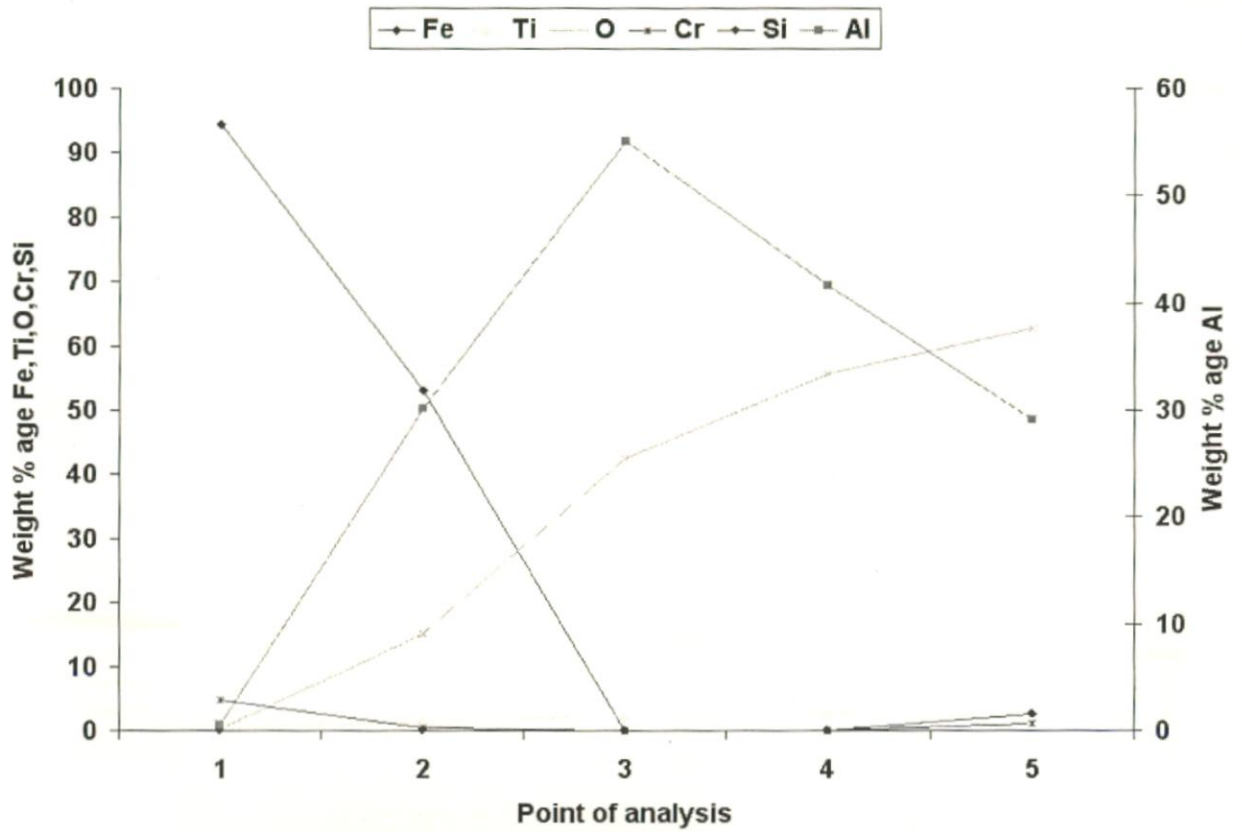


Fig. 7.33: Cross sectional morphology and elemental composition variation across the cross-section of Al_2O_3 -3 wt% TiO_2 coated T11 boiler steels exposed to superheater of the coal fired boiler for 1500 hours at 700°C.

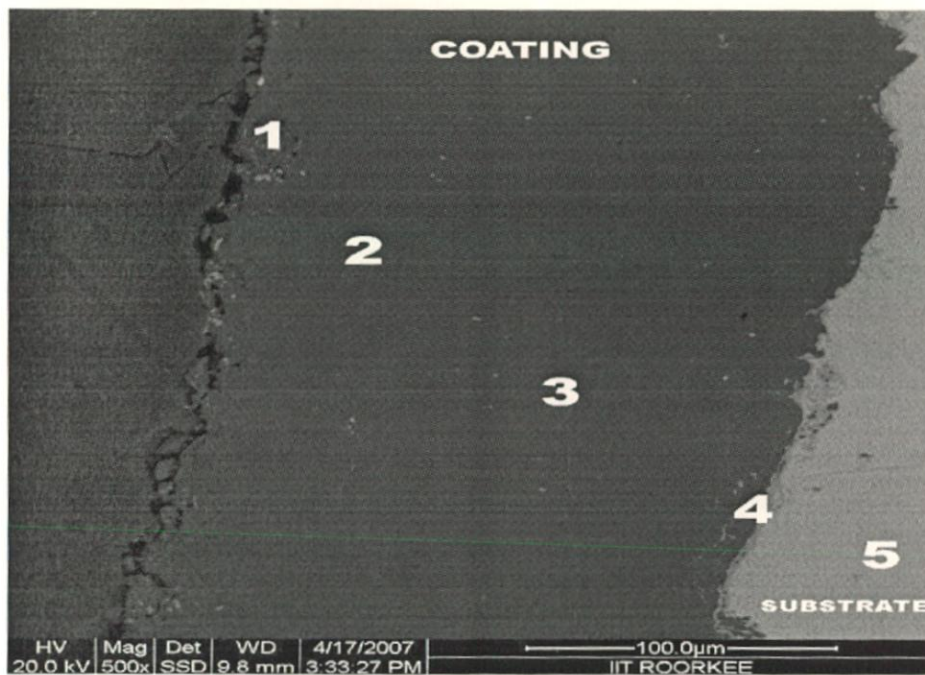
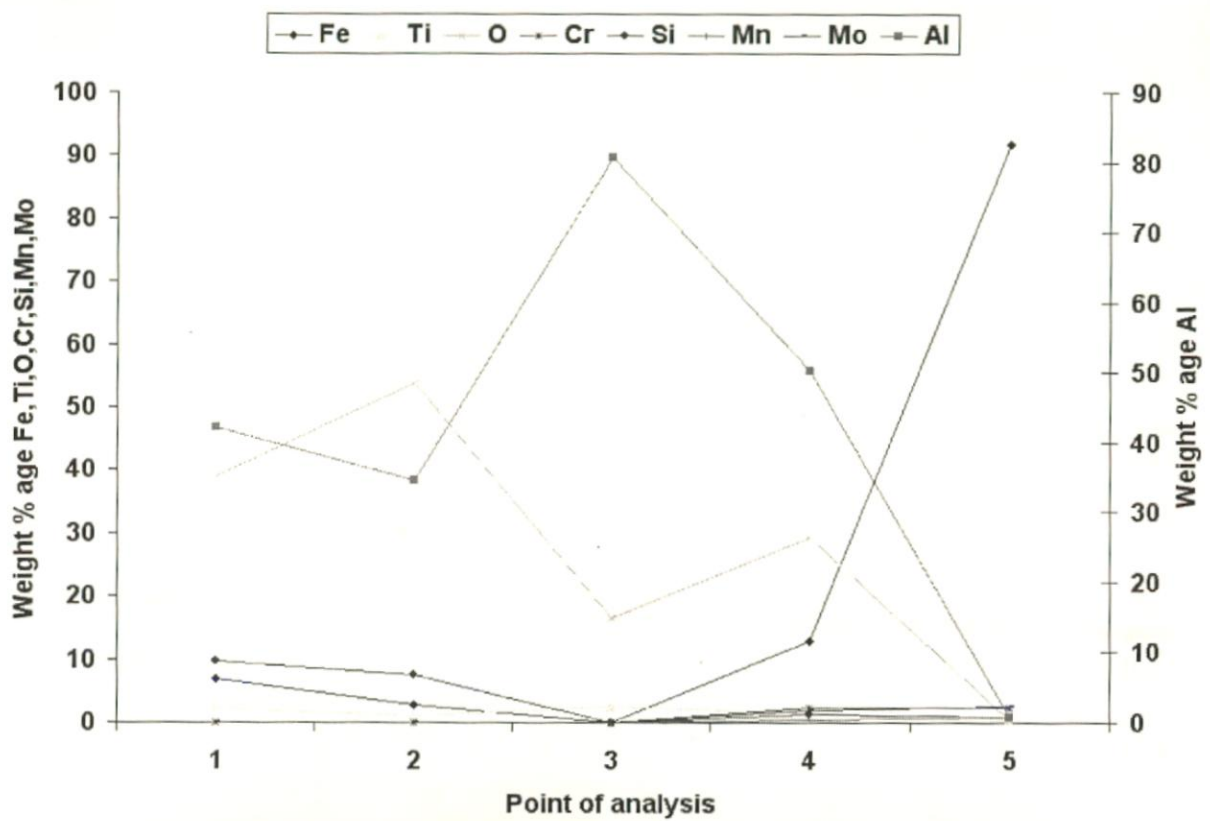


Fig. 7.34: Cross sectional morphology and elemental composition variation across the cross-section of Al_2O_3 -3 wt% TiO_2 coated T22 boiler steel exposed to superheater of the coal fired boiler for 1500 hours at 700°C.

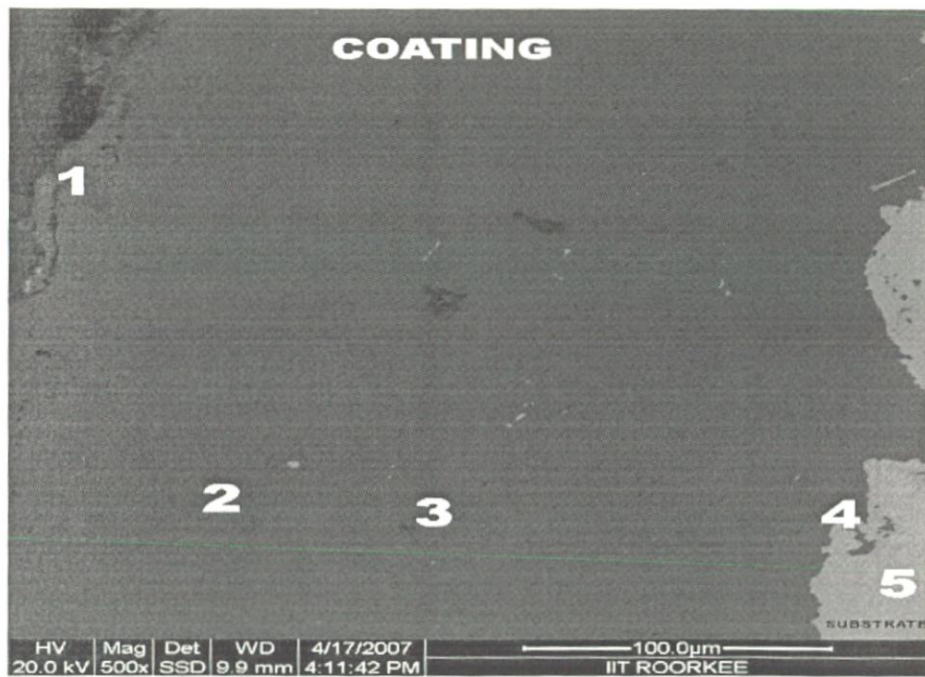
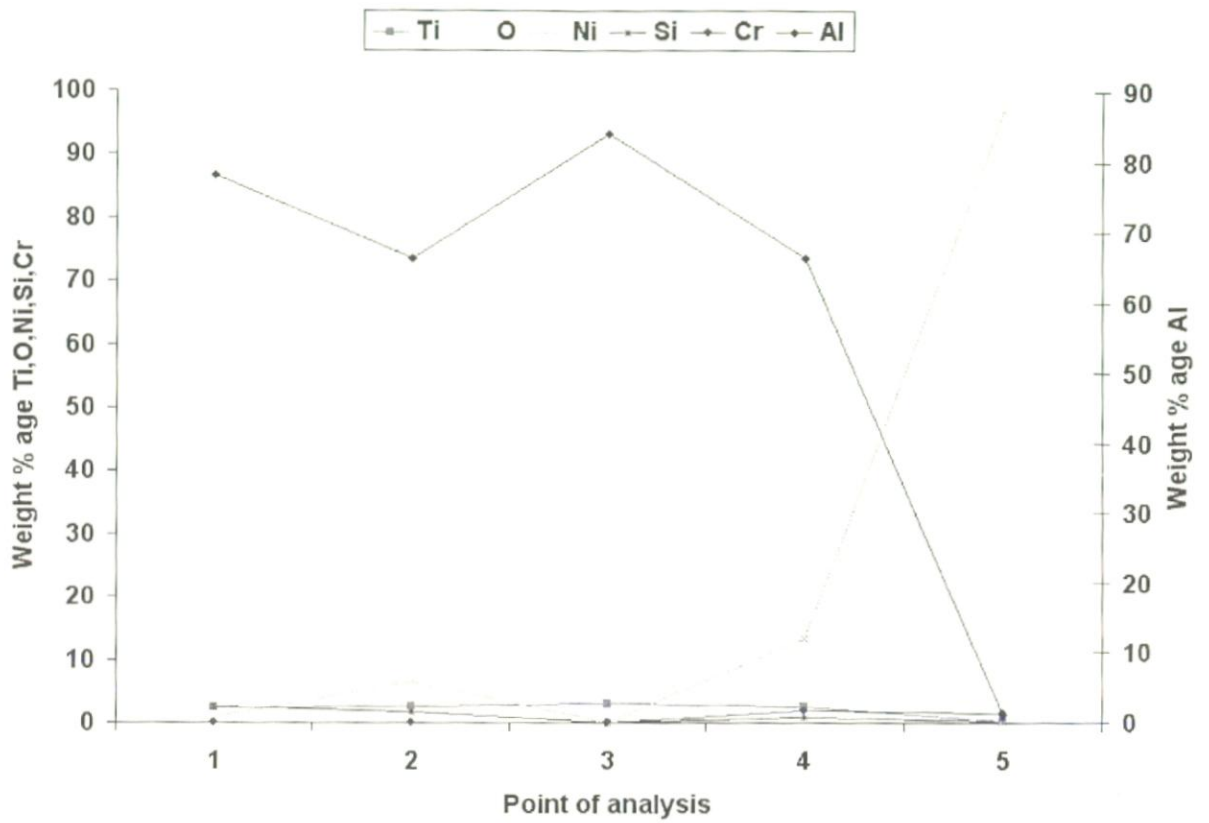


Fig. 7.35: Cross sectional morphology and elemental composition variation across the cross-section of $\text{Al}_2\text{O}_3\text{-3wt\%TiO}_2$ coated Superni 600 superalloy exposed to superheater of the coal fired boiler for 1500 hours at 700°C .

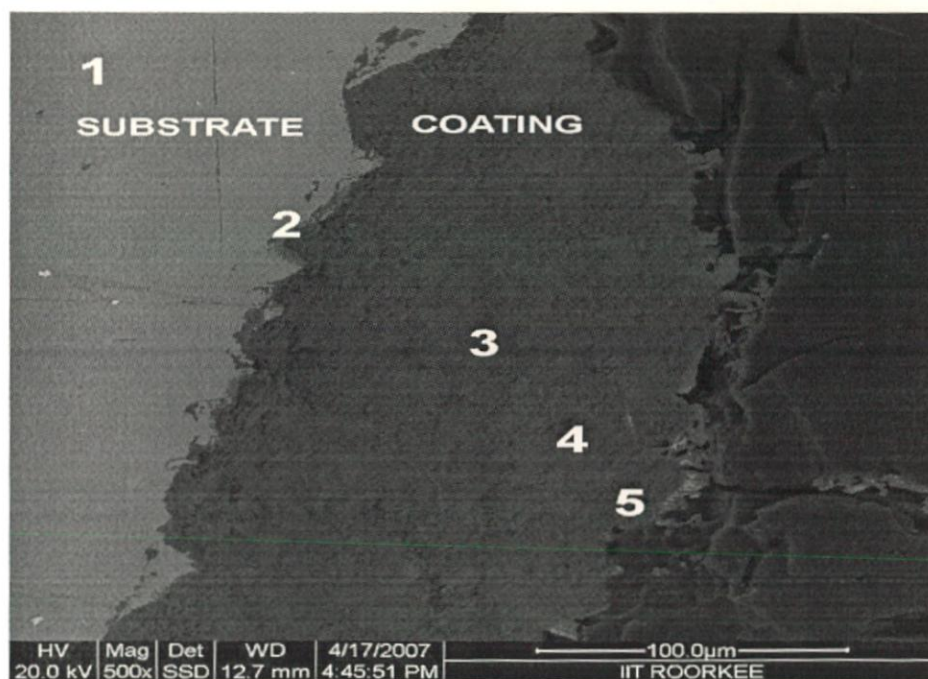
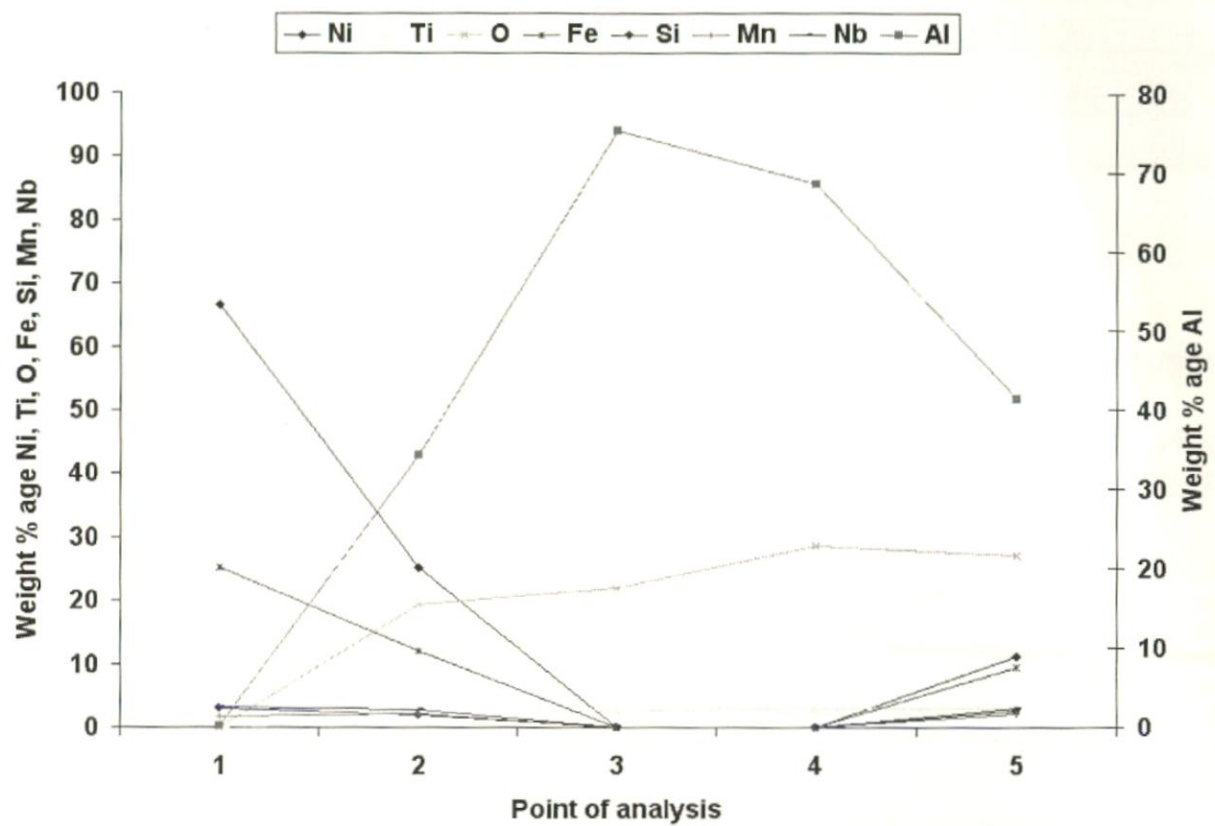


Fig. 7.36: Cross sectional morphology and elemental composition variation across the cross-section of $\text{Al}_2\text{O}_3\text{-3wt\%TiO}_2$ coated Superni 718 superalloy exposed to superheater of the coal fired boiler for 1500 hours at 700°C .

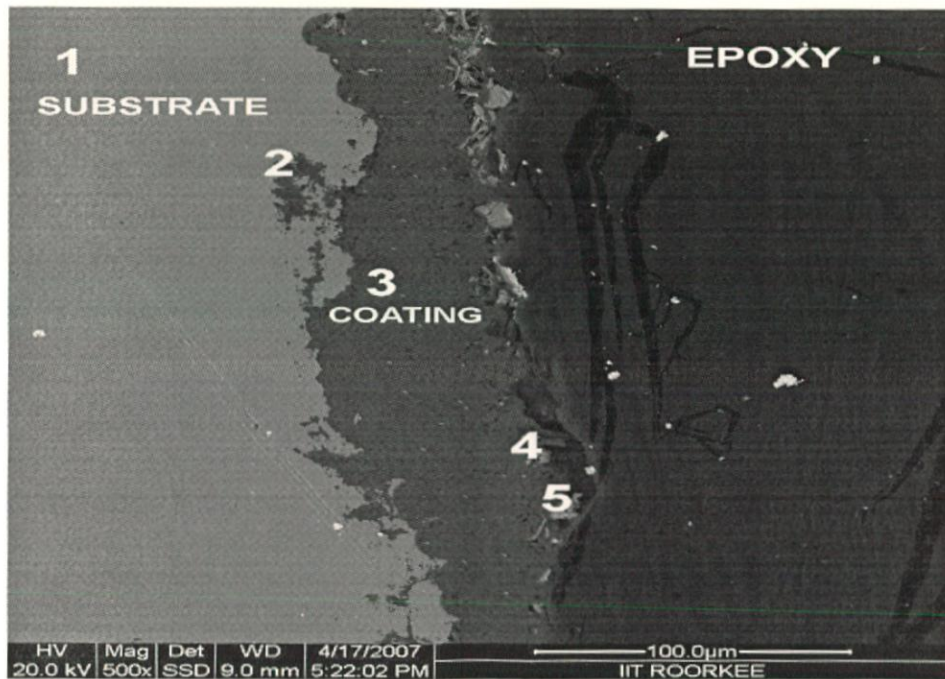
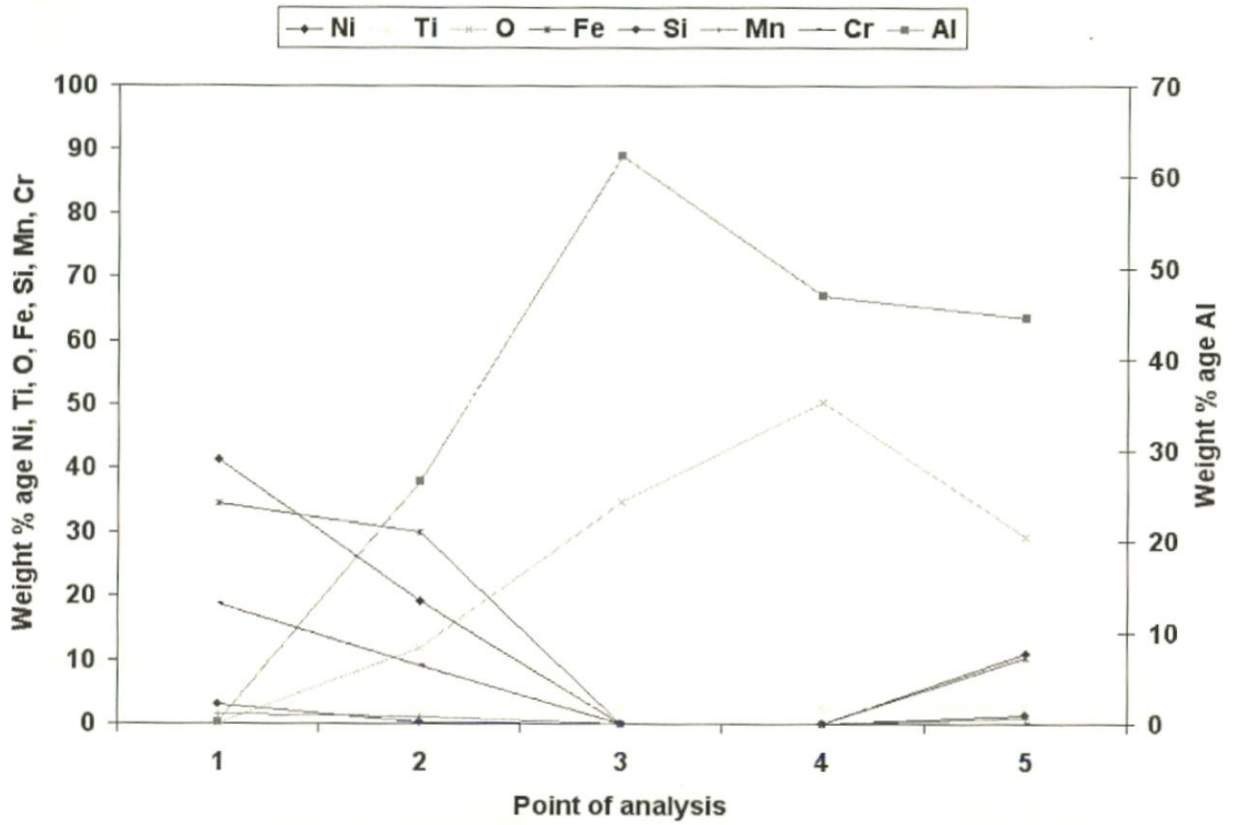


Fig. 7.37: Cross sectional morphology and elemental composition variation across the cross-section of $\text{Al}_2\text{O}_3\text{-3wt\%TiO}_2$ coated Superfer 800 superalloy exposed to platen superheater of the coal fired boiler for 1500 hours at 700°C .

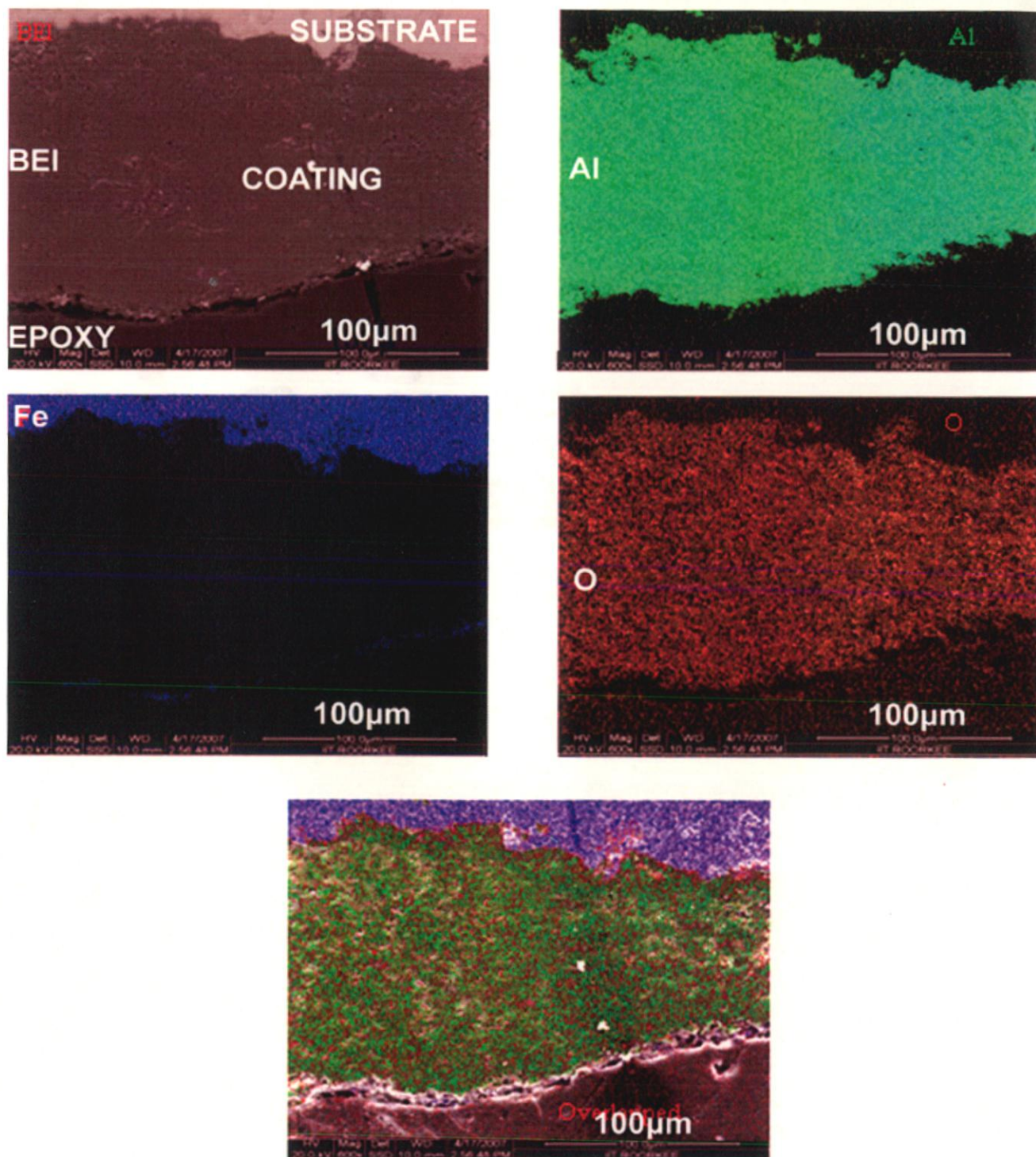


Fig. 7.38: Back scattered electron image and the corresponding x-ray mappings of cross section of $\text{Al}_2\text{O}_3 - 3 \text{ wt}\% \text{ TiO}_2$ coated T11 steel after 1500 hours exposure in boiler.

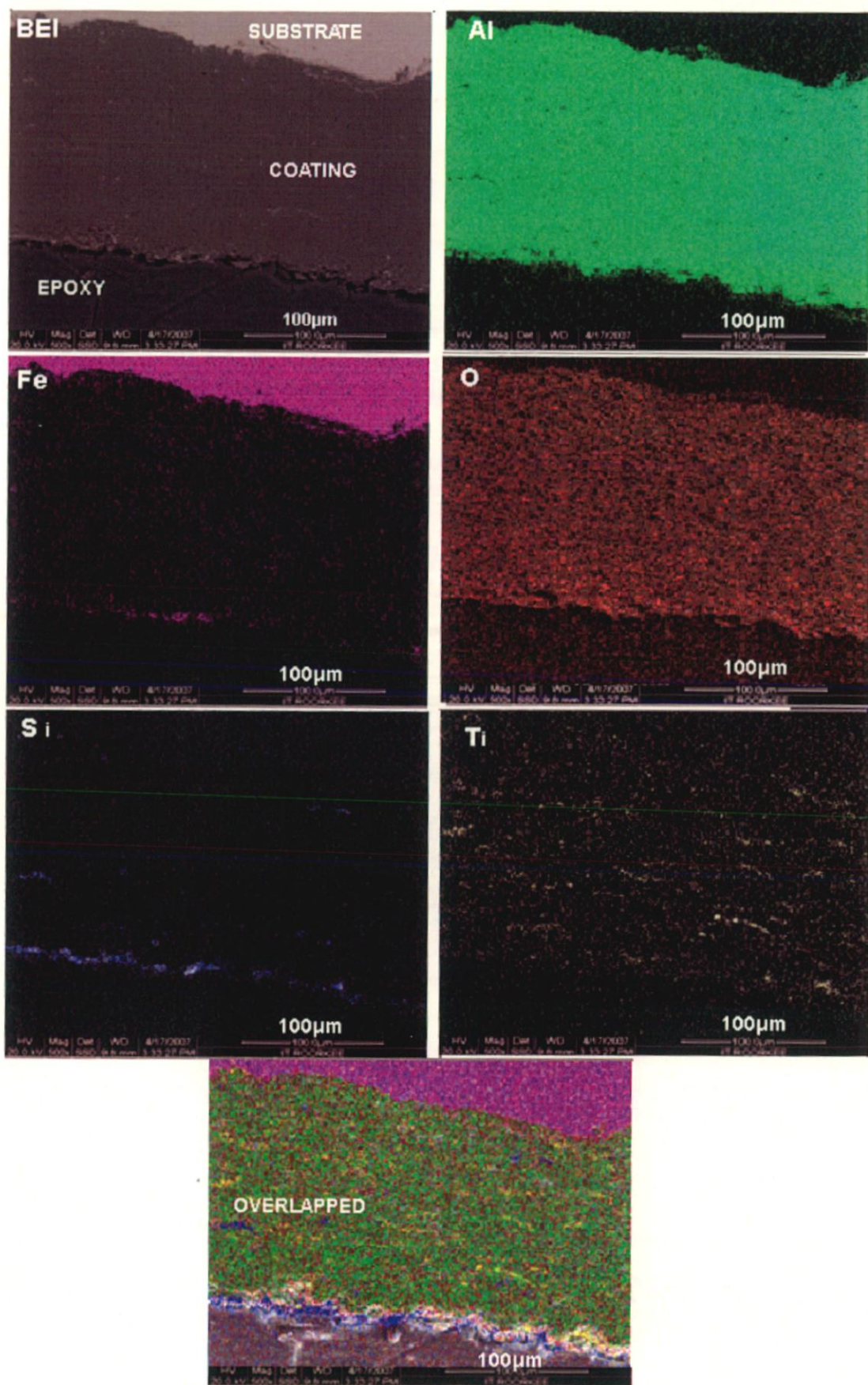


Fig. 7.39: Back scattered electron image and the corresponding x -ray mappings of cross section of $\text{Al}_2\text{O}_3 - 3 \text{ wt}\% \text{ TiO}_2$ coated T22 steel after 1500 hours exposure in boiler.

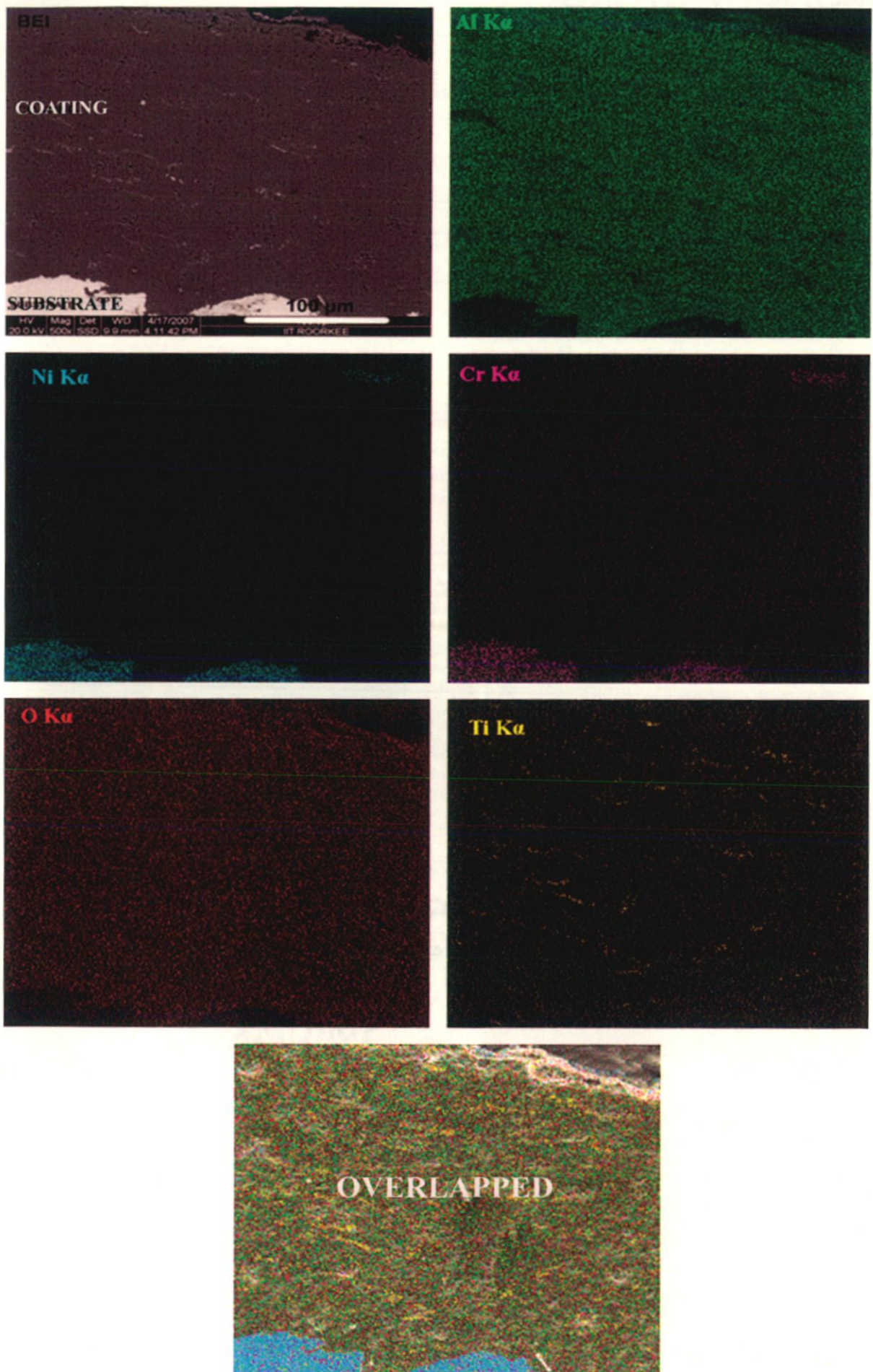


Fig. 7.40: Back scattered electron image and the corresponding x -ray mappings of cross section of Al_2O_3 - 3 wt% TiO_2 coated superalloy Superni 600 steel after 1500 hours exposure in boiler.

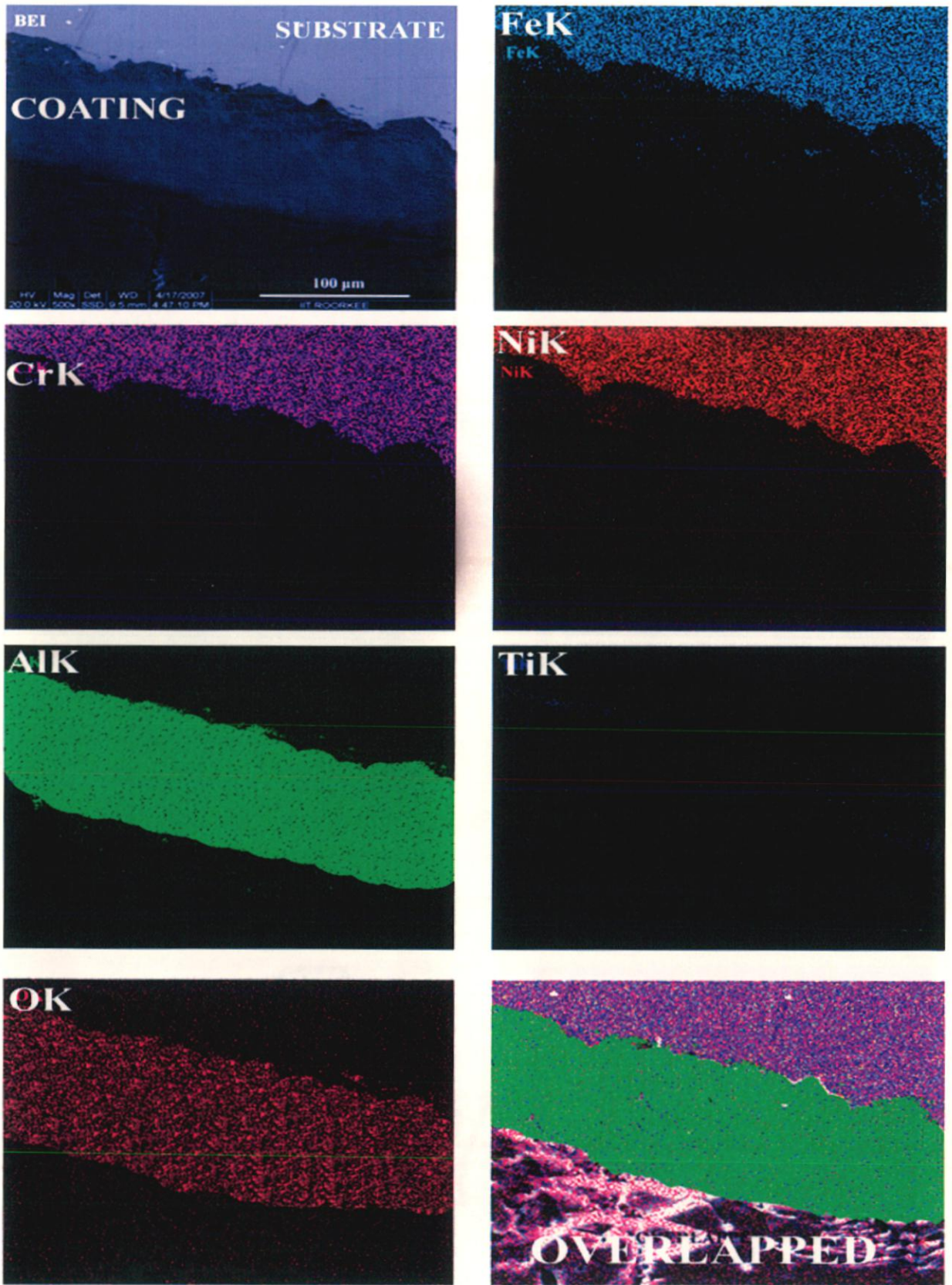


Fig. 7.41: Back scattered electron image and the corresponding x -ray mappings of cross section of Al_2O_3 - 3wt% TiO_2 coated superalloy superni 718 after 1500 hours exposure in boiler.

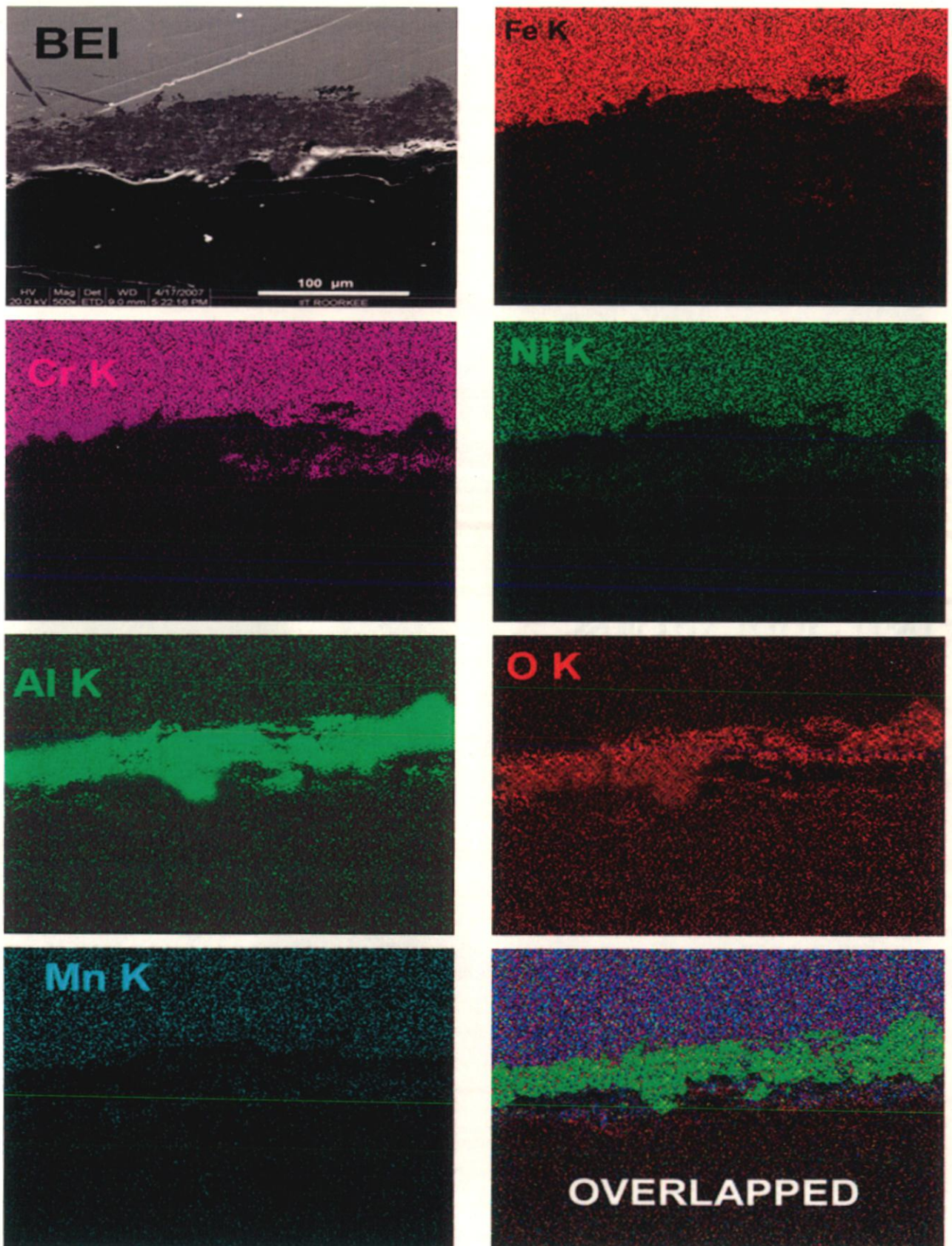


Fig. 7.42: Back scattered electron image and the corresponding x -ray mappings of cross section of Al_2O_3 - 3 wt% TiO_2 coated superalloy superfer 800 after 1500 hours exposure in boiler.

7.2 SUMMARY OF RESULTS

Results obtained after 1500 hours exposure of coated and bare alloys to the superheater zone of the coal fired boiler at around $700\pm 10^{\circ}\text{C}$ are summarised in Table 7.1.

Table 7.1: Summary of the results for uncoated and coated alloys after 1500 hours of exposure to superheater zone of the coal fired boiler at around 700°C .

Base Alloy	Coating	Weight Change (mg/cm^2)	Thickness lost (mm)	Corrosion rate mils per year (mpy)	XRD analysis	Remarks
T11	Uncoated	-105.05	2.08	478.13	Fe_2O_3 , Fe_3O_4 , FeS , Al_2O_3 , ZnO , MnO and SiO_2	Massive scale along with presence of embedded ash. Scale was fragile and intense spalling was observed.
	Al_2O_3 - 3wt% TiO_2	9.88	0.15	35.61	Al_2O_3 , Al_2TiO_5 , TiO_2 , SiO_2 , Fe_2O_3 CaO	There is a presence of minor cracks on the surface and hills and craters are formed on the coating surface. No spalling was observed.
T22	Uncoated	-42.48	1.71	393.81	Fe_2O_3 , Fe_3O_4 , FeS , Al_2O_3 , Mn_3O_4 and SiO_2	Scale was bulky and porous with continuous network of cracks with presence of embedded ash. Massive spalling was observed.
	Al_2O_3 - 3wt% TiO_2	7.51	0.12	29.42	Al_2O_3 , Al_2TiO_5 , TiO_2 , SiO_2 , Fe_2O_3 CaO	Fly ash deposits found to be embedded on the scale. No spalling and cracking but there is formation of craters, grooves and valleys on the coating surface.

Superni 600	Uncoated	11.62	0.22	50.11	Fe ₂ O ₃ , Al ₂ O ₃ , Ni, NiO, Ni(Fe) and SiO ₂	The Bluish scale on the matrix regions was significantly flatter and no spallation of the scale. Localised Cracks developed in the scale and indicated tendency for spallation.
	Al ₂ O ₃ - 3wt%TiO ₂	4.96	0.13	30.35	Al ₂ O ₃ , Al ₂ TiO ₅ , TiO ₂ , SiO ₂ , CaO	Fly ash deposits found to be embedded on the scale. No spalling and cracking. There is presence of pits and craters and velligies on the scale surface.
Superni 718	Uncoated	7.11	0.23	52.94	Fe ₂ O ₃ , Al ₂ O ₃ , Ni, NiO and Ni(Fe)	Very Thin scale formed with a tendency for spalling. Scale had Localised Cracks and internal corrosion, with surface unevenness created by formation of hills and craters
	Al ₂ O ₃ - 3wt%TiO ₂	2.34	0.13	31.31	Al ₂ O ₃ , Al ₂ TiO ₅ , TiO ₂ , SiO ₂ ,Fe ₂ O ₃ CaO	Fly ash deposits found to be embedded on the scale. No spalling and cracking
Superfer 800	Uncoated	14.35	0.25	59.54	Fe ₂ O ₃ , Al ₂ O ₃ , Ni, NiO, Ni(Fe) and Cr ₂ O ₃	Black coloured fragile and irregular scale formed indicated heavy spallation and considerable internal corrosion attack along with formation of craters and hills
	Al ₂ O ₃ - 3wt%TiO ₂	6.99	0.19	45.57	Al ₂ O ₃ , Al ₂ TiO ₅ , TiO ₂ , SiO ₂ , CaO	Fly ash deposits found to be embedded on the scale. No spalling and cracking observed.

7.3 DISCUSSION

In this section the results of erosion corrosion studies on substrate alloys and Al₂O₃-3 wt% TiO₂ coated alloys exposed to superheater region of coal fired boiler after 1500 hrs at 700°C have been discussed.

7.3.1 Uncoated alloys

The XRD and EDX analysis has shown the presence of ash deposits on the surface of the specimens. The interaction of ash with the oxide scales is further supported by X-ray mapping analysis (Figs. 7.17, 7.18, 7.19, 7.20 and 7.21). The corrosion scale formed on the boiler steels was made up only of iron oxide as revealed by XRD. Some fly ash particles were also found embedded into the iron oxide layer. Cross section examination by SEM of the tested samples for 1500 hours showed that the corrosion scale was only made of iron oxide. Backscatter electron image of the corrosion scale showed presence of oxygen throughout the scale. From the surface morphologies, it can also be seen that the layer of the corrosion scale is generally porous. Porous and non adherent scale with tendency to severe spalling and cracking has been observed for the boiler steels used in present investigation. Wang (1988) has also observed severe scaling and spalling for 2.25Cr-1Mo steel during 1000 hours cyclic study at 740°C in medium-BTU coal fired boiler. Iron, silicon and aluminium in substantial amount along with oxygen were the detected elements in the surface layer suggesting interaction of ash with oxide layer. Similar observations have been reported by Harb et al. (1990), Sidhu (2003), Sidhu (2006) and Ramesh (2008). The fly ash particles embedded in the outer layer contained silicon, aluminum, oxygen and in some particles there were also small amounts of potassium, magnesium, calcium and manganese. In the study reported by Pan and Riley (2003), it was disclosed that the SA-210 (A36) steel tested at the windows on the second floor of the boiler suffered a high corrosion rate. Further during this study, use of a higher chlorine containing coal resulted in higher SA-213T-22 corrosion in the superheater area.

In boiler conditions an oxide layer of Fe₃O₄ and or Fe₂O₃ is formed on the surface as shown in Fig. 7.43. This hard oxide layer protects the tube from metal

wastage. However inefficient combustion at times creates localised reducing conditions or allows direct contact of chlorine and carbon with the oxide layer. At high temperature and high heat flux, complex chemical reactions takes place, leading to the formation of iron sulphide (FeS), which owing to its higher molar volume may crack the protective layer. Also low melting compounds may be formed, wasting the metal. If chlorine is present in the flue gas, it diffuses through the oxide layer, making the protective layer porous and therefore less protective (Basu et al, 2000). Also with the deposition of ash, volatile alkali sulphates (Na_2SO_4) and sulphur trioxide (SO_3) produced during combustion diffuse through the ash to initiate corrosion. These compounds and the iron oxide from the oxide scale from the tube wall or from ash deposit itself react to form complex alkali metal trisulphates.

The scale formed on the steel mainly consisted of Fe_2O_3 and Fe_3O_4 as is indicated in XRD graphs. Oxide scale formed in these steels is continuously eaten away by fluxing and particle impact. The oxide scale formed was porous and less adherent. There was indication of massive scale along with presence of embedded ash at some points. There is a presence of pits and hills in scale clearly indicating the combined effect of erosion and corrosion caused by combined action of flue gases along with impact of fly ash. When erodent impact an oxide-covered surface, any damage to the oxide scale will result in an increase in the oxidation rate in the damaged region, and the extent of the increase will depend on whether oxide is cracked, chipped, or physically removed. As in present investigation, Alloys experience accelerated degradation when their surfaces are coated by a thin film of fused salt in an oxidizing environment and are continuously exposed impact of ash particles. The hot corrosion is commonly accompanied by the formation of a porous and non-protective oxide scale, which has been mostly attributed to the condensation of salts that attacks the protective oxide scale (Elliott et al, 1988 and Lai et al, 1983).

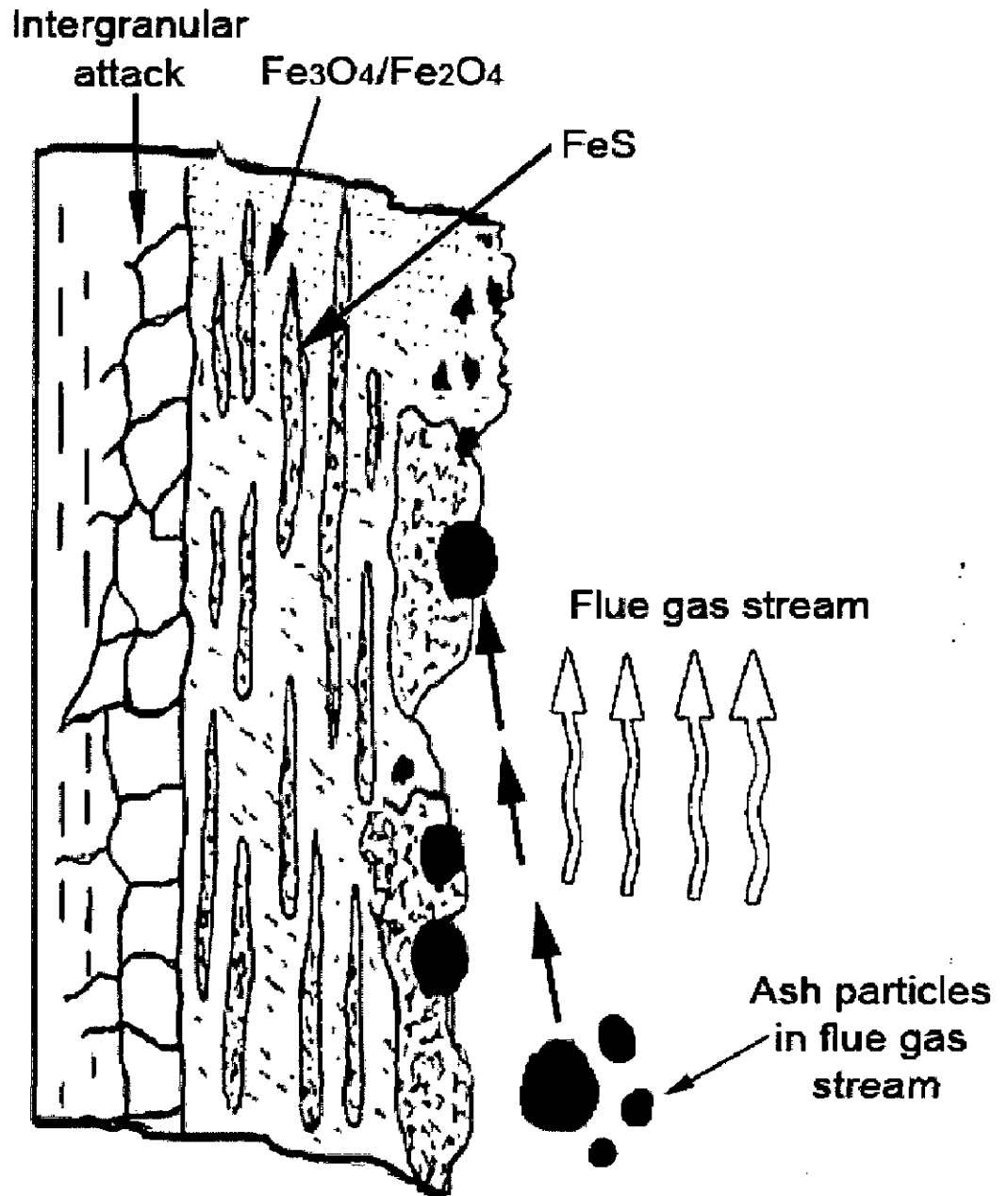


Fig. 7.43: Schematic diagram showing scale growth and probable erosion corrosion mechanism for the uncoated boiler steel exposed to actual boiler environment at 700°C for 1500 hours.

The oxide scale growth occurs by diffusion of iron from the steel to the surface of the scale to react with oxygen and oxygen diffusion through the oxide scale to the metal scale interface to react with iron (French, 1983). The greater volume of iron oxide scale in case of boiler steels has also been reported by Prakash et al. (2001) and Srikanth et al (2003) in their study on failure analysis of superheater tubes of coal fired boilers.

The growth of oxide scale occurs by the diffusion of iron from steel to the surface of scale to react with oxygen and oxygen diffusion through the oxide scale to the metal scale interface to react with iron (French 1983). Sidhu et al 2001 also reported the greater volume of iron oxide layer formation on boiler steels. Boiler steels indicated weight loss instead of weight gain due to spalling. Identical results have also been reported by Wang (1988). Compositional analysis of the boiler steels shown by SEM/EDS studies showed the major elements were iron, silicon and aluminum, with small amounts of calcium, potassium, magnesium, zinc and sodium.

EDX analysis depicted the build up of ash deposits on the surface of scale which is unfavorable and thus leads to severe corrosion attack. Interaction of ash with the scale is evident from the presence of Si, Ca, Mn, P, S, Al and Fe along with oxygen. Iron oxide phase was more loosely distributed in the scale. In the middle part of the slag piece fly ash particles were observed. A gray phase containing a significant amount of calcium was found at the outer part of ash deposit. As ash deposits build up, volatile alkali sulphates like Na_2SO_4 and SO_3 (sulphur trioxide) produced during combustion starts diffusing through the ash and starts corrosion reactions. These alkali sulphates, sulphur trioxide along with iron oxide present in the oxide scale then further reacts to form complex alkali metal trisulphates having low melting point are in the molten state at the operating temperature of the boiler. These molten compounds react with the scale which leads to corrosion. The appearance of scale formed on the steels is very porous and fragile. There is also a formation of chromium oxide. Similar observations were reported by Pan and Riley (2003), it has been reported that corrosion scales on the T22 samples generally consisted of two distinct layers: the inner layer of Fe (Cr) oxide, and the outer layer made up of iron oxide and fly ash particles.

For the present investigation, superalloys under study have not shown any detectable change on visual observation. These have shown small weight gain as compared to weight gain by boiler steels as shown in Fig. 7.2. This small weight gain may be due to the oxidation

and deposition of ash particles on exposed surface surfaces during the 1500 hours testing. This has been reported by Levy (1995) that surfaces of the specimen can add or subtract weight from chemical reactions such as oxidation. In all the superalloys, thin oxidized layer has been observed. Minor cracks on the surface scale have also been observed in some cases. The thickness loss in case of superalloys is very small as compared to thickness loss in case of boiler steels.

In XRD analysis, mainly the peaks of Ni, Ni Fe and indicate presence of some oxides like SiO_2 , Fe_2O_3 and Al_2O_3 . Presence of oxides has been confirmed by EDX analysis of the surface (Figs. 7.9 to 7.11). The main constituents on the exposed surface of superalloys consists of Si, Al, Cr, Ni and Fe along with O and minor constituents like Ca, Zn, Ti, Mo etc. From this it can be inferred that superalloys have been oxidized accompanied with erosion by fly ash impact. Fly ash particles embedded on the surface can also be seen in X-ray mapping of the cross section of the superalloys. In his study Sidhu (2006), also observed ash particle embedment on Ni base superalloy when exposed to actual industrial environment of a coal fired boiler. The presence of mixture of bed material constituents in the outer scale deposits during erosion corrosion of tubing superalloys in combustion boiler environment has also been observed by Levy (1993). Formation of hills and craters on the exposed surface has been observed indicating erosion effect of fly ash particles. Similar results were observed by Mishra 2006.

In cross sectional analysis, in case of Superni 600, there is thin Ni rich band in the substrate from which Cr has depleted as shown in Fig. 7.19. Also there is presence of embedded silica particle. While in case of Superni 718, (Fig. 7.20) a thin scale was observed on the surface. From X-ray mapping, Fe, Ni and Cr are coexisting with oxygen as very thin layers at the top most scale. Fig 7.44 shows the schematic diagram showing probable erosion corrosion mechanism for the uncoated superalloy Superni 600 exposed to actual boiler environment at 700°C for 1500 hours. As compared to other superalloys, Superfer 800 has shown thick scale (Fig. 7.21) in which Si, Mg and Al particles can be seen coexisting with oxygen in the elemental maps. Ni rich layer is present in the substrate at the interface. Also Ni and Cr are coexisting with oxygen at the top of the scale. The scale by itself mainly consists of iron along with oxygen which indicates the formation of Fe_2O_3 . Probable erosion corrosion mechanism for the uncoated superalloy Superfer 800 exposed to actual boiler environment at 700°C for 1500 hour is shown in Fig. 7.45. In his study Mishra 2006 has also reported the embedment of fly ash particles on the top layer of the exposed surface.

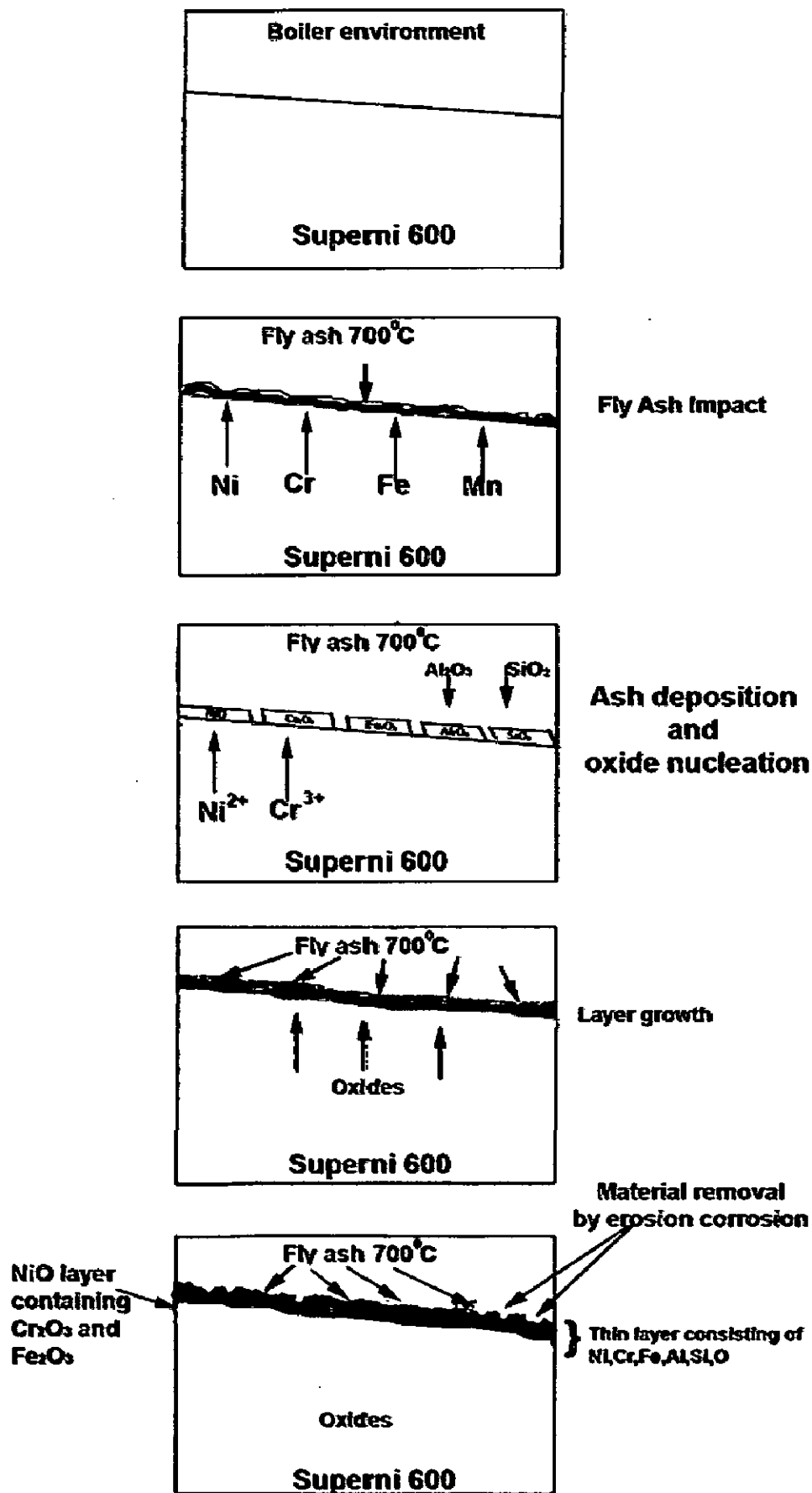


Fig. 7.44: Schematic diagram showing probable erosion corrosion mechanism for the uncoated superalloy Superni 600 exposed to actual boiler environment at 700°C for 1500 hours.

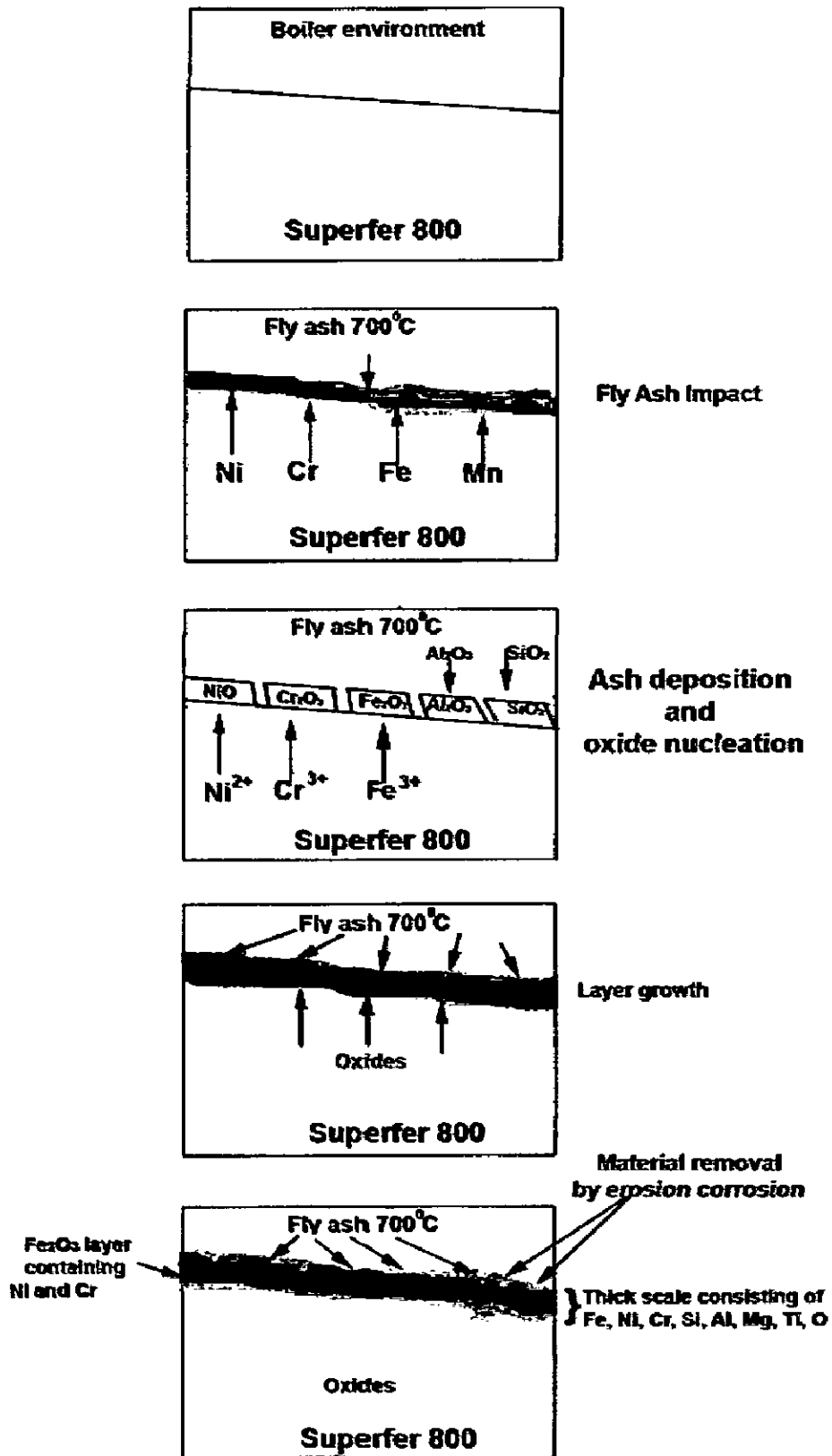


Fig. 7.45: Schematic diagram showing probable erosion corrosion mechanism for the uncoated superalloy Superfer 800 exposed to actual boiler environment at 700°C for 1500 hours.

7.3.2 Coated alloys

The Al_2O_3 -3 wt % TiO_2 coatings deposited on boiler steels and Ni-and Fe-based superalloys behaved very well in the boiler environment at 700°C . Due to the very low porosity of the developed coating, there was hardly any penetration of the corrosive species into the coating. Coating was unaffected by any attack. The attack was limited to edges only otherwise coating acted as a shield between the corrosive environment and the metallic substrate and effectively hindered the corrosive species from migrating into substrate. The coating surface contained almost solely alumina with few streaks of Titania. Alumina titania coated alloys have shown better spallation resistance. Coating remained essentially adherent to the substrate. Continuous impact of fly ash and other particles entrapped in the air blast resulted in thickness loss of the coatings. The thickness lost of the coating was 0.1548, 0.1279, 0.1319, 0.1361, 0.1981 mm in T11, T22, Superni 600, superni 718 and superfer 800 respectively as indicated in Fig.7.24. The X-ray diffraction analysis indicated main constituent of the coated samples as Al_2O_3 , Al_2TiO_5 , TiO_2 , SiO_2 , CaO and small fraction of Fe_2O_3 in few samples. Presence of SiO_2 and CaO , is an indicative of fly ash on the surface of exposed samples which was further verified by EDX analysis. The detection of Si, Ca, Na, Mo, Fe along with O is an indication of embedded ash. There is a presence hills and craters on the surface along with pits and cracks which is a clear indication of combined effect of erosion and corrosion caused by combined action of flue gases and fly ash. Minor micro cracks on the surface were detected but there was no evidence of formation of oxides from the substrate alloys. Hills and craters were formed on the surface indicating effect of erosion which was limited to the surface only. The coating has protected the surface very well by covering the surface of the substrate alloys. This may be due to the fact that Al_2O_3 probably hinders the grain boundary diffusion of the elements. As a consequence, there is no oxide scale growth. The compact and protective Al_2O_3 layer separated the metal substrate from the boiler environment. As a result, the coating improved the resistance. From weight gain and thickness loss data it can be inferred that the protection to the base metals has been provided by the coating. The minimum erosion corrosion loss in case of Al_2O_3 -3 wt % TiO_2 coatings might be attributed to the compact and less porous structure. The more

compact and less porous the coating, the higher is its erosion-corrosion resistance (Wang et al, 1992). Main phases identified in all the coated specimens are Al_2O_3 , Al_2TiO_5 , TiO_2 , SiO_2 , CaO and Fe_2O_3 after 1500 hours exposure to the coal fired boiler environment. The formation of iron oxide in the top scale of few coated alloys after exposure to boiler environment might be due to ash deposition. The Al_2O_3 -3 wt% TiO_2 composite coating was no longer oxidized and acted as an effective inert barrier to improve the isothermal and cyclic oxidation resistance of alloys exposed to boiler environment for 1500 hours. The composite coating possessed very dense structure, high thermal stability and excellent cracking/spallation resistance.

COMPREHENSIVE DISCUSSION

The important results of the present investigations are discussed in this chapter. This chapter describes the current investigation giving comparative performance of the uncoated and D-gun coated alloys. The performance of these uncoated and coated alloys for ambient and elevated temperature erosion, oxidation, molten salt corrosion in aggressive environment of Na_2SO_4 -60% V_2O_5 under cyclic conditions at an elevated temperature of 900°C and actual working environment of the coal fired boiler has been discussed.

8.1 EROSION STUDIES

The room temperature as well as elevated temperature volumetric erosion rate at 30° and 90° impact angles for uncoated and coated alloys is shown in Fig. 8.1. The boiler steels have shown very poor erosion resistance when compared with superalloys. While among the superalloys, the Ni based superalloys have shown better erosion resistance than iron based superalloy.

At room temperature testing, the boiler steels under study have shown higher erosion rate while superalloys have shown low volume erosion rate. The erosion rates at 30° impact angle at room temperature can be arranged in following order:

$$T11 > T22 > \text{Superfer 800} > \text{Superni 718} > \text{Superni 600}$$

In boiler steels, the poor erosion resistance may be attributed to the small amount of alloying elements in these steels while in case of superalloys, Superfer 800 has shown marginally more volume erosion loss as compared to volume erosion loss in other superalloys. Mishra (2006) also observed the similar trend in his study on superalloys. The difference in erosion rate is marginal in case of superalloys and may be dependent on the grain size, thermo mechanical factors, types of micro constituents of particular superalloy and their distribution, presence of impurities etc. While at normal impact, the erosion volume loss is less as compared to the erosion rate at 30° impact and the sequence of erosion rate of alloys based on the data at normal impact angle is:

$$T22 > T11 > \text{Superfer 800} > \text{Superni 600} > \text{Superni 718}$$

The erosion rate has shown an increase when testing temperature was raised to condition 2 i.e. substrate temperature 400°C and surrounding atmosphere to 900°C. Based

on the present data the erosion rates in terms of volume loss per unit of erodent for the substrate for 30° impact angle can be arranged in following order:

T11>T22>Superfer 800 > Superni 718 > Superni 600

At this temperature, the relative erosion resistance of Superfer 800 at 30° impact angle is least among the superalloys under study, while Superni 600 has shown maximum erosion resistance. Here at this temperature, erosion rate of all the alloys have increased substantially except that of Superfer 800 superalloy where there is only marginal increase in erosion rate. While at normal impact, the erosion rate is less as compared to the erosion rate at 30° impact and the sequence of erosion rate is:

T22 > T11> Superfer 800 > Superni 600 > Superni 718

At condition 2 also, the erosion rates of alloys were greatest at 30° impact angle, which is the characteristic erosion behaviour of ductile material and erosion behavior is almost similar to metallic erosion at room temperature. Superfer 800 has shown maximum erosion loss among the superalloys, while Superni 718 has shown minimum erosion loss at normal impact angle. At this temperature, there is no oxide scale formation and even if there is any oxide scale, it will be very thin and thus will behave like metal and erosion will follow metallic erosion mechanism.

On further increasing the testing temperature to 600°C of substrate and to 900°C for surrounding atmosphere i.e. at condition 3, the erosion rate has shown further increase. The volume erosion loss has increased almost double as that at room temperature. The erosion rates for 30° impact angle at condition 3 can be arranged in following order:

T11>T22>Superfer 800 > Superni 718 > Superni 600

At oblique impact angle, here also Superfer 800 has followed the same trend as that at condition 1 and condition 2 i.e. it has shown the maximum erosion loss among the superalloys while Superni 600 has shown maximum erosion resistance. While at 90° impact, the erosion rate is less as compared to the erosion rate at 30° impact and the sequence of erosion rate of alloys based on the data at normal impact angle is:

T11>T22 >Superfer 800 > Superni 718 > Superni 600

At this temperature erosion is affected by oxidation. The impact induces stresses in the developed scale layer, reducing the critical thickness for spallation and thereby accelerating the oxidative attack. At this temperature, erosion takes place from the thick oxide scale.

In case of Al₂O₃-3 wt% TiO₂ coated alloys, when erosion testing was performed at room temperature i.e. at condition 1; the erosion rate of all the coated alloys is almost same with small deviations. With increase in temperature, i.e. when the temperature of coated substrate was raised

- ▣ At Condition 1 (Ambient Temperature)
- At Condition 2 (Sample Temperature 400°C & Air Temperature 900°C)
- At Condition 3 (Sample Temperature 600°C & Air Temperature 900°C)

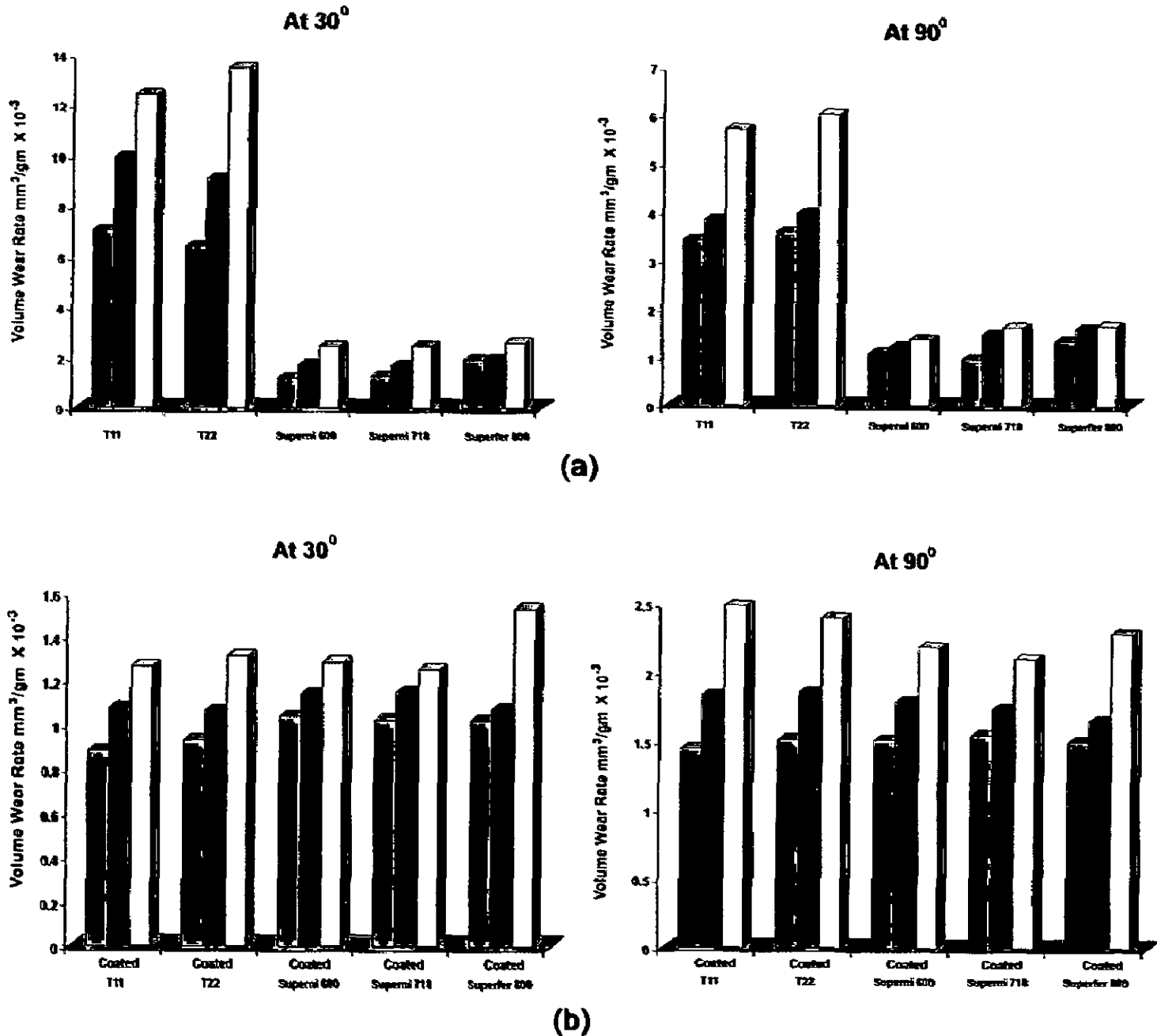


Fig. 8.1: Variation in Volumetric Erosion rate with change in temperature at 30° and 90° impact angles for (a) uncoated alloys and (b) Al₂O₃-3 wt% TiO₂ coated alloys.

to 400°C and surrounding atmosphere to 900°C, there is substantial increase in volume erosion rate of all the coated alloys under study at 90° impact. At oblique angle i.e. at 30°, the volume erosion rate is less as compared to at 90°. On further increasing the substrate temperature to 600°C, volume erosion rate is also increased substantially. The erosion rate is less at 30° impact angle as compared to one at 90° impact angle. It has been observed that erosion rates of coated alloys impacted at low angles do not increase rapidly as the temperature increases, suggesting that alloys tend to show typically brittle behaviour at elevated temperatures. A tendency for erosion rate to increase with temperature has been observed in coated alloys. At normal impact, the rise in erosion rate is much higher for given increase in temperature. The effect of temperature on the erosion rate has been studied by Zhou and Bahadur (1995) and they have reported that the effect of temperature on erosion is significant above 400°C and the rate of increase in erosion rate is greater at higher temperatures.

8.2 OXIDATION ENVIRONMENT AND MOLTEN SALT ENVIRONMENT

The coatings have behaved well and provided the necessary protection to the base metal during testing in air and molten salt environment. The weight change (mg/cm^2) for uncoated and detonation gun coated alloys subjected to cyclic oxidation for 50 cycles at 900°C indicated that weight gains for all the coated alloys are considerably lower than that of uncoated alloys. Bulky and porous scale with continuous network of cracks was observed on the uncoated boiler steels. The uncoated boiler steels suffered intense spalling of the scale. The scale formed on the steel consisted of iron oxide mainly.

Among the boiler steels, T22 steel has shown poor oxidation as well as molten salt resistance than T11 steel at 900°C during cyclic testing. Though T22 steel contained higher amount of chromium (2.5%) relative to T11 steel having only 0.98% chromium. The reason may be due to the presence of higher amount of Mo (1.08%). Further T11 steel showed inferior resistance to Na_2SO_4 -60% V_2O_5 environment which may be attributed to reaction of molten salt with MoO_3 to form lower melting point phase like Na_2MoO_4 which could have led to acidic fluxing of the protective oxide scale as suggested by Fryburg et al (1984) and Pettit and Meier (1984). In superalloys Superni 600 and Superni 718, rapid oxidation rate has not been observed and very small weight gains have been observed and steady state with the progress of exposure time, in spite of the fact that some minor deviations are observed. The bar charts showing the overall weight gains in air and molten salt environments after 50 cycles for the coated and uncoated alloys are presented in Figs. 8.2 and 8.3 respectively. From the bar charts, it can be inferred that among the alloys under

study, boiler steels have shown poor resistance against the oxidation as well as molten salt environment. In superalloys, Superfer 800 has indicated a minimum resistance to air oxidation amongst the superalloys under study. Superni 600 has been found to be most resistant to the air oxidation as well as molten salt corrosion among all the superalloys. Superfer 800 suffered accelerated hot corrosion in the form of intense spalling and sputtering of its scale. On the bare alloys, especially in boiler steels, the oxide scale formed is fragile and irregular, and penetrates deeply into the substrates, thereby reducing the thickness of sound metal. In molten salt environment, the scale formed on the bare superalloys is fragile and irregular. The fluxing action of the molten salt on the surface of the bare alloys is also clearly evident (Figs. 6.49 and 6.50). The EDX analysis and elemental maps obtained after total 50 cycles of exposure to the molten salt environment indicate that all the coatings have protected the base alloys against the penetration of oxygen and other corrosive species, coatings are in good contact with the substrate .

8.4 INDUSTRIAL ENVIRONMENT

In actual industrial environment, when uncoated alloys as well as coated alloys were exposed to superheater zone of coal fired boiler at 700°C for 1500 hours, these encountered both erosion as well as corrosion phenomenon. The temperature in this zone was 700± 10°C and high velocity stream in this zone carried many undesirable elements. In uncoated specimens, fouling was observed from the scanning electron micrographs due to condensed phases of the ash. Coal ash carried by the flue gas in the form of small particles form sintered and fused deposits on the superheater and reheater surfaces, thereby providing the environment in which complex sulphates are formed causing metal degradation. From EDX analysis, it has been revealed that, higher amount of Si, Al and Fe along with O was present on the surfaces in the form of condensed ash which initiates the corrosion mechanism on the surfaces.

Al₂O₃-3 wt% TiO₂ coatings, in general, have shown good resistance to the industrial environment consisting of actual working condition of the coal fired boiler and all the coated alloys performed better than the uncoated alloys. The bar chart indicating the total extent of material thickness lost of uncoated and Al₂O₃-3wt%TiO₂ coated alloys after 1500 hours exposure to superheater zone of coal fired boiler at around 700°C is shown in Fig.8.4. From the bar chart it is clear that minimum thickness loss is shown by Superni 600 superalloy among all the uncoated alloys tested while uncoated boiler steels have shown massive thickness loss.

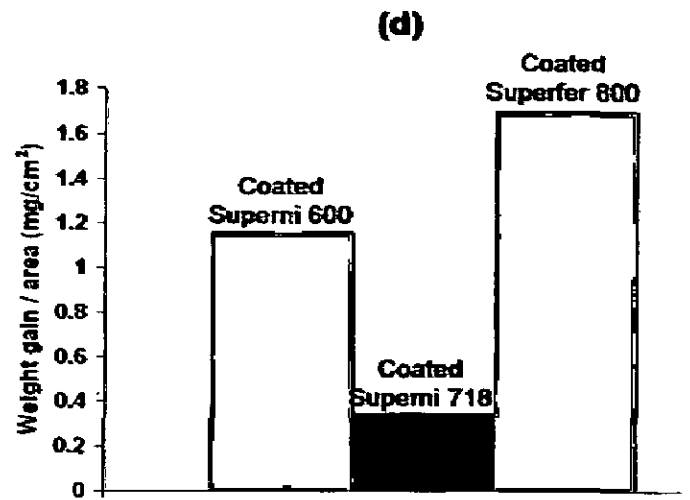
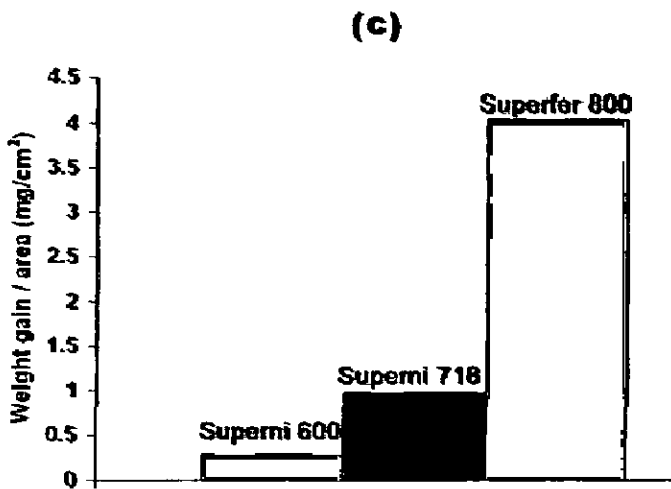
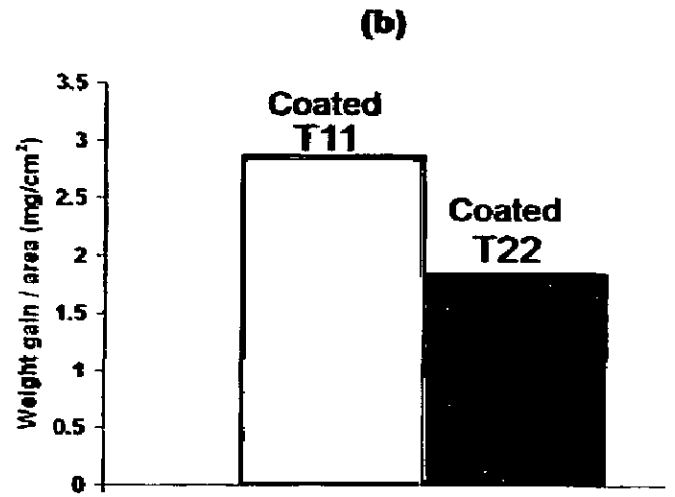
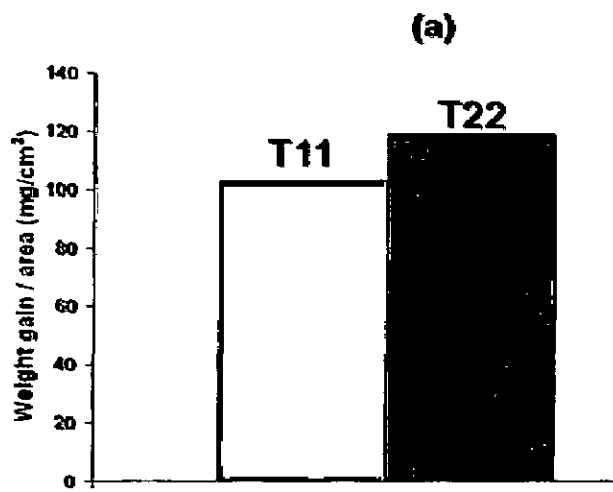


Fig. 8.2: Bar charts showing cumulative weight gain (mg/cm^2) for the uncoated and coated alloys subjected to cyclic oxidation in air at 900°C for 50 cycles.
 (a) Uncoated Boiler steels (b) Coated Boiler steels (c) Uncoated Superalloys (d) Coated Superalloys

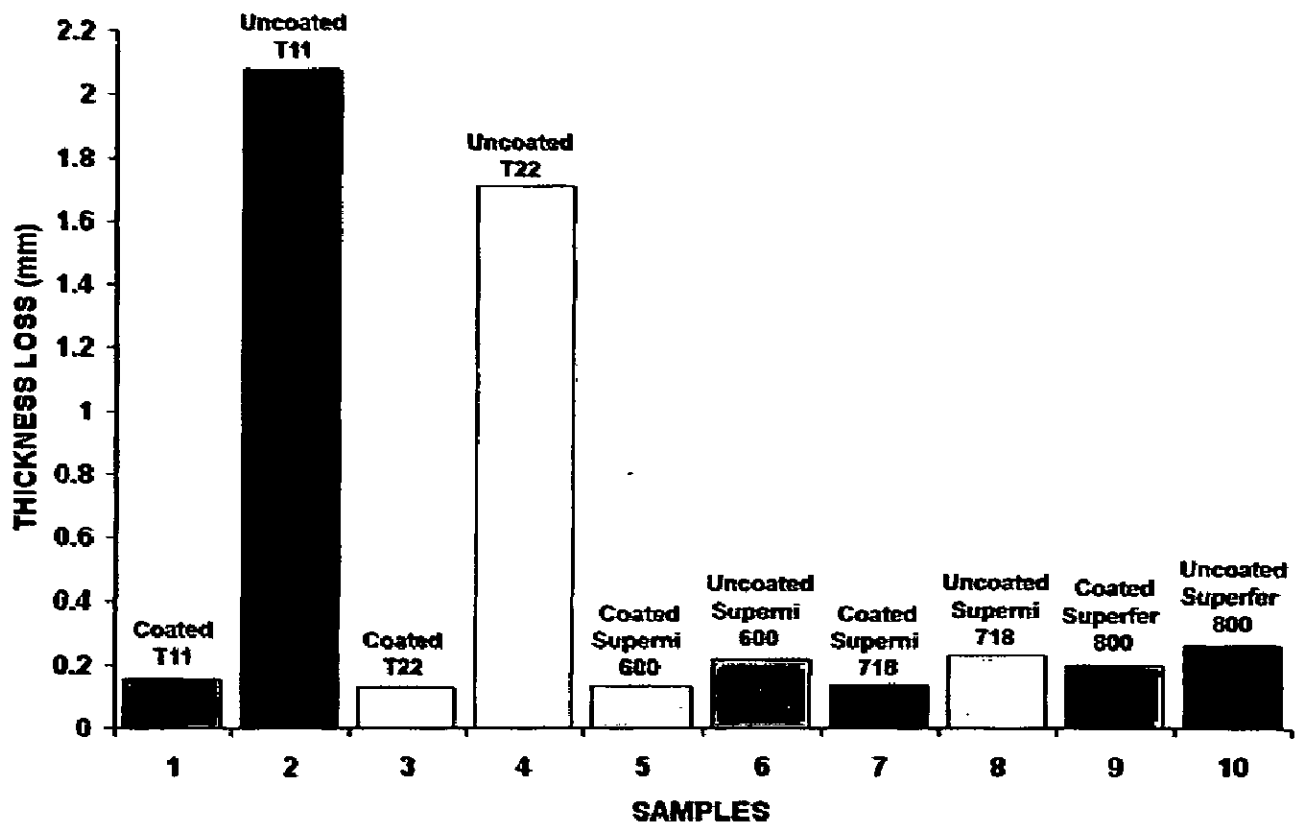


Fig. 8.4: Bar chart indicating the thickness lost in mm for the uncoated and Al₂O₃-3wt%TiO₂ coated alloys after 1500 hours exposure to the coal fired boiler at 700°C.

Comparing the erosion corrosion loss of Al_2O_3 -3 wt% TiO_2 coating on different substrate alloys, it can be inferred that the difference in thickness loss with respect to substrate is not much i.e. it is almost same in all the coated alloys irrespective of the substrate alloy. When compared to uncoated alloys thickness loss is very less. There is no evidence of formation of oxides from the substrate alloys though there is a presence of minor cracks on the surface in few cases and also there is an indication of erosion with the formation of hills and craters on the surface but these could not expose the surface of the substrate alloys and coating has protected the surface very well. This may be due to the fact that Al_2O_3 probably hinders the grain boundary diffusion of the elements. As a consequence, there is no oxide scale growth. The compact and protective Al_2O_3 layer separated the metal substrate from the boiler environment. As a result, the coating improved the hot corrosion resistance. X-ray mapping after 1500 hours exposure to boiler environment is shown in Fig.7.38 to 7.42 respectively. The elemental maps of the coated alloys indicated that the substrate alloys are safe from the oxygen and other corrosive species attack. Alumina-titania coating is intact with all substrate alloys. Thus in boiler environment coating has acted as barrier against erosion and corrosion of all the alloys under testing. Also the coating remained intact even after 1500 hours of cyclic study so it can be concluded that the coating will enhance the life of the components in the evaluated environment.

The relatively better resistance shown by the D-gun sprayed Al_2O_3 -3wt% TiO_2 coatings may be attributed to formation of more compact and denser coating which might be responsible for maximum erosion and corrosion resistance. Wang et al (1992) have also suggested correlation between the erosion-corrosion resistance to compactness and the density. More the compactness and lesser the porosity higher is the erosion-corrosion resistance. Even after 1500 hours exposure in the actual boiler environment , there is very little degradation shown by the coatings. Al_2O_3 -3wt% TiO_2 coating remained integral with respective substrates alloys throughout the exposure time in air, molten salt and actual industrial environment. However, while selecting a particular coating for a specific application, various other factors such as substrate compatibility, adhesion, porosity, the possibility of repair or recoating, inter diffusion, the effect of thermal cycling, resistance to wear and cost should also be considered (Sidky and Hocking, 1999).

CONCLUSIONS

The conclusions from the present investigation on Al_2O_3 -3 wt% TiO_2 coatings obtained by Detonation Gun spray process on two types of boiler steels namely SA213-T11 (T11) and SA213-T22 (T22) and three type of superalloys namely Superni 600, Superni 718, Superfer 800 The coated and uncoated alloys were subjected to oxidation in air, molten salt (Na_2SO_4 -60% V_2O_5) and actual coal fired boiler environments. The salient conclusions resulting from the present investigation can be summarised as follows:

1. Alumina-titania coatings could be successfully obtained by detonation gun spray process. All these coatings showed very less porosity (<1%). Dense coatings with the thickness in the range of 200-250 μm were successfully obtained. Coating possessed distinct layered structure, i.e. aluminum-rich regions separated from titanium rich regions.
2. As sprayed coatings revealed the presence of both original α Al_2O_3 phase and some γ - Al_2O_3 phase. Some of α Al_2O_3 got transferred to γ - Al_2O_3 phase during coating formation.
3. The microhardness along the cross section of the coatings is found to vary with the distance from the coating substrate interface. The coating has shown very high value of hardness in the range of 862 to 1056 Hv.

EROSION STUDIES:

Substrate alloys

4. At room temperature i.e. Condition 1, in all the uncoated alloys, boiler steels have shown the inferior erosion resistance while among the superalloys, Fe- based superalloy exhibited marginally higher erosion rate at both the impact angles.
5. At 30° impact, among the uncoated alloys boiler steels have shown the maximum erosion volume loss while superalloys have given very low erosion rates. Erosion rates can be arranged in following order:

T11>T22>Superfer 800 > Superni 718 > Superni 600

6. In case of normal impact, the erosion rate is less as compared to the erosion rate at 30° impact and the sequence of erosion rate of alloys can be arranged as :
T22>T11>Superfer 800 > Superni 600 > Superni 718
7. When erosion testing temperature was raised to 400°C and surrounding atmosphere to 900°C i.e. to condition 2, the erosion rate has shown an increase. The erosion rates for 30° impact angle can be arranged in following order:
T11>T22>Superfer 800 > Superni 718 > Superni 600
8. In case of normal impact at condition 2, the erosion rate is less as compared to the erosion rate at 30° impact and the sequence of erosion rate of alloys based on the data at normal impact angle is:
T22>T11>Superfer 800 > Superni 600 > Superni 718
9. When erosion testing temperature was raised to 600°C and surrounding atmosphere to 900°C (condition 3), the erosion rate has shown further increase. The erosion rates for 30° impact angle at condition 3 can be arranged in following order:
T11>T22>Superfer 800 > Superni 718 > Superni 600
10. In case of normal impact at condition 3 , the erosion rate is less as compared to the erosion rate at 30° impact and the sequence of erosion rate of alloys at normal impact angle is:
T11>T22 >Superfer 800 > Superni 718 > Superni 600

Coated alloys

11. For coated alloys, at room temperature testing, the erosion rate in terms of volume loss for the Al₂O₃-3wt%TiO₂ coated substrate alloys is between 0.883 to 1.041 X 10⁻³ mm³/ gm at 30° impact. While in case of normal impact, it lies between 1.447 to 1.550 X 10⁻³ mm³/ gm. The generalized behaviour of the all the coated alloys was brittle in nature.
12. As the temperature of testing increased to 400°C of coated substrate and 900°C of surrounding atmosphere, there is substantial increase in volume erosion rate of all the coated alloys under testing at 90° impact while there is small increment in volume erosion rate at 30° impact. It has been observed that erosion rates of coated alloys impacted at low angles do not increases as rapidly as the temperature increases.

13. At 90° impact, the rise in erosion rate is much higher for given increase in temperature. At room temperature erosion rate lies between 1.447-1.55 X10⁻³mm³/gm and at condition 2, erosion rate lies between 1.653-1.858 X10⁻³mm³/gm and on further increase in temperature i.e. at condition 3, erosion rate increases in the range of 2.108-2.486 X10⁻³mm³/gm.
14. It has been observed that all the coatings have maintained adherence with the substrates alloys under study during the erosion testing at all the temperatures. Lower erosion losses observed for coatings might be attributed to relatively low porosity and compact and dense microstructure of the coatings.

OXIDATION STUDIES IN AIR AND HOT CORROSION STUDIES IN Na₂SO₄-60%V₂O₅ MOLTEN SALT MIXTURE:

Substrate alloys

15. The uncoated alloys subjected to cyclic oxidation in air and hot corrosion in Na₂SO₄-60%V₂O₅ molten salt, showed higher weight gains than that of coated alloys. Especially in case of boiler steels there was formation of thick scale with multilayered cracking.
16. The boiler steels suffered intense spalling of oxide scale in both the environments. In case of superalloys, there was no spalling in oxidation testing but some internal localized cracks were observed.
17. In hot corrosion testing, boiler steels suffered intensive spalling and cracking and also in all the superalloys under testing, there was formation of thin and fragile scale and also spallation was observed.

Coated alloys

18. Coated alloys subjected to cyclic oxidation in air, hot corrosion in Na₂SO₄-60%V₂O₅ molten salt, showed lower weight gains than that of uncoated alloys. The coating remained intact and there was no spalling or sputtering of the coating. The superior performance of coating can be attributed to continuous and protective nature of the D-gun sprayed coatings.

EROSION CORROSION STUDIES IN SUPERHEATER OF COAL FIRED BOILER:

Substrate alloys

19. In Boiler steels T11 and T22, the scale was fragile and showed severe spalling during the exposure in the superheater zone for 1500 hours in cycles of 100 hrs each. Frequent spalling was due to the fact that the scales consisted of multi-layered structure of iron oxides. The enhanced corrosion was mainly induced by the presence of corrosion species in the combustion products. In superalloys, the scale formed was thin and there was negligible spalling of the scale and it remained intact throughout the study. Superalloys exposed to boiler conditions have shown a fine surface scale mainly consisting of Al_2O_3 , SiO_2 , NiO , Fe_2O_3 and Cr_2O_3 . The scale was significantly flatter and no spallation of the scale has been seen. At 700°C , a well adherent corrosion scale was formed which mainly consisted of NiO . There is presence of minor cracks on the surface scale and also there was an indication of erosion with the formation of hills and craters on the surface.
20. After testing in the boiler environment, ash deposits embedded on the surfaces of the exposed samples were observed. T11 and T22 steels have indicated Fe_2O_3 as the main constituent of scale with minor peaks of Al_2O_3 , SiO_2 , ZnO and MnO which is indicative of deposition of fly ash on the surface of exposed steel. In case of superalloys Ni is main constituent in the scale with peaks of Fe_2O_3 , NiO , Al_2O_3 , SiO_2 and NiFe .
21. The thickness of metal lost is 2.0782 mm and 1.7117 mm in T11 and T22 steels respectively while in case of superalloys, thickness loss is 0.2178, 0.2301 and 0.2588 mm for Superni 600, Superni 718 and Superfer 800 respectively.
22. Presence of erosion characteristics like hills and craters on the scale along with pits and cracks has been observed which a clear indication of combined effect of erosion and corrosion caused by combined action of flue gases along with impact of fly ash.

Coated alloys

23. Al_2O_3 - 3 wt% TiO_2 coated T11, T22, Superni 600, Superni 718 and Superfer 800 substrate alloys showed better resistance to corrosion and erosion. Coating remained intact throughout the study.

24. There is no evidence of formation of oxides from the substrate alloys though there is a presence of minor cracks on the surface and also there is an indication of erosion with the formation of hills and craters on the surface but these could not expose the surface of the substrate alloys and coating has protected the surface very well. This may be due to the fact that Al_2O_3 probably hinders the grain boundary diffusion of the elements. As a consequence, there is no oxide scale growth.
25. The coatings were found beneficial in increasing the resistance to oxidation and hot corrosion in air, molten salt and coal fired boiler environment for all the alloys under study. The coatings have been very effective in improving the erosion and corrosion resistance of the substrate alloys under study and will be very beneficial in this type of environment. The compact and protective Al_2O_3 coating has separated the metal substrate from the environment. As a result, the coating has protected the alloys.
26. The temperature, at which the coatings have been found useful for the given substrate alloys in reducing the corrosion, can enhance the productivity by a significant fraction particularly in case of boilers.
27. Based on the findings of the present study, Al_2O_3 - 3 wt% TiO_2 coating showed superior performance in cyclic condition in laboratory as well as in real coal fired boiler environment. Also this coating has been found to be successful in maintaining its integrity with its respective substrates throughout the exposure to both the erosion and corrosion environments of the study, without any significant spalling of its oxide scales. This coating may prove suitable for boilers and other similar high temperature applications for erosion and corrosion prevention.

SUGGESTIONS FOR FUTURE WORK

In light of the significant results observed in the present study, some of the recommendations for future work are as follows:

1. Splat-substrate interactions may be studied to see how the particle is altered during the spray coating process, how they bond to the substrate. Detailed study of the influence of process variables on the quality of detonation gun sprayed coatings can be carried out.
2. The coating potential of Alumina-titania for other applications on metal substrates by detonation gun spraying can be explored.
3. Mechanical characterization to evaluate the interface bond strength of the coatings.
4. Attempts can be made to estimate the useful life of the detonation gun sprayed Al_2O_3 -3 wt % TiO_2 coatings by mathematical modeling.
5. Severe erosion condition testing can be explored by taking the erosion parameters viz. particle velocity, exposure temperature to still higher values.
6. Erosion testing can be made at other angles so that if any difference in erosion rate may be studied in more detail.
7. Studies may be conducted to investigate the erosion corrosion behavior of the thermal sprayed coatings obtained by other processes such as Cold spraying, Kinetic spraying etc.
8. Nano powders along with conventional powders can be tried and investigated for better properties.
9. Artificial neural network analysis for predicting the results can be explored. An analytical modeling can be carried out for predicting erosion behavior of detonation gun sprayed coatings.
10. The coatings behaviour can be studied in the actual running boiler for longer duration may be for few years by providing these coatings on the actual boiler tubes.

REFERENCES

1. Adams, B.E.M., Peeters, K.K.E, Diederren, H.S.W. and Wijnhoven, J.P.F, (2004), "Preventing boiler corrosion", *Waste Management World*, pp. 83-88.
2. Ahila, S., Ramakrishna Iyer and Radhakrishnan, V.M., (1994), "Measurement of Hot Corrosion of 2.25 Cr-1 Mo steel-347H steel Welded joint in K_2SO_4 -NaCl mixture," *Materials Letters*, Vol. 18, pp. 243-245.
3. Ahmed, R. and Hadfield, M. (1997), "Experimental measurement of the residual stress field within thermally sprayed rolling elements", *Wear*, 209, pp. 84-95.
4. Ajayi O. O. and Ludema. K. C., (1991), "Effect of microstructure on wear modes of ceramic materials", in: Ludema K.C., Editor, *Wear of Materials*, The American Society of Mechanical Engineers, New York, pp. 307-318.
5. Albina D.O., (2005) Doctoral thesis, "Theory and experience on corrosion of waterwall and superheater tubes of waste-to-energy facilities," Columbia University, New York.
6. Albina D.O., Millrath K. and Themelis N.J., (2004), "Effects of feed composition on boiler corrosion in waste to energy plants", 12th North American Waste to Energy Conference (NAWTEC 12), Georgia, USA.
7. Alkhimov, A. P., Kosarev, V. F. and Papyrin, A. N. (1990), "Method of cold gas-dynamic deposition" *Sov. Phys. Dokl.*, 35(12), 1047-1049 *Transl. American Inst. of Phys.*, 1991(As referred by *The Science and Engineering of Thermal Spray Coatings*, Chapter 3, page 96)
8. Alman D.E., Tulczak J.H., and Hawk J. (2002), "An assessment of the erosion resistance of iron-aluminide cermets at room and elevated temperatures", *Wear*, vol.329, pp.602-609.
9. Alman D.E., Tulczak J.H., Hawk J., and Hebster M. (1999), "Elevated temperature erosion of cermets" *Mater Science and Engineering A*, vol. 261, pp.245-251.
10. Arsenault B., Champagne P., Lambert P. and Dallaire S., (1989), "Zinc Nickel coating for improved adherence and corrosion resistance", *Surface and Coating Technology*, vol.37, pp. 369-378.
11. Arsenault, B., Legoux J.G., and Hawthorne H., (1997), "Slurry erosion of high velocity oxy fuel thermal sprayed coatings", in *Thermal Spray: A United Forum for Scientific and Technological Advances*, ASM International.

12. Arsenault, B., Legoux J.G., Hawthorne H., (2001) "HVOF process optimisation for the erosion resistance of WC-12Co and WC-10Co-4Cr coatings", in *Thermal Spray 2001: New Surfaces for a New Millenium*, (Ed.)C.C. Berndt, K.A. Khor, and E.F. Lugscheider, ASM International, Materials Park, Ohio, USA, pp.1051-1060.
13. ASM Handbook, (2001), "Properties and Selection: Irons, steels and high performance alloys," Vol. 1, ASM Publication, Materials park, Ohio., U.S.A.
14. ASTM standard, Designation: G76-07 (2007), Standard test method for conducting erosion tests by solid particle impingement using gas jets, West Conshohocken, PA 19428-2959, United States, pp.1-6.
15. Bahadur, S. and Badruddin R., (1990), "Erodent particle characterisation and the effect of particle size and shape on erosion", *Wear*, 138, pp. 189-208.
16. Barbooti, M. M., Al-Madfai, S. H. and Nassouri, H. J., (1988), "Thermochemical Studies on Hot Ash Corrosion of Stainless Steel 304 and Inhibition by Magnesium Sulphate," *Thermochimica Acta*, Vol. 126, pp. 43-49.
17. Barkalow, R.H. and Pettit, F.S., (1979), "Corrosion/erosion of materials in coal combustion gas turbines," *Proc. Conf. Corrosion/Erosion of Coal Conversion System Materials*, Berkeley, USA, Jan 24-26 1979, NACE, Houston, TX, pp. 139-173.
18. Bartuli C, Bertamini L., Matera S., Sturlese S , (1995), "Investigation of the formation of and amorphous film at the ZrO_2 - Y_2O_3 /NiCoCrAlY interface of thermal barrier coatings produced by plasma spraying", *Materials Science and Engineering A* , vol. 199 (2) pp. 229-237.
19. Beltzung F., Zambelli G., Lopez E., and Nicoll A.R. (1989), "Fracture toughness of plasma sprayed ceramic coatings", *Thin Solid Films*, vol. 181, pp. 407-415.
20. Bennett, A.P. and Quigley, M.B.C. (1990), "The spraying of boiler tubing in power stations", *Welding and Metal Fabrication*, November, pp.485-489.
21. Berger, L. M. (2004), Titanium oxide-new opportunities for an established coating material, in *Proceedings of the International Thermal Spray Conference'04*, CD-Rom, ISBN 3-87155-792-7, DVS-Verlag, Dusseldorf, Germany.
22. Blough, J. L., Stanko, G. J., Krawchuk, M. T., (1999) "Superheater Corrosion in Ultra-Supercritical Power Plants, Long-Term Field Exposure at TVA's Gallatin Station," Palo Alto, CA: Electric Power Research Institute, TR-111239.
23. Bluni, S.T., and Marder, A.R., (1996), "Effects of thermal spray coating composition and microstructure on coating response and substrate protection at high temperatures" *Corrosion*, Vol. 52, No.3, pp.213-218.

24. Borisov, Yu.S., Stachov, E.A. and Klimenko, V.S. (1990), "Detonation spraying: equipment, materials and applications", in *Thermische Spritzkonferenz TS90*, Vol. 90, DVS, Düsseldorf, Germany, pp. 26-32.
25. Bornstein, N. S., (1996) "Reviewing sulfidation corrosion-yesterday and today", *Journal of Materials*, pp.37-39.
26. Branco Jose Roberto Tavares, Gansert Robert, Sampath Sanjay, Berndt Christopher C., Herman Herbert, (2004), "Solid Particle Erosion of Plasma Sprayed Ceramic Coatings" *Materials Research*. vol. 7. No.1.pp147-153.
27. Buckley, D.H., (1981), "Surface effects in adhesion, friction, wear and lubrication", in: *Tribology Series 5*, Elsevier Scientific Publishing Company, Amsterdam, Netherlands.
28. Budinski K. G., (1988), "Surface engineering for wear resistance", Prentice-Hall, Inc., New Jersey, USA.
29. Budinsky, K.G. (1995), "Abrasion resistance of transport roll surfaces", *Wear*, Vol. 181-183, pp.938-943.
30. Bunshah, R. F., (1994), "Hand book of deposition technologies for films and coatings-science, technology and applications", 2nd edition, William Andrew Publishing/Noyes, Park Ridge.
31. Chatterjee, U. K., Bose, S. K. and Roy, S. K., (2001), "Environmental degradation of metals," Pub., Marcel Dekker, 270 Madison Avenue, New York.
32. Christman, T., and Schewmon, P.G., (1979), "Erosion of a strong aluminum alloy", *Wear*, vol. 52, pp. 57-70.
33. Cullity, B. D., (1978), *Elements of X-ray Diffraction*, 2nd edition, Addison-Wesley Publishing Company Inc., London.
34. Cutler, A.J.B. and Raask E., (1981), "External corrosion in coal-fired boilers: Assessment from laboratory data", *Corrosion Science* (41), pp. 789-800.
35. Dallaire, S., Levert H., and Legoux J.G., (2001), "Erosion resistance of arc-sprayed coatings to iron ore at 25 and 315°C", *Journal of Thermal Spray Technology*, 10(2), pp. 337-350.
36. Das S., Saraswathi Y. L., Mondal D. P., (2006) "Erosive-corrosive wear of aluminum alloy composites: Influence of slurry composition and speed", *Wear*, Vol. 261, pp. 180-190.

37. Das, S. K., Godiwalla, K. M., Mehrotra, S. P., Sastry, K.K.M. and Dey, P. K., (2006) "Analytical model for erosion behaviour of impacted fly-ash particles on coal-fired boiler components", *Sadhana*, vol. 31, no. 5, pp. 583-595.
38. Davis J.R., Editor, (2004) *Handbook of thermal spray technology*, ASM International, Materials Park, Ohio, USA.
39. Deb, D., Ramakrishna Iyer, S., and Radhakrishnan, V. M., (1996), "Assessment of high temperature performance of a cast nickel base superalloy in corrosive environment," *Scripta Materialia*, Vol. 35, pp. 947-952.
40. Eaton, H.E. and Novak R.C., (1989), "Erosion of plasma sprayed porous zirconia under differing conditions, in corrosion and particle erosion at high temperatures", V. Srinivasan and H. Vedula, Editors. *The Minerals, Metals and Materials Society*. pp. 269-280.
41. Elliott P., Ansari A. A., and Nabovi R., (1988) "Behavior of selected commercial alloys during high temperature oxychloridation" *Corrosion Science*, vol. 44, pp. 544-554.
42. Emmerich R, Eenders B, Martin H, Stippich F, Wolf G K, Anderson P E, Kudelha J., Lukac P., Hasuyama H., Shima Y, (1997), "Corrosion protection ability of Al₂O₃ coatings deposited with ion beam assisted deposition", *Surface and Coating Technology*, vol. 89 (1-2), pp. 47-51.
43. Engineer Manual 1110-2-3401, *Engineering and Design-Thermal Spraying: New Construction and Maintenance*, (1999) CECW-ET, , Department of the Army, U.S. Army Corps of Engineers, Washington, DC 20314-1000.
44. Erickson L.C., Westergård R., Wiklund U., Axen N., Hawthorne H.M. and Hogmark S., (1998) "Cohesion in plasma-sprayed coatings-a comparison between evaluation methods", *Wear*, 214, pp.30-37.
45. Evans, A.G. and T.R. Wilshaw, (1976), "Quasi-static solid particle damage in brittle solids-I. Observations, Analysis and Implications", *Acta Metallurgica*, Vol. 24, pp. 939-956.
46. Evans, A.G. and T.R. Wilshaw, (1977), "Dynamic solid particle damage in brittle materials: an appraisal", *Journal of Materials Science*, vol. 12, pp. 97-116.
47. Fernandes, S.M.C., Correal, O.V. and Ramanathan, L.V., (2008), "High temperature erosion-oxidation behavior of steels", *INCAST Proceedings of the International Conference on Aerospace Science and Technology 26-28 June 2008, Bangalore, India*.
48. Fervel, V., Normand, B. and Coddet, C. (1999), "Tribological behavior of plasma sprayed Al₂O₃-based cermet coating", *Wear*, Vol. 230, pp. 70-77.

49. Filmer H.L., Hochstrasser J., Nicoll A.R., and Rangaswamy S., (1990), "Plasma spray deposition of alumina-based ceramic coatings", *Ceramics Bulletin*, vol. 169 (No. 12), pp. 1955-1958.
50. Finnie, I. (1960), "Erosion of surfaces by solid particles", *Wear*, vol.3, pp. 87-103.
51. Finnie, I. and McFadden, D.H., (1978), "On the velocity dependence of the erosion of ductile metals by solid particles at low angles of incidence," *Wear*, Vol. 48, pp.181-190.
52. Finnie, I., (1958), "The mechanism of erosion of ductile metals," *Proceedings of the Third U.S. National Congress of Applied Mechanics*, pp. 527-532.
53. Finnie, I., (1995), "Some Reflections on the Past and Future of Erosion", *Wear*, 186-187, pp.1-10.
54. Fryburg, G. C., Kohl, F. J., Stearns, C. A. and Fielder, W. L., (1982), "Chemical Reactions Involved in the Initiation of Hot Corrosion of B-1900 and NASA-TRW VIA," *The Journal of The Electrochemical Society*, Vol. 129, No. 3, pp. 571-85.
55. Gage, R. M., Nestor, D. M. and Yenni, Y.M. (1962), "Collimated electric arc powder deposition process", US Patent, 3 016 447.
56. Gaskell, D.R., (1973), "Introduction to Metallurgical Thermodynamics", 2nd edition. McGraw-Hill, New York, NY, p.287.
57. Gee M.G., Gee R.H. and McNaught I., (2003), "Stepwise Erosion as a Method for Determining the Mechanisms of Wear in Gas Borne Particulate Erosion", *Wear*, pp.1-11.
58. Giannini, G. and Ducati, A. (1960), "Plasma stream apparatus and method", US Patent 2 922 869.
59. Gitanjaly, (2003) Doctoral thesis, "Role of Inhibitors on Hot Corrosion of Superalloys in $\text{Na}_2\text{SO}_4\text{-V}_2\text{O}_5$ Environment," Indian Institute of Technology Roorkee, India.
60. Gledhill, H.C., Turner, I.G. and Doyle, C: (1999), "Direct morphological comparison of vacuum plasma sprayed and detonation gun sprayed hydroxyapatite coatings for orthopaedic applications" *Biomaterials*, 20, pp. 315-322.
61. Goberman, D., Sohn, Y.H., Shaw, L., Jordan, E. and Gellm, M. (2002), "Microstructure development of $\text{Al}_2\text{O}_3\text{-13wt.\%TiO}_2$ plasma sprayed coatings derived from nanocrystalline powders" *Acta Materialia*, vol. 50, issue 5, pp. 1141-1152.
62. Goebel, J. A., Pettit, F. S. and Goward, G. W., (1973), "Mechanisms for the Hot Corrosion of Nickel-Base Alloys," *Metallurgical and Materials Transactions B*, Vol. 4, pp. 261-275.

63. Goldstein Joseph I., Newbury Dale E., Echlin Patrick, Joy David C., Fiori Charles, Lifshin Eri, (1992), *Scanning Electron Microscopy and X-Ray Microanalysis: A Text for Biologists, Materials Scientists, and Geologists*. 2nd edition, New York: Plenum Press.
64. Grabke, H.J, Reese E. and Spiegel M. (1995), "The effects of chloride, and sulfur dioxide in the oxidation of steels below deposits", *Corrosion Science* (7), pp.1023-1043.
65. Guessasma S, Bounazef Mokhtar, Nardin Philippe and Sahraoui Tahar (2006), "Wear behavior of alumina-titania coatings: analysis of process and parameters" *Ceramics International* vol.32, pp. 13-19.
66. Guo D. Z., Li F. L., Wang J. Y., Sun J. S. (1995), "Effects of post-coating processing on structure and erosive wear characteristics of flame and plasma spray coatings", *Surface and Coatings Technology*, Vol. 73, Issues 1-2, pp. 73-78.
67. Haanapell V.A.C , Fransen T, Greedink B , Gellings P J and Stroosnijder M F, (1991), "The properties of protective oxide scales containing serium on alloy 800H in oxidising and oxidising sulfidising environments", *Oxidation of Metals* vol. 35, pp. 405-414.
68. Habib, K.A., Saura, J.J., Ferrer, C., Damra, M.S., Giménez, E., Cabedo, L., (2006) "Comparison of flame sprayed Al₂O₃/TiO₂ coatings: Their microstructure, mechanical properties and tribology behavior", *Surface & Coatings Technology* vol.201, pp.1436-1443.
69. Hack, H., and Stank, G., (2007) "Experimental Results for Fireside Corrosion Resistance of Advanced Materials in Ultra-Supercritical Coal-Fired Power Plants" 32nd International Technical Conference on Coal Utilization & Fuel Systems, Clearwater, Florida, USA
70. Halling, J. and Arnell, R.D., (1984), "Ceramic coatings in the war on wear", *Wear*, Vol. 100, pp. 367-380.
71. Hancock, P. and Nicholls, J.R., (1988), "Application of fracture mechanics to failure of surface oxide scales," *Material Science and Technology*, Vol. 4, pp. 398-406.
72. Hansen, J.S., (1979), "Relative erosion resistance of several metals, Erosion: Prevention and Useful Applications," STP 664, ASTM, pp.148-162.
73. Harb, J.N. and Smith, E.E., (1990), "Fireside corrosion in PC-Fired boilers", *Progress in Energy and Combustion Science*, Vol.16, pp.169-190.
74. Hartfield-Wunsch S.E., Tung S.C., (1994) "The effect of microstructure on the wear behaviour of thermal spray coatings" in: C.C. Berndt, S. Sampath Eds., *Proc. 7th National Thermal Spray Conference*, Boston, MA, ASM International, pp.19-24.

75. Hawthorne F.M., Erickson L. C., Ross D., Tan H. and Trockzynsko T., (1997), "The microstructural dependence of wear and indentation behaviour of some plasma-sprayed alumina coatings", *Wear*, vol. 203-204, pp. 709-714.
76. Hawthorne, H.M., Arsenault B., Immarigeon J. P., Legoux J. G., Parameswaran V. R., (1999), "Comparison of slurry and dry erosion behaviour of some HVOF thermal sprayed coatings", *Wear*, vol. 225-229, pp.825-834.
77. Haynes J.A, Rigeny E D, Ferber M K and Porter W D, (1996), "Oxidation and degradation of a plasma sprayed thermal barrier coating spray system", *Surface and Coating Technology*, Vol. (86-87) (1), pp. 102-108.
78. He C., Wang Y. S., Wallace J. S. and Hsu S. M., (1993), "Effect of microstructure on the wear transition of zirconia-toughened alumina" *Wear*, vol.162 -164, pp 314-321.
79. He Y., Lee K. Tewari N, S. and Miller R. A., (2000), "Developments of refractory silicate Ytria stabilized zirconia dual layer thermal barrier coatings", *Journal of Thermal spray technology*, vol. 9(1) pp. 59-67.
80. Hearley, J. A., Little, J.A., and Sturgeon, A. J., (1999), "The erosion behaviour of Ni Al intermetallic coatings produced by high velocity oxy-fuel thermal spraying," *Wear*, Vol. 233-235, pp. 328-333.
81. Heath, G. R., Heimgartner, P., Irons, G., Miller, R. and Gustafson, S., (1997), "An Assessment of Thermal Spray Coating Technologies for High Temperature Corrosion Protection," *Materials Science Forum*, Vol. 251-54, pp. 809-16.
82. Heiman R.B., (1996), "Plasma spray coating, principle and application", VCH, Weinheim, Germany.
83. Heimann, R.B. (1996), "Applications of plasma-sprayed ceramic coatings", *Key Engineering Materials*, Vols. 122-124, pp. 399-442.
84. Hidalgo H. V., Varela F.J.B., Menendez A.C., Martinez S.P., (2001), "A Comparative Study of High-Temperature Erosion Wear of Plasma-Sprayed NiCrBSiFe and WC-NiCrBSiFe Resistance Coatings under Simulated Coal-Fired Boiler Conditions", *Tribology International*, Vol.34, pp. 161-169.
85. Hidalgo V H, Varela F.J. B., Calle J M, and Menendez A C, (2000), "Characterisation of NiCr flame and plasma sprayed coatings for use in high temperature regions of boilers" *Surface Engineering* 16, pp. 137-142.
86. Hidalgo V. H., Varela F. J. B., Martinez S. P., and Espana S. G., (1999), *Proceedings of the United Thermal Spray Conference, Germany*, pp. 683-686.

87. Hidalgo V.H., F.J. Belzunce Varela, and E. Fernandez Rico, (1997). "Erosion Wear and Mechanical Properties of Plasma-Sprayed Nickel-and Iron-Based Coatings Subjected to Service Conditions in Boilers", *Tribology International*, Vol. 30, No. 9, pp. 641-649.
88. Higuera, H. V., Belzunce, F. J. and Carrilez, M. A., (1998), "Characterization and High Temperature Behavior of Thermal Sprayed Coatings Used in Boilers" in Coddet, C., (Ed.) *Proceedings of 15th International Thermal Spray Conference, Thermal Spray: Meeting the Challenges of the 21st Century (Nice, France)*, Vol. 1, pp. 617-621.
89. Hjörnhede A., Norling R. and Olefjord I., (2000), "Erosion corrosion of coatings and steels at 550°C", in: P. Neumann, D. Allen, E. Teuckhoff (Eds.), *Proceedings of the International Conference EUROMAT'99*, Wiley-VCH, Weinheim, Germany, pp. 411-416.
90. Hocking M.G., (1993), "Coating resistant to Erosive/Corrosive and severe environment", *Surface and coating Technology*, vol. 62, pp. 460-466.
91. Hussainova I. and Antonov M. (2003), "Elevated temperature wear of chromium carbide based cermets", *Proceedings of the Estonian Academy of Sciences Engineering*, vol.9/4, pp.261-271.
92. Hutchings I.M. and Levy A.V., (1989), "Thermal effects in the erosion of ductile metals" *Wear*, vol.131, pp.105-121.
93. Hutchings I.M., (1992 A), "Tribology: Friction and Wear of Engineering Materials", Edward Arnold, London.
94. Hutchings, I M., (1992B), "Ductile-Brittle transitions and wear maps for the erosion and abrasion of brittle materials", *Journal of Physics D: Applied Physics*, 25, pp. A212-A221.
95. Hutchings, I.M. and Winter R. E., (1974), "Particle erosion of ductile metals; A mechanism of material removal", *Wear* Vol. 27, pp.121 -128.
96. Hutchings, I.M., (1992A), *Tribology: Friction and Wear of engineering materials*. London: Edward Arnold.
97. Irons, G. (1994), "Investigation of erosion resistant chromium carbide coatings sprayed with the high pressure HVOF process", in *Thermal Spray Industrial Applications*. Boston, Massachusetts: ASM International, Materials Park, Ohio., USA.
98. Irving, R., Knight, R. and Smith, R.W. (1993), "The HVOF process-the hottest topic in the thermal spray industry", *Welding Journal*, pp. 25-30.

99. Iyer, S. R., Iyer, K. J. L. and Radhakrishnan, V. M., (1987), "High Temperature Corrosion of a Ni-Base Superalloy by Vanadium," Proceedings of 10th ICMC, Madras, India, Vol. IV, pp. 3665-70.
100. John, R. C., (1999), "Compilation and use of corrosion data for alloys in various high-temperature gases," Corrosion 99, Paper 99073, Houston, Texas, NACE International.
101. Jones, D.A., (1996), Principles and Prevention of Corrosion, 2nd Edition, Upper Saddle River, NJ Prentice Hall
102. Jordan, E.H., Gell, M., Sohn, Y.H., Goberman, D., Shaw, L., Jiang, S., Wang, M., Xiao, T.D., Wang, Y. and Strutt, P. (2001), "Fabrication and evaluation of plasma sprayed nanostructured alumina-titania coatings with superior properties" Materials Science and Engineering A, vol. 301 pp. 80-89.
103. Kadyrov, E. and Kadyrov, V. (1995), "Gas dynamical parameters of detonation powder spraying", Journal of Thermal Spray Technology, 4, pp. 280-286.
104. Kadyrov, V., (1988), "Detonation gas powder technique", in Proceedings of the International Symposium on Advances in Thermal Spraying Technologies and Allied Coatings, High Temperature Society of Japan, Osaka, Japan, pp. 43-48.
105. Kamachi K., Magome M., Ueno K., Ueno G., Yoshioka T., (1991), "A joint study on properties of plasma sprayed alumina coatings" in Proc. 3rd National Thermal Spray Conference, Long Beach CA, ASM International, pp. 497-501.
106. Kamaraj, M., (2003), "Rafting in single crystal nickel-base superalloys-An overview," Sadhana - Academy Proceedings in Engineering Sciences, Vol. 28 (1-2), pp. 115-128.
107. Kane, R. H., (1980), "Characterization of high temperature gaseous environments," Corrosion, Vol. 36, No. 3, pp. 112-118.
108. Kang, C.T., Chang, S.L., Pettit, F.S. and Birks, N., (1985), "Synergisms in the degradation of metals exposed to erosive high-temperature oxidising environments," in G. Simkovich and VS. Stubican (eds.), Transport in Non- nonstoichiometric Compounds, Plenum, New York, pp. 411-427.
109. Kang, C.T., Pettit, F.S. and Birks, N., (1987), "Mechanisms in the simultaneous erosion-oxidation attack of nickel and cobalt at high temperature," Metallurgical and Materials Transactions A, Vol. 18, pp.1785-1803.
110. Karlsson A., Moller P. and Johansen V., (1990), "Iron and steel corrosion in a system of O₂, SO₂ and alkali chloride. The formation of low melting point salt mixture", Corrosion Science (30), pp. 153-158.

111. Kaur M, Singh H, Prakash S, (2008) "A survey of the literature on the use of high velocity oxy-fuel spray technology for high temperature corrosion and erosion corrosion resistant coatings", *Anti Corrosion Methods and Materials*, Vol. 55, No.2, pp.86-96.
112. Kay, A. (1987). "Jet Kote application for corrosion protection", in *Thermal Spray: Advances in Coatings Technology*, D.L. Houck (Ed.), ASM International, Materials Park, Ohio., USA, pp. 393-397.
113. Kerby, R. C. and Wilson J. R., (1973), "Corrosion of Metals by Liquid Vanadium Pentoxide and the Sodium Vanadates," *Trans. ASME*, pp. 36-44.
114. Khanna, A.S. and Gnanamoorthy, J., B., (1982), "Post breakaway oxidation kinetics of two ferritic steels," *Oxidation of Metals*, Vol. 18, pp. 315-331.
115. Kharlamov, Y. A., (1987), "Detonation Spraying of Protective Coatings" *Materials Science and Engineering*, pp.1-37.
116. Kingswel R. I, Rickerby D.S., Scott K.T., Bull S.J., (1991), "Comparison of the erosive wear behaviour of vacuum plasma sprayed and bulk alumina" in *Proc. 3rd National Thermal Spray Conference*, ASM International, pp. 179-185.
117. Kingswell, R., Rickerby D.S, Bull S.J., Scott K.T., (1991), "Erosive wear of thermally sprayed tungsten coatings", *Thin Solid Films*, 198, pp 139-148.
118. Kleis, I. R. and Kullu P (2008), *Solid Particle Erosion Occurrence, Prediction and Control*, Springer-Verlag London.
119. Knight, R. and Smith R.W., (1998), "Thermal spray forming of materials," *Powder Metal Technologies and Applications*, Chapter in *ASM Handbook* ASM International, pp. 408-419.
120. Kobayashi, Y. and Yamaguchi, S. (2004) "Development of thermal sprayed coatings applied for boiler tube", in *Proceedings of the International Thermal Spray Conference '04*, CD-Rom, ISBN 3-87155-792-7, DVS-Verlag, Düsseldorf, Germany.
121. Koch, G.H., Brongers, M.P.H., Thompson, N.G., Virmani, Y.P., Payer, J.H. (2001), *corrosion cost and preventive strategies in the united states*, Technical Report No.FHWA-RD-01-156
122. Kolta, G. A., Hewaidy, L. F. and Felix, N. S., (1972), "Reactions between Sodium Sulphate and Vanadium Pentoxide," *Thermochimica Acta*, Vol. 4, pp. 151-64.
123. Kosel, T.H., (1992), "Solid particle erosion, in: Friction," in: *Lubrication and Wear Technology*, ASM Handbook, Vol.18, pp. 199-213.

124. Krishnamoorthy, P. R., Seetharamu, S., and Sampathkumar, P., (1993), "Influence of the mass flux and impact angle of the abrasive on the erosion resistance of materials used in pulverized fuel bends and other components in thermal power stations," *Wear*, Vol. 165, pp. 151-157.
125. Kübarsepp J, Klaasen H, Mikli V, Viljus M. (2002), "Erosive Wear of TiC-base Cermets" *Proc. of Kaunas Univ of Techn and Acad of Sci of Lithuania. Materials Science*, vol.8/4, pp.486-88.
126. Kumar S., Subramanya Sarma V. and Murty, B.S., (2008), "A statistical analysis on erosion wear behaviour of A356 alloy reinforced with in situ formed TiB₂ particles," *Materials Science and Engineering A*, vol. 476, pp. 333-340.
127. Lai G.Y., (1991), "High temperature corrosion: issues in alloy selection", *Journal of Materials*, 43:11, pp.54-60.
128. Lai Y., Rothman M. F., Baranow S., and Herchenroeder R. B., (1983) "Recuperator Alloys for High-Temperature Waste Heat Recovery" *J. Metals*, vol.7, pp.24-27.
129. Lai, G. Y., (1990), *High temperature corrosion of engineering alloys*, ASM Inter. Book, Materials Park, Ohio, American Society for Metals,
130. Langer, G., Kremsner, A. and Polak, R. (2005), "TeroComposite™ - coating solutions against high-temperature corrosion and erosion in boiler applications", in *Proceedings of the International Thermal Spray Conference '05*, CD-Rom, ISBN 3-87155-793-5, DVS-Verlag, Dusseldorf, Germany.
131. Lathabai, S., Ottmuller, M., and Fernandez, I., (1998), "Solid particle erosion behaviour of thermal spray ceramic, metallic and polymer coatings", *Wear*, vol. 221, pp. 93-108.
132. Legoux J.G., Arsenault B., Immarigeon J.P., Parameswaran V.R., Hawthorne H., (1999) "Slurry and dry erosion of arc sprayed metal and composite coating", in *Tagungsband Conference proceeding*, (Ed.) E. Lugscheider, P.A. Kammer, (Pub.) DVS Deutscher Verband für Schweißen, Germany, , pp.422-427
133. Leushake U., Krell T , Schulz U, Peters M , Kaysser W A, and Rabin B H, (1997), "Microstructure and phase stability of E-B PVD alumina/zirconia for thermal barrier coatings applications", *Surface and Coating Technology*, vol. 94-95, pp. 131-136.
134. Levin I., Bendersky, L.A., Brandon, D.G., Rühle M., (1997), "Cubic to monoclinic phase transformations in alumina", *Acta Materialia*, 45 (9), pp 3659-3669
135. Levy A V, Slamovich E and Jee N (1986), "Elevated temperature combined erosion-corrosion of steels", *Wear*, vol.110, pp117-149.

136. Levy A. V., (1988), "The erosion-corrosion behavior of protective coatings", *Surface and Coatings Technology*, vol.36, pp.387-406.
137. Levy A., (1986), "The platelet Mechanism of Erosion of Ductile Metals," *Wear*, vol. 108, pp. 1-21.
138. Levy A.V., Azhazadeh M., and Hickey G., (1984) "The effect of test variables on the platelet mechanism of erosion", Rep. LBL-17835, (Lawrence Berkeley Laboratory, University of California, Berkeley, CA, U.S.A.)
139. Levy, A. and Wang B., (1988), "Erosion of hard material coating systems", *Wear*, 121, pp. 325-346.
140. Levy, A., (1983), "Erosion mechanisms in ductile and brittle materials, in erosion by liquid and solid impact", Sixth International Conference, Cavendish Laboratory, University of Cambridge: Cambridge, England, pp.39.1-39.7.
141. Levy, A., (1988), "The erosion corrosion behaviour of protective coatings", *Surface and Coatings Technology*", pp. 387-406.
142. Levy, A.V., (1993), "The erosion-corrosion of tubing steels in combustion boiler environments", *Corrosion Science*, Vol. 35 (5-8), pp. 1035-1043.
143. Levy, A.V., (1995), *Solid particle erosion and erosion-corrosion of materials*. ASM International. Materials Park, Ohio, USA.
144. Levy, M., Huie, R. and Pettit, F., (1989), "Oxidation and Hot Corrosion of Some Advanced Superalloys at 1300 to 2000 F (704 to 1093°C)," *Corrosion*, Vol. 45, No. 8, pp. 661-674.
145. Leyens C. , Schulz U, Pint B.A., and Wright I.G., (1999), "Influence of Electron Beam physical vapour deposited thermal barrier coating microstructure on thermal barrier coating system performance under cyclic oxidation conditions", *Surface and Coating Technology* , vol.120-121, pp. 68-76.
146. Li Y. S., Niu Y, and Wu W.T., (2003), "Accelerated corrosion of pure Fe, Ni, Cr and several Fe-based alloys induced by ZnCl₂-KCl at 450°C in oxidizing environment." *Material Science and Engineering A*, 345, pp.64-71.
147. Li, Chang-Jiu and Ohmori, Akira (1996), "The lamellar structure of a detonation gun sprayed Al₂O₃ coating" *Surface and Coatings Technology*, vol. 82, (3), pp. 254-258.
148. Li, M. H., Sun, X. F., Li, J. G., Zhang, Z. Y., Jin, T., Guan, H.R. and Hu, Z. Q., (2003), "Oxidation Behaviour of a Single-Crystal Ni-Base Superalloy in Air-I: At 800 and 900°C," *Oxidation of Metals*, Vol. 59, No. 5-6, pp.591-605.

149. Liebhard, M. and Levy A., (1991), "The effect of erodent particle characteristics on the erosion of metals", *Wear*, 151, pp.381-390.
150. Lin Xinhua, Zeng Yi, Ding Chuanxian and Zhang Pingyu (2004) "Effects of temperature on tribological properties of nano structured and conventional Al₂O₃-3 wt. % TiO₂ coatings", *Wear*, vol. 256, pp.1018-1025.
151. Lin, X., Zeng, Y., Zhou, X. and Ding, C., (2003) "Microstructure of alumina-3 wt.% titania coatings by plasma spraying with nano structured powders", *Material Science Engineering A*, 357, pp. 228-234.
152. Luo, H., Goberman, D., Shaw, L. and Gell, M., (2003) Indentation fracture behaviour of plasma-sprayed nanostructured Al₂O₃-13 wt.%TiO₂ coatings. *Materials Science and Engineering A*, 346, pp.237-245
153. MacAdam S.S. and Stringer J., (1995), "The circumferential distribution of wastage on in-bed tubes in fluidized bed combustors," *Wear*, 186-187, pp. 325-331.
154. Makela, A., Vuroisto, P., Lahdensuo, M., Niemi, K. and Mantyla, T. (1995), "Rolling contact fatigue testing of thermally sprayed coatings" *International Journal of Fatigue*, 17, pp. 305.
155. Margadant N, Siegmann S, Patscheider J, Keller T, Wagner W, Ilavsky J, Pisacka J, Barbezat G, and Fiala P, (2001), "Microstructure- Property relationships and cross-property-correlations of thermal sprayed Ni-alloy coatings", *Proceedings of the International Thermal Spray Conference*, pp. 643-646.
156. Mbabazi J. G., Sheer T. J. and Shandu R., (2004), "A model to predict erosion on mild steel surfaces impacted by boiler fly ash particles", *Wear*, vol. 257, no. 5-6, pp. 612-624.
157. McPherson R., (1989), "A review of microstructure and properties of plasma sprayed ceramic coatings", *Surface and Coating Technology*, vol. 39/40, pp. 173-181.
158. McPherson, R. (1973), "Formation of meta stable phases in flame and plasma prepared alumina", *Journal of Materials Science*, vol. 8, pp. 851-858.
159. McPherson, R. (1980) "On the formation of thermally sprayed alumina coatings", *Journal of materials science*, 15, pp. 3141-3149
160. *Metals Handbook*, (1975), 'Failure analysis and Prevention,' Vol. 10, ASM Publication, Metals Park Ohio., USA.
161. Mishra S. C., Sahu Anupama, Das Rojaleena, Satapathy Alok, Sen S., Ananthapadmanabhan P. V. and Sreekumar K. P., (2008), "Microstructure, adhesion, and

- erosion wear of plasma sprayed alumina-titania composite coatings”, *Journal of reinforced plastics and composites*, DOI: 10.1177/0731684407087758, SAGE Publications.
162. Mishra S.B. (2006), Doctoral thesis, “Development of erosion-corrosion wear resistant coatings on superalloys”, Indian Institute of Technology Roorkee, India.
 163. Mishra, S.B., Chandra, K. and Prakash, S. (2008), “Characterisation and erosion behaviour of NiCrAlY coating produced by plasma spray method on two different Ni-based superalloys,” *Materials Letter*, Vol. 62, pp. 1999-2002.
 164. Mishra, S.B., Chandra, K., Prakash, S. and Venkataraman, B (2006), “Erosion performance of coatings produced by shrouded plasma spray process on a Co-based superalloy,” *Surface and Coating Technology*, Vol. 201, pp. 1477-1487.
 165. Mishra, S.B., Prakash, S. and Chandra, K., (2006), “Studies on erosion behavior of plasma sprayed coatings on a Ni-based superalloy,” Vol. 260, pp. 422 - 432
 166. Misra, A. and Finnie I., (1981), “On the size effect in abrasive and erosive wear”, *Wear*, 65, pp. 359-373.
 167. Misra, A. K., (1986), “Mechanism of Na₂SO₄-Induced Corrosion of Molybdenum Containing Nickel-Base Superalloys at High Temperatures,” *The Journal of The Electrochemical Society*, Vol. 133, No. 5, pp. 1029-1037.
 168. Miyoshi Kazuhisa, Sutter James K., Mondry Richard J., Bowman Cheryl, Ma Kong, Horan Richard A., Naik Subhash K., and Cupp Randall J., (2003) “Measurements of Erosion Wear Volume Loss on Bare and Coated Polymer Matrix Composites” NASA/TM-2003-212628
 169. Morgen-Warren, E.J. (1992), “Thermal spraying for boiler tube protection”, *Welding and Metal Fabrication (UK)*, Vol. 60, pp. 25-31.
 170. Murakami K., Okamoto T., Matsumoto H. (1989), “Characterization of flame-sprayed coating layers of high carbon and high silicon irons” *Material Science and Engineering A*, Vol. 112, pp.185-191.
 171. Musil J., Alaya M and Oberacker R, (1997), “Plasma sprayed duplex and graded partially stabilized zirconia thermal barrier coatings: Deposition Process and properties”, *Journal of Thermal spray Technology*, vol. 6 (4), pp.449-455.
 172. Naerheim Y., Coddet C., Droit P., (1995), “Effect of thermal spray process selection on the tribological performance of WC-Co and Al₂O₃-TiO₂ coatings” in *Proceedings 8th Surface Modification Technologies (SMT8)*, The Institute of Materials, London, pp. 734-746.

173. Nanni, P., Buscaglia, V., Asmundis, C. D. and Roy, S. K., (1987), "Sodium Sulphate Induced Hot Corrosion of Pure Fe, Mn and Cr in Combustion Gas," Proceedings of 10th ICMC, Madras, India, Vol. IV, pp. 3413-22.
174. Natesan, K., (1976), "Corrosion-Erosion Behavior of Materials in a Coal-Gasification Environment," Corrosion, Vol. 32, No. 9, pp. 364-70.
175. Natesan, K., (1985), "High-temperature corrosion in coal gasification systems," Corrosion, Vol. 41, No. 11, pp. 646-55.
176. Natesan, K., (1993), "Applications of coatings in coal-fired energy systems," Surface and Coatings Technology, Vol. 56, pp. 185-197.
177. Nerz, J.E., Kaufold R., Kushner Jr. B.A., and Rotolico A., (1991), "Reduction of solid particle erosion by using HVOF and HEP Coating Deposition Methods", In Thermal Spray Coatings: Properties, Processes and Applications. Pittsburgh, Pennsylvania: ASM International.
178. Nicholls, J.R., Deakin M.J., and Rickerby D.S., (1999), "A comparison between the erosion behaviour of thermal spray and electron beam physical vapour deposition thermal barrier coatings", Wear, 233-235, pp.352-361.
179. Nielsen, H.P., Frandsen, F.J., Dam-Johansen, K., and Baxter, L.L., (2000), "The implications of chlorine-associated corrosion on the operation of biomass-fired boilers", Progress in Energy and Combustion Science (26), pp. 283-298.
180. Niemi K., Sorsa P., Vuoristo P., Mantyla T., (1994), "Thermally sprayed alumina coatings with strongly improved wear and corrosion resistance" in: C.C. Berndt, S. Sampath Eds., Proc. 7th National Thermal Spray Conference, ASM International, pp. 533-536.
181. Niemi K., Vuoristo P. and Mantyla T., (1994), "Properties of Alumina-Based Coatings Deposited by Plasma Spray and Detonation Gun Spray Processes", Journal of Thermal Spray Technology, Vol. 3(2), pp 199-203.
182. Norling R. and Olefjord I., (2003), "Erosion-corrosion of Fe- and Ni-based alloys at 550°C", Wear, vol. 254, pp.173-184.
183. Norling R., and Olefjord I., (2000), "Erosion-corrosion of 304 tubes in bubbling fluidised beds at 550 °C", Material Science Forum, vol. 369-372, pp.515- 522.
184. Normand B. , Fervel V., Coddet C., Nikitine V. (2000), "Tribological properties of plasma sprayed alumina-titania coatings: role and control of the microstructure", Surface and Coatings Technology, vol. 123 , pp 278-287

185. Otero, E., Pardo, A., Hernaez, J. and Perez, F. J., (1992), "The Corrosion of Some Superalloys (At 1000 K) in Molten Eutectic Mixture 60% V₂O₅-40% Na₂SO₄. The Influence of the Oxygen and Carbon Residues," *Corrosion Science*, Vol. 34, pp. 1747-57.
186. Pajonk G and Steffans H. D., (1997), "Corrosion behavior of coated materials, *Fresenius Journal of analytical chemistry*", vol.357 (1-2), pp. 285-290.
187. Pantelis D. I., Psyllaki P and Alexopoulos N, (2000), "Tribological behavior of plasma sprayed Al₂O₃ Coatings under severe wear conditions", *Wear* 237(2), pp 197-204.
188. Pawlowski L., (1995), "The science and engineering of thermal spray coatings", John Willey and sons, USA.
189. Pettit, F. S. and Giggins, C. S. (1987), "Hot Corrosion, Ch 12", *Superalloys II*, Sims C. T., Stolof, N S and Hagel W. C. (Eds.) Wiley Pub., N.Y.
190. Pettit, F. S. and Meier, G. H., (1984), "Oxidation and Hot corrosion of Superalloys," *Superalloys 85* Eds. (1985), M. Gell, C. S. Kartovich, R. H. Bricknel, W. B. Kent, J. F. Radovich (Eds.), The Metallurgical Society of American Institute of Mining, Metallurgical and Petroleum Engineers (AIME), Warrendale, Pennsylvania, pp. 651-687.
191. Poorman, R. M., Sargent, H. B. and Lamprey, H. (1955), "Method and apparatus utilizing detonation wave for spraying and other purposes" US Patent 2 714 553.
192. Prakash, S., Singh, S., Sidhu, B. S. and Madeshia, A., (2001), "Tube failures in coal fired boilers," *Proc. National Seminar on Advances in Material and Processing*, Indian Institute of Technology, Roorkee, India, pp. 245-253.
193. Quadir T and Schewmon P G (1981), "Solid particle erosion mechanisms in copper and two copper alloys", *Metallurgical and Materials Transactions A*, vol. 12, pp.1163-1176.
194. Rabiei, A., Mumm D.R., Hutchinson J.W., Schweinfest R., Ruhle M, Evans A.G., (1999), "Microstructure, deformation and cracking characteristics of thermal spray ferrous coatings", *Materials Science and Engineering A*, 269, pp.152-165.
195. Rademakers P., Hesseling W. and Wetering J., (2002), "Review on corrosion in waste incinerators, and possible effects of bromine." TNO Report
196. Ramachandran K, Selvarajan V, Ananthapadmanabhan P.V, Sreekumar K.P.(1998) "Microstructure, adhesion, microhardness, abrasive wear resistance and electrical resistivity of the plasma sprayed alumina and alumina-titania coatings", *Thin Solid Films* 315, pp144-152

197. Ramesh M.R. (2008), Doctoral thesis, "Studies on the role of HVOF coatings in improving resistance to hot corrosion and erosion", Indian Institute of Technology Roorkee, India
198. Ramesh, C. S., Seshadri, S. K. and Iyer, K. J. L., (1991), "A survey of aspects of wear of metals," Indian Journal of Technology, Vol. 29, pp. 179-185.
199. Ramm D.A.J., Clyne T.W., A.J. Sturgeon, S. Dunkerton, (1994), "Correlations between spraying conditions and microstructure for alumina coatings produced by HVOF and VPS", in: C.C. Berndt, S. Sampath, Eds., Proc. 7th National Thermal Spray Conference, ASM International, pp. 239.
200. Ramm D.A.J., Hutchings I.M. and Clyne T.W., (1993), "Erosion resistance and adhesion of composite metauceric coatings produced by plasma spraying" J. Phys. IV France 03 pp C7-913-C7-919
201. Rapp, R. A. and K. S. Goto, (1981), "The Hot Corrosion of Metals by Molten Salts," Symposium on Fused Salts, J. Braunstein and J. R. Selman (Eds.), The Electrochemical Society, Pennington, N. J., pp.159.
202. Rapp, R. A., and Zhang, Y. S., (1994) "Hot corrosion of materials: fundamental studies", Journal of Materials, pp.47-55.
203. Rishel, D.M., Pettit, F.S. and Birks, N., (1990), Some principle mechanisms in the simultaneous erosion and corrosion attack of metals at high temperatures" in Levy, A.V., (ed.) Proceedings of Conference on Corrosion-Erosion-Wear of Materials at Elevated Temperatures, NACE, Houston, TX, paper no. 16, pp.1-23.
204. Roberge, P. R., (2000), Handbook of Corrosion Engineering, McGraw-Hill Professional; 1st edition, New York
205. Rogers, P.M., Hutchings, I.M. and Little, J.A., (1995), "Coatings and surface treatments for protection against low-velocity erosion-corrosion in fluidized beds," Wear, Vol. 186/187, pp. 238-246.
206. Rogers, P.M., Shipway, P.H., Hutchings, I.M., Little, J.A., (1991), "The erosion-corrosion of plasma sprayed alumina coatings on a low chromium steel", in Levy A.V. (Ed.) Proceedings of the 4th Berkeley Conference on Corrosion-Erosion-Wear of Materials at High Temperatures, NACE: Houston, Texas, p. Paper 35.
207. Roy M, (2006) "Elevated temperature erosive wear of metallic materials", Journal of Physics D: Applied Physics, vol.39, pp101-124.
208. Ruff, A.W. and S.M. Wiederhorn, (1979), "Erosion by solid particle impact", in Treatise on Materials Science and Technology, pp.69-125.

209. Sadique, S. E., Mollah, A. H., Islam, M. S., Ali, M. M., Megat, M. H. H. and Basri, S., (2000), "High-Temperature Oxidation Behavior of Iron-Chromium-Aluminum Alloys," *Oxid. Met.*, Vol. 54, Nos. 5-6, pp. 385-400.
210. Safai S., (1979), Doctoral thesis, "A microstructural investigation of plasma sprayed metal and oxide coatings," State University of New York, Stony Brook, University Microfilm No. 7919359
211. Samad, A. A., Lugscheider, E., Bobzin, K. and Maes, M. (2004), "Tribological behaviour of thermally sprayed ceramic coatings in contact with 100 Cr6 steel at high temperatures", in *Proceedings of the International Thermal Spray Conference'04*, CD-Rom, ISBN 3-87155-792-7, DVS-Verlag, Dusseldorf, Germany, pp.1-4.
212. Saravanan P., Selvarajan ,V. Rao D.S., Joshi S.V. and Sundararajan G., (2000) "Influence of process variables on the quality of detonation gun sprayed alumina," *Surface and Coatings Technology*, 123, pp. 44-54
213. Satapathy Alok, (2005), Doctoral thesis, "Thermal spray coating of red mud on metals ", National Institute of Technology Rourkela, India
214. Schneider Klaus Erich, Belashchenko Vladimir, Dratwinski Marian, Siegmann Stephan , Zagorski Alexander, (2006), "Thermal spraying for power generation components" Wiley-VCH Verlag GmbH & Co. KGaA, Weinheim
215. Schwarz, E. (1980), "Detonation for nuclear and related industries", in *Proceedings of the 9th International Thermal Spray Conference*, Hague, Netherlands, pp. 91-101.
216. Schwetzke, R. and Kreye H., *Cavitation* (1996), "Erosion of HVOF coatings", in *Thermal Spray: Practical Solutions for Engineering Problems*. ASM International.
217. Scott K.T., Kingswell R., (1991) in: Rickerby D.S., Matthews A. (Eds.), *Advanced Surface Coatings. A Handbook of Surface Engineering*, Chapman and Hill, New York: Blackie USA, p. 215.
218. Seiersten, M. and Kofstad, P., (1987), "The Effect of SO₃ on Vanadate-Induced Hot Corrosion," *High Temp. Technology*, Vol. 5, No. 3, pp. 115-122.
219. Sheldon G.L. and Finnie I. (1966), "On the ductile behavior of nominally brittle materials during erosive cutting", *Journal of Engineering for Industry-Transactions of the ASME*,88, pp. 387-392
220. Shi, L., (1993), "Accelerated Oxidation of Iron Induced by Na₂SO₄ Deposits in Oxygen at 750°C- A New Type Low-Temperature Hot Corrosion," *Oxidation of Metals*, Vol. 40, Nos. 1-2, pp. 197-211.

221. Shida Y and Fujikawa H (1985), "Particle erosion behaviour of boiler tube materials at elevated temperature", *Wear*, vol.103, pp 281-296.
222. Shui, Z.R., Wang, B.Q., and Levy, A., (1990), "Erosion of protective coatings", *Surface and Coatings Technology*, vol. 43/44, pp. 875-887.
223. Sidhu B. S. and Prakash S., (2005), "Degradation behaviour of Ni₃Al plasma sprayed boiler tube steels in actual conditions of energy generation system," *Journal of Materials Engineering and Performance*, Vol. 14, pp. 356-362.
224. Sidhu B. S. and Prakash S.,(2006A), "Performance of NiCrAlY, Ni-Cr, Stellite-6 and Ni₃Al coatings in Na₂SO₄-60% V₂O₅ environment at 900°C under cyclic conditions," *Surface and Coatings Technology*, Vol. 201, pp. 1643-1654.
225. Sidhu B. S. and Prakash, S., (2006B), "Erosion-corrosion of plasma as sprayed and laser remelted Stellite-6 coatings in a coal fired boiler," *Wear*, Vol. 260, pp. 1035-1044.
226. Sidhu B. S. and Prakash, S., (2006C), "Evaluation of the behavior of shrouded plasma spray coatings in the platen superheater of coal-fired boilers," *Metallurgical and Materials Transactions*, Vol. 37A, pp. 1927-1936.
227. Sidhu B. S., (2003), Doctoral thesis, "Studies on the role of coatings in improving resistance to hot corrosion and degradation," Indian Institute of Technology Roorkee, India.
228. Sidhu B.S., D. Puri, and S. Prakash, (2005), "Mechanical and metallurgical properties of plasma sprayed and laser remelted Ni-20Cr and Stellite-6 coatings", *Journal of Materials Processing Technology* 159, pp. 347-355.
229. Sidhu B.S., D. Puri, S. Prakash, (2004), Characterisation of plasma sprayed and laser remelted NiCrAlY bond coats and Ni₃Al coatings on boiler tube steels, *Materials Science and Engineering A*, 368, pp.149-158.
230. Sidhu H. S., Sidhu B. S. and Prakash, S. (2007), "Solid particle erosion of HVOF sprayed NiCr and Stellite-6 coatings," *Surface and Coatings Technology*, Vol. 202, pp. 232-238.
231. Sidhu T.S. (2006), Doctoral thesis, "Studies on the hot corrosion behaviour of HVOF coatings on some Ni & Fe. base Superalloys", Indian Institute of Technology Roorkee, India.
232. Sidhu, T.S., Prakash S. and Agrawal R.D., (2005), "Hot corrosion of some superalloys and role of high-velocity oxy-fuel spray coatings - a review," *Surface and Coating Technology*, Vol. 198, pp. 441-446.

233. Sidhu, T.S., Prakash, S., and Agrawal, R.D., (2006), "Hot corrosion studies of HVOF NiCrBSi and Stellite-6 coatings on a Ni-based superalloy in an actual industrial environment of a coal fired boiler," *Surface and Coatings Technology*, Vol. 201, pp. 1602-1612.
234. Sidky P.S., Hocking M.G. (1999) "Review of inorganic coatings and coating processes for reducing wear and corrosion", *British Corrosion Journal*, Vol. 34, Number 3, , pp. 171-183
235. Simms N.J., Oakey J.E., Stephenson D.J., Smith P.J., Nicholls J.R., (1995), "Erosion-corrosion modeling of gas turbine materials for coal-fired combined cycle power generation", *Wear* 186-187, pp. 247-255.
236. Singh H. (2005), Doctoral thesis, "Hot corrosion studies on plasma spray coatings over some Ni and Fe based superalloys", Indian Institute of Technology Roorkee, India.
237. Singh Hazoor (2006), Doctoral thesis, "Role of HVOF coating in improving material degradation at elevated temperature", Punjab Technical University, Jalandhar India
238. Singh T and Sundararajan G (1990), "The erosion behavior of 304 stainless steel at elevated temperatures", *Metallurgical and Materials Transactions A*, vol. 21, pp 3187-3199.
239. Singh, H., Puri, D., Prakash, S, (2005), "Some studies on hot corrosion performance of plasma sprayed coatings on a Fe-based superalloy", *Surface and Coatings Technology*, Vol. 192, No. 1, pp. 27-38.
240. Singh, H., Puri, D., Prakash, S. and Phase, D.M., (2006), "Cyclic Oxidation Behavior of some Plasma Sprayed Coatings in Na₂SO₄-60%V₂O₅ Environment," *Journal of Materials Engineering and Performance*, Vol 15, No. 6, pp. 729-741.
241. Smith, R.G., (1974), "The basic principles of detonation spraying", in *Science and Technology of Surface Coatings*, B.N. Chapman, and J.C. Anderson (Eds), Academic Press, London, UK, pp. 262-271.
242. Smith, R.W. and R. Knight, (1995), *Thermal Spraying I: Powder consolidation -from coating to forming*. *Journal of the Minerals, Metals and Materials Society*, pp. 32-39.
243. Sobiecki J R, Ewertowshi J , Babul T, Wierzchona T (2004) "Properties of alumina coatings produced by gas-detonation method", *Surface and Coatings Technology* Vol.180 -181, pp. 556-560
244. Soderberg, S., Hogmark, S., Engman, U., Swahn, H., (1981) "Erosion classification of materials using a centrifugal erosion tester", *Tribology International*, pp.333-343.

245. Spiegel M., Grabke H.J., (1991), "High temperature corrosion of low and high alloy steels in simulated waste incineration atmospheres", in: Bryers R.W., editor. "Incinerating municipal and industrial waste. Fireside problems and prospects for improvement, New York: Hemisphere, pp.758-762
246. Stachowiak Gwidon W. and Batchelor Andrew W., (2001) *Engineering Tribology - Second Edition - Butterworth-Heinemann.*
247. Stack, M.M., Stott, F.H. and Wood, G.C., (1991), "Erosion-corrosion of preoxidized Incoloy 800H in fluidized bed environments: effects of temperature, velocity, and exposure time," *Materials Science and Technology*, Vol. 7, pp.1128-1137.
248. Stephenson, D.J. and Nicholls J.R., (1995), "Modelling the influence of surface oxidation on high temperature erosion", *Wear*, 186-187 pp. 284-290.
249. Stephenson, D.J. and Nicholls, J.R., (1990), "Role of surface oxides in modifying solid particle impact damage", *Materials Science and Technology*, Vol. 6, pp. 96-99
250. Stephenson, D.J. and Nicholls, J.R., (1993), "Modeling erosive wear" *Corrosion Science*, Vol. 35, pp. 1015-26.
251. Stephenson, D.J., (1989), "Predicting the high temperature erosion behaviour of materials used in gas turbines", *Corrosion Science*, Vol. 29, pp. 647-656.
252. Stephenson, D.J., Nicholls, J.R., and Hancock, P., (1985), "The erosion of gas turbine blade materials by solid sea salt", *Corrosion Science*, Vol. 25, pp. 1181-1192.
253. Stephenson, D.J., Nicholls, J.R., and Hancock, P., (1986), "Particle-surface interactions during the erosion of aluminide-coated MarM002", *Wear*, Vol. 111, pp.31-39.
254. Stoltenhoff, T., Voyer, J. and Kreye, H. (2002), "Cold spraying - state of the art and applicability", in *Proceedings of the International Thermal Spray Conference 2002 Essen*, E. Lugscheider and C.C. Berndt (Eds), DVS Verlag, Dusseldorf, Germany, pp. 366-374.
255. Stott, F. H. (1998), "The role of oxidation in the wear of alloys", *Tribology International*, Vol. 31, Issues 1-3, pp.61-71.
256. Stott, F. H., Wet D J De and Taylor, R. (1994), "The degradation resistance of Thermal barrier coatings to molten deposits at very high temperatures", *Transactions of the Materials Research Society, Japan*, Vol. 14 A, pp.135-140.
257. Stringer, J. and Wright, L.G., (1987), "Erosion/corrosion in FBC boilers," *Proc. of a Workshop on Wastage of In-Bed Surfaces in Fluidized-Bed Combustors*, EPRI, Palo Alto, CA, paper 1.1.

258. Stringer, J., Stallings, J.W. and Wheeldon, J.M., (1989), "Wastage in bubbling fluidized-bed combustors: an update", in: A.M. Manaker (Ed.), Proc. 10th Int. Conf. on Fluidized Bed Combustion, San Francisco, CA, April 30-May 3, 1989, ASME, New York, NY, pp. 857-862.
259. Stroosnijder M. F., Mevrel R. and Bennett M. J., (1994), "The interaction of surface engineering and high temperature corrosion protection", *Materials at high temperature* vol. 12 (1) , pp. 53-66.
260. Sturgeon, A.J., (1993), "Thermal spray technology", *Materials World*, pp. 351-354.
261. Suckling M. and Allen C., (1995), "The design of an apparatus to test wear of boiler tubes", *Wear*, 186-187, pp.266-272.
262. Sue, J.A. and Tucker, R.C. (Jr), (1987), "High temperature erosion behaviour tungsten and chromium carbide based coatings", *Surface and Coatings Technology*, vol. 32, pp.237-248.
263. Sundararajan G, Prasad K.U.M , Rao D.S. Joshi S.V. (1998), "A comparative study of tribological behavior of plasma and d-gun sprayed coatings under different wear modes" *Journal of Materials Engineering and Performance*, Vol. 7, Number 3, pp. 343-351.
264. Sundararajan, G., (1984), "The effect of temperature on solid particle erosion", *Wear*, Vol. 98, pp. 141-149.
265. Swaminathan, J., Raghavan, S. and Iyer, S. R., (1993), "Studies on the Hot Corrosion of Some Nickel-Base Superalloys by Vanadium Pentoxide," *Trans. IIM*, Vol. 46, No. 3, pp. 175-81.
266. Tabakoff W., (1995), "High-temperature erosion resistance of coatings for use in turbomachinery", *Wear*, vol.186-187, pp.224-229.
267. Tabakoff, W and Vittal, B V R, (1983), "High temperature erosion study of INCO 600 metal", *Wear*, vol. 86, pp 89-99.
268. Tani, K. and Nakahira, A. (2004), "Latest case study and subject of thermal spray technology in Japan", in *Proceedings of the International Thermal Spray Conference'04*, CD-Rom, ISBN 3-87155-792-7, DVS-Verlag, Dusseldorf, Germany. pp. 18-24.
269. Thornton J.A. and Chin J., (1977), "Structure and heat treatment characteristics of sputter deposited alumina", *Ceramics Bulletin*, 56 (5), pp. 504-512.
270. Thorpe, M. L., (1993), *Thermal spray industry in transition*, *Advanced Materials and Processes*, Vol. 143 (No. 5), pp.50-56.

271. Tillack, D.J., and Guthrie, J.E., (1992), "Wrought and cast heat-resistant stainless steels and nickel alloys for the refining and petrochemical industries", NiDI Technical Series 10071, Toronto Canada, Nickel Development Institute, 1992. (As referred by the Handbook of Corrosion Engineering, Chapter 3, page 265)
272. Tilly G.P., (1973), "A Two Stage Mechanism of Ductile Erosion," *Wear*, vol. 23, pp. 87-96.
273. Tiwari, S. N. and Prakash, S., (1996), "Hot Corrosion Behaviour of an Iron-Base Superalloy in Salt Environment at Elevated Temperatures," *Proceedings of Symposium on Metals and Materials Research, IIT, Madras, 4-5th July*, pp. 107-17.
274. Tiwari, S. N. and Prakash, S., (1997), "Studies on the hot corrosion behaviour of some superalloys in $\text{Na}_2\text{SO}_4\text{-V}_2\text{O}_5$," *Proceedings of SOLCEC, Kalpakkam, India*, pp. C33.
275. Tiwari, S. N., (1997), "Investigations on Hot Corrosion of Some Fe-, Ni- and Co-Base Superalloy in $\text{Na}_2\text{SO}_4\text{-V}_2\text{O}_5$ Environment under Cyclic Conditions," Ph. D. Thesis, Metallurgical and Materials Engineering Department, UOR, Roorkee, India.
276. Tiwari, S. N., (1997), Doctoral Thesis, "Investigations on hot corrosion of some Fe-, Ni- and Co-base superalloy in $\text{Na}_2\text{SO}_4\text{-V}_2\text{O}_5$ environment under cyclic conditions," University of Roorkee, Roorkee, India.
277. Toma, F. L., Bertrand, G., Klein, D., Coddet, C. and Meunier, C. (2005), "Photocatalytic decomposition of nitrogen oxides over TiO_2 coatings elaborated by liquid feedstock plasma spraying", in *Proceedings of the International Thermal Spray Conference'05*, CD-Rom, ISBN 3-87155-793-5, DVS-Verlag, Dusseldorf, Germany.
278. Tomaszek, R., Pawlowski, L., Gengembre, L., Laureyns, J., Znamirovski, Z. and Zdanowski, J. (2006), "Microstructural characterization of plasma sprayed TiO_2 functional coating with gradient of crystal grain size", *Surface and Coatings Technology*, 201, pp. 45-56.
279. Tomaszek, R., Znamirovski, Z., Pawlowski, L. and Zdanowski, J. (2007), "Effect of conditioning on field electron emission of suspension plasma sprayed TiO_2 coating", *Vacuum*, 81(10), pp. 1278-1282.
280. Tucker R.C., Jr., (1994), *Thermal spray coatings, surface engineering*, Vol. 5, ASM Handbook, ASM International, Materials Park, Ohio, USA, pp.497-509.
281. Tucker, R.C., Jr (1982) "Plasma and detonation gun deposition techniques and coating properties", in *Deposition Technologies for Films and Coatings*, R.F. Bunshah (Ed.), Noyes Publishers, Park Ridge, NJ, USA, pp. 454-489.

282. Venugopal Krishnarao, Agrawal Manish, (2008) "Evaluation of arc sprayed coatings for erosion protection of tubes in atmospheric fluidised bed combustion (AFBC) boilers", *Wear*, vol. 264, pp.139-145.
283. Verdon, C., Karimi A., and Martin J.L., (1997), "Microstructural and analytical study of thermally sprayed WC-Co coatings in connection with their wear resistance", *Materials Science and Engineering A*, 234-236, pp.731-734.
284. Vicenzi J., Villanova D.L., Lima M.D., Takimi A.S., Marques C.M., Bergmann C.P. (2006), "HVOF-coatings against high temperature erosion (~300°C) by coal fly ash in thermoelectric power plant", *Materials and Design* 27, pp. 236-242
285. Viswanathan, R., Colemana K., Rao U., (2006), "Materials for ultra-supercritical coal-fired power plant boilers" *International Journal of Pressure Vessels and Piping*, pp. 778-783.
286. Vuoristo P., Niemi K., and Mantyla T., (1991), "Hard oxide coatings deposited by plasma and detonation gun spraying techniques", in Sandmeier S. B, Eschnauer H., Huber P., and Nicoll A.R., (Ed.), *Proceedings 2nd Plasma-Technik-Symposium*, Lucerne, Switzerland, pp. 323-331.
287. Walsh, P. and Tabakoff W., (1990), "Comparative erosion resistance of coatings intended for steam turbine components", in C. Bellanca, (Ed.) *International Joint Power Generation Conference*, Boston, pp.1-8.
288. Walsh, P., (1992), "Erosion resistant coatings at steam turbine temperatures", *PWR-Steam Turbine Generator Developments for the Power Generation Industry*, 18, pp.123-128.
289. Walsh, P.N., Quets J.M., and Tucker R.C. (Jr), (1994), "The effects of erodent particle size and composition on the erosion of chromium carbide based coatings", *PWR-Advances in Steam Turbine Technology for the Powder Generation Industry*, 26, pp.261-265.
290. Wang B., (1996), "Erosion-corrosion of thermal sprayed coatings in FBC boilers", *Wear*, vol. 199, pp 24-32.
291. Wang, B., Geng G., and Levy A., (1991), "Erosivity of particles from operating fluidised bed combustor," *Wear*, 150, pp.107-124.
292. Wang, B.Q. (1995A), "The Elevated Temperature Erosion Behaviour of HVOF Tungsten Carbide Cermet Coatings", in *Thermal Spray Science and Technology*, Houston, Texas: ASM International, Materials Park, Ohio.,USA.

293. Wang, B.Q. and Geng, G.Q. (1990), "Erosion corrosion of thermal spray coatings", *Surface and Coatings Technology*, 43/44, pp. 859-874.
294. Wang, B.Q. and Lee S.W. (1997), "Elevated temperature erosion of several thermal sprayed coatings under the simulated erosion conditions of In-Bed tubes in a fluidised bed combustor", *Wear*, 203-204, pp. 580- 587.
295. Wang, B.Q. and Lee., S.W. (1995), "Erosion of AISI 1018 steel and several thermal sprayed coatings under simulated in-bed tube erosion conditions of fluidised bed combustors", in *Fluidised Bed Combustion*, ASME.
296. Wang, B.Q. and Luer K., (1994), "The relative erosion-corrosion resistance of commercial thermal sprayed coatings in a simulated circulating fluidized bed combustor environment, in *Thermal Spray Industrial Applications*", C.C. Berndt and S. Sampath, Editors., ASM International, Materials Park, Ohio., USA: Boston, Massachusetts, pp.115-120.
297. Wang, B.Q. and Shui, Z.R., (2002), "The hot erosion behaviour of HVOF chromium carbide-metal cermet coatings sprayed with different powders". *Wear*, 253, pp. 550-557.
298. Wang, B.Q. and Verstak A., (1999), "Elevated temperature erosion of HVOF Cr₃C₂/TiC -NiCrMo cermet coating" *Wear*, 233-235, pp. 342-351.
299. Wang, B.Q., (1995B), "Erosion-corrosion of coatings by biomass fired boiler fly ash", *Wear*, 188, pp. 40-48.
300. Wang, B.Q., (1996A), "Erosion-Corrosion of thermal sprayed coatings in FBC boilers", *Wear*, vol. 199, pp. 24-32.
301. Wang, B.Q., (1996B), "The dependence of erosion corrosion wastage on carbide/metal binder proportion for HVOF Carbide-Metal Cermet coatings", *Wear*, vol. 196, pp.141-146.
302. Wang, B.Q., (1999), "Chromium titanium carbide cermet coating for elevated temperature erosion protection in fluidised bed combustion boilers", *Wear*, 225-229, pp.502-509.
303. Wang, D., (1988), "Corrosion Behavior of Chromized and/or Aluminized 21/4Cr-1Mo Steel in Medium-BTU Coal Gasifier Environments," *Surf. Coat. Technol.*, Vol. 36, pp. 49-60.
304. Wang, F., Lou, H., Bai, L. and Wu, W., (1989), "Hot Corrosion of Yttrium modified Aluminide coatings," *Material Science and Engineering - A*, vol. 121, pp. 387-389.

study, boiler steels have shown poor resistance against the oxidation as well as molten salt environment. In superalloys, Superfer 800 has indicated a minimum resistance to air oxidation amongst the superalloys under study. Superni 600 has been found to be most resistant to the air oxidation as well as molten salt corrosion among all the superalloys. Superfer 800 suffered accelerated hot corrosion in the form of intense spalling and sputtering of its scale. On the bare alloys, especially in boiler steels, the oxide scale formed is fragile and irregular, and penetrates deeply into the substrates, thereby reducing the thickness of sound metal. In molten salt environment, the scale formed on the bare superalloys is fragile and irregular. The fluxing action of the molten salt on the surface of the bare alloys is also clearly evident (Figs. 6.49 and 6.50). The EDX analysis and elemental maps obtained after total 50 cycles of exposure to the molten salt environment indicate that all the coatings have protected the base alloys against the penetration of oxygen and other corrosive species, coatings are in good contact with the substrate .

8.4 INDUSTRIAL ENVIRONMENT

In actual industrial environment, when uncoated alloys as well as coated alloys were exposed to superheater zone of coal fired boiler at 700°C for 1500 hours, these encountered both erosion as well as corrosion phenomenon. The temperature in this zone was 700± 10°C and high velocity stream in this zone carried many undesirable elements. In uncoated specimens, fouling was observed from the scanning electron micrographs due to condensed phases of the ash. Coal ash carried by the flue gas in the form of small particles form sintered and fused deposits on the superheater and reheater surfaces, thereby providing the environment in which complex sulphates are formed causing metal degradation. From EDX analysis, it has been revealed that, higher amount of Si, Al and Fe along with O was present on the surfaces in the form of condensed ash which initiates the corrosion mechanism on the surfaces.

Al₂O₃-3 wt% TiO₂ coatings, in general, have shown good resistance to the industrial environment consisting of actual working condition of the coal fired boiler and all the coated alloys performed better than the uncoated alloys. The bar chart indicating the total extent of material thickness lost of uncoated and Al₂O₃-3wt%TiO₂ coated alloys after 1500 hours exposure to superheater zone of coal fired boiler at around 700°C is shown in Fig.8.4. From the bar chart it is clear that minimum thickness loss is shown by Superni 600 superalloy among all the uncoated alloys tested while uncoated boiler steels have shown massive thickness loss.

293. Wang, B.Q. and Geng, G.Q. (1990), "Erosion corrosion of thermal spray coatings", *Surface and Coatings Technology*, 43/44, pp. 859-874.
294. Wang, B.Q. and Lee S.W. (1997), "Elevated temperature erosion of several thermal sprayed coatings under the simulated erosion conditions of In-Bed tubes in a fluidised bed combustor", *Wear*, 203-204, pp. 580- 587.
295. Wang, B.Q. and Lee., S.W. (1995), "Erosion of AISI 1018 steel and several thermal sprayed coatings under simulated in-bed tube erosion conditions of fluidised bed combustors", in *Fluidised Bed Combustion*, ASME.
296. Wang, B.Q. and Luer K., (1994), "The relative erosion-corrosion resistance of commercial thermal sprayed coatings in a simulated circulating fluidized bed combustor environment, in *Thermal Spray Industrial Applications*", C.C. Berndt and S. Sampath, Editors., ASM International, Materials Park, Ohio., USA: Boston, Massachusetts, pp.115-120.
297. Wang, B.Q. and Shui, Z.R., (2002), "The hot erosion behaviour of HVOF chromium carbide-metal cermet coatings sprayed with different powders". *Wear*, 253, pp. 550-557.
298. Wang, B.Q. and Verstak A., (1999), "Elevated temperature erosion of HVOF Cr₃C₂/TiC -NiCrMo cermet coating" *Wear*, 233-235, pp. 342-351.
299. Wang, B.Q., (1995B), "Erosion-corrosion of coatings by biomass fired boiler fly ash", *Wear*, 188, pp. 40-48.
300. Wang, B.Q., (1996A), "Erosion-Corrosion of thermal sprayed coatings in FBC boilers", *Wear*, vol. 199, pp. 24-32.
301. Wang, B.Q., (1996B), "The dependence of erosion corrosion wastage on carbide/metal binder proportion for HVOF Carbide-Metal Cermet coatings", *Wear*, vol. 196, pp.141-146.
302. Wang, B.Q., (1999), "Chromium titanium carbide cermet coating for elevated temperature erosion protection in fluidised bed combustion boilers", *Wear*, 225-229, pp.502-509.
303. Wang, D., (1988), "Corrosion Behavior of Chromized and/or Aluminized 21/4Cr-1Mo Steel in Medium-BTU Coal Gasifier Environments," *Surf. Coat. Technol.*, Vol. 36, pp. 49-60.
304. Wang, F., Lou, H., Bai, L. and Wu, W., (1989), "Hot Corrosion of Yttrium modified Aluminide coatings," *Material Science and Engineering - A*, vol. 121, pp. 387-389.

305. Wang, J, Zhai C S, Yang Yi and Sun Bao-De (2006) "Vickers microindentation and statistical analysis of microhardness of detonation sprayed nanocomposite Al₂O₃-TiO₂ coatings" *Journal of Composite Materials*, Vol 40, pp. 943 -954
306. Wang, You, Jiang, Stephen, Wang, Meidong, Wang, Shihe, Xiao, T. Danny and Strutt, Peter R. (2000), "Abrasive wear characteristics of plasma sprayed nanostructured alumina/titania coatings", *Wear*, vol. 237, Issue 2, pp. 176-185.
307. Wayne, S.F. and Sampath S., (1992), "Structure/property relationships in sintered and thermally sprayed WC-Co", *Journal of Thermal Spray Technology*, 1(4), pp.307-316.
308. Wayne, S.F., Baldoni J.G., and Buljan S.T., "Abrasion and erosion of WC-Co with controlled microstructures", *Tribology Transactions*, 1990. 33(4), pp.611-617.
309. Westergard R, Erickson L C, Axen N, Hawthorne H M, and Hogmark S, (1998), "The erosion and abrasion characteristics of alumina coatings plasma sprayed under different spraying conditions", *Tribology International* vol.31(5) pp.271-279.
310. Westergard R., Axen N., Wiklund U., and Hogmark S., (2000), "An evaluation of plasma sprayed ceramic coatings by erosion, abrasion and bend testing", *Wear*, 246, pp. 12-19.
311. Wiederhorn S .M and Hockey B .J, (1983) "Effect of Material Parameters on the Erosion Resistance of Brittle Materials", *Journal of Materials Science and Technology*, vol.18, pp 766-780.
312. Wiklund U., Hedenqvist P., Hogmark S, Stridh B and Arbell M, (1996), "Multilayer coatings as corrosion protection of Zirc alloy", *Surface and Coating Technology*, vol. 86-87 (1-3), pp. 530-534
313. Wilms, V. and Herman, H. (1976), "Plasma spraying of Al₂O₃ and Al₂O₃-Y₂O₃", *Thin Solid Films*, vol. 39, pp. 251-262.
314. Winkler, R., Bultmann, F., Hartmann, S. and Burkard, H. (2003), "316L - an alternative to NiCr bond coats for Cr₂O₃-coatings on anifox rolls", in Moreau, C. and Marple, B. (Eds.): *Thermal Spray 2003: Advancing the Science and Applying the Technology*, ASM International, Materials Park, Ohio., USA, pp.149-152.
315. Wood, R.J.K., Mellor B.G., and Binfield M.L., (1997), "Sand erosion performance of detonation gun applied tungsten carbide/cobalt-chromium coatings", *Wear*, 211, pp. 70-83.
316. Wright, I.G., Sethi, V.K. and Nagarajan, V., (1991), "An approach to describing the simultaneous erosion and high-temperature oxidation of alloys", *Journal of Engineering for Gas Turbines and Power*, Trans. ASME, Vol. 113, pp. 616-620.

317. Xia, Z., Zhang X., and Song J., (1999), "Erosion resistance of plasma sprayed coatings", *Journal of Materials Engineering and Performance*, 8(6), pp.716-718.
318. Xiaoou, H. and Yufen, L. (2005), "The current situation and future of thermal spraying industry in China", in *Proceedings of the International Thermal Spray Conference'04*, CD-Rom, ISBN 3-87155-792-7, DVS-Verlag, Dusseldorf, Germany.
319. Xu, H.H.K. and Jahanmir, S. (1996), "Transitions in the mechanism of material removal in abrasive wear of alumina", *Wear*, vol. 192, pp. 228-232.
320. Yin Zhijian, Tao Shunyan, Zhou Xiaming, Ding Chuanxian (2008) "Microstructure and mechanical properties of Al₂O₃-Al composite coatings deposited by plasma spraying", *Applied Surface Science* 254, pp.1636–1643
321. Zahs, A., Spiegel, M. and Grabke J.H, (2000), "Chloridation and oxidation of iron, chromium, nickel and their alloys in chloridizing and oxidizing atmospheres at 400-700°C, *Corrosion Science* (42), pp. 1093-1122.
322. Zhang X. S., Clyne T. W. and Hutchings I. M., (1997), "Relationship between microstructure and erosive wear resistance of plasma sprayed alumina coatings", *Surface Engineering*, vol. 13(5), pp. 393-401.
323. Zhang, Y., Y.B. Cheng, S. Lathabai, (2000) "Erosion of alumina ceramics by air- and water-suspended garnet particles", *Wear*, 240, pp.40-51.
324. Zhou Jianren and Bahadur Shyam (1995), "Erosion characteristics of alumina ceramics at high temperatures", *Wear*, vol.181-183, pp.178-188.
325. Zywitzki O. and Hoetzsch G, (1995), "Effect of plasma activation on the phase transformation of aluminum oxide", *Surface and Coatings Technology*, vol. 76/77, Issue 1/3 pp. 754-762.